NATIONAL INSTITUTE FOR FUSION SCIENCE

Proceeding of A3 Foresight Program Seminar on Critical Physics Issues
Specific to Steady State Sustainment of High-Performance Plasmas
11-14 July, 2017, Sapporo, Japan

Edited by Shigeru MORITA, Liqun HU and Yeong-Kook OH

Proceeding of A3 Foresight Program Seminar on Critical Physics Issues Specific to Steady State Sustainment of High-Performance Plasmas

11-14 July, 2017, Sapporo, Japan

Edited by

Shigeru MORITA, Liqun HU and Yeong-Kook OH

Abstract

The A3 Foresight Program titled by "Critical Physics Issues Specific to Steady State Sustainment of High-Performance Plasmas", based on the scientific collaboration among China, Japan and Korea in the field of plasma physics, has been started from August 2012 under the auspice of the Japan Society for the Promotion of Science (JSPS, Japan), the National Research Foundation of Korea (NRF, Korea) and the National Natural Science Foundation of China (NSFC, China). The main purpose of this project is to enhance joint experiments on three Asian advanced fully superconducting fusion devices (EAST in China, LHD in Japan and KSTAR in Korea) and other magnetic confinement devices to solve several physics key issues on steady state sustainment of high-performance plasmas. The eleventh meeting of the A3 program was held in Sapporo, Japan, 11-14 July, 2017, as the tenth A3 seminar on the collaborative research, which was hosted by National Institute for Fusion Science, to check and review on-going joint research activities including scientific results during past five years and to discuss the future plan after termination of A3 program. Two oral sessions for presentations by PhD and post-doctoral students were also provided. The topics in the seminar includes steady state sustainment of magnetic configurations, edge and divertor plasma control and confinement of alpha particles.

Key words: superconducting fusion device, magnetic confinement, toroidal plasmas, high-performance plasmas, steady state sustainment, edge plasma, divertor plasma, edge stability, high-energy particle, alpha particle and fusion plasma simulation.

Organization Committee

Shigeru MORITA (National Institute for Fusion Science, Japan)

Liqun HU (Institute of Plasma Physics, Chinese Academy of Sciences, China)

Yeong-Kook OH (National Fusion Research Institute, Korea)

Program Committee

Shigeru MORITA (National Institute for Fusion Science, Japan)

Liqun HU (Institute of Plasma Physics, Chinese Academy of Sciences, China)

Yeong-Kook OH (National Fusion Research Institute, Korea)

Satoru SAKAKIBARA (National Institute for Fusion Science, Japan)

Kato DAIJI (National Institute for Fusion Science, Japan)

Naoko ASHIKAWA (National Institute for Fusion Science, Japan)

Satoshi OHDACHI (National Institute for Fusion Science, Japan)

Mitsutaka ISOBE (National Institute for Fusion Science, Japan)

Yasushi TODO (National Institute for Fusion Science, Japan)

Conference Secretariats

Chihiro SAKO (National Institute for Fusion Science, Japan)

Yoshio KAMIYA (National Institute for Fusion Science, Japan)

Shaohua DONG (Institute of Plasma Physics, Chinese Academy of Sciences, China)

Noh-Yeong OH (National Fusion Research Institute, Korea)

Preface

The first meeting of A3 foresight program on Plasma Physics hosted by NFRI (Korea) was held in Jeju Island, Korea on 22nd August, 2012 as coordinator meeting to initiate the A3 program.   The first A3 seminar hosted by NIFS (Japan) and the second A3 seminar hosted by ASIPP (China) were held in Kushiro, Japan during 22-25 January, 2013 and in Beijing, China during 20-23 May, 2013, respectively.   Concrete planning of collaborative research was made and possible scientific progresses done in steady state sustainment of high-performance plasmas were also discussed in two seminars. Many young scientists joined in these seminars.   The third A3 seminar hosted by NFRI was held in Gyeongju, Korea, during 3-4 November, 2013, to report the progress and achievement of on-going A3 collaboration.   The fourth A3 seminar hosted by NIFS, the fifth A3 seminar hosted by ASIPP, the sixth A3 seminar hosted by NFRI were held in Kagoshima, Japan, during 23-26 June, 2014, in Nanning, China, during 6-9 January, 2015 and in Chuncheon, Korea, 19-22 May, 2015 to discuss the achievement of collaborations and summarize an intermediate report within the A3 scientific framework, respectively.   In the seventh A3 seminar hosted by NIFS held in Gotemba, Japan, 1-4 December, 2015, and the eighth A3 seminar hosted by ASIPP held in Yinchuan, China, 17-20 May, 2016, discussions were made on the evaluation report to our intermediate reports prepared by JSPS (Japan), NFR (Korea) and NSFC (China).   Possible modifications in the A3 collaboration along the evaluation report were also investigated in addition to regular check and review of on-going collaborations.

The tenth A3 seminar hosted by NIFS was held in Sapporo, Japan, 11-14 July, 2017, following the ninth A3 seminar in Jeju, Korea, 22-25 November, 2016, to check and review the on-going A3 collaboration including scientific results during the past five years.   A future plan after termination of A3 program was also discussed in the seminar.   The presentations in the seminar are made along the following four categories;

        I. Steady state sustainment of magnetic configurations,
        II. Edge and divertor plasma control
            IIa. Transport of edge and divertor plasmas
            IIb. Stability of edge plasma
        III. Confinement of alpha particles
        IV. Theory and simulation.

In the meeting totally 58 participants joined (18 from Japan, 25 from China and 15 from Korea) including conference secretaries and 55 oral presentations were made in

the seminar. As a special topics in this seminar, achievement of a steady plasma discharge with H-mode over 100s having no tungsten accumulation in EAST, start of high-temperature first wall discharges in KSTAR and initial results of deuterium discharges in LHD are reported. In addition, progress of Chinese demo reactor, CFETR, and a new construction of stellarator device at SWJTU in China were also reported. Two oral sessions were set up for PhD and post-doctoral students.

The seminar was completed with great success, clarifying significant progress in collaborative researches along A3 program physics categories mentioned above and also contributing to the fostering of young scientists and PhD students. The organizing and program committees are deeply grateful to all participants and acknowledge foundation of three countries (NSFC in China, JSPS in Japan and NRF in Korea) for strong and continuous supports. Based on their supports and corporation the seminar was steadily and successfully concluded.

Shigeru MORITA, Liqun HU and Yeong-Kook OH

Chairpersons of the Organizing Committee

11th A3 Foresight Program Workshop
11–14 July, 2017 Sapporo, Japan

,

Contents

LHCD studies towards long-pulse plasma with high performance in EAST

B J Ding for LHCD group, EAST team and collaborators

Institute of Plasma Physics, Chinese Academy of Sciences, Hefei 230031, China

Abstract

Lower hybrid current drive (LHCD) is an important heating system for long pulse plasma with high performance in EAST. The effect of LH (lower hybrid) wave frequency on LHCD characteristics has been studied on EAST for the first time with two different frequencies (2.45 and 4.6 GHz), showing that higher frequency improves penetration of the RF power into the plasma core, leading to a better effect on plasma characteristics. The improvement in LHCD is mainly ascribed to a reduction in parametric instability (PI) and a lesser extent collisional absorption (CA) in the edge region with the 4.6 GHz wave, demonstrating the role and mitigation of parasitic effects of edge plasma. These results are encouraging that LHCD is essential for current profile control in reactor grade plasmas.

1. Introduction

In order for the tokamak to be a commercially viable energy source, it will be necessary to operate these devices in 'advanced' modes characterized by high energy confinement and high fractions of the non-inductive bootstrap current [1]. LHCD [2-4] in principle satisfy this current profile control need, but the coupled radiofrequency (RF) power faces the challenge of effectively penetrating into the main plasma at the relatively high edge density, possibly due to PI [5, 6], CA [7] and scattering by density fluctuation (SDF) [8,9] in the edge region. Here, we describe experiments and analysis that demonstrate the beneficial effects of increasing LH frequency on LHCD at high density.

2. Experiment and results

The typical discharge (#54439) waveforms with a coupled power ($P_{LH} \sim 1$MW) and an almost constant density ($n_e = 2.0 \times 10^{19}$m^{-3}) in a LSN configuration are shown in Fig. 1. The peak value of the antenna power spectrum has a refractive index along the direction of the toroidal magnetic field of $N_{//0} \approx 2$, which satisfies the wave accessibility condition for the operating condition [10]. It is seen that the residual voltage
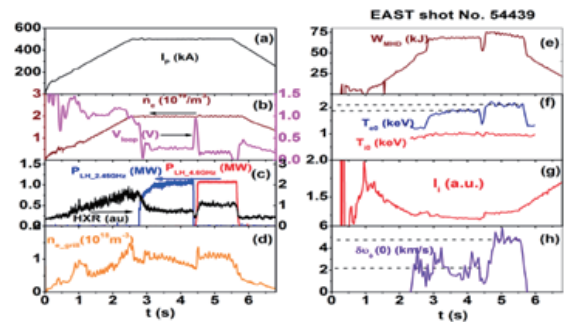
Fig. 1 Typical waveforms with 2 LH frequencies

(V_{loop}) (Fig.1 (b)) at 2.45 GHz (0.27V) is larger than with 4.60 GHz (0.15V), implying a higher CD efficiency with a higher LH source frequency. Consistently, higher hard X-ray emission (HXR) from fast electrons is observed. Better plasma heating effect also occurs for 4.6 GHz as indicated by plasma stored energy (W_{MHD}), central electron temperature (T_{e0}) and central ion temperature (T_{i0}) measured by a X-ray Crystal Spectrometer (XCS) [11]. Also, the internal inductance (l_i) is higher with 4.6 GHz operation, indicating a more peaked current profile. A larger change of plasma rotation (co-current) occurs in the core with 4.6 GHz measured by XCS during LHCD phase, possibly due to the different LH power deposition and the absorbed LH wave momentum [12]. Frequency spectra detected by an RF probe located outside the machine, which documents the occurrence of wave-plasma interactions shows (see Fig. 2) that a clear spectral broadening of the LH pump wave (Δf_p) occurs and is larger for 2.45GHz (1.6MHz) than for 4.6GHz case
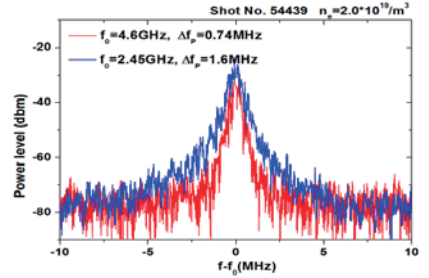
Fig. 2 PI measurements

(0.74MHz) [13], which is measured at 20 dB below the peak (for the line frequency, $\Delta f_p \lesssim 0.1$ MHz).

Further experiments with 3 densities are performed, demonstrating that the above PI effect on LHCD capability. The typical waveforms are shown in Fig. 3, showing that with the density increase, the difference in Vloop increases, in agreement with the change in ECE, suggesting a higher CD capability at 4.6GHz wave.
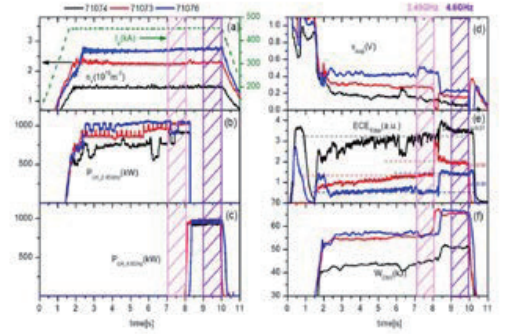
Fig. 3 Typical waveforms with 3 densities

Results show that a stronger LHCD effect occurs by operating at 4.6 GHz than at 2.45 GHz in terms of driven current, plasma heating, modification of current profile, plasma rotation, and RF probe spectrum signals. Furthermore, such discrepancy increases with density.

3. Analysis

Effects of PI and SDF in modifying the initial wave spectrum, as well CA, may play an important role in determining properties of wave propagation and damping in the plasma, hence possibly affecting power deposition and current drive. With the experimental parameters in Fig. 1, using a ray-tracing/Fokker-Planck code (C3PO/LUKE) [14], power deposition and driven current profiles were calculated using the initial nominal antenna spectrum [13]. Though the calculated driven current with 2.45GHz wave is somewhat smaller (about 10kA) than with 4.6 GHz wave, it cannot completely account

2

for the experimental discrepancy (~100kA) estimated by the loop voltage, which is little affected by the change of electron temperature. Therefore the contributions of PI and SDF effects should be considered.

Using the same edge plasma parameters for 2.45 GHz and 4.6 GHz LHCD plasmas, the effect of SDF on the power spectrum *vs.* the parallel refractive index has been evaluated following Ref. 15. Results show that the drift-wave scattering has a negligible effect, producing a spectral broadening $\Delta N_{//}$ less than about 0.25 for 2.45 GHz source and less than about 0.15 for 4.6 GHz source in the region of the LH power absorption (r/a ~ 0.9). Compared to the PI induced spectral broadening $\Delta N_{//} \gg 1$ in the edge region with relatively low (15 eV) edge electron temperature, such broadening is not dominant. Therefore, the different LHCD effect observed with different source frequencies should be not ascribed to the SDF.

Conversely, signatures of PI could be recognized in the aforementioned RF probe spectra that clearly indicate non-linear wave plasma interaction attributable to PI mechanism. With standard EAST parameters in Fig. 1, using the LHPI (Lower Hybrid Parametric Instability) code [16], which has the special feature of modeling the PI mechanism retaining convective losses due to plasma inhomogeneity and finite extent of the pump wave region, the calculated frequencies and growth rates of PI driven mode are shown in Fig. 4, in which the EAST antenna dimensions, edge plasma parameters of $n_{ea} = 4 \times 10^{17}$ m^{-3} and $T_{ea} = 30$ eV, and $n_{//} = 5$ of the low frequency driving quasimode have been considered. For the pump frequency of 4.60 GHz, the analysis shows that the PI mechanism is mostly driven by a low frequency quasi-mode having a maximum homogeneous growth rate ($\gamma/\omega_0 \approx 8 \times 10^{-4}$) that is slightly smaller (by about 20%) than for operating frequency of 2.45 GHz, implying a stronger PI effect in the case of 2.45 GHz source operation, consistent with the RF probe data. Further modeling (Fig. 5) done by MIT group [17] shows that, with the edge density increase, a stronger PI growth rate increases for the 2.45GHz wave, indicating the PI could be more dominant at higher density.
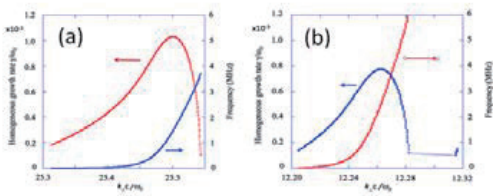
Fig. 4 PI modelling ($n_{ea} = 4 \times 10^{17}$ m^{-3} $T_{ea} = 30$ eV). (a) 2.45GHz, (b) 4.6GHz
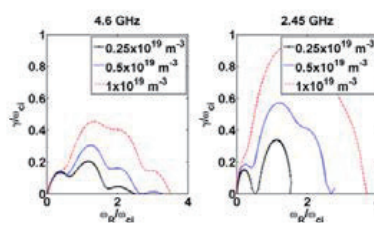
Fig. 5 PI modeling for different edge densities
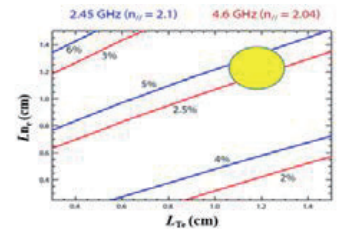
Fig. 6 Round trip loss contours *vs* scale lengths in SOL

In addition, CA loss in the edge region could be another candidate for the discrepancy since CA damping should decrease as a function of frequency [7]. For the typical scale length of $Ln_e \sim L_{Te} \sim 1.2$ cm in EAST, WKB analysis of the absorption based on a plane-stratified SOL model (see Fig. 6) shows that the CA loss

in the SOL for a LH wave passing into and out of the SOL (i.e. the 'round trip') is about 5% at 2.45 GHz and half that at 4.6 GHz, being in agreement with the results with GENRAY code [18]. Although this 'round-trip' damping through the SOL is low, the cumulative damping after several passes is by no means negligible since the core electron temperature is not high enough for the waves to be absorbed in a single pass into the plasma and the LH rays actually undergo many radial reflections in the SOL as indicated by the ray tracing /Fokker Planck simulations.

4. Conclusion

Available data of experiments performed on EAST show that, compared to 2.45GHz, operation at higher frequency (4.6 GHz) improves penetration of the coupled RF power into the plasma core. Studies show that such beneficial behavior could be a consequence of the diminished parasitic effects of the plasma edge expected to occur through PI and CA mechanisms. In addition, the parasitic effects would be further diminished under reactor conditions where a markedly warmer edge and core plasma would exist as compared to present experiments. These results bode well for the use of the LHCD actuator as an essential tool for current profile control in a thermonuclear fusion reactor.

References: [1] S. C. Jardin *et al*, Fusion Engineering and Design 38, 27–57 (1997). [2] N.J. Fisch. Phys. Rev. Lett. 41 873 (1978). [3] S. Bernabei *et al*, Phys. Rev. Lett. 49 1255 (1982). [4] N. J. Fisch, Rev. Mod. Phys. 59 175 (1987). [5] C. S. Liu and V. K. TRIPATHI, Phys. Rep.130143 (1986). [6] R. Cesario *et al*, Phys. Rev. Letters, 92 175002 (2004). [7] P. T. Bonoli et al, Phys. Fluids 29 2937 (1986). [8] Y. Peysson *et al*., Plasma Phys. Contr. Fusion 53 124028 (2011). [9] N. Bertelli et al, Plasma Phys. Control. Fusion 55 074003 (2013). [10] Y. Takase *et al*, Phys. Fluids 28 983 (1985). [11] B. Lyu *et al*., Rev. Sci. Instrum. 85 11E406 (2014).   [12] B Chouli et al, Plasma Phys. Control. Fusion 56 095018 (2014). [13] M. H. Li *et al*., Physics of Plasmas 23, 102512 (2016). [14]Y. Peysson *et al*, Plasma Phys. Control. Fusion 54 045003 (2012). [15] P. L. Andrews and F. W. Perkins Phys. Fluids 26 2537 (1983). [16] R. Cesario *et al*., Nucl. Fusion 54 043002 (2014). [17] S. G. Baek et al., *Nucl. Fusion* **55** 043009 (2015). [18] C. Yang *et al*., Plasma Phys. Control. Fusion 56 125003 (2014).

Reversed I$_p$ operation with counter neutral beam injection in KSTAR

Jayhyun Kim[1], J.W. Lee[2], M.J. Choi[1], S.H. Ko[1], G.Y. Park[1], H.H. Lee[1], Jung-hee Kim[1],
H.S. Kim[1], J.S. Ko[1], W.H. Ko[1], M. Joung[1], S.J. Wang[1], H.S. Han[1], M.H. Woo[1],
the KSTAR team, and the KSTAR collaborators

[1]National Fusion Research Institute, Daejeon, Republic of Korea
[2]Seoul National University, Seoul, Republic of Korea

Abstract

The current and rotation profiles in tokamak-type devices are known to have a great influence on the confinement performance and stability of fusion plasma. KSTAR neutral beam injection (NBI) system with highly tangential geometry in toroidal direction has a significant impact on the current and rotation profiles. In order to maximize the non-inductive current driving (CD) efficiency, the NBI in KSTAR normally enters into the co-current direction. However, in this study, we investigated the physical phenomena due to the current and rotation profiles changed by the NBI in the counter-current direction. Due to the combination of a counter non-inductive CD centered at the core region and an inductive CD penetrating from the edge region, a reversed shear safety factor q profile with high q_{min} (> 2) was maintained for 4 seconds in the flat-top phase of plasma current. In addition, it is confirmed that the shearing of the external counter-torque and the intrinsic co-torque formed the rotation profile having the steep gradient at the edge pedestal region. As a result, the quiescent period without edge localized mode is maintained for about 1 second in the H-mode phase.

1. Experimental set-up

For long pulse steady state operation, the heating systems of KSTAR are designed and manufactured to enable efficient current drive. Thus NBI, the main auxiliary heating device in KSTAR, has the geometry of tangential injection in co-current direction. 2nd NBI, which will be in operation after 2018 campaign, is also being manufactured in the same geometry with 1st NBI.

As shown in figure 1 below, KSTAR has both plasma current and toroidal magnetic field set clockwise when viewed from above. The toroidal magnetic field coils using a unipolar power supply are not capable of changing the current direction. On the other hand, poloidal magnetic field coils using a bipolar power supply are, in principle, capable of applying a bi-directional current freely thus can make plasma current in both directions. However, since blip resistors installed to obtain a momentary high loop voltage for plasma startup cannot be used in a reverse current (*i.e.*, counter-clockwise current), a low voltage plasma startup technique through plasma pre-ionization is needed. We stabilized the efficiency of 2nd harmonic ECH pre-ionization through field structure with trapped particle configuration [LeeJW2016IAEA].
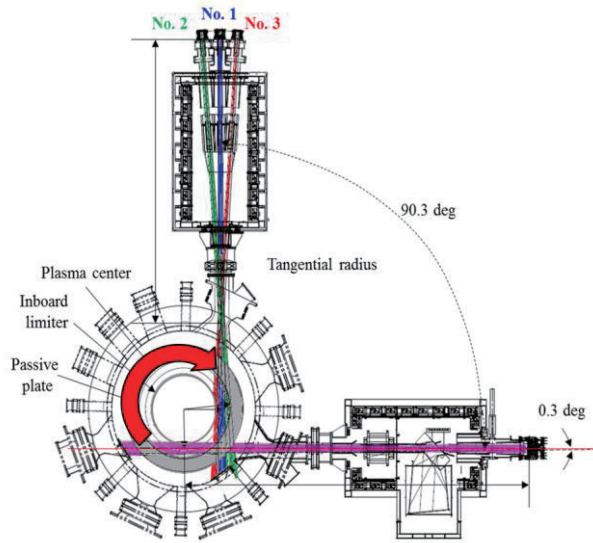
Figure 1. Geometry between vacuum vessel and NBI system in KSTAR. Red half circle arrow depicts the direction of plasma current direction.

2. Effect on current profile due to counter current drive

The current distribution of tokamak plasma is determined by the sum of inductive and non-inductive drive currents. In counter-NBI discharge, unlike the conventional co-NBI discharge, the direction of the inductive drive current becomes opposite to that of the non-inductive drive current. This leads to the formation of a hollow plasma current distribution in the core of the plasma where the non-inductive drive is peaked.

Figure 2 shows the reversed shear shape of resulting q profile by the thus formed hollow plasma current distribution. Not only does it have a reversed shear shape, but it also has a q_{min} value higher than 2 due to the relatively weakened core current density. This tendency is prominent when compared to similar conventional co-NBI discharges. As shown in figures 2c) and 2d), the conventional co-NBI discharge with similar plasma current and NBI power has a centrally peaked current distribution and a monotonically increasing q profile.

Reversed shear q profile is known to play an important role in advanced operation with internal transport barrier (ITB). However, the counter NBI discharge mentioned in this paper did not show neither improvement of plasma confinement performance nor the formation of ITB. The reason for this is that once the counter NBI has a large loss due to prompt loss at the moderate level of plasma current (several hundred kA), it does not satisfy the threshold power required for ITB formation. Although not mentioned in this paper, the energetic particle driven geodesic acoustic mode (EGAM) was first observed in counter NBI discharge of KSTAR due to the change of fast ion distribution according to mentioned prompt loss. Furthermore, in the case of counter NBI discharge, ExB shearing changes to the unfavorable side due to the external counter torque in momentum balance equation, so the phenomenon that the ITB threshold power itself increases by factor of two or three times has already been reported through the DIII-D experiment [CMGreenfield2000PoP].

6
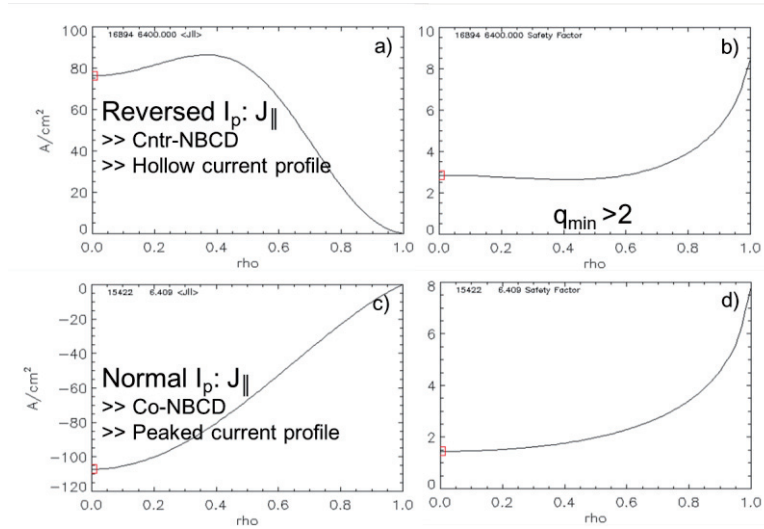
Figure 2. Comparison of current drive effect between counter- and co- NBI discharges: KSTAR shots #16894 (counter NBI in reversed I_p) and #15422 (co NBI in normal I_p). a) Current profile in #16894, b) resulting q profile in #16894, c) current profile in #15422, and d) resulting q profile in #15422.

3. Effect on rotation profile due to counter torque

In H-mode discharge, the intrinsic torque source of the plasma is located near plasma edge pedestal and the intrinsic torque direction is known to be the same as the plasma current direction [RiceJE2016PPCF]. On the other hand, in the case of external torque injected by NBI, most of the NBI torque is peaked near plasma core in KSTAR. In case of counter NBI discharge which is opposite to the plasma current, strong rotation shear is expected in the vicinity of the plasma edge because the direction of intrinsic torque is opposite to that of external torque.
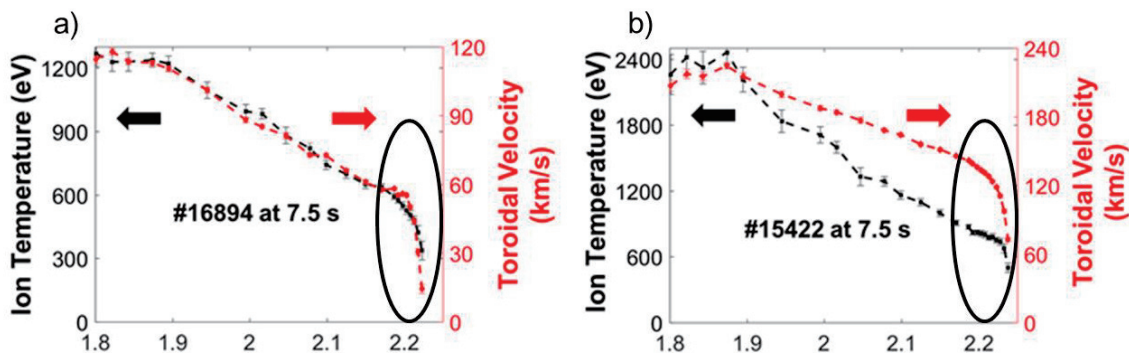
Figure 3. Comparison of rotation profile with regarding to ion temperature profile between counter- and co-NBI discharges: KSTAR shots #16894 (counter NBI in reversed I_p) and #15422 (co NBI in normal I_p). a) Ion temperature profile (black) and rotation profile (red) in #16894. b) Ion temperature profile (black) and rotation profile (red) in #15422.

Figure 3 shows current and ion temperature profiles in counter- and co- NBI discharges, respectively. In figure 3, note that in the case of counter NBI discharge, the rotation profile tends to be steeper than the ion temperature profile, whereas in the case of co NBI discharge, this tendency is reversed. This indicates that the rotation profile can steepen the rotation profile according to the injection direction of the NBI compared to that of plasma current. The ion temperature profile is not affected by the relative orientation of the plasma and NBI.

The reason why the absolute values of ion temperature and rotation are different between co- and counter- NBI discharges is because the actual absorption power is different due to the strong prompt loss mentioned in the previous section.

4. Perspective to quiescent H-mode due to steep edge rotation shear

In the previous section, we discussed about the strong edge rotation shear by counter NBI. Edge rotation pedestal is routinely observed in the H-mode discharge of KSTAR even with co-NBI, which is not well observed in other devices under co-NBI conditions. In H-mode discharge, strong edge rotation shear is the most important factor for making quiescent H-mode without ELM crashes although there still exist other requisites such as low edge collisionality (or density) [BurrellKH2001PoP].
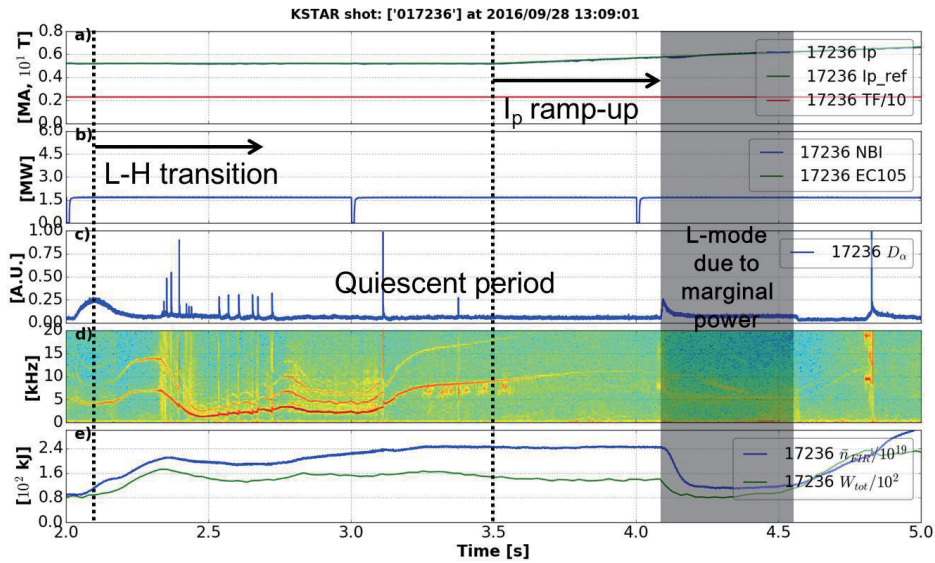
Figure 4. Quiescent period of H-mode without ELM crashes in counter NBI discharge. a) Measured plasma current (blue), programmed plasma current (green), and 1/10 scaled toroidal field (red). b) Injected NB power. c) D_∞ signal. d) Spectrogram of Mirnov coil. e) Line averaged density and stored energy. Shaded region depicts L-mode phase.

Figure 4 shows the H-mode phase without ELM crashes in counter NBI discharge. Unlike the conventional ELM-free phase, confinement is maintained constant during the quiescent period instead of the persistent stored energy and density increase. In addition, complicated forms of multi-harmonics can be observed in the Mirnov coil signal.

8

For more detailed local analysis, the analysis using electron cyclotron emission imaging (ECEI) measurement is used. As shown in figure 5, strong mode activity exists near the edge pedestal, and this mode activity has multiple harmonics. Comparisons with edge harmonic oscillations reported in other devices would normally require additional interpretation, but these edge mode activities appear to play an important role in maintaining the quiescent period.
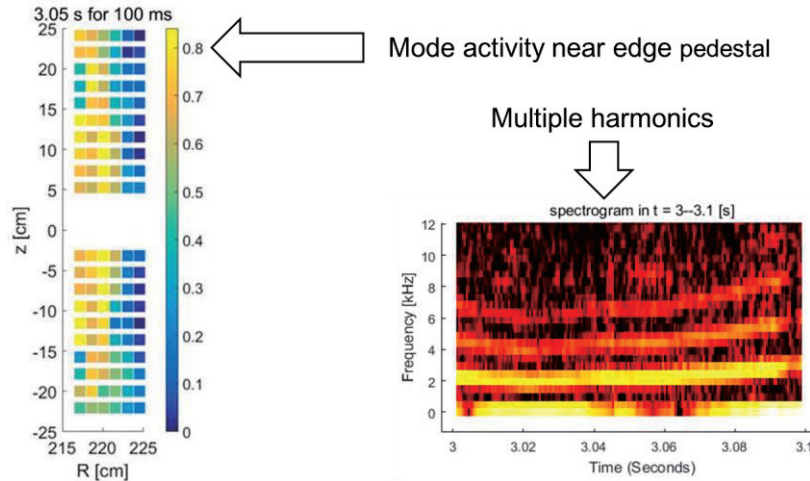
Figure 5 Cross coherence in edge ECEI view and spectrogram of edge ECEI channel.

6. Summary

In this paper, current and rotation profiles changed by counter NBI are discussed with using reversed I_p operation. As expected, by injecting counter NBI, we achieved hollow current profile and resulting reversed shear in q profile with high q_{min}. Furthermore, more strong rotation shear was observed in edge pedestal region and the width of rotation is even narrower than that of ion temperature profile. Typically, the tendency of pedestal widths is opposite in co-NBI discharge. The quantitative analysis is on-going to isolate the amount of edge intrinsic torque.

However, as mentioned in the above, counter NBI has a considerable level of prompt loss at moderate I_p level (~ several hundred kA), thus it is necessary to increase the plasma current to nearly MA level for more quantitative analysis and comparison. We will perform comparative analysis between counter- and co-NBIs in high I_p discharge under the condition of negligible difference in prompt loss compared to co-NBI. It is also a main research topic to implement and study quiescent H-mode, which is one of candidates in ITER operation for satisfying $Q=10$ mission.

References

[LeeJW2016IAEA] J.W. Lee eta al., IAEA fusion energy conference (2016).

[CMGreenfield2000PoP] C.M. Greefield et al., Phys. Plasmas **7** (2000) 1959.

[RiceJE2016PPCF] J.E. Rice, Plasma Phys. Control. Fusion **58** (2016) 083001.

[BurrellKH2001PoP] K.H. Burrell et al., Phys. Plasmas **8** (2001) 2153.

Characteristics of plasma current quench during disruptions in the KSTAR tokamak

J.G. Bak, Heung S. Kim, S.H. Hahn, I.S. Choi, Hyun S. Kim, J. Kim and I.S. Choi

National Fusion Research Institute, Daejeon, Korea

Email : jgbak@nfri.re.kr

The characteristics of plasma current quench during disruptions, which are occurred mainly due to the vertical displacement events (VDEs), are investigated by using disruption data for the pre-disrupted plasma current of 0.4 – 1.0 MA during the experimental campaign of 2013 -2017 in the KSTAR tokamak. The instantaneous and linear current quench rates evaluated from the maximum value of the time derivative and the slope of the linear fit in the phase of the current quench are up to 200 MA/s and 75 MA/s, respectively. The current quench rate (CQR) does not linearly depends upon the magnitude of plasma current in the range of plasma current, especially the value of the CQR is saturated for above 0.6 MA. The current quenches with the double exponential decay structure, which consists of faster slope followed by slower one, are also detected. The slower slope is due to the runaway electron (RE) plateau whose magnitude is less than 0.2 MA, and the sustainment time of the RE plateau linear depend on the plasma current. In addition, toroidal eddy current with a smaller negative dip followed by a larger positive peak is induced on the passive stabilizer in the phase of current quench due to the downward VDE, and the magnitude of the positive peak and time difference between the peak and the dip depend on the plasma current. Finally, the vertical displacement during the VDE causing the current quench depend on the magnitude of $|dI_p/dt|_{max}$, and the values of vertical growth rate are mostly from 50 s^{-1} to 80 s^{-1} for above 0.4 MA. The results from experimental investigations on disruption are reported.

1. Introduction

Plasma disruption is a critical issue in a large tokamak device such as the ITER because the heat and electromagnetic loads on them during the disruption may cause the major damages on the in-vessel conducting structures. Thus, the study on the plasma disruption has been carried out in the most of tokamaks in order to find the method for mitigating it or reducing the number of its occurrence during plasma discharges [1-2].

Most of major plasma disruptions were eventually occurred due to the vertical displacement events (VDEs) during plasma discharges in the KSTAR tokamak. After the occurrence of disruption, sometimes several conditioning shots were carried out to recover the plasma performance required for the experiment. For understanding the plasma disruptions in the KSTAR, the current quench rate and time, properties of the runaway electron (RE) plateau and toroidal eddy currents in the phase of current phase were experimentally investigated for the pre-disrupted plasma current $I_{p,predisrupt}$ of 0.4 -1.0 MA by using disruption data due to the downward VDEs during the experimental campaign of 2013- 2017 in the KSTAR. Here, the vertical growth rates were also mentioned.

In this paper, the experimental investigation of the current quench rate and time in the KSTAR are described in Sec. 2. The characteristics of the RE plateau and the eddy current in the phase of current quench are presented in Sec. 3. Finally, the summary is given in Sec. 4.

2. Current quench rate

The instantaneous current quench rate (ICQR) is directly obtained from the maximum value of the time derivative $|dI_p/dt|_{max}$ in the phase of current quench as shown in Fig. 1(a). The disruption data obtained in the experimental campaign of 2013-2016 were used to investigate the relationship between $|dI_p/dt|_{max}$ and $I_{p,predisrupt}$. There is the linear dependence between the ICQR and plasma current $I_{p,predisrupt}$ in the range of $I_{p,predisrupt} < 0.6$ MA. However, the value of ICQR saturates to ~ 200 MA/s as increasing $I_{p,predisrupt}$ (above 0.6 MA) as shown in Fig. 1(b), which differs with what we expect from the relationship between the ICQR and $I_{p,predisrupt}$. Here, the 'red curve' looks like an upper bound of $|dI_p/dt|_{max}$, which was obtained from the exponential fit to the selected data for the disrupted shots in the campaign of 2016. Only maximum value of

$|dI_p/dt|_{max}$ for a given $I_{p,predisrupt}$ was selected as a data point for the fit. The instantaneous quench time was estimated from the inverse of the ICQR, and its minimum value was about 2.9 ms.

The linear current quench rate (LCQR) was also evaluated by using the slope from the linear fit on the current quench curve. Here, three different intervals, such as such as 90 % - 60 %, 90 % - 30 %, and 80 % - 20 % levels of $I_{p,predisrupt}$, were used for the linear fit on the curve (see Fig. 1(a)). The $LCQR_{9060}$ from the 90 % - 60 % level, which was used for the evaluation of the CQR without the contribution of the runaway electrons (REs), was nearly equal to the ICQR. However, the $LCQR_{8020}$ from the 80 % - 20 % level, which have been used for evaluation of the averaged CQR in the NSTX and JET [3,4], and the value was up to ~75 MA/s that was about one third of the ICQR. The averaged quench time was estimated from the inverse of the $LCQR_{8020}$ and its minimum value was about 6.3 ms. In addition, it was thought that the larger discrepancy between the $LCQR_{8020}$ and ICQR might be due to the long tail at the level of less than 30% of $I_{p,predisrupt}$. The long tail might be the contribution of the REs as reported in the JET [5].

Fig. 1. (a) Typical wave-form of current quench and its time derivative, together with linear fits on the intervals given in the phase of the quench, (b) the ICQR versus the predisruption plasma current and (c) the $LCQR_{8020}$ versus the predisruption plasma current. Here, Experimental conditions were following: toroidal field $B_T = 0.9 – 3.5$ T (mostly, 1.8 T and 2.0 T), plasma elongation $\kappa = 1.4 – 2.0$, plasma density $n_e = (0.5 – 4.0) \times 10^{19}$ m^{-3}, and stored energy $W_{tot} = 0.04 – 0.8$ MJ.

3. Runaway electron plateau and eddy current

Due to the long tail the level of less than 30% of $I_{p,predisrupt}$, the waveform of the current quench had a double exponential decay structure with faster and slower R/L times, which were evaluated from two exponential fits on 90-30 % and 30-5 % levels of plasma current, respectively (see Fig. 2(a)). The slower R/L time was four times the faster one and the slower slope might be due to the formation of the RE plateau at the lower plasma level (< 0.1 MA) in the phase of the quench. But the RE plateau had small slope, which was different from the RE plateau, with almost a constant level, reported in the JET [5]. In addition, there are normally two positive peaks in the loop voltage measured at the outboard midplane in the phase of the current quench, and the first peak appears near the time of $|dI_p/dt|_{max}$, and the second one is detected near the end of the RE plateau as shown in Fig. 2(b), which is quite similar to the result observed in the FTU [6]. The two peaks were detected in the loop voltage when the RE plateau was observed in the phase of the current quench. Interestingly, the time difference between the two peaks, which corresponds to the sustainment time of the RE plateau, is linearly correlated with the magnitude of plasma current I_{p0} as shown in Fig. 2(c). However, there was no clear dependence of the magnitude of RE plateau on the plasma current as reported in the JET [5].
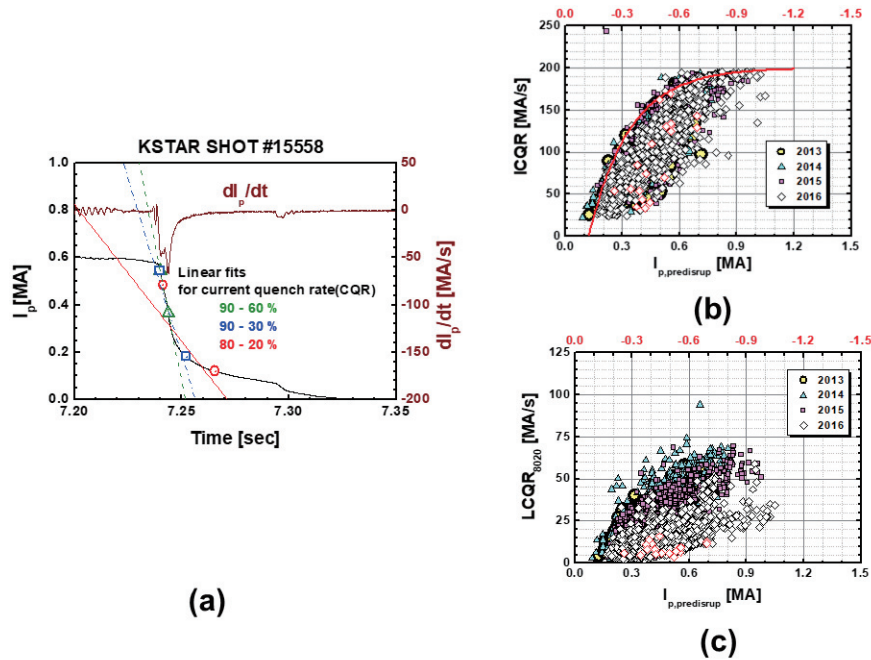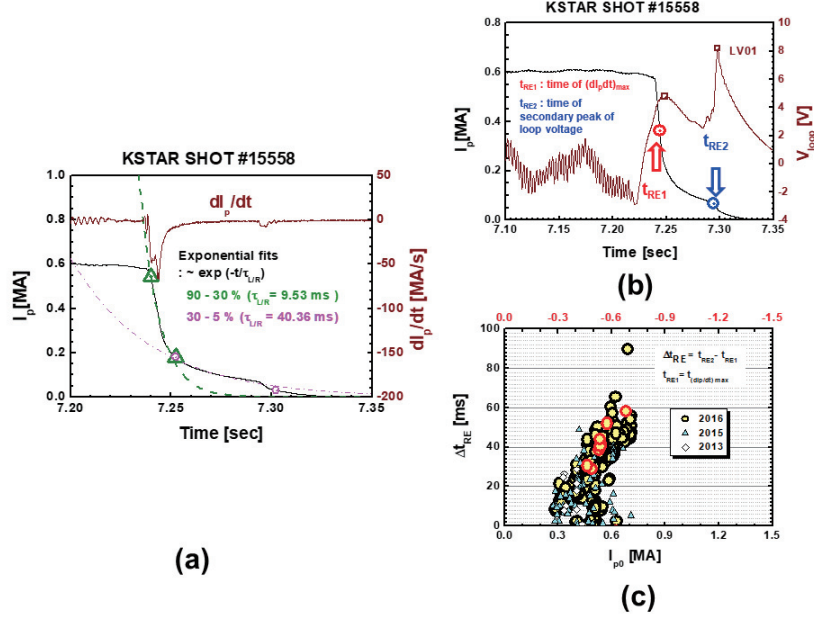
Fig. 2. (a) Typical wave-form of current quench and its time derivative, together with exponential fits on the intervals given in the phase of the quench, (b) a typical wave-form of current quench together with loop voltage showing two peaks that may be related to runaway electron (RE) plateau and (c) the sustainment time of the RE plateau versus plasma current.

Fig. 3 (a) shows the time evolutions of some parameters in the phase of a current quench due to the downward vertical displacement event (VDE) during a plasma discharge. Here, toroidal eddy current (EC) induced on the lower passive stabilizer (PS) has a negative dip followed by a larger positive peak. The dip and the peak appear before and after the time at the $|dI_p/dt|_{max}$, respectively. However, there was only a positive peak in the EC signal measured at the upper PS as it was expected. The magnitude of the peak $I_{eddy,peak}$ exponentially grows for higher value of $|dI_p/dt|_{max}$ as seen in Fig. 3(b). However, the dependence of the magnitude of the dip $I_{eddy,dip}$ upon the value of $|dI_p/dt|_{max}$ is weaker than the case of the peak. Thus, there is a clear exponential decayed structure between ratio of $I_{eddy,dip}$ to $I_{eddy,peak}$ and $|dI_p/dt|_{max}$ as shown in Fig. 3(c), which can be easily expected from Fig. 3(b).
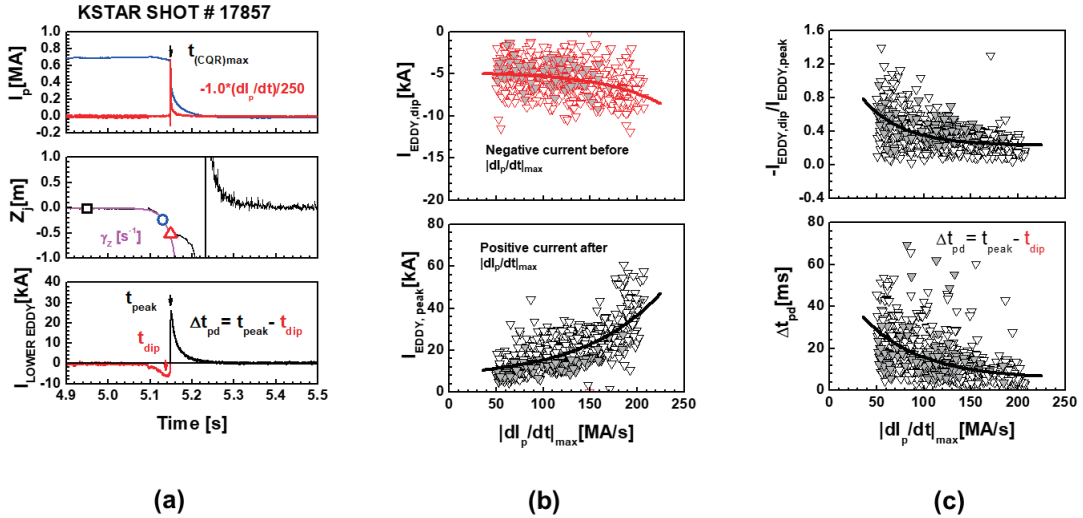
Fig. 3. (a) time evolutions of plasma current and its time derivative (top), the vertical displacement Z_j together with its vertical growth rate γ_z (middle) and eddy current induced on the lower passive stabilizer (bottom) during a current quench, (b) magnitudes of negative dip (top) and positive peak (bottom) of the eddy current versus ICQR, and (c) ratio between magnitudes of the negative dip and the positive peak (top) and time difference between positive peak and negative dip (bottom) versus ICQR. Here, experimental conditions in two campaigns of 2016 and 2017 were following: $B_T = 1.2 - 3.1$ T (mostly, 1.8 T and 2.0 T), $\kappa = 1.2 - 1.9$, $n_e = (0.5 - 4.0) \times 10^{19}$ m^{-3}, and $W_{tot} = 0.04 - 0.8$ MJ.

The EC with a negative dip followed by a larger positive peak was also observed during a VDE in the EAST [7]. In addition, it is found that the elapsed time from the dip to the peak exponentially decreases as $|dI_p/dt|_{max}$ becomes higher as seen in Fig. 3(c).

Finally, three vertical positions in the current quench, such as a neutral position $Z_{j,neutral}$, the position just before disruption $Z_{j,predisrupt}$ and the position at the time of $|dI_p/dt|_{max}$ $Z_{j,peak}$, were evaluated from the magnetic equilibrium reconstruction by using the EFIT code. Fig. 4 (a) shows the trend of the three vertical positions for different $|dI_p/dt|_{max}$ in the downward VDEs. Here, both values of $Z_{j,predisrupt}$ and $Z_{j,peak}$ become smaller for higher value of $|dI_p/dt|_{max}$ and the value of $Z_{j,neutral}$ is about -2 cm for the most VDEs. The vertical growth rate γ_z of the downward VDE was evaluated from Z_j (see middle of Fig. 3(a)) by using the method as mentioned in [8]. Here, there is a weak linear dependence between γ_z and I_p for the range of $I_p <$ 0.4 MA, but the values of γ_z are scattered for above 0.4 MA as seen in Fig. 4(b). For above 0.4 MA, the values of γ_z are mostly distributed from 50 s^{-1} to 80 s^{-1} as shown in Fig. 4(c).

(a) **(b)** **(c)**
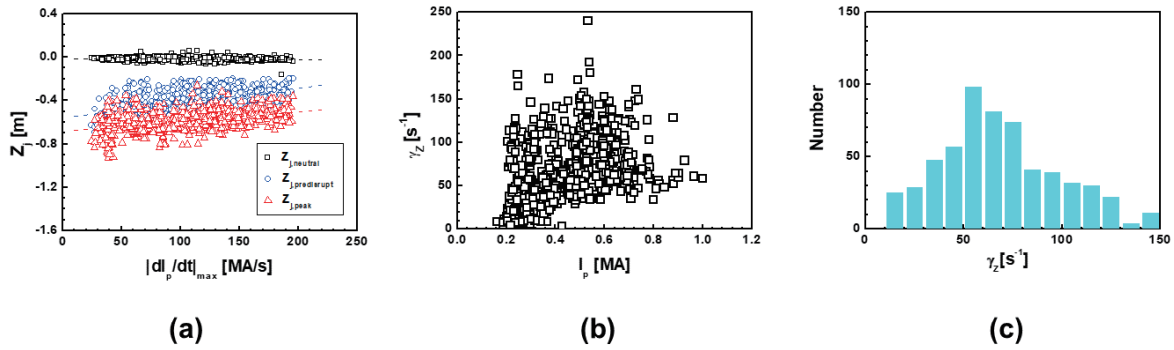
Fig. 4. (a) Three vertical displacements Z_js versus the ICQR, (b) the vertical growth rate versus plasma current and (c) the distribution of γ_z for $I_p > 0.4$ MA during VDEs. Here, disruption data during the downward VDE during the experimental campaign of 2016 are used.

4. Summary

We found several interesting characteristics from the experimental investigations in the current quench. Firstly, there was upper bound in both instantaneous and linear current quench rate for 0.4 -1.0 MA, and the current quench curve had a double exponential decay structure with faster and slower R/L times. Secondly, the sustainment time of the RE plateau became longer for higher plasma current. Thirdly, the magnitude of the positive peak in the toroidal eddy current and the elapsed time from the negative dip to the peak in the current quench became shorter for higher $|dI_p/dt|_{max}$ during the downward VDE. Finally, the growth rate of the downward VDEs was mostly 50 - 80 s^{-1}. Further quantative analysis on experimental data will be carried out in order to understand these characteristics.

References
[1] G. Pautasso *et al.*, *Nucl. Fusion* **42** (2002) 100-108.
[2] A. Savtchkov, PhD thesis, Forschungszentrum Julich, 2003.
[3] S. P. Gerhardt *et al.*, *Nucl. Fusion* **49** (2009) 025005.
[4] V. Riccardo *et al., Plasma Phys. Control. Fusion* **47** (2005) 117-129.
[5] V.V. Plyusnin *et al.*, *Nucl. Fusion* **46** (2006) 277.
[6] J.R. Martin-Solis *et al.*, *Phys. Rev. Lett.* **97** (2006) 165002.
[7] C. D. Long *et al.*, *Chin. Phys. B* **24** (2015) 025205.
[8] R. Albanese *et al.*, *Nucl. Fusion* **44** (2004) 999-1007

Experimental studies of LHCD's effect on plasma rotation on EAST

B. Lyu[1], X.H. Yin[2], J. Chen[2], R.J. Hu[2], Y.Y. Li[1], F.D. Wang[1], J. Fu[1], B.J. Ding[1], M. Wang[1], F.K. Liu[1], H.Q. Liu[1], Q. Zang[1], Y.J. Shi[2,3], B.N. Wan[1] and EAST team[1]

[1]Insitute of Plasma Physics, Chinese Academy of Sciences, Hefei 230031, China

[2]School of Nuclear Science and Technology, University of Science and Technology of China, Hefei 230026, China

[3]Department of Nuclear Engineering, Seoul National University, Seoul 151-742, Korea

Abstract

New experimental results from 4.6GHz LHW driven plasma rotation were presented, which confirmed the fact that the rotation was originated at the plasma edge. LHCD-induced rotation change decreased with I_p and density and evolves at a time scale much longer than plasma temperature and stored energy. Rotation change is closely correlated with current density profile, both of which evolve at a similar time scale. Direct effect from LHW momentum input was observed to result in ctr-current rotation change, followed by co-current resulting from possible j×B force.

1. Introduction

Rotation and its shear play important roles in tokamak plasmas since they can reduce the MHD instabilities [1,2] and enhance the confinement [3,4]. At present, rotation is driven by direct NBI momentum injection in most tokamak devices, which is predicted to be not efficient on ITER and future reactors due to large machine size, high density and beam energy [5]. The study of the rotation without external momentum injection, the so-called "intrinsic rotation", is important for improving predictions for plasma rotation in ITER and future fusion reactors. As one of intrinsic rotation driving methods, LHCD-driven rotation has been reported on Alcator C-mod [6,7,8], JT-60U [9], Supra Tore [10,11] and EAST [12] to induce toroidal rotation change.

A 4.6GHz LHCD system was deployed on EAST [13,14] in 2014, which enabled plasma rotation studies at different LHCD frequencies [15]. In this paper, the typical characteristics of the 4.6GHz LHCD-driven rotation are presented. The preliminary analyses of LHCD induced rotation and its dependence on plasma parameters are performed.

2.Experiment observation of 4.6GHz LHCD induced plasma rotation

Development of 4.6GHz LHW system on EAST adds capability for non-inductive current drive, which also provides tools for RF-driven rotation physics. Fig. 1 presents waveforms of three similar LSN LHCD discharges with different LHCD powers (1MW, 1.5MW and 1.8MW) and the relationships between rotation increment and various parameters during the three shots. The rotation increment increases with LHCD power as seen on JT-60U [9] and C-mod [6,8]. Besides, an obvious hysteresis between the rotation velocity δu_ϕ and T_e (W_{mhd}) is shown, with amplitudes of change increasing with LHCD power while the

slope is almost kept unchanged. The phenomena show the different time scales of electron heating and ion rotation velocity change induced by LHCD and the time scales are independent of LHCD power. The hysteresis confirms that the rotation is driven indirectly. The relationship between the increment δu_ϕ and the decrement in the internal inductance (δl_i), which is used to characterize the broadening of the current density profile induced by LHCD, is observed. The results are similar to those observed on C-mod [8] except for the different rotation direction. In addition, the rotation increases with central safety factor q_0. Both the increase of q_0 and the decrease of l_i indicate that the flattening of the plasma current density profile plays an important role in accelerating toroidal rotation.
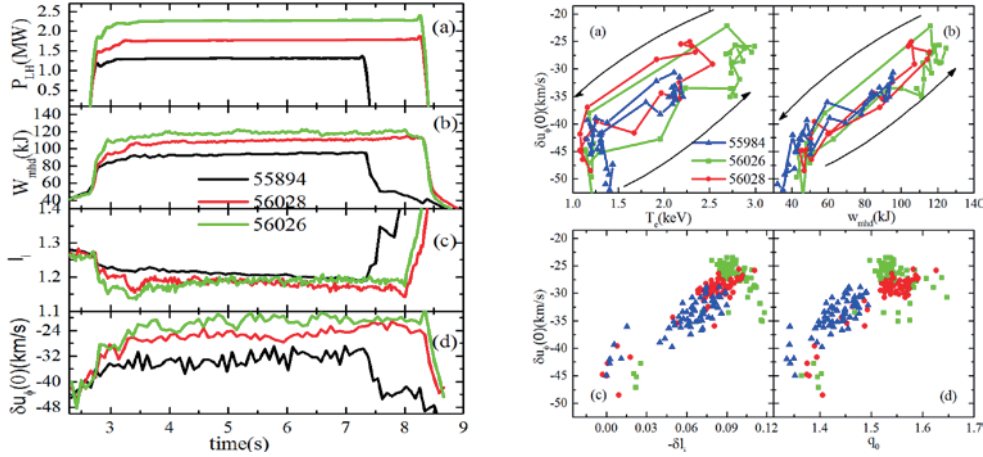
Fig.1 left:Waveforms of 3 LSN 4.6GHz LHCD shots (#55984,#56026, #56028) on EAST: (a) I_p, (b) n_e, (c) P_{LHCD}, (d) δu_ϕ; right: Variations of trajectory in δu_ϕ with (a) T_e/T_i and (b) W_{mhd} for discharges with LHW at varying power; δu_ϕ versus (c) δl_i , (d) q_0 for discharges with LHW at varying power.

A comparison of LHCD rotation drive with different frequencies is carried by injecting LHW of 2.45 GHz and 4.6 GHz at different times during an L-mod discharge [15]. Fig. 2 shows the experimental results for one discharge with 2.45GHz and 4.6GHz LHCD at a similar injected power, while electron density and plasma current are kept unchanged. It was seen that the difference in loop voltage V_{loop} and W_{mhd} was obvious between two injection periods, which indicates better current driven and heating efficiency for 4.6GHz LHCD. Also, from the rotation measurements, larger rotation change is also observed for 4.6GHz. The profiles of the electron temperature, ion temperature and change of toroidal rotation in three conditions (ohmic condition, 2.45 GHz LHCD injection and 4.6 GHz LHCD injection) of this discharge shows that 4.6 GHz LHCD has a stronger electron heating and rotation driving efficiency in the observed region ($\rho<0.6$) than 2.45 GHz LHCD, with no difference in ion heating. During the injection of the 2.45 GHz LHCD in the shot, the rotation driven by the LHCD is in the edge region ($\rho>0.4$), while the rotation in the whole profile changes with the injection of the 4.6 GHz LHCD. The difference may be related to the power deposition. The simulated deposition profiles [15] showed that 4.6G Hz LHCD was absorbed around $\rho=0.3$ and $\rho=0.6$, while the 2.45 GHz LHCD was absorbed in $\rho=0.6$ region.
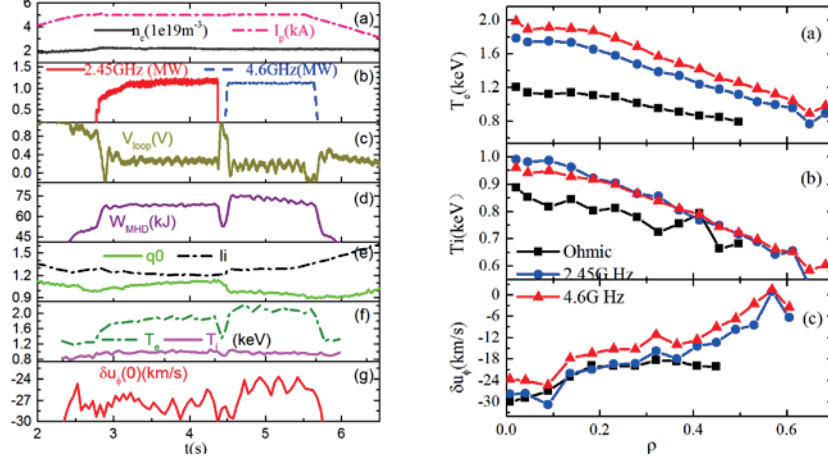
Fig. 2 **left:**Waveforms of an LSD LHCD shot (#54439) on EAST: (a) I_p, and n_e, (b) P_{LHCD}, (c) V_{loop}, (d) W_{mhd}, (e) l_i and q_0 (f) T_i, T_e and (g) δu_ϕ; **right**: Profiles of (a) T_e, (b) T_i, and (c) δu_ϕ under three different discharge conditions.
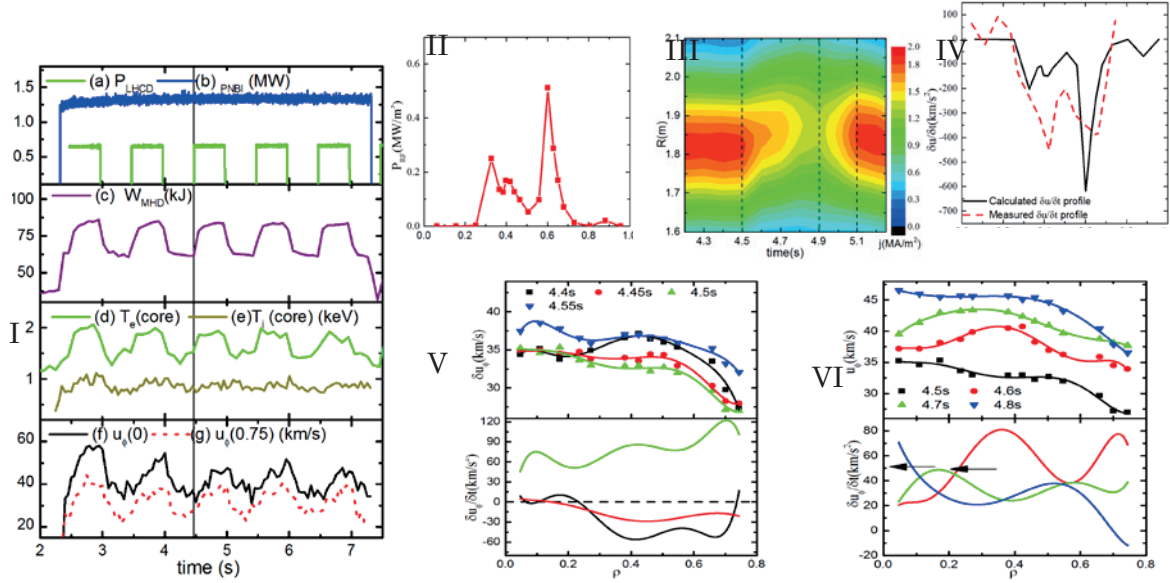
Fig. 3 **I**:The waveforms of a USN 4.6GHz LHW shot (#70944) on EAST. (a) P_{LHCD}, (b) P_{NBI}, (c) W_{mhd}, (d) T_i, (e) T_e (f) δu_ϕ (central) velocity (g) δu_ϕ (edge); **II**: LH Power deposition during the shot; **III**: current density profiles from 4.2 s to 5.2 s for the shot; **IV**: Calculated and measured $\delta u/\delta t$ profile induced by the LH injection; **V** and **VI**: Profiles of the δu_ϕ and $\delta u_\phi/\delta t$ before 4.6 GHz LHW (balck box points) and during LHW

Similar to the results in C-mod [6] and Tore Supra [10], EAST discharges show that change of the rotation decreases with I_p and n_e. LHW is injected into an ohmic discharge in the above-mentioned shots with background rotation in counter-current direction. Additionally, another shot, during which the LHW inject into a NBI discharge, is applied, shown in Fig. 3. With the NBI application, the rotation before the LHW is in co-current direction. ~15km/s co-current increase in core region and ~8km/s co-current increase in edge region of rotation are measured by CXRS. And the time scale for the evolution of the δu_ϕ is same with the evolution of the current density, which confirms that plasma current density profile plays an

important role in accelerating toroidal rotation in LHCD discharge.

Profiles of the δu_ϕ and $\delta u_\phi/\delta t$ before and during the LHW application, shows that after the injection of the LHW (4.45 s), an obvious counter-current change of rotation around $\rho\sim0.4-0.7$, is observed during the first 50 ms. The ctr-current increment is mainly due to the LH wave injected momentum. According tto the results from JET [16] and Tore Supra [10,11], the torque injected by LH is related to the LH power: $\boldsymbol{S_{LH}}=(\boldsymbol{n_\phi}\times\boldsymbol{R_0}/\boldsymbol{c})\times\boldsymbol{P_{LH}}$, and the calculated $\delta u/\delta t$ profile agreed well with the measured results. During the 50-150ms, the change of rotation turned to the co-current direction at $\rho\sim0.4-0.7$, the change may be due to the $\boldsymbol{J}\times\boldsymbol{B}$ force that LHCD induced a radial current to drive the plasma in the co-current direction. Then during the 150-350ms after the LH injection, the rotation increases in co-current direction at the whole observed positions. And the process is probably due to the intrinsic torque from residual stress and momentum transport.

4. Conclusions

This study presents plasma rotation behaviors with 4.6GHz LHCD injection. Typically, the 10-20 km/s co-current rotation change and the transport of rotation velocity from edge to core are observed. The relationship between plasma parameters and rotation is also investigated, indicating that rotation increases with LH power increasing and decreases with increasing of plasma current and density. Besides, rotation decreases with l_i increasing and increases with q_0 increasing. Hysteresis between rotation and T_e (or W_{mhd}) is observed, suggesting different response times between the electron heating and rotation acceleration by LHCD. A comparison between the rotations driven by 4.6G LHCD and 2.45G LHCD on EAST is also presented, in which higher frequency LHCD could induce more rotation changes. The change of toroidal rotation after the LHW inject into a NBI discharge has been studied with application of the CXRS diagnostic. 5km/s ctr-current rotation change in LH deposition region after the LH injection has been observed which is due to direct effect from LHW momentum input and followed by co-current direction change from possible $\boldsymbol{J}\times\boldsymbol{B}$ force.

References

[1]   Bondeson A and Ward D J Phys. Rev. Lett. 1994 72 2709-2712

[2]   Betti R and Freidberg J P Phys. Rev. Lett. 1995 74 2949-2952

[3]   Craddock G G and Diamond P H Phys. Rev. Lett. 1991 67 1535-1538

[4]   Terry P W Rev. Mod. Phys. 2000 72 109-165

[5]   Doyle E J, Houlberg W A, Kamada Y, et al. Nucl. Fusion 2007 47 S18-S127

[6]   Rice J E, Podpaly Y A, Reinke M L, et al. Nucl. Fusion 2013 53 093015

[7]   Rice J E, Ince-Cushman A C, Bonoli P T, et al. Nucl. Fusion 2009 49 025004

[8]   Ince-Cushman A, Rice J, Reinkeet M al. Phys Rev Lett 102, (2009).

[9]   Koide Y, Tuda T, Ushigusa K, et al.   Plasma Phys. Control. Nucl. Fusion Res. 1992, Vol 1. 777-789

[10] Chouli B, Fenzi C, Garbet X, et al. Plasma Phys. Control. F. 2014 56 095018

[11] Chouli B, Fenzi C, Garbet X, et al. Plasma Phys. Control. F. 2015 57 125007

[12] Shi Y, Xu G, Wang F, et al. Phys. Rev. Lett. 2011 106 235001

[13] Wan B N, Li J G, Guo H Y, et al. Nucl. Fusion 2013 53 104006

[14] Wan B N, Li J G, Guo H Y, et al. Nucl. Fusion 2015 55 104015

[15] Li M H, Ding B J, Liu F K, et. al. Phys. Plasmas 2016 23, 102512

[16] Eriksson L G, Hellsten T, Nave M F F, et al. Plasma Phys. Control. F. 2009, 51

Influence of toroidal rotation on Tearing modes

Huishan Cai[1], Jintao Cao[2], Ding Li[1,2]

[1]University of Science and Technology of China, Hefei, Anhui 230026, P. R. China

[2]Institute of Physics, CAS, Beijing 100190, P. R. China

Abstract

Tearing modes stability analysis including toroidal rotation is studied. It is found that rotation affects the stability of tearing modes mainly through the interaction with resistive inner region of tearing mode. The coupling of magnetic curvature with centrifugal force and Coriolis force provides a perturbed perpendicular current, and a return parallel current is induced to affect the stability of tearing modes. Toroidal rotation plays a stable role, which depends on the magnitude of Mach number and adiabatic index Γ, and is independent on the direction of toroidal rotation. For $\Gamma > 1$, the scaling of growth rate is changed for typical Mach number in present tokamaks. For $\Gamma = 1$, the scaling keeps unchanged, and the effect of toroidal rotation is much less significant, compared with that for $\Gamma > 1$.

1. Introduction

Tearing mode, one of the most dangerous magnetohydrodynamics (MHD) instabilities in the magnetically confined plasmas, can negatively impact the performance of tokamak discharge. It can change the topology of magnetic field, lead to the formation of magnetic island, increase the local radial transport, and reduce the plasma confinement of tokamak. Even, it can cause a macroscopic relaxation event, and lead to the plasma disruption. Actually, many disruption events in the tokamak discharge were caused by tearing modes (including neoclassical tearing modes). The neoclassical tearing modes (NTMs), caused by the loss of bootstrap current in the island due to the flatten pressure, can limit the maximum achievable β

($\beta = 2\mu_0 p / B^2$, where p and B are the pressure and magnetic field, respectively) in tokamak discharge[1]. Hence, understanding the physics of tearing modes (including NTMs) is one of the critical physical problems to achieve steady-state and high confinement for present or future tokamak devices, such as the International Thermonuclear Experimental Reactor (ITER)[2].

In plasma discharge, unbalanced neutral beam is often used to heat plasmas. Correspondingly, it can result in strong toroidal plasma rotation. Some experiments have shown that Mach numbers up to unity were found during the unbalanced high power neutral beam injection (NBI)[3-7]. For such high rotation, toroidal rotation would affect MHD instabilities significantly. There are some experimental results that toroidal rotation would stabilize tearing modes[8-13]. In DIII-D, it was shown that onset threshold of NTMs increases as ``co-injected'' rotation increases, while it keeps unchanged for increasing rotation in the counter direction[12]. However, the experiment in ASDEX-U found that onset threshold of NTMs increases with both co and counter rotation increasing[13]. The experimental results are still lack of sound

theoretical explanation. Lots of theoretical works have been devoted to understanding the effect of rotation on tearing modes[14-22]. In **Ref**.[19], by extending the works[23,24] to include rotation, it was shown that the stability criterion Δ' of tearing modes is enhanced by rotation, and the effect is insignificant. The simulations[20,21] both showed that tearing mode is stabilized mainly by the magnitude of rotation rather than rotation shear in the toroidal model. It was understood analytically that a stabilizing effect on Δ' appears due to the `Shafranov' shift in the profile of equilibrium current induced by the rotation in **Ref**.[20], which is contrary to above mentioned results in **Ref**.[19]. In this work, we will investigate the effect of rotation on linear tearing modes. Physically, in the presence of toroidal rotation, the centrifugal and Coriolis forces appear in the inertia term. The perturbations of pressure and density have sidebands due to the compressibility and the poloidal dependence of equilibrium profiles induced by rotation. Then the magnetic curvature would couple with pressure, centrifugal and Coriolis force, which results in a perpendicular current. Correspondingly, a return parallel current is induced. Thus, the stability of tearing modes would be affected. Based on the above physical picture, we will show that the effect is significant if the adiabatic index $\Gamma > 1$ and Mach number is not very small. We will also point out that the effect mainly comes from the physics in the resistive inner region of tearing modes.

2. Influence of toroidal rotation on tearing modes

The detailed calculation can be referred to the paper [34]. By a series of derivation, we can obtain the dispersion of tearing modes including toroidal rotation, as

$$\left(1 + 2q_s^2\right)^{-1/4} \hat{\gamma}^{3/4} \left(\hat{\gamma}^2 + \frac{(\Gamma + 4M^2 + M^4)\hat{\gamma}^2 + (\Gamma - 1)\beta M^4 /(2q_s^2 \gamma_0^2)}{\hat{\gamma}^2 \gamma_0^2 / \beta + \Gamma /(2q_s^2)} \right)^{1/4} = 1 \qquad (1)$$

where $\hat{\gamma} = \gamma / \gamma_0$, $\hat{\gamma}_0 = \left(1 + 2q_s^2\right)^{-1/5} \hat{\eta}^{3/5} \hat{\Delta}'^{4/5}$ is the growth rate of tearing modes without toroidal rotation.

In general, $\beta / \gamma_0^2 >> 1$ is satisfied for typical tokamak. Then, Eq.(1) can be reduced to

$$\left(1 + 2q_s^2\right)^{-1/4} \hat{\gamma}^{3/4} \left(\frac{(1 + 2q_s^2)\Gamma^2 + 2q_s^2 M^2 (4\Gamma + M^2)}{\Gamma^2} \hat{\gamma}^2 + \frac{M^4 \beta}{\gamma_0^2} \frac{\Gamma - 1}{\Gamma} \right)^{1/4} = 1 \qquad (2)$$

It can be seen that the effect of toroidal rotation is reflected by the Mach number, and connected to compressibility. The effect also depends on the adiabatic index Γ, which is needed to be determined by kinetic theory. Here, we analyze the rotation effect for different Γ.

For $\Gamma > 1$, when $M^4 \beta / \gamma_0^2 >> \hat{\gamma}^2$, one can obtain

$$\hat{\gamma} = \left(1 + 2q_s^2\right)^{1/3} \left(M^4 \beta \frac{\Gamma - 1}{\Gamma}\right)^{-1/3} \gamma_0^{2/3} \qquad (3)$$

It can be found that the growth rate of tearing modes $\Gamma \propto \eta M^{-4/3} \beta^{-1/3}$ and $\hat{\gamma} < 1$ in this limit, namely toroidal rotation plays a stable role on tearing modes. The condition can be rewritten as $M^4 \beta >> (\Gamma - 1)^{-2/5} \hat{\Delta}'^{8/5} \hat{\eta}^{6/5}$. For the typical parameters in tokamak, given $M \sim 0.1$, $\hat{\eta} \sim 1 \times 10^{-7}$, the above condition is easily satisfied in plasma with unbalanced neutral beam injection heating. Under this condition, tearing modes are dramatically affected by toroidal rotation, and the scaling of growth rate is

also changed.

For very low rotation, $M^4\beta/\gamma_0^2 << \hat{\gamma}^2$, it can be obtained

$$\hat{\gamma} = \left(1 + \frac{2q_s^2 M^2(4\Gamma^2 + M^2)}{\Gamma^2(1 + 2q_s^2)}\right)^{-1/5} \qquad (4)$$

Under this condition, the scaling of the growth rate of tearing modes keeps unchanged, and is little affected by rotation, since $M << 1$ in this limit. The above two limits can also be justified in **Fig**.1, where the solid line is plotted based on Eq.(1), the dash and dotted lines are plotted based on Eqs.(38) and (39), respectively. In **Fig**.1, the typical parameters in tokamak are given as follows: $\hat{\eta} \sim 1 \times 10^{-7}$, $\beta = 1\%$, the mode numbers m=2,n=1, adiabatic index $\Gamma = 1.67$, and $\hat{\Delta}' = 1$ is set. It can be seen that the growth rate decreases as the Mach number increases, and is significantly reduced for $M > 0.08$. For $M > 0.08$, the growth rate obtained from Eq.(2}) matches well with that from Eq.(1). For typical tokamaks, such as MAST[3], DIII-D[4], NSTX[5], JET[6], ASDEX-U[7], the Mach number can be up to 0.5 - 1. Thus, toroidal rotation would dramatically stabilize tearing modes for typical tokamaks.

As pointed out above, the effect of rotation depends on the adiabatic index, especially for $\Gamma = 1$. For $\Gamma = 1$, the behavior of toroidal rotation effect on tearing modes is different from that for $\Gamma > 1$. It can be obtained from Eq.(2) that

$$\hat{\gamma} = \left(1 + \frac{2q_s^2}{1 + 2q_s^2} M^2(M^2 + 4)\right)^{-1/5} \qquad (5)$$

The scaling of growth rate keeps unchanged, much different from that under the condition $M^4\beta >> (\Gamma - 1)^{-2/5}\hat{\Delta}'^{8/5}\hat{\eta}^{6/5}$ for $\Gamma > 1$. The toroidal rotation still stabilizes tearing modes, which can be seen from **Fig**.2. In **Fig**.2, it can be found that the growth rate decreases with M increasing, while the rotation effect on tearing modes is much less significant than that for $\Gamma = 1.67$.

Based on the above results, toroidal rotation always plays a stable role on tearing modes. This is consistent with the results in the previous simulations[20,21]. In **Ref**.[20], the result was understood analytically that a stabilizing effect on Δ' appears due to the `Shafranov' shift in the profile of equilibrium current induced by the rotation, which is contrary to that in **Ref**.[19]. In **Ref**.[19], it was shown that toroidal rotation effect on stability criterion is small. In the next section, it will also be shown that toroidal rotation effect on stability criterion is small due to the small Mach number. In **Ref**.[20], it was shown that the stabilizing effect mainly comes from the Coriolis force in the resistive layer. Our results also show that toroidal rotation affect tearing modes mainly through the interaction with the resistive inner region. It is pointed out that the above result still can not explain the results in the experiments[12-13]. In these experiments, neutral beam is injected tangentially, then the effects of energetic ions on tearing modes should be considered, and it has been shown that the effects of energetic ions are important[30-32].
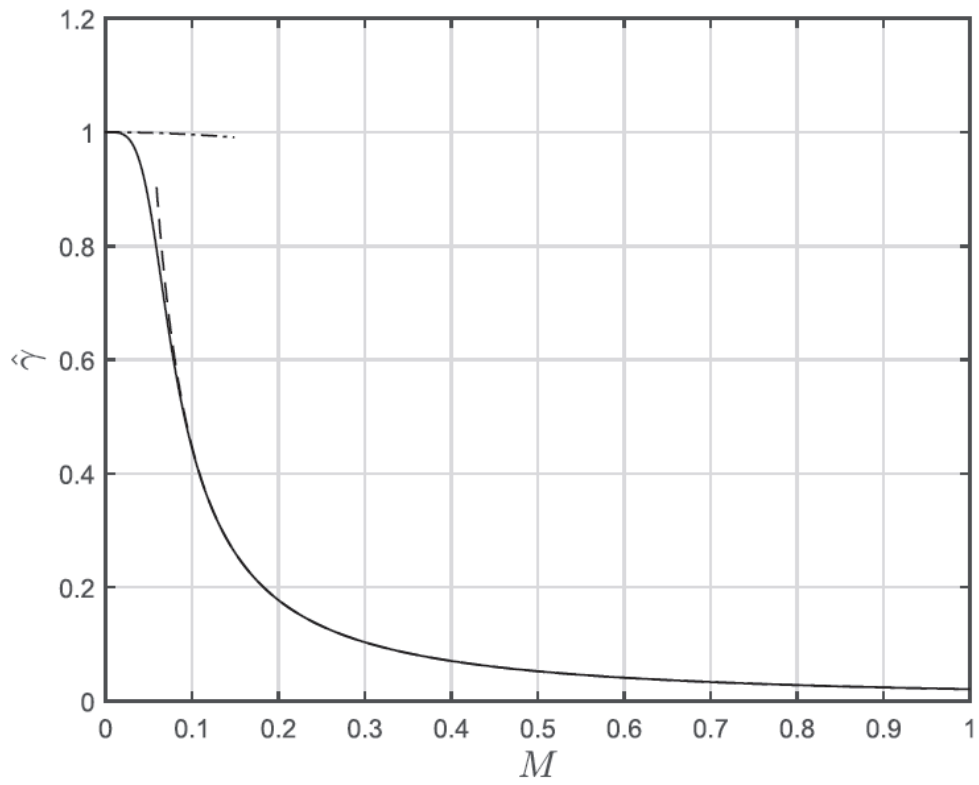
Figure 1. The growth rate of tearing modes against Mach number
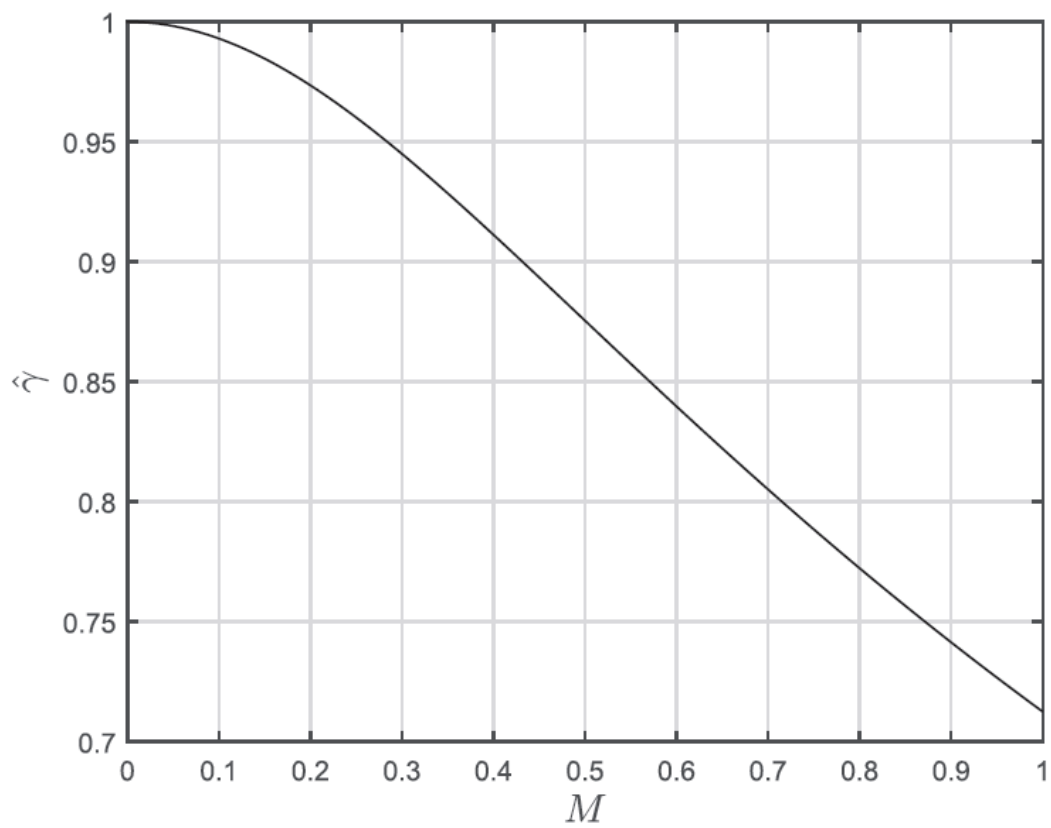
Figure 2. The growth rate of tearing modes against Mach number

References

[1] T. C. Hender *et al.*, Nucl. Fusion **44**, 788(2004).

[2] T. C. Hender *et al.*, Nucl. Fusion **47**, s128(2007).

[3] R. Akers, P. Helander, A. Field, C. Brickley, D. Muir, N. J. Conway, M. Wisse, A. Kirk, A. Patel, A. Thyagaraja, and C. M. Roach, and the MAST and NBI teams, *Proceedings of the 20th IAEA Fusion Energy Conference* (IAEA, Vienna, 2005), paper EX/4-4.

[4] W. M. Solomon, K. H. Burrell, L. R. Taylor, R. J. Fonck, P. Gohil, D. J. Gupta, R. J. Groebner, G. J. Kramer, G. R. McKee, and R. Nazikian, *Proceedings of the 20th IAEA Fusion Energy Conference* (IAEA, Vienna, 2005), paper EX/P4-10.

[5] J. E. Menard, R. E. Bell, E. D. Fredrickson, D. A. Gates, S. M. Kaye, B. P. LeBlanc, S. S. Medley, W. Park, S. A. Sabbagh, A. Sontag, D. Stutman, K. Tritz, and W. Zhu, and the NSTX Research Team, Nucl. Fusion **45**, 539(2005).

[6] J. S. deGrassie, L.-G. Eriksson, and J.-M. Noterdaeme, and JET EFDA Contributors, *Proceedings of the 16th Topical Conference on Radio Frequency Power in Plasmas* (AIP, Melville, NY, 2005), AIP Conference Proceedings Vol. 787, p. 110.

[7] R. Fischer, L. Giannone, K. Lackner, R. M. McDermott, E. Viezzer, H.P. Zehrfeld, and the ASDEX Upgrade Team, 42nd EPS Conference on Plasma Physics, P1.117 (2015).

[8] J. L. Luxon, Nucl. Fusion **42**, 614(2002)

[9] M. Ono, S. M. Kaye, Y.-K. M. Peng, G. Barnes, W. Blanchard, M. D. Carter, J. Chrzanowski, L. Dudek, R. Ewig, D. Gates, R. E. Hatcher, T. Jarboe, S. C. Jardin, D. Johnson, R. Kaita, M. Kalish, C. E. Kessel, H. W. Kugel, R. Maingi, R. Majeski, J. Manickam, B. McCormack, J. Menard, D. Mueller, B. A. Nelson, B. E. Nelson, C. Neumeyer, G. Oliaro, F. Paoletti, R. Parsells, E. Perry, N. Pomphrey, S. Ramakrishnan, R. Raman, G. Rewoldt, J. Robinson, A. L. Roquemore, P. Ryan, S. Sabbagh, D. Swain, E. J. Synakowski, M. Viola, M. Williams, J. R. Wilson, and NSTX Team, Nucl. Fusion **40**, 557(2000).

[10] M. Keilhacker and JET Team, Plasma Phys. Controlled Fusion **41**, B1(1999).

[11] R. J. La Haye, D. P. Brennan, R. J. Buttery, and S. P. Gerhardt, Phys. Plasmas **17**, 056110(2010).

[12] R. J. Buttery, R. J. La Haye, P. Gohil, G. L. Jackson, H. Reimerdes, E. J. Strait, and the DIII-D Team, Phys. Plasmas **15**, 056115(2008).

[13] S Fietz, M Maraschek, H Zohm, M Reich, L Barrera, R M McDermott and the ASDEX Upgrade Team, Plasma Phys. Control. Fusion **55**, 085010(2013).

[14] A. Bondeson and M. Persson, Phys. Fluids **29**, 2997(1986).

[15] R. L. Dewar and M. Persson, Phys.¥ Fluids B **5**, 4273(1993).

[16] G. Urquijo, S. N. Bhattacharyya and A. Sen, Phys.¥ Plasmas **4**, 239(1997).

[17] D. Chandra, A. Sen, P. Kaw, M. P. Bora and S. Kruger, Nucl. Fusion **45**, 524(2005).

[18] R. Coelho, E. Lazzaro, Phys. Plasmas **14**, 012101(2007).

[19] A. Sen, D. Chandra and P. Kaw, Nucl. Fusion **53**, 053006(2013).

[20] D. Chandra, A. Thyagaraja, A. Sen, C. J. Ham, T. C. Hender, R. J. Hastie, J. W. Connor, P. Kaw and J. Mendonca, Nucl. Fusion **55**, 053016(2015).

[21] S. Wang and Z. W. Ma, Phys. Plasmas **22**, 122504(2015).

[22] R. L. White, R. Fitzpatrick, Phys. Plasmas **22**, 102507(2015).

[23] J. W. Connor, S. C. Cowley, R. J. Hastie, T. C. Hender, A. Hood and T. J. Matin, Phys. Fluids **31**, 577(1988)

[24] C. C. Hegna and J. D. Callen, Phys.¥ Plasmas **1**, 2308(1994).

[30] Huishan Cai, Shaojie Wang, Yinfeng Xu, Jintao Cao and Ding Li, Phys. Rev. Lett. **106**, 075002(2011). [31] Huishan Cai and Guoyong Fu, Phys. Plasmas **19**, 072506(2012).

[32] Huishan Cai, Nucl. Fusion **56**, 126016(2016).

[34] Huishan Cai, Jintao Cao, Ding Li, Nucl. Fusion **57**, 056006(2017)

A coupled study of plasma rotation and transport

C. Bae[1,2], J. Kim[1], M. J. Choi[1], L. Terzolo[1], T. Rhee[1], H. S. Kim[1], S. G. Lee[1,2], Y. Ma[1]

[1] National Fusion Research Institute, Gwahak-ro, Yuseong-gu, Daejeon 305-806, South Korea
[2] University of Science and Technology, Daejeon, South Korea

Abstract

The toroidal angular torque contributions of all the ion species (deuterium fuel, carbon, and argon) in axisymmetric NBI-heated KSTAR tokamak plasmas are investigated in this work, based on the first principles with the same set of first-order poloidal perturbations. To account for all the contributions in the toroidal torque balance, the convective torques are neoclassically calculated and the torques from the deuterium and impurity sources with their atomic effects kinetically-simulated by TRANSP code are also included in the analysis. Neoclassical Toroidal Viscosity (NTV) torques are calculated based on the collisionality-extended Braginskii's decomposition and its axisymmetric torques are calculated with the gyroviscous contribution in realistic Shafranov-shifted D-shaped flux surfaces with the first-order poloidal asymmetries considered, based on the extended neoclassical formalism in an earlier work [Bae et. el., Nucl. Fusion 53 (2013) 043011]. The results, analyzed with the upgraded version of the nonlinear GTROTA code [Bae et al., Comp. Phys. Communications 184 (2013) 2571-2587], show that the toroidal torque balance is mostly maintained by the competition between two largest contributions: anomalous Vr cross B and frictional torques. With all other torques being much smaller by an order of magnitude, they provide detailed balances to yield the observed rotation and predicted transport profiles in the investigated NBI-heated tokamak discharges. It is also shown that the rotation and transport of all the ions species can be significantly different with their disparate collisionality throughout the radial range, consequently affecting their radial transport.

1. Introduction

Typically, particle transport studies in confined plasmas solve the continuity equation,

$$\frac{\partial n_a}{\partial t} + \nabla \cdot \left(n_a \vec{V}_a \right) = S_a^0,$$ (1)

where the "radial" fluxes of each species a, $n_a \vec{V}_a$, are closed with assumed physical functions of density and convection with their respective diffusive and convective coefficients (D and V). Theoretically, the proper closure of (1) must be done by solving the momentum balance equation,

$$n_a m_a \frac{\partial \vec{V}_a}{\partial t} + n_a m_a \left(\vec{V}_a g\nabla \right) \vec{V}_a + \nabla p_a + \nabla g \vec{\pi}_a = n_a e_a \left(\vec{E} + \vec{V}_a \times \vec{B} \right) + \vec{F}_a^1 + \left(\vec{S}^1 - m_a \vec{V}_a S^0 \right),$$ (2)

but understanding the difficulties in working out all the terms in (2), especially the convective and viscous forces, all the effects from (2) have been approximated significantly with D and V coefficients. Plasma rotation studies, on the other hand, have to handle (2) as is and deal with as many terms as possible for higher accuracy. NCLASS code[1], based on Hirschman-Sigmar rotation model, is the most famous for solving for rotations and radial electric field (Er) of multiple ion species in plasmas. Another major plasma rotation study[2, 3] was done based on the Stacey-Sigmar model, which retains all the terms in (2) with the first-order poloidal variations (better known as "poloidal asymmetries") in density, velocity, and electrostatic potential considered but at the risk of solving extremely nonlinear set of equations to calculate the rotations of multiple ion species. GTROTA[4], a nonlinear code written based on the Stacey-Sigmar approach, neoclassically calculates the toroidal and poloidal velocities (Vt and Vp), Er, and poloidal asymmetries for toroidally-axisymmetric plasmas. Recent upgrades to GTROTA allow calculations of the effective (or anomalous) radial velocities (Vr) and the corresponding fluxes. Also with the recent upgrades in the calculation of the toroidal electric field based on the time evolution of flux values, GTROTA can neoclassically calculate all the non-negligible terms in the toroidal torque balance (with $\langle \ \rangle$ noting flux surface averaged),

$$\left\langle Rm_a n_a \frac{\partial V_{a\phi}}{\partial t}\right\rangle + \left\langle Rn_a m_a \left(\vec{V}_a \mathbf{g}\nabla\right)V_{a\phi}\right\rangle + \left\langle R\frac{1}{h_\phi}\frac{\partial p_a}{\partial \phi}\right\rangle + \left\langle R\left(\nabla\vec{\mathbf{g}\tau}_a\right)_\phi\right\rangle =$$

$$\left\langle Rn_a e_a\left(-\frac{1}{h_\phi}\frac{\partial \Phi}{\partial \phi}-\frac{\partial A_\phi}{\partial t}\right)\right\rangle + \left\langle Rn_a e_a\left(V_{ar}B_\theta - V_{a\theta}B_r\right)\right\rangle + \left\langle RF_{a\phi}^1\right\rangle + \left\langle RS_{a\phi}^1\right\rangle - \left\langle Rm_a V_{a\phi}S_a^0\right\rangle \qquad (3)$$

and all the neglected terms plus any high-order perturbation effects are collectively defined to be "anomalous" or "*effective* $Vr \times B_\theta$" by assuming that most anomalous effects cause radial movement of the ion species. This *effective* $Vr \times B_\theta$ allows a prediction of radial fluxes for all the ions species to couple plasma rotation study with particle transport. In this work, analysis results of the four axisymmetric KSTAR discharges (two H-modes with Ar injected and two L-modes without any impurity injection) are presented and discussed with a simulation of tungsten impurity in tokamak plasmas.

2. Rotation analysis results

Fig. 1 shows the calculated Vt, Vp, and Er for one of the H-modes analyzed (#5505-2500ms). Overall, the calculated Vt's for all the discharges analyzed stays within 10% of the measurements, providing confidence in other calculation results, including predicted "effective Vr" and its corresponding "effective or anomalous" radial fluxes. Note that GTROTA[4] uses the Miller flux surface geometry[5] for higher accuracy in rotation and Er calculations. Thus the red Er profile in Fig. 1 is calculated with Miller geometry while the black profile calculated with circular flux surface assumption, which is commonly used by experimentalists to get Er from rotation measurements.
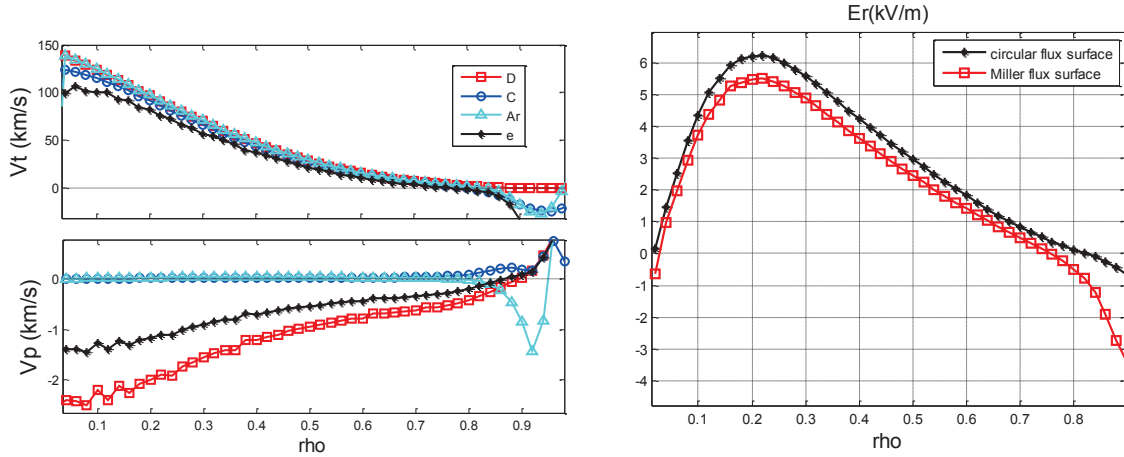
Fig. 1. Vt, Vp, and Er for KSTAR #5505-2500ms(Vt: positive co-Ip / Vp: positive outboard mid-plane)

3. Comparisons of toroidal torque contributions

Fig. 2 shows all the calculated torque density terms in (3) and the effective radial fluxes in the discharge #5505-2500ms, with positive being in co-Ip direction. Overall, we find that the main torque competition is between the frictional and the anomalous torques for all the ion species in the tokamak plasmas. For deuterium, other torques are not completely negligible but are for all the impurities. It is interesting to find that two dominant torque terms for carbon and Ar are showing completely opposite torque directions, which is consistent with all other discharges analyzed, which will be the subject of further investigations.

4. Discussion

The coupling of plasma rotation and transport studies introduces a direct calculation of effective Vr for all the ions in confined plasmas based on the basic principle of closing (1) with (2). From the fact that two most dominant toques come from the frictional and anomalous effects, the collisionalities of all

the ion species seem to play an important role in determining their relative torque balance. The left figure in Fig. 3 shows the ranges of normalized collisionalities for all three ion species in the discharge #5505-2500ms. We see that the impurities become more collisional as their mass gets heavier while deuterium collisionality covers from the banana regime in the core to the Pfisch-Schluter regime in the edge. A simulation study by simply replacing Ar with tungsten(W) in #5505-2500ms also shows notable shifts in these collisionalities and as a consequence shows that the relative torque contributions of all the ions show notable shifts even with the changes in 1% heavy impurity species as shown in Fig. 4. Investigation of collisionality effects will continue in the future with more diverse discharges analyzed from diverse tokamak devices.
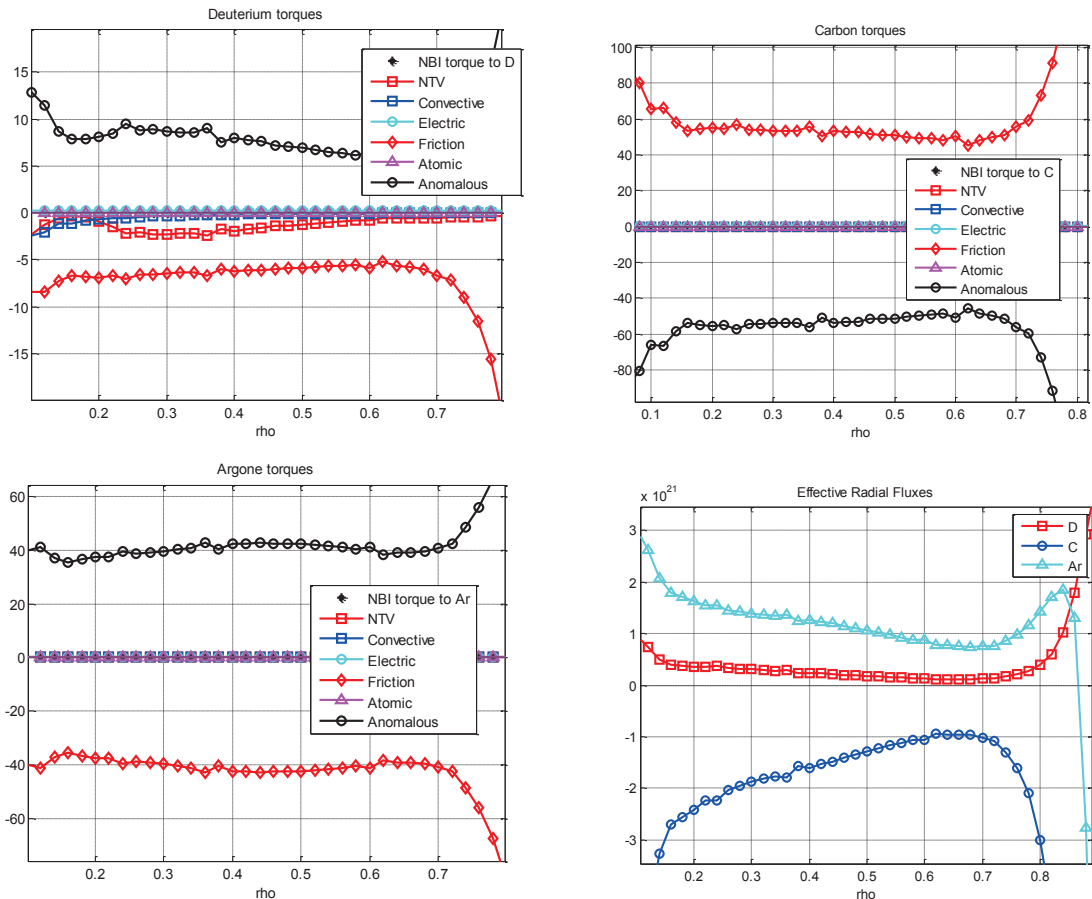
Fig. 2. Toroidal torque density comparisons and effective radial fluxes for #5505-2500ms
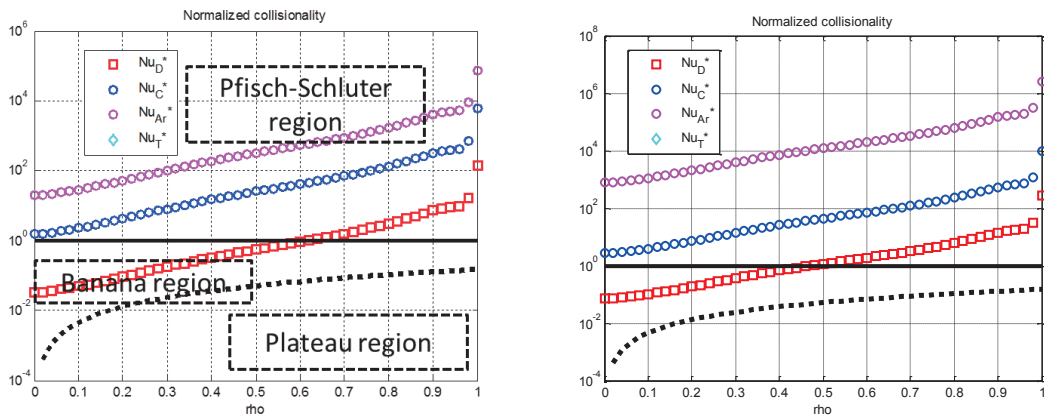
Fig. 3. Normalized collisionalities (Ar in the right figure is for W)

28
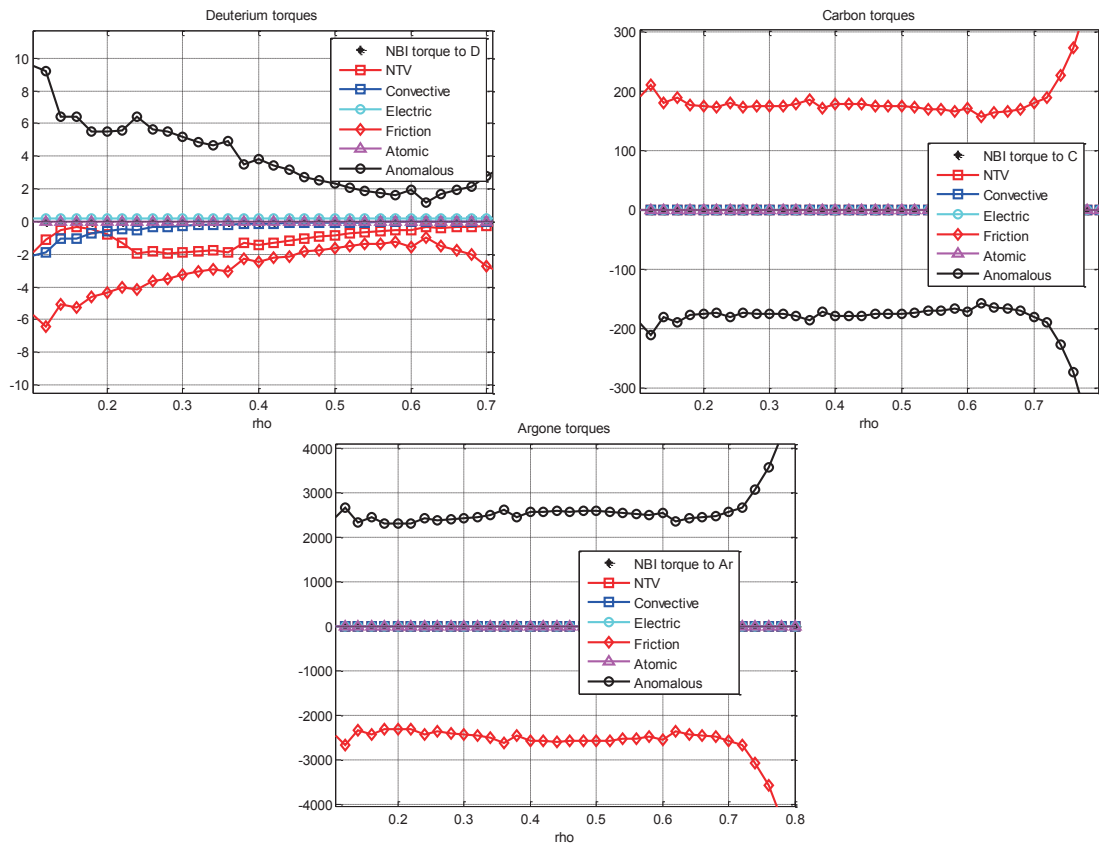
Fig. 4. Simulation results with Ar replaced with W in #5505-2500ms

4. Conclusion

A coupled study of plasma rotation and transport will continue in the future to answer practical questions in plasma researches such as the collisionality effect to the rotation and transport of multiple ion species. This study is aimed at providing theoretical and numerical models to calculate plasma rotation and transport of deuterium based on the impurity measurements, which are readily available in most discharges, while providing self-consistent calculations of rotation and effective radial fluxes coupled based on the first principle of closing (1) with (2).

References
[1] W.A. Houlberg, K.C. Shaing, S.P. Hirshman, M.C. Zarnstorff, Phys. of Plasmas, 4 (1997) 3230-3242.
[2] C. Bae, W.M. Stacey, W.M. Solomon, Nucl. Fusion, 53 (2013) 043011.
[3] C. Bae, W.M. Stacey, S.G. Lee, L. Terzolo, Phys. of Plasmas, 21 (2014).
[4] C. Bae, W.M. Stacey, T.D. Morley, Comp. Phys. Communications, 184 (2013) 2571-2587.
[5] R.L. Miller, M.S. Chu, J.M. Greene, et. al., Phys. of Plasmas, 5 (1998) 973-978.

Stability of the KSTAR H-mode plasma boundary with perpendicular flow shear

G. S. Yun[1], Y.M. Oh[1,2], H.J. Hwang[1], J. E. Lee[1], M.H. Kim[1], J. Lee[3], and M. Leconte[4]

[1]Pohang University of Science and Technology, Pohang 37673, Korea

[2] Beijing Computational Science Research Center, Beijing 100193, China

[3]Ulsan National Institute of Science and Technology, Ulsan 44919, Korea

[4]National Fusion Research Institute, Daejeon 34133, Korea

Abstract

The boundary of high-temperature plasma confined by a toroidal magnetic field structure (a.k.a. tokamak) often shows quasi-periodic relaxation oscillations between high and low energy states. On the KSTAR tokamak, the relaxation oscillation consists of a quasi-steady state characterized by field-aligned filamentary eigenmodes, an abrupt phase transition into non-modal filamentary structure, and its rapid burst leading to a large loss of heat and particle. We propose a phenomenological yet very general model including the effects of time-varying perpendicular flow shear, turbulent transport, and pressure profile. Our model shows that the amplitude and shear of the flow across the plasma boundary are the key parameters determining the nonlinear oscillation. Numerical solutions for a range of the flow amplitude and shear indicate that a steady-state exists only for weak flow. This result suggest that (1) the abrupt transition from the quasi-steady eigenmode to the non-modal state is due to an increase of the flow, and (2) the suppression of filament burst by external magnetic perturbations can be achieved via the reduction of the shear flow.

1. Introduction

In conventional tokamaks, edge-localized modes (ELMs) are described as semi-periodic explosive transport events in the boundary of high confinement (H-) mode plasmas that are triggered by exponentially growing ballooning and external kink modes on the low field side (LFS) of the plasma. Note that the term 'ELM' indicates a magnetohydrodynamic (MHD) eigenmode or the edge transport event triggered by the crash of the mode depending on the context. In this article, the latter is termed as 'ELM crash' or simply 'crash' for clarity. The explosive crashes associated with ELMs are most easily detected by optical emission signals (Dα line) which captures the aftermath of the collapse of the edge confinement, i.e., the particle and heat flux into the scrape-off layer across the last closed flux surface (LCFS).

Some MHD modes prior to the onset of crash called precursors have been occasionally observed by magnetic pickup coils (Mirnov probe). However, it has not been clear whether those precursor modes were the same ELMs driven by ballooning and external kink modes or something different. The ELM crashes are empirically classified [1] according to the dependence of the crash cycle frequency (f_{crash}) on the energy flux through the separatrix (P_{LCFS}) and the existence of the magnetic precursor: Type I ELM crashes show $df_{crash}/dP_{LCFS} > 0$ with larger crash amplitude without precursor while Type III ELM crashes show

df_{ELM}/dP_{LCFS} < 0 with smaller crash amplitude without precursors.

The ELMs and their crashes visualized by an advanced imaging diagnostics [2] with microsecond time resolution on the KSTAR tokamak appear substantially more complex than the conventional picture. The time-resolved images revealed that the modes evolve in three distinctive stages as illustrated in Figure 1: (1) Quasi-steady (stable) filamentary mode [3] with long life time (up to ~100 ms), (2) Abrupt structural transformation into non-modal filaments near the onset of crash [4], and (3) Multiple filament bursts during the crash phase (Fig.1d). In the quasi-steady state, abrupt mode transitions are often observed in the middle of the inter-crash period [5] (Fig.1c)
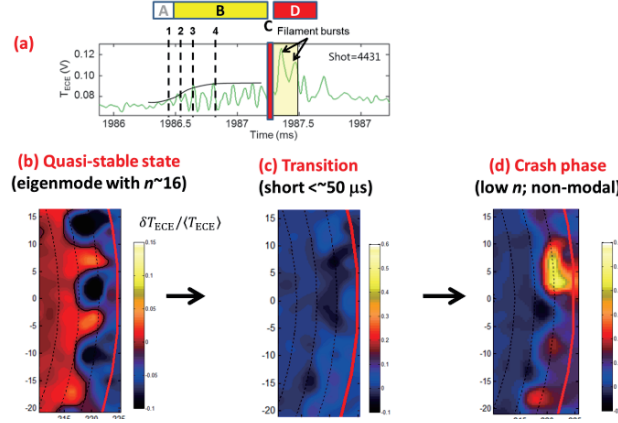
Figure 1 (a) Example of ELM cycle on KSTAR (#4431, H-mode discharge). Reproduced from [2]. The time trace is the intensity of electron cyclotron emission (ECE) from the low field side mid-plane. The labels B, C, and D indicate the quasi-steady state, the transition period, and the crash phase, respectively. (b-d) ECE images showing the transition from an eigenmodes-like filament structure in the quasi-stable state to a non-modal structure in the crash phase period via a short transition period.

2. Ginzburg-Landau model with time-varying perpendicular shear flow for the ELM dynamics

To understand the nonlinear ELM dynamics, a Ginzburg-Landau model for the perturbed pressure was proposed [6] based on reduced MHD equations and, in particular, the effect of the shear was analyzed showing that there can exist a linearly stable steady state for small shear but not for large shear [7]. Recently, the model was extended to consider the time-varying flow shear [8] and found that it is the key to accessing different dynamical states. The model equation for a pressure perturbation mode $\tilde{p} = p(x,t)\exp(-i\omega t + k_y y)$ with a prescribed time-varying perpendicular flow, $u_y(x,t) = A(t)V_s(x) + u_0$ with the profile $V_s(x) = \tanh sx$ and the amplitude $A(t)$, has the form of a generalized Ginzburg-Landau equation (GLE) given by

$$\partial_t \tilde{p} + iA(t)V_s(x)\tilde{p} + \gamma|\tilde{p}|^2\tilde{p} = (-iu_0 + \gamma_L)\tilde{p} + \chi\nabla^2\tilde{p} \qquad (1)$$

where γ_L is the linear growth rate of the mode, γ_N is the nonlinear damping which accounts the increasing

transport for larger $\tilde{p}$, and χ is the diffusion coefficient due to turbulent fluctuations. Figure 2(a) summarizes numerical solutions to the GLE revealing a sharp boundary separating the steady-state region and the oscillatory-state region, corresponding to low shear flow and high shear flow, respectively.
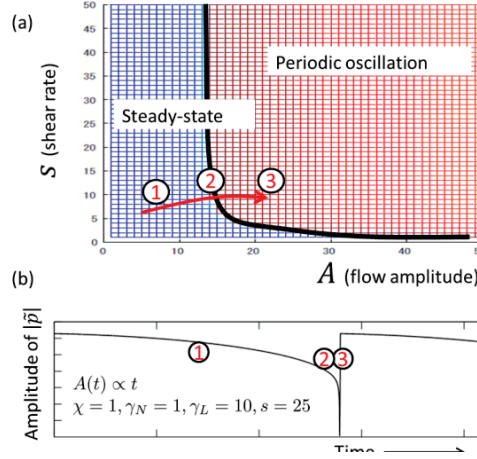
Figure **2** Transition from the steady state to the oscillatory state. (a) The two types of solutions to the GLE in *A-s* space are sharply separated by a boundary (thick solid curve labeled by ②). (b) Example of a numerical solution to the GLE, showing the transition from quasi-steady state ① to the non-steady (oscillatory) state ③.

This result provides a natural interpretation on the experimentally observed transition from the quasi-steady eigenmode (phase B in Fig.1 or state ① in Fig.2) to the crash phase (phase D in Fig. 1 or state ③ in Fig. 2). An numerical example of the rapid transition is demonstrated in Fig.2(b), where the flow shear amplitude $A(t)$ is linearly increased. According to this GLE model, a quasi-steady eigenmode will initially grow. As the flow increases (e.g. due to the development of radial electric field [1] and the associated buildup of pressure gradient) and eventually passes the transition boundary, the steady state can no longer exist, which is consistent with the experimental observation of the abrupt disappearance of the eigenmode (Fig. 1(b)). The subsequent appearance of nonmodal filament is not accounted by the GLE model, which remains as a future work. Note that it is the nonmodal filament which bursts and initiates the collapse of the boundary [4].

The GLE model can be easily extended to include multiple modes [8]. When two modes are included, the model can reproduce even the mode transitions during the inter-crash period that were observed frequently on the KSTAR H-mode discharges [5]. In this case, it is again the time-varying flow shear $A(t)$ which determines the dominant mode [8].

The GLE model can also provide similar interpretation for the suppression of ELM crash in H-mode discharges by resonant magnet perturbation (RMP). The RMP can reduce the flow shear in the edge (which would correspond to the reversed arrow direction in Fig.2(a)), thereby, only quasi-steady eigenmodes can exist in the edge. On the KSTAR, quasi-stable eigenmodes were routinely observed when the crash was suppressed by *n*=1 RMP [9], supporting the scenario based on the GLE model.

3. Summary

The GLE model captures the salient features of the ELM dynamics observed on the KSTAR despite its limitations such as prescribed $A(t)$ and constant γ_L. The GLE model predictions are consistent with the semi-periodic oscillations of the boundary of the H-mode plasmas through distinct stages, namely, quasi-stable state(s) of eigenmodes-like filaments with intermediate n and abrupt transition to nonmodal filament (low-n). This dynamic oscillation is mainly controlled by time-varying perpendicular flow according to the GLE model because the perpendicular flow profile determines the stability of eigenmodes (oscillatory vs. steady). The GLE model can also provide a qualitative explanation for the ELM crash suppression by RMP. The RMP reduces the flow below the threshold (Fig. 2(a)) and thereby the non-bursting quasi-stable eigenmode(s) can exist.

Acknowledgements

References

[1] H. Zohm, "Edge localized modes (ELMs)", Plasma Phys. Control. Fusion **38** (1996) 105–128.

[2] G.S. Yun *et al.*, "Quasi 3-D ECE Imaging System for Study of MHD instabilities in KSTAR", Rev. Sci. Instrum. **85** (2014) 11D820.

[3] G.S. Yun *et al*., "Two-dimensional visualization of growth and burst of the edge-localized filaments in KSTAR H-mode plasmas", Phys. Rev. Lett. **107** (2011) 045004.

[4] J.E. Lee *et al.*, "Solitary perturbations in the steep boundary of magnetized toroidal plasma", Scientific Reports **7** (2017) 45075.

[5] J.E. Lee *et al.*, "Toroidal mode number transition of the edge localized modes in the KSTAR plasmas", Nucl. Fusion **55** (2015) 113035.

[6] M. Leconte, Y.M. Jeon, and G.S. Yun, "Ginzburg-Landau model in a finite shear-layer and onset of transport barrier nonlinear oscillations: a paradigm for type-III ELMs", Contributions to Plasma Physics, **56** (2016) 736–741.

[7] Y.M. Oh, G.S. Yun, and H.J. Hwang, "Mathematical analysis of long-time behavior of magnetized fluid instabilities with shear flow", https://arxiv.org/abs/1706.08036

[8] Y.M. Oh, H.J. Hwang, M. Leconte, and G.S. Yun, "The effect of time-varying flow-shear on the nonlinear stability of the boundary of magnetized toroidal plasmas", https://arxiv.org/abs/1708.04031

[9] J. Lee et al, "Nonlinear interaction of edge-localized modes and turbulent eddies in toroidal plasma under n=1 magnetic perturbation", Phys. Rev. Lett. **117** (2016) 075001

Precursors and Control of ELMs in Stellarator/Helical Plasmas

K. Toi, S. Ohdachi, K. Ogawa, Y. Suzuki, LHD Experiment Group

National Institute for Fusion Science, Toki 509-5292, Gifu, Japan

Abstract

In contrast to H-mode plasmas in tokamaks, resistive interchange modes (RICs) are thought to be most likely candidate of an ELM trigger in present-day stellarator/helical plasmas. In H-mode plasmas of LHD, two types of ELMs are observed, depending on the magnetic axis position of the vacuum field, R_{ax}. In an inward-shifted configuration of R_{ax}=3.6m, n=3/m=2 mode fluctuations destabilized in L-phase are further increased by edge transport barrier formation and lead to triggering high frequency small ELMs. Three components b_r, b_θ and b_φ of magnetic fluctuations of n=3/m=2 mode are enhanced with the nearly same amplitude, i.e., $b_r \sim b_\theta \sim b_\varphi$. The growth of b_r during nonlinear phase of RICs indicates magnetic island formation by RICs. Moreover, the generation of b_φ comparable to b_θ suggests that plasma compressibility would suppress rapid growth of RICs and avoid exciation of harmful large ELMs. On the other hand, in an outward-shifted configuration of R_{ax}=3.9m, RICs are clearly suppressed just after the L-H transition. However, large amplitude ELMs are triggered by n=1/m=1 RIC in this configuration, leading to substantial drop of the plasma stored energy. Just before an ELM onset, magnetic fluctuations b_r and b_θ of n=1/m=1 RIC grow rapidly, while b_φ fluctuations unchange. In this case, nearly imcompressive plasma displacement might grow just before the ELM, and lead to large amplitude ELMs.

1. Introduction

Edge localized modes (ELMs) in tokamak plasmas are thought to be triggered by peeling (or kink) mode, ballooning mode, or their combination[1,2]. These instabilities are destabilized by steep pressure gradient and/or high toroidal current density in the pedestal or edge transport barrier (ETB) region. Control methods of ELMs are being developed, based on understanding of the characteristics of such MHD instabilities[3]. On the other hand, ELMs were also observed in W7-AS stellarator[4] and LHD [5, 6]. The likely candidate of an ELM trigger was thought to be resistive interchange mode (RIC), because ETB region is stable against ideal interchange mode. The RIC is a pressure driven instability destabilized at the rational surface located in magnetic hill region. In net plasma current free stellarator/helical plasmas, current driven instabilities observed in tokamak plasmas are stable. ELM characteristics and the control methods in stellarator/helical devices may have some differences for those in tokamaks.

In this paper, we discuss characteristics of ELMs in H-modes obtained in two typical magnetic configurations of LHD. That is, one is the inward-shifted configuration of R_{ax}=3.6m, and the other the outward-shifted configuration of R_{ax}=3.9m. Here, R_{ax} is the magnetic axis position of the vacuum field. Although high frequency small ELMs are excited accompanying RICs even during H-phase in the former configuration (R_{ax}=3.6 m), low frequency large ELMs are excited in the latter configuration (R_{ax}=3.9 m),

interrupting ELM free phase where RICs are suppressed [7-9].

2. ELMs in the inward-shifted configuration of R_{ax}=3.6 m

The waveforms of a typical H-mode in the R_{ax}=3.6 m configuration is shown in Fig.1(a). High frequency ELMs having small amplitude are excited, although the time resolution of H_α emission signal in this figure is not high enough to indicate the high frequency ELMs clearly. The L-to-H transition takes place at t= 4.165 s. The electron temperature (T_e), density (n_e) and pressure (P_e) profile at t=4.133 s (just blue points: before the transition) and t=4.200 s (red points: just after the transition) are compared in Fig.1(b). The T_e profile remains unchanged, while n_e profile exhibits enhanced edge gradient after the transition. The edge gradient of P_e is increased due to the increase in n_e near the edge. This increase at the transition noticeably enhances n=3/m=2 magnetic fluctuations which are already destabilized in L-phase, as shown in Fig.2. All three components of magnetic fluctuations, i.e., radial (b_r), poloidal (b_θ) and toroidal (b_φ) are measured by using a magnetic probe-cube placed in a horizontally elongated section. After transition, ELMs are excited with high repetition rate but small amplitude, synchronizing n=3/m=2 magnetic fluctuation bursts. As seen from Fig.2, b_r fluctuations are clearly enhanced, synchronizing with b_θ fluctuations.
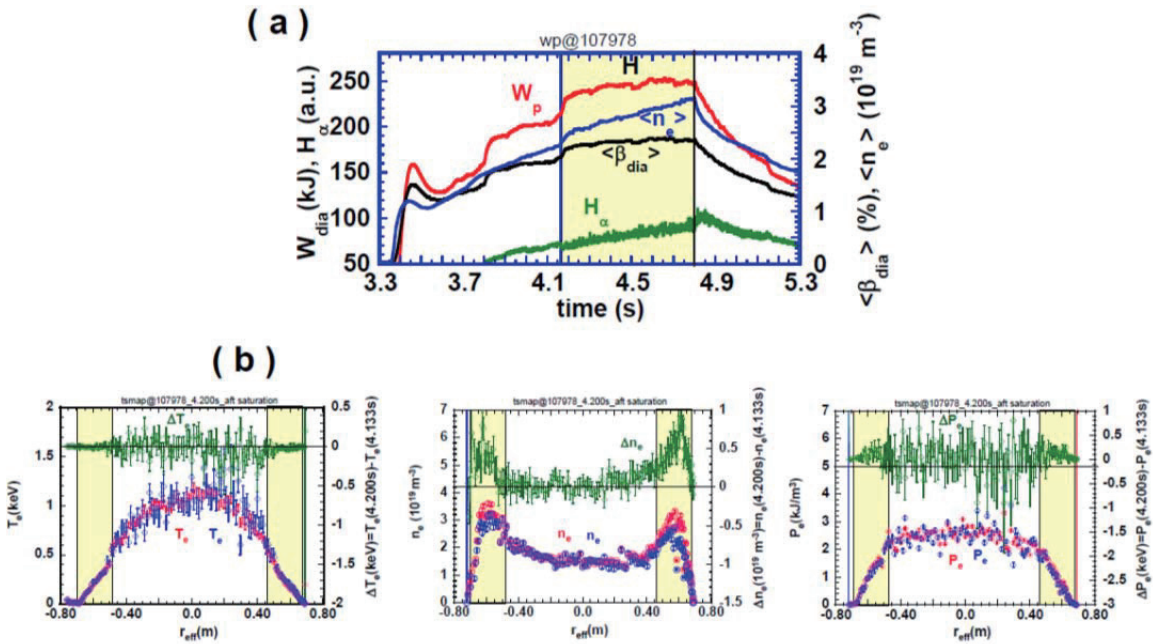
Fig.1 (a) Waveforms of a typical H-mode plasma obtained in the R_{ax}=3.6 m configuration on LHD. (b) Comparison of T_e, n_e, P_e and their increases by the L-to-H transition t=4.165 s, where the profiles are measured at t=4.1333 s (blue points: before the transition) and t=4.200 s (red points: after the transition). The increases in T_e, n_e and P_e are shown with green points. The profiles are plotted as a function of the effective minor radius r_{eff} derived from the T_e data by Thomson scattering.
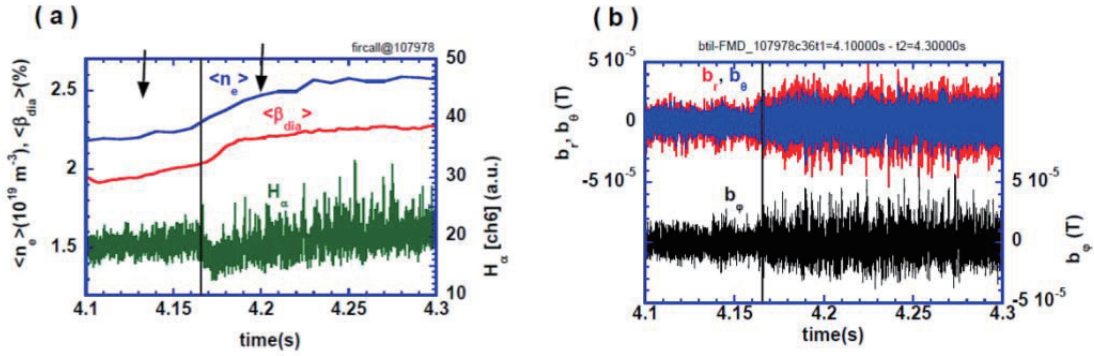
Fig.2 (a) Zoomed waveforms arounf the L-to-H transition in the H-mode shot shown in Fig.1.   The radial profiles of T_e, n_e and P_e are measured at two time slices indicated by arrows in Fig.(a).   (b) Time evolutions of b_r, b_θ and b_φ across the transition.

3. ELMs in the outward-shifted configuration of R_{ax}=3.9 m

In this configuration, several large amplitude ELMs interrupt the ELM free phase where n=1/m=1 magnetic fluctuations destabilized in L-phase are clearly suppressed, as shown in Fig.3 (a).   The changes in T_e, n_e and P_e profiles are similar to those in the R_{ax}=3.6m configuration, as shown in Fig.3(b).   That is, T_e-profile remains unchanges in ELM free H-phase and L-phase, while the edge region of n_e-profile dramatically increases, developing ETB. P_e profile in H-phase has a steep gradient near the edge because of n_e-increase in the edge.   In H-modes of this magnetic configuration, more steeper pressure gradient in the ETB is realized, compared with that in the R_{ax}=3.6 m configuration shown in Fig.1(b).   It should noted that magnetic fluctuations are suppressed for the P_e-profile having steep gradient at the edge in H-phase, but are enhanced for the P_e-profile with loose gradient in L-phase, as seen from Figs. 3(a) and (b).
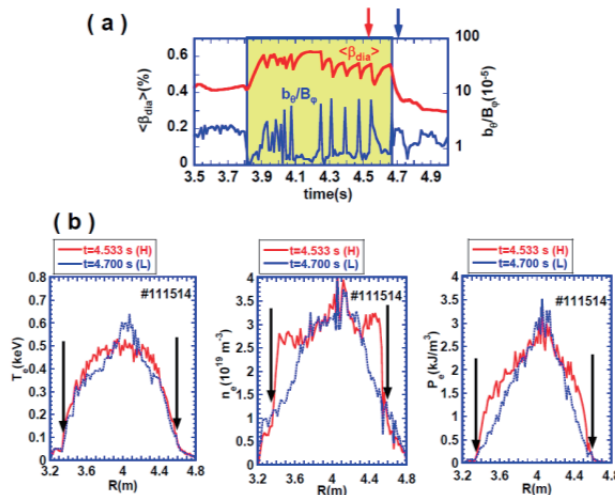
Fig.3 (a) Waveforms of a typical H-mode plasma obtained in the R_{ax}=3.9 m configuration on LHD. Time evolution of b_θ/B_φ is shown with a log-scale.   (b) Comparison of T_e, n_e, P_e and their increases by the L-to-H transition at t=4.165 s, where the profiles are measured at t=4.1333 s (before the transition) and t=4.200 s (after the transition).   The profiles are plotted as a function of the major radius R by Thomson scattering in the horizontally elongated section.

Magnetic fluctuations b_r and b_θ having $n=1/m=1$ structure quickly grow from a few milliseconds before the ELM onset, and lead to a large ELM onset (Figs.4(a) and (b)).   As seen from Fig.4(b), b_φ fluctuations do not show any visible change and then grow dramatically at the onset of the large ELM, and then glowrapidly during the ELM.
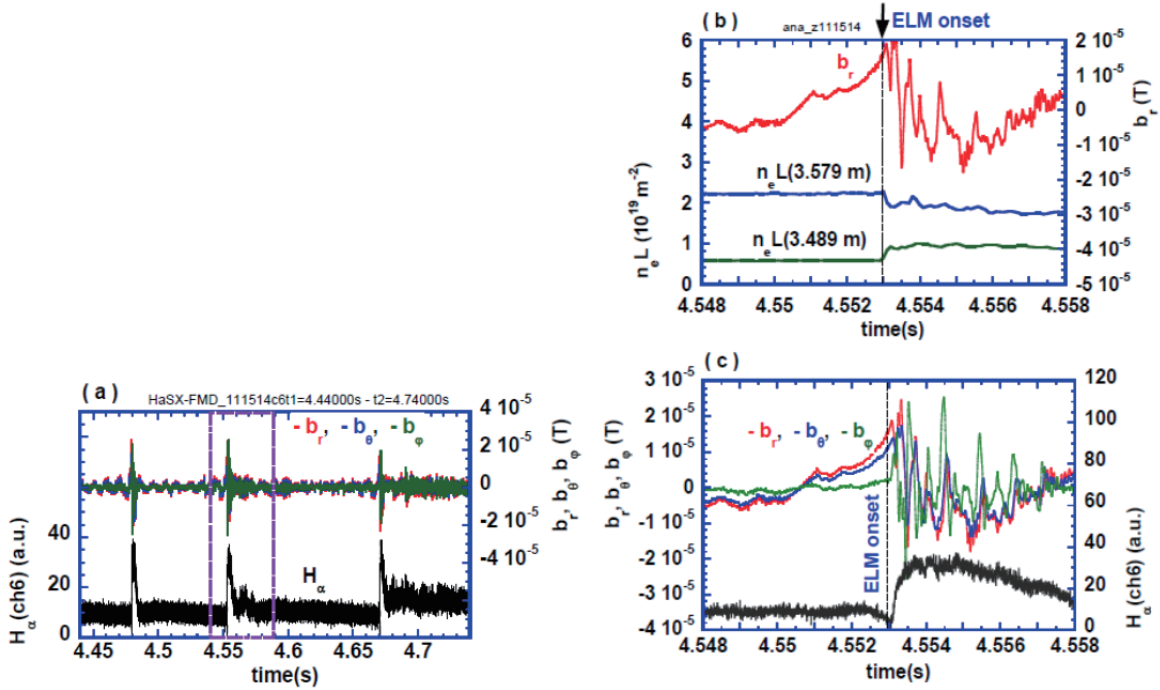
Fig.4 (a) Time evolution of magnetic fluctuations b_r, b_θ and b_φ in the phase three ELMs.   The third ELM quenches the H-pahse and goes back to L-pahse.   (b) Zoomed evolutions of b_r and line electron densities at two edge chords, where the $n_eL(3.579m)$ is just inside the ETB, and $n_eL(3.489m)$ just outside the ETB. The vertical line indicates the ELM onset defined with the drop in $n_eL(3.579$ m).   (c) Time evolutions of b_r, b_θ and b_φ together with the H_α emission signal.

4. Possible ELM control methods

In LHD, the large ELMs triggered by $n=1/m=1$ RICs were converted to small ELMs by resonant magnetic field perturbations (RMPs) dominated by $n=1/m=1$ Fourier components.   This lead to successful ELM mitigation [9].   The repetition frequency of large ELMs was ~5 Hz to ~ 50 Hz in the case without RMPs.   The frequency of mitigated ELMs by RMPs was ~50 Hz to ~150 Hz.   It should be noted that the latter frequency is lower than the frequency of ELMs in the R_{ax}=3.6 m configuration, i. e.,   ~0.2 kHz to ~ 4 kHz [8].   The characters of thus mitigated ELMs seem to be different from those of ELMs in the R_{ax}=3.6 m configuration.   Time evolutions of magnetic fluctuations b_r, b_θ and b_φ of mitigated ELMs are shown in Fig.5.   They are quite similar to that in large ELMs shown in Fig.4, except the repetition frequency and amplitude.

ELM mitigation by RMPs is caused by slight reduction of the edge pressure gradient.   That is, global energy confinement is slightly degraded by reduction of the edge pressure gradient using RMPs.   The

technique using RMPs is successfully demonstrated in tokamaks where current driven peeling mode and pressure driven ballooning mode are key players in triggering ELMs. In LHD, RMPs also reduce the edge pressure gradient, slightly degrading edge stability against RICs. For medum beta plasmas in stellaratot/helical devices such as LHD, RICs are dominantly destabilized near the edge and can trigger ELMs. Linear growth rate of RICs is reduced as $S^{-1/3}$ and $\hat{s}^{-2/3}$, where S and $\hat{s}$ are magnetic Reynold number and the global magnetic shear. Paid attention to the character of RICs, the increase in S and/or $\hat{s}$ by electron heating (ECH) and current drive (ECCD) by electron cyclotron waves may be effective for ELM control. Actually, the increase of S by on-axis ECH was effectively suppressed $n=1/m=1$ RICs destabilized near the edge, which also lead to suppression of energetic-ion driven resistive interchange mode (EIC) [11]. Optimum combination of ECH or ECCH with RMPs will be a promising control method of RICs and ELMs in future stellarator/helical devices.
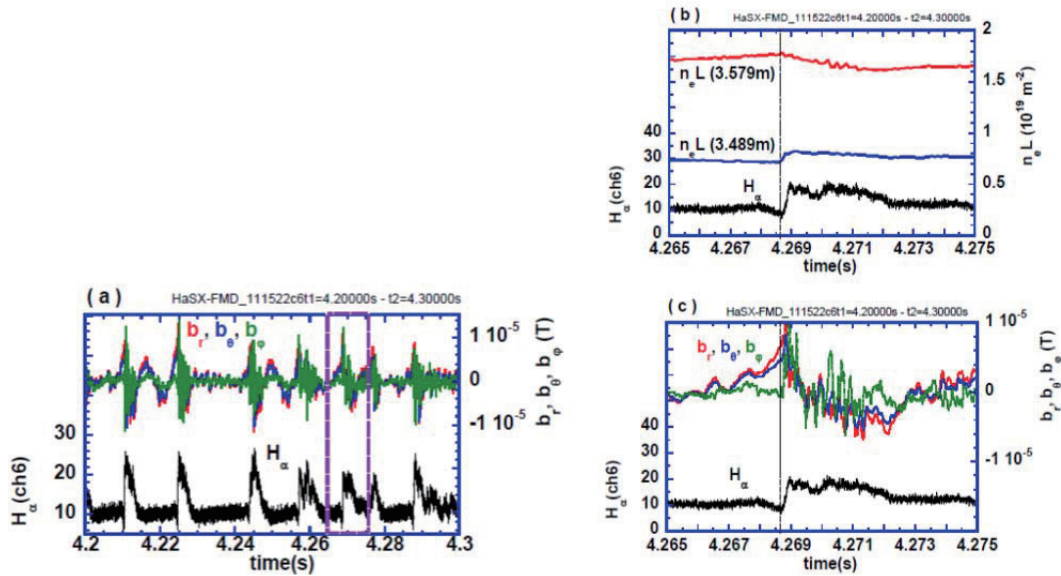
Fig.5 (a) Time evolution of magnetic fluctuations b_r, b_θ and b_φ in the phase seven small ELMs mitigated by RMPs. (b) Zoomed evolutions of b_r and line electron densities at two edge chords, where the n_eL(3.579m) is just inside the ETB, and n_eL(3.489m) just outside the ETB. The vertical line indicates the ELM onset defined with the drop in n_eL(3.579 m). (c) Time evolutions of b_r, b_θ and b_φ together with the H_α emission signal.

4. Discussions

In the inward-shifted (R_{ax}=3.6m) and outward-shifted (R_{ax}=3.9 m) configurations of LHD, b_r fluctuations are induced as well as b_θ fluctuations, when steep pressure gradient region is formed in the plasma edge by L-to-H transition. In particular, large growth of b_r together with b_θ just before the ELM onset are clearly observed in the R_{ax}=3.9 m configuration. The observation of b_r fluctuations suggests that a tearing parity mode of $n=1/m=1$ RIC would grow, generating magnetic islands near the plasma edge having steep pressure gradient region where the rational surface of $\iota=1$ (ι: rotational transform) locates. In

the framework of the linear MHD theory, the RIC eigenfunction of radial displacement or scalor potential has an even function localized at the rational surface, that is, has an interchange parity. However, the eigenfunction of RIC having an interchange parity is not conserved during nonlinear evolution of RIC, and the tearing parity mode can be excited[12]. The tearing parity mode in RIC can generate magnetic island through magnetic reconnection. The above mentioned experimental results may be interpreted along this recent theoretical work.

The other important fnding is that b_φ fluctuations are enhanced having nearly the same amplitude with b_θ during the growth of resistive interchange modes, as seen from the H-mode plasmas in the R_{ax}=3.6 m configuration. According to MHD theory, $b_\varphi/b_\theta \sim (n/m)(r/R) \sim 1/4$ is inferred for the LHD plasma on the assumption of no radial plasma current [13]. The oberserved b_φ fluctuations are much larger than the prediction. MHD theory also tells us an approximate relation between toroidal magnetic fluctuations and plasma compressibility. That is, the ratio to the equilibrium toroidal field B_φ is expressed as, $\frac{b_\varphi}{B_\varphi} \approx$

$-div\xi_\perp$. Here, it is assumed that plasma displacement by RICs is dominated by that perpendicular to the equilibrium magnetic field. Enhanced b_φ fluctuations during nonlinear evolution of RICs and ELM exciation in the R_{ax}=3.6m configuration suggest that plasma compressibility might suppress rapid growth of RICs and relax to small and weak ELMs. A few theoretical works support the above possibility [14, 15]. During the growth of n=1/m=1 RIC in the R_{ax}=3.9m configuration, b_φ fluctuations are not enhanced until the onset of large ELMs or small ELMs mitigated by RMPs, as shown in Figs. 4 and 5. In the H-mode phase of the configuration plasma compressibility would not play a key role in contrast to that in the R_{ax}=3.6m configuration. Condition that plasma compressibility would play an important role in enhancing stability effects of RICs is under investigation in various H-mode plasma of LHD.

5. Summary

ELMs observed in H-mode plasmas of LHD exhibit different characters, depending on the inward-shifted (R_{ax}=3.6m) or the outward-shifted configuration (R_{ax}=3.9m). In the R_{ax}=3.6m configuration, high frequency and small amplitude ELMs are usualyy excited by the growth of n=3/m=2 RICs in the plasma edge region, after the L-to-H transition. On the other hand, in the R_{ax}=3.9 m configuration n=1/m=1 RIC is clearly suppressed by the transition, which realizes ELM free pahses much longer than the global energy confinement time. The ELM free phase is interrupted by a large amplitude ELM with low repetition frequency. In the former configuration, three components b_r, b_θ and b_φ of magnetic fluctuations are enhanced having nearly same amplitude just after the transition. In the latter configuration, b_r and b_θ rapidly grow a few milliseconds before the large ELM onset, while b_φ does not grow until the ELM onset. Growth of b_r fluctuations indicates generation of the tearing parity mode in resistive interchange modes and resulting magnetic island formation and ELM generation. Moreover, growth of b_φ fluctuations typically observed in the R_{ax}=3.6 m configuration suggests that plasma compressibility would contribute to suppression of harmfully large growth of RICs. Further studies of stiblizing effects of RICs by plasma compressibility, high magnetic Reynold number and global magnetic shear are needed in dedicated experiments of LHD.

References

[1] P.B. Snyder et al, Phys. Plasmas **9** (2002) 2037.

[2] G.T.A. Huijsmans et al, Phys. Plasmas **22** (2015) 021805.

[3] A. Loarte et al, *Progress in the ITER physics basis*, chapter4 Nucl. Fusion **47** (2007) S203.

[4] A. Weller et al, Phys. Plasmas **8** (2001) 931.

[5] K. Toi et al., Nucl. Fusion **44** (2004) 217.

[6] K. Toi et al, Phys. Plasmas **12 (**2005) 020701.

[7] K. Toi et al, Fusion Sci. Technol. **58** (2010) 61.

[8] F. Watanabe et al, Contrib. Plasma Phys. **50 (**2010) 651.

[9] K. Toi et al, Nucl. Fusion **54 (**2014) 033001.

[11] X.D. Du et al., Phys. Rev. Lett. **118** (2017) 125001.

[12] M. Sato and A. Ishizawa, Phys. Plasmas **24** (2017) 082501.

[13] I.H. Hutchinson, *Principles of Plasma Diagnostics*, 2ⁿᵈ edition, Cambridge University Press, 2002.

[14] J. Todoroki, Plasma Fus. Res. 2002, www.jspf.or.jp/RCPDF/RC0011.pdf.

[15] O. Yamagishi et al., Phys. Plasmas **10** (2003) 2871.

Simulation Study of Quasi-snowflake divertor with Ne seeding

S.F. Mao[1], Y.F. Zhou[1], Z.P. Luo[2] and M.Y. Ye[1,2]

[1]School of Nuclear Science and Technology, University of Science and Technology of China, Hefei, Anhui 230026, PR China

[2]Institute of Plasma Physics, Chinese Academy of Sciences, Hefei, Anhui 230031, PR China

Abstract

To exhaust the huge power from core plasma, snowflake Divertor (SFD) is thought as a possible candidate for future fusion reactor. Because carbon is not allowed to use due to the unacceptable tritium retention, radiative impurity, such as neon, nitrogen and/or argon, is necessary to be seeded to radiate the power and therefore reduce the heat load onto divertor target. Meanwhile, the impurity concentration should be kept low to avoid degradation of plasma performance. In this study, a SOLPS simulation is performed for the SFD and lower-single null (LSN) divertor of China Fusion Engineering Test Reactor (CFETR) with neon seeding from the outer baffle. The puffing rate is scanned to have a ratio of radiated power to the power into the scrape-off layer (which is 100 MW in this study) up to ~ 80%. Along with the increasing of radiation power ratio, the effective charge number is increasing up to about 2.6-2.8. Furthermore, the outer divertor of SFD is found to have a abrupt transition to complete detachment while the inner divertor is re-attached, when the total radiation power is about ~ 50 MW.

1. Introduction

It is crucial to exhaust the huge power come from core plasma in future fusion reactor. For a fusion reactor of 1 -2 GW fusion power, considering the auxiliary heating power and core radiation, ~200 MW will enter into the scrape-off layer (SOL) [1] and exhausted in the divertor. However, for the divertor target, the heat flux has to be limited below 10 MW/m^2 [2]. The traditional LSN divertor, which is now adopted in ITER, may be of insufficient ability to exhaust the heat power for future fusion reactor. To find an effective way to reduce the heat flux onto divertor target, advanced divertor configurations, such as SFD [3,4], X-divertor [5], Super-X divertor [6] and X-point target divertor [7] are proposed with modified magnetic equilibrium, where an extra X point is introduced in addition to the single null in traditional divertor configuration [8].

Among the advanced divertors, SFD has the advantages that the sets of PF coils and divertor geometry are more compatible with the traditional divertor. In a snowflake divertor configuration, the flux expansion is significantly increased in comparison with traditional single-null divertor, which is of benefit to increase the wetted area and therefore decrease the peak heat load onto the divertor target. Meanwhile, the connection length and radiation volume are also increased in SFD configuration, which is considered of

benefit to radiate the power in scrape-off layer (SOL). SFD has already been achieved in TCV [9], NSTX [10], DIII-D [11] and EAST [12]. Significant decrease in heat flux onto divertor target is identified in experiment [13].

To reduce the heat load onto the divertor target, radiating the heat power by seeded impurities, such as neon, nitrogen and/or argon, are necessary in future fusion reactor, because the intrinsic carbon impurity existed in most tokamak experiments is not allowed in fusion reactor due to the tritium retention problem. As mentioned by Ryutov et al. [4], the increased geometrical connectivity between divertor and main SOL in SFD, due the flux expansion above the main X point, may lead to increased impurity flow to the upstream, which would cause the degradation of plasma performance.

To study the impurity screening effect under different ratio of radiation power to the power into SOL, a SOLPS [14] simulations are performed on the SFD and LSN divertor in CFETR [15-18] with neon seeding from outer baffle. Settings of the simulation are given in section 2, and the simulation results are shown in section 3. Section 4 contains the conclusion.

2. Simulation Settings

The key parameters of superconducting CFETR are: P_{fus} = 200 MW, I_p = 10 MA, B_T = 5.0 T, R = 5.7 m, a = 1.6 m, $\kappa \sim 2.0$, $q_{95} \geq 3$, $\beta_N \sim 2$ and P_{aux} = 100 ~150 MW. Assuming P_{rad} in core region is about 40 MW, $P_{SOL} = 0.2\ P_{fus} + P_{aux} - P_{rad}$ = 100 MW is assumed. The SFD configuration for CFETR is shown in Fig. 1. The distance between two nulls is 1240.58 mm, which is still far from the exact SF configuration and is named quasi-snowflake (QSF) here. The comparison of the connection length from the out-middle plane to the outer target between QSF and LSN configuration, are shown in Fig. 2. In QSF, the connection length is increased by a factor of ~1.5.
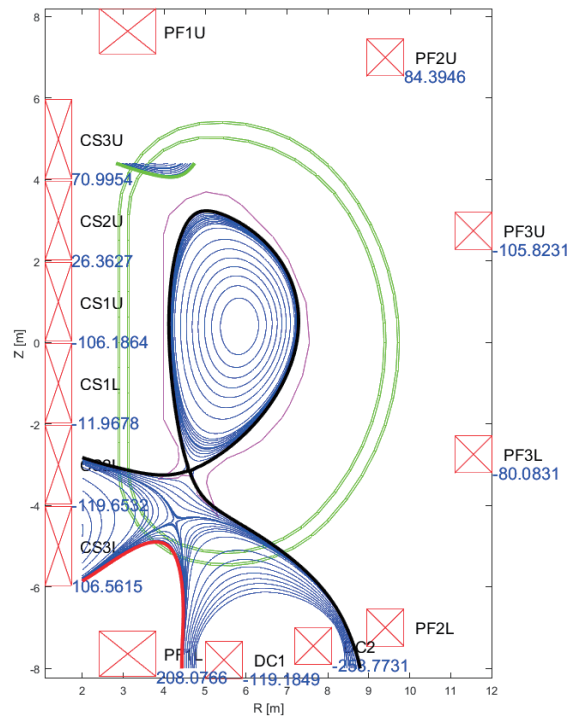
Fig. 1 SFD configuration for CFETR.
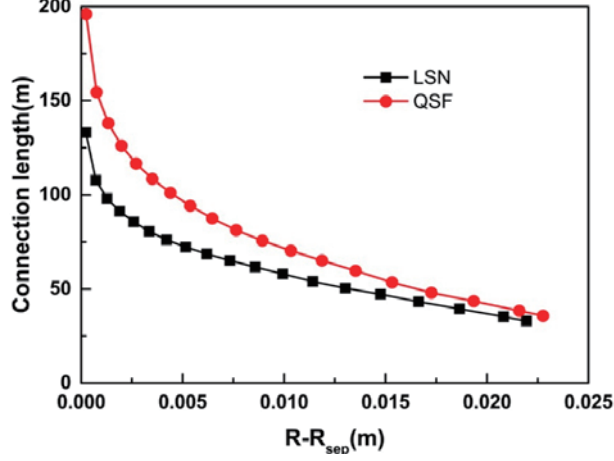
Fig. 2 Comparison of the connection length from the outer-middle plane to the outer target between SFD and LSN configuration.

Fig. 3 shows the computational grid for SFD and LSN. In the simulation, the D ion density is fixed to 8.0×10^{19} m^{-3} at core-edge interface, while the 100 MW power from core plasma is assumed equally divided by ions and electrons, i.e. $P_i = P_e = 50$ MW. Neon impurity is seeded from the outer baffle, and assumed zero flow at core-edge interface. The cross-field transport coefficients are set as: $D_\perp = 0.3$ m^2/s; $\chi_e = \chi_i = 1.0$ m^2/s.
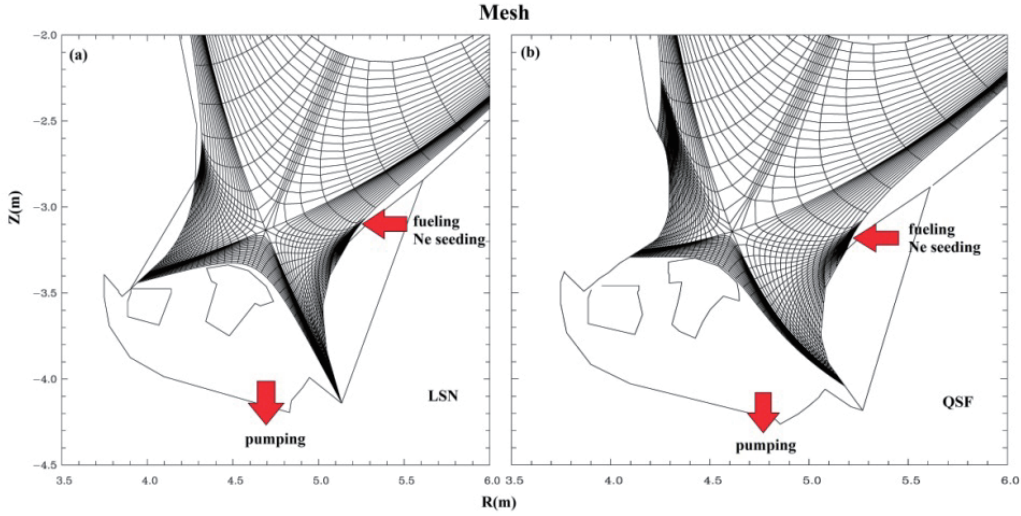
Fig. 3 Computational grid in SOLPS for (a) LSN and (b) QSF.

3. Simulation Results

In this work, the neon seeding rate is scanned to achieve different total radiation power P_{rad} up to ~ 80 MW. For all cases, the upstream condition is similar: ne and Te of separatrix at outer-middle plane is in the range of $2.0\text{-}2.4 \times 10^{19}$ m^{-3} and 260-300 eV, respectively. The relation between effective charge number Z_{eff} at core-edge interface and P_{rad} is shown in Fig. 4. Along with the increasing radiated power, the Z_{eff} is increasing. For the highest radiated power, the Z_{eff} is increased up to $\sim 2.6\text{-}2.8$, which is a typical value in present experiments, but higher than the expected value for ITER. The Z_{eff} for QSF is slightly larger than

that for LSN expect for the highest radiated power. For the case of total radiation power larger than ~ 75 MW, the impurity radiation region is moving into the separatrix for LSN, while for QSF the power is still radiated in the divertor, due to the advantage of increased connection length for QSF.
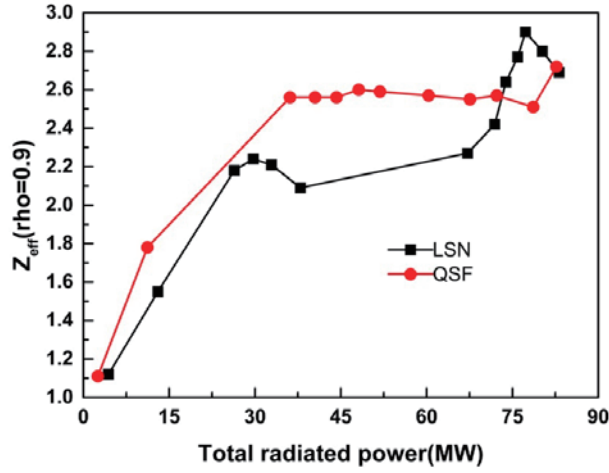
Fig. 4 Z_{eff} at the core-edge interface versus total radiated power for QSF and LSN.

The peak heat flux q_{pk} onto inner and outer divertor is shown in Fig. 5 for QSF and LSN. Before total radiated power reaches ~ 50 MW, the q_{pk} for both divertors are similar, where the inner divertor is already detached and outer divertor is still in the high-recycling regime. By increasing the neon seeding rate, the q_{pk} for both inner and outer target of LSN divertor is further decreasing, however, the abrupt jump appears for both inner and outer target for QSF. The outer divertor plasma is then completely detached, while a detach-attach transition happens in inner divertor for QSF.
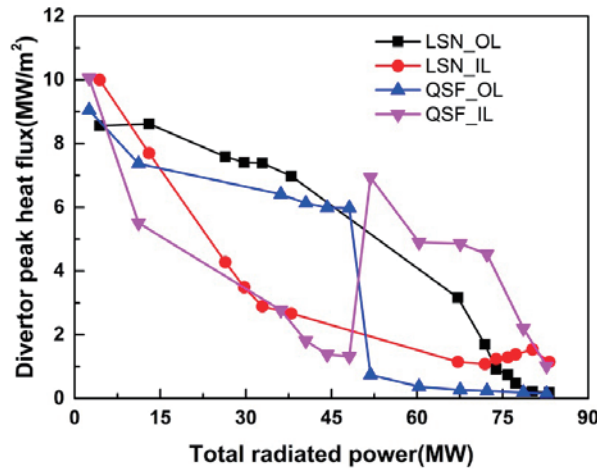
Fig. 5 Peak heat flux onto inner and outer divertor for QSF and LSN under different total radiated power.

In Fig. 6, the power flow into the inner and outer divertor together with the impurity radiation power is shown. It can be seen that both Z_{eff} (Fig. 4) and the power flow into divertor is continued for QSF during the transition, which means that the upstream conditions are not apparently influenced. However, the power flow into the outer divertor is almost radiated completely, which is related to the transition to complete detachment. At the same time, the radiated power in inner divertor is dropped by a factor of ~ 3, the

divertor is then re-attached. The change in the radiation power in the divertor region is the result of different impurity screening effects. Further work is needed to understand the transition for QSF.
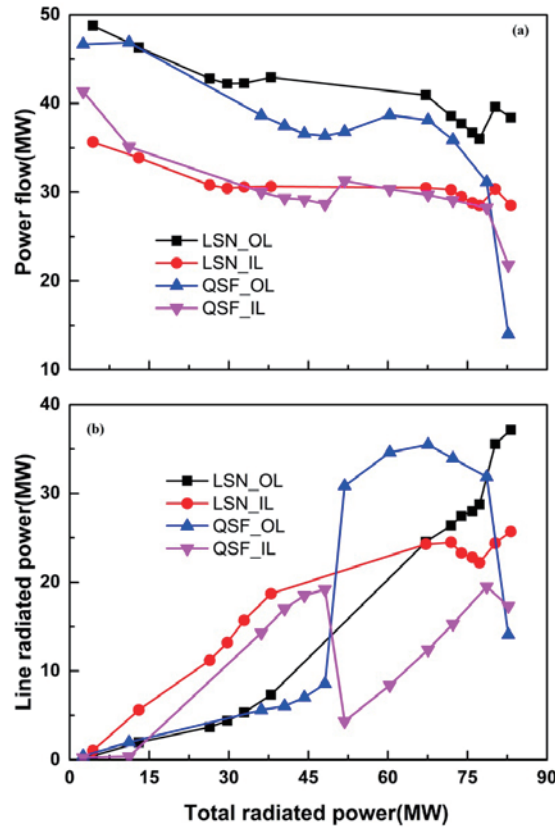
Fig. 6 (a) The power flow into inner and outer divertor and (b) the radiated power in corresponding region for QSF and LSN.

4. Conclusion

SOLPS simulation study of the QSF divertor for CFETR with neon impurity seeding is performed. The simulation results show that, when the radiation power ratio is increased up to ~80%, the Z_{eff} in the core region is lower than about 2.6-2.8 for QSF configuration, which is similar to the LSN configuration. Further analysis of the heat flux onto inner and outer divertor targets shows that a abrupt transition appears near the total radiation power ~ 50 MW for QSF. The outer divertor is complete detached after the transition, while the power flow into the divertor is almost completely radiated. Meanwhile, the radiation in the inner divertor is decreased by a factor of ~3, and the inner divertor is then re-attached. Further work is needed to understand the cause of this transition.

Acknowledgements

References

[1] F. Najmabadi and the ARIES Team, Fusion Eng. Des. **38** (1997) 3.

[2] Y. Shimomura, M. Keilhacker, K. Lackner, et al., Nucl. Fusion **23** (1983) 869.

[3] D.D. Ryutov, Phys. Plasmas **14** (2007) 064502.

[4] D.D. Ryutov, R.H. Cohen, T.D. Rognlien, et al., Phys. Plasmas **15** (2008) 092501.

[5] M. Kotschenreuther, P. Valanju, S. Mahajan, et al., Phys. Plasmas **14** (2007) 072502.

[6] P. Valanju, M. Kotschenreuther, S. Mahajan et al., Phys. Plasmas **16** (2009) 056110.

[7] B. LaBombard, E. Marmar, J. Irby, et al., Nucl. Fusion **55** (2015) 053020.

[8] F. Wagner, G. Becker, K. Behringer, et al., Phys. Rev. Lett. **49** (1982) 1408.

[9] F. Piras, S. Coda, B.P. Duval, et al., Phys. Rev. Lett. 105 (2010) 155003.

[10] V.A. Soukhanovskii, J.W. Ahn, R.E. Bell, et al., Nucl. Fusion 51 (2011) 012001.

[11] V.A. Soukhanovskii, S.L. Allen, M.E. Fenstermacher, et al., J. Nucl. Mater. 463 (2015) 1191.

[12] B.N. Wan, J.G. Li, H.Y. Guo, et al., Nucl. Fusion **55** (2015) 104015.

[13] D.D. Ryutov, V.A. Soukhanovskii, Phys. Plasma **22** (2015) 110901.

[14] D. Coster et al., Further developments of the edge transport simulation package SOLPS, in: Proc. of the 19th IAEA Conference, Fusion Energy, TH/P2-13, October, 2002.

[15] B.N. Wan, S.Y. Ding, J.P. Qian, et al., IEEE Trans. Plasma Sci. **42** (2014) 495.

[16] Y.T. Song, S.T. Wu, J.G. Li, et al., IEEE Trans. Plasma Sci. **42** (2014) 503.

[17] Z.P. Luo, B.J. Xiao, Y. Guo, M.Y. Ye, IEEE Trans. Plasma Sci. **42** (2014) 1021.

[18] S.F. Mao, Y. Guo, X.B. Peng, et al., J. Nucl. Mater. **463** (2015) 1233.

Carbon density in gap of castellated tungsten blocks in 2015 and 16 KSTAR campaign

Eunnam Bang[1], Suk-ho Hong[1,2,3], Kyungmin. Kim, Hongtack Kim[1]

[1]KSTAR research center, National Fusion Research Institute, Daejeon, Korea

Abstract

In this paper, we report the results from a series of experiment using special tungsten block tiles performed in KSTAR on fuel retention inside the gap of castellated blocks of different shapes and heights. Results are presented a comprehensive understanding on deposition procedure inside the gap and would give valuable information on the Be deposition inside the gap of castellated tungsten tiles in ITER. For the experiment, we have manufactured tiles consisting of four different shapes of tungsten blocks. These tungsten block tiles are exposed to L- and H-mode discharges during 2014-2016 campaign, then removed from the vacuum vessel after the campaign for further analysis. The contribution of the ion and charged exchange neutral can be separated on deposition pattern. From the carbon density profiles of castellated tungsten blocks in 2015, the least carbon is deposited on shadowed and open side of ITER chamfer shape among four kind shapes: conventional, trapezoidal, ITER chamfer, rounded. And on shadow side of ITER chamfer shape, the ion is least penetrated into the gap. In 2016 campaign, the reversed Ip plasmas were achieved for 28 shots. In these shots, the tungsten blocks were exposed to outer strike point for 5 seconds. From these reversed I_p plasma, the deposition patterns into the gap of 2015 and 2016 are different. The contribution of reversed I_p is calculated and this affected to the retention into the gap although short time of reversed I_p plasma. So it is assumed that the carbon deposition is saturated in a short plasma time.

1. Introduction

Plasma and plasma facing components (PFCs) are interacted like Fig. 1 [1]. This interaction is consisted of deposition, erosion, re-deposition and co-deposition and so on. PFCs of next generation of fusion machines like ITER or DEMO will be castellated to improve their thermos-mechanical strength and to increase heat load handling capability. Fuel retention inside co-deposited layers along the gap of castellation influences the in-vessel fuel inventory which is limited by nuclear safety authority, e.g., 700g in ITER [2, 3]. So many researchers have simulated the fuel deposition in the gap [2, 4]. Fig. 2 is the ion particle flux in the gap from TEXTORE [4]. This ion flux is used to calculation of carbon deposition density. Fig. 3 shows that the simulation result of poloidal gap in KSTAR marker time (KM01: conventional shape, perfect aligned case). This result is compared with the experimental data. A series of experiment using special tungsten block tiles performed in KSTAR on fuel retention inside the gap of castellated tungsten blocks of different shapes used in various tokamaks. And the ion penetration depths into the gap will be compared according to the shapes and radial recess. And results of 2015 and 16 campaign are compared for the carbon deposition pattern into the gap. The KSTAR marker tile KM02 is same shape and different of plasma condition in 2015 and 16 campaign. In 2016 campaign, the reversed I_p plasma was experimented for 28 shots. During these shots, the W blocks were exposed about 5 sec. From

this differences, the contribution of reversed I_p plasma to the carbon deposition be analyzed. Results presented a comprehensive understanding on deposition procedure inside the gap and would give valuable information on the Be deposition inside the gap of castellated tungsten tiles in ITER.
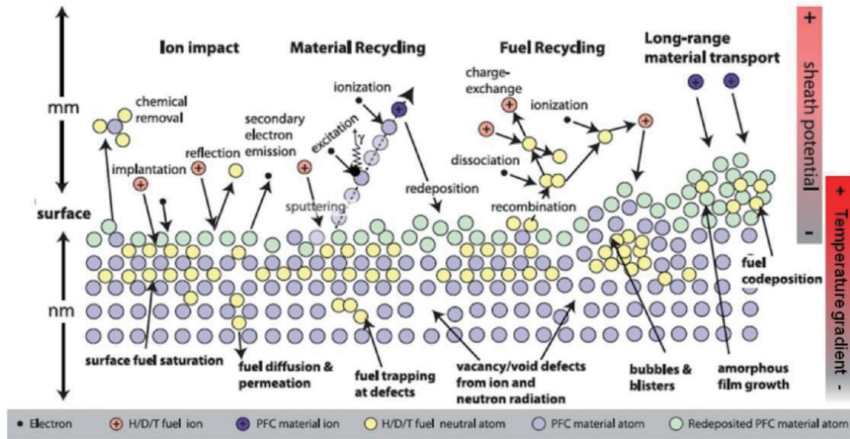
Fig 1. Schematic illustration of the plasma surface interaction process [1].
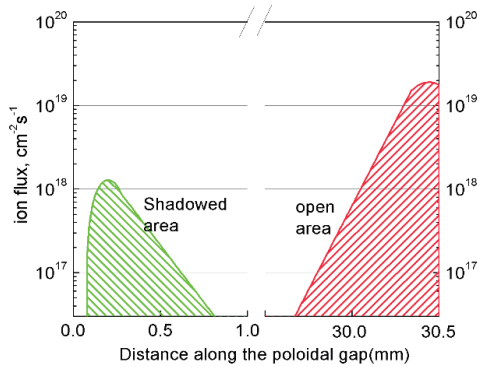
Fig 2. Distribution of the ion flux into conventional gap [4].
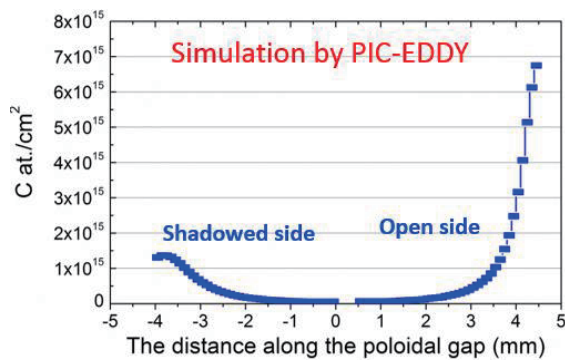
Fig 3. Simulation result of KM02_0:0

2. Experimental Setup, Diagnostics and Analyses

2.1 Tungsten castellated blocks since 2014 campaign

In order to study deposition amount and pattern in the gap of tungsten divertor, castellated tiles based on tungsten (W), copper (Cu), and copper-chrome-zirconium (CuCrZr) alloy are fabricated. Base design of the block is similar to the ITER divertor monoblock. The base block has rectangular structure with a dimension of 30 mm × 20 mm × 12 mm. The blocks in the first four rows of KM00-2014 are aimed to measure the deposition amount and pattern depending on different shapes and edge [5]. The blocks are then installed at central divertor of KSTAR with a graphite cover to protect the side of the blocks and leading edges. During the plasma shot, the position of the outer strike point of typical KSTAR L- and H-mode discharges lay on central and the outer divertor, tungsten blocks installed at the central divertor, are exposed to the plasmas for as long as possible as Fig. 4.
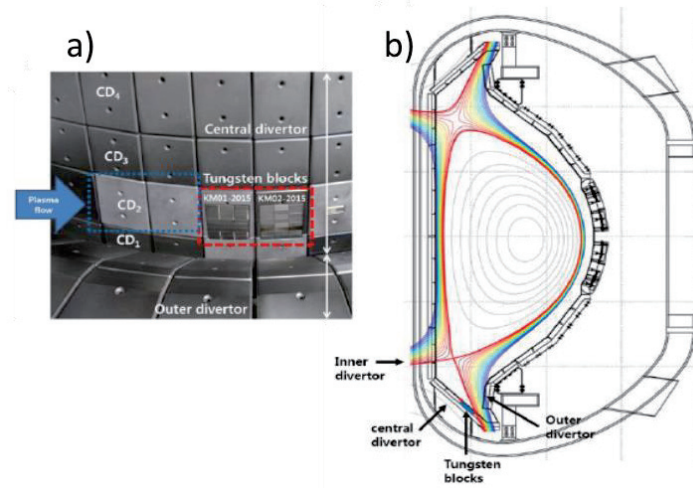
Fig 4. Picture of assemble and location of W block

2.2 Tungsten castellated blocks in 2015 campaign

A dedicated experiment was designed to understand 1) ELM/inter ELM heat load on leading edge (including melting) and on misaligned blocks. Fig. 5 shows a schematic description of different design of tungsten blocks. Leading edge blocks based on the regular rectangular shape with different "intentional" misalignment of 0.3, 0.6, 1.0, and 2.0 mm with respect to perfectly aligned case were fabricated. In KM02-2015, leading edge blocks for the ELM/inter ELM heat load experiment were positioned. In order to avoid parasitic emission from nearby leading edges, blocks were aligned at zig zag position as shown in Fig. 5. Note that the intrinsic misalignment caused by engineering limits has been carefully considered and minimized down to a level of less than 0.05 mm. In 2015 campaign, the total plasma duration is about 12410 seconds, the W blocks exposed for 3150 sec of forward I_p plasmas.
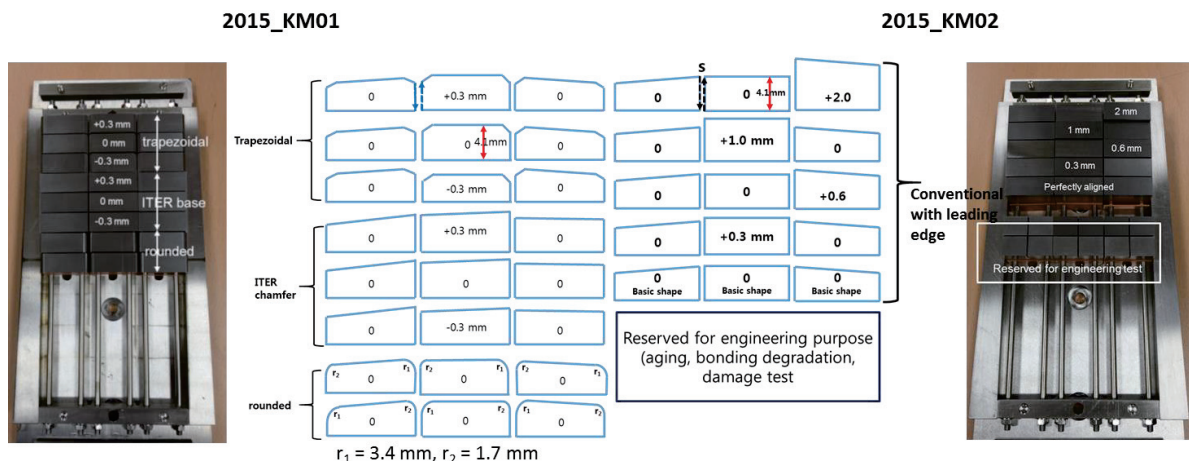
Fig 5. A schematic description and picture of tungsten blocks (2015_KM01 and 02). Label S indicates the direction of S coordinate (set zero at the left bottom corner of the gap).

2.3 Tungsten castellated blocks in 2016 campaign

KM01 W block have ITER shape with edge beveled of 0.5 mm on poloidal and toroidal gap and

realistic misalignment of ±0.3, 0.2, 0.1 mm. And KM02 is same with 2015. In 2016 campaign, the total plasma duration is about 12480 seconds, the W blocks exposed for 2400 sec of forward I_p plasmas and 5 seconds of reversed I_p plasmas.

2016_KM01   **2016_KM02**

ITER chamfer with edge beveled
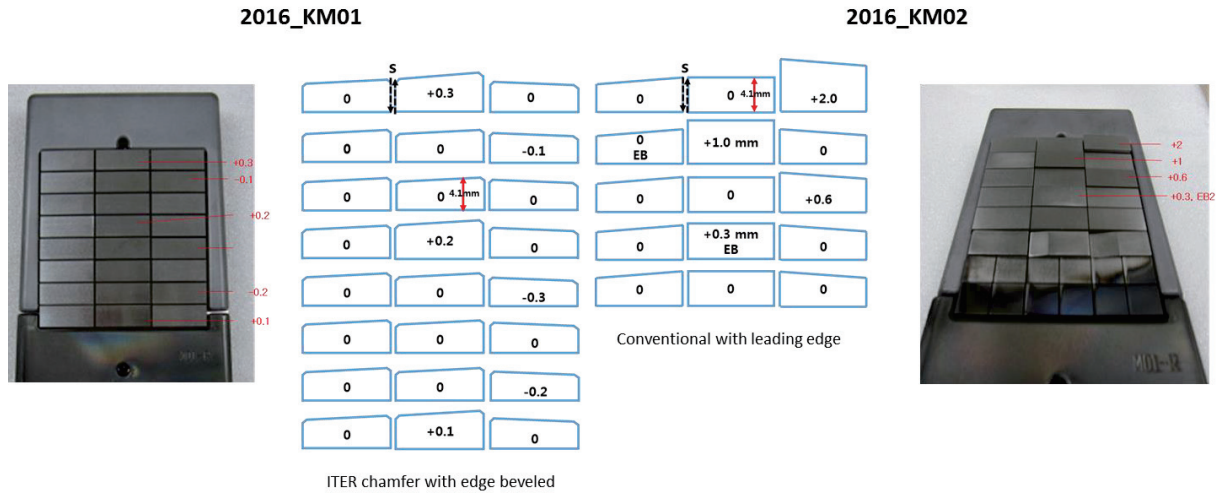
Fig 6. A schematic description and picture of tungsten blocks (2016_KM01 and 02). Label S indicates the direction of S coordinate (set zero at the left bottom corner of the gap).

2.4 EPMA measurements

After each campaign, KM00-2014 and KM02-2015 were taken out from the divertor for various analyses including EPMA (Electron Probe Micro-Analysis, SHIMADZU 1600) measurement. The carbon contents are measured by EPMA with typical setting parameters of 15 keV accelerating voltage, 20 nA beam current, and 1 um^2 beam size. In order to have complete deposition patterns on the blocks, EPMA measurements were performed along the lines with an interval of 0.1 mm on the both sides in each gap of blocks. Note that the EPMA signals show a minimum level of 1×10^{15} C atoms/cm^2, and this level of carbon contents has been reached at around 4 mm down from the gap entrance (S=0).

3. Results and Discussion

3.1 Surface carbon density on the gap of 2015_KM01

Tungsten blocks at the central divertor has been exposed to various plasmas. Although we have observed the blocks assuming that the same amount of heat flux has applied to the tungsten blocks due to the toroidal symmetry. After campaign, the tungsten blocks were measured surface carbon density on poloidal toroidal gap by EDS.

50
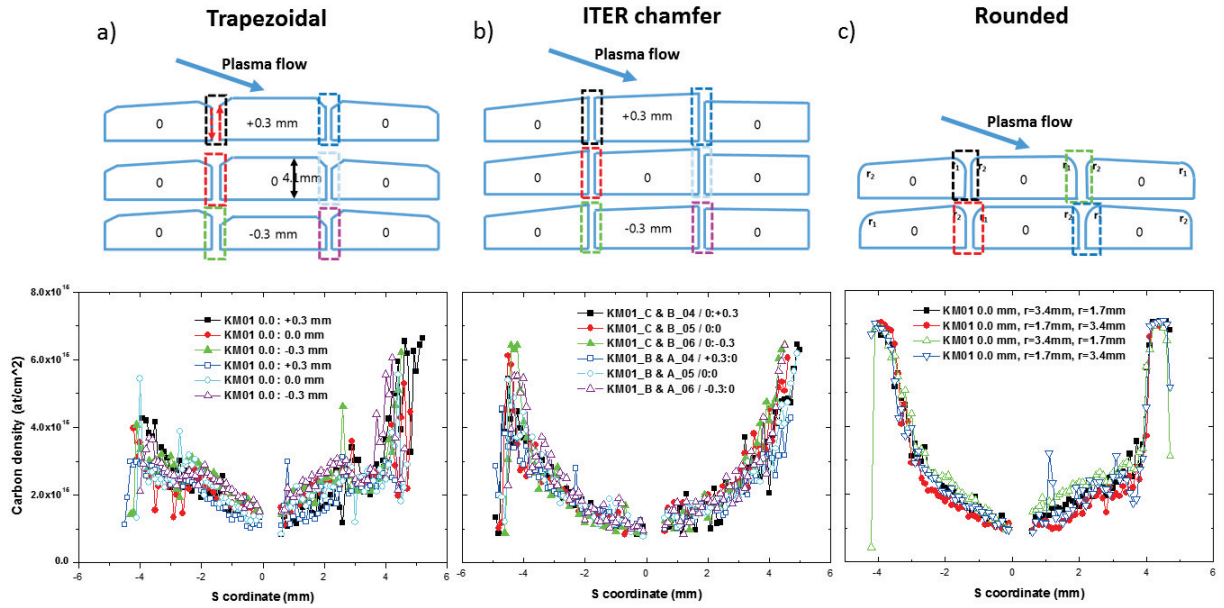
Fig 7. Carbon deposition density into the gap a) Trapezoidal, b) ITER chamfer and c) Rounded shape of KM01_2015.

3.2. Deposition profiles contributed by CX neutrals and C ions from 2015_KM02

Due to the different contribution of C ions and charge exchange (CX) neutrals, deposition patterns inside gaps of various shapes of castellation are different [6, 7]. CX neutrals are not affected by electric and magnetic fields, they can go freely anywhere inside the tokamak vacuum vessel unless they are ionized by collision with electrons. By using leading edges, we could separate the contribution of ions and CX neutrals: The gaps behind leading edges are hidden from the ions due to the higher height of the edge than aligned ones, which act like "barriers" to the ions entering the gaps as Fig. 8a). Since ions cannot enter the gap freely, one can expect that the deposition would be dominated by CX neutrals. The carbon deposition patterns on shadow and open side in the gap are almost the same and symmetric meaning that the deposition process occurred on both sides in the gap was identical and didn't depend on the direction of incoming particles. Note that the grey line at the open side in Fig. 8a) is just a mirror-reflected curve of that at the shadowed side. This reveals that the CX neutrals are responsible for the deposition. On the other hand, Fig. 8b) show the deposition patterns in the gaps between two perfectly aligned blocks at four different locations. First of all, the deposition patterns from different locations are almost identical indicating that the physical process responsible for the deposition in the gaps was well reproduced at each block. Second, the deposition pattern is different from that caused by CX neutrals shown in Fig. 8a) and not symmetric. When a leading edge is present, contribution of ions will be significantly changed resulting in different deposition profiles in the gap in front of the leading edge. Fig. 8c) shows deposition profiles between perfectly aligned blocks and leading edge blocks along S coordinate. In both cases of shadowed and open (leading edge) sides, the amount of deposition increases as the leading edge height increases (label 1 and 2). Two possible interpretations could be made: 1) Ions are bounced back from the side wall and deposited on the shadowed side wall, 2) deposited layers on the open side were bombarded by ions and eroded carbon atoms/molecules were deposited on the shadowed side wall.
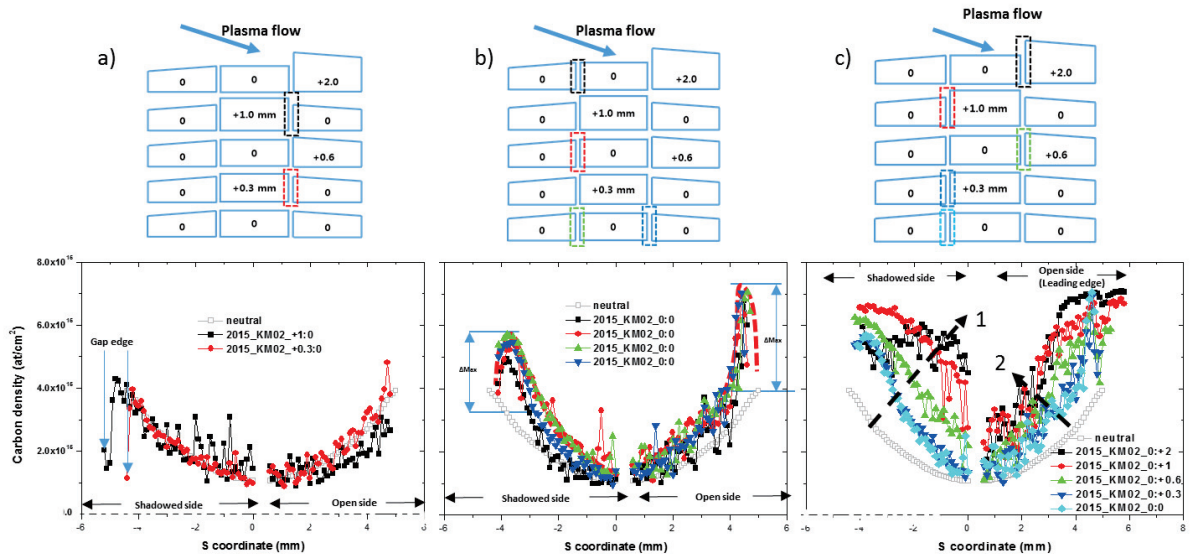
Fig 8. Carbon deposition density in the gap of conventional shape a) barrier of gap to the plasma flow, b) perfect aligned and c) leading edge height of gap

3.3. Ion contribution on deposition

From the carbon deposition amount and pattern in the gap, averaged carbon deposition amounts by ion are compared according to shapes and radial recess as Fig. 9a). And Fig. 9b) indicated that how much deep ion into gap. There are 4 kinds of shape: trapezoidal, ITER chamfer, rounded, conventional, and 5 kinds of radial recess: 0, 0.3, 0.6, 1.0, 2.0 mm. In ITER shape, carbon is the least deposited inside gap on both side and ion has the least penetration on shadow side. In erosion experiment by ICWC, ICWC could effectively erode thin films up to 6 mm below the gap. Those gives and average erosion rate of 0.08 nm/s at mid-plane [8].
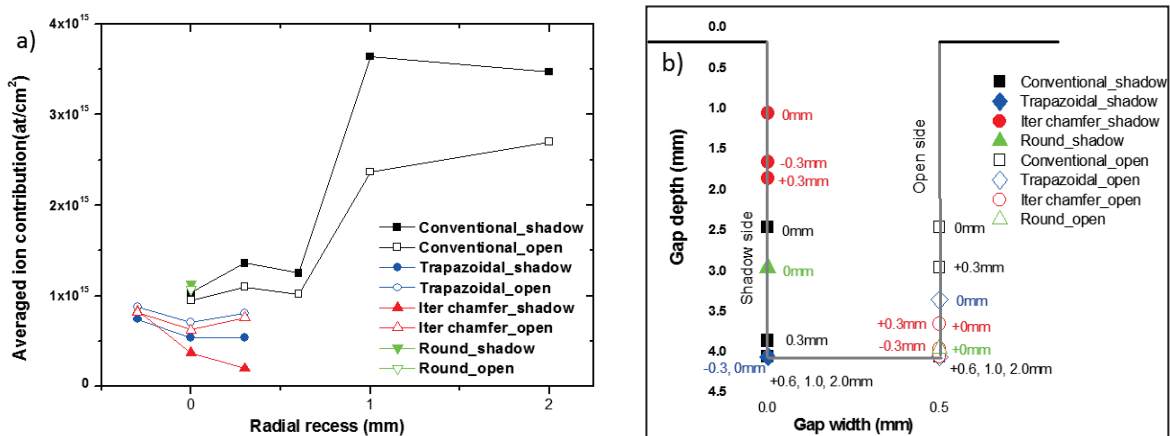
Fig 9. a) Averaged carbon density due to ion, b) how much deep ion into gap on 4 kinds shapes

3.4. Reversed I_p contribution on deposition in 2016_KM02

2016_KM02 tungsten block is same to 2015. But the carbon deposition amount and pattern of 2016_KM02 is different to 2015_KM02. Because the reversed I_p plasma achieved at 2016 campaign. The total plasma duration is similar between 2015 and 16 campaigns. So we can assume that the neutral

contribution is same, and the reversed ion contribution in two gaps in Fig. 10 is calculated. The carbon density in perfectly aligned gaps is compared between 2015 and 16 in Fig. 11b) and d), and ion contribution in Fig. 11c) and e). In Fig 11c), the ion contribution is different on shadow and open side as simulation result of Fig. 2. But ion contribution is symmetry on shadow and open side in Fig. 11e). This is due to the reversed ion contribution. So it is concluded that the carbon deposition is saturated in short time exposure.
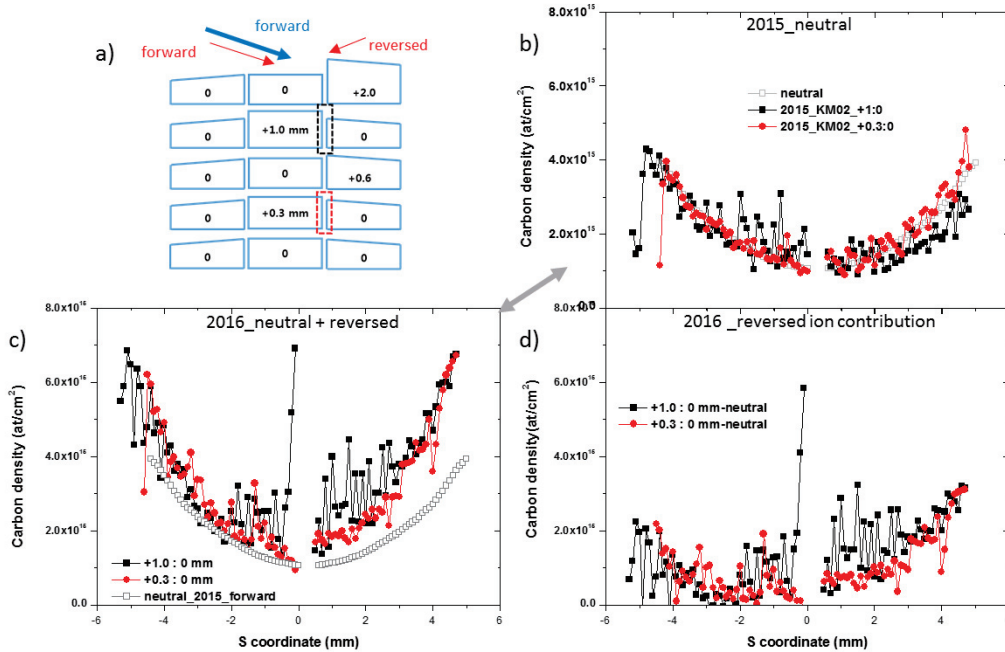
Fig 10. a) Schematic picture of KM02, b) carbon density in two gaps of a) in 2015, c) in 2016, d) reversed ion contribution in 2016.
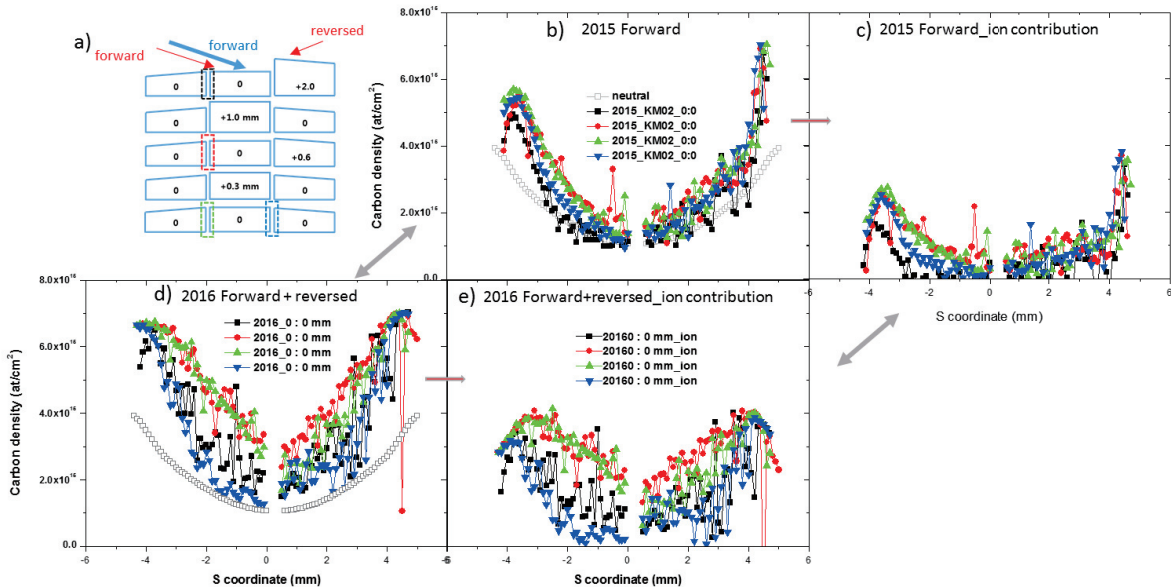
Fig 11. a) Schematic picture of KM02, b) carbon density in four gaps of a) in 2015, c) forward ion contribution, d) carbon density in 2016, e) forward and reversed ion contribution in 2016.
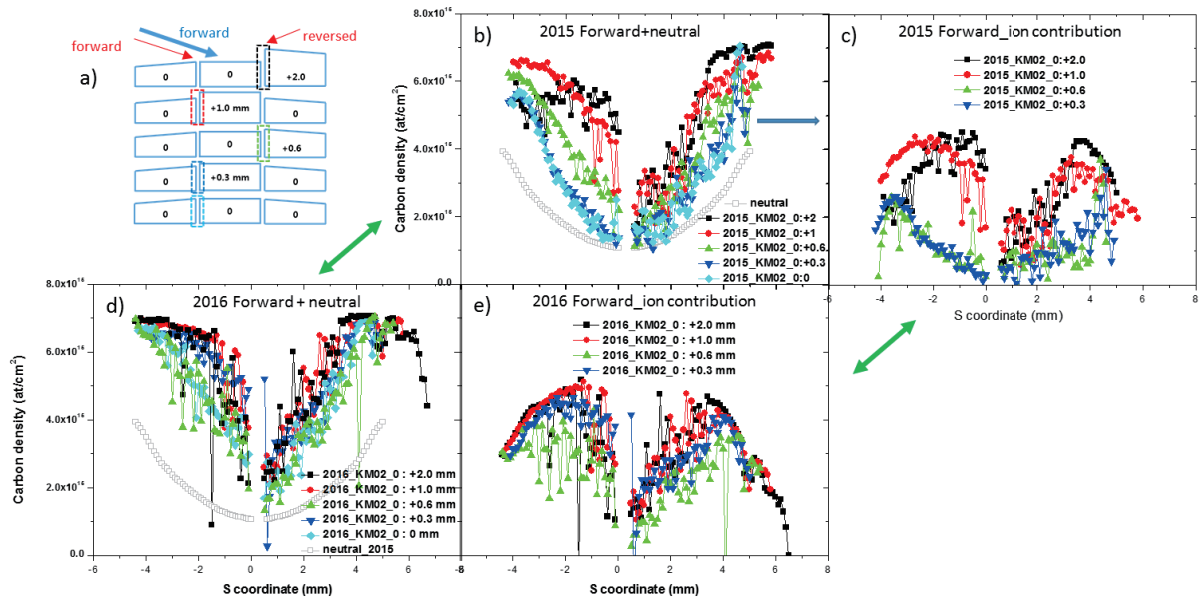
Fig 12. a) Schematic picture of KM02, b) carbon density in four gaps of a) in 2015, c) forward ion contribution, d) carbon density in 2016, e) forward ion contribution in 2016.

This is confirmed in Fig. 12. The forward ion contribution calculated to subtracting the neutral contribution of 2015 as Fig. 12c) and e). The ion contribution of black and red line (0:+2.0 and 0:+1.0 mm gaps) in 2015 and 16 is nearly same. Because these gaps behinds to reversed ion, but green and blue lines are affected to that due to have lower edge heights of 0.6 and 0.3mm respectively. In these case, the lower edge height not be perfect barrier to reversed ion. That affects to carbon deposition in the gap.

4. Summary

A series of experiment using special tungsten block tiles were performed in KSTAR on fuel retention inside the gap of castellated blocks of different shapes. We have varied the shapes and edge heights to find the minimum deposition tungsten shape. After long term exposure of tungsten block, we have analyzed the deposition inside the gaps of castellation. The carbon density on ITER chamfer shape is the lowest in to the four shapes. And by comparing the surface density in the gaps of different shapes of KM02-2015, contribution of each species (ions, CX neutrals) can be separated. ITER chamfer type is the least carbon deposited by ion contribution into the gap, and ion is the least deep into gap on shadow side. These deposition can be removed by ICWC [8], this experiment have to be planed for divertor region and tungsten materials. The W blocks of 2015 and 16 are compared to carbon density and pattern. The reversed plasma is very shorter than forward plasma in 2016, but the effect appears clearly. It is said that the deposition is saturated in a short time of plasma exposure. This is needed to be simulated and compared in a short plasma duration.

References

[1] Jaime Marian, et al., Nucl. Fusion 57, 2017, 092008

[2] A. Litnovsky, et al., J. Nucl. Mater. 386-388 (2009) 809-812.

[3] Suk-Ho Hong, et al., Fus. Sci. Technol. 68 (2015) 36.

[4] D Martveev, et al., Plasma Phys. Control. Fusion 52, 2010, 075007

[5] E. N. Bang, et al., Nuclear Materials and Energy, 2017, In Press.

[6] S.-H. Hong, et al., Fus. Eng. Des. 109–111 (2016) 872

[7] K. Ohya, et al., Fus. Eng. Des. 81 (2006) 205

[8] Suk-Ho Hong, et al., Fusion Engineering and design. 109-111, 2016, 426-431

ELM Heat Load on Castellated Tungsten Blocks

S.-H. Hong[1,2,*], R. Pitts[3], H. H. Lee[1], E.N. Bang[1], K. M. Kim[1], H. T. Kim[1]

[1]National Fusion Research Institute, Daejeon, 305-333, Korea.

[2]Department of electrical engineering, HanYang University, Seoul, 133-791, Korea

[3]ITER Organization, St. Paul Lez Durance, France

Abstract

ELM heat load on the castellated blocks were examined by comparison of divertor IR and COMSOL calculation. It seems that ELM (edge localized mode) heat loads on the leading edges can be described by optical approach. The responses of the tungsten blocks to inter-ELM/ELM heat loads seem to be identical.

1. Introduction

It is mandatory to solve issues on heat and particle loads on plasma-facing components (PFCs) for commercial fusion reactors. Through years, fusion machines have changed in-vessel components to metallic walls such as tungsten (W), which have higher melting point and low erosion yield. Nevertheless, there are misalignments of the order of several hundreds of microns, cannot be avoided due to inevitable engineering tolerances. For instance, entire graphite tile structures inside the KSTAR vacuum vessel have a misalignment level of ~0.5 mm caused by 3D tilting of individual tile [1], which is larger than engineering limit for ITER castellation (0.3 mm) [2]. Such misalignment causes leading edges, which will be exposed directly to plasmas with much higher q_{edge}, which is defined as $q_{edge} = q_{\parallel}\cos\theta$. For instance, $q_{\perp} = q_{\parallel}\sin\theta = 1.0$ MW/m^2 in an inter-ELM (edge localized mode) heat load case with $\theta = 3°$ in KSTAR divertor results in $q_{edge} = 19.1$ MW/m^2.

Inter-ELM heat load on leading edges were carefully studied by installing castellated tungsten blocks with intentionally misalignments of 0.3 mm, 0.6 mm, 1.0 mm, and 2,0 mm: A series of multi-purpose, brazed W blocks (W-Cu-CuCrZr) were fabricated and monitored by divertor IR from the top. The response of the W blocks was simulated by COMSOL multiphysics. The results from IR measurements and COMSOL simulation are consistent with each other indicating that the inter-ELM heat load on the misaligned leading edges was optical, and a simple calculation with geometrical projection can be used to foreseen the heat load on divertor blocks with arbitrary shapes [3].

In this paper, we would like to extend our research to heat load during ELM crash. This is quite challenging, since the typical ELM rise time is about ~50 μs, while the acquisition speed of divertor IR is usually slower than that of the ELM rise time. Fig. 1 shows the time evolution of peak temperature of 0.3 mm leading edge block during ELMy H-mode measured with block measured with two different acquisition speed: a) slow acquisition speed (125 Hz) and b) fast acquisition speed (2.7 KHz). As the strike point was slowly moving

towards 0.3 mm leading edge and as soon as the block is wetted, the peak temperature was increased in both cases. The main difference is, the measurement with slow acquisition speed couldn't catch all individual ELMs but small numbers, while that of fast acquisition speed show all individual ELMs. We will discuss on the validity of measured temperature profiles first.

This paper is organized as follows. In section 2, the experimental setup and analysis methods will be briefly described. In section 3, results will be discussed in detail. Finally, a conclusion will be given.
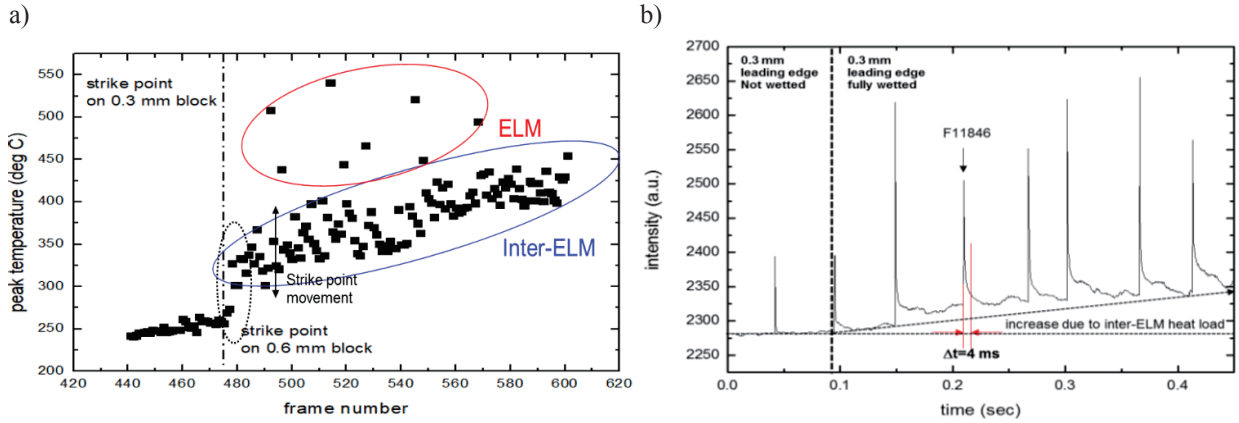
Fig. 1. Time evolution of peak temperature of 0.3 mm leading edge block measured with a) slow acquisition speed (125 Hz), b) fast acquisition speed (2.7 KHz).

2. Experimental Setup and Analysis Methods

Castellated tungsten blocks have four different leading edge heights of 0.3, 0.6, 1.0, and 2.0 mm along perfectly aligned blocks. Gap distance between blocks in both poloidal and toroidal direction is 0.5 mm. Through extremely careful procedure, maximum level of intrinsic misalignment was less than 0.05 mm, confirmed by 3D laser position measurement. The assembled tungsten block tile is installed on the central divertor target region of KSTAR, within the field of view of an infra-red (IR) thermography system consisting of a IR camera, (FLIR SC6101), focusing optics (3 m long periscope) with zoom-in lens system, and vacuum cassette. The spatial resolution of IR system with zoom-in lens system is ~0.4 mm/pixel on the block surface. The parallel power flux q‖ impinging on the various W blocks were measured by power flux density on flat regions of the surrounding graphite tiles, and calculated by NANTHELOT (Numerical Analysis for THErmal Load Onto Target) code [4]. We assume that the same heat flux was applied to the leading edges of tungsten blocks.

COMSOL transient analysis has been performed to calculate the response of W blocks to the heat flux patterns with an emissivity of $\varepsilon = 0.2$ at 100 °C and the angle of incidence of 3 °. Deposited heat load (q‖) on the surface of the block obtained from the measurements is used as input parameter (e.g., 0.65 and 0.7 MW/m2). Note that neither finite Larmor orbit effect nor sheath effect is involved in (optical approximation). Obtained 2D temperature profiles of the tungsten blocks are then compared with that of IR measurements. Note that the blocks were already exposed to H-mode plasmas before the target frames of interest (FOI), leading to the increase of base temperature of blocks.

3. Results

As shown in Fig. 1a), only small numbers of ELMs were detected by divertor IR with slow acquisition speed. Are those temperature profiles meaningful and could be used to make some interpretation of ELM heat load? First of all, it is needed to validate the temperature profiles measured with both slow and fast acquisition speed. In Fig. 1b), it is clearly seen with fast acquisition speed that the effect of ELM peak heat load diminishes within about 4 ms after the ELM crash. 125 Hz acquisition means 8 ms, thus it is natural that frames of ELM crash were lost, unless IR camera catches some of them by "luck". This situation has been modeled by COMSOL as shown in Fig. 2. We have tried to reconstruct measured inter-ELM temperature profiles of both perfectly aligned (0.0 mm) and 0.6 mm leading edges by applying a heat flux level of 1 MW/m^2 with an exposure time of 0.1 s. This task is not physically meaningful, because this is nothing more than constructing initial temperature distribution as close as possible for ELM heat load calculation. Black lines (solid and dash-dot) in Fig. 2 show the temperature distribution of inter-ELM before the ELM crash. We assume that an ELM with 6 MW/m^2 heat flux has been crashed on the leading edge with a characteristic IR rise time (τ_{IR}) of 400 μs. The temperature profiles just after the ELM crash were depicted in Blue lines with maximum temperature of 540 °C. Note that the shape of the temperature profiles before and during ELM was not changed much but the peak temperature increases largely. 10 ms after the ELM, the peak temperature was reduced rapidly down to 440 °C as similar to the behavior seen in Fig. 1b). Here, ELM heat load was removed, but inter-ELM heat load of 1 MW/m^2 was continuously applied.
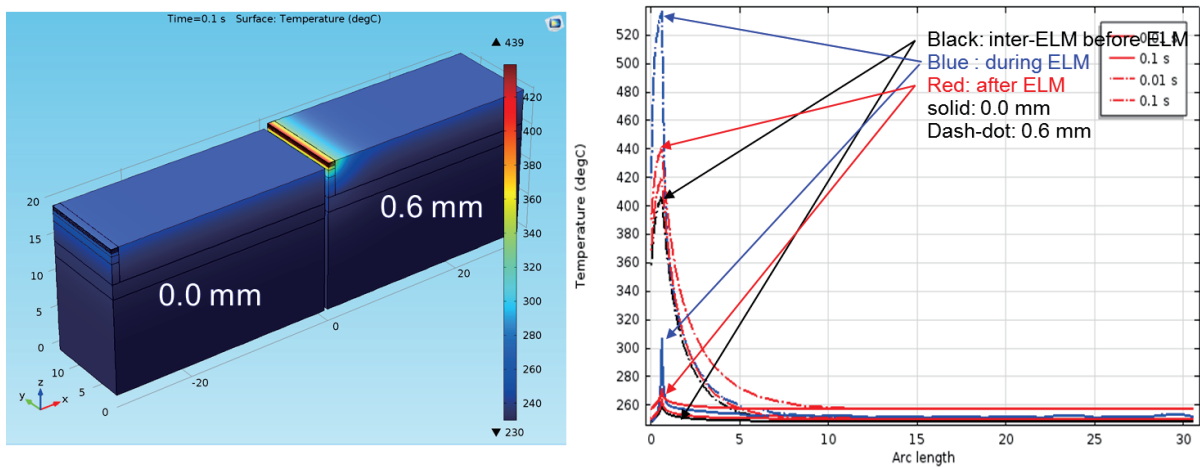
Fig. 2. COMSOL simulation of sequential frames before/during/after ELM crash.

From the results, it seems that ELM temperature profile measured with slow acquisition speed could be used to estimate effect of ELM heat load and corresponding response of the tungsten block qualitatively. To confirm this, a different analysis has been performed. Fig. 3 shows temperature profiles of inter-ELM and during ELM, and their normalized profiles. Surprisingly, normalized temperature profiles of both inter-ELM/ELM heat loads were almost identical, meaning that the responses of tungsten blocks to inter-ELM/ELM heat loads are identical. This leads to a conclusion that ELM heat load might be optical, too, as we have demonstrated in previous publication [3].
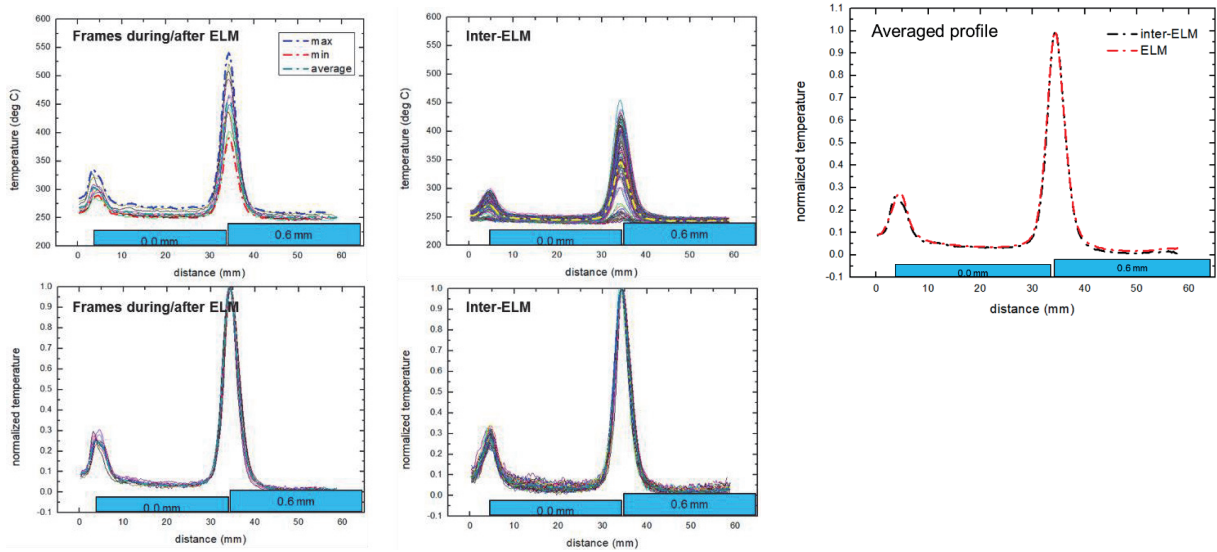
Fig. 3. Measured/normalized temperature profiles of inter-ELM/ELM heat loads.

4. CONCLUSION

Fig. 4. Shows the main conclusion of this paper. Inter-ELM/ELM heat load seem to be calculated by optical approach. Nevertheless, there is no consideration of Larmor orbit effect or sheath effect, which are very important to predict edge melting/response of individual tungsten block.
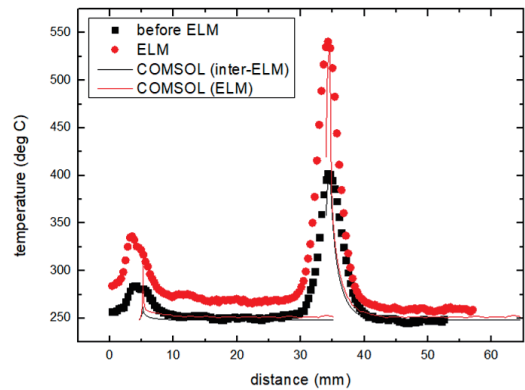
Fig. 4. Measured/calculated temperature profiles of inter-ELM/ELM heat loads

References

[1] S. -H. Hong et al., Fus. Sci. Technol. **68** (2015) 36

[2] R. A. Pitts et al., "Physics conclusions in support of ITER W divertor monoblock shaping", NME, in press

[3] S. -H. Hong et al., "Inter-ELM heat loads on tungsten leading edge in the KSTAR divertor", NME, in press

[4] C. S. Kang et al., Rev Sci Instrum. **87** (2016) 083508

Deuterium retention on tungsten after divertor plasma exposure in KSTAR

N. ASHIKAWA[1),2)], E. BANG[3)], S.H. HONG[3)], S. SON[3)], J.G. Bak[3)], K. KATAYAMA[4)]

[1)]*National Institute for Fusion Science, Toki, 509-5292 Japan*
[2)]*SOKENDAI, Toki, 509-5292 Japan*
[3)]*National Fusion Research Institute, Daejeon, 305-806 Korea*
[4)]*Kyushu University, Kasuga, 816-8580 Japan*

Abstract

Deuterium profiles on molybdenum (Mo) specimen exposed divertor plasmas have been measured by glow discharge optical emission spectroscopy (GD-OES) in KSTAR. Depth profiles of carbon (C), hydrogen (H) and deuterium (D) on Mo holder at different points were measured by GD-OES. Higher carbon amount at an attached position by divertor plasmas is shown. Spatial profiles of hydrogen isotopes (D, H) and C show different characterizations. Highest incident divertor flux energy is estimated at the peak of divertor plasma and retained D at this attached position of plasmas is lower than that at peripheral region after a plasma exposure of 18 seconds.

1. Introduction

Tungsten (W) is a candidate material for plasma-facing components because of a low solubility and a low sputtering yield for hydrogen isotopes. During long pulse plasma discharges in fusion devices, W surfaces will be modified due to a physical sputtering and a re-deposition on plasma facing materials. And different structures from a comparison with deposited W layer and W bulk have been produced. Therefore, the evaluation of hydrogen bulk materials but also deposited layers is required. Moreover, tritium desorption property from deposited W layers has to be also understood for tritium recovery. Lab-scale experiments on hydrogen isotope behavior in deposited W layer formed by plasma sputtering has been performed in Kyushu University [1]. In addition, in order to discuss hydrogen isotopes behavior in deposited W layers formed in a fusion reactor, the characterized deposited layer should be exposed to energetic particles having energy distribution in the fusion experimental devices.

In this work, two kinds of specimens of deposited W layers, which was produced by hydrogen plasma sputtering in Kyushu University (Japan) and Lanzhou institute of chemical physics (China), are exposed to deuterium divertor plasma in KSTAR [2], and surface analyses were operated in NIFS. An advantage of this deposited W layer is characterized target materials with known parameters. The obtained results will be useful also for understanding hydrogen isotope retention in fusion devices.

2. Experimental setup in KSTAR

KSTAR is a superconducting tokamak as a magnetic fusion devices in NFRI, Korea [2]. Two kinds of material manipulators at divertor legs and the midplane of low field side, named "the multi-purpose mid-plane manipulator system", are available in KSTAR. In this experiment, W and deposited W specimens were exposed to divertor plasmas using the divertor manipulator in KSTAR. A systematic

diagram of a poloidal cross-section around the divertor manipulator at K sector of KSTAR is shown in Fig.1. Our own sample holders, the rectangular sample holders of 50 mm x 20 mm, were made by molybdenum and set on the divertor manipulator as shown in Fig.1 (b). A thermocouple was connected to specimens on the holder.

The divertor manipulator was installed to divertor sheet plasma during one or two plasma discharges and specimens were exposed to plasmas. This system don't have a real time monitor system and we cannot see plasma attachment as real time observations. Hence we judged plasma exposures by sustained plasmas. Surface morphologies are measured by a digital optical microscope and a depth profile of elements is measured by a glow discharge optical emission spectroscopy (GD-OES).
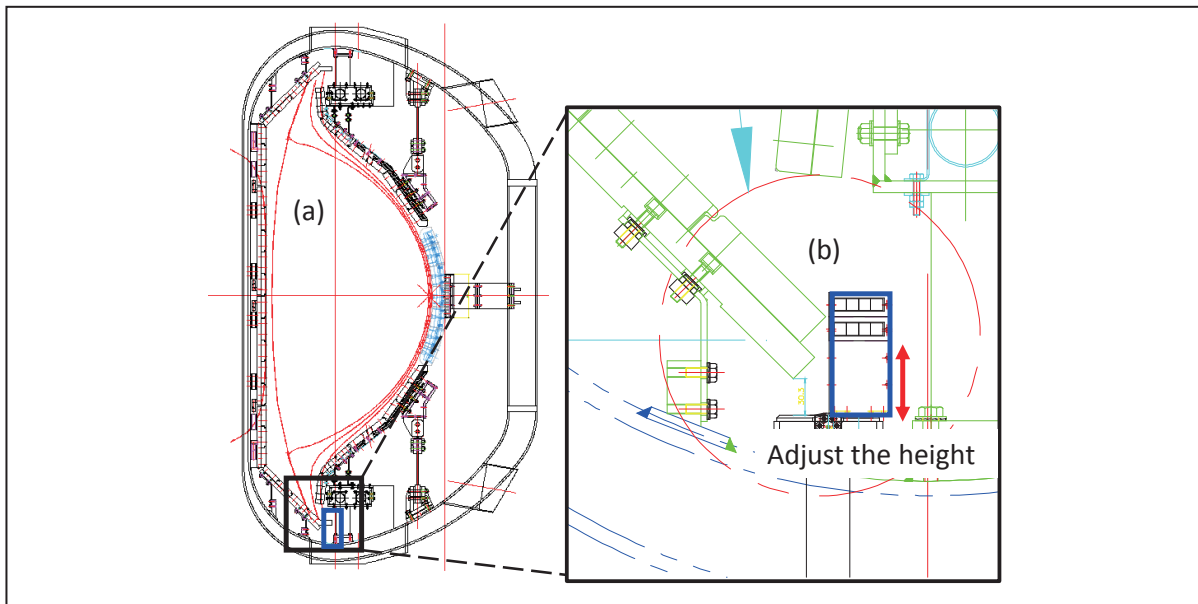
Figure 1 (a),(b) A schematic diagram of sample holders at divertor manipulator in KSTAR. Drawings (a) at a cross-section with divertor sheet plasma directions (b) at a front side of the base holder with two sample holders [6].

3. Results and discussions

A picture of two Mo holders with W specimens is shown in Fig. 2. The vertical position of the sample holders was adjusted as shown in Fig.1 (b) and the sample holders were exposed to two plasma discharges at different positions. In Fig.2, regions of two red solid lines are strike points of divertor sheet plasmas on the sample holders. Blue lines show direction of divertor plasma flows and Right side in this picture is private region. Specimens at two yellow circles had weight measurements using micro-balance and weigh losses over a few micro grams were observed, due to erosions by plasmas. In this work, different characterizations of W specimens were used and then amounts of C, D, H on W specimens simply can not be compared. W specimens were set in Mo sample holders and these had an ethanol cleaning before plasma exposure as the same experimental procedure, and then spatial profiles of C, D, H are observed using Mo holder after divertor plasma exposure.
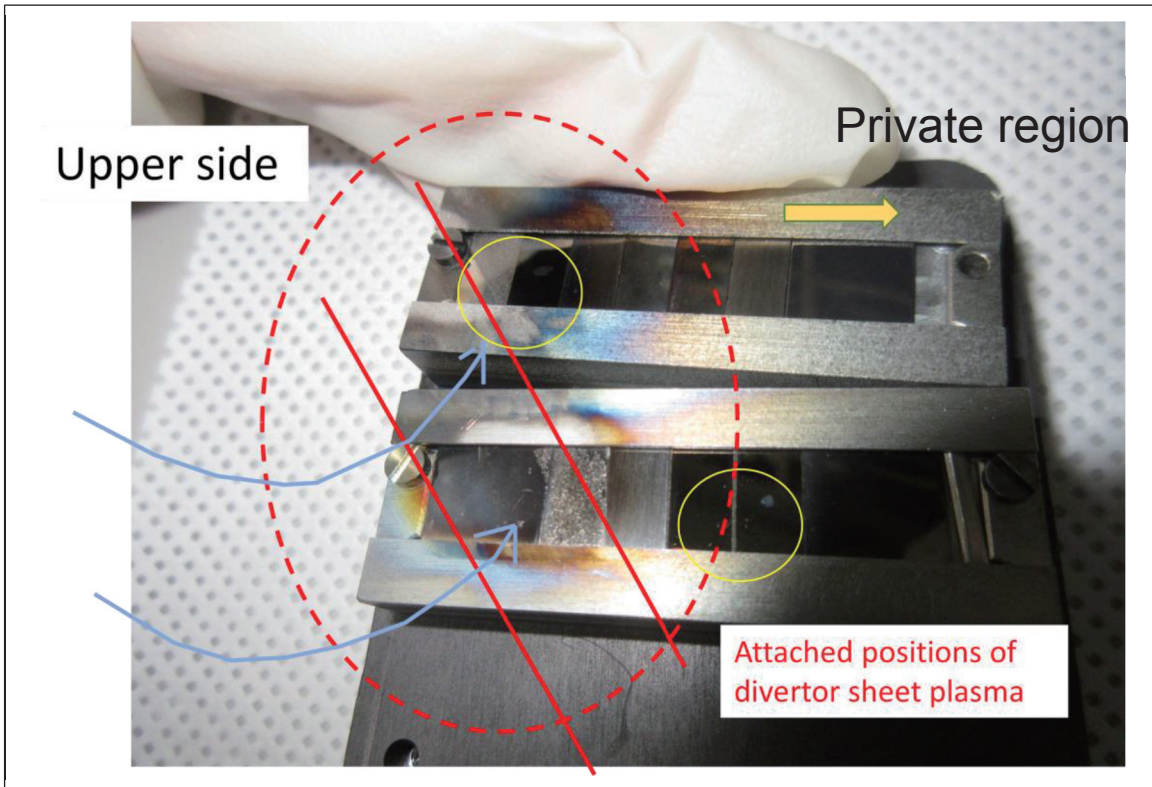
Figure 2 A picture of sample holders with specimens at lines 1 and 2 after divertor sheet plasma exposures in KSTAR. Two red solid lines are strike points of divertor sheet plasmas. Blue lines show direction of divertor plasma flows. Right side in this picture is private region. Specimens at two yellow circles had weight measurements using micro-balance.
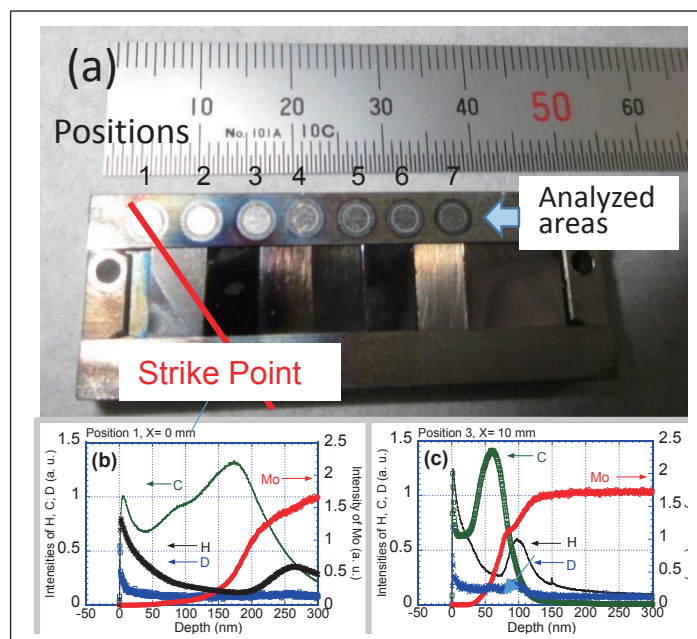
Figure 3 (a) A picture of Mo holder with seven analyzed areas by GD-OES. (b)-(c) Depth profiles of H, D, C, Mo measured by GD-OES at the position 1, and 3. [6]

Figure 3 (a) shows a picture of the 1st Mo holder and an attached position by divertor strike point is shown. Using Mo folder, which had the same characterization of materials for analyzed areas, depth profiles of hydrogen, deuterium, carbon and Mo measured by a glow discharge optical emission spectroscopy (GD-OES) are shown in Fig.3 (b)-(c). H, D, C intensities seem like to be zero at the position 7 in Fig.3 (a), because the position located shadow area for plasmas by in-vessel components. Hence, detected intensities of H, D, C at other positions are related to plasma bombardments. KSTAR has graphite divertor targets and a graphite cover for the base sample holder was used in the divertor manipulator. Sources of carbon impurities are estimated from eroded divertor target. A thick carbon impurity is observed at the divertor strike point and thicknesses of carbon are decreasing toward far distance from the strike point. Two peaks of hydrogen at the surface and interface are shown.

From a comparison between D intensities at positions 1 and 3, a highest intensity at the top surface at the position 3 is observed to compare with D intensity at the position 1. Higher heat flux from plasmas at the divertor strike point, at the position 1 occurred and then both phenomenon of D trapping and releasing occurred during plasma exposure, hence retained D at the position 1 is lower than that at the position 3.

4. Summary and future works

Depth profiles of C, H and D on Mo holder at different points were measured by GD-OES, after divertor plasma exposure in KSTAR. Higher carbon amount at an attached position by divertor plasmas is shown. Amounts of hydrogen isotopes (D, H) and C show different characterizations at different positions. Highest incident divertor flux energy is estimated at the peak of divertor plasma and retained D at this attached position of plasmas is lower than that at peripheral region after a plasma exposure of 18 seconds.

In future work, deuterium retention at different locations, at the first walls [4], have been compared using specimens with the same characterizations. In addition, a comparison with laboratory experiments and tokamaks, EAST [5] and KSTAR, is planned.

5. Acknowledgements

References
[1] Y.K. Oh, et al., J. of the Korean Physical Society 49 (2006) S1.
[2] S.K. Hong, et al., Fusion Sci. and Tech., 63 (2015) 36.
[3] N. Ashikawa, K. Katayama, et al., NIFS-PROC-102 "Proceeding of A3 Foresight Program Seminar, May 2016 Yinchuan"
[4] S.K. Hong, et al., Nuclear Mater. and Energy (2017) accepted.
[5] K. Katayama, N. Ashikawa, et al., Nuclear Mater. and Energy (2017) accepted.
[6] N. Ashikawa, E. Bang, et al., to Plasma and Fusion Research (submitted).

First Mirror in-situ cleaning using radio frequency plasma on EAST for ITER edge Thomson scattering system

J.L. Chen*, R. Yan, H. Xie

Institute of Plasma Physics, Chinese Academy of Sciences, Hefei 230031, Anhui, P.R. China

Abstract

First mirrors are the key element of all optical and laser diagnostics in ITER. Facing the plasma directly, the surface of the first mirrors could be deposited with contaminants eroded from the first wall (tungsten and beryllium) which would result in the degradation of the reflectivity. It emphasizes the necessity of the first mirror in-situ cleaning for ITER. The cleaning results using radio frequency capacitively coupled plasma are reported for a mock-up (200-300 mm) of ITER's Edge Thomson Scattering mirror performed for the first time in a tokamak. The cleaning properties, namely removal of contaminants and homogeneity of cleaning were investigated with molybdenum mirrors insets (25 mm diameter) located at 5 positions over the plates (center to edge) on which 10 nm of aluminium oxide, used as beryllium proxy, were deposited. The cleaning efficiency was evaluated by means of Energy Dispersive X-ray Diffraction, reflectivity measurements and X-ray Photoelectron Spectroscopy. Using argon or neon plasma without magnetic field in laboratory and with 1.7 T magnetic field in EAST tokamak, the aluminium oxide films were homogeneously removed without the magnetic field and the cleaning efficiency with magnetic field was about 40 times higher. These results are promising for plasma cleaning baseline scenario of ITER.

1. Introduction

The first mirror (FM) is one of the most critical elements of the ITER optical and laser diagnostic systems. Facing the plasma directly, the FM would be degraded due to the erosion by the energetic particles and the redeposition of the sputtered first wall materials and the deposition of the wall conditioning material [1]. It is extremely important for a proper reliable optical diagnostic to keep the surface relief pattern i.e. the roughness of a polycrystalline mirror 50 times less than the wavelength of the reflected light in order to minimize the effect of diffuse reflection on the measurements [2]. To avoid such roughening effects, mirrors shall have as small as possible grain sizes and preferably similar crystal orientation to be homogeneously sputtered. These requirements can be fulfilled, for instance, by using a single crystal or by coating the surface with nanometer-size crystallites (Nc). On the other hand, FMs situated deeply in the diagnostic ducts and divertor region are expected to suffer from net deposition. The absorption and interference effects of deposition are responsible for the significant decrease of reflectivity. To mitigate the deposition, duct with fins were tested in JET, or baffle with the aperture geometry in EAST and mirror heating in DIII-D as well as the gas feeding in TEXTOR were investigated and showed some effectiveness. However, the complete mitigation of deposition is almost impossible and furthermore, one of the most promising FM materials, molybdenum (Mo) is easy to be oxidized. Therefore, the research on FM cleaning is indispensable. Laser cleaning of the deposited layer by ablation [3] and plasma cleaning [4] are the two main cleaning methods. The laser cleaning gave satisfactory results even on Be deposits but the

implementation in ITER diagnostic systems would be more challenging from a technical and engineering point of view. Plasma cleaning is considered as the most promising cleaning technique to remove deposits from FMs [5]. Previous experiments using aluminium (Al) as Be proxy [6] demonstrated that the Al and alumina (Al_2O_3) deposits on 18 and 98 mm diameters Mo mirrors were successfully removed by using argon (Ar) plasma with 13.56 MHz radio frequency (RF). The mirrors maintained good optical properties with ion energies ranging from 150 to 350 eV. All laboratories experiments performed by several groups worldwide demonstrated the feasibility of this technique but pointed out the urgent need to upscale the tests to mirror mock-ups in real tokamaks. In this paper, plasma cleaning of the small insets mirror (with 25 mm diameter) embedded in the edge Thomson Scattering (ETS) mock-up in EAST was investigated.

2. Radio frequency plasma in-situ cleaning system in EAST

EAST is a medium size tokamak with the major radius of 1.85 m and the minor radius of 0.45 m. It has the ITER-like magnetic field configuration, which makes it as an ideal experimental platform for the researches on the ITER relevant FM cleaning issues. The FM in-situ cleaning system was inserted in EAST via the Material and Plasma Evaluation System (MAPES) [7] located in the H sector of EAST device. The mirror was mounted on the head of the MAPES manipulator as shown in figure 1. Five small insert small insert mirrors, with a diameter of 25 mm, were made of polished SS substrate with about 600 nm Nc Mo on the surface. Then the 10 nm Al_2O_3 were deposited on the surface in the laboratory and cleaned in EAST. The RF power was fed from the generator through a matchbox to the vacuum feedthrough with a 2-meter coaxial cable and with a 7-meter Bayonet Neill–Concelman cable fixed along the bellows. The FM cleaning head was placed in EAST vacuum chamber at the major radius of 2.4 m. To have an angle between the mirror surface and the toroidal magnetic field similar to what isexpected in ITER, experiments were performed at 5 and 20 degrees.
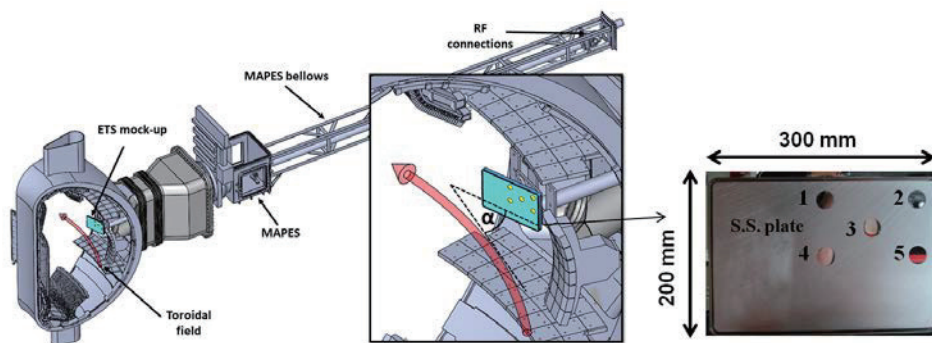
Figure 1. Illustration of the ETS mock-up fixed on the MAPES manipulator and inserted in EAST.

3. Test experiment for the in-situ cleaning system

Before the FW cleaning in EAST, test experiment of the in-situ cleaning system has been performed. In the laboratory, RF power of 70 W is needed to get a self-bias of -200 V. However, the self-bias was kept constant to -200 V by using 188 W for cleaning at MAPES without magnetic field. This may result from a 3 times longer coaxial cable in MAPES than that in the laboratory. In EAST, with the B field, the self-bias was much more different. As shown in fig. 2, the amplitude of the self-bias was decreased with increasing

B field. The self-bias increased first and then reached a saturation value as we increased the B field for both 20 and 5 degree. As noticed this evolution also depends of the angle between the mirror and the magnetic field line, and grazing angle lead to lower the amplitude of the self-bias. At 5°, the minimum voltage amplitude was reached at 0.4 T. By increasing the excitation power, the amplitude of the self-bias was increased for a given gas pressure without magnetic field. The self-bias obtained in EAST and in MAPES were not identical (respectively -165 V and -200 V). This discrepancy could arise from geometrical differences in terms of grounded environment between the two setups or the effect of the residual magnetic field affecting the discharge. For a given power and magnetic field in EAST, a reduction by a factor 2 of self-bias amplitude was measured when the pressure is increased from 0.01 Pa to 0.5 Pa. This result is particularly important for ITER as a large negative self-bias absolute is requested to etch contaminants away while the RF power should be kept as low as possible to avoid overheating of the transmission lines.
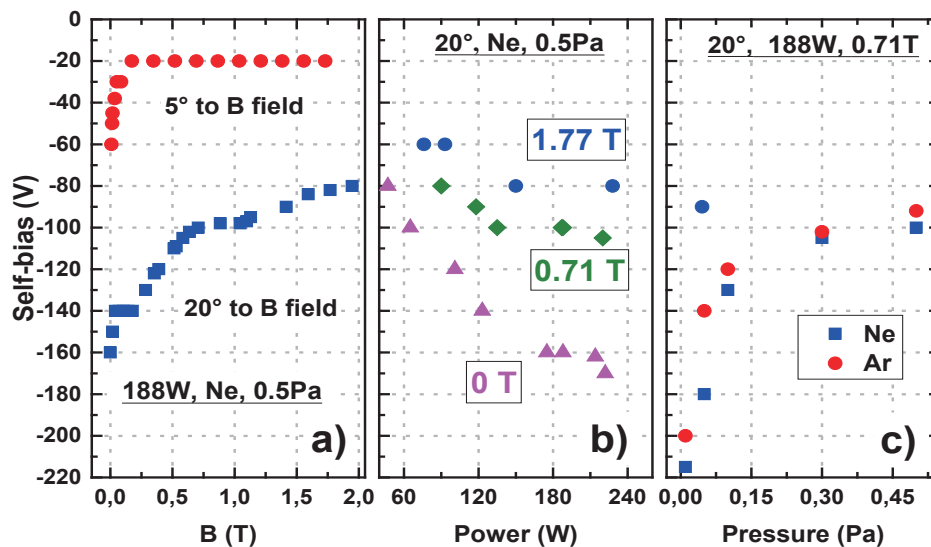
Figure 2. Self-bias versus (a) magnetic field intensity at 5 and 20°, (b) RF power applied to themirror and (c) gas pressure and gas type.

4. FM in-situ cleaning with/without notch filter in EAST

It is well-known that the water cooling system is essential in ITER because of the harsh operation environment. Therefore, the FM in-situ cleaning for the mirror with a water cooling system has been designed. The cooling water will directly go through the FM and the cooling water pipe will be on ground potential. This means that during the FM cleaning in ITER the self-bias may not been developed on the FM. It can be realized by a special length of cooling water pipe. In EAST, a dedicated structure called notch filter is used to simulate the cleaning of FM with water cooling. It is consisted of a T connector along the RF transmit cable. A 3.8 meter coaxial cable with the inner conductor and outer braid connector was connected to the T connector. The notch filter is a DC shorted and AC conducting circuit. By using it, non self-bias can be performed during the FM cleaning. In the following, the experimental results for the cases without and with notch filter are shown.

4.1. Cleaning without notch filter

Experimental results for the case of without notch filter are shown in this section. For the 20° case, the 10 nm coating of Al_2O_3 strongly reduced the reflectivity especially in the visible range (as shown in figure 3). During the cleaning, the maximum self-bias achieved was -80 V with 188 W, 0.5 Pa Ne at 1.77 T. After 30 min cleaning, XPS measurements were carried out and revealed an oxidized Mo film (typically 20 % at.), carbon and oxygen as well as up to 3 % at. of Al for T3 and T5 mirrors. As revealed by SEM observations, the surface lost its initial nanocrystalline structure due to the sputtering. In addition, some large dust particles already present on the mirror before cleaning led to the appearance of contrasted area mainly consisting of Al (measured by EDS). The total reflectivity of mirrors T1-T5 after cleaning was recovered to the level of the pristine ones. For T1 and T2, the higher reflectivity after cleaning is typically observed when removing the surface oxidized Mo layer. Due to physical sputtering during cleaning process, the diffuse reflectivity of the mirrors was increased, especially in the visible range. For mirror T4 and T5, the higher diffuse reflectivity was correlated to the increased roughness indicated in the same figure. Ra of pristine mirrors was 15 nm in average. An inhomogeneous cleaning process with stronger sputtering in the middle of the mock-up was demonstrated.
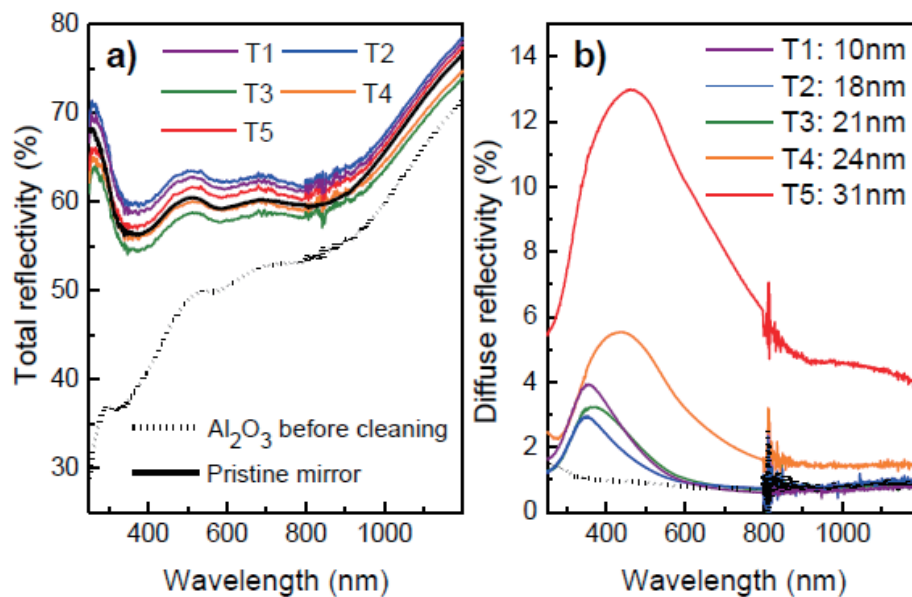
Figure 3.Total and diffuse reflectivity of mirrors for the case of without notch filter cleaned at 20°.

For the 5° case, the maximum self-bias achieved was -20 V (Fig 4) while the cleaning parameters were kept constant (1.77 T, 188 W, 0.5 Pa, Ne, 30 min). After cleaning, XPS revealed Al only for F5 and F2, about 1.8 % and 17.4 % at. respectively. Iron was detected for all mirrors as traces while not detected for 20°. The origin of iron is the stainless steel ETS mock-up. SEM observations revealed similar results as for 20° namely a systematic presence of nanocrystalline Mo as well as shadowing effect due to large dust particles present on the surface. In the shadowed area, Al was always detected by EDS. For this experiment, after dismounting the insets the orientation of the mirrors was physically marked and highlighted the fact that the direction of the shadowed area is parallel to B field orientation. The total reflectivity of all the mirrors was recovered after cleaning except for the mirror F2 which still had 17.4 % at. of Al on the surface

as measured by XPS. Similar with mirrors cleaned at 20°, the diffuse reflectivity of mirrors F1-F5 increased after cleaning, which is correlated with the measured roughness, especially for F4 and F5. Like the mirrors cleaned at 20°, an inhomogeneous sputtering was present.
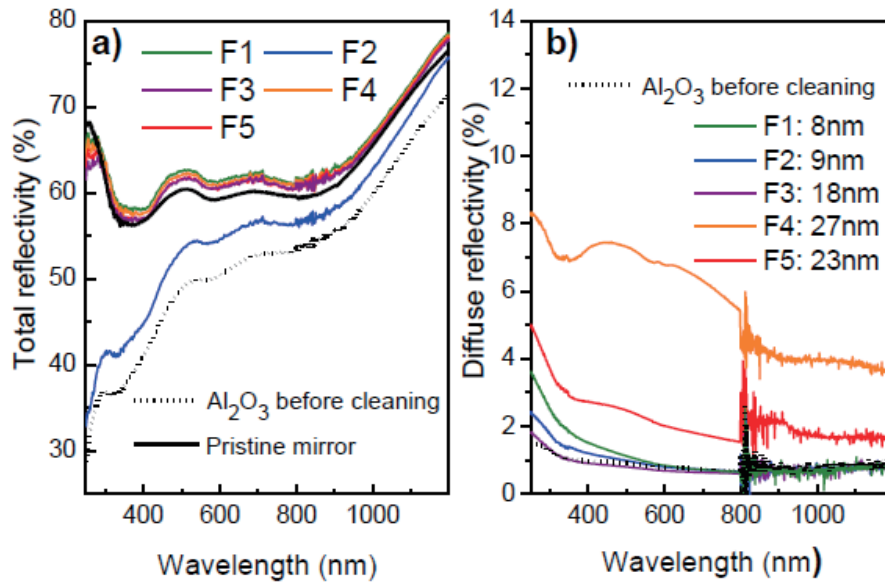
Figure 4.Total and diffuse reflectivity of mirrors for the case of without notch filter cleaned at 5°.

4.2. Cleaning with notch filter

The cleaning with the notch filter at 20 degree has been performed in EAST. The cleaning parameters were the same with the case of without the notch filter at 20 degree except for the self-bias. No self-bias is added in the experiment. After cleaning for half an hour, the Al was appeared on all the mirrors. Only small amount of Mo was observed in the most central mirror. As shown in figure 5, the total reflectivity of all the mirrors recovered only for small extent. It illustrates that the cleaning with the notch filter was slower than that without the notch filter. Moreover, the most central mirror didn't show much recovery of the total reflectivity. We estimated this may result from the enhanced sputtering directions, which were along these two directions pointed opposite the center of the FM mock-up. For the diffuse reflectivity, there is no much difference for all the mirrors. The edge mirror (T5) has a tendency to get a higher diffuse reflectivity. The SEM and other characterizations are undergoing.
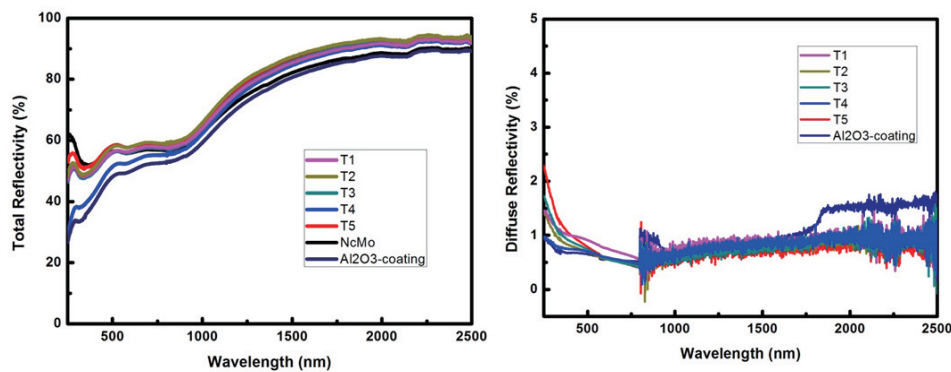
Figure 5. Total and diffuse reflectivity of mirrors for the case of with notch filter cleaned at 20°.

5. Summary and outlook

The plasma cleaning campaign in an operating tokamak EAST with a relevant B field (toroidal, 1.7 T) has been performed. Some promising results are obtained: It was possible to run Ar or Ne discharges on 200×300 mm^2 large mirror for several hours with 1.7 T field; it was impossible to reach a desired self-bias. (-20 and -80V instead of -200V); cleaning was effective and was about 40 times faster than that in the laboratory; cleaning with the notch filter was slower and more homogeneous than that without the notch filter. In the near future, more study of in-situ plasma cleaning are foreseen: Plasma potential measurements will be performed; closer investigations will be conducted regarding the cleaning efficiency looking at self-bias and ion fluxes; new experiment should be performed by looking on the homogeneity of the cleaning on the whole mirror; first mirror in-situ cleaning will integrates with the real diagnostic system (such as the CXRS) in EAST.

References

[1] Walsh M, Andrew P, Barnsley R, et al., ITER diagnostic challenges (IEEE) (2011) 1–8

[2] Voitsenya V, Costley A E, Bandourko V, et al., Rev. Sci. Instrum. 72 (2001) 475–82

[3] Skinner C H, Gentile C A and Doerner R, et al. Rev. Sci. Instrum. 83 (2012) 10D512

[4] Moser L, Marot L, Eren B, et al., Nucl. Fusion 55 (2015) 63020

[5] Bock M F M D, Barnsley R, Bassan M, J. Instrum. 11 (2016) P08010–P08010

[6]Marot L, Linsmeier C, Eren B, et al. Fusion Eng. Des. 88 (2013)1718–21

[7] Ding F, Luo G-N, Pitts R A, J.Nucl. Mater. 455 (2014) 710–6

Ion fractional abundance measurements of highly charged W^{q+} ions based on visible M1 lines

D. Kato[1,2,3], M. Goto[1,2], T. Oishi[1,2], S. Morita[1,2], H.A. Sakaue[1], I. Murakami[1,2], N. Nakamura[4], K. Fujii[5], X.-B. Ding[6] and C.-Z. Dong[6]

[1]National Institute for Fusion Science, Toki 509-5292, Gifu, Japan

[2]Dept. of Fusion Science, SOKENDAI, Toki 509-5292, Gifu, Japan

[3]Dept. of Advanced Energy Engineering, Kyushu University, Kasuga 816-8580, Fukuoka, Japan

[4]Inst. for Laser Science, Univ. of Electro-Communications, Chofu 182-8585, Tokyo, Japan

[5]Dept. of Mechanical Eng. and Sci., Kyoto University, 615-8540, Kyoto, Japan

[6]Key Lab. of Atomic and Molecular Physics and Functional Materials of Gansu Province, College of Physics and Electronic Engineering, Northwest Normal University, Lanzhou, China

Abstract

The tungsten ion fractional abundance measurement has been attempted using M1 lines in a near-UV region from highly charged tungsten ions in LHD based on the tungsten pellet injection. For the purpose vertical profiles of the M1 lines of W^{26+} and W^{27+} ions are measured with absolute intensity. The measured profiles are fitted to theoretical profiles constructed with local photon emission coefficients of the M1 lines and tungsten ion density distributions. The measured fractional ion abundance ratio of W^{27+}/W^{26+} coincides with ionization equilibrium values at electron temperatures of 1 keV or below, however the experimental values are systematically smaller at higher temperatures.

1. Introduction

The ion fractional abundance measurement of tungsten ions in fusion plasmas is very important for accurate understanding of the tungsten transport [1]. The precise measurement serves as a benchmark for evaluation of tungsten atomic data used in transport models. Recently, ion abundance peaks on local electron temperatures have been inferred experimentally at LHD using measured magnetic-dipole (M1) line spectra in a near-UV region emitted from highly charged tungsten ions in the ground states [2]. The previous work demonstrated the usefulness of the M1 lines for tungsten measurements, although absolute values of the ion densities are yet to be accessible. In the present work, the absolute ion densities of W^{26+} and W^{27+} are obtained with local photon emission coefficients of the M1 lines calculated by a collisional-radiative model including proton collision effects.

2. Experimental method

Tungsten was introduced into the LHD plasmas by injecting a polyethylene pellet (0.6 mm long and 0.6 mm diameter) containing a tungsten wire. Size of the tungsten wire in the polyethylene tube is 0.15 mm in diameter and 0.6 mm in length. Number of tungsten atoms in the single pellet is estimated roughly to be 6.6

$\times\ 10^{17}$. The pellet is accelerated by pressurized He gas of $10 - 20$ atm and injected with the angle of $12°$ tilted from the normal to the toroidal magnetic axis. Time-resolved (sampling times for 38 ms at every 100 ms) emission spectra are measured using a Czerny-Turner visible-UV spectrometer (grating of 1200 gr/mm and slit width of 50 μm) equipped with a CCD detector. Photon emission is detected through optical fibers at 44 lines of sight along the vertical direction $Z = -0.6 \sim 0.6$ m of a horizontally elongated poloidal cross section. The poloidal cross section is asymmetric with respect to $Z = 0$ because the cross section is $6°$ tilted from the normal to the toroidal magnetic axis.

Discharges for present measurements were started with electron cyclotron heating followed by tangential hydrogen neutral beam injection (NBI) heating. Figure 1 shows the time sequence of plasma parameters during the present measurement. By the pellet injection at $t = 4.0$ s, the central electron temperature (T_e) decreases from about 3 keV down to 2 keV in 100 ms following a stepwise enhancement of the radiation power. The line-averaged electron density (n_e) increases rapidly after the pellet injection. The line-averaged n_e keeps increasing gradually until $t = 5.4$ s, while the central T_e is kept almost constant at about 1 keV. From $t = 5.4$ s, the central T_e starts to rise, while the line-averaged n_e turns to decrease. The radiation power also decreases accompanying an increase of the stored energy.
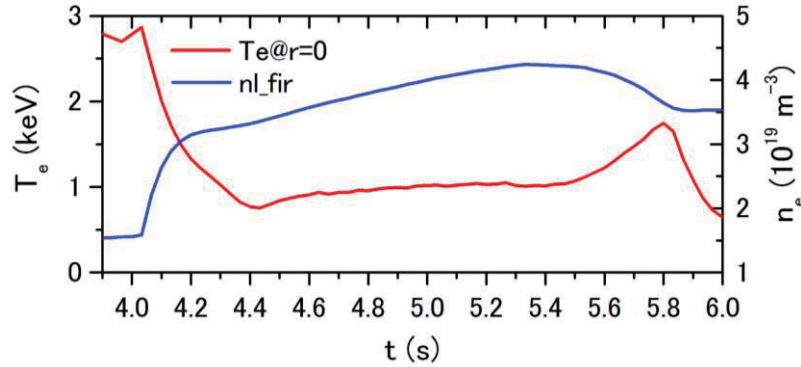
Fig. 1 Time sequence of the central electron temperature (red curve) and the line-averaged electron density (blue). Tungsten pellet is injected at t = 4.0 s.

3. Vertical profile of M1 line intensity

Figure 2 shows the horizontally elongated poloidal cross section and experimental vertical profiles of two M1 lines of W^{26+} and one M1 line of W^{27+}. The two M1 lines of W^{26+} are observed at 333.70 nm and 335.73 nm which are identified as $4f^2\ ^3F_4 \rightarrow\ ^3F_3$ and $4f^2\ ^3F_4 \rightarrow\ ^1F_4$, respectively. The M1 line of W^{27+} at 337.73 nm is identified as $4f\ ^2F_{7/2} \rightarrow\ ^2F_{5/2}$. The vertical profile of an emission line due to transition from the upper level j to the lower level i is theoretically expressed as

$$I(Z) = A_{ij} \times \int n_j^{(q)} n_q n_W dX,$$

where A_{ij} is a transition rate, $n_j^{(q)}$ a fractional population of the upper level, n_q a fractional ion abundance of W^{q+}, and n_W tungsten density. The fractional population of the upper level, which depends on local electron temperature T_e and density n_e, is calculated by a collisional-radiative model (see the next

chapter) using radial profiles of T_e and n_e measured by Thomson scattering. A radial distribution of $n_q n_W$ is represented by a Gaussian basis set centered at discretized radial coordinates ρ_i $(i = 1, \cdots, N)$ as

$$n_q n_W \equiv n_{Wq+} = \frac{1}{\sqrt{2\pi\sigma^2}} \sum_{i=1}^{N} e^{-(\rho-\rho_i)^2/(2\sigma^2)} b_i.$$

The coefficients b_i are obtained by χ^2-fitting of experimental vertical profiles with the theoretical formula. Solid curves in Fig. 2 are the fitted profiles. The upper and lower half of the vertical profile are fitted separately to investigate poloidal asymmetry in the radial distribution of n_{Wq+}.
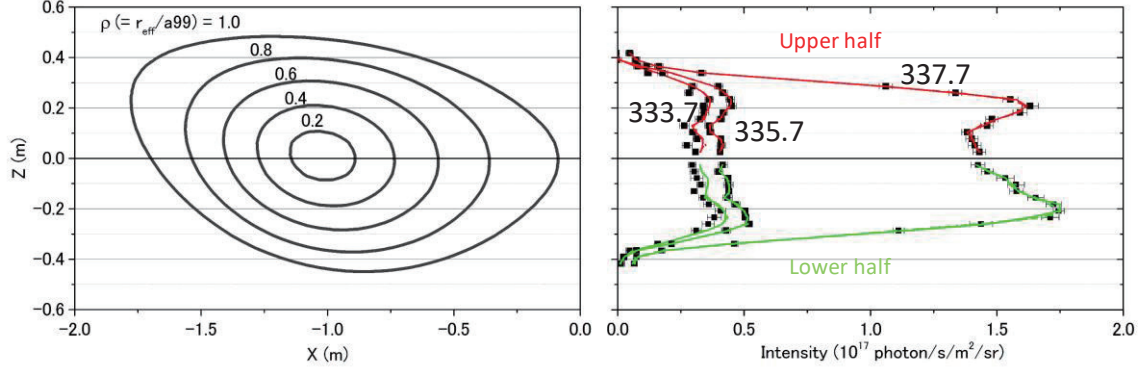
Fig. 2 Poloidal cross section and vertical profiles of M1 line intensities: The two M1 lines of W^{26+} at 333.70 nm and 335.73 nm and one M1 line of W^{27+} at 337.73 nm. Red and green curves are χ^2-fittings with the upper and lower-half of the vertical profiles, respectively.

4. Collisional-radiative model for M1 lines of W^{q+} ions in the ground state

M1 line spectra of W^{q+} ions in the ground state are calculated by a collisional-radiative (CR) model including proton collisions. In the CR model, fractional populations of excited levels $n_i^{(q)}$ of W^{q+} are obtained by solving the quasi-stationary state equation,

$$\left[\sum_{j \neq i} \left(n_e C_{ji}^e + n_p C_{ji}^p \right) + n_e S_i^{q \to q+1} + \sum_{j < i} A_{ji} \right] n_i^{(q)} = \sum_{j \neq i} \left(n_e C_{ij}^e + n_p C_{ij}^p \right) n_j^{(q)} + \sum_{j > i} A_{ij} n_j^{(q)},$$

where n_e and n_p are electron and proton densities, respectively, C_{ij}^e and C_{ij}^p (de-)excitation rate coefficients by electron and proton collisions, respectively, $S_i^{q \to q+1}$ ionization rate coefficients by electron collisions, A_{ij} transition rates, and n_q fractional ion abundances of W^{q+}. The collisional rate coefficients are calculated from cross sections assuming the Maxwellian velocity distribution of electrons and protons. The energy levels, the radiative transition rates and electron distorted-wave cross sections are calculated using HULLAC code [3]. Cross sections of proton collisions are calculated in a semi-classical perturbation approximation [4]. In the present calculations, the electric quadruple interaction between protons and tungsten ions is taken into account and $T_p = T_e$ and $n_p = n_e$ are assumed. It is noted that simple mass-scaling of the electron distorted-wave cross sections underestimates the rate coefficients by many orders of magnitudes. The proton collisions enhance population of W^{27+} in the ground state and the M1 line intensity at 337.7 nm. However, the enhancement is much less significant in the ground state population of W^{26+}.

5. Radial distribution of tungsten ion density of W^{26+} and W^{27+}

Figure 3 shows radial distributions of W^{26+} and W^{27+} ion densities n_{Wq+} obtained from the upper and lower-half of the vertical profiles. The radial distributions have peaks at about 1.0 keV and 1.2 keV, respectively, which agree with values predicted by assuming the ionization equilibrium with the measured electron temperature profile (see the top panel of Fig. 3). The peak positions for the lower-half distributions are apparently shifted outward comparing with those for the upper-half ones, that can be ascribed to poloidal asymmetry in the radial distributions. The upper distributions show other peaks at small ρ (higher T_e) which may be due to blend with emission lines from higher charge states of tungsten ions.

Figure 4 shows the radial profile of the fractional ion abundance ratio of W^{27+}/W^{26+}. The present results agree with values of the ionization equilibrium in a region at where the ion densities become maxima (around $T_e = 1$ keV), however the results are systematically smaller than the ionization equilibrium values at higher temperatures.
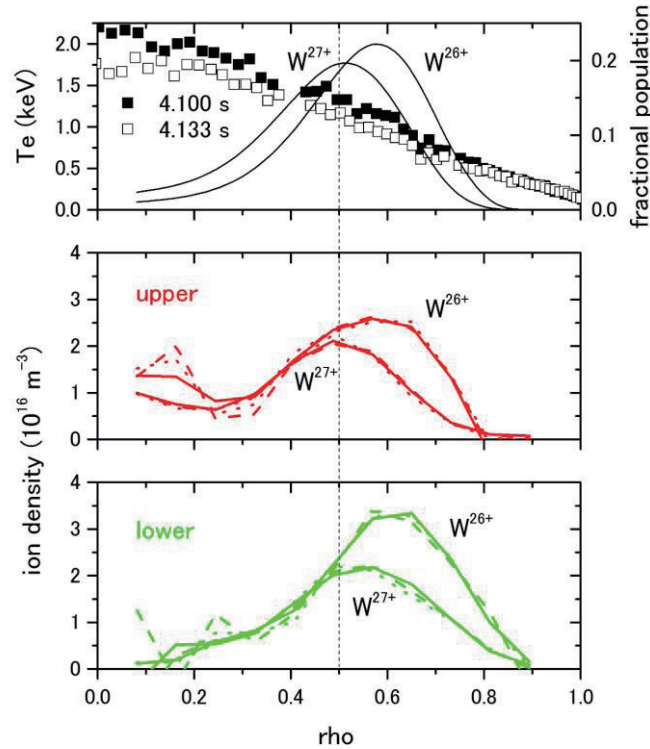
Fig. 3 Radial distributions of W^{26+} and W^{27+} ion densities. Top) ionization equilibrium fractional population of the ions together with measured electron temperature profiles at t = 4.0 s and 4.133 s, Middle) the radial distributions obtained from the upper-half of vertical profiles, and Bottom) the radial distributions from the lower-half of vertical profiles. Solid curves stand for results with the Gaussian width $\sigma = 0.12/a99$, dotted curves $\sigma = 0.1/a99$, and dashed curves $\sigma = 0.08/a99$.
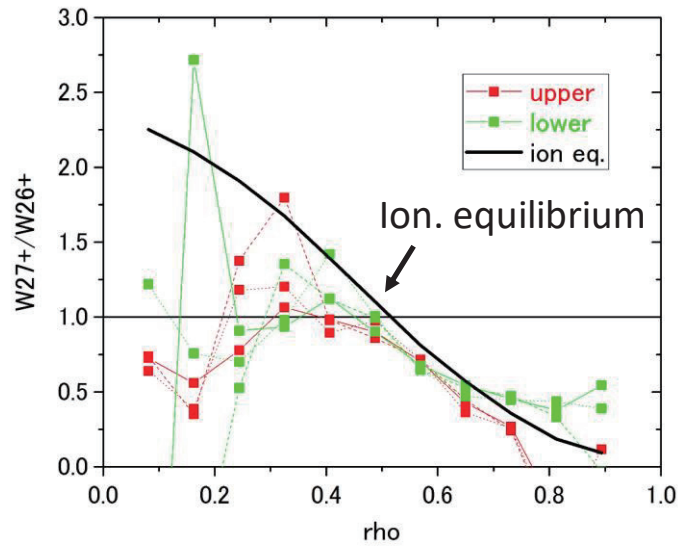
Fig. 4 Ion abundance ratio of W^{27+}/W^{26+}. Red and green squares are results from the upper and lower-half of vertical profiles, respectively. The solid curve is prediction of the ionization equilibrium with the measured electron temperature profile.

References
[1] S.Morita et al., AIP Conference Proceedings **1545** (2013) 143.
[2] K. Fujii et al., J. Phys. B: At. Mol. Opt. Phys. **50** (2017) 055004.
[3] A.Bar-Shalom, M.Klapisch and J.Oreg, J.Quant.Spectr.Radiant.Trans. 71 (2001) 169.
[4] K. Alder et al., Rev. Mod. Phys. **28** (1956) 432.

Study of impurity transport in the HL-2A ECRH L-mode plasmas with radically different ECRH power depositions

Z.Y.Cui[1], K.Zhang[1], S.Morita[2], X.Q.Ji[1], Y.Xu[1], X.T.Ding[1], P.Sun[1], J.M.Gao[1], C.F.Dong[1], D.L.Zheng[1], Y.G.Li[1], M.Jiang[1], D.Li[1], S.D.Song[1], L.M.Yu[1], W.L.Zhong[1], Z.B.Shi[1], B.Z.Fu[1], P.Lu[1], M.Huang[1], B.S.Yuan[1], YiLiu[1], Q.W.Yang[1]

[1]Southwestern Institute of Physics, P. O. Box 432, Chengdu 610041, China
[2]National Institute for Fusion Science, Toki 509-5292, Gifu, Japan

Abstract

The effect of ECRH on the impurity transport has been investigated in relation to the ECRH power deposition by using the laser blow-off (LBO) method in the HL-2A tokamak. When the ECRH power deposits inside the sawtooth inversion radius (inner-deposited ECRH) an inverse sawtooth oscillation combined with a long-lasting $m/n = 1/1$ mode is observed in the central line of sight (LoS) integrated soft x-ray (SXR) brightness. In contrast, when the ECRH power deposits outside the sawtooth inversion radius (outer-deposited ECRH), the normal sawtooth appears in the central LoS-integrated SXR signals. Aluminum trace impurity is then injected into two discharges with inner- and outer-deposited ECRH. Temporal behaviors of the SXR signals are analyzed with a one-dimensional impurity transport code, and radial structures of impurity transport coefficients are estimated. The result shows that the radial transport of the Al ions is strongly enhanced in the inner-deposited ECRH discharge. In particular, an outward convective velocity is significantly developed with the positive value of $V(r)$, while the $V(r)$ in the ohmic discharges takes negative value at the whole plasma radii. The simulation result also indicates that the centrally peaked Al profile appeared in the outer-deposited ECRH discharges can be effectively flattened by the inner-deposited ECRH. Modification of the impurity transport is discussed in the presence of the MHD mode.

1. Introduction

In next-generation fusion devices the reduction of impurity concentration in core plasmas is of great importance not only for the decrease in the line radiation loss but also for mitigation of the fuel dilution and the bremsstrahlung radiation to achieve high-performance plasmas in the high density regime. In experiments, the RF heating, especially the electron cyclotron resonance heating (ECRH) has been widely applied as an effective tool to control impurity accumulation in the plasma core [1]. With ECRH, an increase in the central impurity diffusivity and suppression of the convective pinch, sometimes even a reversal to the outward convection, have been observed [2, 3]. However, the interaction between the edge plasma and the first wall generally becomes strong during the ECRH along with the increase of non-thermal electrons. This could cause a serious concern for ITER in which a high-Z material such as tungsten will be used as the plasma facing components. Therefore, understanding of impurity behaviors with ECRH and related physics are necessary. The possible interpretation for the strong increase of

impurity diffusivity and positive (outward) convection could be due to an enhancement of turbulence [4]. A flattening of the electron density may also play a role on the reduction of the neoclassical impurity pinch. Recently, a long-lasting m/n = 1/1 MHD activity was observed in the AUG experiment when the ECRH was applied [5]. The relation between the saturated MHD activity and the impurity density profile has also been discussed. In the HL-2A tokamak (R/a = 165/40 cm), the impact of ECRH on the impurity transport has been studied with trace impurity injection and variation of the ECRH power deposition. The relation between the ECRH power and the MHD mode as well as the inverse sawtooth oscillation are also examined.

Fig.1 Time evolution of main plasma parameters in two discharge with different ECRH deposition positions.

2. Experimental results with Al injection

In HL-2A, aluminum as the trace impurity has been injected by LBO technique into two discharges with inner- and outer-deposited ECRH. The time evolution of the main plasma parameters for the two discharges are illustrated in figure 1. The two discharges have almost the same plasma parameters except the toroidal magnetic field B_t which leads to the ECRH power deposition layer at r_{ECRH} = 24 cm for the outer-deposited ECRH discharge (dashed lines) and r_{ECRH} = 0.8 cm for the inner-deposited ECRH discharge (solid lines). As shown in the figure, the central electron temperature is higher in the inn-deposited ECRH discharge than that in the outer-deposited ECRH discharge. The corresponding electron temperature profile is peaked in the plasma center for the former and flat for the latter.

The time trace of the central chord of the SXR signals is plotted in figure 2(a) for the outer- and in figure 2(d) for the inner-deposited ECRH cases. The time period to check the sawtooth behaviors is taken just before the trace impurity injection. The central temperature of the two discharges is shown in figure (b) and (e). It is clearly visible that the normal sawtooth appears in the outer-deposited ECRH discharge while the inverse sawtooth is present in the inner-deposited ECRH discharge. The MHD activities are analyzed with the central SXR signal. The spectrogram is shown in figure 2(c) and (f) for the outer- and inner-deposited ECRH discharges, respectively. In figure 2(c), the mode exists very short and is just a precursor before the sawtooth crash. In contrast, the mode lasts for almost a whole sawtooth period for the inner-deposited ECRH discharge in figure 2(l). A strong MHD mode can be also seen from the ECE measurement in figure 2(e).

As shown in figure 1, Al ions are injected at t = 0.6 s in the two discharges with outer- and inner-deposited ECRH. The temporal behaviors of the SXR signals are compared between them for several SXR chords from the edge to the center in figure 3(a-e).
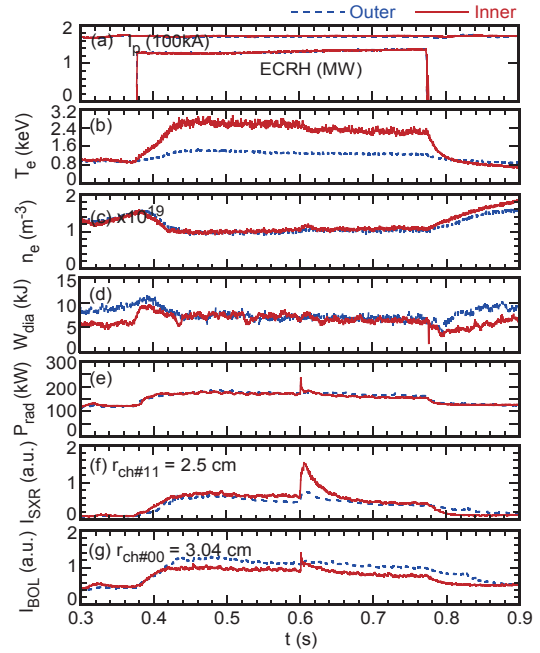
76
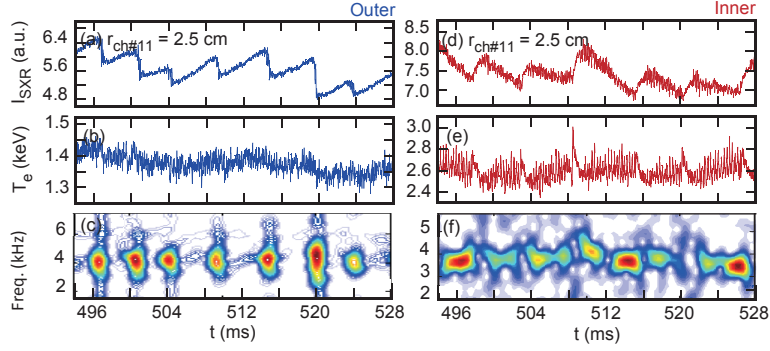
Fig.2 Time evolution of central chord of SXR signals (a), (d) and temperature (b), (e), and spectrogram of central SXR signal for outer- (left panel) and inner- (right panel) deposited ECRH discharges, respectively.

An ohmic discharge with similar plasma parameters is also plotted for comparison. The intensity of the SXR signal is normalized with its maximum and the background prior to the impurity injection is subtracted. In general, after impurity injection intensities of SXR signals show a rapidly increase and gradually decrease along the time development of the discharge. In figure 3, the increase and decrease of the SXR intensity are quite fast for the two ECRH discharges when compared with the ohmic discharge for all chords. On the other hand, the increase and decrease in the central chords of SXR signal are even more quick for the inner-deposited ECRH discharge than that in the outer-deposited ECRH case, as shown in figures 3(d) and (e). The time to reach its maximum in the central SXR signal is t = 606 ms for the inner-deposited ECRH discharge, t = 612 ms for the outer-deposited ECRH discharge and t = 634 ms for the ohmic discharge. It suggests that the penetration of the Al ions is significantly slow for the ohmic

discharge, fast for the inner-deposited ECRH discharge and in the middle for the outer inner-deposited ECRH discharge.

However, when looking at the time trace of the SXR signals outside the sawtooth inversion radius, as shown in figure 3(a-c), the increase of the SXR signal is faster for the outer-deposited ECRH discharges than that for the inner-deposited ECRH discharges. It is opposite to the central range where the increase of the SXR signal is fast for the inner--deposited ECRH case. The decrease of the SXR signal in the outside sawtooth inversion radius is obviously slower for the outer-deposited ECRH discharges than that for the inner-deposited ECRH discharges. The change is identified by the sawtooth inverse radii, which is around $r_{inv} = 8$ cm for the two ECRH discharges. The different time evolution of the SXR signals inside and
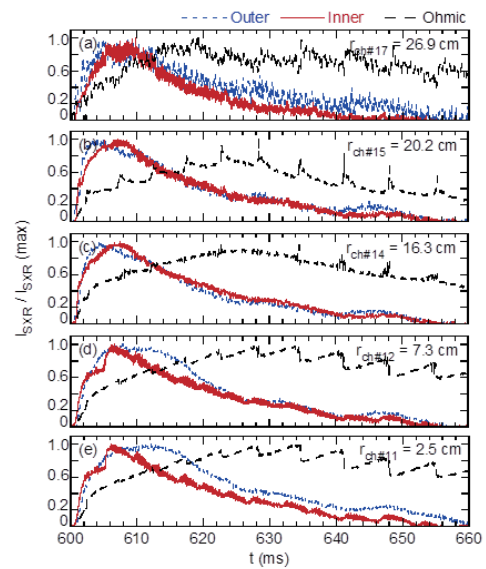
Fig.3 Time evolution of normalized SXR intensity at several chords for outer- and inner-deposited ECRH discharges, and a ohmic discharge.

outside the sawtooth inversion radius for the two ECRH discharges could refer to the change of the impurity transport in addition to the change of the plasma parameters, such as the electron density and temperature profiles with the inner- and outer -deposited ECRH.

3. Simulation with 1D impurity transport code

In order to quantitatively obtain the impurity transport coefficients, diffusion coefficient D and convection velocity V, a one dimensional impurity transport code STRAHL [6] has been applied. The measured plasma parameters of these discharges, especially the electron density and temperature profiles, are used as the input data in the code.   The STRAHL code starts from an initial guess of the transport coefficient radial profiles.   It solves the coupled continuity equations and reconstructs the emission measurements.   Then the transport coefficients are modified iteratively until the difference between the reconstructed signals and the measured ones is minimized.   The obtained impurity transport coefficients with good fitting the experimental results of the three discharges are shown in figure 4.   The simulation results indicate that for the ohmic discharge, the diffusion coefficient at the outer part of the

Fig.4   Radial profiles of (a) diffusion coefficient D, (b) convective velocity V and ratio of V to D for the three discharges.

plasma is much larger than that at the plasma center, e.g. $D = 0.9$ m^2/s at $\rho = 0.8$ and $D = 0.2$ m^2/s at $\rho = 0$. On the other hand, the convection velocity takes negative value in the whole plasma radii.   This entire inward convective velocity reflects the peaked density profile of impurity.   The ratio of V to D in figure 4(c) also confirms an inward movement of Al ions along the whole radial range.

For the outer-deposited ECRH discharge, the diffusion coefficient is significantly enhanced in the whole plasma range but the profile shape keeps similar to the ohmic case.   On the contrary, the convection velocity in the outer-deposited ECRH discharge has a totally different profile from the ohmic case, i.e. the value is positive at mid radius of plasma $0.4 < \rho < 0.7$.   A much small value of V appears in the center at $\rho < 0.4$ in negative.   The ratio V/D clearly suggests that the impurity flux is enhanced in the plasma center, while the outward flux appears in the outer part of the plasma.   For the inner-deposited ECRH discharge, on the other hand, the radial profile of the diffusion coefficient in the inner-deposited ECRH discharge is similar to that in the outer-deposited ECRH discharge, but the value is a little different. $D(\rho=0) = 1$ m^2/s is obtained for the inner-deposited ECRH discharge while $D(\rho=0) = 0.3$ m^2/s is for the outer-deposited ECRH discharge.   They increase to $D(\rho=1) = 10$ m^2/s for the former and 11 m^2/s for the latter.   The change of D just reflects the time evolution of the SXR between the two ECRH discharges, as shown in 3. Moreover, the value and the profile of the convective velocity are considerably different between the two ECRH discharges.   An outward convective velocity appears almost along the whole radial range ($\rho \leq 0.8$). The ratio V/D in the inner-deposited ECRH discharge also directs outwards and is much larger than that of the outer-deposited ECRH discharge for the whole plasma region.   This indicates a significant increase of
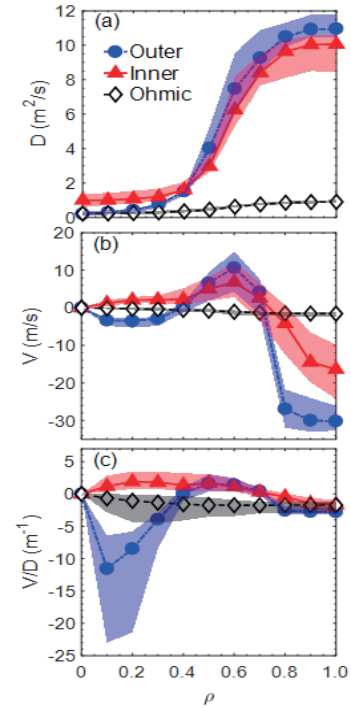
the outward flux of the impurity.

The calculated Al ions density profile also confirms that a large amount of Al ions are transferred to the plasma center and a clear impurity accumulation appears at $\rho \leq 0.3$ where the peaking factor becomes large (see figure 4(c)) in the outer-deposited ECRH discharge. On the contrary, the inner-deposited ECRH discharge seems to have less radial transport and a flat impurity density profile is formed. In the ohmic discharge, most of the Al ions deposited in the plasma edge gradually moves toward the plasma center, reflecting the presence of the inward convection at the whole plasma radii.

5. Summary

The effect of the ECRH on the impurity transport has been investigated by changing the ECRH deposition layer against the sawtooth inversion radius in the HL-2A tokamak. For the purpose Al is injected by LBO method in two different ECRH discharges with power deposition inside and outside the sawtooth inversion radius. Temporal behaviors of SXR array signals after the LBO are analyzed with the impurity transport code, STRAHL. In the inner-deposited ECRH discharge with inverse sawtooth activity, a spatially continued outward convection is observed in the central plasma region of $\rho \leq 0.7$ and an inward convection is observed in the edge plasma range of $\rho \geq 0.7$, while an inward convection always appears at the whole plasma radii in the ohmic discharge. The diffusion coefficient is enhanced in the whole plasma range compared to the ohmic discharge. As a result a flat Al density profile is obtained with the inner-deposited ECRH. In the outer-deposited ECRH discharge, on the other hand, an inward convection is observed in a narrow region of the plasma center ($\rho \leq 0.4$), while the diffusion coefficient profile is similar to the inner-deposited ECRH case. This change in the convective velocity forms a centrally peaked Al density profile. The result strongly suggests an effect of the m/n = 1/1 mode on the impurity transport.

References

[1] R.Dux, et al., Plasma Phys. Control. Fusion **45**(2003)1815.

[2] J.Hong, et al., Nucl. Fusion **55**(2015)063016.

[3] Z. Y. Cui et al., Nucl. Fusion 53 (2013) 093001.

[4] C. Argioni, et al., Phys. Rev. Lett. 96(2006)095003.

[5] M. Sertoli, et al., Nucl. Fusion 55(2015)113029.

[6] R. Dux, 2006 Technical Report No 10/30 IPP Garching Germany.

Dependence of carbon impurity flow in the edge stochastic magnetic field layer of LHD on the magnetic field configuration

T. Oishi[1,2], S. Morita[1,2], S. Y. Dai[3], M. Kobayashi[1,2], G. Kawamura[1], X. L. Huang[1], Y. Liu[2], M. Goto[1,2], and the LHD Experiment Group[1]

[1]National Institute for Fusion Science, Toki 509-5292, Gifu, Japan

[2]Department of Fusion Science, Graduate University for Advanced Studies, Toki 509-5292, Gifu, Japan

[3]Key Laboratory of Materials Modification by Laser, Ion and Electron Beams (Ministry of Education), School of Physics, Dalian University of Technology, Dalian 116024, PR China

Abstract

The parallel flow of carbon impurity in a thick stochastic magnetic field layer called "ergodic layer" located at the edge plasma of Large Helical Device (LHD) is studied by space-resolved vacuum ultraviolet (VUV) spectroscopy using a 3 m normal incidence spectrometer.   The carbon flows have directions same as the friction force calculated with a three-dimensional simulation code, EMC3-EIRENE, in both inward and outward shifted magnetic configurations with the position of the magnetic axis, R_{ax}, of 3.6 m and 3.9 m, respectively.   The carbon flows have directions same as the friction force in both inward and outward shifted configurations.   In the case of R_{ax} = 3.9 m, the flow has a large value even in the low density regime.

1. Introduction

Stochastization of edge magnetic fields is extensively studied not only for the ELM mitigation but also for the plasma detachment and the impurity transport.   A thick stochastic magnetic field layer called "ergodic layer" of the large helical device (LHD) consists of stochastic magnetic fields with three-dimensional structure intrinsically formed by helical coils, while well-defined magnetic surfaces exist inside the last closed flux surface [1].   It is therefore extremely important to study the impurity behavior and transport in the ergodic layer and to compare with those in the scrape-off layer of tokamaks.   In LHD, it is found that carbon impurities are screened by the presence of the ergodic layer [2] and iron impurities are more effectively screened.   As a result, the iron density in core plasmas of LHD is found to be extremely low despite the stainless steel vacuum vessel [3].   The effect of "impurity screening" has been also compared among several kinds of magnetic configurations with the different position of the magnetic axis, R_{ax}.   It has been revealed that the impurity screening effect is more obvious in the outward-shifted magnetic configuration with R_{ax} = 3.9 m and a thick ergodic layer than the inward-shifted magnetic configuration with R_{ax} = 3.6 m and a thin ergodic layer [2].   A transport model for the impurity behavior in the ergodic layer has been proposed considering the parallel momentum balance on impurity ions along a magnetic field line connecting the core plasma and the divertor plate [4].   A transport model for the impurity behavior in the ergodic layer has been proposed considering the parallel momentum balance on impurity ions along a magnetic field line connecting the core plasma and the divertor plate based on the

following equation;

$$m_Z \frac{\partial V_{Z\parallel}}{\partial t} = -\frac{1}{n_Z} \frac{\partial T_Z n_Z}{\partial s} + ZeE_\parallel + m_Z \frac{V_{i\parallel} - V_{Z\parallel}^{imp}}{\tau_s} + 0.71 Z^2 \frac{\partial T_e}{\partial s} + 2.6 Z^2 \frac{\partial T_i}{\partial s},$$

(1)

where five terms in the right-hand side are contributions of impurity ion pressure gradient, parallel electric field, friction force between bulk ions and impurity ions, electron thermal force, and ion thermal force, in the order. Among these terms, the friction force terms and the ion thermal force term are the dominant terms. When the ion density gradient increases, the friction force increase resulting the impurity flow is directed toward divertor plates, which means the impurity screening. On the other hand, when the ion temperature gradient increases, the ion thermal force increases resulting that the impurity flow is directed toward the core plasmas, which means the impurity accumulation. Based on the model, the parallel flow of the impurity ions is considered to be a key mechanism to determine impurity distributions in the ergodic layer. Therefore, in this study, measurement of carbon impurity flow is attempted by using a space-resolved VUV spectroscopy and relation between the flow and the impurity screening effect is discussed.

2. Measurements of flow velocity of the carbon impurity

Figure 1 shows a typical waveform of a discharge with a magnetic configuration with $R_{ax} =$ 3.6 m and the toroidal magnetic field, B_t, of 2.75 T. Power of the electron cyclotron heating (ECH) and the neutral beam injection based on the negative ion sources (n-NBI) central electron temperature and central electron density, and the plasma stored energy are shown together. The discharge initiated by ECH is grown by three n-NBI beams with total port-through power of 10 MW and maintained with a flat-top phase for 1 s as shown in Fig. 1. A space-resolved VUV spectroscopy was attempted in the flat-top phase of the discharges by using a 3m normal incidence VUV spectrometer [5]. The edge flow profile is investigated with high spatial resolution by using the viewing angle of the edge profile measurement of the VUV spectroscopy from Doppler shift of the second
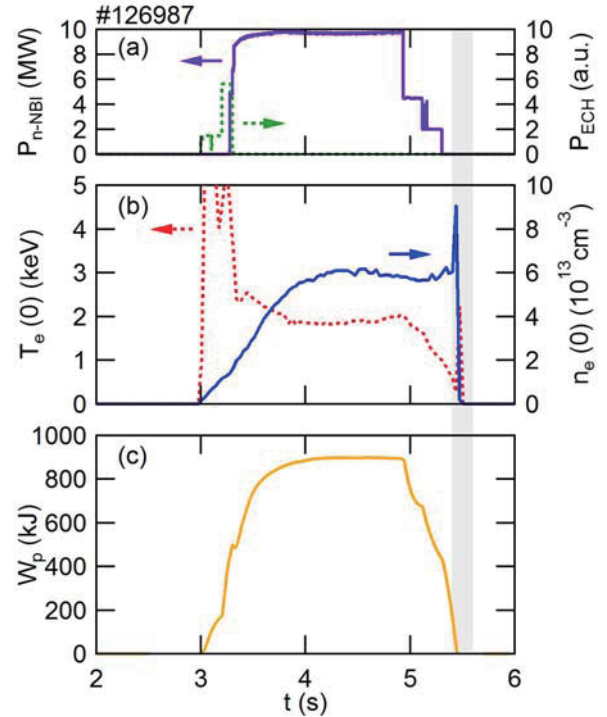
Fig. 1 Typical waveform of a discharge in which the space-resolved VUV spectroscopy is attempted. (a) ECH and n-NBI power, (b) central electron temperature and central electron density, and (c) plasma stored energy.

81

order of CIV line emission (2 × 1548.20 Å) at a horizontally-elongated plasma position of LHD.

Figure 2(a) shows vertical profiles of flow velocity at the bottom edge of the ergodic layer derived from CIV 1548.20 × 2 Å line emission measured by VUV spectroscopy for the line averaged electron density, n_e, of 2.9, 4.2, and 6.0 × 10^{13} cm^{-3} with a magnetic configuration with R_{ax} = 3.6 m and B_t = 2.75 T. The observation range of the edge profile measurement of the VUV spectroscopy is also shown in Fig. 2(b). The measured flow velocity is projection of the flow along the observation chord which can be approximately considered to be the direction of the plasma major radius.   Therefore, a variable of v_R is used to indicate the measured flow value.   Positive and negative sign in the horizontal axis of Fig. 2(a) corresponds to the outboard an inboard direction along the plasma major radius, respectively.   As increasing the electron density, the flow velocity toward the outboard direction develops clearly with the maximum value at Z = -480 mm, which is a location close to the outermost region of the ergodic layer. This direction is also same as the friction force in the parallel momentum balance for R_{ax} = 3.6 m calculated with EMC3-EIRENE code [6].

We compared the results with a magnetic configuration of R_{ax} = 3.9 m and B_t = 2.539 T as shown in Fig. 3.   Figure 3(a) indicates that the flow is directed toward the inboard direction with the maximum value at Z = -480 mm.   This direction is also same as the friction force in the parallel momentum balance for R_{ax} = 3.9 m calculated with EMC3-EIRENE code, even though it is opposite direction to that of R_{ax} = 3.6 m case.   The maximum value of the flow does not depend on the electron density within the density
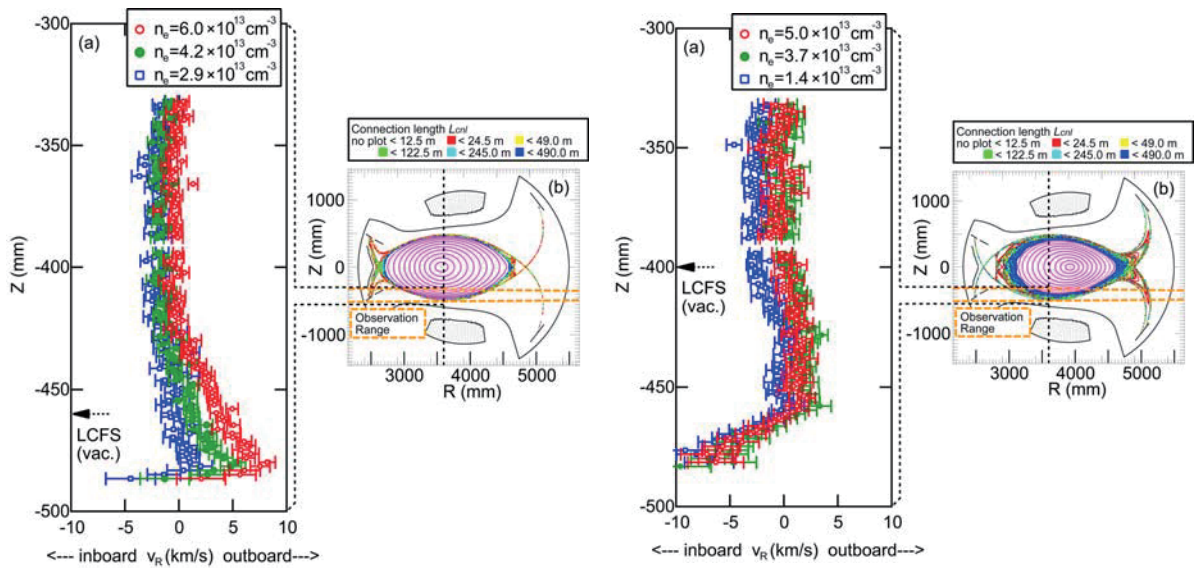
Fig. 2   (a) Vertical profiles of flow velocity at the bottom edge of the ergodic layer derived from the Doppler profile of the second order of CIV line emission (2 × 1548.20 Å) measured by VUV spectroscopy for inward-shifted magnetic configuration with R_{ax} = 3.6 m.   (b) The observation range of the VUV spectroscopy.

Fig. 3   (a) Vertical profiles of flow velocity at the bottom edge of the ergodic layer derived from the Doppler profile of the second order of CIV line emission (2 × 1548.20 Å) measured by VUV spectroscopy for outward-shifted magnetic configuration with R_{ax} = 3.9 m.   (b) The observation range of the VUV spectroscopy.

range employed in this experiment.

The electron density dependence of the maximum value of the observed flow is summarized in Fig. 4. All plots in the figure have directions same as the friction force even though the flow directions are opposite between $R_{ax} = 3.6$ m and $R_{ax} = 3.9$ m. In the case of $R_{ax} = 3.9$ m, the flow has a large value even in the low density regime. It might have some relationship with the fact that the impurity screening effect for $R_{ax} = 3.9$ m is larger than $R_{ax} = 3.6$ m. Further experiments and simulations in the low density regime are needed to clarify the density dependence of the impurity flow, which remains as a future study.

Fig. 4 Observed C^{3+} flow at the bottom edge of the ergodic layer as a function of density for inward-shifted magnetic configuration with $R_{ax} = 3.6$ m and outward-shifted magnetic configuration with $R_{ax} = 3.9$ m.

3. Summary

The parallel flow of carbon impurity in a thick stochastic magnetic field layer called "ergodic layer" located at the edge plasma of Large Helical Device (LHD) is studied by space-resolved vacuum ultraviolet (VUV) spectroscopy. The carbon flows have directions same as the friction force calculated with a three-dimensional simulation code, EMC3-EIRENE, in both inward and outward shifted configurations with $R_{ax} = 3.6$ m and $R_{ax} = 3.9$ m, respectively. In the case of $R_{ax} = 3.9$ m, the flow has a large value even in the low density regime.

References

[1] T. Morisaki, K. Narihara, S. Masuzaki *et al.*, J. Nucl. Mater. **313-316** (2003) 548.

[2] M. B. Chowdhuri, S. Morita, M. Kobayashi *et al.*, Phys. Plasmas **16** (2009) 062502.

[3] S. Morita, C. F. Dong, M. Kobayashi *et al.*, Nucl. Fusion **53** (2013) 093017.

[4] M. Kobayashi, S. Morita, C. F. Dong *et al.*, Nucl. Fusion **53** (2013) 033011.

[5] T. Oishi, S. Morita, C. F. Dong *et al.*, Appl. Opt. **53** (2014) 6900.

[6] T. Oishi, S. Morita, S. Y. Dai *et al.*, 26th IAEA Fusion Energy Conference, Kyoto, Japan, 17-22 October 2016, EX/7-2.

Modeling of the effects of drifts on edge plasma and impurity transport in EAST

Fuqiong Wang [1], Y. M. Duan [2], X. J. Zha [1], F. C. Zhong [1], L. Q. Hu [2], H. W. Lu [1], L. Li [1]

[1] Department of Applied Physics, College of Sciences, Donghua University, Shanghai 201620, China

[2] Institute of Plasma Physics, Chinese Academy of Sciences, Hefei 230031, Anhui, China

Abstract

The newly developed SOLPS-ITER code package has been used to investigate the effects of drifts on the in-out/up-down asymmetry of divertor heat/particle fluxes in EAST. Characteristics of the divertor heat/particle fluxes in a double null (DN) discharge with $\mathbf{B} \times \triangle B$ points to the upper and lower directions h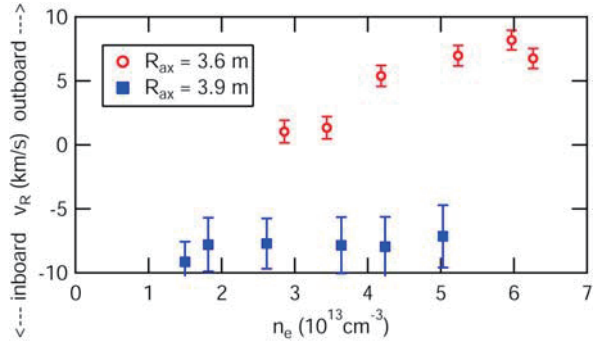ave been investigated by SOLPS-ITER calculations. It is found that the classical drifts will directly affect the parallel plasma flow velocity, and thus affect the divertor asymmetry of particle fluxes. The divertor heat fluxes can also be affected, but not so evidently as that for the divertor particle fluxes. Besides, the influences of classical drifts on the transport properties of W impurity have been investigated by performing the coupled SOLPS-DIVIMP modeling, finding that the leakage of the W impurity from the divertor region to the core will be greatly affected, due to the fact that friction force exerted on the impurity ions has been greatly affected.

1. Introduction

Divertor particle and heat controllability is one of the most critical issues to be solved for the long-pulse and/or high power operation of the future fusion devices, such as ITER and DEMO. EAST, the first fully superconducting tokamak in the world, is designed to study key issues of plasma physics and fusion technology in steady-state operation in support of ITER. As the advance of the EAST experimental campaigns, the heating power has been increased step by step. Thus, divertor asymmetry, a ubiquitous feature in tokamaks, becomes more and more important for the operation and design of EAST divertors, especially for the H-mode discharges [1].

Divertor asymmetry can be driven by the classical drifts [2-9] and the different distributions of the particle and heat sources in the inboard and outboard sides, e.g. enhanced ballooning-like transport near the outboard midplane [10-12]. However, the change of the divertor asymmetry is usually associated with the classical drifts, including the $E \times B$ drift and the grad-B drift . To predict and/or interpret the effects the classical drifts on the divertor asymmetry, modeling on the main characteristics of the divertor heat and particle fluxes in EAST discharges with grad-B drift points towards the upper and lower 'X' point directions has been performed and will be presented in this paper. Besides, the effects of $E \times B$ drift and grad-B drift on the divertor asymmetry have been differentiated. Due to the fact that the plasma flows can been greatly affected by the classical drifts, and thus the friction force, defined as $m\frac{(v_\parallel - v)}{\tau_s}$, exerted on the impurity ions will definitely be affected. We have also studied the influences of classical drifts on the W impurity transport to get hints on how to control the leakage of W impurity from the divertor region to the core.

SOLPS [13-16], the coupling of 2D multi-fluid plasma code B2/B2.5 [16]and the Monte Carlo neutral transport code Eirene [14], has been widely used for the edge plasma and impurity transport modeling. In SOLPS, lots of complicated physics processes, e.g. drifts, ballooning like

transport, etc., can be considered. At present, various versions of SOLPS code packages have been developed, including SOLPS4.x, SOLPS5.x, SOLPS6.x and SOLPS-ITER. Here, in this paper the plasma conditions have been constructed by SOLPS-ITER code [17], which is the latest version of SOLPS. As for the W impurity transport modeling, the Monte Carlo code DIVIMP [18] has been selected to use, since it is more effective than the SOLPS code to be used for the high-Z impurity transport modeling.

This paper has been organized as follows: section 2 will introduce SOLPS-ITER modeling of divertor asymmetry, including the effects of $E \times B$ drift and the grad-B drift on the divertor heat and particle asymmetry. Section 3 will show the SOLPS-DIVIMP modeling of the influence of drifts on the W impurity transport. The summary and conclusions will be presented in section 4.

2. SOLPS-ITER modeling of drifts on the divertor asymmetry

2.1 models used in the simulation
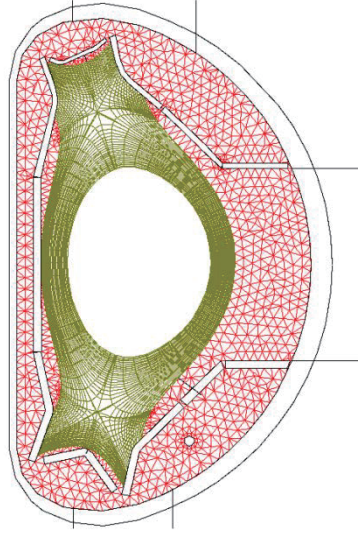
Fig. 1 grids used for the SOLPS-ITER calculation

To investigate the effects of classical drifts on the in-out and up-down asymmetry, a double null (DN) discharge with toroidal field $B_T \sim 2.0T$ has been selected to model. Fig. 1 shows the grids for the SOLPS-ITER calculation, including the quasi-orthogonal grids for the B2.5 calculation and the triangular grids for the EIRENE calculation. The B2.5 calculation grids are generated based on the MHD equilibrium from EFIT code and the EAST geometry. From fig. 1, the B2.5 calculation region extends from the scraped-off layer (SOL) to the region which is often referred to as the outer core by ~5cm. Since the neutral transport cannot be restricted by the magnetic field, so that the calculation region of the neutral transport code EIRENE not only includes the B2.5 calculation region but the gaps between the B2.5 calculation region and the plasma facing components (PFCs), see fig. 1.

Main inputs for the SOLPS-ITER calculation are as follows:

(1) At the inner core boundary, the density of the deuterium ion D$^+$ $n_u = 1.2e19m^{-3}$. The neutral deuterium D^0 density is very low due to the high temperature and strong ionization there. Thus, n$_0$ at the core-edge interface is set to be 0. Also, an assumption that T$_e$=T$_i$ =350 eV is made.

(2) At the divertor target plates, the standard sheath boundary condition is applied. According to

the Bohm criterion, the flow needs to be at least sonic speed at the entrance of the sheath $nV_{\parallel} = nb_x C_s$. With the inclusion of the drifts, the target sheath boundary condition would become []: $nV_{\parallel} + nV_{E \times B} = nb_x C_s$.

(3) At the wall and the dome-side boundaries of PFRs, the radially decay length of the electron and ion temperature λ_T is set to 0.01 m. The ion leakage is given by $\Gamma_{loss} = \alpha c_s n_a$, where c_s is the sonic speed and n_a is the density of the species a, $\alpha = 0.001$ for ions. The ions leak off and recycle to neutrals. The recycling coefficient at the targets and wall is set to be 1.0. The recycling coefficient is set to be 0.95 at the entrances of the pumping holes, giving a pumping speed up to ~70 m³.s⁻¹.

Transport parallel to the magnetic field is assumed to be classical but flux limited: for neutral diffusion, flux is limited to the thermal flux; electron and ion parallel heat fluxes are limited to 30% and 60%, respectively, of the thermal fluxes. Sensitivity of solutions to these flux limits is not considered here, but should not qualitatively affect the results.. Due to the lack of the reliable physical models, the cross-field heat and particle diffusivities are usually assumed to be constant, which is considered to be the simplest and appropriate approximation introducing the least variables. Typically, similar to that for ITER [], assumes that the anomalous particle diffusivity, $D_{\perp} = 0.5 m^2/s$, and the thermal heat diffusivities, $\chi_{\perp i} = \chi_{\perp e} = \chi_{\perp} = 1.0\ m^2/s$. For simplicity, the inward pinch velocity, V_{pinch}, is set to 0.

In the modelling, the atomic and molecular processes involving D^0 neutrals, D_2 molecules, and D_2^+ molecular ions, including charge exchange, ionization, and recombination are controlled self-consistently via an iterative coupling of plasma transport computations with the kinetic Monte-Carlo neutral particle transport simulation code EIRENE. The atomic data for the SOLPS-ITER calculation has been provided by ADAS [19]. Those detailed reactions are shown in table 1.

Table 1. Reactions considered in the EIRENE calculation

Index	Reactions	Type
1	$e + D \rightarrow 2e + D^+$	Ionization
2	$D^+ + D \rightarrow D + D^+$	Charge exchange
3	$e + D_2 \rightarrow 2e + D_2^+$	Ionization
4	$e + D_2 \rightarrow e + D + D$	Dissociation
5	$e + D_2 \rightarrow 2e + D + D^+$	Dissociative ionization
6	$D^+ + D_2 \rightarrow D^+ + D_2$	Elastic collision
7	$D^+ + D_2 \rightarrow D + D_2^+$	Charge exchange
8	$e + D_2^+ \rightarrow e + D + D^+$	Dissociation
9	$e + D_2^+ \rightarrow 2e + D^+ + D^+$	Dissociative ionization
10	$e + D^+ \rightarrow D$	Recombination

2.2 Effects of classical drifts on the divertor asymmetry

By performing SOLPS-ITER calculation with the models presented above, the divertor heat and particle fluxes of the no drift case, normal B_T case and the reversal B_T case have been generated and are shown in fig. 2, where normal B_T means that the grad-B drift ($\mathbf{B} \times \nabla B$) points to the lower 'X' point, while the reversal B_T means that the grad-B drift points to the upper 'X' point. From fig. 2, for the no drift case, no evident in-out and up-down asymmetry have been found.

However, both the peak values and the decay lengths of the divertor D^+ fluxes changes as the change of the direction of toroidal field B_T, i.e. the direction of drift velocity, so that the in-out and up-down divertor particle asymmetry has been evidently changed. Detailed investigation about the relationship between the classical drifts and the decay lengths of the divertor heat and particle fluxes in EAST will be focused and presented on in the future work.

Fig. 2 D^+ fluxes onto the lower inner (LI), lower outer (LO), upper inner (UI) and the upper outer (UO) targets for the no drift case, normal B_T case and the reversal B_T case.
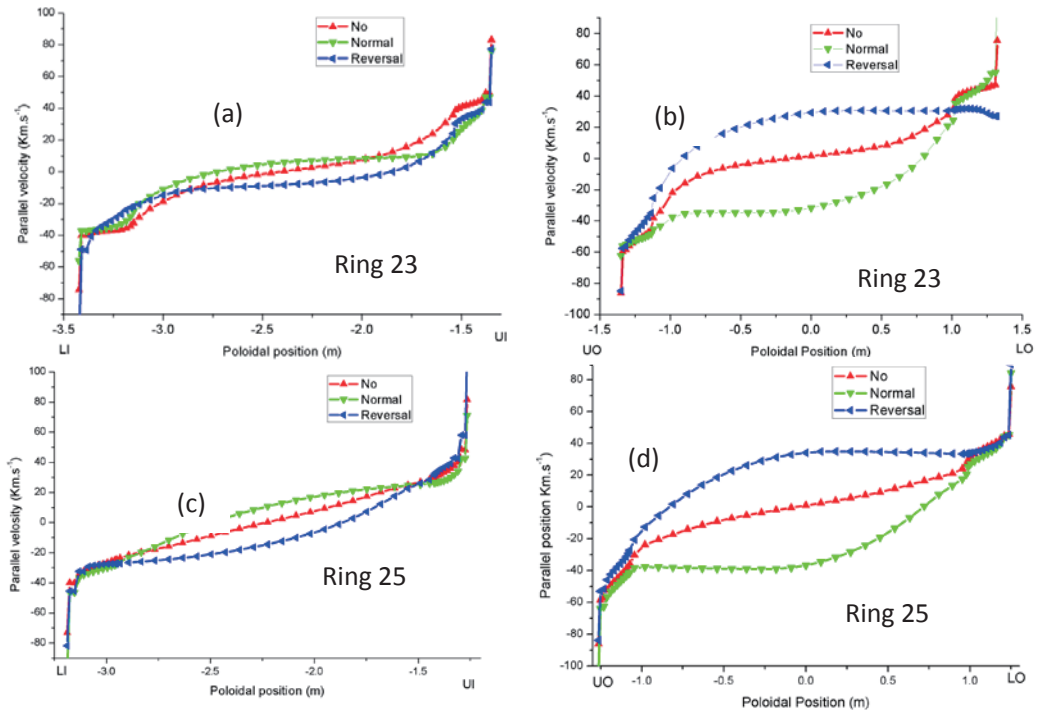
Fig. 3 Parallel plasma flow velocity along the inboard ((a), (c))and outboard ((b), (d))SOL flux tubes (iy=23 ((a), (b)), 25 ((c),(d))) for the no drift case, Normal B_T case and the reversal B_T case

Some recent research [21] finds that the poloidal drift $E_r \times B$ could play a dominant role in the up-down asymmetry, The main physical mechanism can be attributed to the target sheath boundary condition, which must be modified on the account of drifts as follows:

$$nV_\parallel + nV_{E \times B} = nb_x C_s$$

To hold this equation, the parallel velocity ($V_\parallel$) is adjusted according to poloidal drift velocity $V_{E \times B}$. According to fig. 3, the parallel velocity $V_\parallel$ is ~10-100 $Km.s^{-1}$, and $V_\parallel$ has evidently been changed by the classical drifts, so that the plasma conditions, including the plasma density and particle flux will be adjusted by drifts. Also, we have tried to differentiated the effects of grad-B drift and $E \times B$ drift on the divertor divertor particle fluxes. From the calculation, the grad-B drift and $E \times B$ drift velocity have the same orders of magnitude (~$10^3 m.s^{-1}$). Also, the grad-B drift and $E \times B$ drift have almost the same effects on the divertor particle fluxes.

Fig. 4 shows the heat fluxes onto the lower inner (LI), lower outer (LO), upper inner (UI) and the upper outer (UO) divertor target for the no drift case, normal B_T case and the reversal B_T case. From fig. 4, the classical drifts can also have effects on the divertor heat fluxes, including the peak values and the decay lengths of the divertor heat fluxes, but not so evident as the effects on the divertor particle fluxes, the reason for which will be described in the following part.
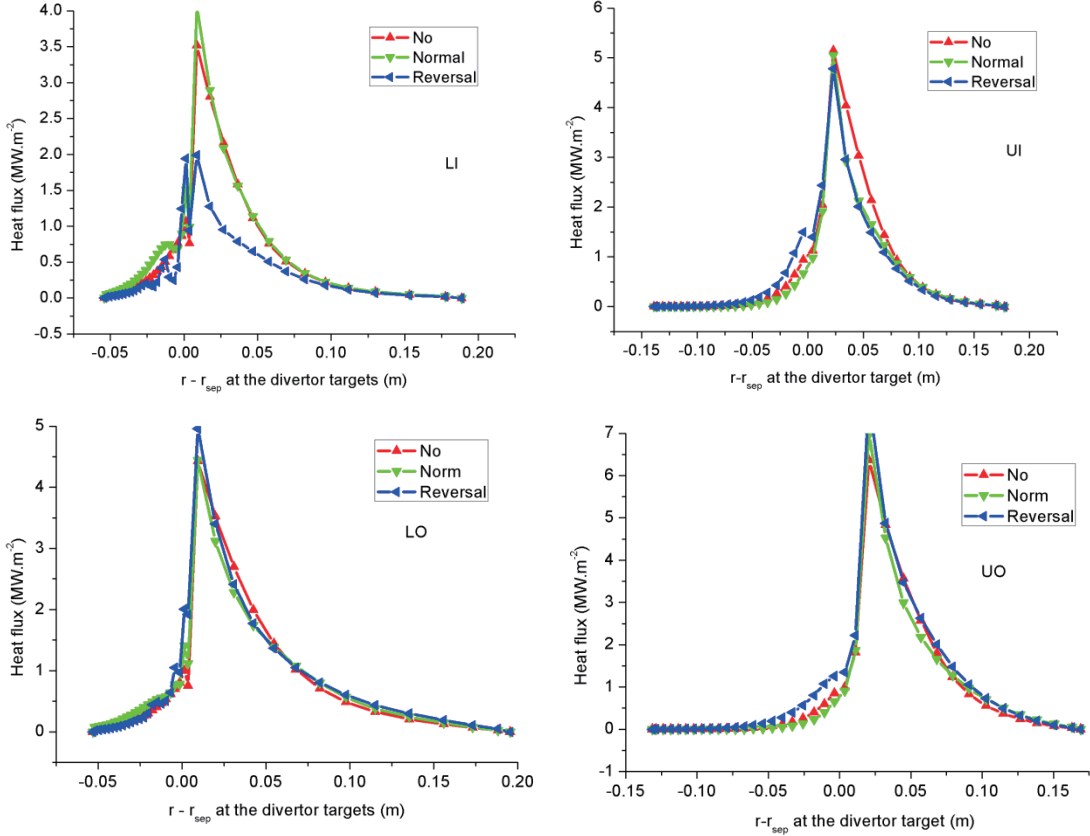
Fig. 4 Total heat flux onto the lower inner (LI), lower outer (LO), upper inner (UI) and the upper outer (UO) targets for the no drift case, normal B_T case and the reversal B_T case.

In the calculation, total heat flux onto the divertor target fht is given by:

fht=fhpe+fhme+fhe+fhmi+fhi+fhj

from which, the total target heat flux consists of the target flux of the potential energy released from the electrons (fhpe) and ions (fhpi), the kinetic energy of the electrons (fhme) and ions (fhmi),

the electric heat energy *fhj*, as well as the heat flux of electrons (*fhe*) and ions (*fhi*) due to the conductive and convective processes. More detailed description of these components of the target heat flux can be seen in reference [20]. Fig. 5 shows the ion heat flux onto the different divertor targets. By comparing fig. 5 and fig. 2, we can see that the divertor D^+ flux and the ion heat flux (*fhi*) have very similar profiles for the same divertor target, so that the divertor ion heat fluxes could also be affected significantly. However, the divertor ion heat flux only take a small part of the total divertor heat flux, as can be seen from the comparison between fig. 4 and fig. 5, so that the total divertor heat flux have not been evidently affected by the classical drift. That is to say, from SOLPS-ITER calculation the classical drifts will mainly affect the divertor ion heat fluxes, while the other components of the total divertor heat fluxes cannot be evidently affected by the usual drifts.
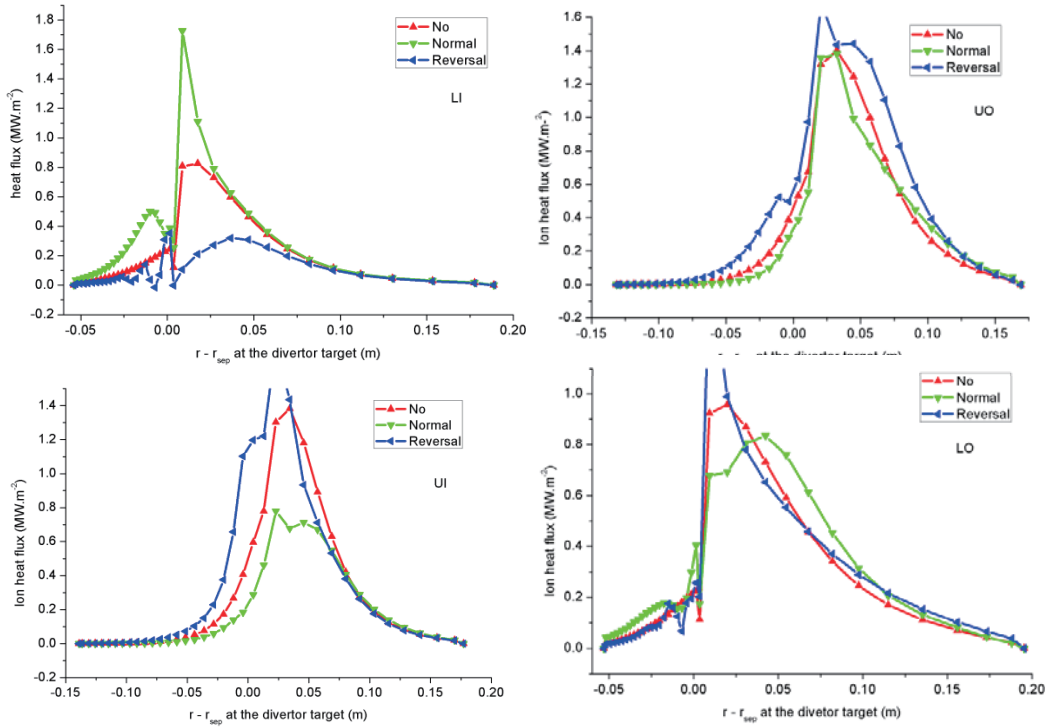
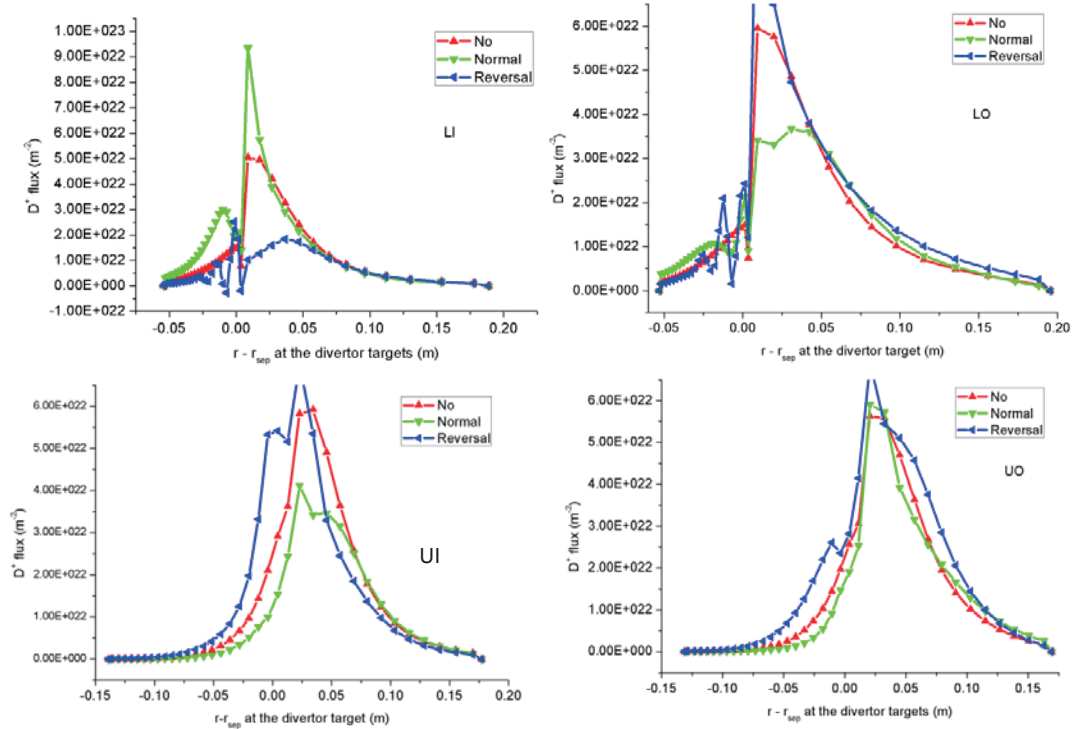Fig. 5 Ion heat flux onto the lower inner (LI), lower outer (LO), upper inner (UI) and the upper outer (UO) targets for the no drift case, normal B_T case and the reversal B_T case

3. Effects of the classical drifts on the W impurity transport

3.1 models for the impurity transport modeling
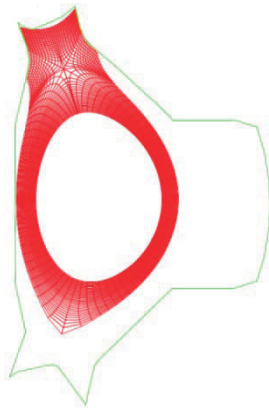
Fig. 6 grids used for the W impurity transport modeling

DIVIMP is a widely used Monte Carlo impurity transport code, which traces the motion and ionization state of the impurities. Although the DIVIMP code has previously been developed for modeling of C impurity transport for the single null discharges, this code is very effective at high-Z (e.g. W) impurity transport modeling. Since in 2014, the upper divertor of EAST has been changed to be made of tungsten, this section will focus on DIVIMP modeling of W impurity transport for an EAST upper single null (USN) discharge. Grids for the calculation are shown in fig. 6. The background plasma conditions (n_e, T_e, T_i, $v_\parallel$, E, …) for DIVIMP calculation has been provided by SOLPS with the models described in section 2.1. Based on the SOLPS provided plasma conditions, the sputtering fluxes of W impurity from the upper divertor of EAST have been calculated. After that, the W atoms W^0 will be launched from the divertor target plates. The launching probability from a specific element of the divertor target plates is proportional to the sputtering flux there. For the W impurity atoms, they are assumed to travel in straight line until they hits at some other surfaces or they are ionized to be impurity ions. When the impurity neutrals strike at the surface of the plasma facing components, they are assumed to be reflected from the surface based on the reflection model coupled in TRIM. Once the W atoms are ionized to be W ions, their parallel-to-B motion and cross-field motion will be treated separately [22].
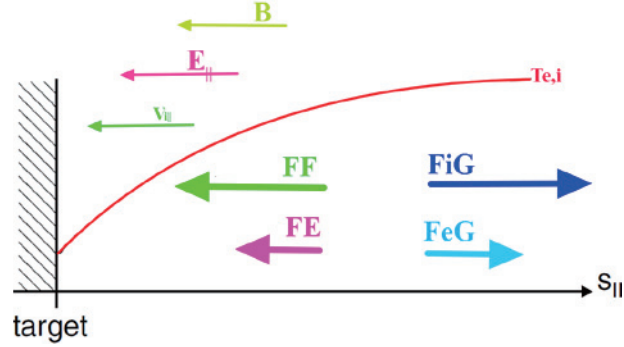
Fig. 7 Forces assumed to be exerted on the impurity ions in the direction parallel to B

The cross-field motion is assumed to be anomalous with the diffusivity $D_\perp = 1.0$ m/s^2 In the direction parallel to B, total force exerted on the impurity ion can be described as [22] follows (see fig. 7):

$$\text{m}\frac{dv}{dt} = F_{total} = -\frac{1}{n}\frac{dp}{ds} + m\frac{(v_\parallel - v)}{\tau_s} + ZeE + \alpha_e\frac{dT_e}{ds} + \beta_i\frac{dT_i}{ds}$$

Where $-\frac{1}{n}\frac{dp}{ds}$ is the pressure gradient force, s is the distance along the magnetic field line,

$m\frac{(v_\parallel - v)}{\tau_s}$ is the friction force, ZeE is the electric force, $\alpha_e\frac{dT_e}{ds}$ and $\beta_i\frac{dT_i}{ds}$ are the electron and ion temperature gradient force respectively. Among all the components of the total force, the thermal force and friction force are usually much larger than others. Usually, the temperature gradient force tends to drive the impurity ions from the divertor region to the upstream, while the friction force tends to drag the impurity ions to the divertor region. Therefore, the leakage of the impurity ions from the divertor region to the core is the competition between the friction force and the thermal force. As is mentioned above, the classical drifts will directly affect the parallel plasma flow velocity $V_\parallel$, and thus the friction force F_{fric} could be definitely affected. Accordingly, we have performed DIVIMP modeling of W impurity transport in EAST for the no drift case, normal

B_T case and the reversal B_T case.

3.2 Effects of drifts on the W production and transport of W impurity
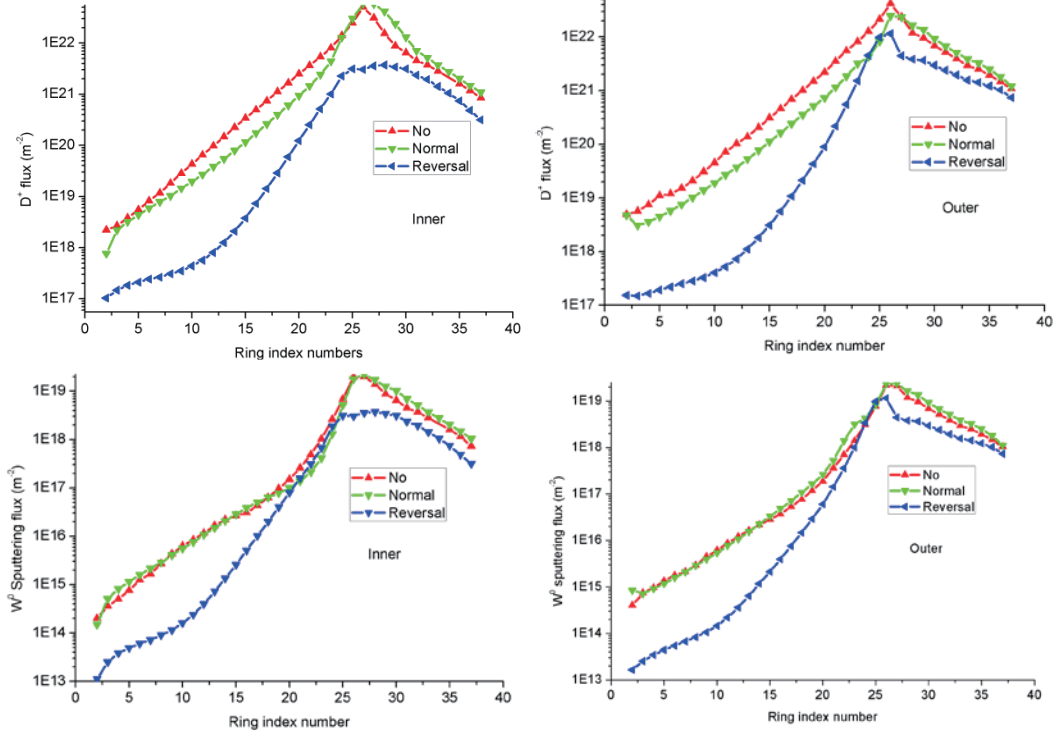
Fig. 8 Calculated D^+ flux and the W^0 sputtering flux from the upper inner and outer divertor respectively.

As is mentioned above, the deuterium ion D^+ flux, as well as the plasma temperature at the divertor region, can be greatly affected by the classical drifts. Therefore, the sputtering flux of the W impurity form the divertor targets due to the bombardment of the D^+ could definitely be affected, just as fig. 8 shows. The calculated W^0 sputtering yield, defined as the ratio of the integrated W sputtering flux (f_w in table 2) to integrated target D^+ flux, is of 10^{-4} orders of magnitude for all the three cases. Also, from fig. 8 the sputtering yield, determined by the D+ flux, the electron and ion temperature (T_e, T_i) at the divertor targets, has been changed as the change of the direction of the drift velocity.

Table 2 shows some important information about the production and transport of W impurity, including the integrated W sputtering flux from the divertor targets f_w, the content of W impurity, i.e. the ratio of the W impurity density to the electron density, in core c_{w_core}, the maximum values of the friction force exerted on the W^{+1} ions F_{fric_max}, and the leakage of the W impurity from the divertor region from which they are sputtered to the core, which is defined to be the ratio of the W impurity density in core to the W impurity density in the divertor region. From table 2, we can see that these different cases have quite different core leakage of W impurity. For this USN discharge, $P_{SOL}=1.0$ MW, $n_u=2.0e19$ m^{-3}, the normal B_T case has the lowest core leakage of W impurity and thus the lowest content of W impurity in core, while the reversal B_T case has the highest core leakage and W content in core. The reason for this is that friction force exerted on the impurity ions in the normal B_T case is much larger than that in the reversal B_T case in most of the divertor region. This result is in consistent with the theory presented in section 3.1. Also, from the

calculation results we may draw a conclusion that the transport processes of W impurity could be controlled by introducing some artificial flows into the plasma.

Table 2 Information about the production and transport property of W impurity for the three cases.

case	f_w	Leakage	c_{w_core}	F_{fric_max}
No drift	2.306E+18	3.882E-03	7.577E-05	4.9E-17
Normal	2.769E+18	2.556E-03	4.939E-05	6.5E-17
Reversal	9.034E+17	1.011E-02	1.645E-04	1.8E-18

4. Summary and conclusions

In this paper, we have performed some preliminary modeling work to investigate the effects of the classical drifts on the divertor particle and heat fluxes. It is found that The usual drifts can evidently affect plasma flow velocity, and thus affect the plasma density and the divertor particle fluxes. The divertor heat fluxes can be affected by the usual drifts not so evidently as that for divertor particle fluxes, the reason for which is that the classical drifts could mainly affect the convective and conductive ion heat flux, taking only a small part of the total divertor heat flux.

Besides, we have investigate the effects of classical drifts on the W impurity transport by performing the coupled SOLPS-DIVIMP modeling, finding that both the production and the transport processes of the W impurity con be affected by the classical drifts. For the case in which the friction force is larger, it has lower W impurity core leakage and lower W content in core. Based on this result, it seems that the transport process of W impurity could be controlled by artificially introducing some flows into the plasma.

In conclusion, the usual drifts, including the grad-B drift and the $E \times B$ play a significant role in the edge plasma and impurity transport. Much future work is still needed to get the quantitative relationship between the classical drifts and the decay length of the divertor heat/particle fluxes and the relationship between drifts and impurity transport.

References

[1] J.B. Liu, H.Y. Guo, L. Wang, et al., Nucl. Fusion **56** (2016) 066006

[2] Eich T. et al 2009 J. Nucl. Mater. 390–1 760–3

[3] Asakura N. et al 2004 Nucl. Fusion **44** 503–12

[4] Faitsch M. et al 2015 Plasma Phys. Control. Fusion **57** 075005

[5] Chankin A.V. et al 2015 Plasma Phys. Control. Fusion **57** 095002

[6] Churchill R.M. et al 2013 Nucl. Fusion **53** 122002

[7] Rozhansky V. et al 2012 Nucl. Fusion **52** 103017

[8] Rognlien T.D. et al 1999 J. Nucl. Mater. 266–9 654–9

[9] Goldston R.J. 2012 Nucl. Fusion **52** 013009

[10] Eich T. et al 2011 Phys. Rev. Lett. **107** 215001

[11] LaBombard B. et al 2004 Nucl. Fusion **44** 1047–66

[12] Boedo J.A. 2009 J. Nucl. Mater. 390–1 29–37

[13] Schneider R. et al 1992 J. Nucl. Mater. 196–198 810

[14] Reiter D. 1992 J. Nucl. Mater. 196–198 80

[15] Coster D.P. et al 1997 J. Nucl. Mater. 241–243 690

[16] Braams B.J. 1986 PhD Thesis Computational Studies in Tokamak Equilibrium and Transport, Rijksuniversiteit, Utrecht, Netherlands

[17] Wiesen S., et al., Journal of Nuclear Materials **463** (2015) 480–484

[18] Stangeby P.C. et al 1988 Nucl. Fusion **28** 1945

[19] Porter G D, et al., Nucl. Mater. 266-269, 917 (1999)

[20] Y. Chen. Phys. Plasma **18**, 062506 (2011)

[21] Rozhansky V, et al., Nucl. Fusion **52** 103017

[22] Stangeby P.C. 2000 The Plasma Boundary of Magnetic Fusion Devices (Bristol: Institute of Physics Publishing)

Studies of impurity source location on edge impurity transport in EAST with EMC3-EIRENE modelling

Shuyu Dai [1]*, T. Xie [1], Q. Shi [1], Y. Feng [2], J. Huang [3], L. Wang [3], L. Zhang [3], J. C. Xu [3], G. Kawamura [4], D.Z. Wang [1]

[1]Key Laboratory of Materials Modification by Laser, Ion and Electron Beams (Ministry of Education), School of Physics, Dalian University of Technology, Dalian 116024, China
[2]Max-Planck-Institute für Plasmaphysik, D-17491 Greifswald, Germany
[3]Institute of Plasma Physics, Chinese Academy of Sciences, Hefei 230031, People's Republic of China
[4]National Institute for Fusion Science, Toki 509-5292, Japan

Abstract

The studies of the edge impurity transport in the scrape-off layer (SOL) of EAST have performed with the three-dimensional (3D) edge transport code EMC3-EIRENE. The carbon impurities of the C^{1+} - C^{3+} are mainly distributed at the private region and X-point region. However, for the higher charge states, the distributions of the C^{4+} - C^{6+} are mainly at the upstream region due to the high ionization potential.

1. Introduction

The studies of impurity transport in the edge plasma have a strong implication for the performance of the fusion facilities. The effective control of edge impurity transport can reduce the impurity penetration into the core plasma [1]. On the other hand, the retention of impurity in the divertor region has a positive effect on the achievement of the radiative divertor plasma, which can mitigate the heat load on the target plates [2]. In addition, the impurity transport into the plasma-shadowed region can result in the fuel retention by co-deposition [3].

In this work, the studies of the edge impurity transport in the scrape-off layer (SOL) of EAST have conducted with the three-dimensional (3D) edge transport code EMC3-EIRENE [4,5]. The EMC3 code was originally developed for the simulation of the edge plasma behaviour in the stellarator of W7-AS [6], which has a more complicated edge magnetic field structure compared to the axisymmetric tokamaks. Due to the good flexibility for treating arbitrary magnetic geometry, the EMC3-EIRENE code has been commonly applied in the edge plasma simulations [7].

The implementation of the EMC3-EIRENE code into the EAST tokamak has been achieved and employed for the studies of edge plasma transport behaviour [8]. In this study, the transport properties of the carbon impurity for different charge states have been investigated with the EMC3-EIRENE code based on the previous works for LHD simulations [9-12]. It is shown that the C^{4+} - C^{6+} ions have a larger penetration depth compared to the C^{1+} - C^{3+} ions. A detailed analysis of the impact of the impurity source location on the edge impurity distribution for different charge states is performed by artificially switching on/off the divertor target erosion in EMC3- EIRENE code. The distributions of the C^{1+} - C^{3+} ions are strongly associated with the impurity source location, while the distributions of the C^{4+} - C^{6+} ions are independent on the impurity source location. In section 2, the setup of EMC3-EIRENE simulations is introduced. In section 3, the simulation results and discussion are given. Finally, a summary is presented in section 4.

2. Setup of EMC3-EIRENE simulations

The EMC3 code is used for the modelling of plasma transport in the arbitrary 3D magnetic configuration. The steady-state Braginskii fluid equations are solved for the mass, momentum and energy transport for ions and electrons by using a Monte Carlo (MC) method. The parallel transport along the magnetic field lines are considered to be classic, while the cross-field transport is assumed to be anomalous. The EIRENE code is used to treat the transport of neutral atoms and molecules by solving the kinetic Boltzmann equations. The self-consistent treatment of the impurity transport has been implemented into the EMC3 code by solving the mass and parallel momentum balance equations for the relevant impurities. The feedback of impurities on the background plasma is handled by the energy loss induced by ionization and excitation of impurities.

The input parameters for the present EMC3-EIRENE simulations are selected same as the previous work [8]. The heating power is 260 kW and the upstream density is 2.3×10^{18} m^{-3} for the ohmic shot 41587, which is employed as the innermost boundary condition for the plasma transport. The outmost boundary condition for the plasma transport is a sink of the particle, momentum and energy with a decay length of several centimeters. The Bohm sheath boundary condition is employed to address the particle and heat loads on the divertor target. The recycling neutral Deuterium from the target plates are simulated by EIRENE code, and the neutral source distribution is proportional to the plasma flux deposition distribution obtained by EMC3.

The erosion process of the divertor target plates is determined by the plasma flux and the sputtering coefficient. At the present version of EMC3, the sputtering coefficient is a free parameter fixed in the simulation, which is assumed to be 0.01 in this study. For the shot of 41587 (2012 experimental campaign), the upper and lower divertor targets are still

made of graphite. For this ohmic shot, the plasma preferably flows down to the lower divertor, the computation grid is still extended to the upper divertor. The perpendicular particle and energy transport coefficients of background plasma ($D_\perp = 0.4$ m^{2}s^{-1} and $\chi_\perp = 2.0$ m^{2}s^{-1}) are used in the modelling according to the previous reciprocating probe measurements [8]. The impurity perpendicular diffusivity D_{imp} (=0.4 m^{2}s^{-1}) is assumed to be the same as the background plasma in the modelling. The toroidal simulation domain has a toroidal length of $30°$. The reversible field line mapping (RFLM) technique has been employed for the transport of individual MC particle across the toroidal block boundary [13,14].

3. Results and discussion

Figure 1 (a) shows the poloidal cross section of the connection length (L_c) distribution. In the upper and lower private regions, the L_c of the open field lines are very short in the range from 10 to 40 m. The outermost region of the SOL, in which the most flux tubes are connected to the upper divertor, has the L_c varying from 40 to 70 m. The very thick flux tube bundles with the L_c around 70-90 m are connected to the lower divertor, which corresponds to 7-9 toroidal turns of the EAST torus (major radius R=1.75 m). Figure 1 (b) presents the poloidal cross section of the plasma density distribution. The thick flux tube bundles connecting to the lower divertor can be the transport channels for the edge plasma, which results in a higher plasma density in the lower divertor region. This would also lead to a stronger recycling flux and target erosion at the lower divertor. The plasma density near the separatrix is about 2.0×10^{18} m^{-3}, and the plasma density is mainly about 0.5-1×10^{18} m^{-3} in the SOL region. Figure 1 (c) shows the poloidal cross section of the plasma temperature distribution. In the SOL region, the plasma temperature is less than 100 eV. Figure 1 (d) displays force balance of $|V_\parallel^{fric}| - |V_\parallel^{ther}|$ between the friction and the thermal forces acting on the carbon impurity. The impurity transport along the magnetic field line is mainly determined by the friction force and ion thermal force [15]. The friction force drives the impurity towards the target plates while the ion thermal force will push the impurity towards the upstream. It can be seen that the region near the separatrix is mainly in the friction force dominant regime. In particular, near the lower X-point region, the thermal force is stronger than the friction force. However, The regions near the lower divertor target are in the friction force dominant regime. In addition, the upper divertor leg regions are also in the friction force dominant regime.
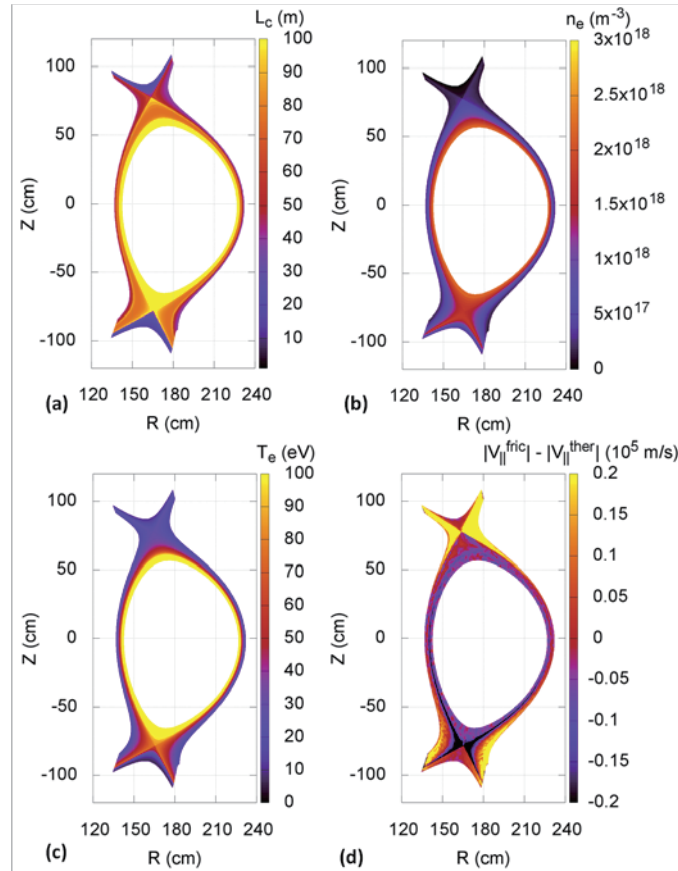

Fig. 1. Poloidal cross sections of the connection length (a), plasma density (b), plasma temperature (c) and force balance of $|V_\parallel^{fric}| - |V_\parallel^{ther}|$ between the friction and the thermal forces (d).

Figure 2 shows the poloidal cross sections of the carbon impurity densities for different charge states. The EMC3-EIRENR code has a flexibility of switching on or off the erosion of divertor target plates. However, the EMC3-EIRENE code would maintain the same total erosion amount of carbon impurity no matter switching off one target plate or switching on all the target plates. All the divertor target plates are switched on for the results shown in Figure 2. The neutral carbon particles are released from the divertor target plate and easily become ionized in the divertor leg region due to the low ionization potential (11.3 eV). The ionization potentials of carbon impurity for different charge states are summarized in Table 1, which are taken from ADAS database [16]. It can be seen that the C^{1+} ions are mainly distributed at the private region of the lower divertor. The lower plasma temperature and density as shown in Figure 1 (b) and (C) lead to the survival of the C^{1+} ions in the lower private region. The C^{2+} ions are mainly populated near the separatrix in the lower private region as shown in Figure 2 (b). The C^{3+} ions can penetrate deeper radially which results in a build-up of the C^{3+} ions near the lower X-point. For the shot of 41587, the erosion of the divertor target plates mainly occurs at the lower divertor targets. The eroded amount of carbon impurity from the upper divertor target plates is about 7.0% of the total carbon erosion amount. Hence, the C^{1+} - C^{3+} ions mainly populate at the lower divertor and private region of torus.

Table 1. Ionization potentials of carbon impurity for different charge states. The data are taken from ADAS database.

Carbon impurity	Ionization potential (eV)
C^{0+} -> C^{1+}	11.3
C^{1+} -> C^{2+}	24.4
C^{2+} -> C^{3+}	47.9
C^{3+} -> C^{4+}	64.5
C^{4+} -> C^{5+}	392.1
C^{5+} -> C^{6+}	490.0
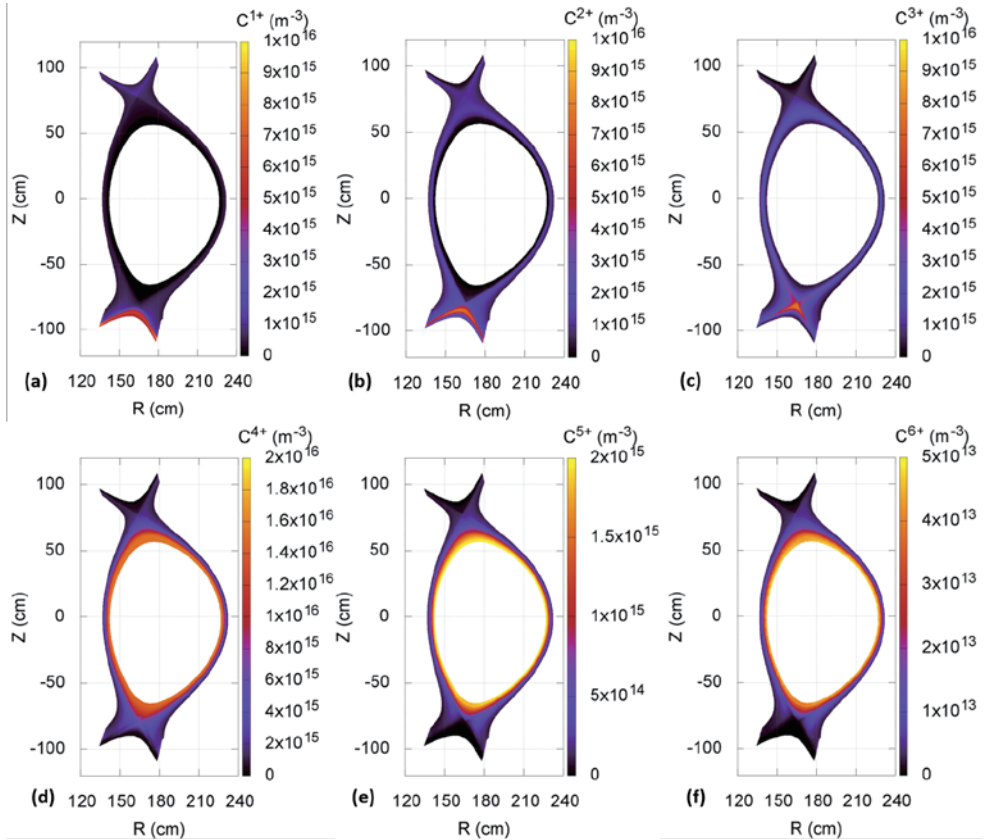
Fig. 2. Poloidal cross sections of the carbon impurity densities for different charge states for C^{1+} (a), C^{2+} (b), C^{3+} (c), C^{4+} (d), C^{5+} (e) and C^{6+} (f). All the divertor target plates are switched on.

The high plasma temperature and density in the SOL region leads to a successive ionization reactions of carbon particles to the high charge states. The distributions of the C^{4+} - C^{6+} ions are mainly at the upstream region near the LCFS where has a high plasma temperature. It can be seen that the density of C^{4+} ions is higher compared to the other charge states. The densities of the C^{5+} and C^{6+} ions reduce one and three orders of magnitude compared to the C^{4+} density, respectively. Since the erosion of the lower divertor target plates is dominant, the studies of the impact of the

impurity source location focus on the lower divertor target. In the EMC3-EIRENE modelling, the erosion of the lower inner and outer divertor target plates are switched off successively to assess their effects on the edge impurity transport characteristics.

4. Summary

The edge impurity transport in the scrape-off layer of EAST have been investigated with the three-dimensional edge transport code EMC3-EIRENE. The distributions of the C^{1+} - C^{3+} are mainly at the private region and X-point region. However, the C^{4+} - C^{6+} ions, which have a deeper penetration depth, are mainly distributed at the upstream region. In order to confirm the simulation results, the dedicated experiments by using argon gas puffing are ongoing. The argon gas can be puffed into the divertor region at the different target plates in EAST. The measurement of argon impurity transport can provide the experimental data to study the impact of the impurity source location on the impurity distribution in the edge plasma.

Acknowledgments

References

[1] G. Federici et al., Plasma-material interactions in current tokamaks and their implications for next step fusion reactors, Nucl. Fusion 41 (2001) 1967.
[2] A. Loarte et al., Chapter 4: Power and particle control, Nucl. Fusion 47 (2007) S203-S263.
[3] J. Roth et al., Tritium inventory in ITER plasma-facing materials and tritium removal procedures, Plasma Phys. Control. Fusion 50 (2008) 103001.
[4] Y. Feng et al., 3D edge modeling and island divertor physics, Contrib. Plasma Phys. 44 (2004) 57.
[5] D. Reiter et al., The EIRENE and B2-EIRENE codes, Fusion Sci. Technol. 47 (2005) 172.
[6] F. Sardei et al., A 3D Monte Carlo code for plasma transport in island divertors, J. Nucl. Mater. 241–243 (1997) 930-934.
[7] Y. Feng et al., Monte-Carlo fluid approaches to detached plasmas in non-axisymmetric divertor configurations, Plasma Phys. Control. Fusion 59 (2017) 034006.
[8] J, Huang et al., Implementation and first application of EMC3-EIRENE to EAST double-null divertor, Plasma Phys. Control. Fusion 56 (2014) 075023.
[9] S.Y. Dai et al., EMC3-EIRENE modelling of edge impurity transport in the stochastic layer of the large helical device compared with extreme ultraviolet emission measurements, Nucl. Fusion 56 (2016) 066005.
[10] S.Y. Dai et al., EMC3-EIRENE simulation of impurity transport in comparison with EUV emission measurements in the stochastic layer of LHD: Effects of force balance and transport coefficients, Contrib. Plasma Phys. 56 (2016) 628-633.
[11] H.M. Zhang et al., Vertical profiles and two-dimensional distributions of carbon line emissions from C2+ - C5+ ions in attached and RMP-assisted detached plasmas of Large Helical Device, Phys. Plasmas 24 (2017) 022510.
[12] S.Y. Dai et al., Effects of varying stochastic layer on edge plasma and impurity transport in 3D EMC3-EIRENE simulations of LHD, Fusion Eng. Des. In press.
[13] Y. Feng and F. Sardei, A simple highly accurate field-line mapping technique for three-dimensional Monte Carlo modeling of plasma edge transport, Phys. Plasmas 12 (2005) 052505.
[14] H. Frerichs et al., Block-structured grids in Lagrangian 3D edge plasma transport simulations, Comput. Phys. Commun. 181 (2010) 61-70.
[15] P.C. Stangeby, The plasma boundary of magnetic fusion devices (Bristol: Institute of Physics Publishing), 2000.
[16] http://open.adas.ac.uk

Island formation in stochastic magnetic field layer during RMP-triggered detached plasmas of LHD

S.Morita[1,2], H.M.Zhang[3], T.Oishi[1,2], X.L.Huang[1], Y.Liu[2] and M.Goto[1,2]

[1]National Institute for Fusion Science, Toki 509-5292, Gifu, Japan

[2]Graduate University for Advanced Studies, Toki 509-5292, Gifu, Japan

[3]Institute of Plasma Physics CAS, Hefei 230026, Anhui, China

Abstract

Edge magnetic island is suddenly formed has been observed during the plasma detachment assisted by resonant magnetic perturbation (RMP) field in Large Helical Device (LHD). Edge impurity profiles are observed at both the top edge near island O-point and the bottom edge near island X-point of LHD plasmas. It is found that the radial location of CIII and CIV differently changes between the top and bottom edges during the RMP-assisted detachment, i.e. 8 cm inside at the top and 2 cm inside at the bottom, while CVI radial location does not change at all. The result indicates a clear evidence of the island formation during the RMP-assisted detachment.

1. Introduction

In Large Helical Device (LHD), the plasma detachment has been steadily maintained without any external impurity gas feed only by supplying the m/n = 1/1 resonant magnetic perturbation (RMP) field at plasma axis position of R_{ax} = 3.90 m [1, 2]. In the R_{ax} = 3.90 m the radial profile of rotational transform, $\iota/2\pi$, becomes relatively flat and the radial position of $\iota/2\pi$ is located in stochastic magnetic field layer outside last closed flux surface (LCFS) where the magnetic field structure is entirely 3-dimensional. The RMP-assisted plasma detachment is triggered when the electron density increases above a threshold value, e.g. 5×10^{13} cm^{-3}. After triggering the detachment an electron temperature flattening suddenly appears in the plasma edge [1]. The temperature flattening covers a wide range of plasma radii, e.g. from the $\iota/2\pi$ = 1 position in the stochastic layer to ρ = 0.9 inside LCFS. It is believed that the magnetic island with m/n = 1/1 mode is rapidly grown up. Therefore, it is important to verify the magnetic island formation during the RMP-assisted detachment. For the purpose a space-resolved extreme ultraviolet (EUV) spectrometer [3-6] is utilized to experimentally examine the magnetic island formation by measuring the vertical profile of carbon line emissions of CIII to CVI during the plasma detachment. The effect of island on the radial location of carbon emissions is investigated at the top and bottom plasma edges close to the m/n=1/1 island O-point and X-point, respectively.

2. RMP-assisted detachment and vertical carbon profiles

The plasma detachment is obtained in neutral-beam heated discharges at high densities above threshold density when the RMP field with m/n = 1/1 mode is supplied to the stochastic layer in which $\iota/2\pi$ = 1 position exists. The discharge waveform with typical detachment is shown in Figs. 1(a) – (c). The RMP

coil current is constantly supplied at I_{coil} = 3340 A during the discharge.   In LHD the m/n=1/1 island formation with two different toroidal phases are possible as '6-O island' and '7-O island' in which the island O-point is located at the outboard midplane of #6 (ϕ = 180°) and #7 (ϕ = 216°) toroidal sections, respectively [1].   Figure 1 shows the 6-O island case.   The detachment transition occurs at t = 5.0 s when the electron density reaches $n_e \sim 5 \times 10^{13}$ cm^{-3}.   The ion saturated current (I_{is}) shown in Fig. 1(b) indicates a sudden decrease in the divertor particle flux.   The electron temperature at the LCFS position ($T_{e,LCFS}$) also gradually decreases after the detachment transition (see Fig. 1(c)).
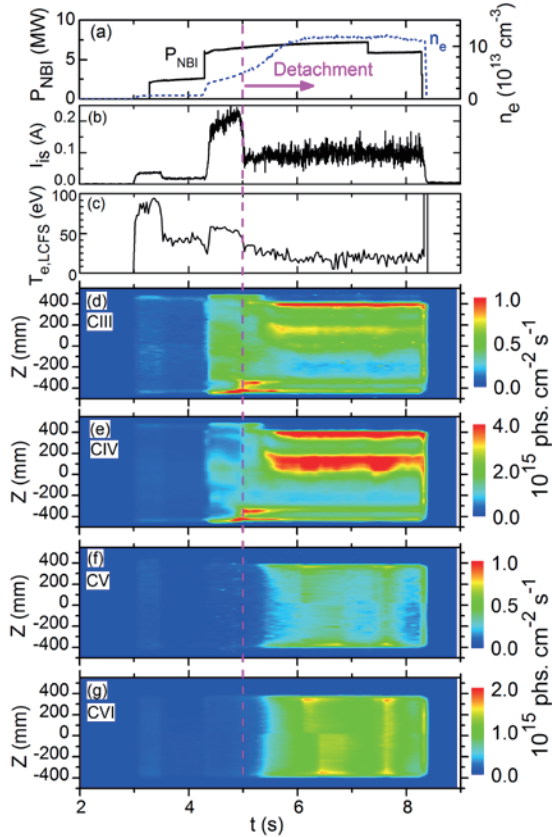
Fig. 1 Time behaviors of (a) NBI port-through power and line-averaged electron density, (b) ion saturation current, (c) electron temperature at LCFS and vertical profiles of (d) CIII (386.203 Å), (e) CIV (384.02 Å), (f) CV (40.27 Å) and (g) CVI (33.73 Å) in RMP-assisted detachment discharge.
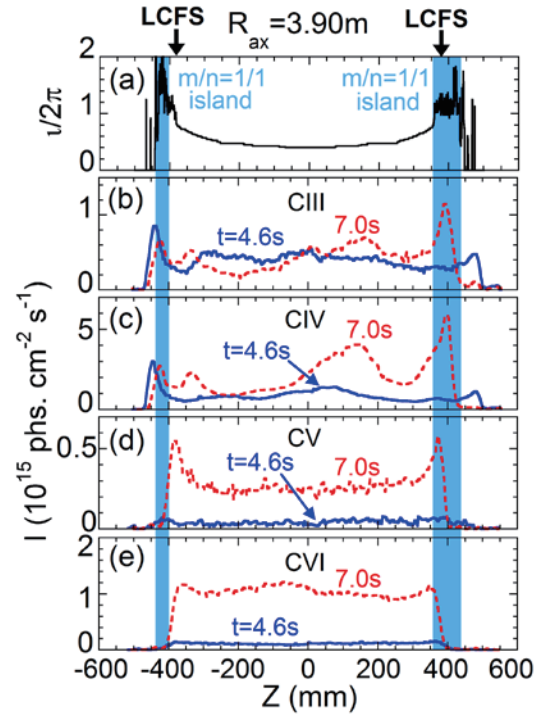
Fig 2 Vertical profiles of (a) rotational transform ($\iota/2\pi$), (b) CIII (386.203 Å), (c) CIV (384.174 Å), (d) CV (40.27 Å) and (e) CVI (33.73 Å) during attached (t= 4.6 s) and detached (t = 7.0 s) phases in Fig. 2.   The radial location of $\iota/2\pi$= 1 is indicated with hutched areas.

Time-developed vertical profiles of CIII (386.203 Å), CIV (384.174 Å), CV (40.27 Å) and CVI (33.73 Å) are also shown in Figs. 1(d), (e), (f) and (g), respectively.   Although the carbon emission intensities increase with electron density at the initial phase of the detachment, behaviors of CIII and CIV are clearly different from those of CV and CVI.   The radial location of CIII and CIV emissions begins to shift inside just before the detachment transition at both top and bottom edges.   On the contrary, the radial location of CV and CVI is entirely unchanged.   These results strongly suggest an influence of m/n = 1/1 magnetic island formation in the plasma edge, which is discussed later in details.

3. Analysis of CIII–CVI vertical profiles

In order to examine the effect of magnetic island on carbon emission profiles, vertical profiles of CIII–CVI are compared with rotational transform in vacuum condition, as plotted in Fig. 2. The observation chords are shown in Fig. 3 with a Poincare plot of the edge magnetic field at #10-O toroidal section for the 6-O island case, which is calculated in the vacuum condition. It is clear that the island O-point is near the top plasma edge, while island X-pint is near the bottom plasma edge. Before the detachment at t = 4.6 s, the CIII in Fig. 2(b) and CIV in Fig. 2(c) have a clear edge peak at both the top and bottom edges due to a long integration of the emission. During the detachment, on the other hand, the second edge peak is newly appeared in the CIII and CIV profiles at the island O-point location of $360 \leq Z \leq$ 430 mm denoted with hatched area. In particular, it is clear in the CIII profile at the top edge, i.e. the weakened first peak at Z = 480 mm and the newly appeared second peak at Z = 400 mm. In addition, the CIII and CIV emissions are also increased at $0 \leq Z \leq 200$ mm reflecting the emission enhancement in the vicinity of outboard X-point divertor separatrix. In contrast, the radial position of CVI located at radially inside of the island is entirely unchanged during the detachment, while the intensity increases. Here, it should be noticed that the CVI intensity during the plasma detachment is still much smaller than that during the plasma attachment without RMP field. It indicates that the RMP field enhances the edge impurity screening.

Fig. 3 Observation chords and Poincare plot of edge magnetic field structure at #10-O toroidal section with m/n = 1/1 island calculated in vacuum condition.

Fig. 4 Time behaviors of CIV (384.174 Å) vertical positions at (a) top and (b) bottom edges and density dependences of CIV vertical positions at (c) top and (d) bottom edges in discharges without (closed triangles) and with (closed circles) RMP.
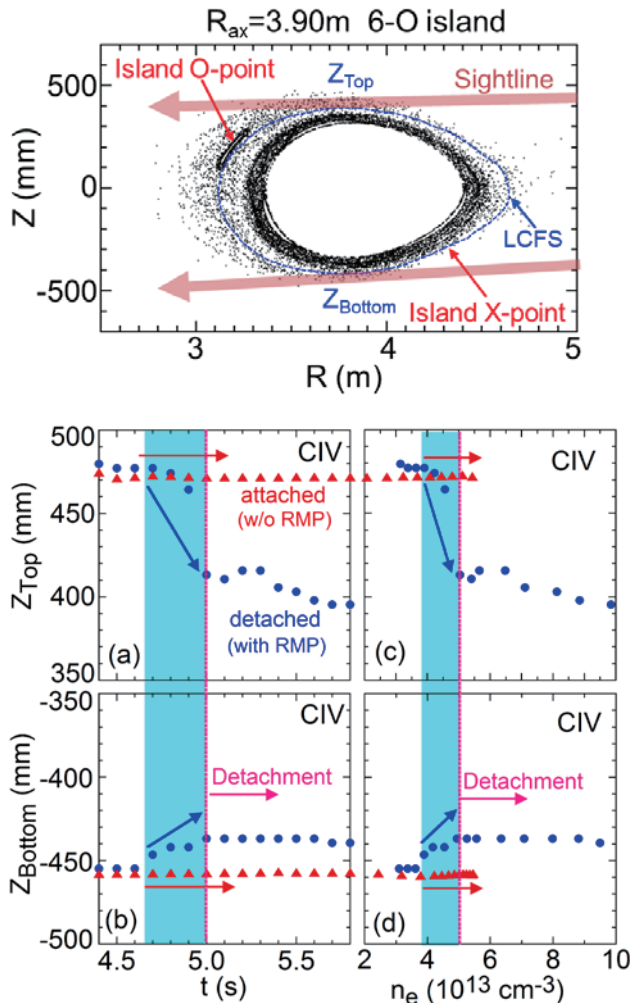
Time behaviors of radial positions in the CIV (384.174 Å) edge peak at the top and bottom edges, i.e. Z_{Top} and Z_{Bottom}, are plotted in Figs. 4(a) and (b), respectively. The closed circles and triangles indicate discharges with and without RMP, respectively. It is clearly seen that the radial position of CIV begins to move radially inside at t = 4.65 s before the detachment transition at both the top and bottom edges in the discharge with RMP, while the CIV radial position is entirely unchanged in the discharge without RMP. The values of Z_{Top} and Z_{Bottom} are also plotted as functions of electron density in Figs. 4(c) and (d) for discharges with and without RMP. It is found that the CIV radial position in the discharge with RMP starts to move when the density reaches 3.8×10^{13} cm^{-3} and the detachment transition occurs at $n_e = 5.0 \times 10^{13}$ cm^{-3} after the CIV radial position is sufficiently changed. In the discharge without RMP, on the other hand, the CIV position is unchanged against density and the detachment does not occur even if the density is higher than 5.0×10^{13} cm^{-3}. In addition, the radial shift in the top edge peak (ΔZ_{Top}) is much larger than that in the bottom edge peaks (ΔZ_{Bottom}) during the detachment, i.e. $\Delta Z_{Top} \sim 80$ mm and $\Delta Z_{Bottom} \sim 20$ mm. As shown in Fig. 3, the island O- and X-points are located near the top and bottom plasma edges, respectively. Therefore, the difference between ΔZ_{Top} and ΔZ_{Bottom} observed here indicates a clear evidence of m/n = 1/1 magnetic island suddenly grown up during the plasma detachment. The result concludes that formation of a big magnetic island expanded into magnetic surface region of ρ=0.9 is possible by supplying the RMP field, even if the magnetic resonance exists in the stochastic magnetic field layer.

4. Summary

The radial distribution of impurity carbon emissions has been measured during plasma detachment in LHD with the space-resolved EUV spectroscopy. The effect of RMP field on the edge impurity emission can be clearly observed from the radial distribution measurement. It is found that the radial position of CIII and CIV radially shifts inside before the RMP-assisted detachment transition, but it is unchanged in general discharges without RMP. The difference in the radial shift between the top and bottom CIV edge peaks experimentally confirms the appearance of m/n = 1/1 island during the plasma detachment.

References
[1] M. Kobayashi, et al., Phys. Plasmas **17** (2010) 056111.
[2] H. M. Zhang, et al., Plasma Fusion Res. **11** (2016) 2402019.
[3] C. F. Dong, et al., Rev. Sci. Instrum. **81** (2010) 033107.
[4] E. H. Wang, et al., Rev. Sci. Instrum. **83** (2012) 043503.
[5] H. M. Zhang, et al., Jpn. J. Appl. Phys. **54** (2015) 086101.
[6] C. F. Dong, et al., Rev. Sci. Instrum. **82** (2011) 113102.

Energetic-particle diagnostics and physics collaborations
in Japan, Korea, and China for the last five years

Mitsutaka Isobe[1,2], Junghee Kim[3], Jiafeng Chang[4], Yipo Zhang[5], Kunihiro Ogawa[1,2], Jun Young Kim[6], Jungmin Jo[7], MunSeong Cheon[3], Hideki Tomita[8], Guoqiang Zhong[4], Tieshuan Fan[9], Yi Liu[5], and Liqun Hu[4]

[1]National Institute for Fusion Science, National Institutes of Natural Sciences, Toki 509-5292, Gifu, Japan

[2]SOKENDAI (The Graduate University for Advanced Studies), Toki 509-5292, Gifu, Japan

[3]National Fusion Research Institute, Daejeon 34133, Korea

[4]Institute of Plasma Physics, Chinese Academy of Science, Hefei 230031, China

[5]Southwestern Institute of Physics, Chengdu 610041, China

[6]University of Science and Technology, Korea

[7]Seoul National University, Seoul 151-744, Korea

[8]Nagoya University, Nagoya 464-8603, Japan

[9]Peking University, Beijing 100871, China

Abstract

Tight collaborations on energetic-ion and neutron diagnostics have been performed between Japan, Korea, and China in the support of the A3 foresight program on critical issues specific to steady state sustainment of high-performance plasmas. As a result of joint works, the scintillator-based fast-ion loss detectors (FILDs) are now being operated in four major fusion devices in east Asia, i.e. the LHD, the KSTAR, the EAST, and the HL-2A. The FILD has revealed significant effects on beam-ion transport associated with various MHD activities resonant and non-resonant with beam ions, e.g. toroidicity-induced Alfvén eigenmode, energetic-particle continuum mode, tearing mode, sawthooth, and major disruption. It also indicated that resonant magnetic perturbation field can lead to loss of beam ions. Furthermore, it has been showed that beam-ion losses were enhanced due to impurity pellet and/or supersonic molecular beam injection. A recent big step is the start of the deuterium operation in the LHD. Comprehensive neutron diagnostics of the LHD are accelerating energetic-particle physics study in a three-dimensional helical plasma.

1. Introduction

Good confinement of energetic ions is crucial for the realization of the future fusion reactor because d-t born 3.5 MeV alpha particles work as a primary heating source and play an essential role in the steady state sustainment of ignition condition. In eastern Asia, nuclear fusion science is now flourishing. Three superconducting fusion devices are successfully running. One is the Large Helical Device (LHD) heliotron in Japan, another is the Korea Superconducting Tokamak Advanced Research (KSTAR) tokamak, and the other is the Experimental Advanced Superconducting Tokamak (EAST) tokamak in China. These devices are equipped with intensive heating systems. In addition to these, confinement study with neutral beam

injection is being performed in the Huan Liuqi-2A (HL-2A) tokamak in China. Lately, the deuterium plasma experiment began in the LHD. Therefore, these four machines can function as a good platform for the study of behaviors of neutral beam-injected energetic ions, perpendicular tail ions accelerated by ion cyclotron resonance wave, and MeV-class fusion products, enhancing a comprehensive understanding of energetic ion behaviors in toroidal fusion plasmas.

Bilateral collaborations on energetic-particle physics study in fusion between east Asian countries, i.e. Japan, Korea, and China have been supported by the A3 foresight program on critical physics issues specific to steady state sustainment of high-performance for the last five years. As a result of joint efforts, scintillator-based fast-ion loss detectors are now successfully working in the four fusion devices. Also, tight collaborations on neutron diagnostics development have been performed. In this paper, energetic-particle/neutron diagnostics and physics collaborations in Japan, Korea, and China for the last five years are summarized.

2. Diagnostics development

2.1. Development of scintillator-based fast-ion loss detector

The scintillator-based fast-ion loss detector (FILD) was originally developed in Princeton Plasma Physics Laboratory (PPPL) for the Tokamak Fusion Test Reactor (TFTR) [1,2]. The FILD functions as a magnetic spectrometer, providing both energy and pitch angle of escaping fast ion reaching the detector simultaneously. In the National Institute for Fusion Science (NIFS), the FILD project was initiated in 1997 in the Compact Helical System (CHS) [3,4] with a help of PPPL and the FILD technology was transferred to the LHD in 2001 [5]. Thereafter, ceaseless efforts have been made on the LHD-FILD to improve its performance [6]. Because NIFS has owned superiority in knowledge and/or experience on the FILD, as for the FILD on the HL-2A, the basic design of the FILD was provided by NIFS, and fabrication and assembly of the detector whole system was subsequently performed in Southwest Institute of Physics (SWIP) [7]. The development of the FILD system for the EAST was also conducted in the same manner [8]. As for the KSTAR-FILD [9], the FILD design stems from the FILD on the ASDEX-U. Practical collaboration on the
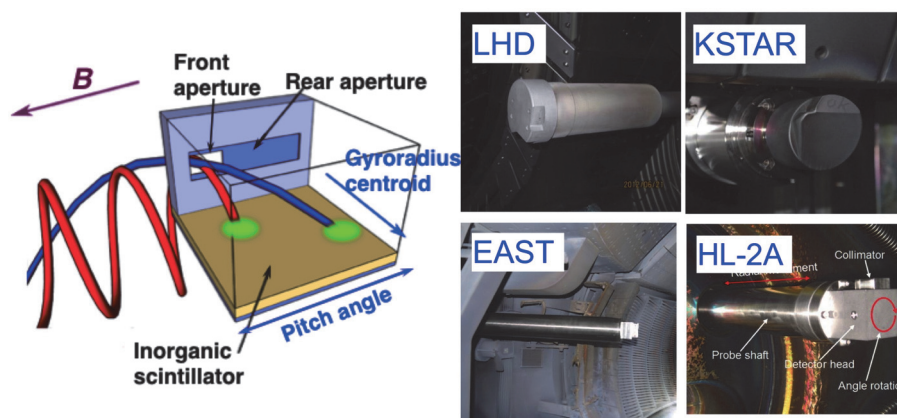

Figure 1. Schematically depicted function of scintillator-based FILD (left) and four pictures of FILDs in the LHD, the KSTAR, the EAST, and the HL-2A (right).

FILD between National Fusion Research Institute (NFRI) and NIFS began in 2011 before the start of the KSTAR-FILD operation. As a result of joint works, installation of the FILD onto the four devices was completed in 2014. The function of the FILD is schematically depicted in Figure 1. Pictures of detector head sections of the four FILDs are also shown in Figure 1. Joint activities on the FILD development and representative physics results obtained with the FILD are summarized in Ref. 10.

2.2 Neutron diagnostics

The deuterium plasma experiment began in the LHD in March 7, 2017. A working gas for a plasma discharge is now deuterium in the LHD, the KSTAR, the EAST, and the HL-2A. Note that neutron diagnostics can work as energetic-ion diagnostics because generated neutrons in beam-heated plasmas are dominated by neutrons due to beam-plasma interactions. Neutron diagnostics in the LHD, the KSTAR, the EAST, and the HL-2A are listed in Table 1.

Table 1. A list of neutron diagnostics in the LHD, the KSTAR, the EAST, and the HL-2A.

Neutron diagnostics	LHD	KSTAR	EAST	HL-2A
Neutron flux monitor	Working [11]	Working [16] Tentative [17]	Working [21, 22]	Working [25]
Neutron activation system	Working [12]	Working [18]	In preparation	-
Neutron profile monitor	Working [13]	In preparation Prototype [19]	Working [22]	Working [26]
Neutron fluctuation diagnostic	Working [14]	-	Working [23]	-
Scintillating-fiber detector	Working [15]	In preparation	-	-
Neutron energy spectrometer	In preparation	Prototype [20]	Working [24]	Tentative [27]

The NFMs in the LHD, the KSTAR, and the EAST consist of ^{235}U fission chambers and high-sensitivity ^{3}He and/or ^{10}B neutron counters. The HL-2A has only a ^{235}U fission chamber for the NFM. The NFMs of the LHD and the EAST are characterized by very wide dynamic range because the system can be operated in both the pulse counting mode and the Campbelling mode. The NFMs in the KSTAR and the HL-2A are operated only in the pulse counting mode. The total neutron emission rate S_n of the LHD is the highest among the four devices. In the first deuterium campaign, the maximum S_n was evaluated to be 3.3×10^{15} (n/s) in the LHD. The vertical neutron camera (VNC) based on eleven stilbene scintillation detectors and neutron collimator made of heavy concrete is successfully
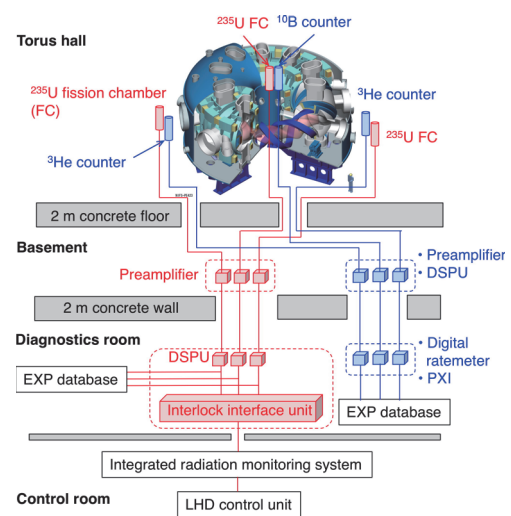
Figure 2. Neutron flux monitor on the LHD.

working in the LHD. Redistribution and losses of beam ions due to resistive interchange modes destabilized by helically trapped beam ions have been clearly observed by the VNC [28]. Neutron profile monitors on the four fusion devices can be seen in Figure 2. In the LHD and the KSTAR, the neutron activation system (NAS) has been working as a shot-integrated neutron yield monitor and triton burnup monitor (see Figure 3). Some of neutron diagnostics development were performed as a joint work. For example, in situ calibration of NFM on the LHD was performed by using a ^{252}Cf of ~800 MBq in November, 2016 together with collaborators of Japan, Korea, and China. Also, in the KSTAR, a neutron spectrometer prototype and a neutron profile diagnostic based on nuclear emulsion technique were tested as a joint work between NFRI and NIFS. As for neutron diagnostics in the two tokamaks in China, argument and information exchange between NIFS and ASIPP/SWIP have been often performed to improve its performance.
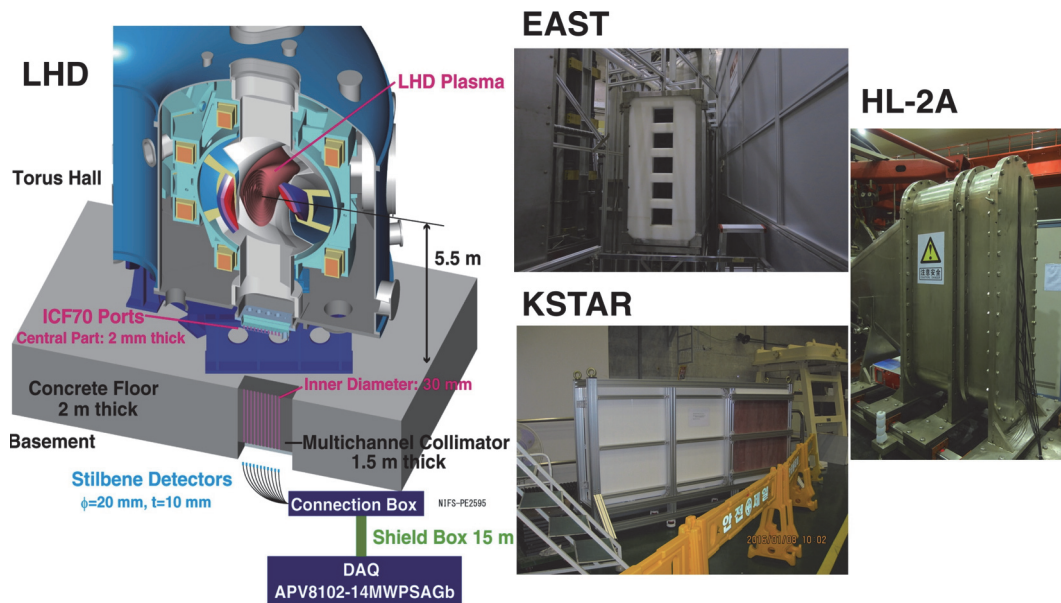
Figure 2. Neutron profile monitors in the LHD, the KSTAR, the EAST, and the HL-2A.
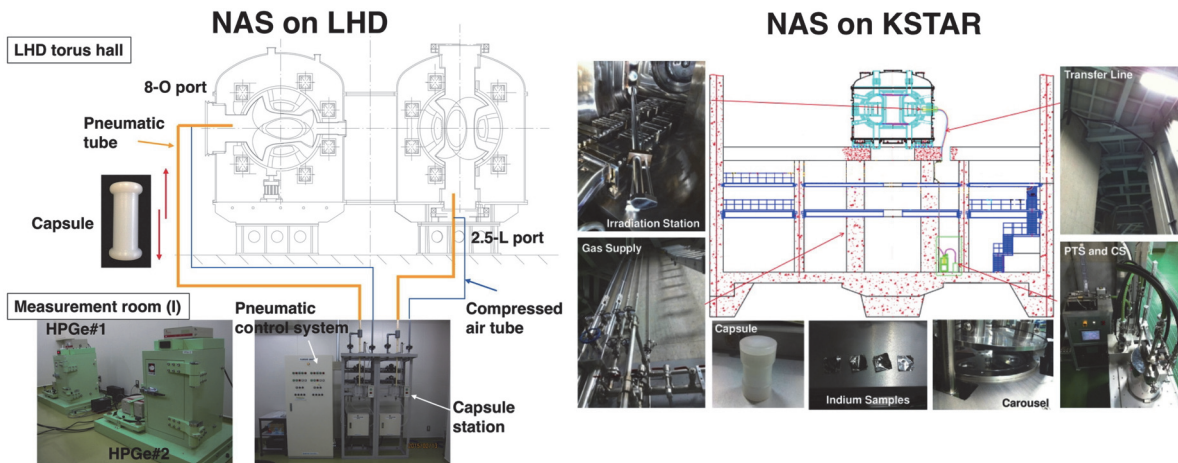
Figure 3. Entire view of neutron activation systems on the LHD and the KSTAR.

3. Experimental results

3.1 Orbits, slowing-down process, and effect of three-dimensionality on energetic ions

Deuterium beam blip experiments were conducted in the HL-2A and the LHD to check whether injected beam ions decelerate classically without loss or not [29-32]. The slowing down of tangentially co-injected beam ions in plasmas with various parameters has been investigated in the HL-2A tokamak by injecting a very short pulse high-energy deuterium beam. In the discharges with electron cyclotron resonance heating (ECRH), the decay rate of the d-d fusion neutron emission measured with the NFM was obviously longer than that in the plasma without ECRH. In addition, the neutron emission decay rate in a higher electron-density n_e plasma was shorter than that in a lower-n_e plasma. The experimental phenomena about the neutron emission decay rate in plasmas with various parameters are well consistent with the theoretical predictions [31]. In the LHD, short pulse neutral beams (NBs) were co-, counter-, and perpendicularly injected into MHD-quiescent plasmas and the decay time of S_n right after NB turn-off were measured with the NFM. The experiment indicates that the neutron decay time agreed with that predicted by the classical slowing down model in the high-n_e regime, i.e, in the short-slowing down time regime. In the low-n_e regime, a discrepancy between measured and predicted neutron decay rate was recognized [32]. The detailed analysis is now ongoing.

Energetic-ion transport caused by non-axisymmetric magnetic fields is one of the oldest issues in fusion. However, attention is now being focused on it again because in recent experiments, three-dimensional (3-D) perturbed magnetic field produced by resonant magnetic perturbation (RMP) coils is often superposed on target plasmas to explore the mitigation condition for the edge localized mode (ELM). As for the LHD, since the magnetic configuration is intrinsically 3-D, confinement of energetic ion has been of a great concern. Because of this background, beam-ion loss characteristics were investigated in various magnetic field configurations in the LHD by using the FILD [33]. Beam-ion losses largely depended on the magnetic axis positions of plasmas and increased as plasma column was shifted outwardly. Also, in the KSTAR, prompt loss characteristics on beam ions were carefully studied by using the FILD [34]. The RMP experiments have been conducted in the four devices. Effects of RMP on behavior of beam-ion loss were significant in the LHD [35] and the KSTAR [36, 37]. Lately, characterization of beam-ion loss due to the RMP field has been initiated in the EAST by using the FILD.

3.2 Effects of MHD instabilities on energetic-ion loss

Effect on magnetohydrodynamics (MHD) on energetic-ion transport and/or loss is one of crucial issues in magnetic confinement fusion since energetic alpha particles may be lost as a result of interaction with energetic-ion-driven MHD instabilities such as toroidicity-induced Alfvén eigenmode (TAE) and energetic-particle continuum mode (EPM). The LHD is equipped with three negative-ion-based neutral beam injectors (N-NBIs), providing fairly high energy neutral beams of which energy is ~180 keV. Beam ions can be therefore super-Alfvénic and TAEs have been often destabilized when the magnetic field strength was set to be below 1 T [38]. Effects of TAE on beam-ion transport and/or loss have been clearly seen by using the E//B-neutral particle analyzer [39] and the FILD [40-44]. EPMs have been preferably destabilized when balance injection of co- and counter-N-NBIs were carried out [45]. Also, effects on MHD instabilities non-

resonant with energetic ions such as a resistive interchange mode and an ELM on beam-ion transport and/or loss have been observed in the LHD [46-48]. In the HL-2A, studies on neutral beam ion confinement and excitation of beta-induced Alfvén acoustic eigenmodes were performed [49]. In addition, in the HL-2A, beam-ion transport and loss due to various MHD modes such as a tearing mode, a long-live mode, a sawtooth crash, and a major disruption were intensively studied by using the NFM and the FILD in the collaboration between SWIP and NIFS [29, 50]. In the KSTAR experiments, beam-ion losses associated with the tearing mode (m/n=2/1) have been observed [36]. Especially it has been revealed that passing beam-ions, which are sensitive to the magnetic island positions, are the primary sources of this core MHD-associated loss.

3.3 Triton burnup study

Triton burnup studies have been conducted in the LHD and the KSTAR as a joint work between NFRI, Seoul National University, and NIFS. In deuterium plasmas, following two primary fusion reactions can take place.

$$d + d \quad \rightarrow \quad {}^{3}He \text{ (0.82 MeV)} + n \text{ (2.45 MeV)}$$
$$d + d \quad \rightarrow \quad t \text{ (1 MeV)} + p \text{ (3.03 MeV)}$$
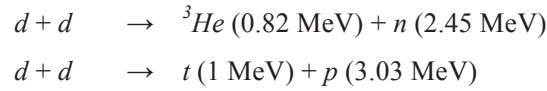
Energetic tritons are characterized by isotropicity in the velocity space and will undergo secondary d-t reactions with background thermal deuterons. Kinetic parameters such as Larmor radius and precessional drift frequency of 1 MeV tritons are almost the same as those of 3.5 MeV alpha particles generated by d-t reaction. Therefore, it can be said that confinement study for 1 MeV tritons in d-d plasmas is equivalent to that for 3.5 MeV alphas in d-t plasmas. In the KSTAR, the triton burnup study was conducted in wide plasma parameter ranges with different n_e and plasma current I_p [51]. So far, the triton burnup ratio defined as the ratio of secondary d-t neutron yield to primary d-d neutron yield has reached about 0.5% in the high-I_p operation of the KSTAR. In the LHD, to examine the triton burnup ratio in various magnetic configurations, the magnetic axis position R_{ax} in vacuum were scanned from inward shifted (R_{ax}=3.55 m) to outward shifted cases (R_{ax}=3.9 m). The results indicated that the triton burnup ratio increased as the plasma column was shifted inwardly as expected from confinement property of helically trapped orbit predicted by orbit calculations. The maximum triton burnup ratio evaluated in the first deuterium campaign of the LHD was about 0.45% in B_t/R_{ax} of 2.89 T/3.55 m. To measure time evolution of secondary d-t neutron emission rate, three different scintillating-fiber (Sci.-Fi.) detectors were employed in the LHD. Note that the Sci.-Fi. detector is now operated only in the LHD. Based on the collaboration between NIFS, NFRI, Seoul National University, and National Institute of Technology, Toyama College, development of a large size Sci.-Fi. detector suitable for the KSTAR was initiated.

4. Summary

Research activities based on international collaboration between Japan, Korea, and China on energetic-particle diagnostics development and physics studies on energetic particles are summarized. Energetic-particle and neutron diagnostics have been steadily enhanced in the LHD, the KSTAR, the EAST, and the

HL-2A to obtain a comprehensive understanding of energetic-particle physics in helical system and tokamak in the support of the A3 foresight program. The FILD has been installed in the LHD, the KSTAR, the EAST, and the HL-2A as a result of joint work. Physics studies on energetic ions, e.g. effects of various MHD instabilities, external RMP field, pellet injection etc. are ongoing by using the FILD. The deuterium operation began in the LHD in 7 March, 2017. Neutron signals have become available in the four major fusion devices in east Asia with the start of the LHD deuterium operation in all devices. An environment to enhance further the bilateral collaboration on energetic-particle physics studies between Japan, Korea, and China has been realized. Based on the platform established by the A3 foresight program, the collaboration on energetic-particle physics will be tightly performed hereafter between Japan, Korea, and China.

References

[1] S.J. Zweben, Rev. Sci. Instrum. **60** (1989) 576.

[2] S.J. Zweben, Nucl. Fusion **29** (1989) 825.

[3] D.S. Darrow, M. Isobe *et al*., J. Plasma Fusion Res. SERIES **1** (1998) 362.

[4] M. Isobe, D.S. Darrow *et al*., Rev. Sci. Instrum. **70** (1999) 827.

[5] T. Saida, M. Sasao, M. Isobe *et al*., in Proceedings of Advanced Diagnostics for Magnetic and Inertial Fusion, villa Monastero, Varenna, Italy, 3-7 September 2001, pp133.

[6] K. Ogawa, M. Isobe, and K. Toi, J. Plasma Fusion Res. SERIES **8** (2009) 655.

[7] Y.P. Zhang, Yi Liu, X.B. Luo, M. Isobe *et al*., Rev. Sci. Instrum. **85** (2014) 053502.

[8] J.F. Chang, M. Isobe, K. Ogawa *et al*., Rev. Sci. Instrum. **87** (2016) 11E728.

[9] Junghee Kim, Jun Young Kim, S.W. Yoon *et al*., Rev. Sci. Instrum. **83** (2012) 10D305.

[10] M. Isobe, Junghee Kim, Yipo Zhang *et al*., Fusion Sci. Technol. **72** (2017) 60.

[11] M. Isobe, K. Ogawa, H. Miyake *et al*., Rev. Sci. Instrum. **85** (2014) 11E114.

[12] N. Pu, T. Nishitani *et al*., submitted to Rev. Sci. Instrum.

[13] K. Ogawa, M. Isobe *et al*., Rev. Sci. Instrum. **85** (2014)11E110.

[14] K. Ogawa, M. Isobe *et al*., to be submitted to Plasma and Fusion Research.

[15] M. Isobe, K. Ogawa *et al*., submitted to IEEE Trans. Plasma Sci.

[16] A.C. England, private communication.

[17] Y.-K Kim S.-K Lee *et al*., Journal of Instrumentation **7** (2012) C06013.

[18] M.S. Cheon, Y.S. Lee, A.C. England *et al*., Journal of Instrumentation **7** (2012) C05009.

[19] Y. Izumi, H. Tomita *et al*., Rev. Sci. Instrum. **87** (2016) 11D840.

[20] H. Tomita, F. Yamashita *et al*., Rev. Sci. Instrum. **85** (2014) 11E120.

[21] ZHONG Guoqiang *et al*., Plasma Sci. Technol. **13** (2011) 163.

[22] G.Q. Zhong *et al*., Rev. Sci. Instrum. **87** (2016) 11D820.

[23] N. Pu, Y.B. Zhu, G.Q. Zhong *et al*., Journal of Instrumentation **10** (2015) P12013.

[24] Xing Zhang, Zhongjing Chen *et al*., Nucl. Fusion **54** (2014) 104008.

[25] Yang Jinwei, Song Xianying *et al*., Plasma Sci. Technol. **7** (2005) 2860.

[26] Y.P. Zhang, J.W. Yang, Yi Liu, T.S. Fan *et al*., Rev. Sci. Instrum. **87** (2016) 063503.

[27] YUAN Xi, ZHANG Xing *et al*., Chinese Physics C **37** (2013) 126001.

[28] K. Ogawa, M. Isobe et al., to be submitted to Nucl. Fusion.

[29] ISOBE Mitsutaka, LIU Yi *et al*., Chin. Phys. Lett. **26** (2009) 105201.

[30] Mitsutaka ISOBE, Yi LIU *et al*., Plasma Fus. Res. **6** (2011) 2402107.

[31] Y.P. Zhang, M. Isobe, Yi Liu *et al*., Phys. Plasmas **19** (2012) 112504.

[32] T. Nishitani, K. Ogawa *et al*., to be submitted to Plasma Fus. Res.

[33] K. Ogawa, M. Isobe *et al*., Plasma Fus. Res. **7** (2012) 2402014.

[34] Jun Young Kim, T. Rhee, Junghee Kim *et al*., AIP ADVANCES **6** (2016) 105013.

[35] K. Ogawa, M. Isobe *et al*., Plasma Fus. Res. 9 (2014) 3402097.

[36] Junghee Kim, T. Rhee, Jun Young Kim *et al*., 15th IAEA Technical Meeting on Energetic Particles in Magnetic Confinement Systems, 5-8, September, 2017, Princeton, USA. **O-6**

[37] Jun Young Kim, "*Study on fast-ion loss associated with external magnetic perturbation in KSTAR*", Ph.D. thesis, Nuclear Fusion and Plasma Science, University of Science and Technology, February 2017.

[38] K. Toi, S. Yamamoto *et al*., Plasma Phys. Control. Fusion **46** (2004) S1.

[39] M. Osakabe, S. Yamamoto *et al*., Nucl. Fusion **46** (2006) S911.

[40] K. Ogawa, M. Isobe *et al*., Plasma Fus. Res. 4 (2009) 033.

[41] K. Ogawa, M. Isobe *et al*., Nucl. Fusion **50** (2010) 084005.

[42] K. Ogawa, M. Isobe *et al*., Nucl. Fusion 52 (2012) 094013.

[43] K. Ogawa, M. Isobe *et al*., Plasma Sci. Tech. **14** (2012) 269.

[44] K. Ogawa, M. Isobe *et al*., Nucl. Fusion **53** (2013) 053012.

[45] M. Isobe, K. Ogawa *et al*., Contrib. Plasma Phys. **50** (2010) 540.

[46] K. Ogawa, M. Isobe *et al*., Plasma Fus. Res. **4** (2009) 033.

[47] K. Ogawa, M. Isobe *et al*., Nucl. Fusion **50** (2010) 084005.

[48] K. Ogawa, M. Isobe et al., Nucl. Fusion **56** (2014) 094005.

[49] Liu Yi, Isobe Mitsutaka, Peng Xiao-Dong *et al*., Nucl. Fusion **52** (2012) 074008.

[50] Y.P. Zhang, Yi Liu, W. Chen, Y. Xu, M. Isobe *et al*., Nucl. Fusion **55** (2015) 113024.

[51] Jungmin Jo, MunSeong Cheon, Jun Young Kim *et al*., Rev. Sci. Instrum. **87** (2016) 11D828.

Research Status of Energetic Particle Physics and Diagnostics in KSTAR

Junghee Kim[1], T.N. Rhee[1], S.I. Lee[1], M.S. Cheon[1], J. Jo[2], M. Isobe[3,4], K. Ogawa[3,4], T. Nishitani[3], E. Takada[5], J.W. Yoo[1], J.-Y. Kim[6], S.G. Oh[7], A. Fenyvesi[8], S.H. Son[1], S.H. Hong[1] and the KSTAR team

[1]National Fusion Research Institute, Daejeon 34133, Republic of Korea

[2]Department of Nuclear Engineering, Seoul National University, Seoul 08826, Republic of Korea

[3]National Institute for Fusion Science, Toki 509-5292, Gifu, Japan

[4]SOKENDAI (Graduate University for Advanced Studies), Toki 509-5292, Gifu, Japan

[5]National Institute of Technology (Toyama College), Toyama 939-8630, Japan

[6]Plasmapp Co. Ltd. Daejeon 34127, Republic of Korea

[7]Ajou University, Suwon 16499, Republic of Korea

[8]National Institute for Nuclear Research (MTA Atomki), Debrecen 4026, Hungary

Abstract

Confinement of energetic particle is a big concern to operate the high-performance fusion plasmas in KSTAR like other major fusion devices. Research on the energetic particle dynamics in KSTAR plasmas has been performed for several years with the help of developing the novel diagnostics. Several important topics such as fast-ion loss and energetic particle diagnostics have been advanced in the frame of A3 collaborations. In this paper, the current status of energetic particle research on KSTAR is stated.

1. Introduction

Main origin of fast ions in KSTAR is NBI. Experimental research on the beam-driven fast-ions has been conducted on KSTAR since 2011 by development of fast-ion loss detector (FILD) [1]. After development of the FILD, collaborations on the fast-ion modelling and the diagnostics have been activated and the meaningful physical experimental results have been achieved in the frame of A3 foresight program. Study on the fast-ion dynamics has been started with FILD operation. Hardware development as well as modelling orbits have been actively carried out with the energetic particle researchers in LHD. In this collaboration, main concern about fast-ion physics has been the fast-ion loss associated with the edge resonant magnetic perturbations (RMP) on KSTAR. Various RMP applications using all three rows, which are able to produce versatile poloidal spectra of the magnetic perturbations, have shown the localized and the asymmetric fast-ion loss behaviors [2]. Fast measurement using the PMT (photomultiplier tube) of the FILD has revealed the tearing-mode-induced fast-ion losses at the different pitch-angle ranges [3]. In addition to fast-ion loss physics, energetic particle modes have been investigated. In particular, multiple-n toroidal Alfvén eigenmodes (TAE) have been observed [4], and the EGAM (energetic-particle-driven geodesic acoustic modes) has been excited while the counter-current on-axis NBI is applied through the reversed-Ip experiments [5]. Besides the FILD diagnostic, initial design of FIDA (fast-ion D_α) diagnostic

[6] to investigate the fast-ion profile has been conducted and will be upgraded in 2018 in order to span the observable phase-space of the fast-ions.

For the fusion-product study, the activation probe and the various types of neutron diagnostics have been tested. Activation probe has shown the distinctive radiation from the fusion-born charged particles such as He^3 or proton [7,8]. This result has been confirmed with the measurement using the ITER-prototype neutron activation system (NAS) [9]. Especially NAS diagnostic has been also used for the initial study of triton burn-up in KSTAR [10]. The radiation detector using the PMT and the scintillator have been also tested by strong collaboration with LHD EP researchers [11], and will be operated in high-performance discharges in KSTAR after upgrade of NBI power in 2018 or 2019 campaign. Another crucial topic on the energetic particle physics in KSTAR is about runaway electrons [12-14], however the contents in this paper describe the fast ions mainly.

2. Fast-ion transport study

Fast-ion transport in the fusion plasmas is a big concern of sustainment of high-performance discharge aiming at high yield of fusion reaction. So far the following issues: fast-ion loss and energetic particle modes have been investigated on KSTAR.

2.1. Fast-ion loss detector

A scintillator-based fast-ion loss detector has been installed and operated since 2011 experimental campaign with robust collaboration with NIFS and IPP (ASDEX-U). Detector head has been optimized for surviving under the harsh environment such as high-performance long-pulse discharge. In particular the scintillator (ZnS:Ag) screen and the several PMT DAQ system have been supplied by NIFS EP research team.
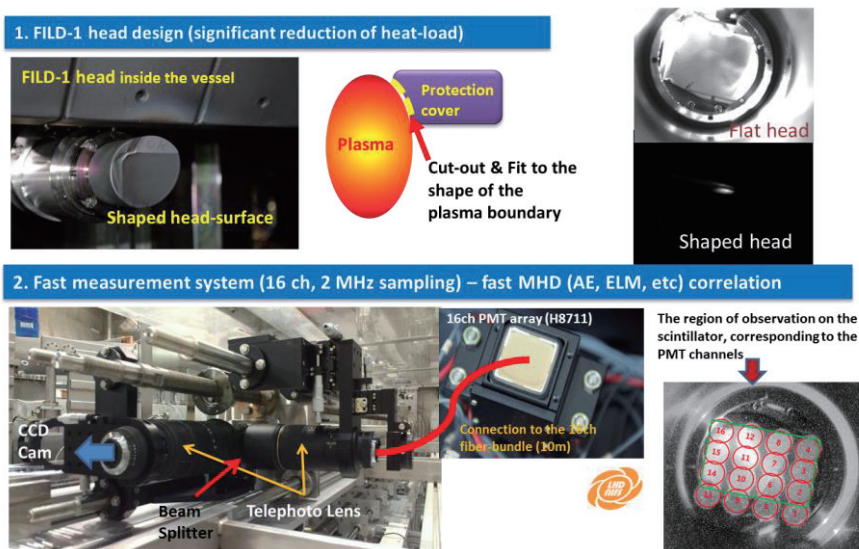

Fig. 1 Fast-ion loss detector installed on KSTAR in the framework of collaborations including A3 foresight program

Modelling of the fast-ion orbits has been devoted to identify the origin of the lost fast-ions. Various pitch-angle ranges of the lost fast-ions have been often observed on the scintillator plate during H-mode

discharge. Deposition location has been compared with the orbit simulation using LORBIT [15], and it has been found that the high-field side edge and the low-field side SOL are the birth positions of the fast-ions having the low pitch-angle (arccos $(v_\parallel/v) < 30°$) prompt-loss (Fig. 2) [16].
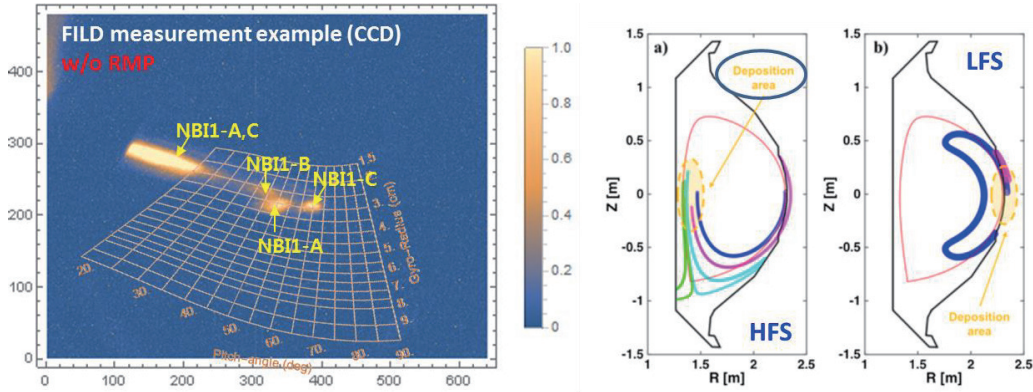
Fig. 2 FILD measurement of the phase-space (left) and the corresponding test-particle simulations using the LORBIT code (right)

2.2 Fast-ion loss associated with the RMP and AEs

KSTAR is known to be an excellent device to test the edge-magnetic perturbations with the help of versatile in-vessel control coils. Resonant magnetic perturbations (RMP) using this IVCC could achieve the ELM mitigation and suppression successfully [17].
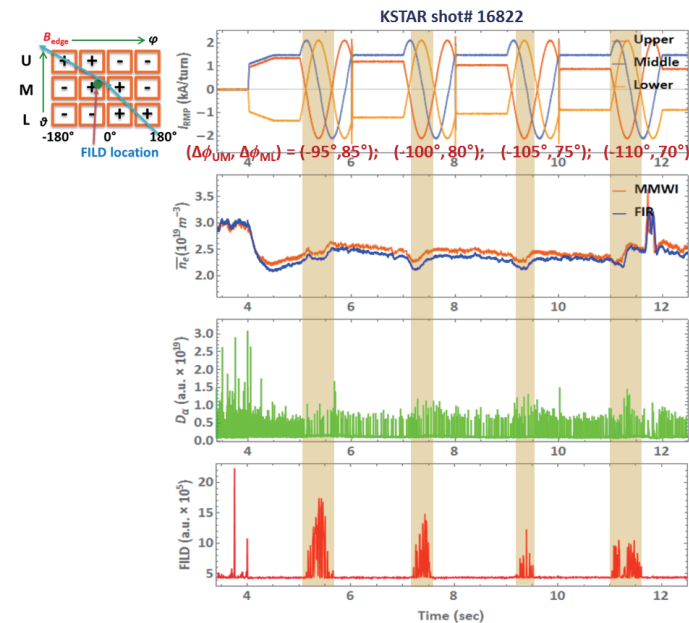
Fig. 3 Intentionally misaligned RMP experiments in KSTAR has shown the reduction of fast-ion loss as the de-phasing increases. Different poloidal spectra of the applied RMP field may give different edge magnetic perturbation configuration (i.e. change in canonical toroidal angular momentum) to the fast-ion orbits at the edge/SOL regions.

Especially in this paper fast-ion loss response under the 'intentionally misaligned' n=1 RMP configuration is described briefly. 'Intentional misalignment' means the non-equal phasing ($\phi_{UM} \neq \phi_{ML}$) of the RMP application and this configuration can be implemented by using the middle-row RMP coils. It has been

found that ELM is successfully mitigated [18] and the localized fast-ion loss intensity decreases as 'de-phasing' increases [19]. This implies that the localized fast-ion load on the first-wall during RMP application can be reduced with keeping the ELM mitigation effect.

Another experimental results that might be affected by enhanced fast-ion transport is fast-ion loss associated with the multiple-n TAEs [4]. When the multiple-n AEs are excited, fast-ion loss increases largely and the neutron emission rate is reduced remarkably. Modelling of core magnetic field / pressure fluctuation as well as change in fast-ion distribution function that may be induced by multiple Alfven eigenmodes is being done using the MEGA code.
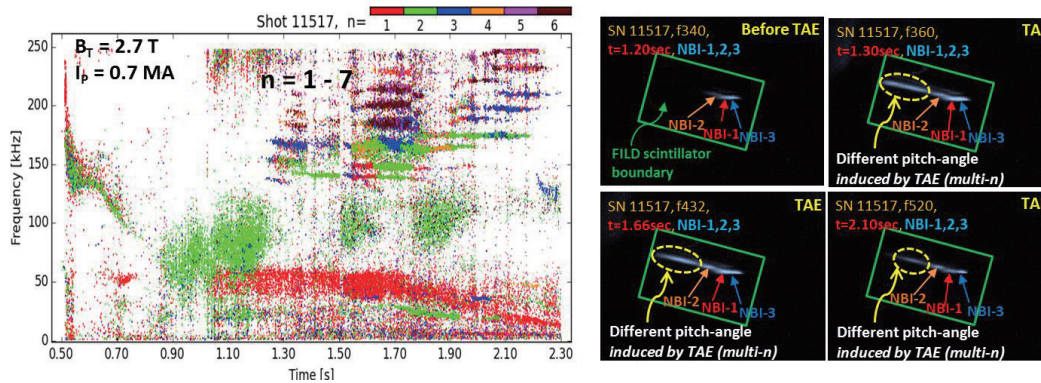
Fig. 4 Fast-ion loss associated with the multiple-n (n = 1 – 7) TAEs. [4]

Last example of the EP-driven modes in this section is the EGAM (energetic particle-driven geodesic acoustic mode). EGAM is one of low-frequency EP-driven modes such as fishbone and is thought to be very important key for the interaction between the supra-thermal ion profile and the thermal ion profile. In 2016 experimental campaign, EGAM has been found while the reversed-Ip experiments have been conducted. This EGAM is driven by the counter on-axis NBI without change beam direction because of the reversed plasma current direction. Counter-NBI causes large amount of fast-ion prompt loss, hence the temporal depict of the fast-ion velocity distribution is occurred. The free energy from this drives the GAM.

EGAM is observed under the low density (less than 1.5×10^{19} m^{-3}) L-mode plasmas, and is disappeared or transformed to different low-frequency modes (n=1 or 2) instantaneously just before the H-mode transition or rising of electron density.
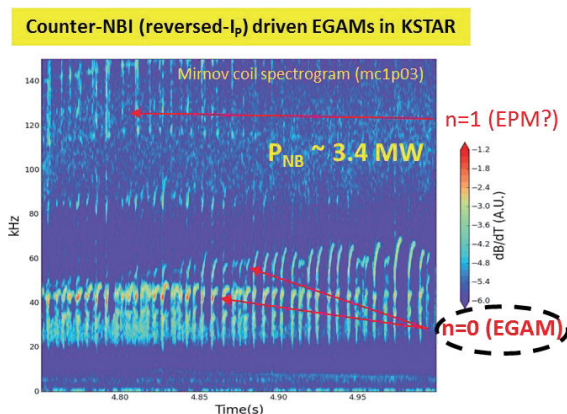
Fig. 5 fast-ion driven EGAM has been found in KSTAR when the counter on-axis NBI (reversed Ip) is applied.

3. Fusion-product study

KSTAR is aiming at high-performance steady-state operation of fusion plasma discharges. 'The high-performance' is characterized by high-beta and high current (mega-ampere). Under this kind of environment, somewhat high confinement of core fast-ions that can participate in the fusion reaction can be achieved, and the role of fusion product is not trivial. Several diagnostic efforts have shown the existence of the D-D fusion products such as fast He^3 and proton with the help of activation probe technique. Measurement of fast charged fusion products have been verified with the NAS (neutron activation system) diagnostic. NAS has also measured the activation by the 14 MeV neutron. These diagnostic results imply that triton burn-up is occurred on KSTAR, and the burn-up ratio has been investigated with the NAS.

Detection of neutrons and escaping fast-protons   Detection of escaping ^{3}He-ions
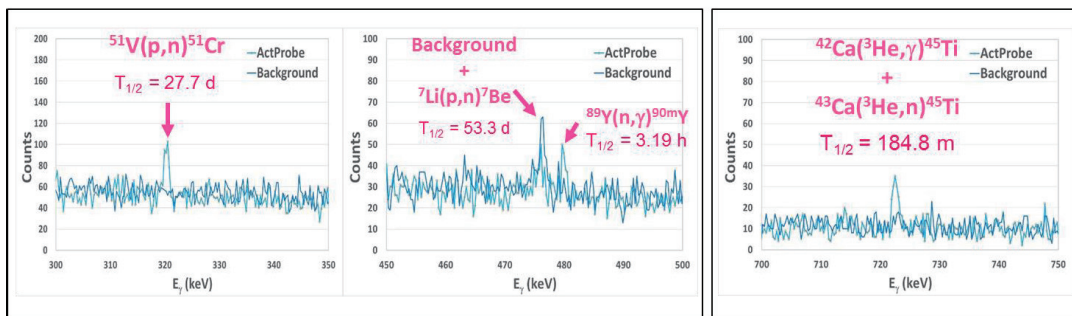
Fig. 6 Measurement example of charge fusion product on KSTAR using the activation probe has shown the existence of MeV-level fast-proton and He^3 ions [8].

Initial measurements (14.1 MeV neutron) using the NAS shows the 0.1 – 0.5 % of triton burn-up ratio. Burn-up increases as plasma current increases because of squeezed banana or potato orbits of 1 MeV tritons.

Clear effect of increased slowing down time ($\propto T_e^{1.5}/n_e$) has been observed only in the case of Ip = 0.5 - 0.6

MA. It is expected that the triton burn-ratio increases as slowing down time increases, but further investigation on the database is desired because the reproducibility of the basic plasma parameters (T_e, n_e) is very important.
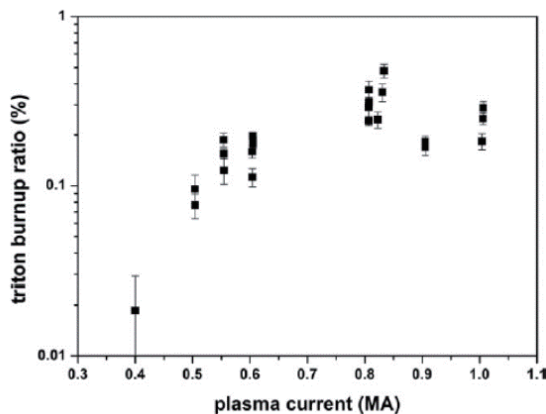
Fig. 7 Triton burn-up ratio increases as plasma current increases. Orbit width of fast triton is squeezing when the plasma current increases (higher poloidal field strength). (Figure depicted in the reference [10])

To enhance research capability of energetic particle physics, it is quite worthwhile developing the novel neutron diagnostics. A close collaboration with NIFS has been continued and the PMT-based detectors and the scintillating fiber system are ready for testing on KSTAR under the high-performance discharges.
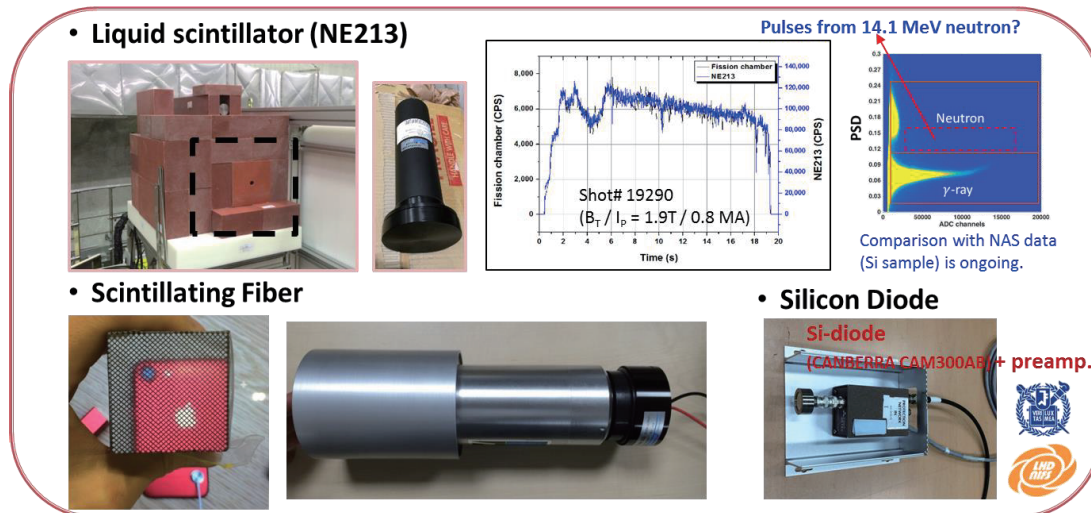
Fig. 8 Active collaboration with NIFS enhances the neutron diagnostic capability and will provide deep understanding of energetic particle physics on KSTAR.

4. Summary and prospects

As performance of fusion plasma increases, understanding of energetic particle behavior becomes crucial. Experimental study including development of novel fast-ion / neutron diagnostics has been carried out and the initial observations have been produced. Fast-ion transport study which has been focused on the fast-ion loss has made a big step toward the enhanced understanding of the physics with the international collaborations including A3 foresight program. At this moment several diagnostic efforts has provided the good start to study the fusion product behavior such as triton burn-up. Based on the research collaboration described in this paper will contribute to explore the 'real' fusion plasma physics.

Acknowledgements

References

[1] Junghee Kim *et al.*, Rev. Sci. Instrum. **83** (2012) 10D305.
[2] J.-Y. Kim *et al.*, The 55th Annual Meeting on the APS Division of Plasma Physics, Nov. 11 – 15 (2013), Denver, Colorado, USA. **JP8.00112**

[3] Junghee Kim *et al*., The 14th IAEA Technical Meeting on Energetic Particles in Magnetically Confinement Systems, Vienna, Austria, 1 – 4 Sep 2015. **O-9**

[4] Junghee Kim *et al*., The 26th IAEA Fusion Energy Conference, Kyoto, Japan, 17 – 21 Oct 2016. **EX/P4-26**

[5] Jayhyun Kim *et al*., The 11th A3 foresight program workshop.

[6] Junghee Kim *et al*., 2017 KSTAR Conference, Muju, Korea, 18 – 20 Jan 2017, **P2-23**

[7] F. Tzika *et al*., Appl. Radiat. Isot. **126** (2017) 121-126.

[8] A. Fenyvesi *et al*., 29th ITPA TG on Diagnostics

[9] M.S. Cheon *et al*., J. Instrum. **7** (2012) 05.

[10] J. Jo *et al*., Rev. Sci. Instrum. **87** (2016) 11D828.

[11] J. Jo *et al*., Rev. Sci. Instrum. (2017), under review.

[12] R.S. Granetz *et al*., Phys. Plasmas. **21** (2014) 072506.

[13] C.S. Kang *et al*., Phys. Plasmas. **21** (2014) 072509.

[14] M.S. Cheon *et al*., Nucl. Fusion **56** (2016) 126004.

[15] M. Isobe *et al*., J. Plasma Fusion Res. **8** (2009) 330.

[16] J.-Y. Kim *et al*., AIP Advances. **6** (2016) 105013.

[17] Y.M. Jeon *et al*., Phys. Rev. Lett. **109** (2012) 035004.

[18] Y. In *et al*., Nucl. Fusion, at press: https://doi.org/10.1088/1741-4326/aa791c

[19] Junghee Kim *et al*., 18th ITPA TG on Energetic Particles

The effects of the RMP application on the energetic particle driven resistive interchange (EIC) mode

S. Ohdachi[1,2], T.Bando[1,2], M. Isobe[1,2], and LHD Experiment group[1]

[1]National Institute for Fusion Science, Toki 509-5292, Gifu, Japan

[2]SOKENDAI(Graduate University for Advanced Studies), Toki 509-5292, Gifu, Japan

'

Abstract

The energetic particle driven resistive interchange (EIC) mode is a new kind of MHD instability observed in LHD. It is excited when the precession motion of the energetic particle and the resistive interchange mode resonate with each other. Significant amount of the energetic particle is lost when the EIC is excited. Since the effects of the EIC is fairly large, the trial for the suppression or the mitigation of the EIC mode is performed in the latest LHD experimental campaign.

1. Introduction

The LHD plasmas are intensively heated by the three tangentially injected NBIs and two perpendicularly (PERP-) injected NBIs as shown in Fig. 1. Perpendicularly injected energetic ions are easily trapped in the helical magnetic-field-ripple of LHD. It was found that when the precession motion of trapped energetic particles (EP) interact with the resistive interchange mode, so-called trapped-energetic-ion driven resistive interchange mode (EIC) is excited [1]. Recently, the NBI system is upgraded for deuterium campaign; the deuterium beams instead of hydrogen are injected. The acceleration voltage of the two PERP-NBIs is thereby increased from 40kV to 60 / 70KV. It is expected that the amount of the trapped EPs is increased significantly.

Bursts of the magnetic fluctuation of EIC are observed less frequently, whereas the amplitude of each bursts is 2~5 times larger than that observed with the hydrogen NBIs as shown in Fig. 2. After the large burst of the magnetic fluctuation (having n=1 structure), chirping-down of the m/n=1/1 mode structure localized at the iota = 1 rational surface is observed. The frequency of the chirping-down mode is similar to the frequency of the poloidal precession frequency of the perpendicular injected NBI particle. This observation supports that these phenomena are caused by the MHD instabilities (resistive interchange mode) affected by the existence of the energetic particles.
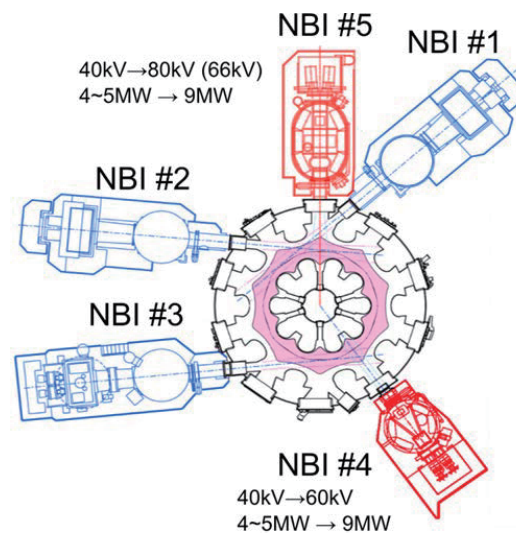
Fig. 1. Arrangements of the NBI heating system of the LHD.

2. Mitigation of the EIC

Since the effects of the EIC on the EPs and the bulk plasmas are quite large, we try to control the EIC. Two methods have been tested to control the EIC.

2.1 Control using RMP using m/n = 1/1 resonant magnetic field perturbation (RMP).

In the previous experiments in LHD, application of the m/n = 1/1 mode structure is effective to control the MHD instability related with iota = 1 rational surface. While the RMP field increases, suppression effects start before the appearance of the flat region of the electron temperature profile, which suggests the penetration of the RMP field. Since EIC mode is destabilized both by the bulk pressure gradient and energetic particle's pressure gradient, control of the MHD instability caused by the bulk plasma

Fig. 2 Comparison of the EIC in Hydrogen / Dueterium campaign.

can affect the stability of the EIC. Fig 3 shows a comparison of the plasma parameters with and without RMP. Before 4.7s, the two discharges are almost identical. There appears EIC modes when no RMP field is applied. The stored energy is decreased slightly. On the other hand, EICs are suppress when the RMP field is applied and neutron emission rate is kept higher. The amount of the energetic particles in the plasma is confined in this case.

It is found that when the EIC is marginally unstable, the EICs are suppressed with the RMP. The suppression / mitigation of the EIC is observed only when the external field does penetrate the LHD plasma. The penetration is confirmed by the flux loop measurement measuring Br and the flat electron temperature profile at the rational surface. This suppression is not caused by the reduction of the energetic particle confined in the plasma since the neutron Emission rate is not changed so much.

Fig. 3: Time evolution of the plasma parameters, such as the stored energy, the central ion temperature and neutron emission rate and magnetic fluctuations are shown.

2.1 Mitigation of the EIC using ECH heating

In order to decouple the MHD and EPs, reduction of the mode width of the resistive interchange mode is effective. It is known that the radial mode width of the interchange mode is estimated by $\delta w \propto \left(\frac{q^2}{S\hat{s}^2}\right)^{1/3}\left(\frac{\beta\kappa_n}{L_p}\right)^{1/5}$. Here, q is the safety factor, S is the magnetic shear, $\hat{s}$ is the magnetic Reynold's number, β is the beta, κ_n is the curvature of the magnetic field and the L_p is the scale length of the pressure gradient. If the electron temperature at the rational surface increases, the mode width will be reduced since the magnetic Reynold's number

Fig. 4: Schematic view of the banana orbit and its radial width.

increases. If the mode width is small enough so that interaction of the energetic particle becomes smaller (see, Fig. 3), the MHD mode and Eps are decoupled. The suppression of the EIC by ECH heating is already reported in lower ion temperature regime [2]. It is also confirmed in deuterium campaign where the ion temperature is higher.

Fig. 4 shows the time evolution of the plasma parameters with and without the ECH heating. The core

plasma is heated by ECH heating from 4.9s. The electron temperature is increased from the center. Even in the mode rational surface of iota = 1, the local electron temperature is increased slightly from 1.6 keV to 1.7~1.8keV. Though the mechanism for this suppression should be carefully confirmed, the effect of the ECH on the EIC is quite clear experimentally. When the EIC is suppressed, there appear complicated magnetic fluctuations which has not been identified.
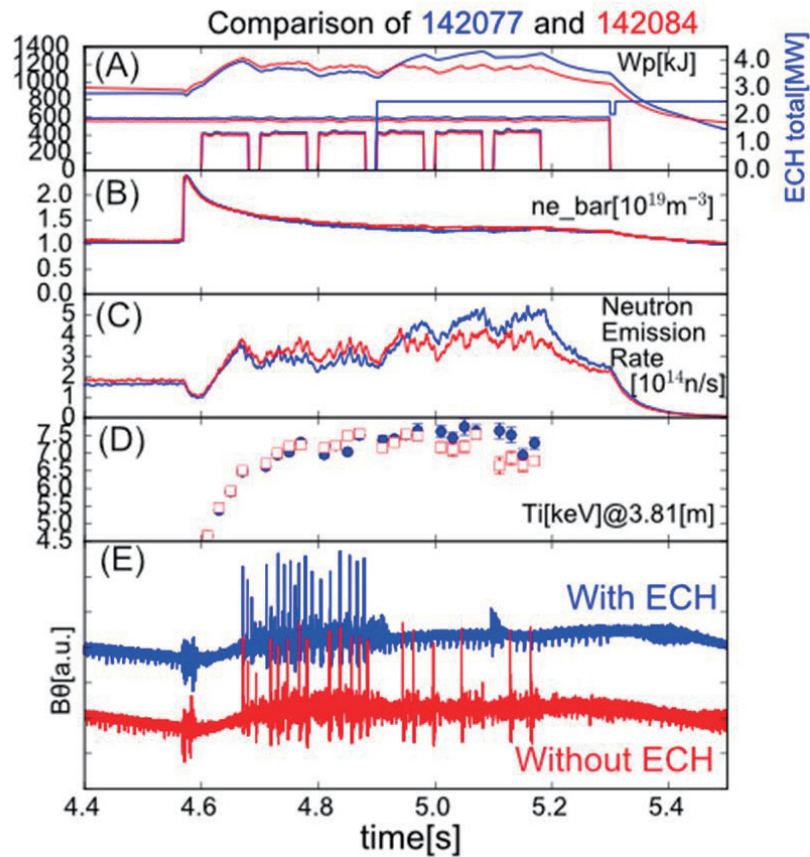
Fig. 5 Comparison of the plasma parameters with and without ECH heating.

In summary, the EIC modes are observed in the deuterium campaign of the LHD where the plasma heated by the perpendicularly injected NBIs. The mitigation/suppression of the EIC using by (1) RMP application and (2) ECH heating is reported.

Acknowledgements

References

[1] X. D. Du, et. al., Phys. Rev. Lett. **114** (2015), 15003

[2] X. D. Du et. al. Phys. Rev. Lett. **118** (2017), 125001

Preliminary Design and R&D of ITER Diagnostic-Radial X-ray Camera

L. Hu[1], K. Chen[1], Y. Chen[1], H. Cao[1], S. Li[1], H. Yu[1], J. Zhan[1], J.Shen[1], S. Qin[1], X. Sheng[1], J. Zhao[1], L. Niu[1], C. Feng[1], J. Ge[1], S. Zhang[1], B. Zhang[1]

[1]Institute of Plasma Physics, Chinese Academy of Sciences, Hefei 230031, China

Abstract

Preliminary design of ITER Radial X-ray Camera (RXC) has been finished. The structure design is optimized and installation process is studied considering the simplification and easiness of maintenance. Remote handling procedures are designed for the system maintenance after being activated. For detector cooling against high environment temperature which can be up to 240℃, a dedicated gas cooling system using heat exchanger is designed. The structure analysis indicates that the stresses and displacements of most of the components under load combinations are within the allowable limits and no Safety Important Component (SIC) boundary is damaged. Through putting B4C material in the front part of Diagnostic Shielding Module (DSM) and around detectors for neutron shielding, the detectors are expected to survive the whole D-D phase. As for electronics, preliminary design of highly integrated pre-amplifier and program controllable mid-amplifier has been completed, both with bandwidth greater than 100 kHz to meet time resolution requirement of 20 kHz. To protect the electronics from intensive neutron and gamma irradiation, shielding cabinet capable of attenuating neutron flux down to 0.0001 and gamma dose 0.01 is designed. Besides, many R&D has been done to support the design. The tests of pre-amplifier and mid-amplifier indicated the electronics had no functional problem when debugging together and generally passed preliminary Electro Magnetic Compatibility (EMC) test and nuclear test. The highly-integrated compact pre-amplifier has been used in EAST and proved useful. To test the feasibility of dedicated gas cooling system for detectors, a cooling test platform was built and preliminary cooling test has been done, indicating that during 250℃ baking the detector temperature is promising to be cooled down to the detector temperature limit of 75℃. To increase signal to noise ratio, large area detector with dark current less than 2nA has been manufactured and worked steadily in EAST experiments.

1. Introduction

Radial X-ray Camera (RXC) is one of the plasma diagnostics [1-4] installed on ITER tokamak. RXC is expected to measure the poloidal profile of the plasma x-ray emission with high spatial and temporal resolution. RXC primarily measure low (m,n) MHD modes, sawteeth, disruption precursors, and used as ELMs indicator. RXC also supplementarily measures plasma position, radiation power, runaway electrons, impurity content, etc [5-7].

As described in the Procurement Arrangement (PA) [7], this system has been credited with basic
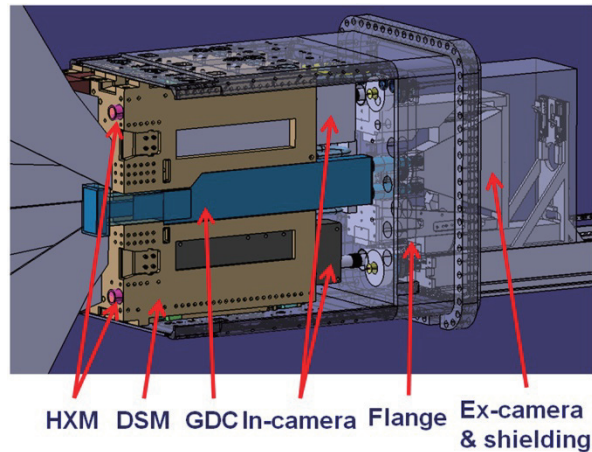
Fig.1 Overall view of RXC.
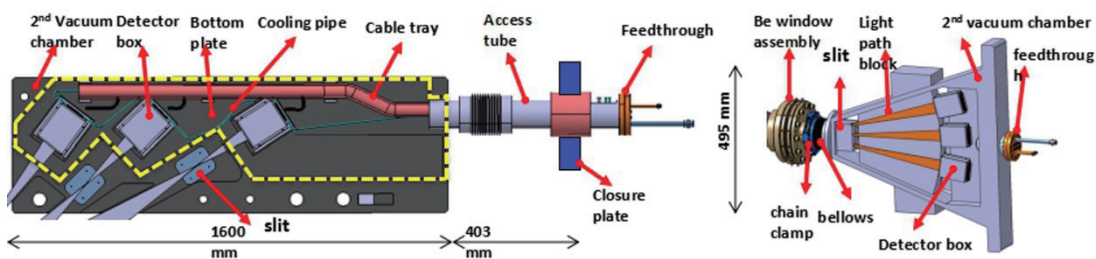
Fig.2 Layout of internal camera and external camera

detectors (silicon detectors) that are expected to operate until the end of the DD phase. However, due to rapid ongoing developments in fast, radiation-tolerant, photon-counting x-ray arrays, it is intended that the camera should be upgraded with such detectors (advanced detectors) at an appropriate time during D-D operations. Besides, advanced detectors are outside the scope of this PA.As a result, the design of this system is based on basic detectors, i.e. silicon linear diode arrays, with compatibility to advanced detectors considered. Overall view of RXC is shown in Fig.1.

As can be seen from Fig.1, RXC, Glow Discharge Cleaning (GDC) and Hard X-ray Monitor (HXM) share middle module of Equatorial 12 port plug [8]. RXC is composed of in-port and ex-port cameras which view the outer and core region respectively through vertical slots in the Diagnostics Shield Module (DSM). Both internal camera and external camera have secondary vacuum housing with beryllium window assemblies. A concrete shielding shell enclosing the external camera is designed to reduce radiation leakage into outside environment.

In the remaining sections, preliminary design, R&D and summary will be presented.

2. Design of camera

Layout of internal camera and external camera is shown in left part and right part of Fig.2, respectively.

As seen from left part of Fig.2, internal camera is composed of rectangular main body (secondary vacuum chamber) and access tube. The secondary vacuum boundary is shaped by dashed formed by stainless steel wall and beryllium window assembly. The access tubed starts from end of main body,

penetrating port flange (closure plate) and ends with feedthrough flange. Main body of internal camera is installed in the large rectangular hole in DSM. The installation sequence is as follows: push the camera into DSM from the back --> fix main body on DSM side wall --> connect the access tube with closure plate through welding.

The layout of external camera is shown in right part of Fig.2. External camera is supported on closure plate through upper and lower legs, and connected to closure plate through vacuum extension welded on closure plate, Be window assembly, chain clamp and double bellow.

Considering detector operation temperature limit is ~75 ℃ and environment temperature inside camera chamber can be up to 240℃[9], a multi-hole gas heat exchanger is tightly attached to detector for dedicated cooling.

To improve machining precision and assemble precision, the internal camera slits are welded with bottom plate firstly and then machined together. The machining of external camera slit and light path block follow the same procedure.

To mitigate nuclear radiation leakage into environment outside closure plate, a concrete shielding shell enclosing the external camera is designed. Through putting B4C material in the front part of DSM and around detectors (not shown in Fig.2 for the sake of simplicity), the detectors are expected to survive the whole D-D phase without detector replacement.

Load combinations of Dead Weight (DW) + Earthquake (EQ), DW+VDE, DW+VDE+EQ, DW+THB+EQ, DW+THO+VDE, etc. were analyzed to study structural integrity. Stress and displacement of most of the components under load combinations are within the allowable limits. No SIC boundary is damaged. Only one point at the pipe (continuous part) and corresponding pipe support inside the internal camera (inside port plug) present high stresses. The structural of the coolant pipe will be optimized continuously in the final design phase. For example, adding S-bend is a good method to reduce the stress. So, it is not difficult to lower the high stresses of pipe and pipe support.

To be compatible with future maintenance operations in nuclear environment where access of workers is strictly restricted or forbidden, remote handling procedures are designed. Note that both internal camera and external camera will be installed and maintained as a whole. The basic procedure to remove internal camera as shown in Fig.3 is: ①disconnection of connectors, weldings, pipes, etc. outside closure plate;②transport the whole port plug and DSM with internal camera inside into hot cell; ③extraction of middle DSM from port plug; ④unbolting of anchoring point of internal camera from DSM; ⑤extraction of internal camera; ⑥ cleaning or replacement of the whole camera. The installation follows the reverse procedure. The basic procedure to remove external camera as shown in Fig.4 is: ①removal of shielding block;② disconnection of connectors, weldings, pipes, etc.; ③disconnection of external camera from closure plate;④ transport of the whole external camera and shielding block into hot cell;⑤ cleaning or replacement of the whole camera. The installation of external camera follows reverse procedure. The only difference is that the installation needs to be adjusted for alignment. Note the external camera and shielding block should be removed first to allow for space for the removal of internal camera and installed lastly in assembly situation. It is obvious that during the installation and removal of internal camera and external camera, several tools have to be used, such as bolt runner, crane, manipulator, cutting/welding tools, etc.
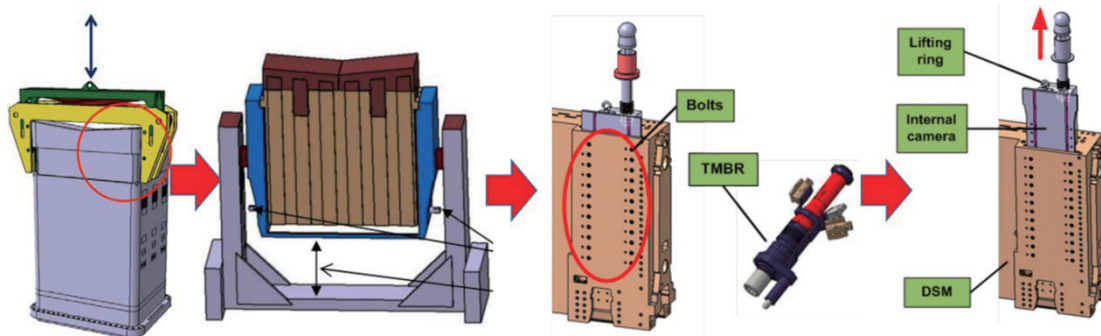
Fig.3 Internal camera maintenance procedure
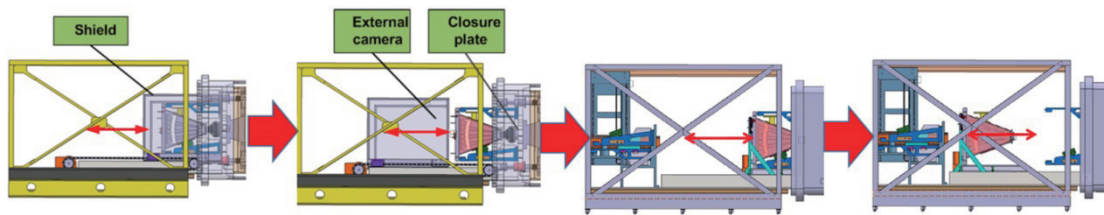
Fig.4 External camera maintenance procedure

To improve RXC signal to noise ratio, the detector active area is designed to be 12mm*4mm for each channel. To meet measurement requirement in PA [7], i.e. localization of MHD modes to a/10 and vertical spatial resolution of 40mm for edge region (r/a>0.85), 64 channels are allocated to central region and another 64 channels to edge region. This chord arrangement is shown in Fig.5 (a). The edge region (r/a from 0.85 to 1) in the low-field-side is covered by ~15 effective chords (observing upper plasma; overlapping has been considered). Similar coverage is observed for the chords looking at the lower plasma. This edge region expands on the vertical magnetic axis to a 600 mm chord. The vertical resolution is then evaluated to ~40mm (600mm/15=40mm) which is the Annex B requirement. It can be noted that, in fact, there will be about 35 chords covering the edge region when counting the upper and lower views. This redundancy of coverage will help to improve the analysis of the plasma soft x-ray emission. Simulation results as shown in Fig.5 (b) and (c) indicate that features of sawteeth and ELMs can be grabbed with the diagnostic. In order to measure detector background noise and heat drift, one single detector is put behind each detector chip. Two marginal channels on adjacent chips which view nearly the same plasma area as that of adjacent detector array made the camera allow for the poloidal position error.

As for electronics, preliminary design of highly integrated pre-amplifier and program controllable mid-amplifier has been completed to process 140 channel of signals, both with bandwidth greater than 100 kHz to meet time resolution requirement of 20 kHz [7]. The number of channels to be processed is 140. The pre-amplifier is designed based on highly-integrated PXI plug-in containing 24 channels each with gain ~ 1.0×10^6 V/A. A customized standard 6U and 8-socket chassis is used for preamplifier housing and EMC compliance. To change the gain and drive long distance (~50m) signal transmission, mid-amplifier is designed based on 3U standard PXI plug-in each with 16 channels. The gain is program controllable by PLC from slow controller. Since there are strong EM and nuclear radiation in port cell and some of the electronics components are susceptible to these external radiations, multi-layer (20cm Iron, 20cm

<div align="center">(a)   (b)   (c)</div>

Fig.5 Chord arrangement and simulation results.(a) Chord arrangement; (b)soft x-ray flux contour with sawtooth; (c) soft x-ray flux contour with ELM.

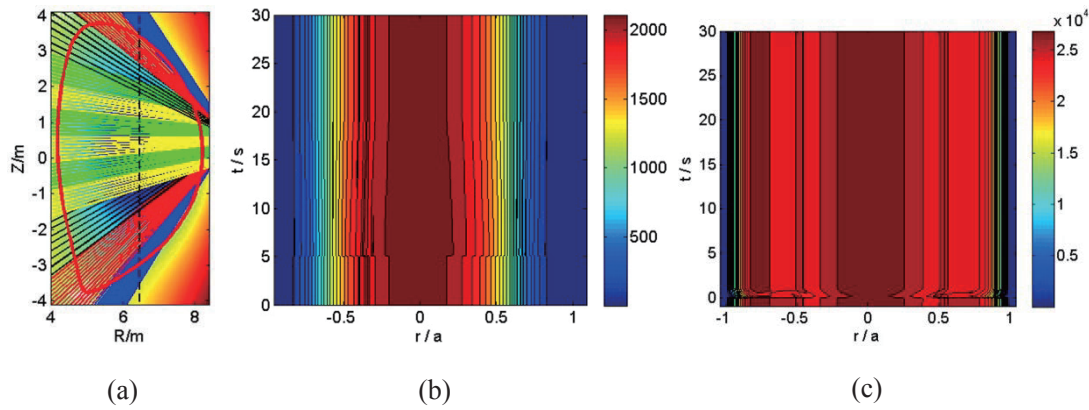boron-contained polyethene and 4cm lead) shielding cabinet is designed to protect the pre-amplifier and mid-amplifier. The simulation results indicate that the neutron attenuation factor is ~0.0001 and gamma ~0.01, which will make the internal neutron flux less than 100 n/cm^2/s and total integrated dose less than 10Gy as required by ITER electronics policy.

I&C design has also been done following the Plant Control Design Handbook [10], diagnostic I&C requirements and ITER hardware and software specification. The I&C function includes: Measurement of Soft X-Ray flux (128 channel of linear array signal+ 12 channel of single detector signal); Calibration for Data AcQuisition (DAQ) card, amplifier and detector; Gain control of mid-amplifier; Gas cooling system control and monitoring (valve, pump, temperature sensor, pressure sensor and flow sensor); Provide equipment health monitoring; Provide standard COntrol, Data Access and Communication (CODAC) distributed control system functions, i.e. Control, monitoring, alarming, data archiving, HMI, etc.; Sequence RXC plant-system operating states (PSOS) to match ITER Common Operating States (COS). I&C functional analysis, architecture design, fast controller design, slow controller design, definition of signals and variables, identification of boundaries and interfaces, cubicle configuration design, software design and state machine design have been completed.

3. R&D and tests

In addition to the design, many R&D has been done to support the design. The pre-amplifier prototype and mid-amplifier have been manufactured and the output noise is ~10 mV and 50-100 mV respectively. The design of the later will be improved to reduce the noise in the future. These two set of amplifiers have been debugged together and no functional problem was found. Prototypes of pre-amplifier and mid-amplifier are shown in Fig.6. Preliminary tests of Radiated Electromagnetic Fields (E-Field) Immunity, Electric Fast Transient (EFT) Immunity and Electrostatic Discharge (ESD) Immunity have been done following standards introduced in Electrical Design Handbook (EDH) [11]. The test results indicated that all the components functions pass the tests except for some minor deviation of 1-2 components like the communication errors of chassis controller's USB devices which however will not be used in ITER. Pre-amplifier was tested with Cf-252 source at neutron flux of ~2.23×10^3 n/cm^2/s and neutron fluence greater than 10^{10}n/cm^2. No change was found in signals of detector and pre-amplifier. In the Co-60 test

(a)   (b)
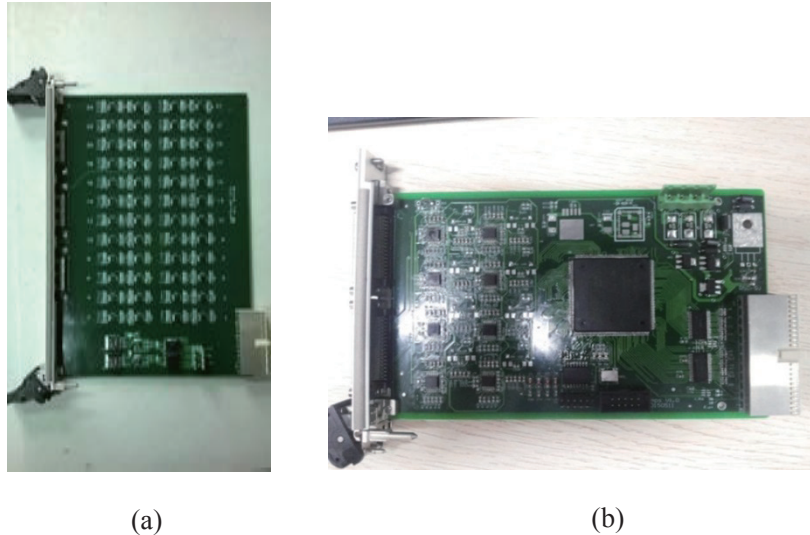
Fig.6 Prototypes of (a) pre-amplifier and (b) mid-amplifier

with gamma dose rate of 0.5 Gy/min and integrated dose of 200 Gy, the pre-amplifier and mid-amplifier worked well during the gamma irradiation, while the power module in the board had some radiation damages. This implies the necessity to increase radiation resistance of the power supply chip.

To test the feasibility of dedicated gas cooling system for detectors, a cooling test platform was built as shown in Fig.7, containing simplified internal camera, baking box housing the internal camera, heat exchanger and supporting equipment and components like heating controller, vacuum pump, air compressor, data acquisition system, etc. In the cooling test, the surface of detector box and cooling pipes were wrapped with several layer of heat insulation. The test results indicate that during 250 $^\circ$C baking with compressed air of pressure 0.5 MPa and flow rate 50L/min, the detector temperature can be cooled down to 85-95 $^\circ$C which is very close to the detector operation temperature limit of 75°C. It is promising that this requirement can be met in the future through optimizing design of insulation, heat exchanger and cooling loop layout.

To increase signal to noise ratio, detector active area is enlarged to 24 mm^2 (~6 times as large as Centronic LD35-5T) and the customized detectors with 35 channels were manufactured and tested. It is found that the dark current is less than 2 nA and worked steadily in EAST experiments. An even larger detector containing 16 channels is envisaged and to be customized in the future.

There are also some I&C tests that has been done on EAST. To test the data acquisition system and the response time from data receiving to calculated data uploading, a set of simplified I&C system including cubicle, DAQ card (PXIe-6368), programmable amplifier, Industrial Personnel Computer and CODAC Core System 4.3 has been built. It is found that the response time is estimated to be 1.4 ms when collecting and processing 200 channel of signals. This response time is sufficient for real time data display.

4. Summary

In summary, preliminary design of RXC has been completed and produced useful results. In the next step, the RXC design will be furthered towards final design review (FDR). All the PDR chits and comments from PDR documents will be considered to optimize the design. The camera design will take into account future detector upgrade and related maintenance between two ITER operation phases. The candidates of
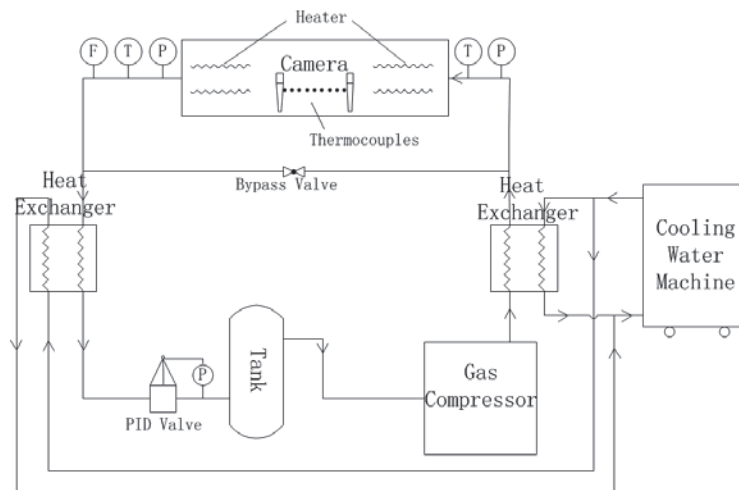
Fig.7 Sketch of cooling test platform

advanced detectors are Low Voltage Ionization Chamber (LVIC) [12], Gas Electron Multiplier (GEM) detector, silicon detector with optimized nuclear shielding [13], etc. The compatibility to LVIC and GEM detectors has been considered in the design, and also for the components in port cell and diagnostic building, e.g. space reservation, electronics nuclear shielding, number of channels, etc. More detailed design related to compatibility to advanced detector will be carried out with input information from ITER organization. Besides, in the final design phase, there will be some prototyping components manufactured and tested to verify the design.

References

[1] C. Watts, et al., NuclearInstrumentsandMethodsinPhysicsResearchA **720** (2013) 7.

[2] V.S.Udintsev, NuclearInstrumentsandMethodsinPhysicsResearchA **623**(2010) 649.

[3] M.G. vonHellermann, et al., NuclearInstrumentsandMethodsinPhysicsResearchA **623**(2010) 720.

[4] V.I. Afanasyev, et al., NuclearInstrumentsandMethodsinPhysicsResearchA **621** (2010) 456.

[5] A. E. Costley, et al., Measurement Requirements and the Diagnostic System on ITER: Modifications Following the Design Review, in: 22nd IAEA Fusion Energy Conference, Geneva, Swiss, 2008.

[6] S. Wang, et al., Electromagnetic behavior on ITER radial soft x-ray camera, in: 2013 IEEE 25th Symposium on Fusion Engineering (SOFE), San Francisco, United States, 2013.

[7] R. Barnsley, Annex B_55 E7_Radial X Ray Camera, private communication, 2013.

[8] G.. Vayakis, et al., Current status of ITER diagnostics development, in:26th ITPA Spring Meeting,

Pohang, Korea, 2014.

[9] L. Hu, et al., Fusion Science and Technology, **70** (2016) 112

[10] J.Journeaux, Plant Control Design Handbook, private communication, 2013.

[11] D.Beltran, EDH Part 4: Electromagnetic Compatibility (EMC), private communication, 2012.

[12] Yu. V. Gott and M. M. Stepanenko, Instruments and Experimental Techniques, **52** (2009) 260.

[13] D. Mazon, et al., Fusion Engineering and Design, **96-97** (2015) 856.

Progress of infra-red imaging video bolometer of KSTAR

Seungtae Oh[1], Juhyeok Jang[2], Byron Peterson[3], Wonho Choe[2], Suk-Ho Hong[1]

[1]National Fusion Research Institute, Daejeon, Korea

[2]Department of Physics, KAIST, Daejeon, Korea

[3]National Institute of Fusion Science, Gifu, Japan

Abstract

KSTAR IRVB diagnostic for KSTAR plasma radiation measurements is successfully implemented with its tomography codes based on the Phillips-Tikhonov algorithm. It was applied to the plasma radiation profile measurements in ELM mitigation experiments using resonant magnetic perturbation (RMP), and it showed that the application of RMP induced the significant radiation profile changes under Ar injections.

1. Introduction

Plasma radiation is the most fundamental measurement of the fusion plasma for the studies of power balance [1], boundary physics studies [2], and impurity transport [3]. The radiation from the plasma core induces fusion power loss and the degradation of plasma confinements. However, radiation from the plasma edge is considered as a good indicator of the mitigation of the heat load on the divertor [2-4]. In addition, the radiation is quite informative for impurity transport studies, ELMs, and disruptions [5-9].

As for the measurement technique for the radiation power from high temperature fusion plasma, the foil bolometry method is widely used due to its flat sensitivity in the wide wavelength range. Conventional resistive bolometer utilizes the electrical resistance changes of the metal grid under the foil temperature changes induced by the radiation. Another type of foil bolometry is the infrared imaging video bolometer (IRVB) using an IR camera. The big advantage of IRVB is its stability against electromagnetic noise compared with resistive bolometers using Wheatstone Bridge.
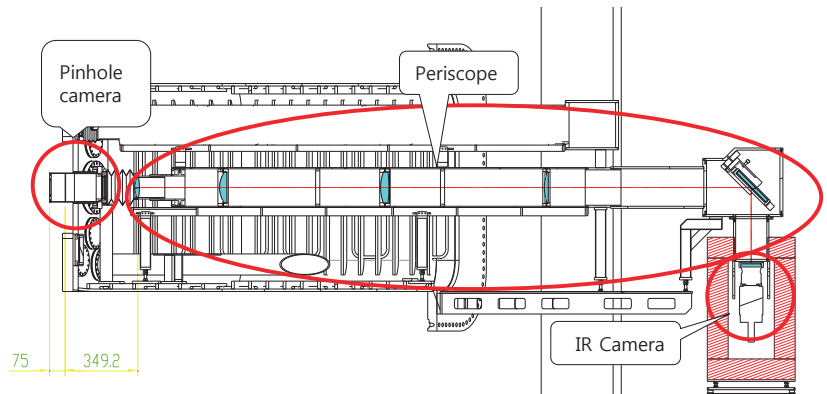
2. KSTAR IRVB setup

Fig.1 KSTAR IRVB setup

Recent development of the KSTAR IRVB can provide edge radiation power for the investigation of energy balance and pedestal characteristics during ELMs. The setup of the KSTAR IRVB is composed of a pin-hole camera, a periscope, and an IR camera as shown in Fig.1. The entire length of the system is 3.5 m, and its height is 1.2 m. As mentioned before, the core part of the system is the pin-hole camera placed inside the vacuum chamber. It has a 2 μm thick 70 × 90 mm² platinum foil and a 5 mm diameter pin-hole. The foil is coated with graphite for the enhancement of radiation absorption and emission, and it can measure up to 7.5 keV of photon energy. The IR image of the foil is to be measured by an IR camera with Indium Antimonide imaging array through a CaF_2 vacuum window. However the system needs a periscope due to the KSTAR structure with a cryostat and the camera protection from the radiations or the magnetic fields. The periscope consists of 4 CaF_2 lenses for relay optics and a mirror to avoid direct radiation exposure to the sensor of the camera. The shielding box of the IR camera is 3 layered with lead, soft iron and borated poly-ethylene. In the operations, the camera is controlled from a remotely located computer.

3. 2D profile reconstruction of plasma radiation

The foil image presents the line integrated plasma radiation as shown in Fig.2. So, to get the cross sectional profile of the plasma radiation from the foil image data, mainly three calculation steps should be taken to convert the foil image into the cross section profile of the plasma power density [10]. The first step is the conversion from foil image data to temperature data. This process is just a scale conversion using a pre-calibrated scale factor. The second step is predicting input radiation power. After getting the temperature profile of the foil, the input power of a line integrated radiation can be calculated using the heat diffusion equation as

$$P(x,y,t) = kt_f(x,y)\left\{\frac{1}{\kappa(x,y)}\frac{\partial T(x,y,t)}{\partial t} - \left(\frac{\partial^2 T(x,y,t)}{\partial x^2} + \frac{\partial^2 T(x,y,t)}{\partial y^2}\right)\right\} + \varepsilon(x,y)\sigma_{SB}(T(x,y,t)^4 - T_0^4) \quad (1)$$

where x and y represent the horizontal and vertical coordinates on the foil, T(x,y,t) denotes the 2D profile of the foil temperature, T_0 represents the temperature of the surroundings, k, t_f and κ are the thermal conductivity, thickness and the thermal diffusivity of the foil, respectively. σ_{SB} and ε are the Stefan-Boltzmann constant and the blackbody emissivity of the foil, respectively [10]. The final third step
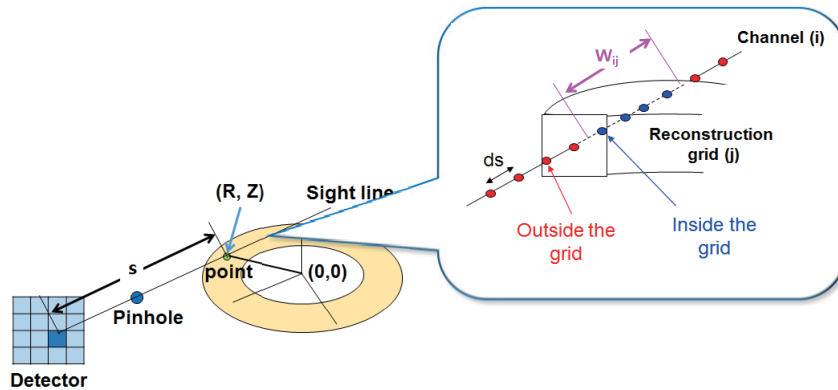

Fig.2 Reconstruction of plasma profile from line integrated radiation power
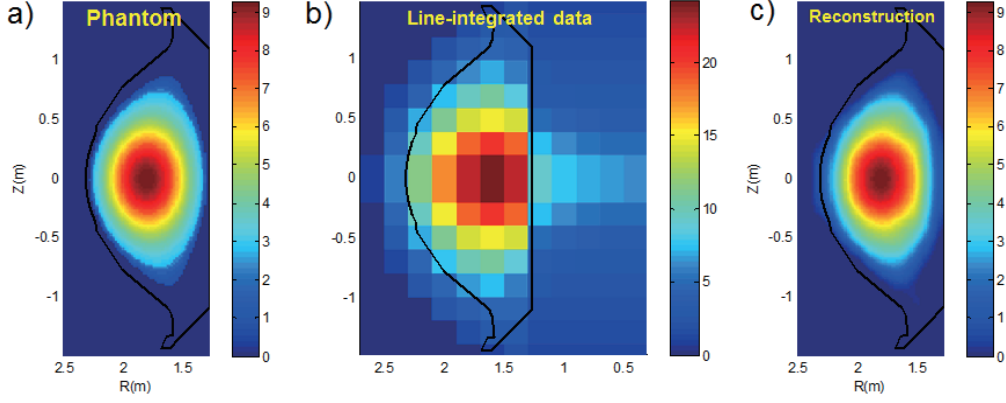
Fig.3 The estimation of KSTAR IRVB reconstruction code: a virtual phantom plasma profile (a) was generated, and the line-integrated data (b) on the foil was then generated with integration weight matrix (W). The 2D profile (c) was successfully reconstructed from the line-integrated data (b) on the foil.

of the reconstruction is the conversion from the line integrated radiation power to the 2D profile of the plasma radiation through Phillips-Tikhonov (P-T) algorithm [11]. When the 2D radiation profile ($\vec{g}$) experiences the geometry integration weight matrix ($\overleftrightarrow{W}$), the final measurement of the line integrated radiation power ($\vec{f}$) at the foil can be expressed as $\vec{f} = \overleftrightarrow{W} \cdot \vec{g}$. Since the inverse matrix of $\overleftrightarrow{W}$ doesn't exist, P-T algorithm to find the 2D radiation profile ($\vec{g}$) adopts the method minimizing total error of the average projection error ($|\vec{f} - \overleftrightarrow{W} \cdot \vec{g}|^2/M$, M means the total detector number) and the perturbation error ($|\overleftrightarrow{L} \cdot \vec{g}|^2$ where and $\overleftrightarrow{L}$ is the Laplacian matrix). The final equation of $\vec{g}$ through the P-T algorithm can be derived as

$$\vec{g}(\gamma) = (\overleftrightarrow{W}^T \cdot \overleftrightarrow{W} + M\gamma \overleftrightarrow{L}^T \cdot \overleftrightarrow{L})^{-1} \cdot \overleftrightarrow{W}^T \cdot \vec{f} \qquad (2)$$

where the regularization parameter γ balances the projection error and the perturbation error. KSTAR IRVB reconstruction code was successfully estimated with virtual plasma phantoms as shown in Fig. 3.

4. Ar injection Experiments

KSTAR IRVB was applied to the plasma radiation profile measurements in ELM mitigation experiments using a resonant magnetic perturbation (RMP) as shown in Fig. 4. It shows radiation profile changes after Ar injections or with RMP applications. The injected Ar trace is 1.7 V during 60 ms from the divertor side. And the plasmas conditions and the applied RMP were respectively H-mode with $I_p \approx 0.5$ MA , $n_e \approx 1.5 \times 10^{19}/m^2$, $T_e \approx 3$ keV, NBI = 2.9 MW under $B_t = 1.8$ T and n=1 90˚ RMP. In the case of the plasma without ELM mitigation, high emissions in the divertor region were shown after the Ar injection. It seems to be caused by the increase of the impurity amount in the divertor region with the injection, and the emission increase in the plasma core region may be caused by the impurity diffusions or transports. However, in the case with ELM mitigation, the emissions at the divertor were similiarily increased after the Ar injection, however the emission change at the plasma core was relatively quite low. It may show the transport mechanism changes after ELM mitigation
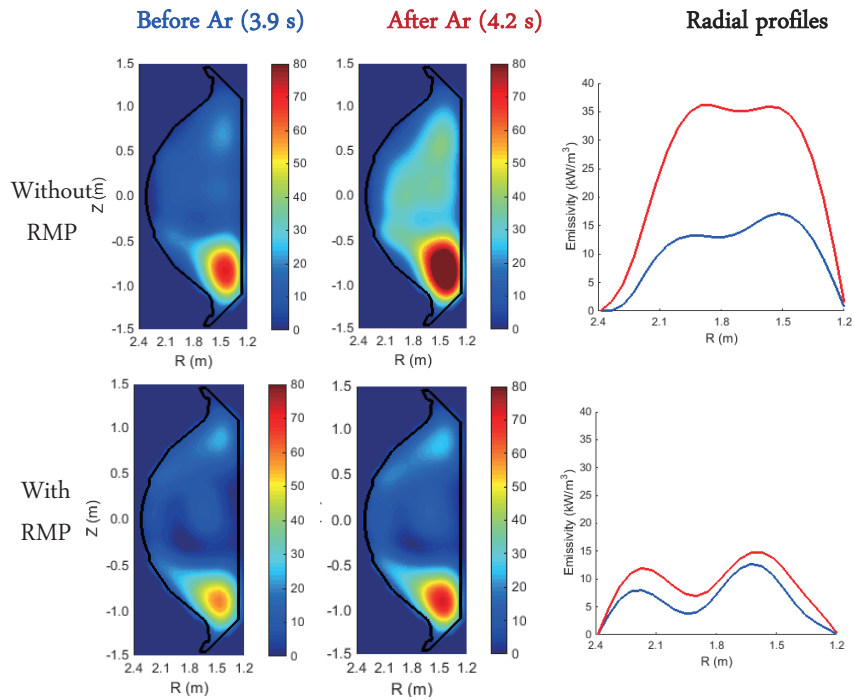
Fig.4 plasma radiation changes with Ar injection and RMP

4. Summary

Plasma radiation measurement is one of the most fundamental measurements for plasma fusion researches. For this diagnostics, KSTAR IRVB was successfully implemented with the development of its reconstruction code based on Phillips-Tikhonov algorithm. In KSTAR experiments, it is producing the radiation profiles, and it showed the meaningful results in the ELM mitigation experiments using RMP through plasma radiation profile measurements.

References

[1] J. A. Goetz, B. Lipschultz, M. A. Graf *et al., J. Nucl. Materials* **220–222 (**1995) 971

[2] A. Kallenbach, M. Bernert, R. Dux *et al., Plasma Phys. Control. Fusion* **55** (2013) 124041

[3] P. Dumortier, P. Andrew, G. Bonheure *et al., Plasma Phys. Control. Fusion* **44** (2002) 1845

[4] J. Rapp, P. Monier-Garbet, G. F. Matthews *et al., Nucl. Fusion* **44** (2004) 312

[5] H. Chen, R. Giannella, N. C. Hawkes *et al., Plasma Phys. Control. Fusion* **43** (2001) 1

[6] M. Valisa, L. Carraro, I. Predebon *et al., Nucl. Fusion* **51** (2011) 033002

[7] A. Huber, K. McCormick, P. Andrew *et al., J. Nucl. Materials* **363–365** (2007) 365

[8] G. Veres, R. A. Pitts, A. Bencze *et al., J. Nucl. Materials* **390–391** (2009) 835

[9] G. Pautasso, Y. Zhang, B. Reiter *et al., Nucl. Fusion* **51** (2011) 103009

[10] B. J. Peterson, H. Parchamy, N. Ashikawa, *et al., Rev. Sci. Instrum.* **79** (2008) 10E301

[11] S. H. Lee, J. H. Kim *et al., Curr. Appl. Physics* 10 (2010) 893

Development of Beam Emission Spectroscopy diagnostic on EAST tokamak

Y. Yu[1], M.Y. Ye[1], H.J. Wang[1, 2], R. Chen[2], Y.F. Wu[1], B.D. Yuan[1], S.B.Gong[1],

Q.J.Yu[1], B. Lyu[2], Y.J. Shi[1], B.N. Wan [2]

[1]School of Nuclear Science and Technology, University of Science and Technology of China, Jinzhai Road 96#, 230026, Hefei, China

[2]Institute of Plasma Physics, Chinese Academy of Sciences, Hefei 230031, China

Abstract

Beam Emission Spectroscopy (BES) diagnostic based on Neutron Beam Injection (NBI) on EAST tokamak (Experimental Advanced Superconducting Tokamak) has been developed. This system consists of 16×8 channels which can diagnose the density fluctuation in a rectangular area of about 20×10 square centimeters in the cross section. The viewing area of BES is adjustable from core to edge by changing the angle of the rotation mirror. The spatial resolution is about or better than 1 centimeter depending on the observed radial position and he temporal resolution is 1μs. NBI modulation experiment during EAST plasma discharge shows BES system is well developed.

1. INTRODUCTION

Although great progress on tokamak physics has been made in the last decades, many physical problems still remain open, such as Internal Transport Barrier[1], pedestal physics[2, 3] and L-H transition [4-6]. This comes partly from the insufficiency of diagnostics and experimental data. Plasma density fluctuation is one of the most important parameters in experimental plasma research and many kinds of diagnostics are developed to measure it, such as Doppler Reflectometer[7, 8], gas puffing imaging[9, 10], phase contrast imaging[11], et al. Among these plasma density diagnostics, BES[6, 12, 13], based on Neutral Beam Injection (NBI)[14, 15], is a sharp tool to get two-dimensional distribution of plasma density fluctuation by measuring Doppler shifted D_α line which is emitted by excited NBI atoms. BES has been widely applied on many tokamaks, such as DIII-D[12, 16], MAST[6, 17], and KSTAR[18, 19] , working from core to edge. In this article, we present the development of BES on EAST tokamak[20, 21].

The rest of this article is organized as follows: the development of BES system is given in section 2 after a brief introduction to principle of BES; first results in NBI modulation experiment is shown in section 3.

2. DEVELOPMENT OF BES DIAGNOSTIC ON EAST

EAST is a superconducting tokamak with 16 D-shape magnets to produce 3.5T toroidal magnetic field and 12 poloidal magnets to induce the plasma current higher than 1 million Ampere. Besides Ohm-Heating, auxiliary heating sources such as ICRF, ECRH, LHW and NBI are used to heat plasma to get high plasma

parameters. When the power of tangential NBI in port A of EAST vacuum chamber is high enough,i.e.2MW,BES system can detect specific Doppler red-shift D_α signal with $\lambda = 659nm$ emitting at the interaction position between NBI and bulk plasma. The light intensity I and the plasma density n briefly follows[22]:

$$\tilde{n}/n = \tilde{I}/I,$$

Where $\tilde{I}$ and $\tilde{n}$ are the fluctuations of I and n. By means of collecting the time series of light intensity, BES can effectively diagnose plasma density fluctuation.

There are two NBI heating systems on EAST tokamak as is shown in Fig.1. Ttwo red lines named NBI-left and NBI-right illustrate the injection path of these two neutral beams. The blue lines represent the light paths from the emitting particles to the first mirror of BES, or in other words, the viewing area.
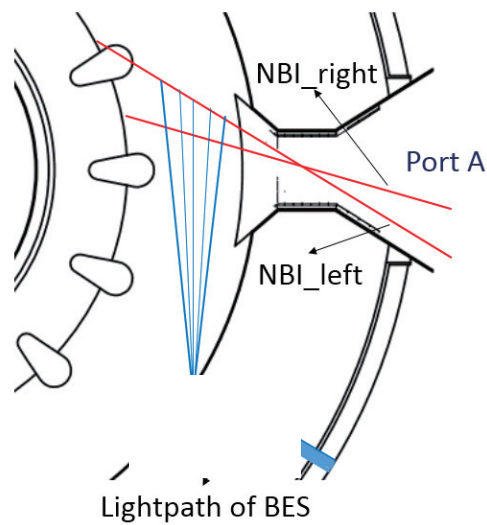
Figure 1.Two red lines named NBI-left and NBI-right show the injection path of these two neutral beams in EAST port A. The blue lines represent the light paths from the emitting particles to the first mirror of BES.

BES system on EAST tokamak consists of five main parts: a long steel sleeve with lens inside to guide emission light, light collection branches, server to save and analyze signals, remote controlling system, and supporting and shielding components.
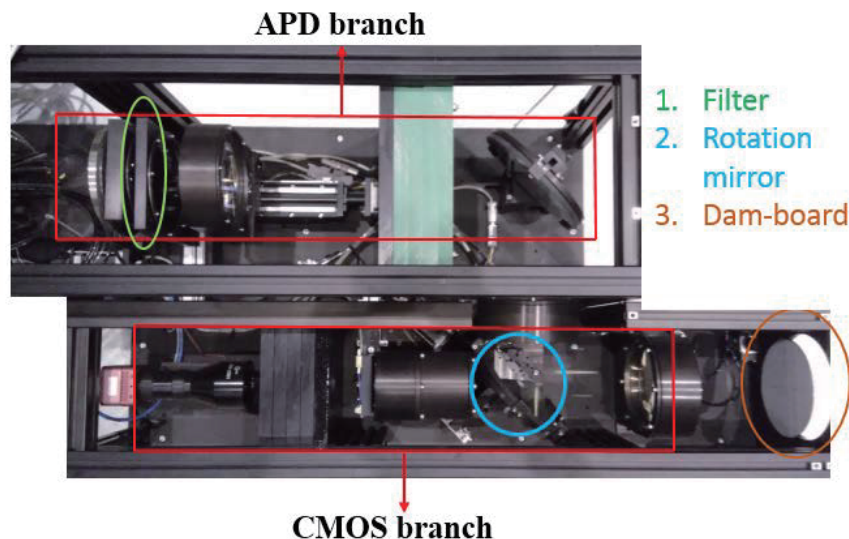
Figure 2. Main parts in the atmosphere of BES system. APD branch and CMOS branch share the same light path. APD branch is used to detecting plasma fluctuations and CMOS branch is used as an observation for something like calibration. The different coloured circles in this figure mark some key components of the system.
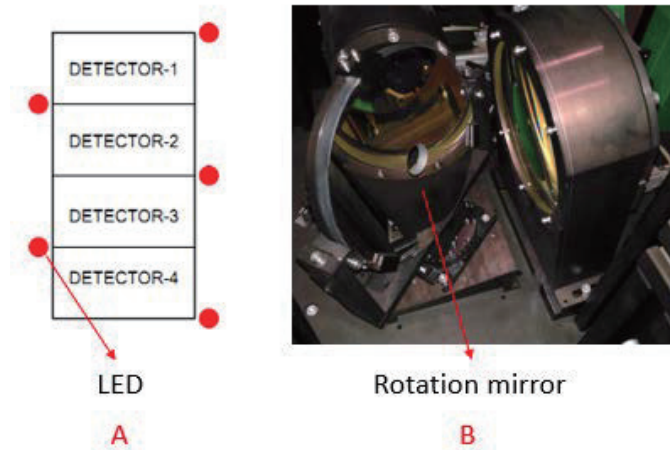
Figure 3. (A): The arrangement of the 128 detection channels of the APD camera, shown as DETECTOR-1 to -4.The five red spots are LEDs which are used for space calibration. (B): It's the rotation mirror that has been marked out in Fig. 2. Light reaches the CMOS camera through the hole in the mirror center.

There are two light collection branches in BES system as is shown in Fig.2: APD (Avalanche Photo Diode camera) branch and CMOS (Complementary Metal Oxide Semiconductor) branch, with a dam-board at the end of the branch. APD branch, which has 16×8 (16 in horizontal and 8 in vertical direction) channels, is used to detect 659nm line, divided into four groups named DETECTOR-1 to -4 (8×4channels per group) as is shown in Fig. 3(A).Five LED (light-emitting diode) bulbs (red spots in fig. 3(A)) around the APD detection channels are used for space calibration which is carefully discussed in section 3. In front of the APD detector, a narrow band-pass filter (1.59nm Full Wave at Half Maximum with a central wavelength of 659nm) is used to filter out the unwanted background line, such as the un-shifted D_α line with a wavelength of 656.1 nm. The rotation-mirror (Fig. 3(B)) reflects signal light to APD branch and it can be rotated in clockwise or anticlockwise to adjust light path, in other words, different view planes along NBI, as is shown in Fig. 4(A). A hole with a diameter of 1cm (Seeing in Fig. 3(B)) is at the right center of the rotation-mirror where emitted light is allowed to pass through. Then we can use CMOS camera for space calibration and catching the trace of NBI during EAST discharging. In figure 4(A), blue, yellow and green lines represent different light paths, corresponding to different diagnosed spatial positions from core to edge. Thus the viewing area is adjustable in EAST cross section by rotating the mirror. Fig. 4(B) shows the cross section of EAST device and the location of BES viewing area. The blue rectangle at the RHS represents the viewing area with 16×8 hollow points in it showing the 128 diagnosed spatial positions.
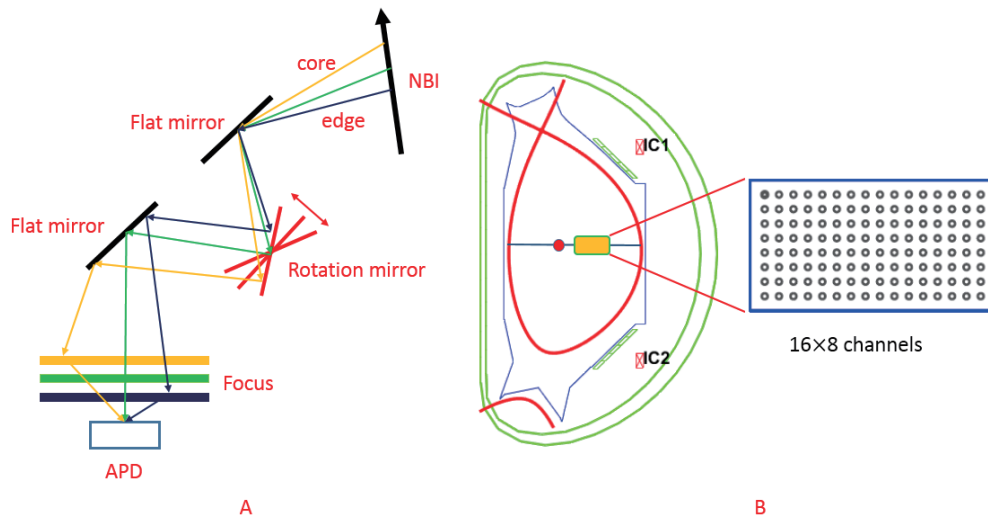
Figure 4. (A): This figure shows the light path from plasma to APD. The reflection angle of the rotation mirror and the light path are changeable by means of rotating the mirror clockwise or anticlockwise. Blue, red and green lines show different light paths and different diagnosed spatial positions from core to edge. (B): The green rectangle in the cross section is zoomed in to the bigger blue one, showing the 128 diagnosed spatial positions which is movable radially.

A 165cm-long sleeve with lenses inside, delivered by Adimtech Kft[23], is located in the vacuum chamber running through the heavy thermal shield of the superconductive tokamak to guide emission light. In Fig.5, A is the first mirror of BES. A shutter (B in Fig.5) is installed in front of the first mirror to protect the mirror from lithiation or high heat flux in some experiments. It is to be noted here that fibers are widely used as the main optical path of BES system on many other tokamaks such as DIII-D[12] and HL-2A, since that fibers can effectively reduce disadvantages from the vibration of the devices in discharging. Thinking of the fact that EAST tokamak dose not vibrate too much and neutron irradiation during plasma campaign, lenses are better than fibers since large flux neutrons may destroy the fibers structure. On the other hand, the number of fibers determines the pixel of the image caught by the APD camera, while lenses are free of pixel limitation.
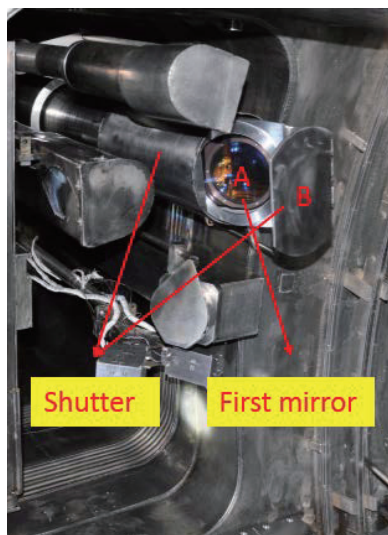
Figure5. BES transmission part (165cm-long sleeve) runs through EAST vacuum chamber with a shutter (B) in front of the first mirror (A).
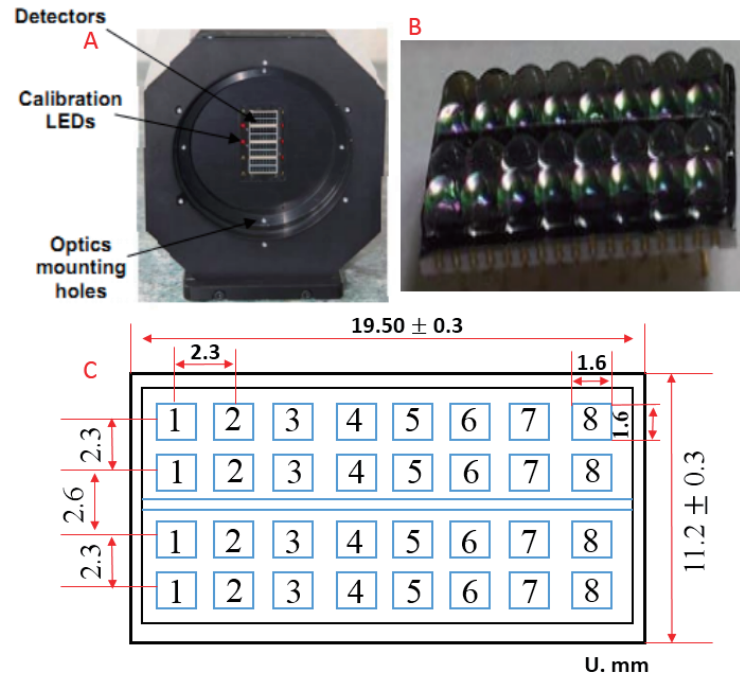
Figure 6. (A) shows the front pale of the S8550 APD camera. (B) is the micro-lens array which are mounted on 128 APD detection channels. (C) draws the detector array. 4×8 detectors are arranged in the detector ceramics housing with a non-negligible gap between two of them.

S8550 (Fig.6 (A)) is chosen as APD camera for BES diagnostic, delivered by Fusion Instruments Kft[24]. It has a sampling frequency of 2MHz which is suitable for wide band turbulence detection. The element size of DETECTOR-1 (seeing Fig.3 (A)) is 1.6mm×1.6mm and the separation between each element center is 2.3mm. Since the gap is comparable to the element size, almost half of signal light is wasted. One of the main defect of BES diagnostic is the small luminous flux, resulted from the high temporal resolution. In order to make better use of signal light, 128 micro-lens array is designed and put 2.2 mm away from the detector plane. Every micro-len has a circular cross section with a diameter of 2.3 mm and can focus all of the signal light onto the corresponding detector, increasing the filling factor to almost 100% (Fig. 6(B)).
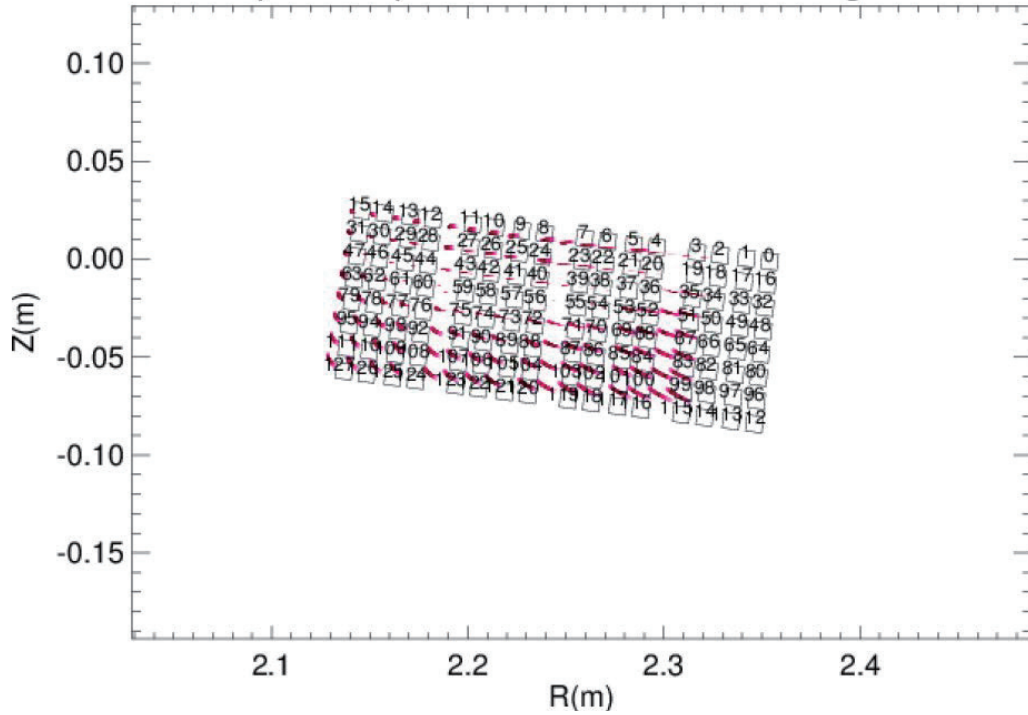
Figure 7. The spatial resolutions of the BES channels simulated by RENATE code.

Neutral beam mode code RENATE, which can calculate beam evolution in plasmas with mixed isotope content and impurity composition by calculating the evolution of several atomic levels and solving the time-dependent rate equations[25], is used to estimate the BES space resolution. Fig.7 shows the geometrical point spread function for the tangential beam on poloidal plane, using the magnetic field data of shot #48079 with a co-current magnetic field configuration[26]. The numbers from 0 to 127 indicate label projections of the 128 detector channels onto the poloidal plane. The emission has been normalized along every line of sight to its highest emission value. The size of the purple smudges indicate a favorable magnetic field configuration, since the magnetic field lines are quasi parallel to the detector lines of sight. As one can see, the radial resolution for this configuration is about 6-8 mm and the poloidal resolution is about 0.8-1 cm, according to the spatial positions.

3. FIRST RESULTS AND CONCLUSION

128-channel BES diagnostic has been developed on EAST tokamak with the ability to measure two-dimensional plasma density fluctuation from core to edge. It has a temporal resolution of 1μs and a spatial resolution of about 1 cm according to the diagnosed position.
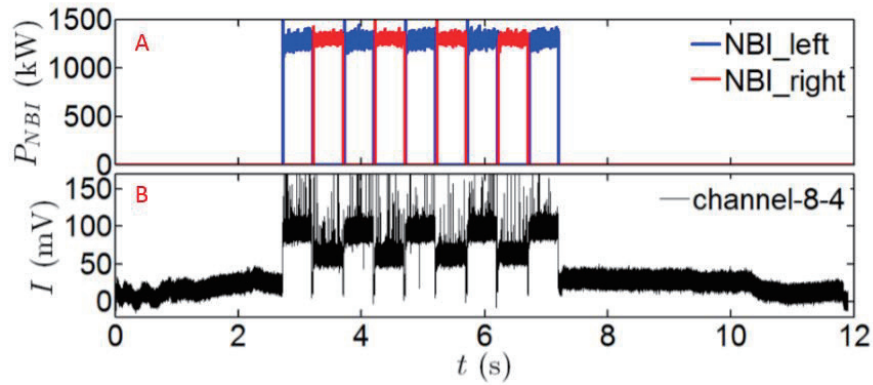
Figure 8. (A) is the waveform of NBI in shot #61497. (B) is the time series of intensity of one BES channel.

Fig.8 (A) shows the NBI waveform in shot #61497. Pulsing powers from NBI_left and NBI_right are used to modulate plasma periodically. The time series of signal intensity of one of the BES channels is drawn in Fig.8 (B). It is obviously that the BES channel does can detect the signal which is consistent with the NBI power. The NBI_left can improve the plasma density much more effectively than NBI_right, which is reasonable because of the difference between these two injecting angles (seeing Fig.1). The signals in other channels are similar and not shown here just for simplicity.

ACKNOWLEDGMENTS

REFERENCES

[1] J. W. Connor, T. Fukuda, X. Garbet, C. Gormezano, V. Mukhovatov, M. Wakatani, I. D. Grp and I. T. G. T. Intern Nucl Fusion **44,** (2004) R1-R49.

[2] A. Y. Pankin, J. W. Hughes, M. J. Greenwald, A. H. Kritz and T. Rafiq Nuclear Fusion **57,** (2017) 022012.

[3] L. Frassinetti, M. N. A. Beurskens, S. Saarelma, J. E. Boom, E. Delabie, J. Flanagan, M. Kempenaars, C. Giroud, P. Lomas, L. Meneses, C. S. Maggi, S. Menmuir, I. Nunes, F. Rimini, E. Stefanikova, H. Urano, G. Verdoolaege and J. Contributors Nuclear Fusion **57,** (2017) 016012.

[4] N. Aiba, M. Honda and K. Kamiya Nuclear Fusion **57,** (2017) 022011.

[5] M. X. Huang, Q. M. Hu, P. Shi, X. L. Zhang, L. Z. Zhu, Z. P. Chen and G. Zhuang Plasma Physics and Controlled Fusion **58,** (2016).

[6] A. R. Field, D. Dunai, N. J. Conway, S. Zoletnik and J. Sarkozi Rev Sci Instrum 80, (2009) 073503.

[7] W. L. Zhong, Z. B. Shi, Y. Xu, X. L. Zou, X. R. Duan, W. Chen, M. Jiang, Z. C. Yang, B. Y. Zhang, P. W. Shi, Z. T. Liu, M. Xu, X. M. Song, J. Cheng, R. Ke, L. Nie, Z. Y. Cui, B. Z. Fu, X. T. Ding, J. Q. Dong, Y. Liu, L. W. Yan, Q. W. Yang, Y. Liu and H.-a. Team Nuclear Fusion **55,** (2015).

[8] W. L. Zhong, Z. B. Shi, Y. Xu, X. L. Zou, X. R. Duan, W. Chen, M. Jiang, Z. C. Yang, B. Y. Zhang, P. W. Shi, Z. T. Liu, M. Xu, X. M. Song, J. Cheng, R. Ke, L. Nie, Z. Y. Cui, B. Z. Fu, X. T. Ding, J. Q. Dong, Y. Liu, L. W. Yan, Q. W. Yang, Y. Liu and H.-a. Team J Instrum **10,** (2015) P10014.

[9] J. M. Sierchio, I. Cziegler, J. L. Terry, A. E. White and S. J. Zweben Review of Scientific Instruments **87,** (2016) 023502.

[10] D. Moulton, Y. Marandet, P. Tamain, P. Ghendrih and M. Groth J Nucl Mater **463,** (2015) 893-896.

[11] R. Fric, E. K. Lindstrom, G. A. Ringstad, K. A. Mardal and P. K. Eide Acta Neurochir **158,** (2016) 2295–2304.

[12] G. McKee, R. Ashley, R. Durst, R. Fonck, M. Jakubowski, K. Tritz, K. Burrell, C. Greenfield and J. Robinson Rev Sci Instrum **70,** (1999) 913-916.

[13] R. L. Boivin, J. L. Luxon, M. E. Austin, N. H. Brooks, K. H. Burrell, E. J. Doyle, M. E. Fenstermacher, D. S. Gray, M. Groth, C. L. Hsieh, R. J. Jayakumar, C. J. Lasnier, A. W. Leonard, G. R. McKee, R. A. Moyer, T. L. Rhodes, I. C. Rost, D. L. Rudakov, M. J. Schaffer, E. I. Strait, D. M. Thomas, M. Van Zeeland, J. G. Watkins, G. W. Watson, W. P. West and C. P. C. Wong Fusion Sci Technol **48,** (2005) 834-851.

[14] Y. J. Xu, C. D. Hu, S. Liu and L. Yu J Fusion Energ **33,** (2014).

[15] Y. L. Lin, Z. M. Liu, P. Sheng, Q. L. Cui, Y. Z. Zhao, X. D. Zhang, R. Zhang and C. D. Hu J Fusion Energ **33,** (2014) 702–706.

[16] T. Gorler, A. E. White, D. Told, F. Jenko, C. Holland and T. L. Rhodes Physics of Plasmas **21,** (2014) 122307.

[17] A. R. Field, D. Dunai, Y. C. Ghim, P. Hill, B. McMillan, C. M. Roach, S. Saarelma, A. A. Schekochihin, S. Zoletnik and M. Team Plasma Physics and Controlled Fusion **56,** (2014) 025012.

[18] Y. U. Nam, S. Zoletnik, M. Lampert and A. Kovacsik Rev Sci Instrum **83,** (2012) 10D531.

[19] M. Lampert, G. Anda, A. Czopf, G. Erdei, D. Guszejnov, A. Kovacsik, G. I. Pokol, D. Refy, Y. U. Nam and S. Zoletnik Review of Scientific Instruments **86,** (2015) 073501.

[20] J. P. Qian, B. N. Wan, L. L. Lao, B. Shen, S. A. Sabbagh, J. Menard, Y. W. Sun, Y. M. Duan, J. H. Li, B. J. Xiao, X. Z. Gong and E. R. Team J Plasma Phys **75,** (2009).

[21] J. P. Qian, B. N. Wan, B. Shen, M. L. Walker, D. A. Humphreys and B. J. Xiao Chinese Phys B **18,** (2009) 2432.

[22] R. J. Fonck, P. A. Duperrex and S. F. Paul Rev Sci Instrum **61,** (1990) 3070-3070.

[23] I. G. Kiss, B. Meszaros, D. Dunai, S. Zoletnik, T. Krizsanoczi, A. R. Field and R. Gaffka Fusion Eng Des **86,** (2011) 1315-1318.

[24] Y. C. Ghim, A. R. Field, S. Zoletnik and D. Dunai Rev Sci Instrum **81,** (2010) 10D713.

[25] D. Guszejnov, G. I. Pokol, I. Pusztai, D. Refy, S. Zoletnik, M. Lampert and Y. U. Nam Rev Sci Instrum **83,** (2012) 113501.

[26] G. Pokol, Ö. Asztalos, Final report for the modeling of the DBES system on the EAST tokamak (internal report) (2014).

Dynamics of runaway electrons in HL-2A with infrared camera system

J.M. Gao, Y.B. Dong, Y. Liu, Y.P. Zhang, C.Y. Chen, W. Li,

X.Q. Ji, Y. Zhou, and Q.W. Yang

Southwestern Institute of Physics, Chengdu, 610041 China

Abstract

A new wide-angle infrared periscope system has been developed for the HL-2A tokamak to measure the synchrotron radiation from the relativistic runaway electrons during plasma disruption discharges. This diagnostic is installed on the outer mid-plane of the tokamak with a tangential view in the direction of electron approach, and its wide-angle design allows to have a full poloidal view of the HL-2A vessel. Measurements of relativistic runaway electrons using this system have been performed, and the dynamics of the relativistic runaway electrons are investigated. In the dedicated experiment of runaway current mitigation during plasma disruption with supersonic molecular beam injection (SMBI), this diagnostic technique has been used to follow the time evolutions of runaway beam, providing direct information about the mitigation process of runaway electrons.

1. Introduction

Runaway electrons with energies in the order of several tens of megaelectron volts (MeV) have been observed during tokamak disruption [1-2] and low density discharges [3]. These relativistic runaway electrons can cause substantial damage to the plasma facing wall components of fusion devices. It is therefore necessary to understand the dynamics of these high-energy runaway electrons in experiments.

Runaway electron is typically investigated by measuring the thick-target bremsstrahlung emission or neutron emission produced by the lost runaway electrons hitting the limiter or vessel structures [4-5]. These methods, however, can not provide the information of runaway electrons directly, especially the relativistic electrons in the core of plasma. Synchrotron radiation emitted by the relativistic runaway electrons is in the (near) infrared wavelength range [6-7], which can easily be detected by thermographic cameras. So the synchrotron radiation may be a powerful tool for direct observation and investigation of the relativistic runaway electrons. It has been applied on several tokamaks, such as TEXTOR-94 [1], EAST [8], J-TEXT [9], to study the dynamics of runaway electrons.

Recently, a wide-angle infrared periscope system has been installed to observe the synchrotron radiation on HL-2A. A 3-m long periscope structure was designed to obtain the wide-angle view allowing a full poloidal view of the HL-2A main chamber. Preliminary results show that an almost circular synchrotron spot is observed during runaway current plateau after plasma disruption and low density discharges. The dynamics of the relativistic electrons, such as the energy, the pitch angle, and the beam radius, are analyzed from the spectral features. Moreover, runaway current mitigation experiments have been carried out with Supersonic Molecular Beam Injection (SMBI) technique [10]. The measurements show the direct information about the mitigation process, characterized by a strongly changed shape of the synchrotron radiation spot after SMBI.

The rest of this paper is organized as follow. The infrared periscope system, as well as the characteristics of the synchrotron radiation spectra in HL-2A, are described in section Ⅱ. According to the synchrotron radiation measurements, the runaway electrons parameters in HL-2A, such as the energy, the pitch angle and the beam radius, are estimated in section Ⅲ. The characteristics of runaway beam during runway current mitigation with SMBI are also presented in section Ⅲ. Finally, section Ⅳ gives the conclusions.

2. Infrared periscope system

A. HL-2A setup

The HL-2A device is a medium size tokamak with double null closed divertor. The geometrical parameters of HL-2A are $R_0 = 1.65m$ and $a = 0.4m$ [11]. Typically, HL-2A is run in the low single null closed divertor configuration with a plasma current of about $130\sim200KA$, toroidal magnetic field of about $1.2\sim1.5T$ and electron density of about $1\sim3\times10^{13}cm^{-3}$. But the poloidal cross section of the plasma in the main chamber is almost circular.
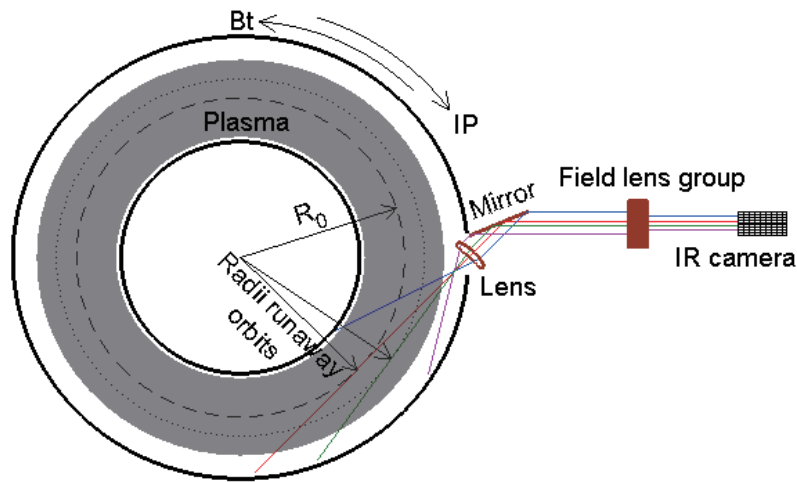
Fig.1. Sketch of infrared periscope system on HL-2A, as well as the directions of magnetic field and plasma current. Using reference points in the vessel wall, the runaway orbits are constructed for pitch angle $\theta = 0$.

According to the HL-2A geometry, a wide-angle infrared periscope system has been develop to investigate the dynamics of runaway electrons. The sketch of the infrared system is shown in Fig.1, which is located in the equatorial plane looking tangentially into the direction of runaway electron approach. In order to image a large section of the tokamak, both in poloidal and toroidal directions, a 3-m long periscope was designed with a field-of-view of 50 degrees. This wide angle allows to have a full poloidal view of the HL-2A vessel (see Fig.4(a)). The optical system presents first the front part, formed by a ZnSe lens and a flat mirror made of stainless steel and coated with gold. The ZnSe lens is located behind a flat stainless steel plane equipped with a small aperture. The combination of the lens and the mirror allows to bend the beam with an angle of 43 degrees, and to collimate the beam towards the next optical components. Then the image of HL-2A vessel can be achieved outside the device by means of the two following ZnSe lenses, as shown in Fig.2. The three ZnSe lenses and the flat mirror form the first part of the optical system, i.e., imaging group.

In order to keep the infrared camera from electric or magnetic interference (especially during the plasma disruption events), a relay group is designed to make the camera far away from the device. The

third part of the optical system is a correction group, which has two functions: first, it is used to adjust the size of the image surface to match that of the detector; second, it is used to suppress the image deformation after many lenses. Therefore, the image is transmitted through the relay group composed of two silicon lenses, then emended by the correction group composed of seven silicon lenses, and finally image on the focal plane array. All lenses are treated with infrared anti-reflective coating. To achieve the positioning of the optical components, all the optical elements are installed on a tube. The imaging group is working under the HL-2A vacuum, which is isolated by a ZnSe window installed between the imaging group and the relay group. Moreover, a shutter is designed to protect the observation window from getting contaminated during siliconization and glow discharge cleaning.

Fig.2 The optical system includes the imaging group, the relay group and the correction group. The relay group and the correction group are isolated from the HL-2A vacuum by the ZnSe window.
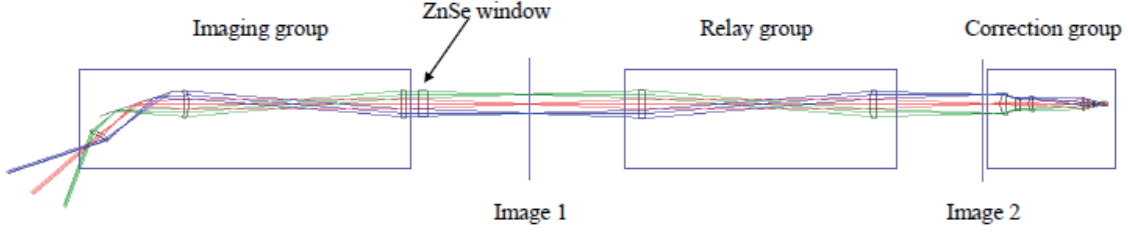
Synchrotron radiation measurements are made with a commercial thermographic camera (FLIR7750L) operating in the wavelength range $8 - 9.4\mu m$. This camera employs a HgCdTe array of 640×512 pixels with a pitch size of $16\mu m$, and the detector is cooled down to 80K by means of a Stirling cooler. The infrared images are digitized to 14 bits, and then they are transferred by Ethernet Gigabit to a remote computer for data analysis and storage. The images are acquired with sampling rates of 114Hz for the full frame. The image frequency, however, is programmable for the fast plasma events study with the sub-windowing modes but at the expense of a reduced array size. The integration time is adjustable by increments of $1\mu s$. External triggering allows the synchronization of the image with the most fleeting of events, which is useful for the data comparison with other plasma diagnostic signals.

B. Synchrotron radiation spectra

The orbit of a relativistic runaway electron in a tokamak consist of three components: the helical motion of the guiding center along the field lines, the gyration about the magnetic field lines with frequency $\omega_{ce} = eB_t/\gamma m_e$, and the drift of the guiding center as a result of the curvature and gradient of the magnetic field. Here m_e is the electron rest mass, $\gamma = 1/\sqrt{1 - v^2/c^2}$ is the relativistic factor and c the velocity of light. The synchrotron radiation emitted by the relativistic electrons is mainly in the forward direction. But due to the gyration motion, the radiation is emitted in a cone with a half opening angle given by the pitch angle of $\theta = {V_\perp}/{V_\parallel}$, where $V_\perp$ and $V_\parallel$ are the perpendicular and parallel (to the magnetic field) velocity of electron respectively. Taking into account the features of the relativistic electron motion in a tokamak, the spectral density of the emitted power is expressed approximately by [7],

$$P(\lambda) = \pi m_e c^3 r_e \sqrt{\frac{2\sqrt{1+\eta^2}}{\lambda^5 R_0 \gamma}} \left[I_0(a) + \frac{4\eta}{1+\eta^2} I_1(a) \right] exp(-\xi) \qquad (1)$$

where r_e is the classical electron radius, $\eta = v_\perp/v_{dr}$ with the drift velocity $v_{dr} = v_\parallel^2/R_0\omega_{ce}$, R_0 is the major radius of magnetic surface, $I_{0,1}(a)$ is the modified Bessel function with $a = {4\pi R_0 \eta}/{3\lambda\gamma^3(1+\eta^2)^{3/2}}$, and $\xi = 4\pi R_0/3\lambda\gamma^3\sqrt{1+\eta^2}$. However, some conditions of $\xi \gg 1, a \leq 1$,

and $\eta \gg 2$ or $\eta \ll 0.5$, must be fulfilled to use Eq. (1) [8]. At $\lambda_m = 8\pi R_0/15\gamma^3\sqrt{1+\eta^2}$, the expression $P(\lambda)$ takes a maximum value

$$P(\lambda_m) \approx 0.1\gamma^7 m_e c^3 r_e (1+\eta^2)^{\frac{3}{2}}/R_0^3 \qquad (2)$$

For typical HL-2A parameters ($R_0 = 1.65m$ and $B_t = 1.4T$), the energy of relativistic runaway electrons is $E_{re} \sim 20 \pm 3 MeV$, and the pitch angle $\theta \sim 0.13 rad$ (see section III). The parameters of ξ, a, and η are estimated as follow, $\xi > 2.5$, $a < 0.6$, and $\eta > 4$. Therefore, according to the Eq. (1) the synchrotron spectra is calculated and shown in Fig. 3. The wavelength λ_m of maximum emission is estimated, and the relationship of the runaway energy with λ_m is also plotted in Fig.3 for the pitch angle $\theta \sim 0.13 rad$. The extremely strong decrease of the spectrum with decreasing λ indicates that the highest energy dominates the spectrum. It also demonstrates that the infrared range between 8 and $9.4\mu m$ seems appropriate for these measurements in HL-2A.
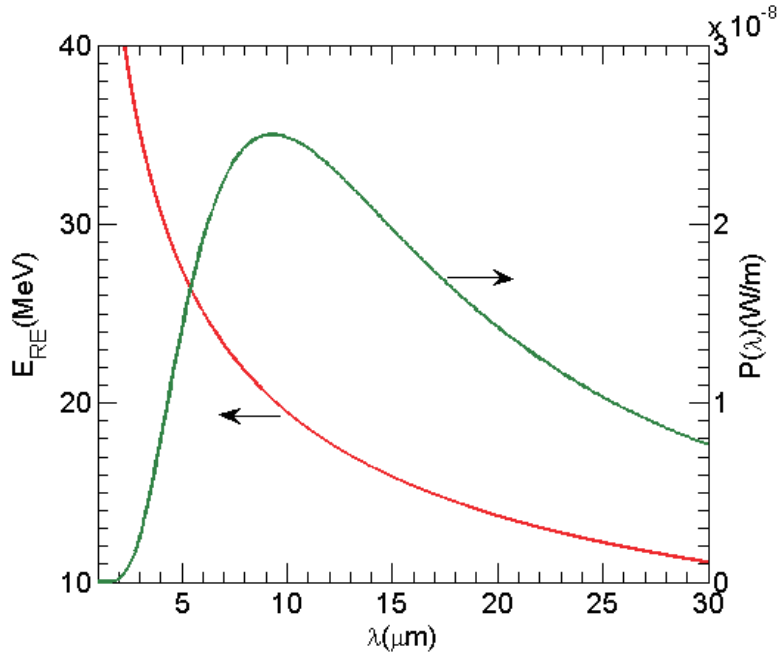
Fig.3. The runaway energy as a function of the wavelength of maximum synchrotron emission with the pitch angle $\theta \sim 0.13 rad$ (red line), and the synchrotron radiation spectra for the runaway energy $E_{re} \sim 20 MeV$ and the pitch angle $\theta \sim 0.13 rad$ for HL-2A.

3. Preliminary results

Recently, the wide-angle infrared periscope system has been installed on the HL-2A tokamak to measure the synchrotron radiation emitted by the relativistic runaway electrons. The first results show the evolution of runaway beam clearly during the mitigation of the runaway current in the plasma disruption.

The runaway current during intentional disruptions caused by argon injection (MGI) has been successfully mitigated with SMBI in HL-2A [12]. Fig.4 shows the evolution of runaway beam during runaway current mitigation. When no synchrotron radiation (Fig.4(a)), the thermal radiation of the vessel wall is clearly recognized. The thermal radiation, including the wall components and diagnostic ports, is a helpful tool for aligning the diagnostic and it provides a suitable reference frame for the position measurements.
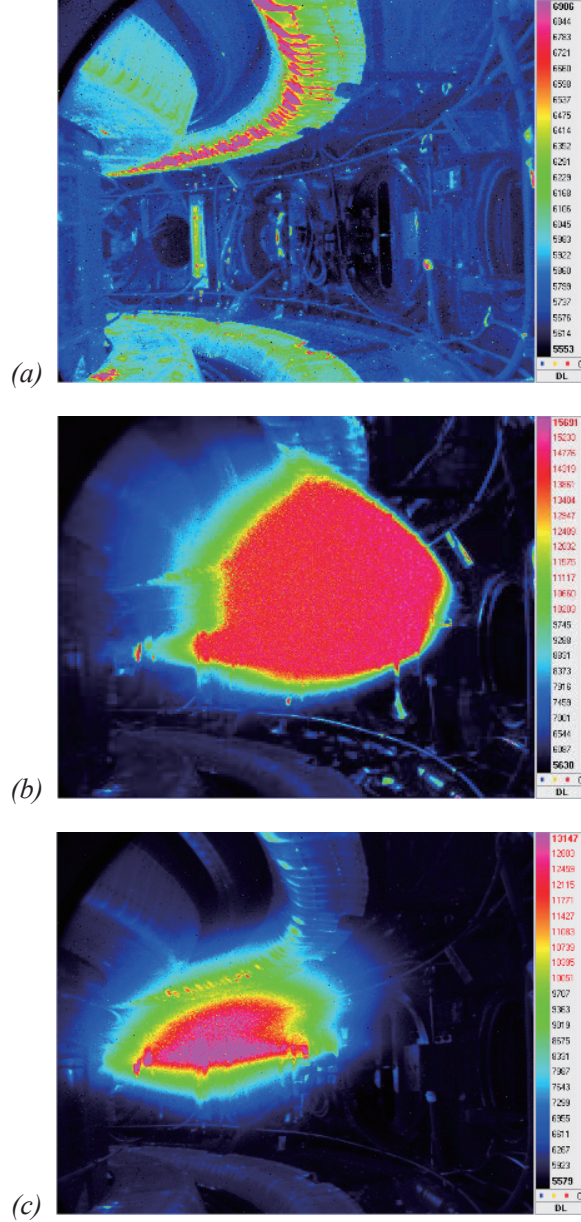
Fig.4. Three frames of images taken by the infrared periscope system of discharge #25431 before plasma disruption (a), during runaway plateau (b), and after SMBI (c).

The runaway current plateau is formed by using a rapid (~1ms), massive injection of argon (gas capacity of 2×10^{21}), as shown in Fig.5. During the runaway current plateau (Fig. 4(b)), an almost circular spot was observed. This automatically indicates that the pitch angle must be sizable. The vertical extent of the synchrotron spot corresponds to the beam radius, and the horizontal extension would be larger by the amount $dr = R(1 - cos\theta) \approx R\theta^2$ than the vertical extent as a result of the toroidal curvature of the electron orbit. Because the toroidal extension of the observed volume is limited by the small opening angle (for HL-2A $2R_0\theta \approx 37cm$ in the toroidal direction), the synchrotron radiation measured by the infrared camera can be interpreted approximatively as a poloidal projection of the runaway beam. With the assumption, the major radii of runway orbits can be estimated, and the construction of the major radii of runway orbits is shown in Fig.1. Therefore, typical HL-2A runaway beam parameters of $r_{beam} = 0.28m$ and $\theta = 0.13rad$ are determined. Because of the curvature drift, the drift orbits of runaway electrons are shifted to the low field side of the magnetic flux surfaces. This

shift is given by $\delta \approx qE_{re}/ecB_t$, and thus the energy of runaway electrons of $E_{re} = 20 \pm 3MeV$ is calculated, which is consistent with the synchrotron spectra (see Fig.3).

After helium injection with SMBI, however, the runway current is mitigated clearly. The image of synchrotron radiation shows that the radius of the synchrotron spot is reduced, and the spot moves inside largely (Fig. 4(c)), indicating a reduced runaway energy and a great loss of relativistic runway electrons. Both of them should be responsible for the mitigation of runaway current.
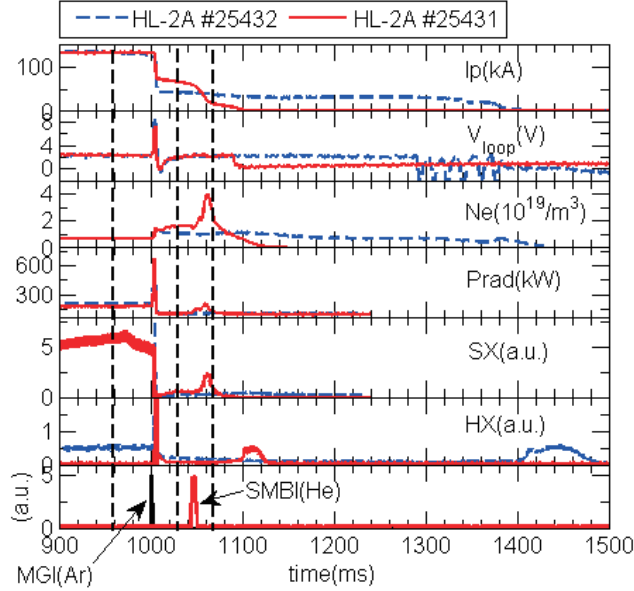
Fig.5. Typical example of runway mitigation in HL-2A. The plasma parameters are plasma current , loop voltage , central line-averaged electron density , plasma radiation , soft x-ray, hard x-ray, and the signals of MGI and SMBI. The dashed lines indicate a long-lived runaway beam for comparison. The vertical dashed lines indicate the time slices of infrared images shown in Fig.4.

4. Conclusions

Synchrotron radiation, emitted by the relativistic runaway electrons, was measured by a new infrared periscope system positioned in the direction of the electron approach on the equatorial plane. This system allows to have a full poloidal view of the HL-2A vessel with a wide-angle field of view. Therefore, the evolutions of runaway beam would be observed clearly. In HL-2A, the runaway beam can be formed easily during intentional disruption discharges with MGI, and is characterized as an almost circular spot. The preliminary results demonstrate that this technique would be a powerful tool for the runaway electron study.

Based on the measurements, the pitch angle $\theta = 0.13rad$ is estimated, and the runaway energy $E_{re} = 20 \pm 3MeV$ is deduced typically. Furthermore, the mitigation of runaway current is achieved with SMBI. The helium gas injection leads to a strongly changed shape of the synchrotron spot, which suggests both the energy and the number of relativistic runaway electrons are reduced, and then the runaway current decreases gradually. It indicates that the SMBI technique is a useful tool for the runaway mitigation.

References

[1] R. Jaspers, N.J. Lopes Cardozo, A. J. H. Donne, et al. Rev. Sci. Instrum. **72** (2001) 466.

[2] E. M. Hollmann, P.B. Parks, N. Commaux, et al. Phys. Plasmas **22** (2015) 056108.

[3] I. Entrop, N.J. Lopes Cardozo, R. Jaspers and K.H. Finken. Plasma Phys. Control. Fusion **40** (1998) 1513.

[4] Y. P. Zhang, Y. Liu, X.Y. Song, et al. Rev. Sci. Instrum. **81** (2010) 103501.

[5] P. V. Savrukhin, Rev. Sci. Instrum. **73** (2002) 4243.

[6] I. M. Pankratov. Plasma Phys. Rep. **22**(1996) 535.

[7] I. M. Pankratov. Plasma Phys. Rep. **25**(1999) 145.

[8] R. J. Zhou, I.M. Pankratov, L.Q. Hu, et al. Phys. Plasmas **21** (2014) 063302.

[9] R. H. Tong, Z.Y. Chen, M. Zhang, et al. Rev. Sci. Instrum. **87** (2016) 11E113.

[10] L.H. Yao, B.B. Feng, C.Y. Chen, et al. 2007, Nucl. Fusion, **47** (2007) 1399.

[11] J.M. Gao, Y. Liu, W. Li, et al. Rev. Sci. Instrum. **85** (2014) 043505.

[12] Y. Liu, Y. B. Dong, Y. Xu, et al. 26th IAEA Fusion Energy Conference (2016), Japan: EX/9-3.

Simulation studies of chirping geodesic acoustic modes and nonlinearly-coupled modes in 3-dimensional LHD equilibrium

H.Wang[1], Y.Todo[1,2], T.Ido[1], Y.Suzuki[1,2]

[1]National Institute for Fusion Science, Toki 509-5292, Gifu, Japan

[2]Graduate University for Advanced Studies, Toki 509-5292, Gifu, Japan

Abstract

Energetic particle driven geodesic acoustic mode (EGAM) in a 3-dimensional Large Helical Device (LHD) equilibrium are investigated using MEGA code. MEGA is a hybrid simulation code for energetic particles interacting with a magnetohydrodynamic (MHD) fluid. The phenomena of chirping primary mode and the associated half-frequency secondary mode are firstly reproduced with the realistic input parameters and 3-dimensional equilibrium. There are good agreements between simulation and experiment on the frequency chirping of the primary mode and on the excitation of the half-frequency secondary mode. It is found that the bulk pressure perturbation and the energetic particle pressure perturbation cancel out with each other, thus the frequency of the secondary mode is lower than the primary mode. Also, it is found that the secondary mode is excited by the energetic particles, not by the nonlinear MHD coupling.

1. Introduction

Geodesic acoustic mode (GAM) is an oscillatory zonal flow coupled with density and pressure perturbations in toroidal plasmas. In the last decade, energetic particle driven GAM (EGAM) is observed in Joint European Torus (JET), DIII-D, and Large Helical Device (LHD). In the DIII-D experiment, drops in neutron emission follow the EGAM bursts suggesting beam ion losses. Also, in the LHD experiment, anomalous bulk ion heating during the EGAM activity suggests a GAM channeling. Then, understanding EGAM is important for magnetic confinement fusion where the energetic particles need to be well confined and the bulk plasma need to be efficiently heated. The EGAM has been extensively studied by both the experimentalists and theorists[1-3]. Recently, in LHD, an abrupt excitation of a half-frequency secondary mode is observed when the frequency of a chirping primary EGAM reaches twice of the GAM frequency[4,5].

2. Simulation model and parameters

A hybrid simulation code for energetic particles interacting with a magnetohydrodynamic (MHD) fluid, MEGA, is used for the simulation of EGAMs[6]. In the MEGA code, the bulk plasma is described by the nonlinear MHD equations. The drift kinetic description and the δf particle method are applied to the energetic particles. A realistic 3-dimensional equilibrium generated by HINT2 code is used for the simulation. This equilibrium data is based on the LHD shot #109031 at time t = 4.94s. At this moment, the EGAM activity is very strong, thus it is good to reproduce the EGAM phenomenon.

In the experiment of LHD, the EGAMs are observed under the bump-on-tail energetic particle distribution. In the present work, a realistic distribution function, which is the same as the experimental observation, is applied. The parameters for the EGAM simulation are based on an LHD experiment, B_0 = 1.5 T, electron density $n_e = 0.1 \times 10^{19}$ m^{-3}, electron temperature at the magnetic axis T_e = 4 keV, and bulk plasma beta value on the magnetic axis equals to 7.2×10^{-4}. The counter-injected neutral beam energy is E_{NBI} = 175 keV. The safety factor q value is q = 2.82 on the magnetic axis and q = 0.84 on the plasma edge, negative normal shear. The major radius of the magnetic axis is R_0 = 3.7 m. Cylindrical coordinates (R, φ, z) are employed. For LHD equilibrium, there are 10 pitches in the toroidal direction. Since the toroidal mode number of GAM is 0, for simplicity, only 1 pitch is used for the present simulation. The numbers of grid points of this pitch in (R, φ, z) directions are (128, 64, 128), respectively.

3. Simulation Results
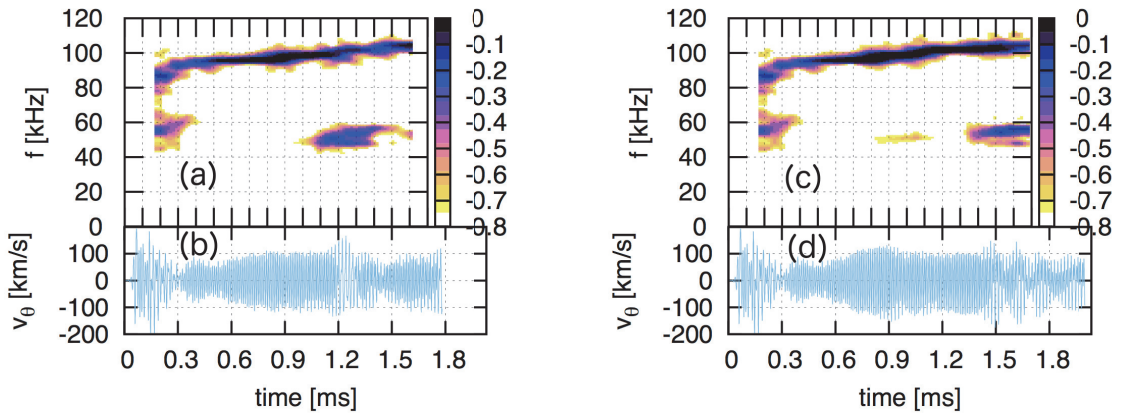
Fig.1 Time evolution of (a) frequency spectrum and (b) poloidal velocity. Another simulation where nonlinear fluid terms are turned off from t = 0.67 ms is shown in panel (c) and (d).

Both the chirping primary mode and the half-frequency secondary mode are reproduced by the MEGA code, as shown in Fig.1(a) and Fig.1(b). The primary mode frequency chirps from 70 kHz. The mode is saturated at t = 0.07 ms, and then, steps into the nonlinear phase. At t = 1.1 ms, the frequency of the primary mode reaches to 100 kHz, and a half-frequency secondary mode with frequency f = 50 kHz is excited nonlinearly. The amplitudes of the 100 kHz mode and 50 kHz mode are close to each other. The simulated phenomenon is very similar to the experimental observation, as shown in Fig.2 of Ref.[4]. Good validations are obtained not only for frequency spectrum, but also mode number, mode profiles, and phase relations. This is the first time to reproduce both the chirping primary mode and nonlinearly-coupled secondary mode with 3-dimensional model and realistic input parameters.

Both the primary mode and the secondary mode are the EGAMs. The question then arises as to why a same mode has 2 different frequencies. In order to clarify the reason, the bulk plasma pressure perturbation δP_{bulk} and the energetic particle pressure perturbation $\delta P_{h\parallel}$ are analyzed, as shown in Fig. 2. For the primary mode, the phase of δP_{bulk} and $\delta P_{h\parallel}$ are the same. The primary mode is driven by both δP_{bulk} and $\delta P_{h\parallel}$, and this

2 different kinds of pressures enhance each other. For the secondary mode, the phase difference between δP_{bulk} and $\delta P_{h\parallel}$ is π. They are in anti-phase, and they cancel out with each other. Thus, the frequency of the secondary mode is much lower than the primary mode.
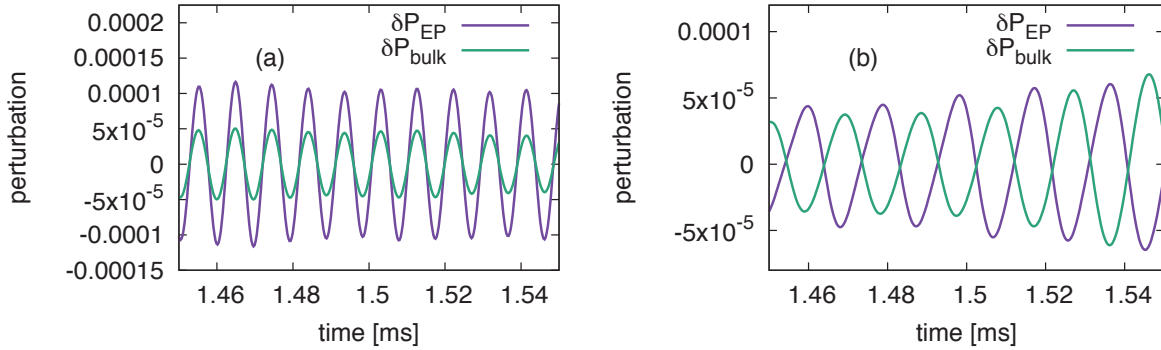
Fig.2 The δP_{bulk} and $\delta P_{h\parallel}$ oscillation of (a) primary mode and (b) secondary mode.

In order to clarify the effects of the fluid nonlinearity, another special linear MHD model is applied. In the present work, simulations are run in 2 stages. In the 1st stage, the nonlinear code is run, until time t = 0.67 ms when the EGAM is completely saturated but the secondary mode has not been excited yet. Then, in the 2nd stage which starts at t = 0.67 ms, both the linear and nonlinear MHD codes are run separately from the end of the 1st stage. In the 2nd stage, the secondary modes appear in both runs, and their amplitudes are close to each other, as shown in Fig. 1(a) and Fig. 1(c). In other words, the secondary mode can be excited even if the MHD equations are linearized. This result is different from that in Ref.[5]. In the present work, the excitation of the nonlinearly-coupled secondary mode is only caused by the kinetic nonlinearity, while the fluid nonlinearity hardly works.
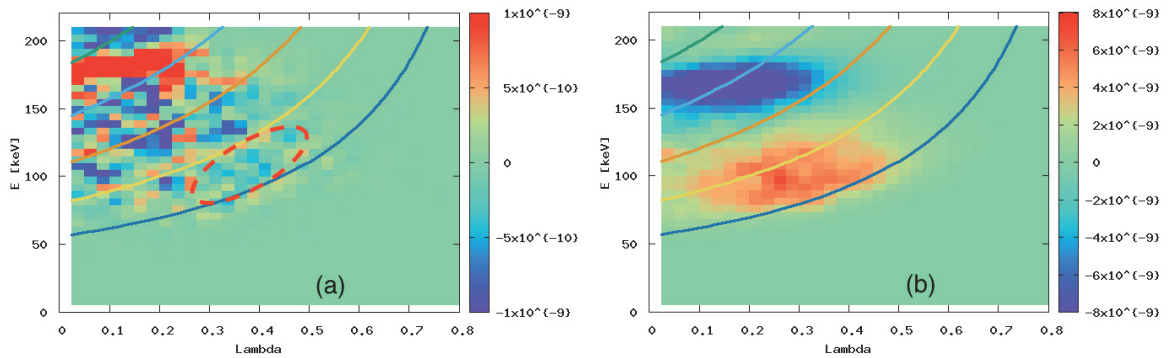
Fig. 3 The (a) energy transfer and (b) δf distribution in (Λ, E) phase space. The 5 curves from bottom to top represent f_{tr} = 50 kHz, 60 kHz, 70 kHz, 80 kHz, and 90 kHz, respectively.

In order to confirm the conclusion that the secondary mode is excited by the energetic particles, the resonant particles are analyzed in phase space. The energy transfer in pitch angle Λ and energy E is analyzed as shown in Fig. 3(a). The particle transit frequency f_{tr} is defined as

$$f_{tr} = \sqrt{(1-\Lambda)(2E/m_h)}/(2\pi q R_0),$$

where m_h is the mass of energetic particles and R_0 is the major radius. The transit frequency f_{tr} is a function of pitch angle Λ and energy E, thus it is able to plot constant f_{tr} curves in (Λ,E) space. Inside the ellipse region, the dominant color is blue, that means the energetic particles lose energy and the energy is transferred to the mode, then the mode is destabilized. The ellipse region is located at $f_{tr} \sim 55kHz$ that is the same as the secondary mode frequency, this suggests the secondary mode is indeed driven by the energetic particles. In addition, δf distribution in (Λ,E) space is investigated and shown in Fig. 3(b). The red region represents positive δf values. In other words, it represents clump structure in phase space. Similarly, the blue region represents hole structure. The formation of hole-clump pair is another evidence to show the strong interactions between energetic particles and the modes.

3. Summary

In summary, 3 conclusions are obtained in the present work. Firstly, the chirping EGAM and the associated secondary mode are reproduced with the 3-dimensional model and realistic parameters for the first time. The simulations are quantitatively consistent with the experiments. Secondly, it is found that the phase differences between δP_{bulk} and $\delta P_{h\parallel}$ is π for the secondary mode. The δP_{bulk} and $\delta P_{h\parallel}$ cancel out with each other, and thus, the frequency of the secondary mode is much lower than the primary mode. Thirdly, it is found that the fluid nonlinearity does not work for the excitation of the secondary mode. This can be confirmed by both the linearization of MHD equations and the resonant particle analysis in phase space.

Acknowledgements

References

[1] R.Nazikian, G.Fu, M.Austin et al., Phys. Rev. Lett. **101** (2008) 185001.

[2] G.Fu, Phys. Rev. Lett. **101** (2008) 185002.

[3] H.Wang, Y.Todo, C.Kim, Phys. Rev. Lett. **110** (2013) 155006.

[4] T.Ido, K.Itoh, M.Osakabe, et al., Phys. Rev. Lett. **116** (2016) 015002.

[5] M.Lesur, K.Itoh, T.Ido, et al., Phys. Rev. Lett. **116** (2016) 015003.

[6] Y.Todo, Phy. Plasmas, **13** (2006) 082503.

ECRH on CFETR- Physics and Technology Needed

Jiangang Li (j_li@ipp.ac.cn), F.K.Liu, Y.P.Zhao, X.J.Wang, M.H.Li, H.D.Xu

Institute of Plasma Physics, Chinese Academy of Sciences, Hefei, China

Abstract: The Chinese Fusion Engineering Testing Reactor (CFETR) is the next device for the Chinese magnetic confinement fusion (MCF) program which aims to bridge the gaps between the fusion experiment ITER and the demonstration reactor DEMO. Operation scenarios have been assessed by integrated modeling based on advanced H-mode physics with high magnetic fields. High frequency electron cyclotron resonance heating will play a key role for H&CD and profile control. Concept design and some R&D activities are presented in this paper.

Introduction

The Chinese Fusion Engineering Testing Reactor (CFETR) [1-2] is the next device for the Chinese magnetic confinement fusion (MCF) program which aims to bridge the gaps between the fusion experiment ITER and the demonstration reactor DEMO. CFETR will be operated in two phases. Steady-state operation and tritium self-sustainment will be the two key issues for the first phase with a modest fusion power up to 200 MW. The second phase aims for DEMO validation with a fusion power around 1 GW.

Operation scenarios have been assessed by integrated modeling based on advanced H-mode physics with high magnetic fields (up to 7T). High frequency electron cyclotron resonance heating (170-230 GHz), lower hybrid current drive (5-7.5GHz), off-axis negative-ion neutral beam injection will be used together with high bootstrap current for achieving steady-state advanced operation.

Fully non-inductive CFETR scenarios have been developed with a self-consistent core-pedestal-equilibrium model. Table one is the baseline scenarios based on the integrated modeling. Different modelling of steady state operation conditions by the combination of ECCD with NNBI, ECCD with high field lower hybrid wave current drive were presented in this table. ECRH will play a key role for H&CD, NTM suppressing, and profile control to get nessosory operation scenarios.

Table 1 Baseline steady state scenarios for CFTER

	Start point	Phase I	Phase II
R_0 , a (m)	6.6,1.8	6.6 , 1.8	6.6, 1.8
P_{NBI} , P_{ECH} (MW)	29.5, 10.0	35.8, 20.0	33.9, 20.1
Fusion Gain Q_{FUS}	2.9	3.0	14.9

P$_{fus}$ (MW)	111	169	811
B$_T$ (T), I$_p$ (MA)	6.0, 7.5	6.0, 7.6	6.0, 10.0
Bootstrap Fraction	60.%	63.6%	84.4%
β$_N$	1.46	1.89	3.15
H$_{98Y2}$	1.3	1.3	1.3
Γ$_{NW}$(MW/m^2)	0.15	0.19	0.92
Diverter Loading P$_{DIV}$/R$_0$ (MW/m)	7.1	10.4	25.8

Concept design for CFETR EC system

Concept design for CFETR EC system for Phase I has been done based on the ITER ECRH system. The first step is 20MW at 170GHz.   Current drive efficiency, optical and engineering arrangements have been assessed from both top and mid-plan port. Table 2 shows modeling results for mid-plane port design. Four mirrors are used at different radial position (-67.5cm to + 67.5 cm), toroidal and poloidal angles. Current drive efficiency of 29kA/MW was obtained at 170GHz. Total 600kA plasma current could be driven by 20MW EC power. 750kA could plasma current could be driven by 20MW EC power at 230GHz at Bt=7.0T from mid-plane port.

Table 2.   Modeling results for the mod-plan port at 170GHz with 5.0T

Height Za（cm）	-22.5	22.5	-67.5	67.5
Max. Icd（kA）/MW	29.5	28.5	29	28.5
Current density（MA/ m^2）	0.6	0.55	0.55	0.45
Optimum Φ	200°	200°	200°	200°
Optimum θ	88°	94°	83°	98°

Similar simulation was carried out from top window injection which showed a higher current drive efficiency. Total 850kA plasma current could be driven by 20MW EC power at 170GHz with Bt = 5T.   1.5MA could plasma current could be driven by 20MW EC power at 230GHz with Bt=7.0T. Further optimization for get the best current drive condition is still under way.

The key sub-system is the antenna. Two options are under concept design which based on current developments of microwave antenna for ITER ECRH system. One is top window launcher and another one is the mid-plane antenna shown in Fig.1. Due to the limitation of space, beam combination will be used. 20 transmission lines which transfer 1MW power each from gyrotron are combined into the mid-plan port. By

combine 5 units into one which handle 5MW per mirror unit. Steering mechanism similar with that used in EAST will be adopted to have capacity for change the power deposition position and for real time NTM suppression. All components inside port are actively cooled with full shielding function. The first steering mirrors are equipped with shutter for preventing plasma contamination during plasma discharge and cleaning.
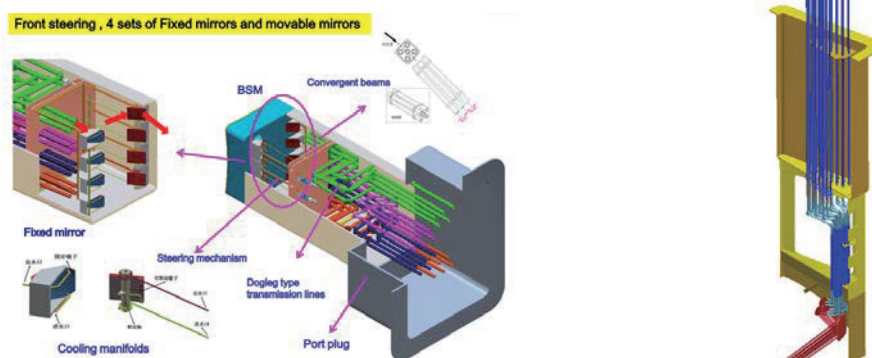

Fig.1 Concept design for mid-plan port antenna   Top port antenna design

Key components R&D

The main technologies needed to fulfill CFETR EC mission are 170GHz/230GHz gyrotrons, long distance transmission, power supply, control and protection system and integrated antenna. Key components R&D started a few years ago, such as helium-free magnet, transmission line and key components, and gyrotron itself.

The first step is to develop a gyrotron shown in Figure 2 (a) with 0.5- 1MW power and 5-10s pulse length at 140GHz.   Fig.2 (b) is related low temperature superconducting magnet with a maximum field 5.8T. The magnets has been fully tested at 4.5K and meets the design requirement. The assembly and commission of the whole system of gyrotron for short pulse system will begin before the end of 2017. The following step for next 5 years is to develop the CW 1MW gyrotron at 170GHz and 230GHz in future.

The R&D of w/g components for CW evacuated transmission line is in good progress. To explore the feasible or optimum fabrication techniques, key prototype components, such as Multi-functional miter bends, pump out tee, bellows, DC break, and gate valve are currently being fabricated. The most difficult transmission line with corrugated geometry has been design, fabricated and tested. One meter and two meter corrugated waveguide transmission lines are technical ready for massive fabrication. High power gyrotron load with 1MW CW capacity is under development.

Summary:

The detailed physical modeling, concept design, research and development activities including R&D on ECRH system for CFETR haven been done for past few years. Modeling results showed a good performance by combination of ECCD, NNBI and

LHCD. Some key components, such as superconducting magnets, CW evacuated transmission line have been successfully developed. Gyrotron is under assembling and commissioning will start soon. The relative technology for experiments is under testing by using EAST ECRH experimental system [3-5] which is used as pre-testing for future CFETR.

Fig.2 (a) short pulse 1MW gyrotron   (b) superconducting magnet

Fig.3 Key components for transmission line

References:
1. Y.Tao Song, et. Al., IEEE TRANS. ON PLAS. SCI., VOL. 42, 495(2014)
2. B.N.Wan et. Al., IEEE TRANS. ON PLAS. SCI., VOL. 42, 503(2014)
3.H.D.Xu, X.J.Wang, F.K.Liu et. al., PST, Vol.18, (2016)442
4. Y. Tang, X. Wang, et. al., Fusion Eng. and Design, 89 (2014) 847–852.
5. Y.Tang, X.Wang et. al., Fusion Engineering and Design 94(1), 2015

Recent Results form HL-2A on MHD Control

Yi Liu, Xiaoquan Ji, Longwen Yan, Shaodong Song, Y.B Dong, Yuan Xu, Jiruo Ye, Min Jiang, Wenjin Chen, Tengfei Sun, Shaoyong Liao, Fei Leng, Chao Yang, Rui Ma, Mei Huang, Xianming Song, Deliang Yu, Zhongbin Shi, Qingwei Yang, Min Xu, Xuru Duan, Yong Liu and HL-2A team

Southwestern Institute of Physics, Chengdu, Sichuan 610225, China

E-mail: yiliu@swip.ac.cn

Abstract

Important advances in control of MHD activities have been made on HL-2A, aided by substantial developments to plasma control, diagnostics and heating systems. The first high coupling efficiency of resonant magnetic perturbation (RMP) with the edge plasma was successfully demonstrated in H-mode plasma on the HL-2A tokamak, such low-hybrid wave has also been found to be advantageous in ELM mitigation. In addition, various ELM mitigation techniques have been investigated, including supersonic molecular beam injection (SMBI). In the MHD research, neoclassical tearing modes (NTMs) driven by the transient perturbation of local electron temperature during the non-local thermal transport events have been observed. Feedback control/suppression of MHD tearing modes with EC heating has been demonstrated. Long-lasting runaway electron plateau was achieved after argon injection and the runaway current beam was successfully suppressed by SMBI. Furthermore, extensive modelling efforts of the plasma response to the resonant magnetic perturbation fields, utilized for controlling the edge localized mode (ELM), help to identify the edge-peeling response as a key factor, which correlates to the observed ELM mitigation in HL-2A tokamak device. The recently observed edge safety factor window for ELM mitigation in HL-2A experiments is explained in terms of the edge-peeling response.

1. Introduction

The stability and performance of tokamak plasmas are routinely limited by various MHD instabilities, such as edge localized mode (ELM), neoclassical tearing modes (NTMs) and disruptions. Resonant magnetic perturbation (RMP), or sometimes simply referred to as magnetic perturbation(MP), has been experimentally established as an efficient way of controlling the large(type-I) edge localized mode (ELM) in H-mode tokamak plasmas. In fact, full suppression of type-I ELM, under ITER relevant (low) collisionality conditions, has been reported on several present-day devices including DIII-D, KSTAR , EAST and ASDEX Upgrade[1,2] . Even in devices where ELM suppression has so far not been achieved, the ELM bursting frequency is significantly increased with reduced amplitude per burst. This is referred to as ELM mitigation, which is still of significant benefit in terms of reducing the peak heat flux load on the plasma facing components[3,4,5,6,7]. In the DIII-D tokamak, a successful control experiment was conducted to suppress NTM activity. The alignment of the ECRH/ECCD power deposition with the NTMs was achieved by varying the horizontal plasma position rather than a steerable launcher mirror[8,10].

On JT-60U, ASDEX Upgrade, Tore Supra, TCV, and TEXTOR, steerable launchers have been used in the suppression experiments of (neoclassical) tearing modes[11,12]. The steerable systems are routinely equipped with a feedback controller for changing the position of the launcher mirrors. The ECRH/ECCD system on ITER will also apply a steerable launcher as actuator for the RT control of NTMs. Efforts on JT-60U, TCV, ASDEX-Upgrade and FTU have promoted the alignment of actual diagnostic information and tearing mode positions into a control system in real time. JT-60U presents an example of 3/2 tearing mode to be detected by combining plasma shape with electron temperature perturbation where a local minimum corresponds to the center of the NTM. This information is used to optimize the injection angle of the steerable mirrors. Recently, a dedicated RT system implemented on HL-2A, a medium sized divertor tokamak with major radius R = 1.65 m and minor radius r = 0.40m, has been developed for the NTM control.

Disruptions are a major threat for future reactor-size tokamaks，its damage can come from overheating of divertor surfaces, electromagnetic loads on conducing structures, and localized impact of relativistic electrons. Disruption mitigation is therefore essential for next-generation tokamaks, including ITER [13]. Massive gas injection (MGI) is one of the candidate methods foreseen as a standard mitigation system for future devices, which aims at reducing the deleterious effects of the disruption. Encouraging results have been obtained on several tokamaks[14]. However, the injection scenario (gas species and amount) is still an open issue. Another important gas jet technique is the Supersonic Molecular Beam Injection (SMBI) [5], which can meet a lot of demanding functional requirements. Runaway electron (RE) generation in the presence of electric fields is common in both laboratory and space plasmas [1]. In laboratory plasmas, much attention has been given to the highly relativistic RE beams that can be generated in tokamak disruptions. Such REs may damage plasma facing components due to their highly localized energy deposition. The potential for detrimental effects increases with plasma current. Therefore, understanding the processes that may eliminate RE beam formation is very important for future reactor-scale tokamaks with high currents, such as ITER .In several tokamak experiments it has been observed that RE generation only occurs above a threshold toroidal magnetic field. While the origin of this threshold is uncertain, it might linked to decreased relative magnetic fluctuation levels [15]. It remains therefore prudent to develop mitigation techniques, which suppress runaway generation.

This paper presents an overview of studies on the control of these instabilities on HL-2A tokamak. The remaining sections of this paper are arranged as follows. Section 1 provides the experimental results of ELM mitigation with RMP coil and its modeling. Section 2 provides the experimental results to detect and suppress the tearing modes in the pilot tests. Some results on the development of mitigation techniques for disruption, such as, massive gas puff, use of SMBI and auxiliary plasma heating, are presented in Section 3. The final section is devoted to the conclusions and discussions.

2. ELM mitigation experiments and Modelling

ELM mitigation has been achieved in several machines, including MAST , ASDEX Upgrade , JET and recently in EAST and HL-2A. Extensive MARS-F modelling has been performed for MAST, ASDEX Upgrade, and EAST. All the modeling results, in comparison with the corresponding experimental observations, so far point to the important role played by the edge-peeling response for achieving the best ELM mitigation . The edge-peeling response, which was first identified in modelling of the JET experiments , is found to be closely correlated to the pronounced plasma surface displacement near the X-point. On the contrary, the other type of the plasma response - the core-kink response - often causes large plasma displacement near the outboard mid-plane, due to the ballooning effect. In the modelling of the MAST ELM mitigation experiments, we found that the ratio of the plasma displacement near the X-point to that at the outboard mid-plane serves as a good indicator for the density pump-out observed in experiments, for both L-mode and H-mode plasmas. In H-mode plasmas, achieving ELM mitigation without causing the mode locking or the H-to-L back transition requires this displacement ratio exceeding certain critical value (about 1.7 for MAST plasmas). In other words, the best strategy for ELM mitigation appears to be maximizing the edge-peeling response and at the same time minimizing the core-kink response.
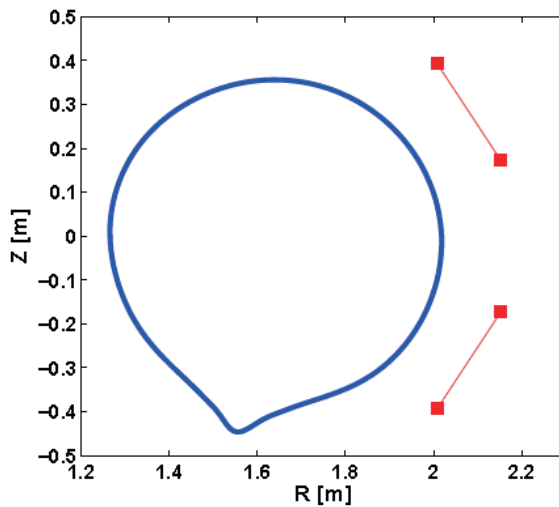
Figure 1: The location and size of the ELM control coils in HL-2A, shown on the poloidal plane together with the plasma boundary shape for discharge 29676 at 820ms.

In the following, we shall report the MARS-F modelling results for the recent ELMmitigation experiments in HL-2A. HL-2A is a medium-sized tokamak with the major radius of R_0=1.65m and the typical plasma minor radius of about 37 cm. A 2×2 ELM control coil system has recently been installed. There are two rows of coils (upper and lower, respectively) as shown in Fig. 1, with each consisting of 2 coils along the toroidal angle ϕ, spanning about 11.4° in ϕ,and being separated from each other by 180° in ϕ.

This coil system generates multiple toroidal RMP field components. By supplying the coil currents flowing in the opposite direction in each row, as in experiments, field components with odd n numbers are created. In HL-2A discharge 29676, which we use in this work for the modelling purpose, the supplied coil current is 4.5 kAt. An analytic estimate shows that the corresponding coil currents for toroidal components n = 1,3,5,7 are 284 A, 280 A, 373A, 262 A, respectively. The amplitude of the first few toroidal components of the coil currents is comparable, as expected.

However, when the generated RMP fields reach the plasma, the (resonant) field components with higher n become significantly weaker, due to the fact that the higher-n and m (m is the poloidal number) components decay faster in the vacuum. The resulting resonant radial field amplitude, at the corresponding rational surface close to the plasma boundary, is compared in Fig. 2. Here, the amplitude of the radial field component, for each m and n, is defined as a dimensionless quantity

$$b_{res}^1 = \frac{1}{R_0^2 B_0} \left| \frac{b \cdot \nabla \psi}{B_{eq} \cdot \nabla \phi} \right|_{mn} ,$$

where B_0 is the vacuum toroidal magnetic field strength at the major radius R_0 (B_0=1.37 Tesla in HL-2A discharge 29676), **b** the perturbed magnetic field due to RMP, ψ the equilibrium poloidal flux function, and **B**$_{eq}$ the equilibrium field. The toroidal harmonic is calculated using the geometric toroidal angle ϕ, whilst the poloidal harmonic is calculated using a PEST-like definition for the poloidal angle χ, which yields a Jacobian being proportional to the square of major radius, R_0. These choices of toroidal and poloidal angles result in a straight-field-line flux coordinate system.

Figure 2 compares b^1_{res} for n = 1,3,5,7 toroidal components. For each n, comparison is also made between the applied vacuum RMP field (dashed lines) and the total perturbed field including the plasma response (solid lines). Moreover, in numerical modelling, for each n, we perform full scans of the coil current phasing angle $\Delta\phi$ between the upper and lower rows, from -180° to +180°. In experiments, with only two coils per row, the only possible choice for the coil phasing is either even parity ($\Delta\phi$ = 0) or odd parity ($\Delta\phi$ = ±180°). In all ELM control experiments carried out so far in HL-2A, only odd parity configuration has been considered.

Comparing the resonant vacuum field components between n = 1,3,5,7, we find the ratio of the peak values (among all coil phasing $\Delta\phi$) is about 169:64:8:1, indicating that the largest role in ELM control is still played by the n = 1 field component in HL-2A, despite a very small coverage of the toroidal angle by the RMP coils. The n = 3 field component, being 3 times smaller than the n = 1 component, may also plays some role.

Inclusion of the plasma response changes the poloidal spectrum of the RMP field. As a consequence, the dependence of b^1res on the coil phasing $\Delta\phi$ also changes. In particular, the peak amplitude of b^1res is reached at different coil phasing, between the vacuum field and the total response field. Defining the coil phasing that maximizes b_{1res} as the "optimal" coil phasing, we find $60°$ shift in the optimal phasing between the total response field and the vacuum field, for the dominant $n = 1$ component. This $60°$ phase shift is close to what has been found for ASDEX Upgrade plasmas as well.
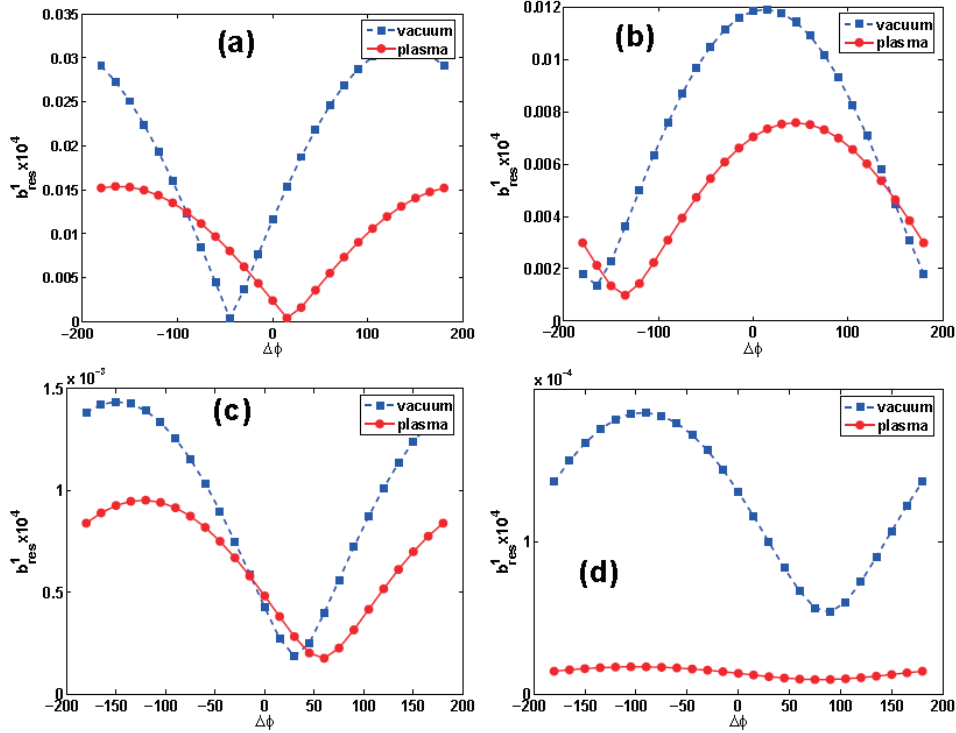

Figure 2: The computed amplitude of the last resonant radial field component, for the vacuum RMP field (dashed lines) and the total response field including the plasma response (solidlines), for the (a) $n = 1$, (b) $n = 3$, (c) $n = 5$, and (d) $n = 7$ field components in HL-2A, with artificial variation of the coil phasing $\Delta\phi$ between the upper and lower rows. The experimental coil phasing corresponds to $\Delta\phi = 180°$.

The amplitude of the plasma normal displacement is also plotted in the poloidal plane in Fig. 3, and compared between the $n = 1$ and the $n = 3$ toroidal components, assuming the odd parity coil configuration. Besides the obvious difference in the overall magnitude of the displacement, the pattern is somewhat different. In particular, the $n = 1$ normal displacement strongly peaks near the X-point, whilst the $n = 3$ displacement is pronounced both near the X-point and in the low field side region of

the torus. The combined effect is still largely the X point displacement peaking with the odd parity coils, which should be in favour of maximizing the control effects on the ELMs in experiments.

Finally, and perhaps most interestingly, is a direct comparison between experiments and modelling for HL-2A, as shown by Fig. 4. Here, we present in Fig. 6(a) the experimentally measured ELM frequency for a series of RMP discharges, where the edge safety factor q_{95} is varied. The ELM frequency is normalized by that from the RMP-off discharges. In the range of q_{95} below 3.5, no ELM mitigation is achieved in HL-2A (with odd parity coil configuration).However, clear ELM mitigation is achieved in a q_{95} window with q_{95} value above 3.6,with more than doubling of the ELM frequency in certain cases.
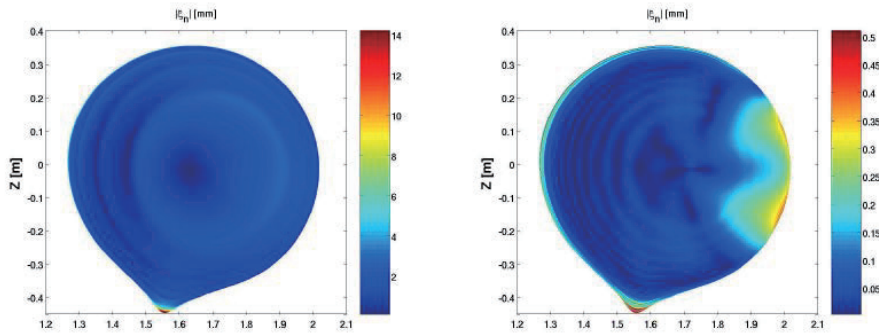

Figure 3: The computed distribution of the plasma radial displacement amplitude at thepoloidal plane, caused by the (a) $n = 1$ and (b) $n = 3$ components of the applied RMP fields in HL-2A. The ELM control coil current is assumed to be 4.5 kAt, with the upper and lower rows in odd parity, as in experiments.

In the MARS-F modelling results shown in Fig. 4(b), we vary q_{95} by scanning the total plasma current, based on the plasma equilibrium from the HL-2A discharge 29676 at 820 ms. We find that, roughly in the same q_{95} window where the ELM mitigation has been observed in experiments, the ratio ξ_X/ξ_M of the computed plasma surface displacement near the X-point, to that of the outboard mid-plane, is maximized. Thus, these MARS-F modelling results for HL-2A, though still not representing an exhausted study, already clearly confirm the role of the edge-peeling response in the ELM mitigation, that we have previously found in other devices.
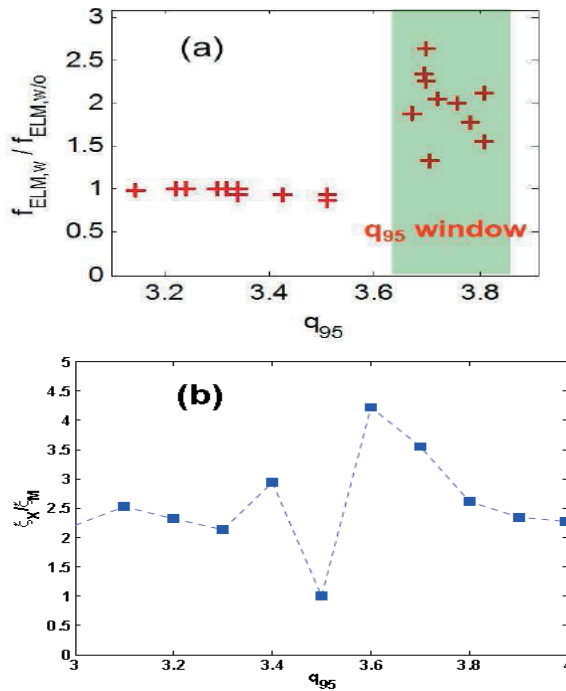
Figure 4: Comparison of the HL-2A experiments versus the modelling results as the safety factor '$q95$ is scanned: (a) the ratio of the ELM frequency with RMP to that without RMP, as measured in experiments, (b) the ratio of the plasma surface displacement near the X-point to that near the outboard mid-plane, as computed by MARS-F.

3. Mitigation of Runaway Current with SMBI

Disruptions are a major threat for future reactor-size tokamaks，its damage can come from overheating of divertor surfaces, electromagnetic loads on conducing structures, and localized impact of relativistic electrons. Disruption mitigation is therefore essential for next-generation tokamaks, including ITER. Massive gas injection (MGI) is one of the candidate methods foreseen as a standard mitigation system for future devices, which aims at reducing the deleterious effects of the disruption. Encouraging results have been obtained on several tokamaks. However, the injection scenario (gas species and amount) is still an open issue. Another important gas jet technique is the Supersonic Molecular Beam Injection (SMBI), which can meet a lot of demanding functional requirements. In this contribution, disruption mitigation experiments performed on HL-2A tokamak with MGI and SMBI technique are reported.

Disruption mitigation experiments with MGI have been carried out on HL-2A with a rapid (~1ms), massive (~10^{21} particles) injection of helium/neon/argon to study various injection scenarios. The behaviors of runaway currents in MGI induced disruptions have been investigated. As shown in figure5, a long-lasting RE plateau is achieved after

phase(top) and image form Fast-framing camera(bottom) showing runaway beam.

162
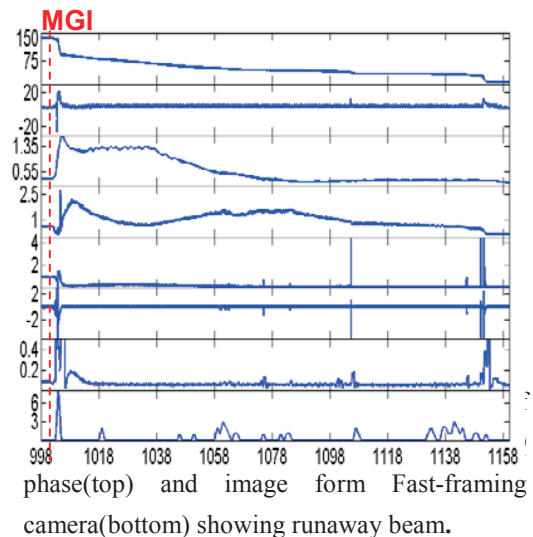
argon injection by MGI even at $B_t = 1.28$ T, much lower than previous B_t threshold found in other tokamaks. It was found that argon injection can cause the generation of runaways carrying up to 30% of the initial plasma current, while disruptions triggered by injection of helium or neon are runaway free.

Furthermore, the runaway current caused by argon injection with MGI was successfully suppressed by SMBI with a number of injected atoms of about 1.0×10^{21}, as shown in Figure 6. Light gases, such as helium, are selected in this experiment for its high efficiency in increasing the density.

These experiments suggest that SMBI might be viable for runaway suppression in future tokamaks even though core penetration of jet neutrals is not achieved. An understanding of this paradox is obtained by modeling, which shows that the initial cooling of the plasma periphery triggers a very rapid growth of low-order tearing mode, resulting in a strochastic region over much of the plasma. This allows rapid transport across the entire plasma, and could explain the effectiveness of SMBI mitigation in HL-2A in spite of the shallow penetration of the neutral gas jet.
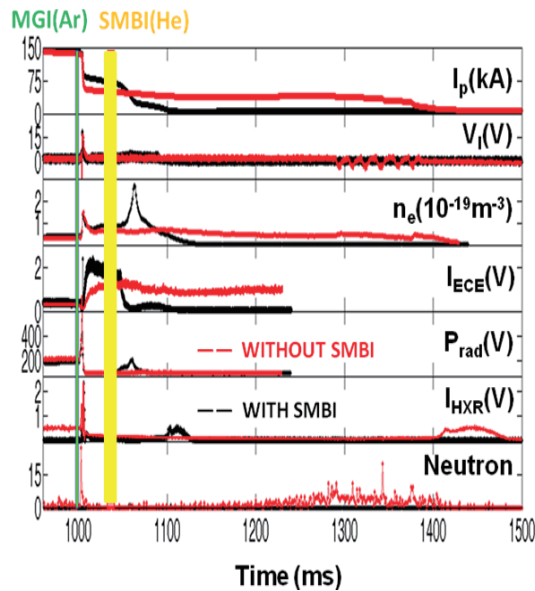
FIG. 6 The disruption was triggered by MGI with Ar gas, and then the runaway current was mitigated by using SMBI to inject He gas.

In addition, a toroidal alfvén eignmode (TAE) was observed during disruptions deliberately triggered by the massive gas injection (MGI) of argon as shown in Figure 7. This mode occurs at the beginning of the current quench and lasts about 1-2 ms. These instabilities appears to be favorable in limiting the RE beam formation. It has been found that the runaway plateau is easy to obtain on the condition of high normalized magnetic fluctuation

163
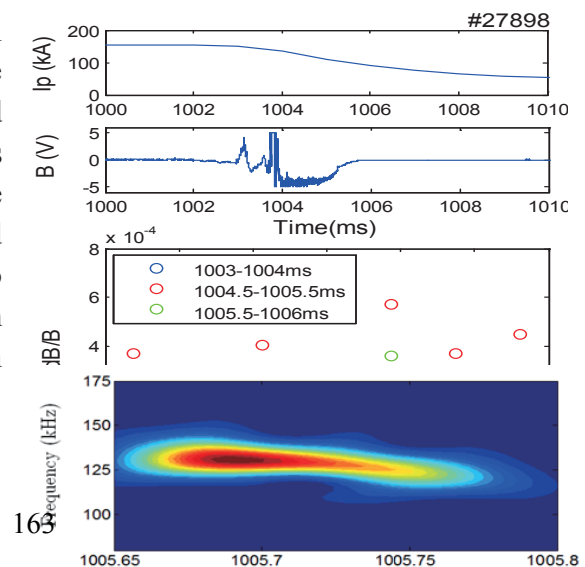
level($\delta B/B_T$), the runaway plateau is even invisible when $\delta B/B_T$ the exceeds the threshold of about 7.8×10^{-4}, incdicating that this magnetic mode plays a scattering role on the RE beam strength.

Dedicated experiments have been carried out with SMBI combined with MGI on HL-2A. Runaway electrons are suppressed only by light gases with SMBI. Furthermore, it is found that TAE mode plays a scattering role on the RE beam strength. These results bring important insights to the suppression of runaway for further simulations and extrapolations to larger devices like ITER.

FIG. 7 High frequency mode during CQ before RE current. The mode level at the plasma core: **dB/B≈5x 10⁻⁴.**

3. **Real-time Control of Tearing Modes with ECRH**

The RT control of NTMs by ECRH with launcher mirror steering has been developedA few RT diagnostics and intelligent controllers achieved precise control of ECRH deposition at a rational surface. A reliable feedback loop has been designed, developed and tested by a proper integration and coordination of several diagnostic systems with plasma control system (PCS). An RT code solves Grad-Shafranov equation with 129X129 grid scale using the advanced parallel computation within 1 ms. The magnetic island location was determined by the RT 'ECE/Mirnov' subsystem with the high spatial resolution less than 1 cm. Motor controller will calculate the control signal with all the possible signals from the reflective memory networking. The stabilization of tearing modes with the ECRH feedback has been demonstrated on HL-2A, as shown in figure 8.
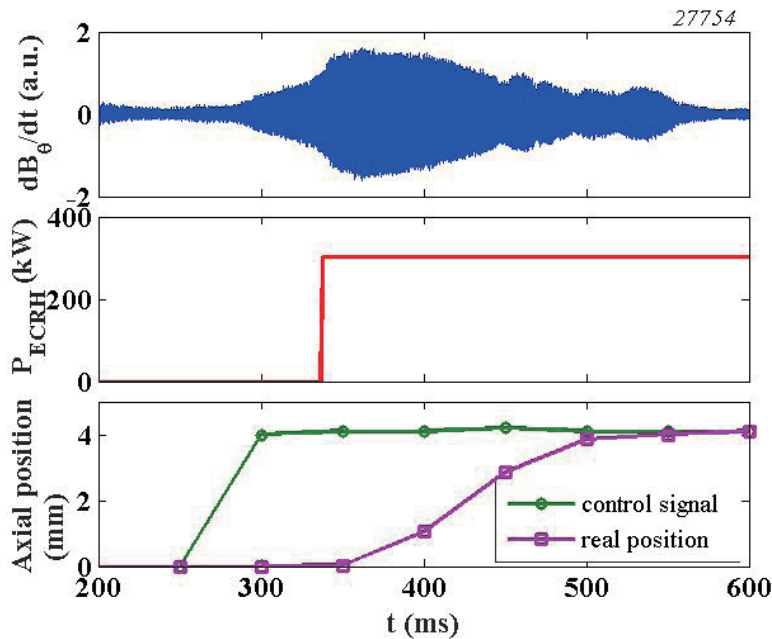

Figure 8. Real time control of tearing mode.

Shown in Fig.8 is a tearing mode to be killed by ECRH in real time with steerable mirror on HL-2A. Main parameters have Bt = 1.3 T and Ip = 170 kA. The RT control system detects the appearance of 2/1 tearing mode at t = 300 ms. The gyrotron is turned on at t = 335 ms after the mode amplitude reaches a threshold for 20 ms. Meanwhile, the launcher mirror is rotated from ▢=0 to the target angle. The mode amplitude continuously increases when the deposition position of the ECRH power is far away from the rational surface. The amplitude begins to drop if both positions are close to each other. The 2/1 mode is completely killed after the ECRH deposition is aligned with the tearing mode with the power of 260 kW. Most of the time during mirror rotation is spent on the communication between main controller and PLC for driving mirror. The poloidal beta and plasma density slightly drop during the existence of the tearing mode. They obviously recover after the mode disappearance. The total control time can be decreased rather largely in future. The NTM suppression in real time will be tested in the next experimental campaign on HL-2A.

4. Conclusion and discussion

This paper presents the progress in MHD control on HL-2A. Firstly, dedicated experiments have been carried out with PMP on HL-2A. To achieve better ELM mitigation, while maximizing the edge-peeling response is essential, minimizing the core-kine response may also be important to avoid undesired side effects (such as core flow damping or H-to-L back transition) on the plasma. For plasma-coil configurations where both the edge-peeling and the core-kink response can be simultaneously large, the best strategy seems to be maximizing the ratio of the plasma X-point to the outboard mid-plane displacement. This is so far the case for MAST and HL-2A plasmas. In fact, this displacement ratio serves as a good indicator of the experimentally observed ELM mitigation window in q_{95} in HL-2A, as shown in this study.

An integrated real-time control approach for suppression and stabilization of neoclassical tearing modes is established on HL-2A. The experimental results demonstrated ability of this real-time control for the tearing mode, i.e. mode detection, alignment with ray tracing, suppression and stabilization. Main control tasks required to perform tearing mode suppression have been successful, notably, the system can align the ECRH/ECCD deposition with a mode center, track the perturbed tearing modes in real time and modulate the ECRH/ECCD power of 1 kHz.

At last, runaway electrons are suppressed only by light gases with SMBI. A toroidal alfvén eignmode (TAE) was observed during disruptions deliberately triggered by the massive gas injection (MGI) of argon. It has been found that the runaway plateau is easy to obtain on the condition of high normalized magnetic fluctuation level($\delta B/B_T$), the runaway plateau is even invisible when $\delta B/B_T$ the exceeds the threshold of about 7.8×10^{-4}, incdicating that this magnetic mode plays a scattering role on the RE beam strength. These results bring important insights to the suppression of runaway for further simulations and extrapolations to larger devices

like ITER.

Acknowledgments

References

[1] Evans T.E. *et al* 2006 *Nat. Phys.* **2** 419

[2] Jeon Y.M. *et al* 2012 *Phys. Rev. Lett.* **109** 035004

[3] Sun Y.W. *et al* 2016 *Phys. Rev. Lett.* **117** 115001

[4] Suttrop W. *et al* 2016 *Plasma Phys. Control. Fusion* at press

[5] Liang Y. *et al* 2007 *Phys. Rev. Lett.* **98** 265004

[6] Kirk A. *et al* 2013 *Plasma Phys. Control. Fusion* **55** 124003

[7] Liu Y.Q. *et al* 2011 *Nucl. Fusion* **51** 083002

[8]T.C. Hender, J.C Wesley, J. Bialek. et al. MHD stability, operational limits and disruptions. Nucl. Fusion 47 S128–S202 (2007)

[9]Qu W X and Callen J D "Nonlinear growth of a single neoclassical MHD tearing mode in a tokamak", University of Wisconsin report, UWPR 85-5 (1985).

[10]Z Chang et al, "Observation of nonlinear neoclassical pressure-gradient-driven tearing modes in

[11]TFTR" Phys. Rev. Lett. 74 4663 (1995).

[12]H R Wilson, J W Connor, R J Hastie and C C Hegna "Threshold for neoclassical magnetic islands in a low collision frequency tokamak", Phys Plasmas 3 248 (1996)

[13] Hender T.C. et al 2007.Nucl. Fusion 47 128–200

[14] Pautasso G. et al 2009. Plasma Phys. Control. Fusion 51 124056

[15] W.W. Xiao. et al 2012.Nucl. Fusion 52(11):114027.

A3 Foresight Scientific Report

Name of visitor: Yasuaki KISHIMOTO
Affiliation: Kyoto University
Category: Ⅲ
Numerical laboratory based on global gyro-kinetic modeling for studying turbulent and MHD events
Duration of visit: 2017 July 11 - 14
Place of visit: Sapporo, Hokkaido, Japan
Responsible person in visiting country: Prof. S. Morita

1. Purpose of the visit

The purpose in participating the conference was to present the activity related to gyro-kinetic based numerical experiment of tokamak, GKNET [1-4], which is a full-f flux-driven global toroidal code with heat and momentum source and sink, and to discuss other A3 participants for the confinement and transport issues, including LHD, EAST and KSTAR. A capability using both adiabatic and gyro-kinetic electrons is now become available in the GKNET, so that not only ion temperature gradient (ITG) mode, but also trapped electron mode (TEM) mode can be treated in global geometry [3]. Recently, the electromagnetic version based on the δf-model has been implemented in linear regime, so that finite-β effects on the ITG mode and also on the kinetic ballooning mode (KBM) can be studied. The GKNET is also going to be incorporated with the electromagnetic gyro-fluid model which includes the effect of non-adiabatic electrons [5]. Magnetic configuration with non-circular poloidal cross section becomes available in the GKNET which can be incorporated with equilibrium code. Recently, effects of magnetic shaping with ellipticity and triangularity on ITG instability have been investigated including the inverse D-shaping [6]
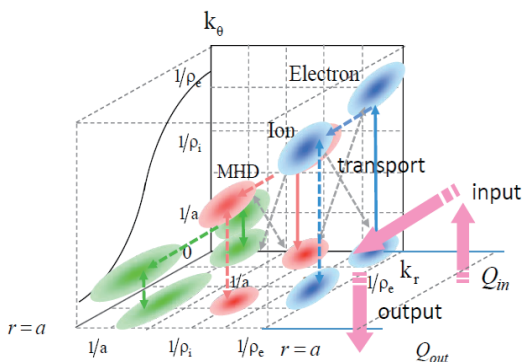
Fig.1: distribution of various scale fluctuations in (k_r, k_θ) plain and radial direction in toroidal plasma and the global effect, e.g. radial spreading, in flux driven system [7].

The global approach in studying confinement and transport in toroidal plasmas is of specific importance. Suh a confined plasma is in a non-thermodynamics equilibrium state sustained by external heat input Q_{in} near center and output Q_{out} near edge, so that the system is not closed but opened to the outside, which feature is shown in Fig.1 [7]. Assuming that the temperature near center T_1 is higher than that near edge T_2, i.e. $T_1 > T_2$, it can be readily seen that such an open system exhibits structure formation inevitably either in real

space and/or phase space since the variation of thermo- dynamics entropy in the system yields a negative value as found, $ds = dQ_{in}/T_1 + dQ_{out}/T_2 = \left(1/T_1 - 1/T_2\right)dQ_{in} < 0$, where $Q_{out} = -Q_{in}$. Namely, such a circumstance with same heat input and output at different radial location are considered in providing a constraint on the structure and dynamics of the fluctuations and then the transport. Using the GKNET, we have studied the characteristics of the transport dominated by ion temperature gradient (ITG) mode using adiabatic electron response and associated turbulent transport as a flux driven system.

It has been well recognized that the toroidal plasmas with L-mode state is found to reveal characteristic structure and dynamics which are not simply explained by local and diffusive Gaussian processes but are dominated by non-local and non-diffusive processes [1]. Three types of non-diffusive events has been found, (1) *radially localized fast time scale avalanche*, (2) *global bursts due to the instantaneous formation of radially extended ballooning modes*, (3) *slow time scale avalanche of $E \times B$ staircase*. The transport is reproduced by their spatio- temporal linkage coupled with neoclassical mean flows. Among them, the process (2) is of specific importance, which is also the origin in causing the process (3).

Here, we elucidated the generation mechanism of the process (3), i.e. the $E \times B$ staircase, which results from zonal flow and pressure governed by the intensity gradient of the ballooning modes, i.e. the process (2). The typical interspace of the staircases is then determined by the radial correlation length of the extended mode. The dynamical evolution of the $E \times B$ staircase causes a new type of long time scale breezing in the transport.

2. The formation mechanism of E×B staircase in toroidal system [4]

Recently, a $E \times B$ shear flow pattern coupled with pressure corrugation, which exhibits quasi-regular long-lived meso- to macro-scale structures, has been found in gyro-fluid and gyrokinetic simulations in global toroidal geometry, where the effect of profile variation incorporated with zonal flows is taken into account self-consistently [7,1]. Dif-Pradalier *et al*. pointed out that the effect of the mean flow plays an important role in forming the quasi-regular temperature corrugations and $E \times B$ shear layers, referring to them collectively as the $E \times B$ staircase [-10].

Here, we investigated the formation and sustainment mechanism of a self-organized global profile and a meso-scale quasi-regular long-lived $E \times B$ shear flow layer coupled with pressure corrugation, the $E \times B$ staircase, based on the simulations by GKNET in for the ITG instability using the adiabatic electron response. The simulations include heat source and sink, neo-classical collisional effects and global equilibrium mean flows. Such a setting is important in studying the transport regulated by non-local and non-diffusive processes and resultant global profile formation, which are suffered from various constraints not only in micro- and meso-scales but also in macro- and/or device scales. We also incorporated with

168

the δf version which is employed to investigate each physics process using the advantage that the background equilibrium mean field can be artificially introduced.

We have found that a radially extended ITG mode is the key and origin in leading the self-organization to the global temperature profile and to the meso-scale isomorphic profiles of radial electric field and ion temperature. Such structures are found to be initiated during the saturation phase of the ITG mode and is established as it evolves into a quasi-steady turbulence. It is noted that these two processes are not independent but coupled with each other through the generation of radially extended ITG mode. The results are summarized as a sequence of the fundamental processes as follows:

1) The global equilibrium mean radial electric field $E_r^{(eq)}$ is established, which satisfies the radial force balance. Such a mean field is essential in regulating the mode structure and then the transport, e.g. diffusive transport due to the neo-classical collisional effect and that due to smaller scale turbulent eddies, non-diffusive and non-local turbulent transport due to various sizes of avalanches and that due to global intermittent bursts.

2) The ITG mode with radially extended meso-scale structure with nearly up-down symmetry with respect to the mid-plain, i.e. the ballooning angle of $\theta_0 \approx 0$, is induced, where the radial correlation length and the growth rate are maximized. This results from the partial cancellation between the diamagnetic shear frequency due to the global profile variation and the poloidal flow shear frequency due to the induced equilibrium mean radial electric field discussed in 1).

3) Due to the radially extended ITG mode, the ion temperature profile is self-organized into *a specific function form* through relaxation process. In the case of the ITG mode where the instability free energy is given by $\varepsilon \equiv R/L_T$, the function tends to *an exponential form*, which makes $\varepsilon \equiv R/L_T$ a radially constant value. The relaxation takes place keeping the same function form but only changing the scale length L_T with a slow time scale.

4) At the same timing of the relaxation discussed in 3), an even-parity zonal flow $\delta E_r^{(ZF)}$ induced by the ITG mode, where the flow direction at the central part and that at both edges are opposite. Therefore, the subsequent suppression of the ITG mode is achieved not by tilting but by bending the mode, disintegrating it into smaller scale eddies. The number of the smaller eddy is topologically three, where the central one and those at both edges rotate in opposite directions.

5) The temperature relaxation δT_i discussed in 3), which is equivalent to the zonal pressure, induces the mean radial electric field $\delta E_r^{(TR)}$ to satisfies the radial force balance. Here, the zonal flow component $\delta E_r^{(ZF)}$ induced by the same radially extended ITG mode discussed in 4) exhibits an in-phase relation, so that the sum of them, i.e. $\delta E_r^{(TR)} + \delta E_r^{(ZF)}$, is reinforced in a self-organized manner. The ratio of the contribution from the zonal flow excitation and mean flow variation is approximately 1:2. Due to the in-phase relation

between $\delta E_r^{(ZF)}$ and $\delta E_r^{(TR)}$, the total equilibrium mean field, i.e. $E_r = \delta E_r^{(TR)} + \delta E_r^{(ZF)} + \delta E_r^{(eq)}$, and then the temperature corrugation measured by $\delta(R_0/L_T)$ exhibits isomorphic profiles. Thus, the staircase structures of E_r and $\delta(R_0/L_T)$ are initiated through the saturation phase.

6) The disintegrated smaller scale eddies due to the even-parity zonal flow discussed in 4) tend to be aligned radially by spontaneous phase matching, thereby recovering radially extended structure.

7) The processes from 3) to 7) are repeated quasi-periodically. Here, the radial location of the $E \times B$ shear layers, temperature corrugation, and ITG mode maintain the positional relationship, so that the $E \times B$ staircase structure is sustained in a self-organized manner accompanied by the intermittent bursts of turbulent transport associated with the repetitive formation of the radially extended ITG mode. Among above whole processes, the equilibrium mean field $E_r^{(eq)}$ plays an important role in causing the phenomena.

3. Remarks

Here, we considered the ITG mode using the adiabatic electron, which is characterized by the diamagnetic frequency ω_d. On the other hand, in the case when kinetic electron is introduced, the trapped electron mode (TEM) is a candidate regulating the turbulent transport. In this case, the sign of the mode frequency is opposite to ω_d, so that the tilting of the mode, which is also opposite to that in the case of ITG mode, is further enhanced, so that the dynamics and structure are different. The study including kinetic electrons is thus an important subject. Electromagnetic effects, which not only change the mode characteristics, e.g. the mode frequency, the radial correlation length, Bloch angle, but also modulate the safety factor and then the magnetic shear, are important.

Reference
[1] K. Imadera et al. 25th Fusion Energy Conference, TH/P5-8 (2014).
[2] Y. Kishimoto et al., 26th Fusion Energy Conference, TH/P3-2 (2016)
[3] K. Imadera et al. 26th Fusion Energy Conference, TH/P3-3 (2016)
[4] W. Wang, Y. Kishimoto, K. Imadera, J.Q. Li, Z.X. Wang, submitted 2017.
[5] A. Ishizawa et al., 17pC34-5, JPS Meeting, Osaka Univ., Japan, March 17 (2017)
[6] K. Obrejan, K. Imadera et al., Computer Phys. Communications, 216, 8-17 (2017)
[7] Y. Kishimoto, A3 Foresight Scientific Report, National Fusion Research Institute (NFRI), Korea, March 12-15, 2017
[8] N. Miyato. et al., Phys. Plasmas **11** 5557, (2004)
[9] G. Dif-pradalier G. and P.H. Diamond P. H. Physical Rev. E **82** 025401, 2011
[10] Dif-pradalier G. et al., Phys. Rev. Lett. **114** 085004 (2015)

Development of fully kinetic code to simulate lower hybrid wave and plasma interactions on EAST

Nong Xiang[1,2], Taotao Zhou[1,2], Xueyi Wang[3], Zhengzheng Men[1,2]

[1]Institute of Plasma Physics, CAS,Hefei 230031 China

[2]Center for Magnetic Fusion Theory,Hefei 230031, China

[3]Physics Department, Auburn Univerisity, AL 36849-5311, USA

Abstract

A particle-in-cell simulation code GCPIC is developed to study interactions of plasmas and lower hybrid waves (LHWs). For the given wave parameters used in LHW experiments on EAST tokamak, the launched wave experiences the mode conversion of slow and fast modes in a typical H-mode discharge. The wave amplitude is enhanced during the back-and forth propagations between the mode conversion layer and the cutoff layer. As a result, the parametric decays are observed near the mode-conversion layer, The pump wave decays into a LHW at a lower frequency which can penetrate the mode-conversion layer and low frequency electromagnetic waves which can resonantly interact with electrons, resulting the electron heating.

1. Introduction

Lower hybrid current drive (LHCD) has been proved to be one of the most promising approaches to achieve steady state operations on tokamaks [1]. It is found experimentally that LHCD efficiency decays rapidly with the plasma density in high density regime, accompanied by the broadening of the launched spectrum [2,3]. Different models have been proposed to account for the experimental observations, in which the parametric decays have been suggested as the main candidates for the reduction of the LHCD efficiency in the high density regime [2,4]. However, no published works yet treat the interactions of LHWs and plasmas consistently. In this work, a particle-in-cell code GCPIC is developed and simulations are carried to investigate the interactions of plasmas and LHWs under EAST LHCD experimental parameters.

2. GCPIC code and simulation setup

The particle-in-cell code GCPIC consists of particle pusher and field solver. The particle velocities are advanced in the cartesian coordinate with the Boris algorithm. The particle positions are advanced in the curvelinear coordinate by converting the velocity from the cartesian coordinate to the curvelinear coordinate. Both electrons and ions are treated in the fully kinetic model.

In the simulations, the inhomogeneity is along x (radial direction) and the magnetic field is in z direction which is assumed to be constant (Fig.1). For LHCD experiments on EAST, the incident LHW frequency is f=4.6GHz. The plasma density at the center $n_0=4*10^{19}$m^{-3} with the profile given in the figures below. and the electron and ion temperatures near the edge are set to Te=Ti=40ev. The peak of the launched spectrum is at n//=2.

3. Simulation results

To benchmark the code we launch a slow wave in two different densities as shown in fig.2. In the lower density case, no mode conversion occurs while in the higher density case the mode conversion appears where the launched wave is partially converted to a fast wave. Such mode conversion process is reproduced in the simulation as shown in fig.3 which confirms our simulations.
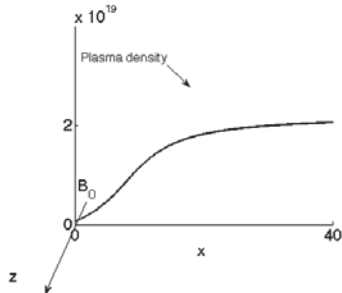

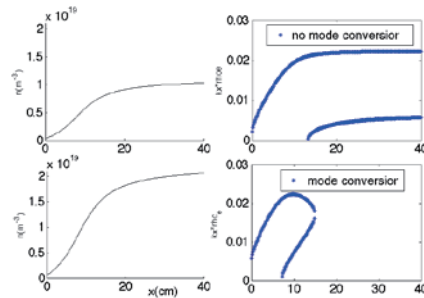Fig.1 Schematic plot of the simulation setup.

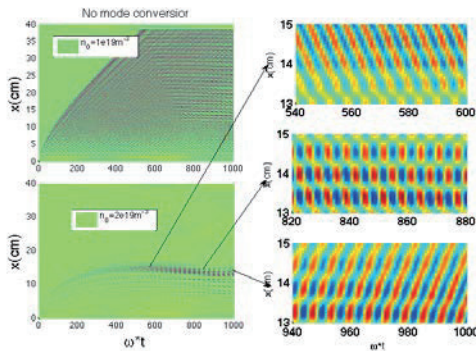Fig.2 Plasma density profiles and dispersion relation.

Fig.3 Contour plot of Ex at different time for different plasma densities.
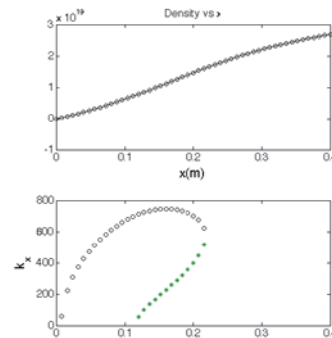

Fig.4 Plasma density profile (top) and LHW dispersion relations.

In reality the LHW is launched outside the scrape-off layer of the tokamak. It is coupled into the plasma by tunneling its cutoff layer. To include the LHW cutoff layer we consider the case shown in fig.4,
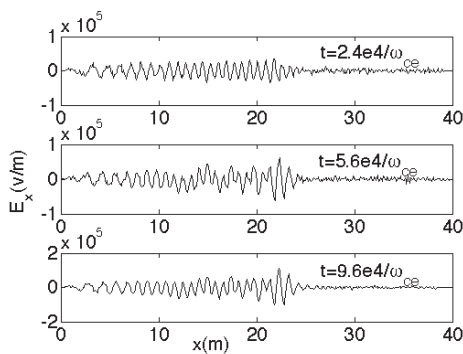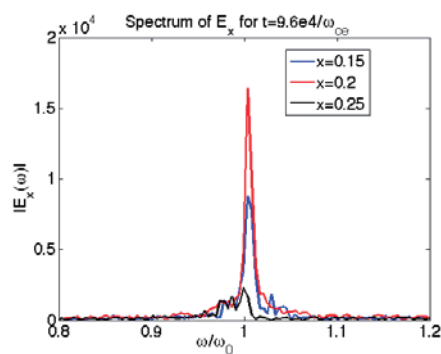

Fig.5 Spatial distribution of Ex at different times.

Fig.6 Spectrum of Ex at different positions

172

in which the cutoff layer is around x=0.02m and the mode conversion layer is around x=0.22m. We put a current source J=J_0sin(ωt) at x=0.05m for J_0=2000A/m². The spatial distribution of Ex is plotted in fig.5. One can see that a slow wave is excited and propagates into plasma. As the slow wave reaches the mode conversion layer, a fast wave is generated and propagates outwards. The spectrum of Ex is shown in fig.6 which demonstrates that the excited mode is the launched LHW.

The distributions of electrons and ions in the phase space is checked and no particle heating is observed. The simulation results agree well with the predictions from the linear theory. If the perturbation current is increased to for J_0=10⁴A/m² , the spatial variations of Ex at different times are shown in fig.7. Differing from that in fig.5, the LHW can penetrate the mode conversion layer. This can be better seen in fig.8 which plots the spatial variation of Ey. The fast wave is generated as the launched wave arrives at the mode conversion layer. With the time going, an electromagnetic wave is excited near x=0.28m. The spectra of Ex at different locations are plotted in fig.9 which clearly shows that different sideband frequencies are produced. At x=0.25m, one can see the peak frequency is shifted to ω-8Ω_{ci}, about 0.96ω_0. As the frequency decreases, it can penetrate the mode conversion layer for the launched wave.
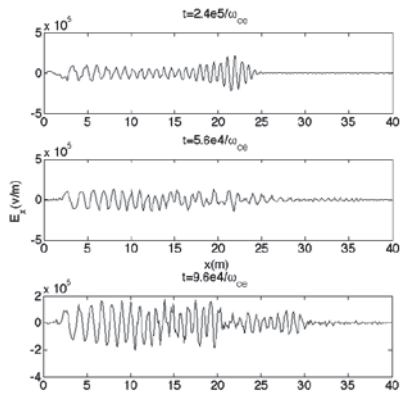
Fig.8 Spatial variations of Ex at different times.
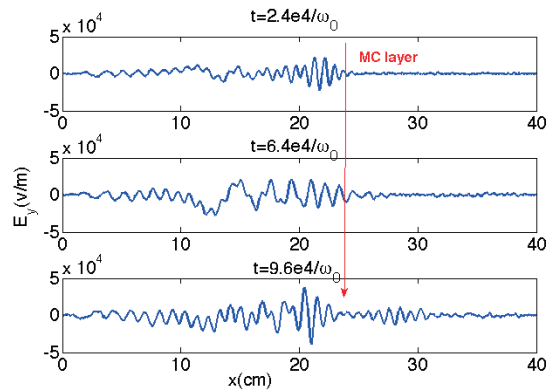
Fig.9 Spatial variations of Ey at different times
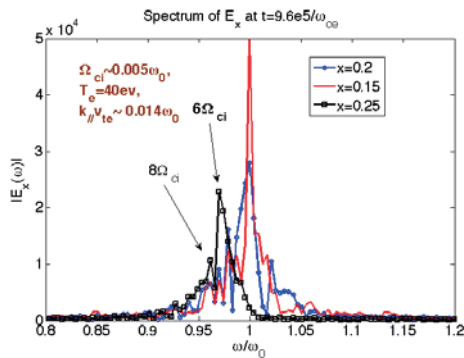
Fig.9 Spectra of Ex at different locations.
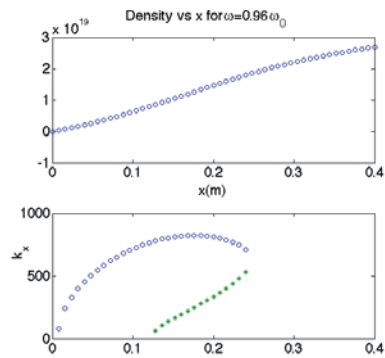
Fig.10 For the given density profile (top), the dispersion curve for the frequency ω=0.98ω_0.

Fig.9 clearly shows the decay of the incident wave into a LHW at lower frequency which can go through the mode conversion layer of the launched wave, and a low frequency electromagnetic wave. Since the phase velocity of these low frequency waves is comparable to the electron thermal velocity, they can

resonantly interact with the electrons and then heat the electrons. The distributions of the electrons in the phase space are plotted in fig.11. Clearly the electron heating occurs while the ion heating is not observed.

Fig.11 Distributions of electrons in the phase space at $t=10^5/\omega_0$ (left) and $t=1.26*10^6/\omega_0$ (right). If the electron temperature is decreased to Te=20ev, it is found that the sideband at $\omega-8\Omega_{ci}$, disappears and at $\omega-6\Omega_{ci}$, instead. The electron heating is still observed.
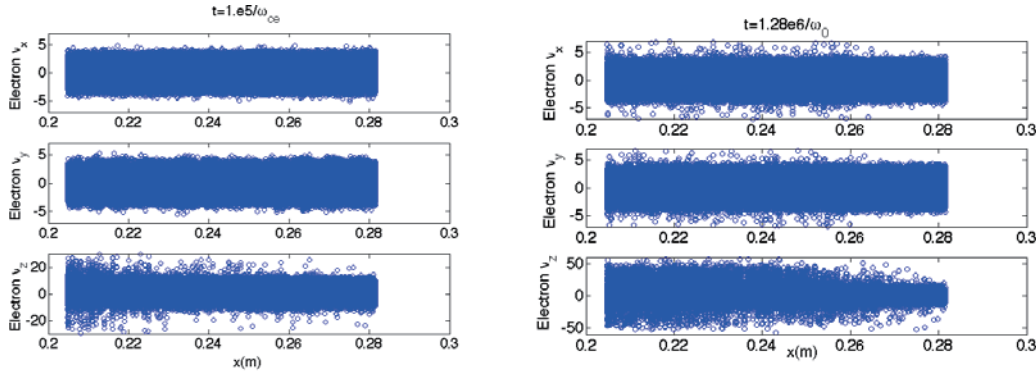
4. Summary

In this work, a particle-in-cell simulation code GCPIC is developed to study interactions of plasmas and lower hybrid waves (LHWs). It is found that for the given wave parameters used in LHW experiments on EAST tokamak, the launched slow wave experiences the mode conversion to the fast modes in a typical H-mode discharge. The wave amplitude is thus enhanced during the back-and-forth propagations between the mode conversion layer and the cutoff layer. As it exceeds a threshold, the parametric decays are observed near the mode-conversion layer, The pump wave decays into a LHW at a lower frequency which can penetrate the mode-conversion layer and low frequency electromagnetic waves interacting resonantly with electrons and resulting in the electron heating. Such parametric decays cause the LHW energy to be deposited near the plasma edge and thus reduce the current drive efficiency.

Acknowledgements

References

[1] N. J. Fisch, Phys. Rev. Lett. **41**, (1978) 873.
[2] R.Cesario, et al., Nucl. Fusion **54** (2014) 043002.
[3] B.J.Ding, et al., Nucl. Fusion **57** (2017) 022022.
[4] Aihui Zhao et al., Nucl. Fusion **53** (2013) 083015.

Recent results of microwave reflectometer systems on EAST

C. Zhou[1], A.D. Liu[1], J.Q. Hu[1], J. Zhang[1], X. Feng[1], J.L. Xie[1], Z. Y. Liu[1], G. Zhuang[1], T. Lan[1], W. X.Ding[2], G. Wang[2]

[1]University of Science and Technology of China(USTC), Hefei, China

[2]University of California, Los Angeles, CA, USA

Abstract

The Profile Reflectometer and eight-channel Doppler Backscattering (DBS8) have worked reliably on EAST tokamak. The profile Rflectometer are used for electric density measurements with the temporal resolution 10/25 μs. The DBS8 are used for turbulence measurements, and the wave number can cover the range 2-15/cm. These two microwave diagnostics system are integrated together at the K-port on EAST. A high harmonic coherent mode in RF-dominating H-mode and the turbulence evolution during neon seed injection will be introduce in this article. The coherent mode structure, with up to 7 harmonics of a fundamental frequency of 12-15 kHz , has been observed in pedestal region during EAST H-mode phase driven by lower hybrid current drive (LHCD). Although such harmonic coherent mode (HCM) has a few similar features as the edge harmonic oscillation (EHO) in the DIII-D QH-mode, some differences between these two modes can still be discerned. Bi-spectral analysis indicates that strong coupling between HCM and high frequency turbulence exists at the HCM peaking location, implying the important role of turbulence in HCM saturation process. The confinement improvement by neon injection in L-mode has been observed in EAST, and the edge radial electric field becomes more negative, while in H-mode it changes little. The detailed results will be presented in this article.

1. Introduction

The high confinement operation (H mode) in toroidal plasma device is always accompanied with edge localized modes (ELM), which can generate unacceptable heat loads to the divertor and the plasma-facing components[1]. Therefore, suppressing or mitigating of the large ELMs is important for the next step magnetic confinement fusion devices. On the other hand, the ELM can induce the impulsive particle transport, which will help prevent the accumulation of impurity and sustain operation performance. The edge harmonic oscillation (EHO) in the quiescent H-mode (QH-mode), which can enhance the particle and impurity transport, can be a potential solution, and they have been observed in various devices. Here an EHO-like oscillation: the harmonic coherent mode (HCM) has also been observed in EAST H-mode operation with lower hybrid current drive (LHCD) or with ion cyclotron resonance heating (ICRH) together by the Doppler backscattering system (DBS). The fundamental frequency is f ~12-15 kHz, and the second to seventh harmonics are quite obvious with the toroidal mode number n = 1 to n = 7, respectively. Although such harmonic coherent mode (HCM) has a few similar features as the edge harmonic oscillation (EHO) in the DIII-D QH-mode, some differences between these two modes can still be discerned. In this

paper, we also investigate the nonlinear wave-wave interaction between the HCM and background turbulence, and through the amplitude correlation method we firstly found that the energy flow between different harmonics of HCM was not always in one direction, and can redistribute the power of different harmonics.

Reduction of heat loading of the divertor target is also crucial for the fusion reactor, and impurity seeding is considered as a primary technique to decrease the heating loading. The confinement improvement by impurity seeding injection has been observed in L-mode operation on several device, which is also observed in EAST by neon injection. And the turbulence evolution during neon injection will be also introduced.

2. Recent results of microwave reflectometer systems on EAST

2.1 Application of Microwave reflectometer system on EAST

Two kind of microwave reflectometer system: the profile Reflectometer and eight-channel Doppler Backscattering(DBS8), have been applied in EAST tokamak for electric density profile and fluctuation measurements. These two system are integrated together at the K port of EAST, and can be used for toroidal coherent measurements with the DBS system at the O port of EAST[1]. The schematic diagram of the two system are show in Fig. 1(a) and (b), respectively. The profile Rflectometer as shown in Fig.1(a) launches microwave into plasma with O-mode and X-mode polarization simultaneously by a same horn, and the reflected signal is also received by this horn which is same to the arrangement used for ITER. The
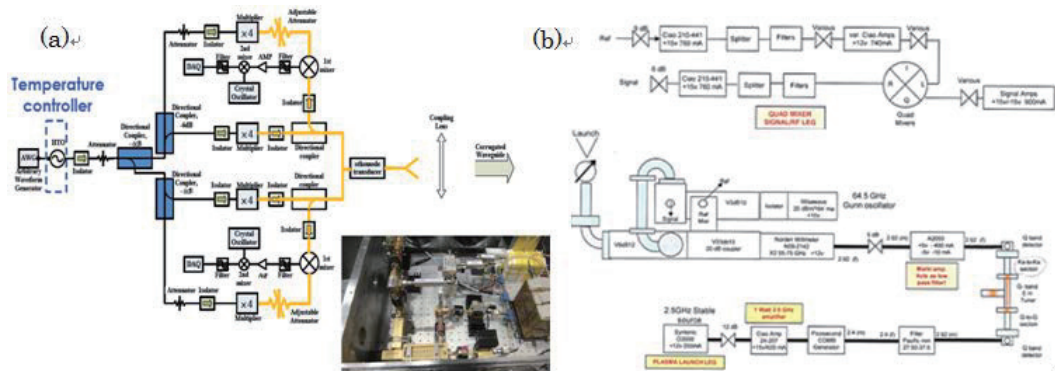
Fig.1 The schematic diagram of the profile Reflectometer (a), and DBS8 (b).

profile Rflectometer contains two subsystem: Q-band system and V-band system, and can cover the density range from 0 to 6.5e19/m^3. The DBS8 system shown in Fig. 1(b) can launch eight different microwave into plasma simultaneously in X-mode, and the frequencies are 55, 57.5, 60, 62.5, 67.5, 70, 72.5 and 75GHz. The wave number range can be from 0-12/cm, which is enough for the turbulence measurements on EAST.

2.2 The harmonic coherent mode in RF-dominating H-mode in EAST

Fig.1 shows an example with a typical lower single null H-mode discharge with ~1 MW ICRH and ~0.8 MW LHCD, plasma current I_P~ 500 kA and B_T ~ 1.8 T. The divertor D_α emission sharply reduces to a low level during L-H transition, after a while further reduces to a lowerlevel to achieve an ELMy-free H-mode operation until an ELM crash. In the ELMy-free phase, line-averaged density increase slowly, while the stored energy, plasma current Ip and injected power remain nearly constant. Accompanying with the ELMy-free H-mode, there is a harmonic coherent mode in the phase derivative spectrum of DBS

signal(Fig.2(f)). The fundamental frequency is 12~5 kHz, and the second to seventh harmonics are quite obvious. One can notice that the HCM is correlated with edge radiation, when HCM appears, the edge radiation measured by XUV shows a faster increasing speed (around 4.21 s in Fig.2(d)), suggesting a larger pressure gradient in pedestal, which intimates that HCM may be a kind of peeling-ballooning mode..
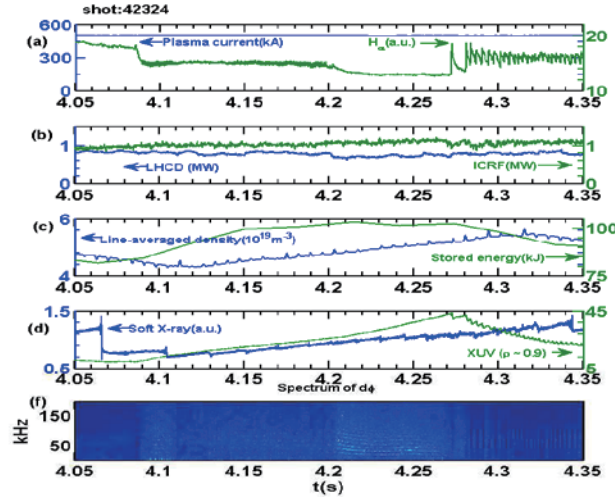

Fig.2 An example of HCM observed in EAST(shot 42324). Time evolution of several plasma parameter:(a) plasma current Ip and divertor D_α emission, (b) the LHCD and ICRF heating power, (c) the line average density and stored energy, (d) soft x-ray at the core palsma and the xuv radiation at ρ~0.9, (f) the phase derivative (dϕ) spectrum of DBS signal. One can see the clearly separated n = 2 ~ 7 harmonic oscillations during the ELM-free operation.

The eight-channel DBS (DBS8) can measure the turbulence at eight different radial location simultaneously, which is helpful to study the radial distribution of the radial electric field (Er) and HCM. Fig.3 is an example of the HCM measured by the DBS8 system. In Fig.3(a), the phase derivative (dϕ) power spectrums of three different probing frequency (55 GHz, 62.5 GHz and 75 GHz, the solid line) and the amplitude power spectrum of the probing frequency 62.5 GHz (the dash line) are represented. Here the radial measurement location of 55 GHz (ρ~0.964) is the most outside one, while that of 75 GHz (ρ~0.89) is
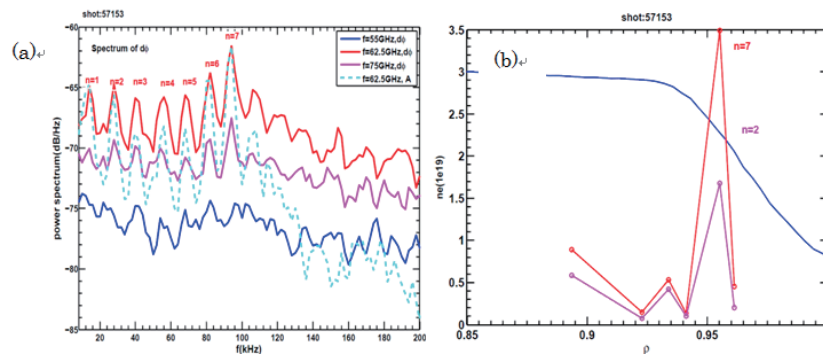
Fig.3 (a) The d=ϕ power spectrums of three different channel of the eight-channel DBS system(the solid line), and the amplitude power spectrum of the probing frequency 62.5 GHz(the dash line);(b) The radial distribution of the second and seventh harmonics of HCM.

the most inside. We can find that the harmonic oscillations in the phase derivative and amplitude spectrum around the radial location ρ~0.955 (the probing frequency 62.5 GHz) are the most significant. And at the

inner location ($\rho\sim0.89$), the amplitude of the oscillations are much smaller, while at the outside location (_$\rho\sim0.964$), the oscillations disappear. We calculate the amplitude of the second harmonic (n = 2) and the seventh harmonic (n = 7) at different radial location showing in Fig.3(b). It should point out that in the two most outside channel we don't observe the harmonic oscillations in the phase derivative spectrum, so there are only six points in Fig.3(b) rather than eight. The second and seventh harmonics both peak around the steep gradient regions of the pedestal (near the top of pedestal), and here the radial location is around ρ= 0:955 which is about 2 ~ 3 cm to the last closed field surface (LCFS). A comparison of the Er measured by the DBS8 in the H-mode with HCM and the H-mode with ELMs has been shown in Fig.4. The red line is the Er profile in H-mode with HCM, and one can find that the Er well is much deeper than that in ELMs H-mode (blue line). Although there are only eight points in the Er profile, we can still determine that the width of the Er profile in HCM H-mode is smaller than in ELMs H-mode at the edge of plasma.
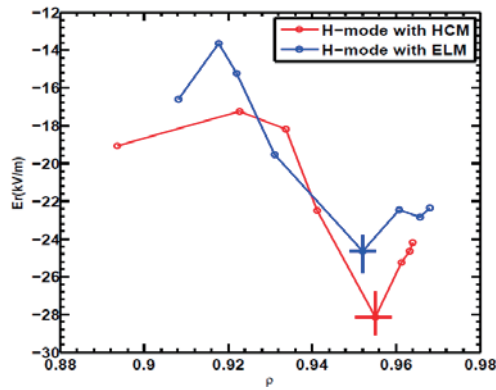

Fig. 4. A comparison of Er profile in H-mode with HCM(red line) and with ELMs(blue line).

In Fig.5 we study the energy flow between the second and the third harmonic of HCM in two different time period: 4.58-4.585 s (the blue line) and 4.585-4.59 s (the red line). Fig5(a) is the DBS signal in the frequency range 10~150 kHz, and we can find that during these two time periods the fluctuations change little. And the calculated root mean square (RMS) are about 0.0739 in 4.58-4.585 s and 0.0733 in 4.585-4.59 s which are almost the same, suggesting that the total energy of HCM changes little during these two time periods. Here we concentrate on the second and the third harmonics, so the pass-band filters are F_1 = 21 - 31 kHz with the centre frequency f_1 = 26 kHz, and F_2 = 35 - 45 kHz with the centre frequency f_2 = 40 kHz, and the low-pass filter is F_3 = 10 kHz. One can notice that in the time period 4.58-4.585 s, the energy flow is from the second harmonic to the third harmonic (the correlation $K(\tau)$ peaks at $\tau> 0$), and the amplitude of second harmonic in the power spectrum is much smaller than the third harmonic. But in the time period 4.585-4.59 s, the energy flow changes its direction, and becomes from the third harmonic to the second harmonic (the correlation $K(\tau)$ peaks at $\tau< 0$). At the same time, the amplitude of the second harmonic in the power spectrum grows up, while the third harmonic amplitude decreases. This means that the energy flow between different harmonics isn't always in the same direction, and can sometimes change its direction, which will redistribute the power of different harmonics.
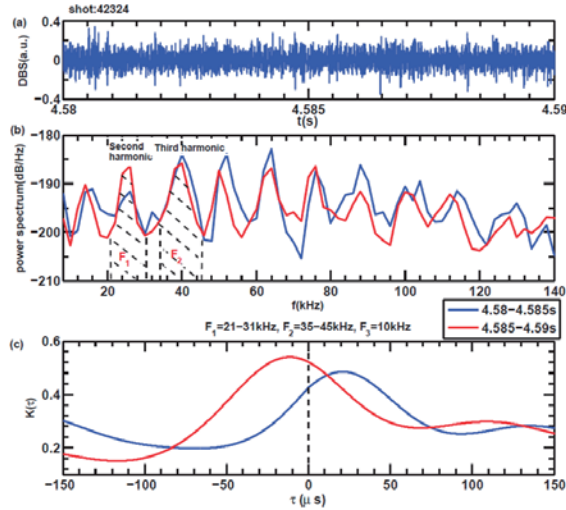
Fig. 5. The energy ow between the second and third harmonics in different periods. The DBS signals (a), the amplitude spectrum of DBS signals (b), and the amplitude correlations of the second and third harmonics (c).

2.3 Turbulence evolution during impurity seed injection
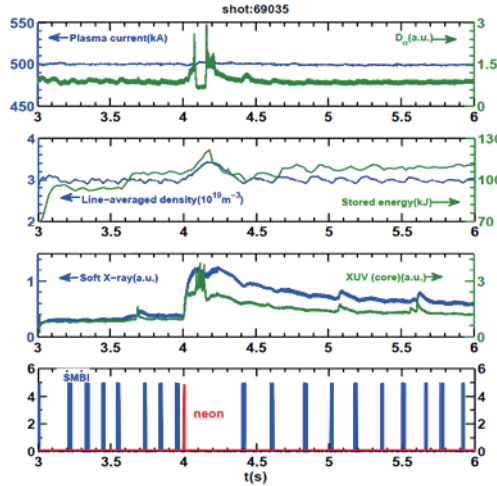
Fig.6. An example of neon seed injection experiments in L-mode.

Fig.6 shows a typical experiment for neon impurity seed injection in L-mode on EAST. We can notice that after neon injection, the line averaged density and the stored energy both show a increasing, while the D_α emission decreases for about 100ms, which suggests that the neon seed injection can improve the confinement in L-mode operation. We calculate the poloidal flow evolution during SMBI(D) and neon injection as shown in Fig.7(a), and one can see that the influence of SMBI(D) and neon on the poloidal flow are quite different: after SMBI(D) the Doppler shift(proportional to the poloidal rotation) increases in the ion diamagnetic drift direction(more positive) at rho~0.97, while after neon injection, the Doppler shift increases in the electric diamagnetic drift direction. A comparison of Er in L-mode, after SMBI(D) and after neon injection is shown in Fig.7(b), and we can see that after SMBI(D) the Er around $\rho=0.97$ becomes more positive while at other locations Er changes little. But after neon injection, the Er becomes more negative at all location inside LCFS.

179

Fig.7. (a) The poloidal flow evolution during SMBI(D) and neon seeding injection, (b) a comparison of E_r in L-mode, after SMBI(D) injection and after neon injection.

References

[1] C. Zhou, A. D. Liu, et al. REVIEW OF SCIENTIFIC INSTRUMENTS 84, 103511 (2013).

Recent progress on hybrid scenario in KSTAR

Youngho Lee, Yong-Su Na and the KSTAR Team

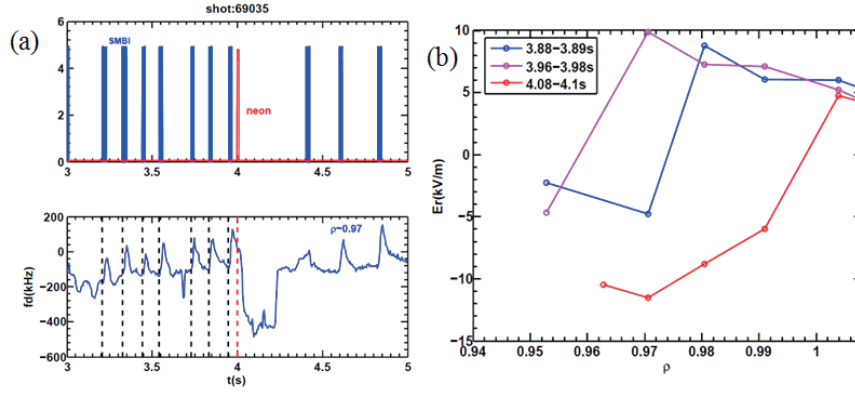Department of Nuclear Engineering, Seoul National University, Korea

Abstract

The recent progress on hybrid scenario in KSTAR is reported. Firstly, the definition of the hybrid scenario in KSTAR is described as $H_{89} > 1.9, \beta_N > 2.2$ sustained longer than $5 \times \tau_E$ at $q_{95} < 6.5$ without or mild sawtooth. Secondly, the characteristics of KSTAR hybrid scenarios are introduced in three perspectives, experimental approaches to access the regime, their categorization by MHD activities, and confinement enhancement against conventional H-modes. Four experimental recipes are used to access the hybrid regime; early heating, plasma current overshoot adjusted early heating, and late heating scenario. The plasma performance shows different properties depending on the type of MHD activities such as fishbone and tearing mode. It is clearly shown that the hybrid scenarios exhibit higher confinement than H-mode according to the KSTAR energy confinement scaling. Lastly, the origin of performance enhancement is investigated. The pedestal enhancement is thought to be the main reason for the confinement improvement with some contribution from core ion heat transport improvement in KSTAR hybrid scenarios.

1. Introduction

The reference scenario of ITER has a typical q-profile of H-mode with central q lower than 1, so sawtooth is expected to occur frequently. Since the sawtooth can seed neoclassical tearing modes (NTMs), the risk of disruption by NTMs is very high in high beta regimes. Therefore, the reference H-mode scenario of ITER must raise the plasma current to obtain a high fusion power gain of Q = 10 at low beta to avoid this risk of disruptions. However, in the 'hybrid' or 'advanced inductive' scenario, q-profile is flat with a central q above 1, so that sawtooth is absent or very small. Therefore, it is possible to maintain a high beta and consequently Q = 10 for longer at lower plasma current than the reference H-mode. Due to this advantage the hybrid scenario has been actively studied in various tokamak devices including KSTAR [1] and included as one of the ITER operation scenarios. In this study, the hybrid scenario in KSTAR is defined based on the conventional features of the hybrid scenario and the characteristics and the performance improvement factors of KSTAR hybrid discharges are studied. In section 2, the detailed process to define hybrid scenario in KSTAR is described. Some characteristics of KSTAR hybrid scenarios are investigated in section 3. In section 4, the origin of the performance enhancement of KSTAR hybrid scenario is studied. A concluding section summarizes and closes the paper.

2. Definition of hybrid scenario in KSTAR

The operation window of hybrid scenario in KSTAR is determined by q_{95}, plasma current (I_P) and sawtooth activities. 445 of H-mode discharges with total neutral beam injection (NBI) power larger than 3.5 MW are plotted in the I_P and q_{95} plane with sawtooth activities in figure 1. Because there are no or very

weak sawtooth activities in hybrid scenario due to flat q-profile ($q_0 \gtrsim 1.0$) as mentioned above, the sawtooth activities present inherently among conventional H-mode discharges. In figure 1, only about 8% of discharges have sawtooth activities with electron cyclotron heating (ECH) sources in the blue window, which means there are no sawtooth activities inherently in the blue window due to larger q_{95} ($\propto B_T/I_P$) and larger I_P with the higher fraction of broad NB current drive. Note that the sawtooth is triggered by central ECH in this regime. On the other hand, about 40% of discharges have sawtooth activities in the red window. ASTRA modelling shows that q(0) goes below unity in this window thus, the red window where sawtooth activities present inherently is the operation windows of hybrid scenario in KSTAR.
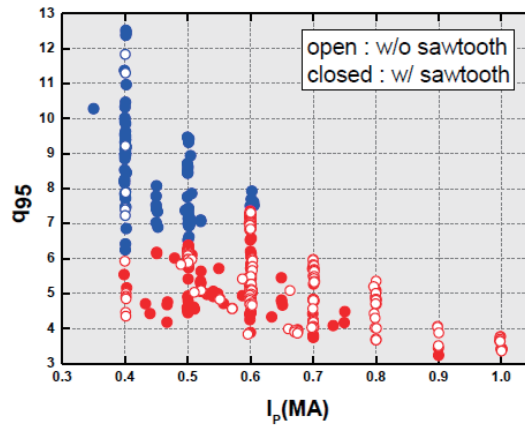
Fig. 1 I_P vs q_{95} plot with sawtooth activities for 445 high heating H-mode discharges in KSTAR

Hybrid scenario in KSTAR is defined as stationary regime with $\beta_N > 2.2$ and $H_{89} > 1.9$ in $q_{95} < 6.5$ without severe sawtooth activities where β_N and H_{89} values are from the real-time equilibrium fitting code, EFIT. Here, the first condition 'stationary' means that the plasma performance factors, β_N and H_{89}, sustain for longer than 5 times of energy confinement time (τ_E) [2]. The second condition in terms of β_N and H_{89} is very important because the discharges of hybrid scenario should have the improved normalized fusion power gain expressed in G-factor ($\equiv \beta_N H_{89}/q_{95}^2$) according to the objective and advantage of the scenario [3]. Due to the strong dependency of G-factor on q_{95}, normalized performance defined as $\beta_N H_{89}$ is also used instead for similar q_{95} discharges. The reference values of β_N and H_{89} refer to the previous study [3] and reflect the fact that the values of the performance factors from the real-time EFIT tend to be 10 % less than the values from the fully iterated EFIT. The third condition, $q_{95} < 6.5$, is from the operation window of hybrid scenario in KSTAR as described. The last condition about no or soft sawtooth activities follows the basic feature of hybrid scenario. As a result, 34 discharges of the black square in figure 2 are classified as hybrid scenario by satisfying this definition in KSTAR.

Fig. 2 H_{89} vs β_N plot with sawtooth activities for the discharges in the red window shown in figure 1 (the operation window of hybrid scenario in KSTAR)

3. Characteristics of KSTAR hybrid scenarios

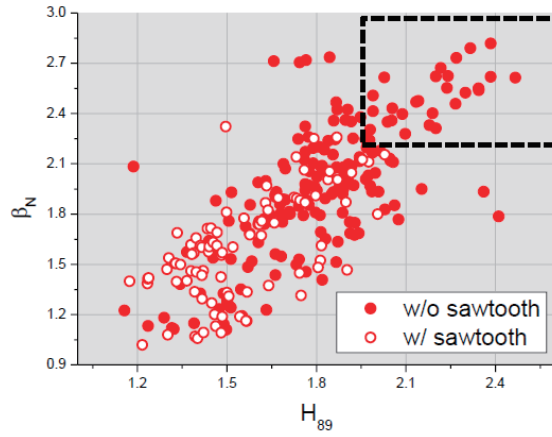Figure 3 shows four experimental approaches to access hybrid regimes in KSTAR. Early heating during the current ramp-up shown in figure 3 (a) has been widely used to obtain hybrid scenario in various tokamak devices [4] and also used for the basic plasma operation scenario in KSTAR. 26 out of 34 hybrid discharges are operated with this approach and transient peaked high performance is usually obtained in the beginning of the high heating phase. The current overshoot recipe shown in figure 3 (b) is used to optimize the magnetic shear profile denoted as s/q in terms of the ITG theory [5]. It has been explored in JET [5] and the early stage of KSTAR project [6]. 1 out of 34 hybrid discharges is operated with this recipe in this database where the main heating is applied after the current overshoot is finalized. The high performance is obtained with 100% non-inductive current drive at the main heating phase but degraded after appearance of the n = 2 mode. Based on the early heating scenario, the main heating time is adjusted to optimize plasma performance as shown in figure 3 (c). 6 out of 34 discharges are operated with this operation scenario where the high performance phase sustains without any harmful MHD modes. In figure 3 (d), full heating is applied in the current flattop phase after the Ohmic current is fully diffused as explored in [4]. 1 out of 34 hybrid discharges is operated with this heating scenario with the similar performance to the adjusted early heating scenario. The safety factor profiles at the high performance phase were taken from MSE-EFIT for figure 3 (c) and 3 (d) which are presented in figure 4 (a) and 4 (b) respectively. Both have flat q profiles around the core and $q_0 \gtrsim 1.0$ exhibiting the typical hybrid scenario feature.

In other tokamaks, hybrid discharges typically have MHD modes such as n = 1 Fishbone or n = 2 NTMs. The hybrid scenarios in KSTAR also exhibit MHD modes and can be classified according to the type of these modes in the plot of the plasma performance and density. Figure 5 (a) shows that the higher normalized performance can be obtained for the hybrid discharges with n = 1 Fishbone, n = 2 mode or no mode in the low density regime. On the other hand, figure 5 (b) presents that the higher G-factor can be obtained with Fishbones in the high density regime. The difference results from the dependency on q_{95}

183

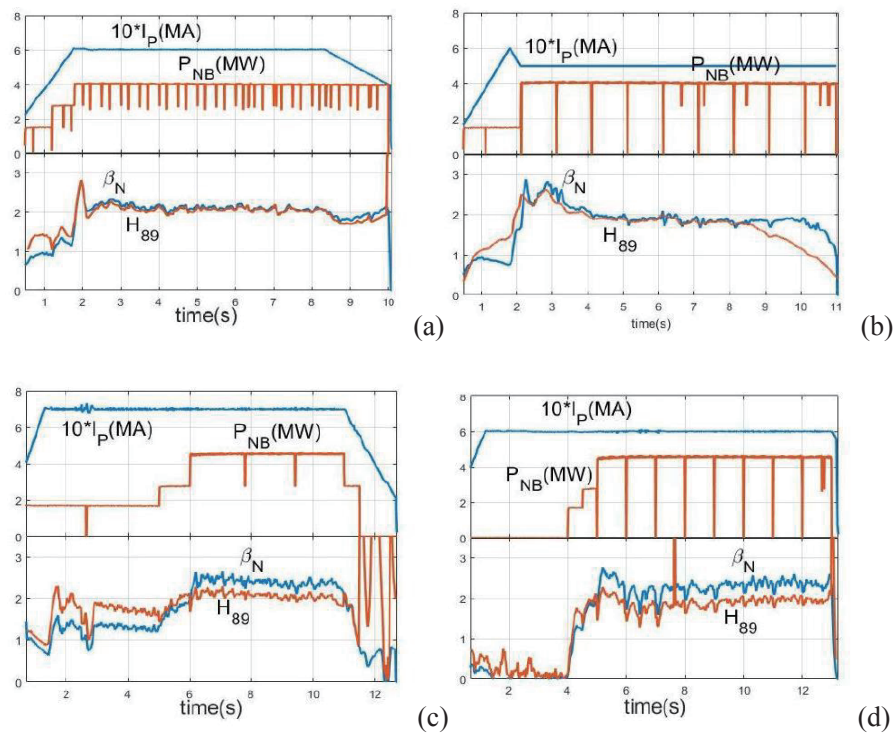Fig. 3 Operation scenario and plasma performance, β_N and H_{89}, plots of 4 experimental approaches
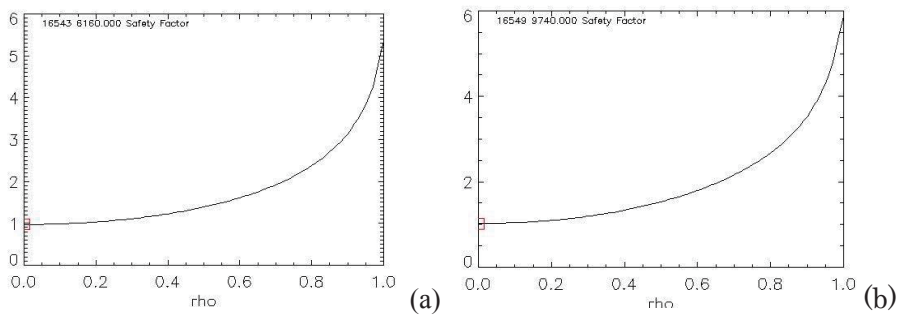
Fig. 4 Safety factor (q) profiles from MSE-EFIT during the high performance phase of figure 3 (c) and (d), respectively
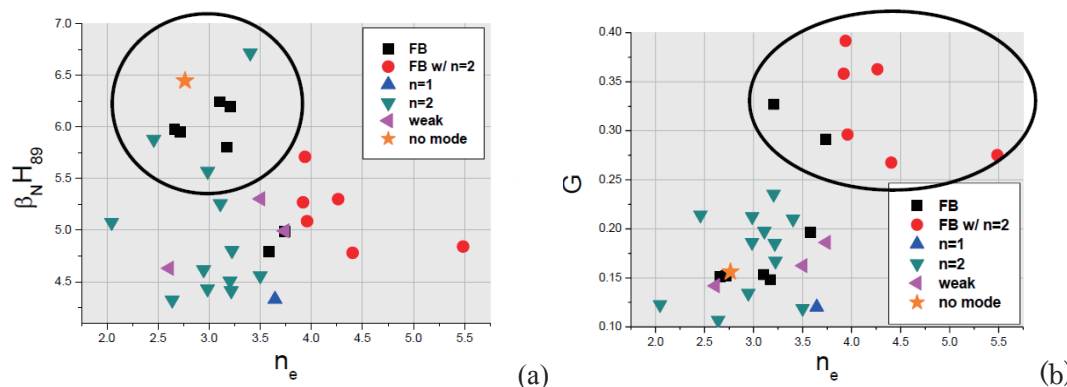
Fig. 5 Performance factors ($\beta_N H_{89}$ and $G \equiv \beta_N H_{89}/q_{95}^2$) vs average density plot with MHD modes at high performance phase of hybrid discharges

Like the hybrid scenarios in other tokamaks, the KSTAR hybrid discharges also tend to have larger energy confinement time than that of conventional H-mode discharges. The H-mode energy confinement time scaling in KSTAR, $\tau_{E,KSTAR,H-mode\ scaling} = 0.793\kappa^{-0.68}I_P^{1.41}B_T^{-0.29}P_L^{-0.69}$ [7] which was derived by including dataset of high beta plasmas, is used to estimate the energy confinement of hybrid discharges. In figure 6, the hybrid discharges shown in red tend to be located above the scaling clearly but, the other H-mode discharges in black spread evenly around it. This implies the hybrid discharges exhibit higher energy confinement than that of standard H-modes in KSTAR.
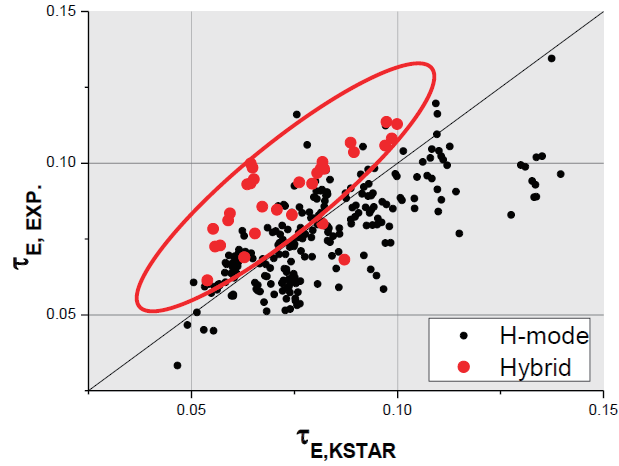
Fig. 6 Experimental energy confinement time of hybrid discharges (red) and H-mode discharges (black) presented in figure 2
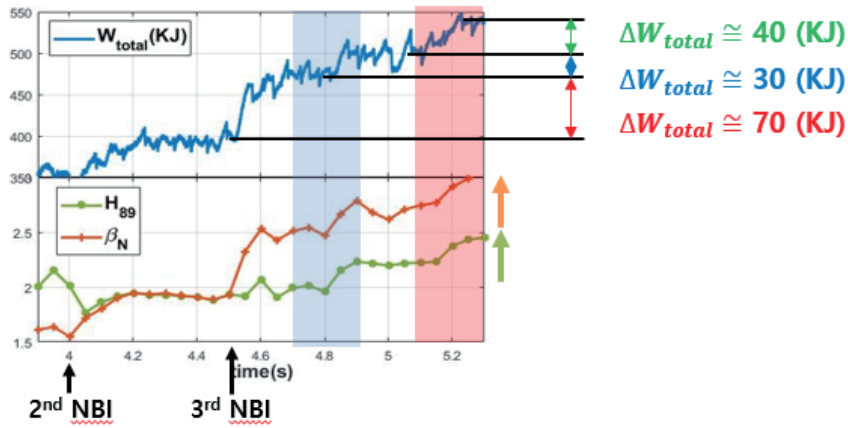
Fig. 7 Time evolution of W_{total}, H_{89} and β_N of #16545 where delayed performance improvement is indicated with the blue and red box

4. Analysis of performance improvement

The origin of improved performance of the hybrid discharges is investigated. Figure 7 shows an example of the adjusted early heating scenario with n = 1 Fishbone (#16545) where β_N increases after each 2nd and 3rd NBI is injected but, H_{89} does not increase. However, delayed performance improvements of β_N, H_{89} and W_{total} (total plasma stored energy) occur at 4.8 s and 5.2 s after the 3rd NBI.
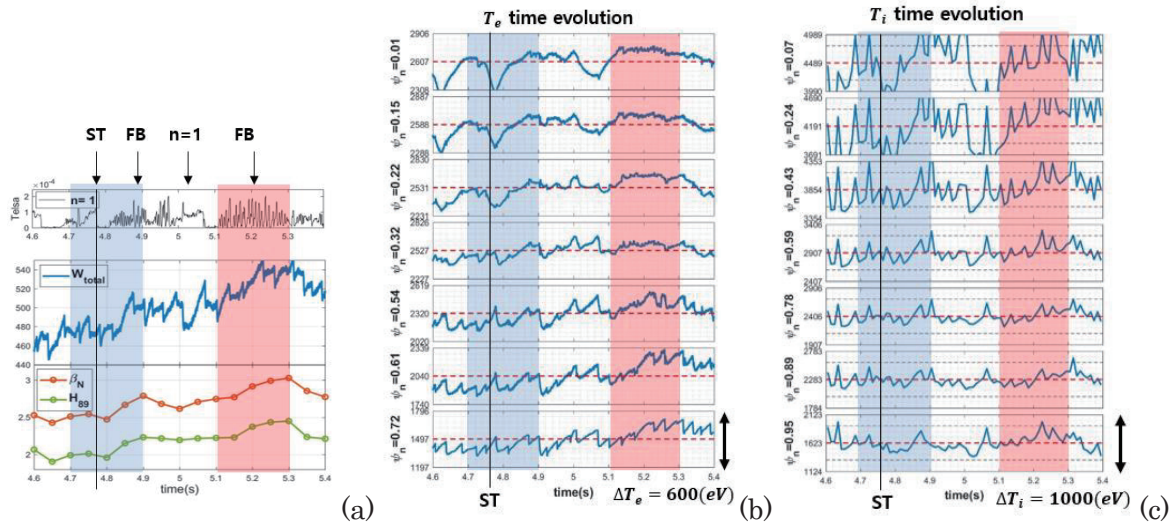
Fig. 8 (a) time evolution of n=1 mode amplitude, W_{total}, β_N and H_{89} (b) time evolution of electron temperature at 7 radial positions (c) time evolution of ion temperature at 7 radial positions
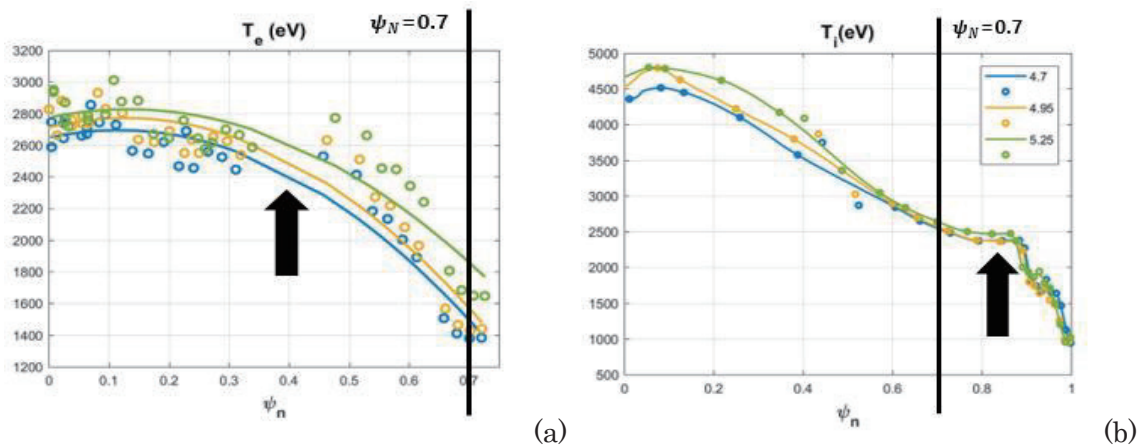
Fig. 9 Changes in (a) electron temperature profiles and (b) ion temperature profiles during the delayed performance improvements

To find the origin of these delayed performance improvements, time evolution of 7 radial positions of the electron (T_e) and ion (T_i) temperature is compared with total plasma stored energy in figure 8. They are from electron cyclotron emission (ECE) diagnostics and charge exchange spectroscopy (CES), respectively and the total plasma stored energy is from the diamagnetic loop signal. It is clearly seen that the increase of W_{total} accompanies the increase of outer T_e in both the blue and red time window. The core T_e is increased via the stiffness. In the red window, the increase of core T_i begins to contribute to the performance improvement. Comparing evolutions of T_e and T_i profiles with W_{total} shows the trend more clearly in figure 9.

186
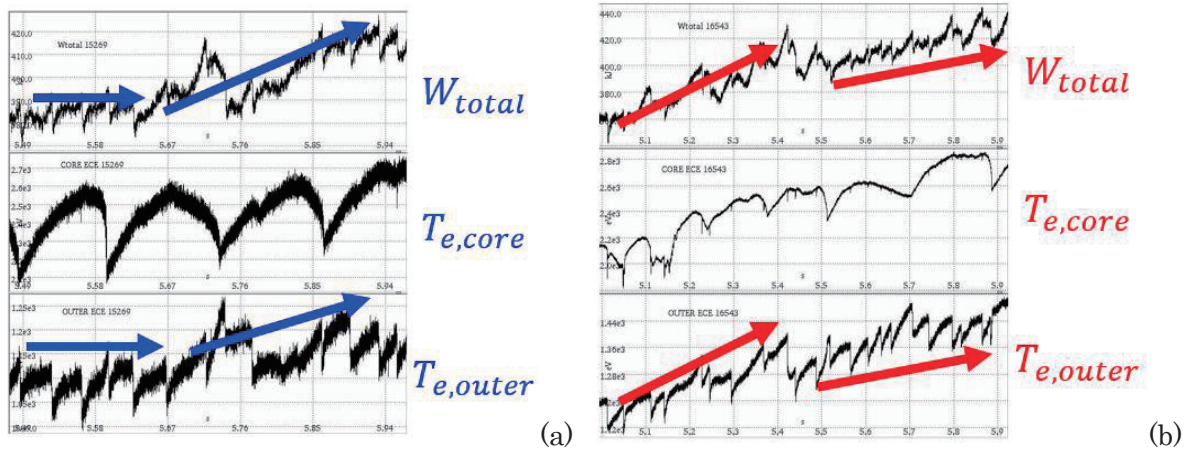
Fig. 10 Time evolution of W_{total}, core T_e and outer T_e during the performance improvement in #15269 (a) and #16543 (b)
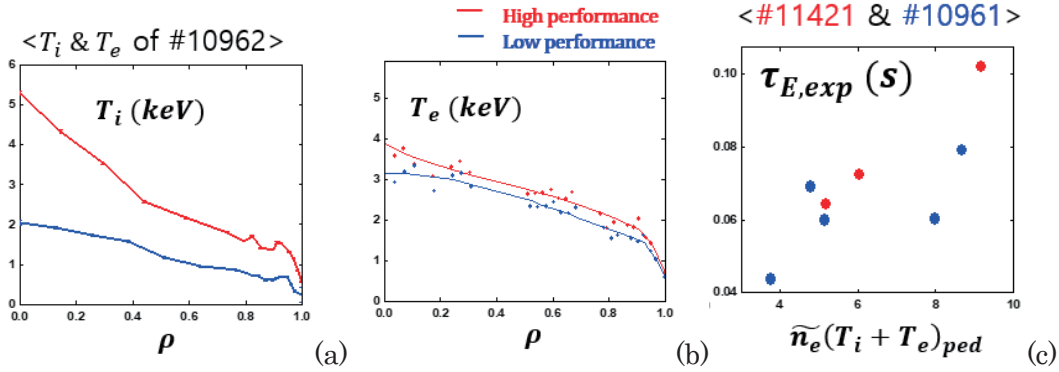
Fig. 11 (a), (b) ion and electron temperature profiles between high and low performance in #10962, (c) relationship between pedestal height and energy confinement time in #11421 and #10961

Figure 10 shows the delayed confinement improvement accompanying increase of outer T_e in other hybrid discharges, #15269 and #16543. Figure 11(a) and (b) show comparison of T_e and T_i profiles between high and low performances in #10962 and figure 11(c) shows the relationship between the experimental confinement time ($\tau_{E,EXP}$) and the pedestal height. As a result, the confinement improvement of the hybrid discharges mainly results from the pedestal enhancement of T_e or T_i as reported in [1] and ASDEX Upgraded [8] together with slight core ion heat transport improvement probably due to fast ions [9].

5. Conclusion

The operation window of hybrid scenario is determined as $q_{95} < 6.5$ by investigating the inherent presence of sawtooth activities of 445 H-mode discharges in KSTAR. Based on the operation window and characteristics of hybrid scenario, the hybrid scenario in KSTAR is defined as stationary $\beta_N > 2.2$ and $H_{89} > 1.9$ in $q_{95} < 6.5$ without severe sawtooth activities. 34 discharges satisfying this condition are classified as hybrid scenarios in KSTAR. The KSTAR hybrid discharges are obtained with four different experimental approaches but can be categorized by their MHD activities and the subsequent confinement property. The origin of improved performance is studied and improved pedestal of electron or ion temperature

is thought to be the main factor with some contribution from core ion heat transport improvement. The cause of pedestal enhancement is still under investigation.

References

[1] Na, Yong-Su, IAEA TM SSO, Nara, Japan (2015)

[2] Luce, T. C., et al., Nuclear Fusion 54.1 (2013): 013015

[3] Luce, T. C., et al., Nuclear Fusion 45.6 (2005): 407

[4] Stober, J., et al., Nuclear Fusion 47.8 (2007): 728.

[5] Hobirk, J., et al., Plasma Physics and Controlled Fusion 54.9 (2012): 095001

[6] Byun, C.S., Currnet Appl. Phys. 1414 (2014)

[7] Kim, H-S., et al., Nuclear Fusion 54.8 (2014): 083012

[8] Na, Yong-Su, et al., Nuclear Fusion 46.2 (2006): 232

[9] Citrin, Jonathan, et al. Physical review letters 111.15 (2013): 155001

Analysis of impurity transport at different magnetic configurations in LHD based on impurity pellet injection and space-resolved EUV spectroscopy

X. L. Huang[1], S. Morita[1,2], T. Oishi[1,2], M. Goto[1,2] and Y. Liu[2]

[1]National Institute for Fusion Science, Toki 509-5292, Gifu, Japan

[2]Graduate University for Advanced Studies, Toki 509-5292, Gifu, Japan

Abstract

Radial profiles of Fe n = 3–2 L_α transition array consisting of emissions from ionization stages of Ne-like Fe^{16+} through Li-like Fe^{23+} ions are simultaneously measured in the LHD by a space-resolved extreme ultraviolet (EUV) spectrometer working in the wavelength range of 10-130 Å. To analyze the measured Fe L_α transition array the one-dimensional impurity transport calculation is carried out with photon emissivity coefficients, electron temperature and density profiles and Fe density profiles assuming the radial structure of transport coefficients, i.e. diffusion coefficient and convective velocity. All peaks in the measured spectrum have been well identified and the radial density profiles of Fe^{16+} through Fe^{23+} ions are derived as a function of the transport coefficients. The impurity transport in neutral-heated discharges with hollow n_e profiles is then compared among three different magnetic configurations of R_{ax} = 3.6 m, 3.75 m and 3.9 m. It is found that the convective velocity is significantly affected by the density gradient of bulk ions, while the diffusion coefficient is entirely anomalous, especially in the edge region. As a result, a largest outward convective velocity is observed in core plasmas inside ρ= 0.7 at R_{ax} = 3.6m configuration.

1. Introduction

Radial transport of impurity ions still remains an important subject in magnetically confined fusion devices, since the plasma performance is entirely affected by the radiation loss and fuel dilution caused by the impurity. In particular, it is an urgent issue to control the influx of heavy impurities because the use of tungsten has been decided for the armor material of the ITER divertor [1, 2]. In a big-size fusion device like ITER, on the other hand, the electron density tends to have a flat profile. In the LHD a variety of density profiles, e.g. hollow, flat and peaked, are formed which are extremely unique compared with those in tokamaks. Therefore, the LHD plasmas give a good opportunity for studying the impurity transport through analysis of the radial structure in the transport coefficient, in particular, in relation to the density and temperature gradients. Analysis on the detail structure of transport coefficients is essential for understanding the radial transport. In addition, the impurity transport could also depend on the magnetic configuration. When the position of magnetic axis changes, the helical ripple varies and thus affects the neoclassical transport. Comparison of the impurity transport coefficients among different magnetic axis configurations is then useful to clarify the contribution of the neoclassical and anomalous transports to the radial impurity flux.

2. Experimental setup

A space-resolved extreme ultraviolet (EUV) spectrometer used in the present study works in the wavelength range of 10 - 130 Å and mainly consists of an entrance slit, a spatial-resolution slit, a gold-coated concave varied-line-spacing (VLS) laminar-type holographic grating with a groove density of 2400 per mm and a charge-coupled device (CCD) detector with 1024×255 pixels (26 μm $\times$ 26 μm/pixel). The EUV spectrometer is installed on a mid-plane port at the backside of a rectangular vacuum extension chamber.   The elevation angle of the central viewing chord is exactly aligned to measure the upper half of the elliptical LHD plasma, i.e. Z = 0–50 cm.   Details of the spectrometer can be seen in reference [3].

3. Analysis of Fe n = 3–2 L_α transition array

Based on the observation of Fe n = 3–2 L_α transition array, radial profiles of total iron density are analyzed in two discharges with peaked or hollow n_e profiles.   The central iron density at the hollow n_e profile is found to be at least an order of magnitude smaller than that at the peaked n_e profile over a wide range of electron densities in the LHD [4].   The detailed result on the spectral analysis of Fe L_α transition array is described in this paper.

A lot of Fe L_α transitions from highly ionized Fe ions are observed in the spectrum.   Since the Fe lines are blended with other Fe lines at several wavelength intervals, the spectrum sometimes is appeared like a pseudo-continuum structure in the wavelength range of 11-16 Å.   Therefore, it is necessary to clarify the composition of each peak in the spectrum.   Figure 1 shows an example of theoretically predicted spectral lines (solid lines) of Fe XVII through Fe XXIV.   In this calculation, it is assumed that the radial profile of total Fe density, n_{Fe} (r), is similar to the electron density profile, n_e (r), i.e. n_{Fe} (r) = 10^{-3} n_e (r).   Here, the ion fractions are calculated with Chianti database in collisional ionization equilibrium [5]. The photon emissivity coefficients (PEC) of the Fe n = 3–2 L_α transition array are calculated by HULLAC code [6].   The local emissivity of the Fe L_α transitions can be derived after Abel inversion based on magnetic surfaces provide by the VMEC code [7].   Considering the spectral resolution of the spectrometer, the theoretical line-integrated spectrum is thus obtained in the calculation.   In Fig. 1 the synthetic spectrum obtained by adding each theoretical spectral line and the experimental spectrum measured at t = 4.3s in shot #124864 with the space-resolved spectrometer.   The wavelengths of spectral intensity peaks agree well between the calculation and experiment.   The intensity peaks for calculating the density profile of iron ions in an ionization stage are as follows; Fe XVII at 17.07 Å, 16.78 Å and 15.02 Å; Fe XVIII at 15.61 Å and 14.32 Å; Fe XIX at 14.72 Å and 13.50 Å; Fe XX at 12.81 Å; Fe XXI at 12.30 Å (blended with Fe XXII and Fe XXIII); Fe XXII at 11.80 Å (blended with Fe XXIII); Fe XXIII at 10.92 Å (blended with Fe XXIV); Fe XXIV at 11.18 Å and 10.62 Å.   Since the intensity peaks of Fe XXI, Fe XXII and Fe XXIII are blended with other lines in higher ionization stage, the density profiles of Fe^{20+} through Fe^{23+} ions are necessary for the consideration of multiple ionization stages.

In order to calculate the absolute value of Fe density profiles, the intensity calibration is essential. The calibration was done based on comparison of radial profiles between EUV and visible bremsstrahlung continua.   In the range of 10-18 Å of Fe n = 3–2 L_α transition array, however, there are only a few wavelength intervals without line radiations.   It may cause certain uncertianty in the calibration. Therefore, the calibration factor obtained in this wavelength range requires a cross-checking with another
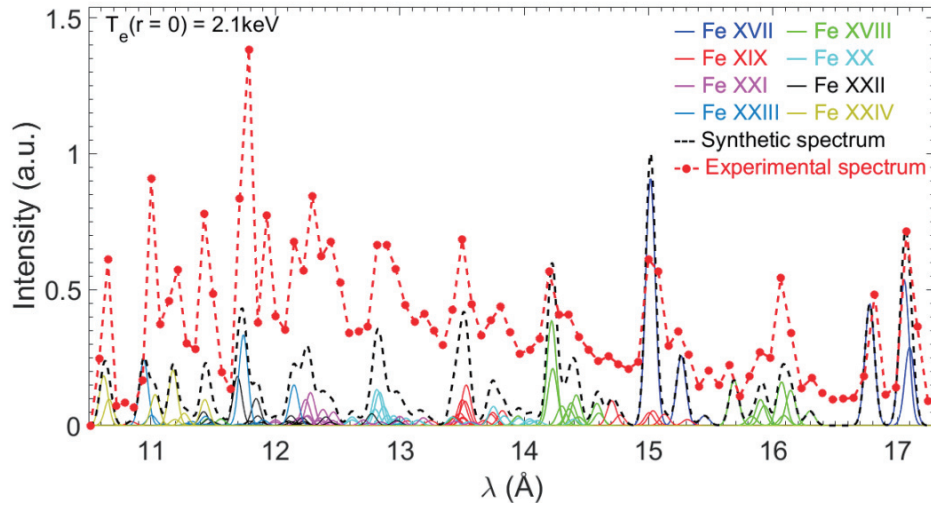
Fig.1 Single-ionization-stage spectra (solid lines) of Fe XVII through Fe XXIV calculated based on PEC data, T_e and n_e profiles, an assumed Fe density profile and assumed ionization equilibrium; the synthetic spectrum (dash line) obtained by combination of the single-ionization-stage spectra and experimental spectrum (dot-dash line) measured at t = 4.3s in shot #124864.
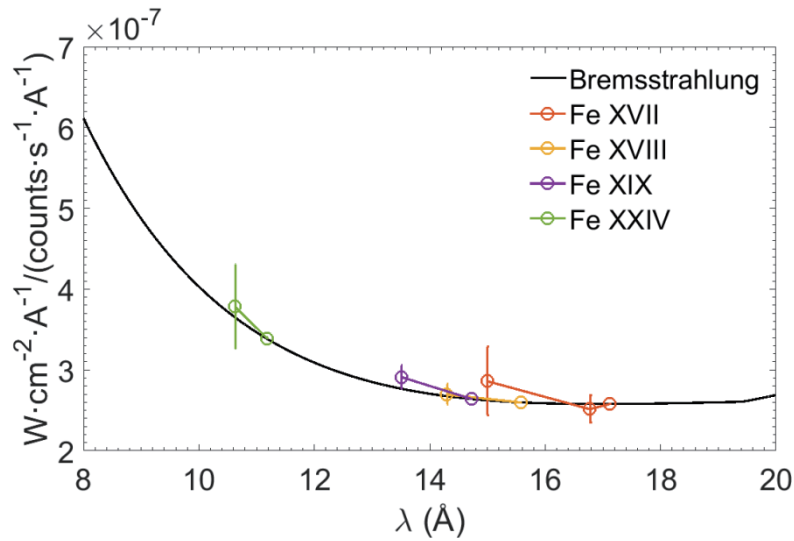
Fig.2 Calibration curve obtained with the bremsstrahlung method (solid line) and calibration factors (open symbols) derived from intensity ratios of Fe emissions on the same ionization stage in shots #124864, #124891 and #125727- #125770.

method.　Here, the intensity ratios between two Fe emissions in the same ionization stage are utilized for the alternative calibration.

　　Two or more spectral intensity peaks in the same ionization stage are chosen at different wavelength intervals and the radial profiles at those intensity peaks are reconstructed into the radial emissivity profiles. Then, a relative calibration factor can be obtained from such emissivity profiles considering the line intensity ratio.　In order to compare with the original calibration factor based on the bremsstrahlung measurement the relative intensity calibration factor is normalized to the original intensity calibration curve.

The result is plotted in Fig. 2 for Fe XVII, Fe XVIII, Fe XIX and Fe XXIV. The relative calibration factors show a good agreement with the original calibration curve within their error bars. The calibration curve used in the present study is thus well verified.

Based on the analysis of Fe n = 3–2 L_α transition array and the calibration coefficients, the density sum of Fe $^{16+}$ through Fe $^{23+}$ ions are calculated. The sum of the ion fractions of these ionization stages is close to unity in the T_e range of 300 eV to 1300eV. Therefore, the density sum of these ionization stages equals to the total Fe density integrated from the plasma edge to the vicinity of plasma center. The Fe^{24+} ions also exist near the plasma center in the cases of $T_e > 1.3$ keV. Nevertheless, we can use the ion fraction data in the equilibrium to evaluate the Fe^{24+} ion density and then calculate the total density of Fe ions because the transport near the plasma center is not so large. Figure 3 shows ratios of total Fe densities between plasma core and edge, so called peaking factor defined as n_{Fe} (ρ=0.3) / n_{Fe} (ρ =0.8), against the peaking factor of electron densities, n_e (ρ=0.3) / n_e (ρ =0.8), for three magnetic configurations of R_{ax} = 3.6m, 3.75m and 3.9m. The Fe density profile changes from hollow to peaked, when the n_e peaking factor increases.
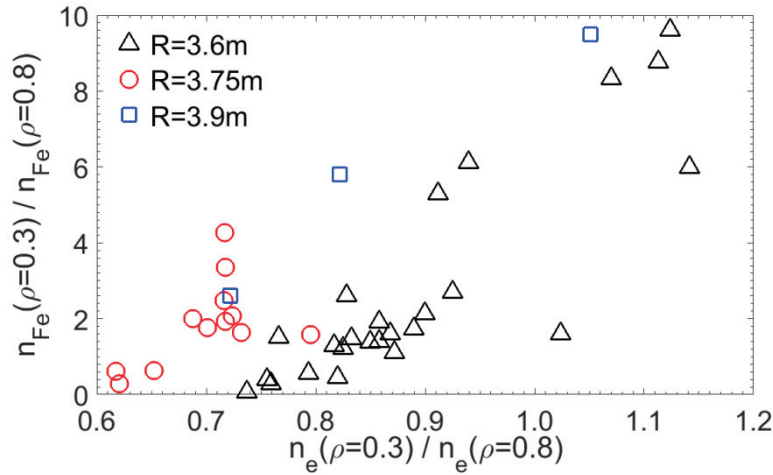
Fig.3 Shape factor of the total Fe density profile, defined as n_{Fe} (ρ=0.3) / n_{Fe} (ρ =0.8) against that of electron density in three magnetic configurations with R_{ax} = 3.6m, 3.75m and 3.9m.

4. Impurity transport analysis at different R_{ax}

A one-dimensional impurity transport code is employed to determine the transport coefficient [8]. It is assumed that the impurity ions satisfy the following equations of transport and continuity.

$$\Gamma_I^K = -D\frac{\partial n_I^K}{\partial r} + V n_I^K \tag{1}$$

$$\frac{\partial n_I^K}{\partial t} = -\frac{1}{r}\frac{\partial}{\partial r} r\Gamma_I^K + n_e\left[S_I^{K-1}n_I^{K-1} - \left(S_I^K + \alpha_I^K\right)n_I^K + \alpha_I^{K+1}n_I^{K+1}\right] \tag{2}$$

where $\Gamma_I^K, n_I^K, D, V, S_I^K$ and α_I^K are the particle flux, the ion density, the diffusion coefficient, the convective velocity, the ionization rate coefficient and the recombination coefficient of impurity ions in the Kth ionization stage, respectively. Positive values of V stand for outward and inward convection.

With given transport coefficients and radial profiles of plasma parameters, the code yields the impurity

ion density profile in all ionization stages as a function of time. The transport coefficient near the emissivity peak can be determined by comparing the emissivity profile between the experiment and the simulation. In order to determine the transport coefficient at the whole plasma radius, the iron emission is simultaneously analyzed in several ionization stages. The minimization of deviation between measured and simulated impurity profiles and time evolution of Fe emissions can determine the transport coefficient profile.

Previous analysis [4] shows that the diffusion coefficient increases with increasing minor radius. This could explain the longer confinement time in the plasma center. On the other hand, an outward convective velocity obviously exists in the core plasma region at $\rho < 0.7$. The convective velocity changes from outward to inward at certain radial plasma location in the peripheral region where the density gradient changes the sign, i.e. from positive to negative. This suggests the convective velocity is correlated with the density gradient.

An impurity pellet injection experiment has been carried out in the LHD for comparison of iron impurity transport at different magnetic axis positions of R_{ax} = 3.6m (inward shifted configuration), 3.75m (standard configuration) and 3.9m (outward shifted configuration) with magnetic field of B_t = 2.5-2.7T.

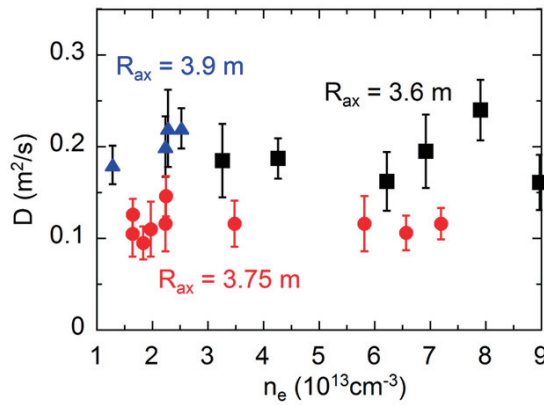Fig. 4 Diffusion coefficient at ρ= 0.5 as a function of density for the cases of R_{ax} = 3.6 m (squares), 3.75 m (circles) and 3.9 m (triangles).
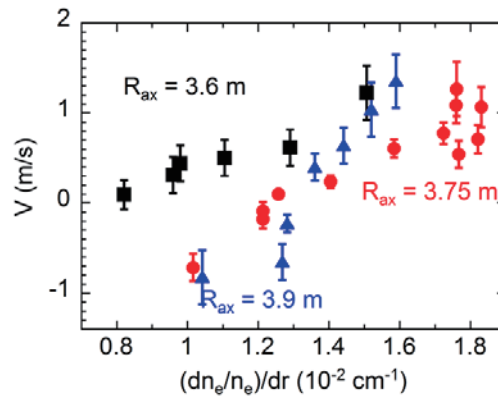

Fig. 5 Convective velocity at ρ= 0.5 as a function of density for the cases of R_{ax} = 3.6 m (squares), 3.75 m (circles) and 3.9 m (triangles).

Transport coefficients at $\rho = 0.5$ at hollow density profiles are compared among the three magnetic configurations. Figure 4 shows the diffusion coefficient D as a function of electron density. The diffusion coefficient has the smallest value at $R_{ax} = 3.75$ m, whereas the neoclassical theory predicts the smallest particle transport at the inward shifted configuration ($R_{ax} = 3.6$ m). This suggests an important role of anomalous transport. Figure 5 shows the convective velocity as a function of normalized density gradient ((dn_e/n_e)/dr) because the convection strongly depends on the density gradient in the LHD as discussed above. The convective velocity can be zero or negative at the normalized density gradient below a threshold value. This threshold seems to be larger at $R_{ax} = 3.75$ m and $R_{ax} = 3.9$ m. Overall the convection is most positive, i.e. outward-directed, at $R_{ax} = 3.6$m. This result of the convective velocity could well explain the difference in the peaking factor of Fe density in the three magnetic configurations as shown in Fig. 3.

6. Summary

The radial profiles of Fe n = 3–2 L_{α} transition are measured in the LHD by a space-resolved EUV spectrometer. The spectral structure of the measured Fe L_{α} transition array is analyzed with threoretically predicted synthetic spectrum calculated with PEC data and experimental parameters. For crosschecking the original calibration curve obtained from the bremsstrahlung, the intensity ratio method is used. As a result, the original calibration factor can be well verified by the intensity ration method.

With help of a transport code, the transport coefficients are obtained analyzing radial profiles of Fe L_{α} transition array. The diffusion coefficient is found to be smallest at $R_{ax} = 3.75$ m in contrast with the prediction of $R_{ax} = 3.6$ m. The convective velocity increases with increasing normalized density gradient. In general, the n_{Fe} profile is hollower at R_{ax}=3.6m than those at R_{ax}=3.75m and 3.9m, corresponding to a larger outward convection velocity when the n_e profile is hollow.

References

[1] Pitts R.A. *et al*. 2009 Phys. Scr. **2009** 014001.

[2] Philipps V. 2011 Journal of Nuclear Materials **415** S2.

[3] X. L. Huang *et al.* 2014 Rev. Sci. Instrum. **85** 11E818.

[4] X. L. Huang *et al.* 2017 Nucl. Fusion **57**086031.

[5] Del Zanna et al., 2015 Astronomy & Astrophysics **573**, A104.

[6] A. Bar-Shalom *et al.* 2001 J. Quant. Spectrosc. Radiat. Trans., **71**, 169.

[7] K. Yamazaki 2003 J. Plasma Fusion Res. **79**, 739.

[8] T. Amano, J. Mizuno, and J. Kako, 1982 Simulation of impurity transport in tokamak, Int. Rep. **IPPJ-616**, Institute of Plasma Physics, Nagoya University.

Determination of tungsten ion density in LHD using unresolved transition array at 27-34 Å

Y.Liu[1], S.Morita[1,2], T.Oishi[1,2], I.Murakami[1,2], M.Goto[1,2], X.L.Huang[2] and H.M.Zhang[1]

[1]Graduate University for Advanced Studies, Toki 509-5292, Gifu, Japan

[2]National Institute for Fusion Science, Toki 509-5292, Gifu, Japan

Abstract

Vertical profiles of tungsten emission lines are measured with a space-resolved EUV spectrometer working in wavelength range of 10-130 Å. The observation range is roughly 0.55 m which corresponds to half of the vertical plasma diameter at horizontally elongated plasma cross section. A series of experiments on the tungsten spectroscopy are conducted in Large Helical Device (LHD) by injecting a tungsten pellet to investigate an evaluation method of tungsten ion density. In LHD, until now, ion charge state distribution of the tungsten unresolved transition array (UTA), from which the emissions are useful for the tungsten diagnostic in edge plasmas of ITER, have been examined by analyzing the emission intensity as a function of central electron temperature and by comparing the vertical intensity profile with the electron temperature profile. As a result, it is found that the tungsten UTA lines at wavelength interval of 32.16-33.32 Å consist of a single ionization stage of W^{24+}. The ADAS database is used for excitation rates of W^{24+} emission lines at this wavelength interval. A tungsten density profile at 32.16-33.32 Å is thus obtained with the local emissivity profile reconstructed from the vertical intensity profile based on measured electron density and temperature profiles.

1. Introduction

In next-generation fusion device, ITER (International Thermonuclear Experimental Reactor), the material of plasma-facing components (PFCs) must have a good capability of tolerating extremely large thermal heat load, in addition to lower erosion and tritium retention rates. For this request, the tungsten with extremely high melting point is adopted for divertor material of ITER instead of carbon material which has been used for many years in toroidal devices [1, 2]. However, the radiation loss from tungsten ions is extremely large compared to that from carbon ions. Once the tungsten concentration exceeds a certain level, the huge radiation loss from tungsten ions leads to a drastic degradation of the plasma performance. Therefore, the tungsten density, n_w, in ITER must be maintained at a low level against the electron density, n_e, e.g. $n_w/n_e < 10^{-5}$ [3]. The tungsten transport study is then important for controlling the impurity accumulation in the plasma core and enhancing the impurity screening in the plasma edge. In LHD, tungsten spectra and vertical intensity profiles have been observed in extreme ultraviolet (EUV) wavelength range by injecting a coaxial graphite pellet included a thin tungsten wire [4]. Use of a traditional laser-blow-off method seems to be difficult in LHD, because a thick stochastic magnetic field layer exists outside the core plasma [5]. The tungsten density profile analysis is then attempted from the local emissivity profile reconstructed from the vertical intensity profile measured at 27-34Å in the tungsten

UTA spectra, of which the wavelength interval consists of line emissions from a single tungsten ionization stage of W^{24+}. The analysis is carried out with the ADAS database based on measured electron density and temperature profiles.

2. Experimental setup

A space-resolved EUV spectrometer, EUV_Short2 [6], is installed on #10-O port of LHD for measuring the spatial distribution of impurity line emissions in the wavelength range of 10-130 Å. A schematic diagram of the spectrometer arrangement is shown in Fig. 1. The optical axis of the spectrometer is perpendicular to the toroidal magnetic field. The spectrometer is composed of an entrance slit, a spatial resolution slit placed in front of the entrance slit, a gold-coated concave varied-lines-spacing (VLS) laminar-type holographic grating and a back-illuminated charge-coupled device (CCD) detector. Since a long distance between the spectrometer and the plasma is necessary for observing the vertical plasma range of 50 cm, which corresponds to half diameter at short axis of the elliptical LHD plasma, the spectrometer entrance slit is placed at 9.457 m away from the plasma center of $R_{ax} = 3.6$ m. The CCD has an effective area of 26.6×6.6 mm^2 with the total number of pixels of 1024×255 (26×26 μm^2/pixel). The vertical profile and spectrum are recorded along the CCD long and short axes, respectively. The CCD detector is operated in two readout modes of full resolution image and sub-image. The full resolution image mode which can yield the best spectral resolution is used only for the spectral resolution test and the line identification because the necessary exposure time is very long. The sub-image mode is used for routine measurement on the impurity profile. A sub-image mode with 204×127 channels is usually used by summing up five adjacent pixels in long axis and two adjacent pixels in short axis. The spectra of impurity emissions are thus obtained with exposure time of 61.5 ms and resultant sampling time of 100 ms. The spectral intensity measured with EUV spectrometers is absolutely calibrated on the basis of simultaneous profile measurements of bremsstrahlung continua in EUV and visible ranges. The vertical observation range of EUV_Short2 is fixed to the observation of upper half plasma ($0 \leq Z \leq 50$ cm).
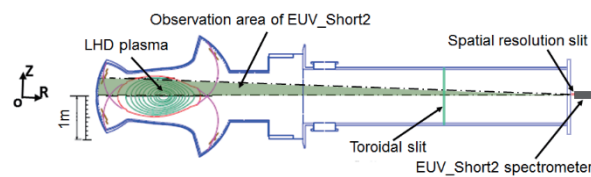
Fig. 1. Side view of space-resolved EUV_Short2 spectrometer.

3. Experimental results

A. Typical discharge with tungsten pellet injection

A series of experiments on tungsten UTA spectroscopy have been carried out in LHD with tungsten pellet injection to find a practical evaluation method of the tungsten ion density. Ion charge state distribution in the tungsten UTA spectrum has been carefully examined in wavelength range of 27-34 Å. The tungsten density has to be analyzed at certain wavelength interval of tungsten UTA which consists of a

single ionization stage.   A typical discharge with tungsten pellet (tungsten wire: 0.05 mm in diameter $\times$ 0.7 mm in length; graphite cylinder: 0.7 mm in diameter $\times$ 0.7 mm in length) injected at horizontal mid-plane is shown in Fig. 2.   A stable discharge is maintained during 4.2-5.0 s by two negative-ion-source-based neutral beams (n-NBI#2 and #3) with injection energy of 180 keV.   A tungsten pellet is injected at t = 4.03 s.   The line-averaged electron density, n_e, quickly increases just after the pellet injection, and also continuously increases with slow rate during the whole n-NBI phase after the pellet injection.   The central electron temperature, T_{e0}, starts to gradually decrease after 0.15 s of the pellet injection.   The total radiation power, P_{rad}, keeps a constant level during the n-NBI phase except for the initial phase of the pellet injection.   The plasma stored energy increased after the pellet injection also starts to decrease after 0.1 s of the pellet injection due to a reduction of edge temperature.
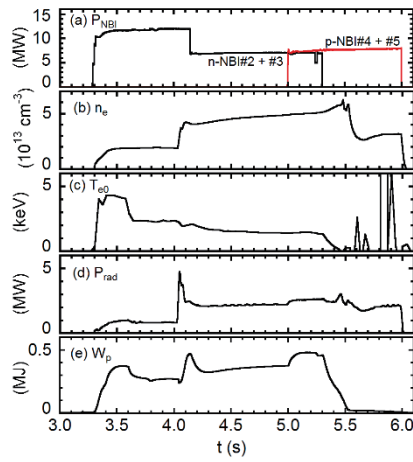
Fig. 2. Discharge waveform with tungsten pellet injected at 4.03 s; (a) NBI input power, (b) line-averaged electron density, (c) central electron temperature, (d) total radiation power and (e) plasma stored energy.
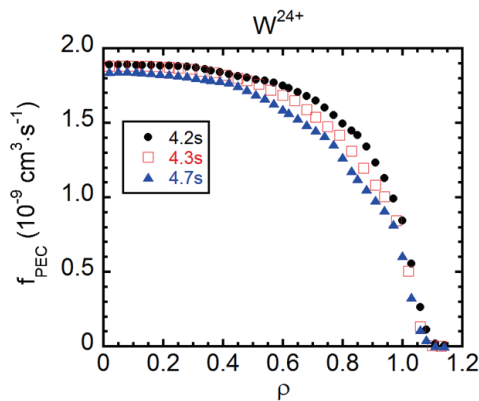
Fig. 3. Photon emission coefficients of W^{24+} at T_{e0}=1.93 (4.2s), 1.70 (4.3s) and 1.45keV (4.7s).

B. Calculation of photon emission coefficients

Based on electron temperature and density profiles measured by Thomson diagnostic, the photon emission coefficient, f_{PEC}, is calculated using the ADAS code.   In Fig. 3, the photon emission coefficients

of W^{24+} at wavelength interval of 32.16-33.32 Å are plotted at t = 4.2, 4.3 and 4.7 s of the discharge shown in Fig. 2 with closed circles, open squares and closed triangles, respectively. The photon emission coefficient at outer plasma positions of $0.45 \leq \rho \leq 1.0$ largely decreases, while the coefficient at inner plasma positions of $\rho < 0.45$ decreases only a little, mainly reflecting a change in the electron temperature profile. The tungsten UTA spectrum observed with EUV_Short2 spectrometer is shown in Fig. 4 with solid line. Photon emission coefficients at 27.20-27.62 (W^{28+}), 28.38-28.70 (W^{27+}), 29.36-30.47 (W^{26+}), 30.69-31.71 (W^{25+}) and 32.16-33.32Å (W^{24+}) calculated by ADAS code are shown in black hatched regions.
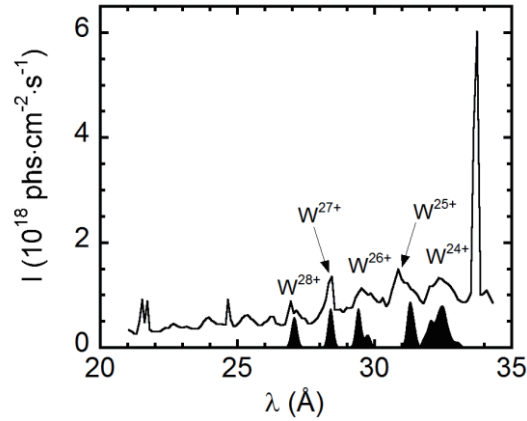
Fig. 4. Tungsten UTA spectrum observed with EUV_Short2 (solid line) and photon emission coefficients calculated by ADAS code (black hatched region).

C. Error estimation of Abel inversion method

Abel inversion method is applied to reconstruct the local emissivity profile from the measured vertical intensity profile under the assumption that the local emissivity is uniform along each magnetic surface. The necessary magnetic surfaces are calculated with three-dimensional equilibrium code, Variational Moments Equilibrium Code (VMEC). The local emissivity profile is expressed by the following matrix:

$$\varepsilon(\rho) = L^{-1}I(Z), \tag{1}$$

where ε, L and I are the local emissivity profile [photons·cm^{-3}·s^{-1}], matrix of chord length [cm] and vertical intensity profile [photons·cm^{-2}·s^{-1}], respectively.

At the first step of Abel inversion, an appropriate set of magnetic surfaces is determined with the VMEC calculation so that the electron temperature profile can be symmetric between inboard and outboard sides along major plasma radius against a derived normalized radius, ρ, since the magnetic surface structure is a function of volume-averaged β values and the pressure profile. During the calculation, the electron temperature profile measured with Thomson diagnostic along the major plasma radius is converted into a function of the normalized radius. The symmetric temperature profile as a function of the normalized radius can be then obtained by adjusting the β value and the pressure profile. The most appropriate magnetic surface structure is finally determined by minimizing the difference in the temperature profiles

between inboard and outboard sides.

Fig. 5. (a) line-integrated vertical intensity, (b) observation chord length, (c) local emissivity after Abel inversion for β = 0.23% (8020) at R_{ax} = 3.75 m, and normalized errors of (d) line-integrated vertical intensity, I_{error}/I, (e) observation chord length, $L_{e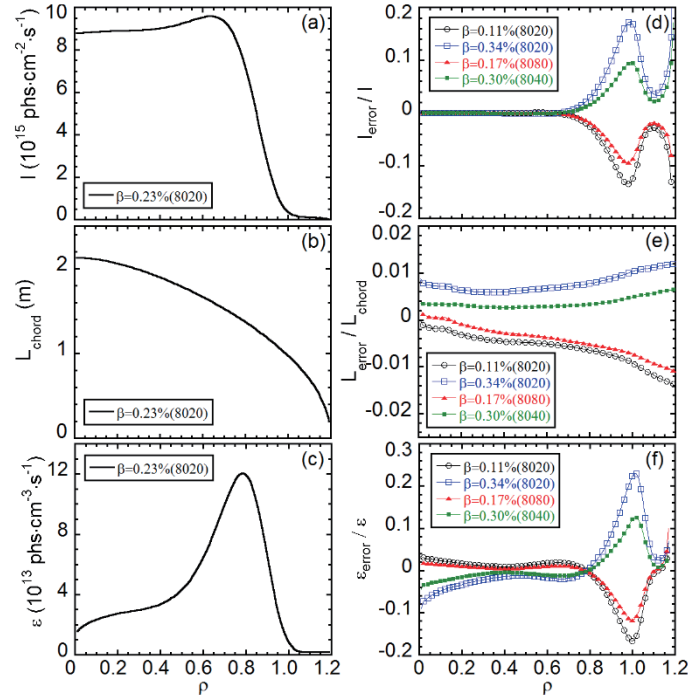rror}/L_{chord}$, and (f) local emissivity, $\varepsilon_{error}/\varepsilon$ for different β and pressure profiles. Notation of "β = 0.23% (8020)" means pressure profile of $P(\rho)=P_0(1-\rho^8)(1-\rho^2)$ with volume-averaged beta of 0.23%, where P_0 is central pressure.

Uncertainty in the local emissivity profile analysis mainly originates in the uncertainty of the magnetic surface structure calculated with the VMEC code. Figures 5(a)-(c) show the vertical intensity, integrated chord length and local emissivity as a function of the normalized radius at outwardly shifted magnetic configuration of R_{ax} = 3.75 m. The pressure profile of $P(\rho)=P_0(1-\rho^8)(1-\rho^2)$ with volume-averaged beta of 0.23% (8020), where P_0 is central pressure, is used for the analysis. In addition, the magnetic surface at ρ > 1.0 is assumed as a simple expansion of the magnetic surface contour at last closed flux surface (LCFS) of ρ = 1.0.

The normalized error of the intensity profile is defined as I_{error}/I, where I_{error} means the difference between two intensity profiles at β = 0.23% (8020) in Fig. 5(a) and another β value or another pressure profile in Fig. 5(d). The definition is also the same for normalized errors of the integrated-chord length profile (L_{error}/L_{chord}) in Fig. 5(e) and the local emissivity profile ($\varepsilon_{error}/\varepsilon$) in Fig. 5(f). The I_{error}/I in Fig. 5(d) and $\varepsilon_{error}/\varepsilon$ in Fig. 5(f) have a large error of ±18% in the vicinity of ρ = 0.97-1.0 for all the assumed magnetic surface structures. On the contrary, the L_{error}/L_{chord} in Fig. 5(e) has a quite different radial structure with smoother radial changes compared to I_{error}/I and $\varepsilon_{error}/\varepsilon$. It means the L_{chord} does not give any serious effect on the final result of $\varepsilon_{error}/\varepsilon$. The $\varepsilon_{error}/\varepsilon$ indicates a considerably large error of ±23% at the maximum value in the plasma edge. Therefore, the error in the tungsten density profile analysis

mainly originates in the error during the local emissivity profile calculation based on the local structure of magnetic surfaces in addition to errors in the measured electron density profile and calculated photon emission coefficients. The error in the electron density profile is estimated to be within 10%. In the present study, however, the error in the photon emission coefficient is ignored from the error evaluation in the tungsten density analysis.
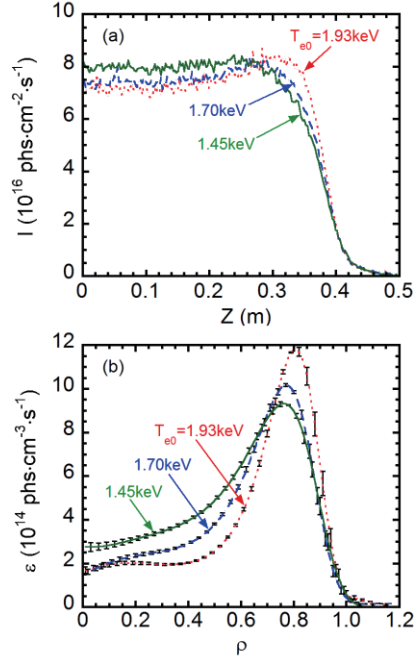
Fig .6. (a) Vertical intensity and (b) local emissivity profiles at T_{e0} = 1.93 (dotted line), 1.70 (dashed line) and 1.45 keV (solid line).

D. Radial density profiles of W^{24+} ions

Vertical intensity profiles of UTA lines at 32.16-33.32Å measured with EUV_Short2 spectrometer are plotted in Fig. 6(a) for three different central electron temperatures of T_{e0} = 1.93 (dotted line), 1.70 (dashed line) and 1.45 keV (solid line). The intensity in the plasma core ($Z \leq 0.25$ m) increases only a little as a function of time, while the intensity in the plasma edge at $Z = 0.32$ m decreases as a function of time. The local emissivity profile reconstructed from the vertical intensity profile is shown in Fig. 6(b). The peak position in the local emissivity profile near ρ = 0.8 clearly moves inside when the electron temperature decreases. The density profiles of W^{24+} ions, $n_{w24+}(\rho)$, are calculated by the equation of

$$n_{w24+}(\rho) = \varepsilon(\rho) / (n_e(\rho) \times f_{PEC}(T_e, n_e)), \qquad (2)$$

where $n_e(\rho)$ is the electron density profiles. The W^{24+} ion density profiles analyzed at T_{e0} = 1.93 (dotted line), 1.70 (dashed line) and 1.45 keV (solid line) are shown in Fig. 7(a). It is obvious that the W^{24+} ion density increases in the plasma core and decreases in the plasma edge when the electron temperature decreases. However, the peak density in the plasma edge distributes in similar ranges of 1.0-1.2×10^{10} cm^{-3}. It means that the tungsten ions stay in the plasma for a considerably long time. The W^{24+} concentration profile, $C_{w24+}(\rho)$, is obtained from the equation of

$$C_{w^{24+}}(\rho) = n_{w^{24+}}(\rho)/ n_e(\rho). \tag{3}$$

The result is plotted in Fig. 7(b). It indicates the W^{24+} concentration gradually decreases as a function of time.
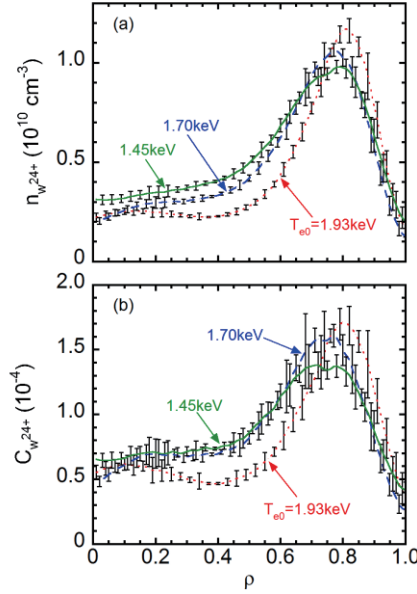
Fig. 7. (a) Density and (b) concentration profiles of W^{24+} ions at T_{e0} = 1.93 (dotted line), 1.70 (dashed line) and 1.45 keV (solid line).

4. Summary

A series of experiments on the tungsten spectroscopy are conducted in Large Helical Device (LHD) by injecting a tungsten pellet to investigate an evaluation method of the tungsten ion density. Photon emission coefficients of W^{24+} in 32.16-33.32 Å at T_{e0} = 1.93, 1.70 and 1.45 keV are calculated by ADAS code. UTA spectrum observed with EUV_Short2 spectrometer is analyzed with the ADAS code. Local emissivity profiles of W^{24+} in 32.16-33.32 Å are reconstructed from vertical intensity profiles based on Abel inversion method and the error in the local emissivity calculation is evaluated. It is found that the error mainly originates in the uncertainty in the evaluation of the magnetic surface structure deformation. W^{24+} density and concentration profiles are calculated at T_{e0} =1.93, 1.70 and 1.45 keV from electron density and temperature profiles, local emissivity profiles and photon emission coefficients. The error of W^{24+} density is evaluated from the errors of the local emissivity profile and electron density profile. Finally, the W^{24+} ion density is determined to be 1.0-1.2×10^10 cm^-3 and the value does not change temporally so much during the discharge.

References

[1] G.F.Matthews, P.Edwards, T.Hirai, et al., Phys. Scr. T128 (2007) 137.

[2] R.A. Pitts, A.Kukushkin, A.Loarte, et al., Phys. Scr. T138 (2009) 014001.

[3] R.Neu, R.Dux, A.Geier, et al., Fusion Eng. Des. 65 (2003) 367.

[4] X.L.Huang, S.Morita, T.Oishi, M.Goto and H.M.Zhang, Rev. Sci. Instrum. 85 (2014) 11E818.

[5] T.Morisaki, S.Sakakibara, K.Y.Watanabe, et al., contrib. Plasma Phys. 40 (2000) 266.

[6] X.L.Huang, S.Morita, T.Oishi, M.Goto and C.F.Dong, Rev. Sci. Instrum. 85 (2014) 043511.

Coherent Mode detected by ECEI in pedestal region on EAST Tokamak

Z.Zhao, J.Xie*, C.Qu, W.Liao, H.Li, T.Lan, A.Liu, G.Zhuang, W.Liu

Department of Modern Physics, University of Science and Technology of China, Hefei 230026, China

Abstract

A coherent mode is detected by electron cyclotron emission imaging (ECEI) diagnostic in the pedestal region during ELM-free phase and inter-ELM phase on the Experimental Advanced Super-conducting Tokamak (EAST). In the normal high confinement regime (H-mode) with co-current neutral beam injection (NBI), the coherent mode grows a few milliseconds after L-H transition, and the mode frequency downshifts from about 45 kHz to 15 kHz lasting for about 100ms before the first ELM crash. It is obvious to say that the mode rotates in the electron diamagnetic direction in the laboratory frame through ECE imaging. Ballooning-like mode structure is identified. The estimated poloidal mode number is $m>25$, and toroidal mode number is $n>5$ for the local safety factor $q \sim 5$. Wave length of the mode increases until the mode saturates, which is consistent with the result that the estimated poloidal mode number decreases. Characteristics of the mode during inter-ELM phase are similar to that during ELM free phase.

1. Introduction

Since the high confinement regime (H-mode) was achieved on ASDEX [1], it has drawn greater attention [2-5] and it is believed to be the promising regime to realize fusion reaction in the magnetic confined devices. The typical characteristic of H-mode is that a transport barrier (so-called pedestal) which leads to steep pressure and current density gradients is formed in the edge plasma [6]. However, a variety of magnetohydrodynamic (MHD) instabilities [7, 8] is induced to the pedestal region due to the gradients. One of the most important instabilities is edge localized mode (ELM), which is a periodical relaxation oscillation causing a diminution in density and temperature in the pedestal [9]. During each burst of ELM, a high peak of heat will load on the target divertor [10] and that limits lifetime of the plasma-facing wall material. Understanding the natural characters of ELMs and control of them are crucial for the present fusion research machines and future fusion power plants, such as ITER [11] and CFETR [12].

In the past decades, ELM has been studied experimentally [13] and theoretically [14, 15]. The theories of ELMs, including the ballooning mode driven by pressure gradient, peeling mode because of edge current, and coupled peeling-ballooning mode [16], has been investigated over the past decades. However, the phenomena of ELMs is too complex to be fully explained by the theories. Generally, the ELMs can be classified into three categories according the relationship between frequency of ELMs and heating power [13]. Type-I ELM precursor modes are identified in JET [17] and so is the quasi-coherent mode in Alcator C-Mod [18]. Some other coherent modes in the steep-gradient pedestal region are also studied via gas puff imaging (GPI) system [19], Mirnov coils [20], and reflectometry [21] on EAST.

Electron cyclotron emission imaging (ECEI), as an advanced two dimension imaging diagnostic, has plenty of advantages to investigate the phenomena of ELMs, which has been proved by the ECEI systems

installed on ASDEX-U [22], DIII-D [23], KSTAR [24]. In the 2014 EAST campaign, details of the coherent mode during ELM-free and inter-ELM phases have been obtained by the ECEI system. The 384 channel (24 vertical X 16 horizontal) ECEI system can cover a very large area of 36 - 70 cm height and 19 - 28 cm width with spatial resolution ~1 - 2 cm and temporal resolution ~1 us. The coherent mode structures are described by 2D imaging of electron temperature fluctuation $\delta T_e / \langle T_e \rangle$, where $\delta T_e = T_e - \langle T_e \rangle$ and $\langle T_e \rangle$ is the time average of electron temperature T_e.

2. Experimental setup

Experimental Advanced Superconducting Tokamak (EAST), which is a fully superconducting tokamak device, aims at achieving long pulse stable H-mode plasma operation [5]. Since the first H-mode in EAST was achieved in 2010, the duration of H-mode plasma reached to 30s [25] in 2012, and this record was updated to 60s in 2016 campaign. The major and minor radius of EAST are R_0=1.85m and a=0.45m, respectively. Top view and cross section of EAST are shown in Figure 1. Related auxiliary heating and diagnostics are located at different ports. In Figure 1 (b), The blue solid line indicating the first wall demonstrates that ITER-like W monoblock upper divertor [26] and normal graphite lower divertor. The blue area indicates 384 channels ECEI detecting region when the toroidal field (TF) strength is $B = 2.25T$ for shot #52327. 32-channel heterodyne ECE radiometer [27] (green square line) can measure the electron temperature profile from core plasma to high field side (HFS) edge plasma. The last closed flux surface (LCFS) given by EFIT [28] is displayed in red dash line. Thus, ECEI can cover the whole pedestal region. It is obvious lower single null (LSN) for this shot. As a typical D-shaped tokamak, the elongation of EAST for this shot is $\kappa \sim 1.62$.
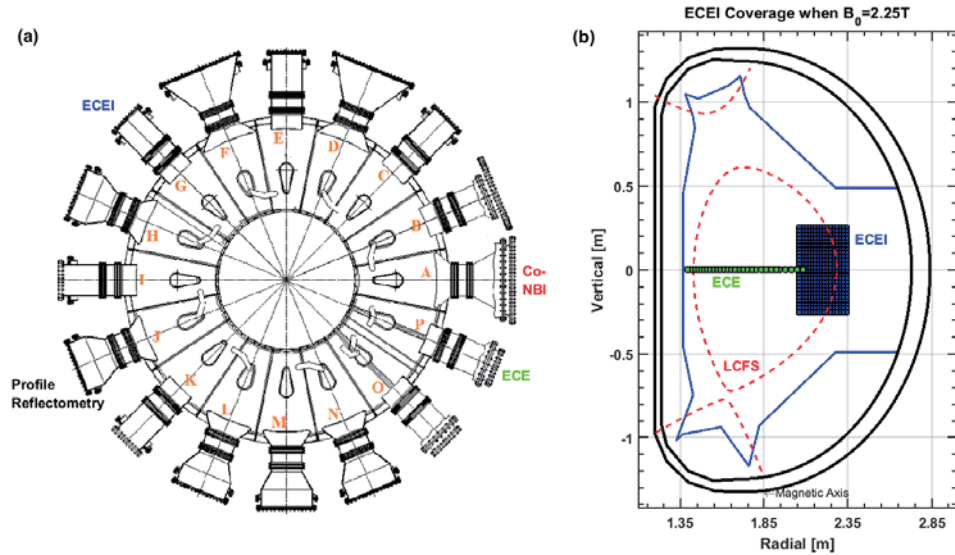

Figure 1. Top view and cross section of EAST. (a) Related auxiliary heating and diagnostics are located at different ports. (b) The blue solid line indicates the first wall; the blue area shows the detecting region of 384-channel ECEI; 32-channel heterodyne ECE radiometer is marked as green square line; last closed flux surface is displayed as red dash line.

Time history of the principal discharge parameters of shot #52327 are demonstrated in Figure 2. Plasma current (IP), line averaged density (<ne>), and central electron temperature (Te) are shown in Figure 2(a), (b) and (c), respectively. The heating power of co-current neutral beam injection (co-NBI) is about 3.6 MW (Figure 2(d)). L-H transitions and H-L transition can be found via the divertor Da signal (Figure 2(e)), with an increase and decrease of line averaged density as shown in Figure 2(b). The n=1 resonant magnetic perturbation (RMP) turns on at 3.2s (Figure 2(d)) and the ELMs are mitigated at same time until the H-L transition occurs at 3.35s. When RMP turns off at 3.49s, L-H transition happens again. The radiation temperature measured by ECEI at the edge plasma region is shown in Figure 2(f). Changes of sawtooth behavior can be found in the central electron temperature, and the radiation temperature is more likely affected by the ELMs.
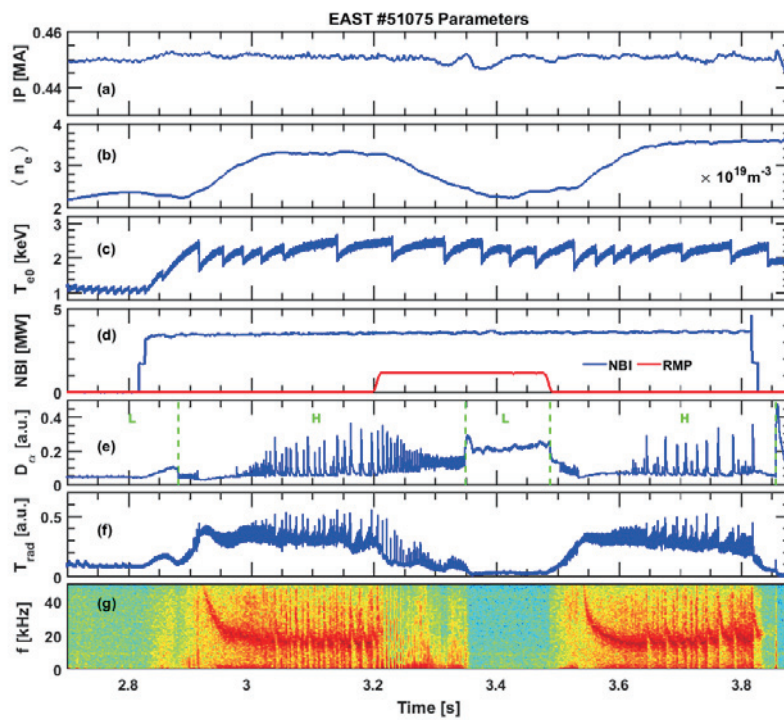
Figure 2. Time history of principal parameters of typical NBI heating discharge on EAST: (a) plasma current IP, (b) line averaged density <n_e>, (c) central electron temperature T_{e0}, (d) power of co-current NBI and amplitude of n=1 RMP current, (e) divertor Da signal, (f) radiation temperature in edge plasma region T_{rad}, (g) spectrogram of the radiation temperature.

3. Coherent mode measured by ECEI

Since the temperature and density of plasma in the edge plasma region drops dramatically, the condition of optical thick ($\tau \quad 1$, τ is the optical thickness) for ECEI is not guaranteed. Thus, ECEI data can be interpreted as radiation temperature T_{rad} containing both electron temperature and electron density [23, 29]. An example of T_{rad} located at $R = 2.260m$ corresponding to cold resonances is demonstrated in Figure 2(f). In the spectrogram of T_{rad}, a coherent mode can be found in the H-mode regime. The mode frequency downshifts from about 45 kHz to 15 kHz lasting for about 100ms in the ELM-free phase. In the inter-ELM phase, the coherent mode can also be found. When the RMP turns on, the radiation temperature

falls down and the coherent mode disappears. The coherent mode will repeat after the second L-H transition.

Evolution of the radiation temperature fluctuation dealt with 5 – 50 kHz band-pass filter and characteristics of the coherent mode during the ELM-free phase are shown in Figure 3. The red line in Figure 3(a) indicates amplitude of the fluctuation and the green dash line denotes moments of the frames in Figure 3(b). The ballooning-like mode structure is clearly shown in the frames. The mode locates just inside the last closed flux surface (LCFS) which is marked as black dash line, and radial width of the mode is about 4 cm. The mode rotates in electron diamagnetic direction in the laboratory frames. Magnetic field shearing maybe account for deformation of the mode structure off mid-plane as shown in Frame-(3). Poloidal mode number of the coherent mode is estimated to larger than 25 ($m > 25$), and the toroidal mode number is greater than 5 ($n > 5$) since the edge safety factor $q_{95} \sim 5$. Wave length of the mode increases from 8.5 cm to 11.7 cm in the four frames, which implies that the poloidal mode number may decrease as the mode grows. During the ELM-free phase from 3.55s to 3.64s, amplitude of the coherent mode increases while other parameters including frequency, poloidal wave number and phase velocity decrease, as shown in Figure 3(c) - (f).
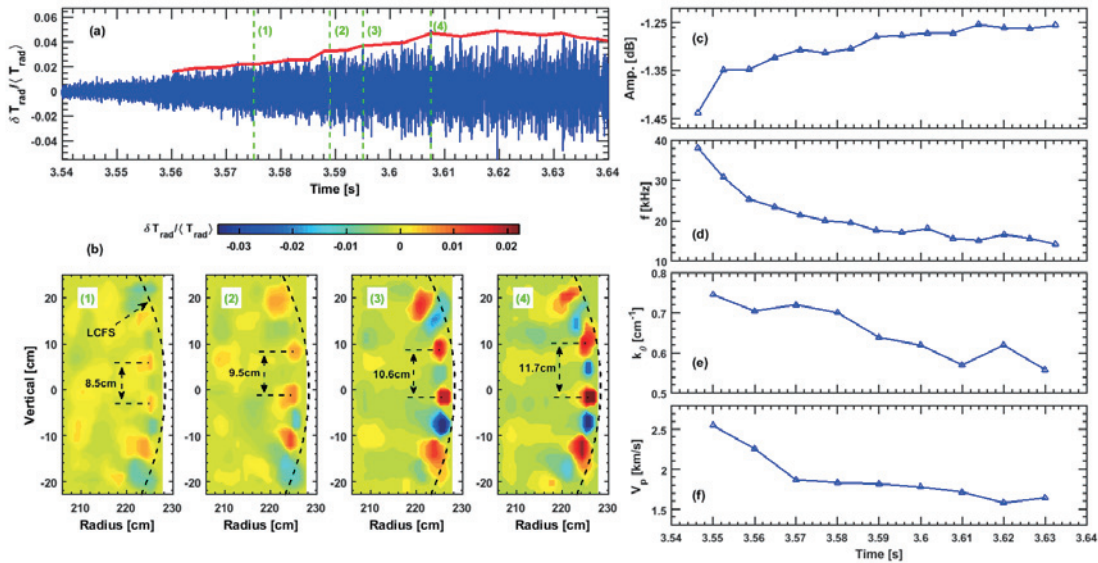
Figure 3. Time history of: (a) the radiation temperature fluctuation, (c) amplitude, (d) frequency, (e) poloidal wave number and (f) phase velocity of the coherent mode during the ELM-free phase. The coherent mode structure is shown in (b): the black dash line is the LCFS, and wave length of the mode is marked in the frames below.

Localization of the coherent mode is also verified by Figure 4. Spectrogram of five channels of radiation temperature measured by ECEI on the mid-plane are shown in Figure 4(a) – (e), and cold plasma resonant position of the the measurement points are denoted in the legends. The coherent mode can just be found in two channels with a 4 cm span, which is consistant with the result discussed in Figure 3. When NBI is turned off at 3.83s, marked as the pink dash line, the coheret mode disappears at $R = 2.260m$ and

appears at $R = 2.221m$, which means the mode moves toward inside. Pedestal density profile measured by reflectometry [30] is give in Figure 4(f). Even through information of density on top of pedestal is missing, the steep pedestal structure can be indentified. It is clear that the pedetal moves towards inside when NBI is turned off. Thus, it is believable that the coherent mode associates with pedestal.
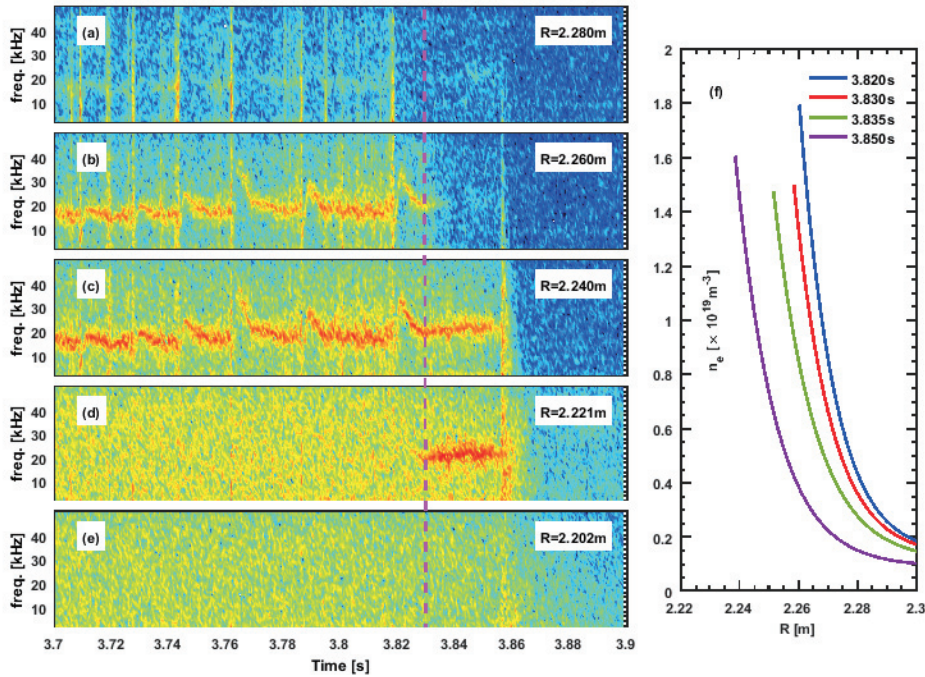
Figure 4. Spectrogram of five channels of radiation temperature measured by ECEI on the mid-plane are shown in (a) – (e). Major radius of the channels are denoted in the legends, and the pink dash line indicates the moment of NBI shutting down. Pedestal density profile measured by reflectometry at four moments is given in (f).

Acknowledgements

References

[1] Wagner F, Becker G, Behringer K, et al., 1982, Physical Review Letters, 49: 1408-1412

[2] Team A, 1989, Nuclear Fusion, 29: 1959

[3] Groebner R, Allen S, Baker D, et al., 1994, Plasma physics and controlled fusion, 36: A13

[4] Team J, 1994, Plasma physics and controlled fusion, 36: A23

[5] Wan B, Li J, Guo H, et al., 2015, Nuclear Fusion, 55: 104015

[6] Hubbard A E, Boivin R L, Granetz R S, et al., 2001, Physics of Plasmas, 8: 2033-2040

[7] Luce T C, Wade M R, Politzer P A, et al., 2001, Nuclear Fusion, 41: 1585

[8] Manickam J, 1992, Physics of Fluids B, 4: 1901-1908

[9] Oyama N, Shinohara K, Kamada Y, et al., 2001, Plasma physics and controlled fusion, 43: 717

[10] Pitts R A, Arnoux G, Beurskens M, et al., 2009, Journal of Nuclear Materials, 390–391: 755-759

[11] Physics E J D W A H Y K V M T H O A P, 2007, Nuclear Fusion, 47: S18-S127

[12] Song Y T, Wu S T, Li J G, et al., 2014, IEEE Transactions on Plasma Science, 42: 503-509

[13] Zohm H, 1996, Plasma Physics and Controlled Fusion, 38: 105

[14] Connor J W, 1998, Plasma Physics and Controlled Fusion, 40: 191

[15] Connor J W, 1998, Plasma Physics and Controlled Fusion, 40: 531

[16] Snyder P B, Wilson H R, Ferron J R, et al., 2002, Physics of Plasmas (1994-present), 9: 2037-2043

[17] Perez C, Koslowski H, Huysmans G, et al., 2004, Nuclear fusion, 44: 609

[18] Mazurenko A, Porkolab M, Mossessian D, et al., 2002, Physical Review Letters, 89: 225004

[19] Wang H Q, Xu G S, Wan B N, et al., 2014, Physical Review Letters, 112:

[20] Wang H, Xu G, Guo H, et al., 2014, Nuclear Fusion, 54: 124001

[21] Gao X, Zhang T, Han X, et al., 2015, Nuclear Fusion, 55: 083015

[22] Boom J E, Wolfrum E, Classen I G J, et al., 2012, Nuclear Fusion, 52: 114004

[23] Tobias B J, Austin M E, Boom J E, et al., 2012, Review of Scientific Instruments, 83: 10E329

[24] Yun G S, Lee W, Choi M J, et al., 2011, Physical Review Letters, 107:

[25] Li J, Guo H Y, Wan B N, et al., 2013, Nat Phys, 9: 817-821

[26] Luo G-N, Li Q, Chen J, et al., 2012, Fusion Science and Technology, 62: 9-15

[27] Han X, Liu X, Liu Y, et al., 2014, Review of Scientific Instruments, 85: 073506

[28] Calabrò G, Xiao B J, Chen S L, et al., 2015, Nuclear Fusion, 55: 083005

[29] Bornatici M, Cano R, Barbieri O D, et al., 1983, Nuclear Fusion, 23: 1153

[30] Zhang S, Gao X, Ling B, et al., 2014, Plasma Science and Technology, 16: 311

Study of helically trapped energetic-ion-driven resistive interchange modes (EIC) with deuterium perpendicularly NBIs in LHD

T. Bando[1], S. Ohdachi[1,2], M. Isobe[1,2], K. Nagaoka[2], Y. Suzuki[1,2], X. D. Du[3], K. Y. Watanabe[2], Y. Narushima[1,2], K. Ogawa[1,2], H. Tsuchiya[2], T. Akiyama[1,2], T. Ido[2], A. Shimizu[2], M. Yoshinuma[1,2], S. Masuzaki[1,2], T. Ozaki[2], R. Seki[1,2], H. Takahashi[1,2], K. Toi[2], M. Osakabe[1,2], T. Morisaki[1,2], and the LHD Experiment Group[2]

[1]SOKENDAI (The Graduate University for Advanced Studies), 322-6 Oroshi-cho, Toki, Japan

[2] National Institute for Fusion Science, National Institutes of Natural Sciences, 322-6 Oroshi-cho, Toki, Japan

[3]University of California, Irvine, CA, USA

Abstract

Energetic particle driven resistive InterChange mode, EIC, was observed in hydrogen plasma experiments of LHD [1]. EICs have been also observed in the recent experimental campaign started from Mar. 2017, using two deuterium perpendicularly (PERP) NBIs. The acceleration voltage and input power of the PERP-NBIs are respectively increased from 40 keV to 60/80 keV and from 6 MW to up to 9/10 MW, compared with those in the hydrogen beam campaign. With those PERP-NBIs, EICs induces larger magnetic fluctuation and larger electrostatic potential. In this study, the change of the neutron emission rate by EICs and mode location of EICs with PERP-NBIs are introduced.

1. Introduction

Energetic particle driven resistive InterChange mode, EIC, was observed in hydrogen plasma experiments of LHD [1]. EIC is destabilized by the resonance between the precession motion of helically trapped energetic ions (EPs) in the peripheral region and the resistive interchange mode (RIC) having an m/n = 1/1 mode structure. In deuterium plasma experiments, EICs induces larger magnetic fluctuation (2~5 times) and occur less frequently, as shown in fig. 1. This red and blue magnetic fluctuations are due to EIC in deuterium and hydrogen experiments respectively.

In deuterium experiments, study of EICs are proceeded with the total neutron emission rate measured by Fission chambers, which gives us the information about amount of EPs, and comparisons of characteristics of EICs between hydrogen and deuterium experiments. In this brief report, the change of the neutron emission rate by EICs and mode locations of EICs with PERP-NBIs are introduced.

2. Change of the neutron emission rate by EICs

In figure 2, the total neutron emission rate and magnetic fluctuations when EICs occur are shown. The neutron emission rate drops by EICs and recovers, then the neutron emission rate drops again. Observed drop of the total neutron emission rate is up to 60%. The induced drop rate of the neutron emission rate is higher with larger magnetic fluctuations as shown in fig. 3. The reason of the tendency may be that larger

loss of EPs induces larger magnetic fluctuation. The amplitude of the magnetic fluctuation is higher with higher electron density. This suggest that the critical value to induce EICs becomes higher with higher electron density. The mechanism of the change of critical values is still investigated.

2.2 Mode location of EICs

Figure 4 show the time evolution of fluctuation of Te measured by ECE and magnetic fluctuation when a EIC occur. Chirping down oscillation with m/n=1/1 structure localizes around ι=1 surface, which eigenfunction has tearing parity, are observed. These characteristics are same as that with hydrogen. The precession frequencies of the EPs from the PERP-NBIs 66 (60) keV are estimated with observed precession frequency. The calculated precession frequency of EICs at ι=1 surfaces is almost the same as the observed precession frequency. This also suggests that EPs around ι = 1 surface resonates with resistive interchange modes.

The formation of large negative potential drop, up to -25 kV, is observed, which is about two times larger than that in the hydrogen campaign [1] as shown in figure 5. The change of the potential occur in the edge region with deuterium PERP-NBIs. This suggests that EPs are expelled by EICs from around the ι = 1 rational surface.

After the formation of electrostatic potential, the gradual increase of Te and ne is observed. It may due to the transport barrier induced by the Er shear. This will be investigated in near future.

Acknowledgements

References

[1] X. D. Du et al, Phys. Rev. Lett 114 155003 (2015)
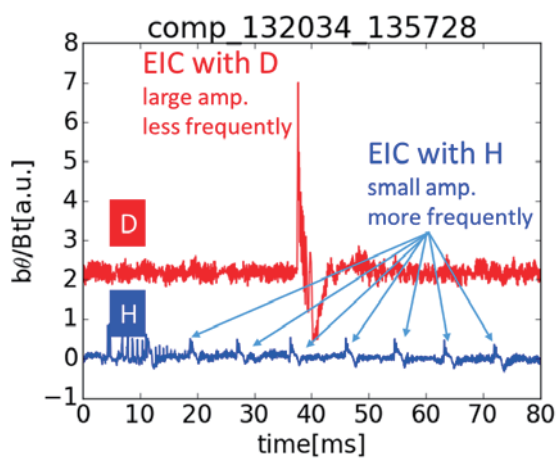
Fig. 1 Magnetic fluctuations induced by

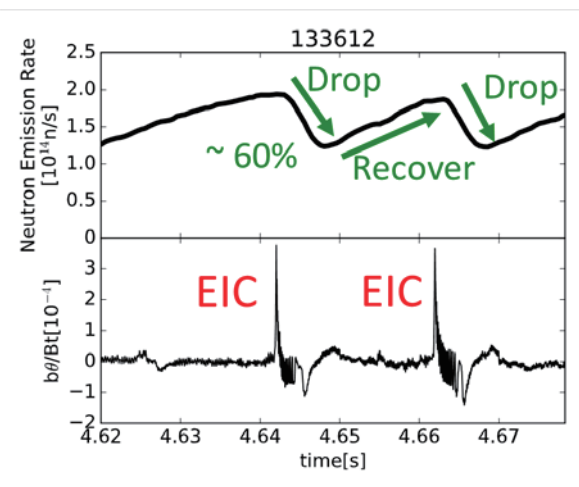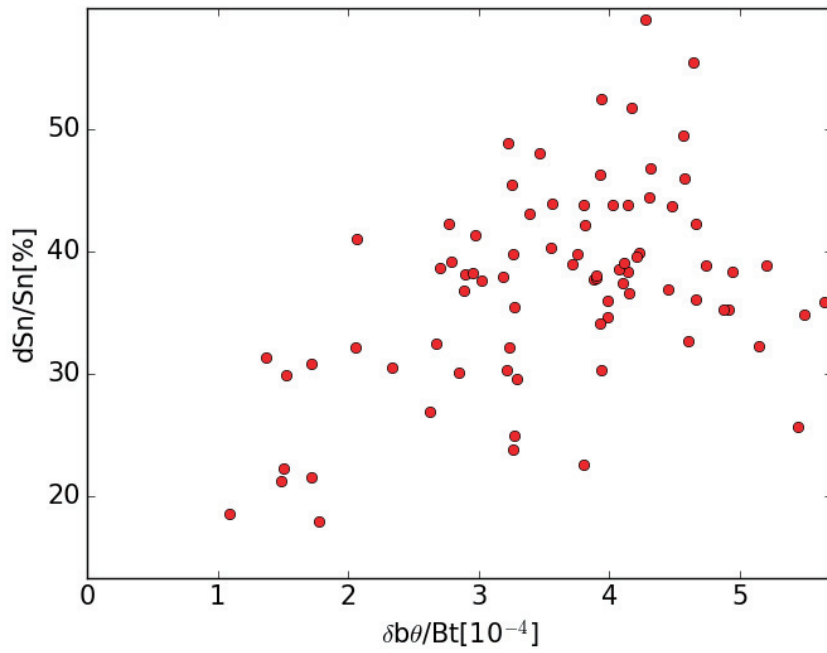Fig. 2 The total neutron emission rate and

Fig. 3 Relationship between the observed magnetic fluctuation when EICs occur and the drop rate of the total neutron emission rate by EICs.
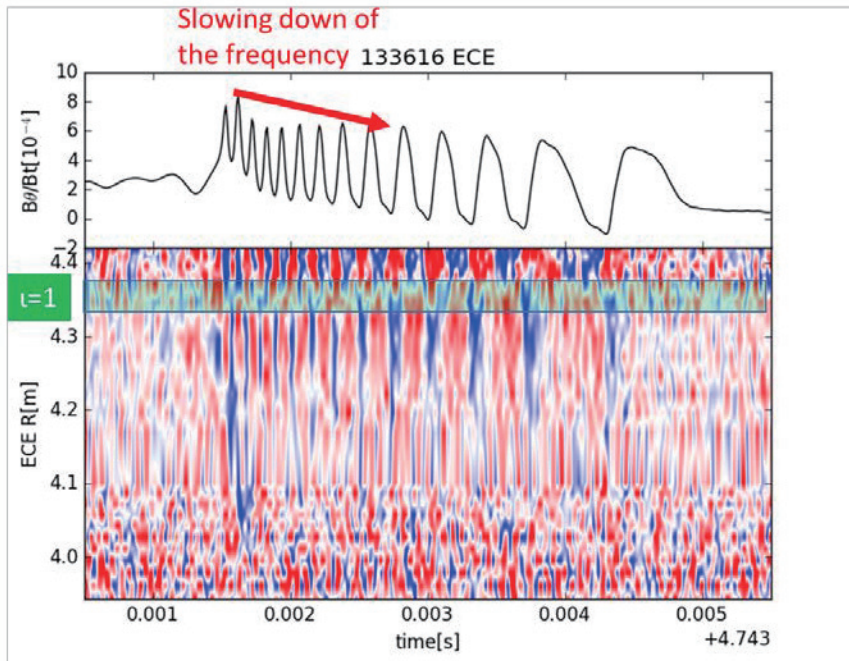

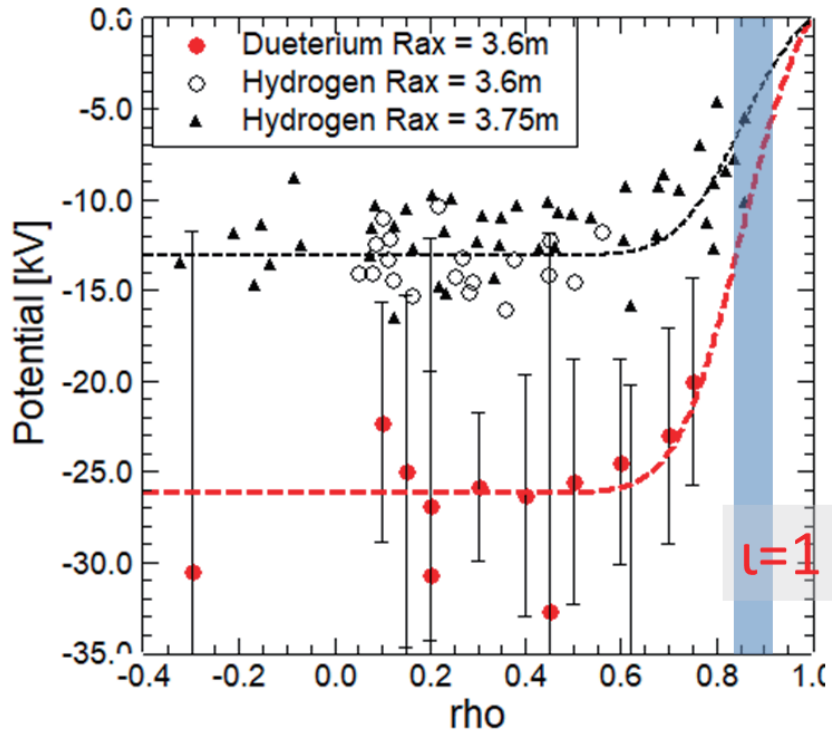Fig. 4 The time evolution of magnetic fluctuation and fluctuation component of Te measured by ECE when a EIC occurs.

Fig. 5 The formed electrostatic potential measured by HIBP in hydrogen or deuterium experiments.

Fast RF diagnostics in KSTAR ELMy H-mode discharge

M.H. Kim[1], S.G. Thatipamula[2], G.H. Choe[1], J.E. Lee[1], M.J. Choi[2], H.K. Park[2,3] and G.S. Yun[1*]

[1]Pohang University of Science and Technology, Pohang, Korea

[2]National Fusion Research Institute, Daejeon, Korea

[3]Ulsan National Institute of Science and Technology, Ulsan, Korea

Abstract

A fast radio frequency (RF) (0.1 – 1 GHz) diagnostics has been developed in KSTAR. Using fast digitization technology (~5 GSa/s), it becomes possible to measure the dynamic changes of the RF emission with sub-μs time resolution. Especially, we found that there exist several distinct stages of RF emission at the pedestal collapse in *H*-mode discharges. Comparison with the electron cyclotron emission (ECE) images has revealed that each stage is related to the condition of the outboard mid-plane edge. First, intensified high-harmonics ion cyclotron emissions (ICE) occur with the appearance of a non-modal filamentary perturbation in the edge within several tens of μs before the collapse. Then, the RF signal becomes broad toward high-frequency range (< 500 MHz) at the crash onset of the non-modal filament. During the collapse, rapid frequency up/down chirp signals (1-3 μs) appear with additional filament bursts. These RF observations can provide clues for ion dynamics at the pedestal collapse.

1. Introduction

Radio frequency (RF) diagnostics are used to observe wave phenomena in ionospheric plasmas [1-2], tokamak plasmas [5] and laboratory experiments (e.g. Space Physics Simulation Chamber [7]). In H-mode toroidal plasmas, the semi-periodic rapid collapse of the edge pedestal involves intense RF emissions from the edge [3-5]. Recent progress in DAQ system enables us to analyze the RF emissions near the collapse with high-resolution (< 1 MHz). For this purpose, we install two different types of RF spectrometers on the KSTAR. [5] One is a filter-bank spectrometer to measure the RF emissions at 16 different frequency bands for the whole discharge duration. The other is a fast digitizer system (~5 GSa/s) to obtain high temporal resolution spectra for specific time windows. These two systems are connected to the antennas located outside the vacuum vessel close to a diagnostic port with large aperture viewport permitting the passage of RF radiations. The bandwidth of the RF system is 0.1 – 1 GHz.

Figure 1 shows an example of *H*-mode discharge in KSTAR. The D_α signal indicates that the pedestal collapses are compound showing both large and small surges. In the electron cyclotron emission (ECE) spectrogram at outer mid-plane edge region, broadband ECE emission occurs during pedestal collapse. In addition, ~60 kHz frequency components often appear in the spectrogram during the inter-crash periods, indicating existence of the edge-localized mode (ELM). The last row of Figure 1 indicates some of the filter-bank RF signals, which vary significantly with the appearance of the ELM frequency components and broadband emission in ECE signal.

The filter-bank system is very useful for measuring the trends of RF emission during one ELM cycle or even in the whole time range of discharge. On the other hand, the fast digitizer system with broadband range is essential to see the detail of the dynamic RF emission spectra.
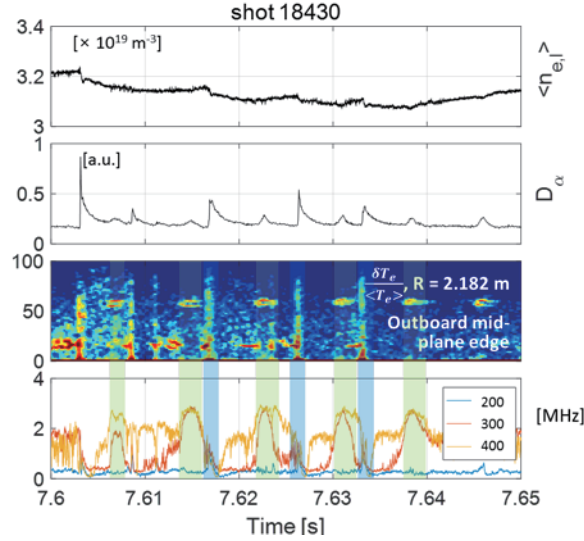
Figure 1. Time traces of line average density, D_α, ECE signal spectrum in outboard mid-plane edge and filter-bank RF signals for KSTAR #18430 (B_T = 2.3 T, I_p = 500 kA, W_{tot} = 140 kJ). In green boxes, 0.3 and 0.4 GHz RF signals are synchronized with ~60 kHz components in the ECE channel. In blue boxes, 0.2 and 0.3 GHz RF channel signals are matched with the broadband ECE spikes at the pedestal collapses.

2. The distinct stages of RF emission near and at the pedestal collapse

Figure 2 describes the RF emission at the pedestal collapse. In Fig. 2(a), the 200 MHz filter-bank RF channel and D_α signals are overlaid around the collapse event. Using the fast RF diagnostic system, we successfully captured the RF spectrum for 370 μs around the onset of the collapse. Here, t_0 is defined as the time point at which the slope of the filter-bank changes drastically. The evolution of the RF emission can be divided into four distinct stages with respect to the time t_0 (Fig. 2(b)).

The first stage, stage A, is characterized by several line emissions in the range of 100 to 300 MHz. The spacing between these lines is 11±0.5 MHz, which corresponds to the deuterium cyclotron frequency (f_{cD}) at the outboard midplane edge (R=218±10 cm). In KSTAR, we frequently observe such discrete spectral patterns during the inter-crash period of *H*-mode discharge.

After that, the stage B starts from t_0 - 90 μs. The f_{cD} harmonics are observed in the range of 100 to 300 MHz similar to stage A. To highlight the difference between stage B and A, magnified spectrogram and high-resolution spectrum graphs are compared in Figure 3(c) and (d), respectively. The main difference between these two stages stands out in the 250 to 350 MHz range. The intensities of high harmonics f_{cD} in that range are increased at stage B. Interestingly, the stage B corresponds to the emergence of the non-modal structure in the outer mid-plane edge region (R ~ 220 cm) as illustrated by the ECE images in Fig. 3(b).
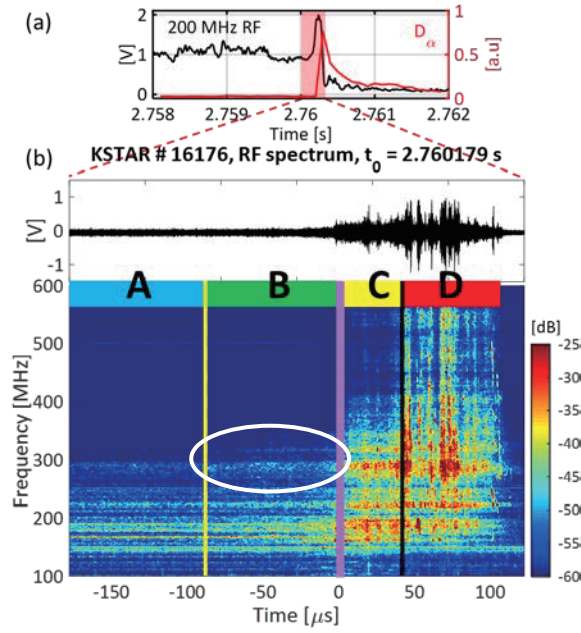
Figure 2. (a) 200 MHz RF signal of the filter-bank spectrometer and D_α in KSTAR #16176 ($B_T = 1.8$ T, $I_p = 520$ kA, $\langle n_{e,l} \rangle = 3.8 \times 10^{19}$ m^{-3}, $W_{tot} = 330$ kJ). (b) RF bursts at the pedestal collapse. The white circle denotes the region of increased emission in stage B.
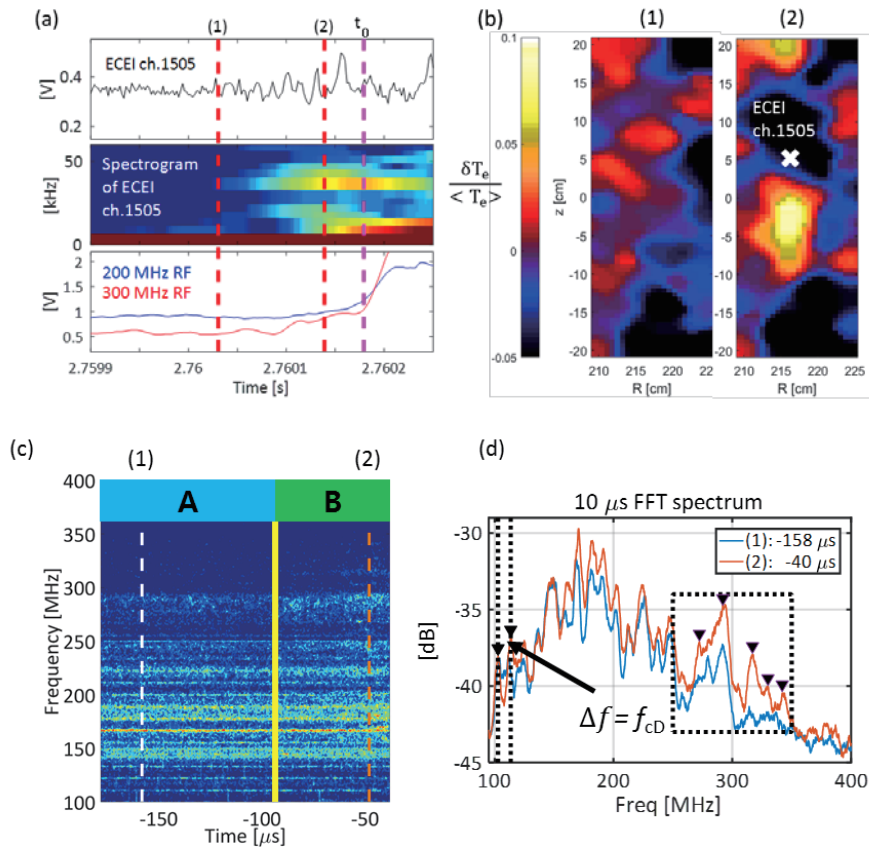
Figure 3. (a) ECE signal in the outer mid-plane edge, its spectrogram and 200, 300 MHz filter-bank RF signals. (b) ECE images at the times (1) and (2). (c) Magnified RF spectrogram in stage A and B. (d) High-resolution spectrum graphs for 10 μs window around the times (1) and (2).

From t_0, the RF emission goes to the next step, stage C. The RF emission is rapidly intensified as seen in the filter-bank channels in Fig.3(a). The corresponding spectrogram shows the emergence of broad emission under 500 MHz as shown in Figure 4(a). In ECE image, the non-modal filamentary structure moves radially outward and starts to burst at around t_0, which initiates the pedestal collapse. This indicates that RF signals can be a good indicator for the crash onset whereas the D_α signal reflects only the aftermath of the collapse.
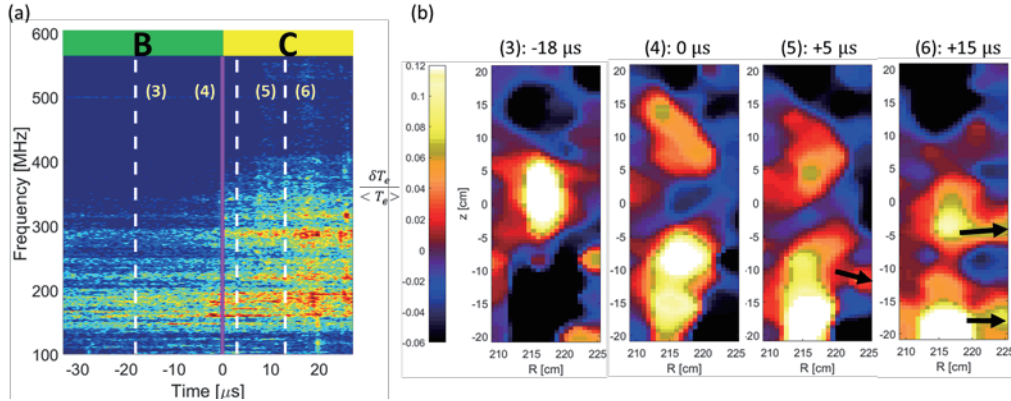
Figure 4. (a) Magnified RF spectrogram in stage B and C. The solid magenta line indicates t_0. (b) $1 - 60$ kHz FFT band-passed ECE images from the time points (3) to (6).

Following the filament burst, the pedestal collapse proceeds. During the collapse, additional filament bursts occur with 1-3 μs rapid up/down chirping in the RF spectrum as shown Figure 5. Most of these chirpings occur in step of f_{cD} at the outer mid-plane edge for broad RF range. For the case of chirpings with f_{cH} stepping, it was shown based on a 1D3V particle-in-cell simulation that a subset of 3MeV fusion protons, born centrally with deeply passing orbits, can drive ICEs via magnetoacoustic cyclotron instability and the chirpings are due to the local density change [10].
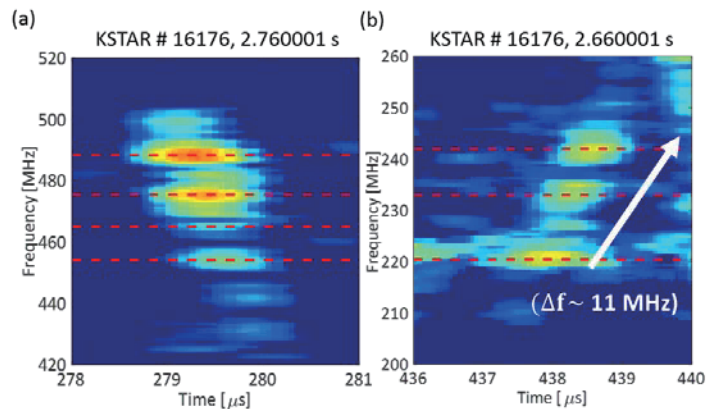
Figure 5. (a) RF burst with chirping down during pedestal collapse. (b) RF burst with chirping up during pedestal collapse.

In summary, this article reports the spectral characteristics of the electromagnetic high-harmonic ICEs and their evolution around the pedestal collapse in H-mode discharge. It is clear that the condition of the

outboard mid-plane edge is important for the ICEs. One possible hypothesis for the ICE generation mechanism may be considered as follows. In H-mode discharge, inhomogeneous radial electric field (E_r) (e.g a well structure) is formed near the plasma periphery [6]. The inhomogeneity in the E_r results in radial shear in poloidal velocity profile because of the $E \times B$ drift. The sheared flow can make electromagnetic ICEs as reported in laboratory experiment [7] and theoretical modeling [8] with the assumption of cold and collisionless plasma condition except the motion of electrons in the parallel direction. Furthermore, the non-modal filamentary structure can enhance the velocity shear as suggested in [4, 9], which can intensify the ICE. The strong velocity shear can also lead the expulsion of filamentary perturbation [9], which can drive the broadband emission like the stage C shown in Fig. 4.

Acknowledgements

References

[1] Bo Thidé et al., Phys. Rev. Letter **49**, 1561 (1982)

[2] B. Chen et al., Astrophysical Journal **736(1)**, 64 (2011)

[3] G.S. Yun et al., Phys. Rev. Letter **107**, 045004 (2011)

[4] J.E. Lee et al., Sci. Rep. **7**, 45075 (2017)

[5] S.G. Thatipamula et al., Plasma Phys. Control. Fusion **58**, 065003 (2015)

[6] K. Itoh and S.I. Itoh, Plasma Phys. Control. Fusion **38**, 1-49 (1996)

[7] E.M. Tejero et al., Phys. Rev. Letter **106**, 185001 (2011)

[8] J.R. Peñano and G. Ganguli, J. Geophys. Res., **107**, 2504 (2002)

[9] J.A. Morales et al., Phys. Plasmas, **23**, 042513 (2016)

[10] B. Chapman et al., 44th EPS Conference on Plasma Physics (2017) P4.401:http://ocs.ciemat.es/EPS2017PAP/pdf/P4.401.pdf

Coherent and incoherent fluctuations in fixed Langmuir probe measurements

Shekar G. Thatipamula, H.S. Kim, J.G. Bak and S.H. Hong

National Fusion Research Institute, Daejeon 34133, Korea

Abstract

The ion saturation current (I_{sat}) on the fixed Langmuir probes in the lower divertor region exhibit coherent oscillations (15~30 kHz) in some high confinement (H)-mode discharges. These fluctuations are observed during the inter edge localized mode (ELM) crashes, possibly in the ELM mitigation phase, dominantly in a narrowband in frequency which varies gradually either up or down. Filamentary modes with similar spectral features are observed in the mid-plane using the beam emission spectroscopy. In another H-mode discharge, bursts or incoherent fluctuations are observed and hence possible intermittency during the ELM suppression phase.

1. Introduction

The fluctuations, turbulence and transport in the fusion plasma boundary are known to play key roles in the improvement of the plasma confinement. Several diagnostic methods are in use today for investigating these phenomena to generate a comprehensive understanding through them. The Langmuir probe technique is perhaps one of the earliest methods, but still finds application in tokamaks today.

The Langmuir probe measurements in tokamaks are limited to the scrape-off layer (SOL) or near the boundary walls, for example the divertor. In KSTAR tokamak, a fast reciprocating probe in the mid-plane has been operational to obtain the plasma density and electron temperature profiles in SOL [1, 2]. A poloidal array of Langmuir probes fixed on the boundary wall including the top / bottom divertors of KSTAR has been useful in monitoring the particle flux and the magnetic strike point.

In the present work, observation of coherent and incoherent fluctuations in the fixed Langmuir probe measurements on KSTAR divertor, from different discharges in 2017 campaign is reported. Interestingly, the coherent fluctuations in the fixed Langmuir probes on divertor are accompanied by similar frequency fluctuations in mid-plane, viewed by the beam emission spectroscopy (BES).

2. Measurement apparatus

The fixed Langmuir probes on KSTAR are made of CFC probe tips of dome type. Each graphite tile is mounted with either two or three probe tips of the array through proper insulation. The schematic cross-section of one probe tip with insulator is shown in Fig.1. In the recent campaign, the discharges were produced with lower single null preferably, hence the measurements were performed using fixed Langmuir
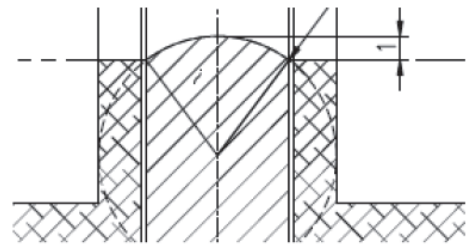
Figure 1. Langmuir probe cross section

probes near the lower divertor region. These probes are schematically shown in the tokamak cross-section in Fig.2, numbered 40 through 63, along with the real time EFIT profile. Each Langmuir probe is biased to about -215V, hence collects the ion saturation current, measured across a shunt resistor and digitized at 400 kS/s. Since these Langmuir probes are fixed in the boundary, the particle flux is incident on the probe surface at grazing angle.

Another useful diagnostic system on KSTAR in the context of the results using fixed Langmuir probes, as described in the following section, is the beam emission spectroscopy (BES). The KSTAR BES system is based on the measurement of D_α emission, which gives an estimate of the density fluctuations. The BES measurements are in 2-D plane with 16 radial × 4 vertical channels. It should be noted here that BES system views the outer SOL in the mid-plane for the results reported here. The measurement location extends both sides of the separatrix, as shown schematically in Fig.3. Hence, the density fluctuations in the plasma edge and SOL can be inferred, and images of the structures may be reconstructed. In the sections that follow, useful results from Langmuir probes and the BES system are described.
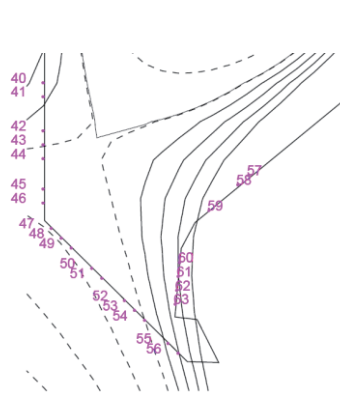
Figure 2. Langmuir probe array with EFIT plot
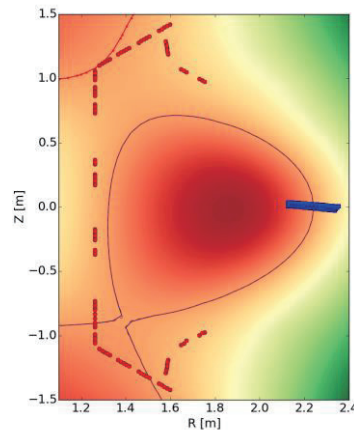
Figure 3(a). BES system view position in mid-plane and Langmuir probes in the boundary
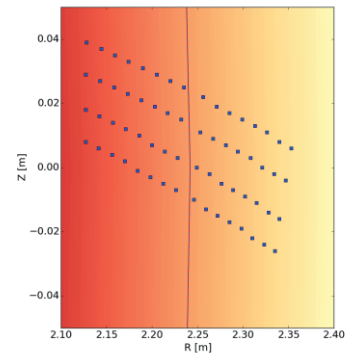
Figure 3(b). BES measurement positions around separatrix (R~2.24 m)

3. Coherent fluctuations

The typical tokamak signals for KSTAR high confinement (H)-mode shot 18585 is shown in Fig.4. For this discharge the magnetic field at the magnetic axis ~1.7 T, plasma current ~0.7 MA, total neutral beam heating power ~3.5 MW, and stored energy ~320 kJ. The time trace of H_α signal indicates edge localized mode (ELM) crashes; the significantly long inter ELM crash periods may imply the ELM mitigation phase. The magnetic configuration from the real time EFIT, as shown in Fig. 2 implies the outer strike point is on the central divertor, in the vicinity of the fixed probe number 54. Interestingly, coherent fluctuations in a narrow frequency band are found in I_{sat}
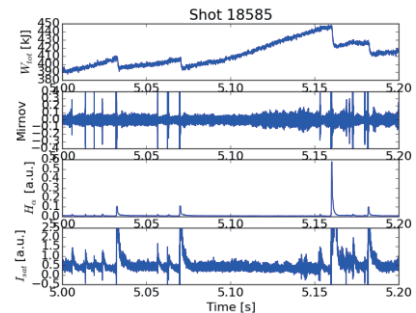
Figure 4. Typical signals for shot 18585

on probes numbered from 60 to 63 on the outer divertor, during the inter ELM crash periods. The time
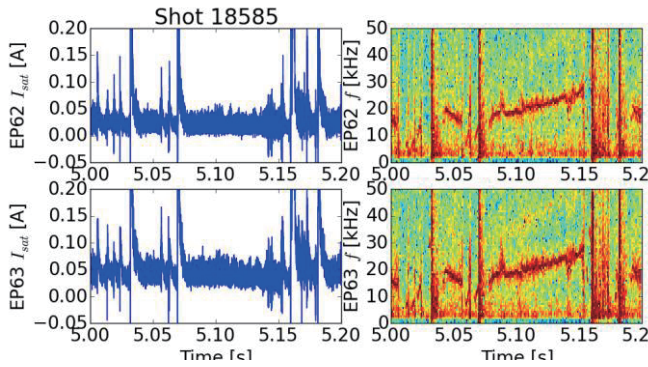
Figure 5. Langmuir probe spectra
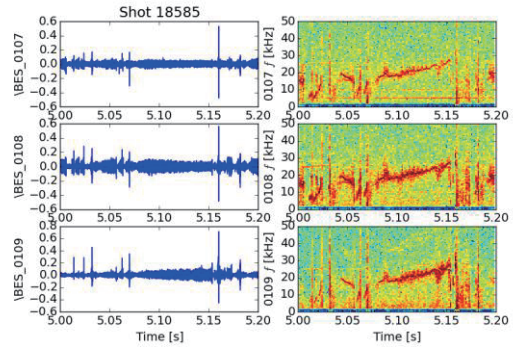
Figure 6. BES spectra near separatrix

series and the spectrogram for two probes are shown in Fig. 5. The frequency of the coherent fluctuations is found typically in the range 15 – 30 kHz, and drifts gradually either up or down during the inter ELM crash as depicted in Fig.5. Coherent modes in this frequency range are routinely observed in the inter ELM crash period, in the plasma edge through imaging systems such as electron cyclotron emission (ECE) imaging [3], and BES systems.

The spectrogram of BES measurements in the mid-plane, is shown in Fig.6 for three channels, around the separatrix. Coherent fluctuations in the inter ELM crash period in a narrow frequency band occur in BES channels, similar to those in Langmuir probes on divertor. The fluctuations are localized radially in the mid-plane but found in all vertical channels, around the separatrix. Filamentary structure is evident on reconstructing the images of density fluctuation from BES measurements. The time evolution depicts, filamentary structures moving down in the BES system view plane. The filamentary structure can be seen from multiple images in Fig.7.
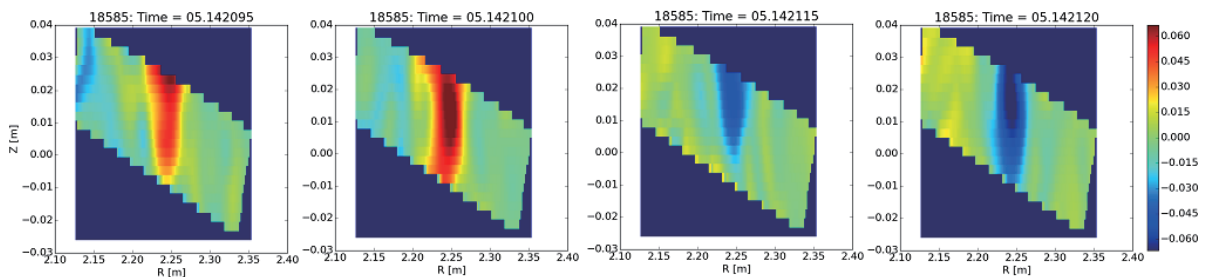
Figure 7. ELM filaments moving downward near separatrix (R~2.24 m)

The observation of ELM filaments in the plasma edge in the mid-plane and the coherent fluctuations of similar frequency by the Langmuir probes on divertor (outside the region of confinement) hints at possible connection. The mechanism behind this connection will be investigated in future.

4. Incoherent fluctuations

In another H-mode KSTAR shot 18559, intermittent fluctuations are observed in fixed Langmuir probe I_{sat} in KSTAR. For this discharge, the magnetic field at the magnetic axis ~1.8 T, plasma current ~0.7 MA, total neutral beam heating power ~2.8 MW, total stored energy ~300 kJ. Magnetic perturbations are

applied at 5 – 28 s. The typical tokamak signals for this discharge are shown in Fig. 8. The ELM mitigation and ELM suppression phases are evident from the H_α time trace.

The first ELM suppression window, starting around 5.5 s is followed by mitigated ELM phase and then another ELM suppression window. The I_{sat} signal on some of the fixed Langmuir probes exhibit bursts. The probability distribution function (PDF) of the I_{sat} fluctuations for probe 54 is shown in Figures 9 and 10, in the first and second ELM suppression phases as depicted by red vertical lines in Fig. 8. In both cases the distribution deviates from the Gaussian; positively skewed in Fig.9 and negatively skewed in Fig.10. If these positive and negative bursts are due to the density blobs and holes respectively or other mechanisms shall be investigated in future.
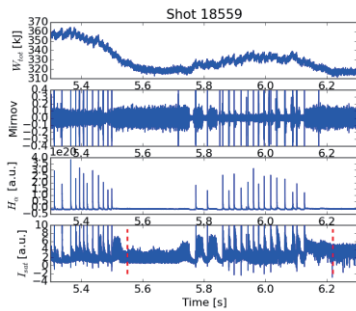
Figure 8. Typical signals for shot 18559
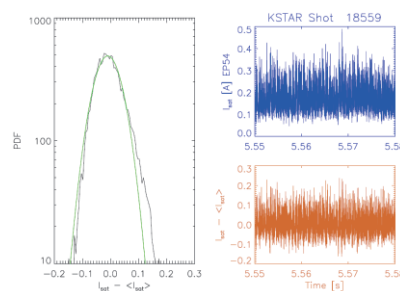
Figure 9. PDF during first ELM suppression window
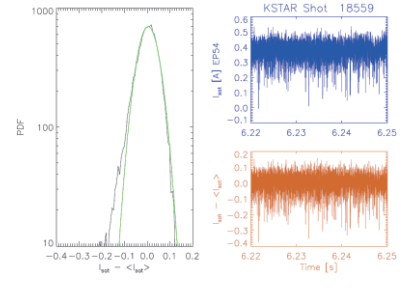
Figure 10. PDF during second ELM suppression window

5. Summary

Coherent fluctuation in the fixed Langmuir probe (I_{sat}) on the divertor is accompanied by ELM filaments of similar frequency in the midplane. In another discharge, incoherent fluctuations with changing sign of skewness occur during the ELM suppression phase. Mechanisms behind these phenomena shall be investigated further.

References

[1] J.G. Bak, H.S. Kim, M.K. Bae et al., J. Nucl. Mater. **463** (2015) 424

[2] H.S. Kim, J.G. Bak, M.K. Bae et al., Fusion Engineering and Design **109-111** (2016) 809

[3] J. Lee, G.S. Yun, M.J. Choi et al., Phys. Rev. Lett. **117** (2016) 075001

The wall retention research by particle balance in KSTAR 2016 experiment

B. Cao[a,b*] ,S. H. Hong[a,c,d+], K. P. Kim[a] and J.W. Juhn[a]

[a]*National Fusion Research Institute, Daejeon Korea*

[b]*Institute of Plasma Physics, Chinese Academy of Sciences, Hefei China*

[c]*Department of Electrical Engineering, Hanyang University, Seoul Korea*

[d]*Department of Accelerator and nuclear fusion physical engineering, Korea University of Science and Technology, Daejeon, Korea*

Email address: [*]*caobin@nfri.re.kr* *and* [+]*sukhhong@nfri.re.kr*

Abstract

The wall retention has been investigated by particle balance in KSTAR 2016 experiment campaign. The total injected fuel particles during discharges are 5.55×10^{24}D, the total removed fuel particles during wall cleaning are 8.34×10^{23}D and the total retained particles are 1.99×10^{24}D with a averaged retention rate of 1.45×10^{20} Ds^{-1}. The daily wall retention research shows that there is wall saturation after a long time discharges during one day. After wall saturation, it is hard to achieve high quality plasma discharge. The difference of wall retention between different discharge types is studied in this work. The results show that the wall retention is independence from plasma current and density. The main parameters, which could affect the wall retention, are pulse length and injected particles. There are a lot of particles outgassing from wall after disruption, which could lead to negative wall retention.

1. Introduction

The control of long term fuel retention is one of the most critical issues for both ITER and other Tokamaks aiming at operating in steady-state conditions [1-3]. And particle balance is a reliable method for this research. Wall retention affects fuelling efficiency, plasma density control and the neutral particle density in the plasma edge, which in turn affects plasma confinement [1]. Furthermore, excessive tritium accumulation in the first wall will introduce a safety problem for the next fusion device, such as ITER. The limit of maximum tritium retained in first wall for ITER is 700g [1, 3].

There are three main fuel retention mechanisms: absorption, implantation and co-deposition [4]. Normally the absorbed particles will release after the discharges. The implantation depth is limited by incident particle energies and the first wall temperature. Both of the two kind retentions could reach saturation. Once the surface is saturated, wall pumping capability will be decreased. And it can be recovered by means of wall cleaning, baking, and even disruptive discharges. But there is no saturation for co-deposition [2-5].

Wall retention research in current tokamak could provide good database for future device such as ITER. Particle balance is a more convenient method compared with post-mortem analysis [6]. Global particle balance analysis is popularly used in different tokamaks. The first particle balance results in KSTAR are shown in reference [7]. In this paper, we will show the fuel retention research in KSTAR last year experiment campaign. The relation between plasma parameters and fuel retention is studied.

2. Calibration of fueling systems

Korea Superconducting Tokamak Advanced Research (KSTAR) is a full superconducting tokamak with a 1.8m major radius and 0.5m minor radius, and it has single-null divertor plasma configurations [8]. In the KSTAR 2016 experiment campaign the magnetic field (B_t) is from 1.2T to 3T. There are three different fueling systems installed on the KSTAR: Gas Puffing (GP), Supersonic Molecular Beam Injection (SMBI) and Neutral Beam Injection (NBI).

GP through piezoelectric valves installed for the fast response is the main source of fuel both for prefilling the vacuum chamber and for controlling the density during plasma operation. The effective fueling rate of piezoelectric valves are calibrated every year just before experiment [9]. An example of calibration data is shown in figure 1, the gas puffing rate can be calculated by the function as below:

$$\Gamma_{GP}(D/s) = 10^{20}(aU_{pv}^3 + bU_{pv}^2 + cU_{pv} + d) \tag{1}$$

where Γ_{GP} is the puffing rate in Ds^{-1} and U_{pv} is the imposed voltage of the piezoelectric valves in volts. The parameters for all piezoelectric valves of KSTAR in 2016 experiment campaign are shown in table 1.
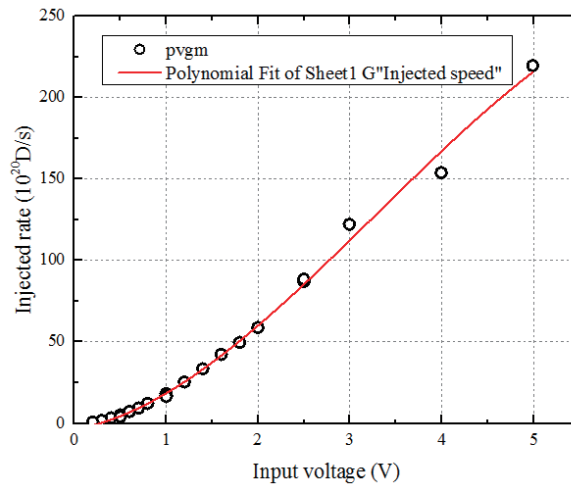
Fig. 1. Calibration of piezoelectric valve of puffing speed, the black points are the puffing rates under different input voltages and the red line is the fitting of these points.

Valve	a	b	c	d
PVGM	-0.072	1.72	1.221	-0.062
PVJL	-3.171	22.736	5.361	-0.691
PVDB	-0.072	1.72	1.221	-0.062
PVOM	-22.233	91.377	26.982	-0.899
PVIM	-0.065	-0.708	22.519	-0.636

Table 1. The parameters of KSTAR piezoelectric valves in 2016 experiment campaign

SMBI is an innovative concept of fueling method used in many tokamaks such as HL-2A, JET and EAST [10-11]. It bursts fuel in supersonic gas phases so that substantial amounts of the gases are quickly transported to the edge of plasma, and those fuels are expected to penetrate into deeper regions of the plasma edge. As shown in figure 2, the amounts of injection by SMBI are correcting with SMBI operation pulse length. The averaged result of SMBI injection in KSTAR 2016 experiment campaign rate was:

$$\Gamma_{smbi}(D/s) = 2.93 \times 10^{22} + \frac{1.29 \times 10^{19}}{t_{smbi}} \tag{2}$$

where Γ_{smbi} is the injection rate of SMBI in Ds^{-1} and t_{smbi} is the SMBI operation pulse length in s.
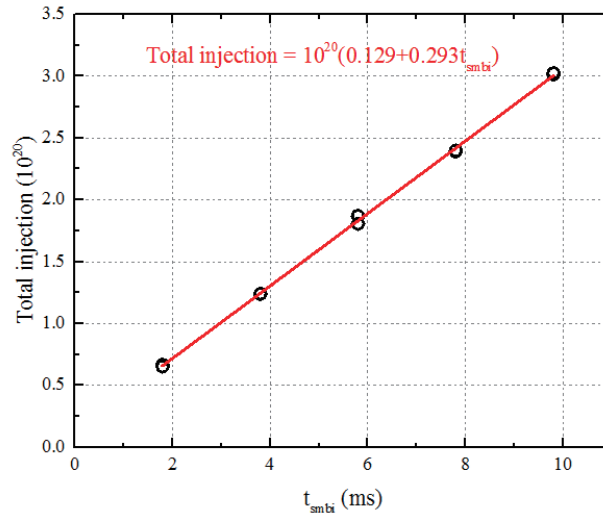
Fig. 2. SMBI calibration results

NBI is the main source of heat power in KSTAR, but the NBI not only provide the source of energy and the deuterium particles. Particle injection via the NBI system is evaluated by

$$\Gamma_{NBI}(D/s) = 6.25 \times 10^{21} \cdot \sum_{n=1}^{3} \frac{P_{NBI,n}}{E_{NBI,n}} + 4 \times 10^{16} E_{NBI,n} \tag{3}$$

where Γ_{smbi} is the injection rate of SMBI in Ds^{-1}, P_{NBI} is the injected power of NBI in MW, E_{NBI} is the injected particle energy in keV. The last part is a small quantity of neutral deuterium from the NBI chamber as calibration from without any NBI beam.

3. Particle balance

Particle balance used the difference between the puffed particles and the pumped particles to calculate the retained particles in the wall. The particle retention rate Γ_{wall} is calculated by the function below:

$$\Gamma_{wall} = \Gamma_{GP} + \Gamma_{smbi} + \Gamma_{NBI} - \Gamma_{pump} - \frac{dN_p}{dt} - \frac{dN_V}{dt} \tag{4}$$

Γ_{pump} is the exhausted particle rate by the KSTAR pumping system:

$$\Gamma_{pump} = P \cdot S_{eff} \tag{5}$$

where P is the measure pressure of vacuum vessel, S_{eff} is the effective pumping speed of vacuum pumping system. The effective pumping speed for KSTAR is 13.56 m^3s^{-1} without inner cryo-pump and 43.56 m^3s^{-1} with inner cryo-pump. And when NBI system connected with the main camber, the NBI system would provide an additional effective pumping speed of 28.44 m^3s^{-1}.

N_p is the deuterium ions in the plasma:

$$N_p = \frac{n_e}{L_{chord}} \cdot V_{plasma} \tag{6}$$

where n_e is the line integral density and L_{chord} is the length of chord. The V_{plasma} is the plasma volume.

N_v is the neutral particles in the vacuum vessel:

$$N_v = P \cdot (V_{vessel} - V_{plasma}) \tag{7}$$

where V_{vessel} is the volume of KSTAR vacuum vessel, it is about 110 m^3.

We do the similar error analysis as [7]. The error of particle injection is about 5% from the fuelling systems calibration. The error of pumping speed of pumping systems is about 10%, and the error of exhausted particles is about 5% from pressure measurement, the total error of exhausted particles is about 15%. The amount of injected particles is about 2~3 times than retained particles, so the error of total retained particles is about 25%. During experiment we used the retained particles divided by the total

injected particles as retention fraction and the retained particles divided by discharge pulse length as retention rate.

4. Experimental results

4.1 Total fuel retention of KSTAR 2016 campaign

Figure 3 shows the whole particle balance in KSTAR 2016 experiment campaign: injected, removed by GDC at night and early morning, and accumulated retained particles. During GDC at night and early morning the removed rate by GDC is about $3.5\times10^{17}\,Ds^{-1}$, we used the data cross the total GDC time at night and early morning to calculate the removed particles by GDC every day. From figure 3, it is clearly seen that the total retention increased as a function of plasma duration time. At the beginning of this campaign there is a negative retention due to the low injected particles in experiment, the GDC at night and early morning removed more particles than retained during experiment at day. The total shots of 2016 KSTAR experiment campaign is 2424 (including the dummy shots), the total plasma duration time is 12857s, the total injected particles is 5.55×10^{24} D, the total removed particles by GDC is 8.34×10^{23} D and the total retained particles is 1.99×10^{24} D. The total retention fraction for the whole 2016 experiment campaign is about 35.8% and the averaged retention rate is about $1.45\times10^{20}\,Ds^{-1}$. The retention fraction is higher than 21% in KSTAR 2010 experiment campaign [7] because of the longer shot's pulse length. The longer pulse shot normally need more injected particles, the retention fraction increased with injected particles. The total injected particles (5.55×10^{24} D) and retained particles (1.99×10^{24} D) in KSTAR 2016 experiment campaign are about an order of magnitude bigger than injected particles (5.3×10^{23} D) and retained particles (1.1×10^{23} D) in KSTAR 2010 experiment campaign [7].
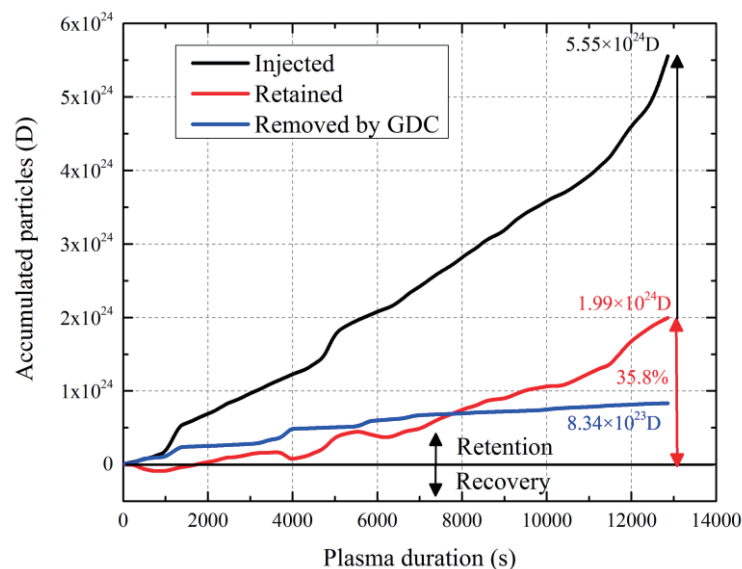
Fig. 3 Total accumulated particles of injected (black), removed by GDC during night and early morning (blue), and the retained in 2016 KSTAR experiment campaign (red) as a function of accumulated plasma duration. The detail number of total injected, removed by GDC and retained particles are shown in Table 2.

The number of retained particles and retention fraction of discharges (not including the dummy shots) obtained using particle balance are shown in figure 4. In this figure, the plasma current < 100 kA and pulse length < 1s are consider as failed discharges. The plasma current decay time define as the '60% linear decay' time, which is the time required for a 60% drop of the pre-disruption plasma current, from 95% to 35% [13], and the plasma current quench rate is also calculated from this 60% decay. In figure 4, the shots with plasma current quench after discharges larger than 40 MAs^{-1} are consider as disruptive discharges, and the shots with plasma current lower than 40 MAs^{-1} are consider as non-disruptive discharges (normal discharges) [7]. From figure 4(a), the retained particles increased with the injected particles. As shown in figure 4(b), with the increasing of injected particles the range of retention fraction was getting more and more narrow. While the number of injected particles is larger than 4×10^{21} D, there is no negative retention fraction even for disruptive discharges. The retention fraction is up to 80% with a very low deviation when the injected particles larger than 1.2×10^{22} D. The total injected and retained particles of 1275 normal discharges are 3.78×10^{24} D and 2.52×10^{24} D, the averaged injected and retained particles for normal discharges are 2.96×10^{21} D and 1.97×10^{21} D and the averaged retention fraction for normal discharges is about 66.6%. The total injected and retained particles of 352 disruptive discharges are 7.15×10^{23} D and 1.81×10^{23} D, the averaged injected and retained particles for disruptive discharges are 2.03×10^{21} D and 5.14×10^{20} D and the averaged retention fraction for disruptive discharges is about 25.3%. The total injected and retained particles of 621 failed discharges are 8.52×10^{22} D and -2.79×10^{22} D, the averaged injected and retained particles for failed discharges are 1.37×10^{20} D and -4.49×10^{19} D and the averaged retention fraction for failed discharges is about -32.7%. The averaged retention fraction for disruptive discharges is lower than that for normal discharges.
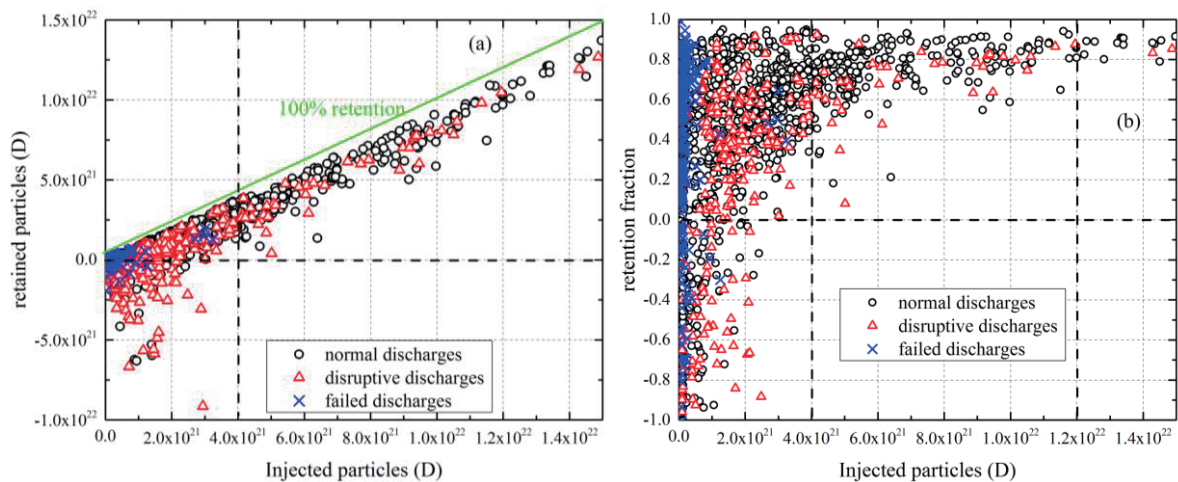
Fig. 4. Retained particles and retention fraction versus injected particles

4.2 Daily fuel retention analysis

There are total 58 days discharges in 2016 KSTAR experiment campaign. The average daily injected particles are 7.94×10^{22} D and average retained particles are 4.68×10^{22} D. Figure 5 shows the daily retention rate and retention fraction versus the total injected particles of every day. It is clearly, there is a strong correction between retention and injection. The averaged daily retention rate increased with the total injected particles during this day. For low total injected particles of one day ($<5 \times 10^{22}$ D), sometimes the fuel retention could be negative. The average daily retention rate increased up to about 7.5×10^{20} D/s with the injected particles, the averaged retention rate of all these days is about 2.2×10^{20} D/s, and most averaged daily retention rate is below than 4.5×10^{20} D/s. The maximum daily retention fraction is about 80%. While the injected particles more than 1×10^{23} D during one day, the daily average retention fraction is about 60%~80%.
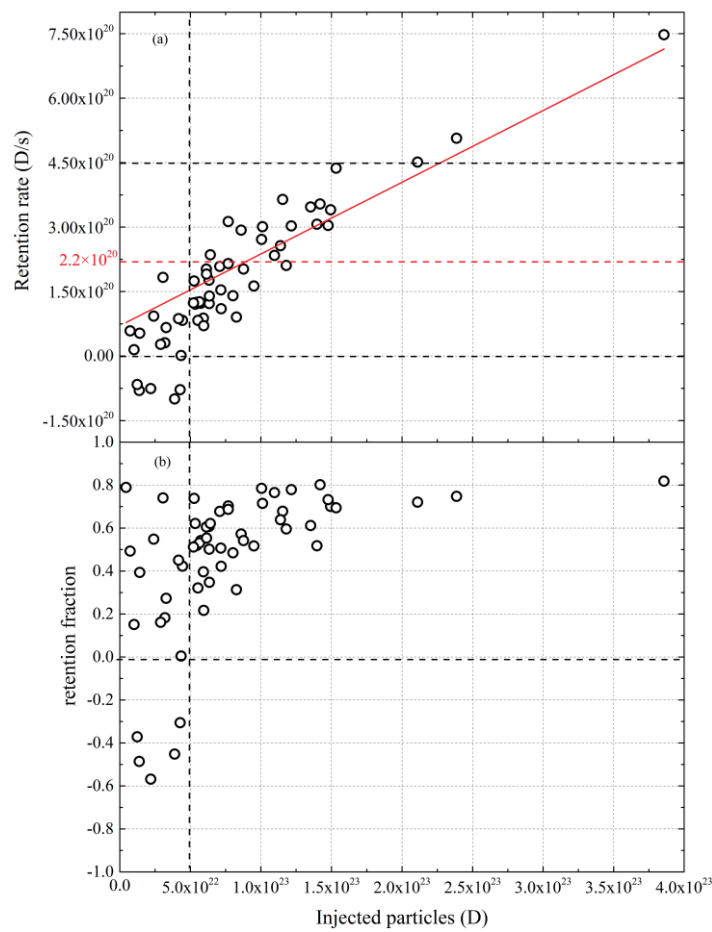
Fig. 5 Daily retention rate and fraction versus daily injected particles

4.3 The effect of plasma parameters on fuel retention

Retention is the process between plasma and first wall, and plasma scenario plays an important role in this process. In this part we chose the soft landing shots with positive retention in 2016 KSTAR experiment campaign and tried to find out the relation between retention and these plasma parameters.

4.3.1 The plasma parameters not affect fuel retention

Plasma current is a main parameter for plasma confinement [14]. And the wall retention would affect the density feedback [15]. We tried to find out the plasma current and electron density would affect fuel retention or not. Unfortunately there is no correction between plasma current, electron density and fuel retention. Then after that, we tried electron temperature, toroidal magnetic field and NBI injected power. The fuel retention is independent from all these plasma parameters.

4.3.2 Pulse length

The relationship between pulse length and retention is very important to predict retention on ITER. The correlation between pulse length and retention rate was shown in [7]. But the pulses lengths are less than 7s in this paper. In KSTAR 2016 experiment campaign the longest discharges is up to 70s. Figure 6 shows the correlation between and averaged retention rate at different plus length (larger range) versus the injected particles. The results are similar with paper [7], for pulse length lower than 25s, the retention rate increased with injected particles. As the pulse length increased, the gradient of retention rate decreased that indicating that retention decreased. For pulse length longer than 25s, the retention rate is around 1.9×10^{20} Ds^{-1}, which is quite similar with Tore Supra (2×10^{20} Ds^{-1}) [16].
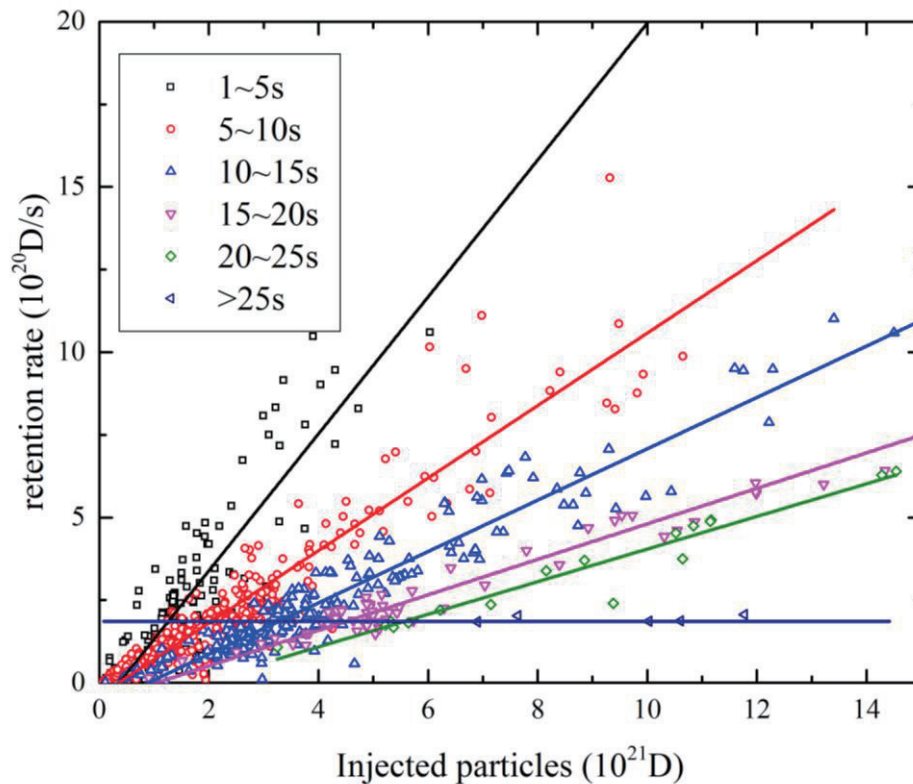
Fig. 6 Retention rate versus injected particles for different pulse length

4.3.3 Ohmic, L-mode and H-mode discharges

The H-mode is the projected baseline operational scenario for the International Tokamak Experimental Reactor (ITER) [17]. The difference of fuel retention for Ohmic, L-mode and H-mode discharges is very important to predict the fuel retention on ITER. Figure 7 shows the correlation between retention fraction for Ohmic, L-mode and H-mode discharges versus the injected particles. From figure 7, there is no difference for Ohmic, L-mode and H-mode discharges at injected particles more than 6×10^{21} D. At this range of injected particles the retention fraction is very high (60%~90%). But for at range of $1\sim6\times10^{21}$ D of injected particles, the retention fraction for H-mode discharges is lower than for Ohmic and L-mode discharges. From figure 8, for similar injected particles, the H-mode discharges had a little higher electron density than L-mode and Ohmic discharges. This means the H-mode discharges had a liter higher fueling efficiency for low injection ($<6\times10^{21}$ D). Since the retention has strong correction with injected particles. This is the reason for lower retention fraction for H-mode discharges with low injected particles.
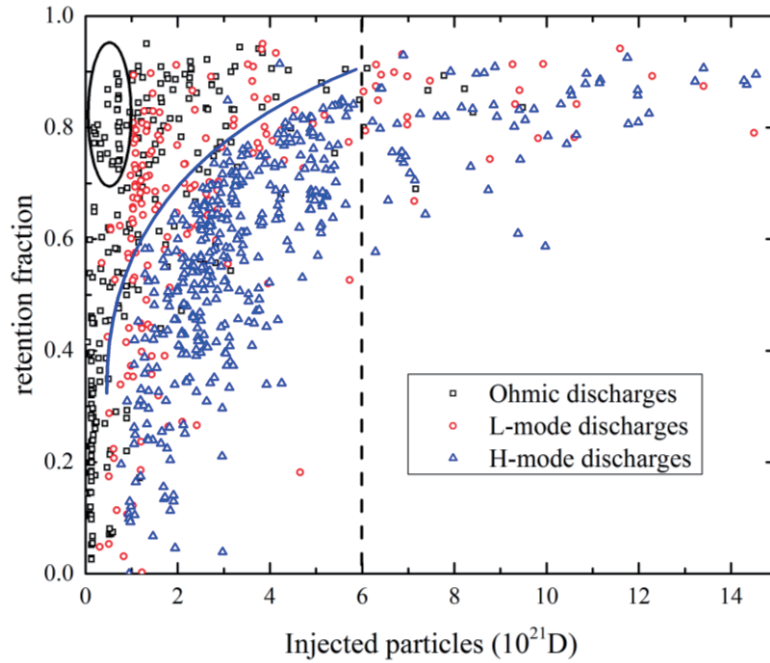
Fig. 7 Retention fraction versus injected particles for Ohmic, L-mode and H-mode
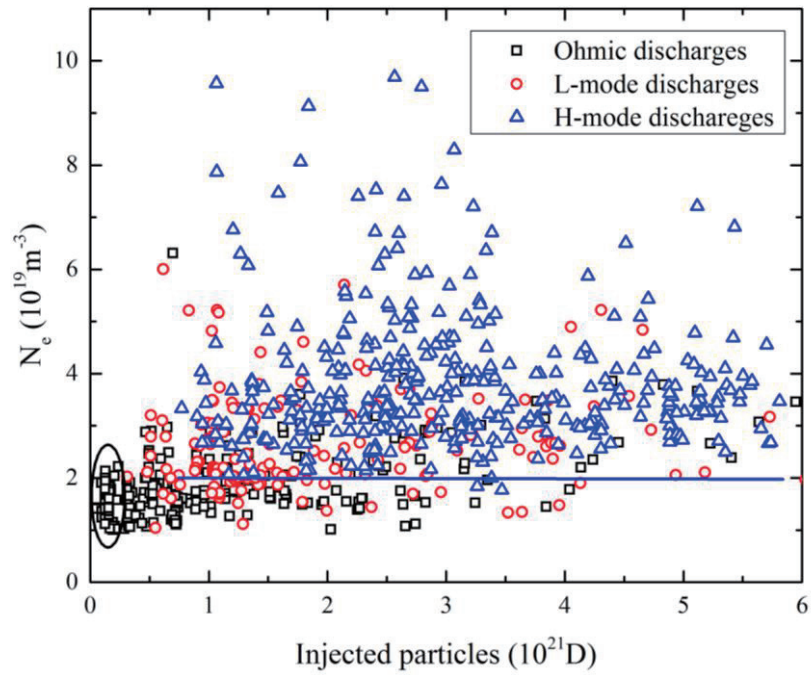
Fig 8 Maximum electron density as a function of the total injected particles

4.4 Fuel recovery by disruptive discharges

As show in part 4.1, the averaged retention of disruptive shots is lower than non-disruptive shots in KSTAR 2016 experiment campaign. Disruptions release more particles than non-disruption was also observed in EAST [18], JET [19], Tore Supra [20], Alcator C-mod [21] and DIII-D [22]. After disruption, a lot of high energy particles directly deposited on the first wall, which would cause more particles released from the first wall. Sometimes there is a negative retention after disruption, which means net fuel recovery after disruption. From figure 4 there is no negative retention (net fuel recovery) with high injected particles (more than 4×10^{21} D) even for disruptive shots. All these negative retention shots are shorter than 10s, most of them are about 2~4s. We chose the shots' pulse length at 2~4s, and showed on figure 9 and figure 10.
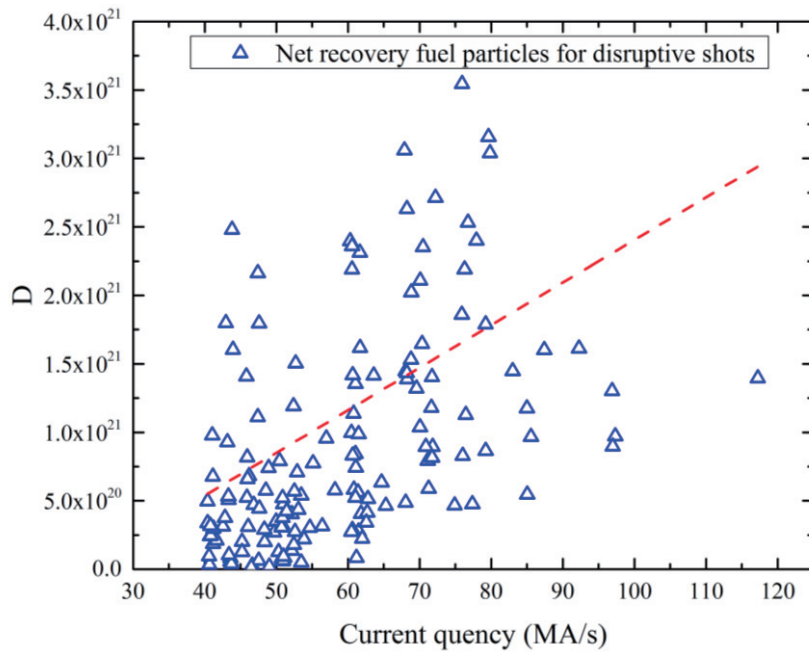
Fig. 9 Net fuel recovery for disruptive shots versus current quench rate

Figure 9 shows the correcting between net fuel recovery and current quench rate after disruption. The current quench rates have been calculated from the current decrease from 95% to 35%. From this figure the net fuel recovery after disruption had weekly affected by the current quench rate.
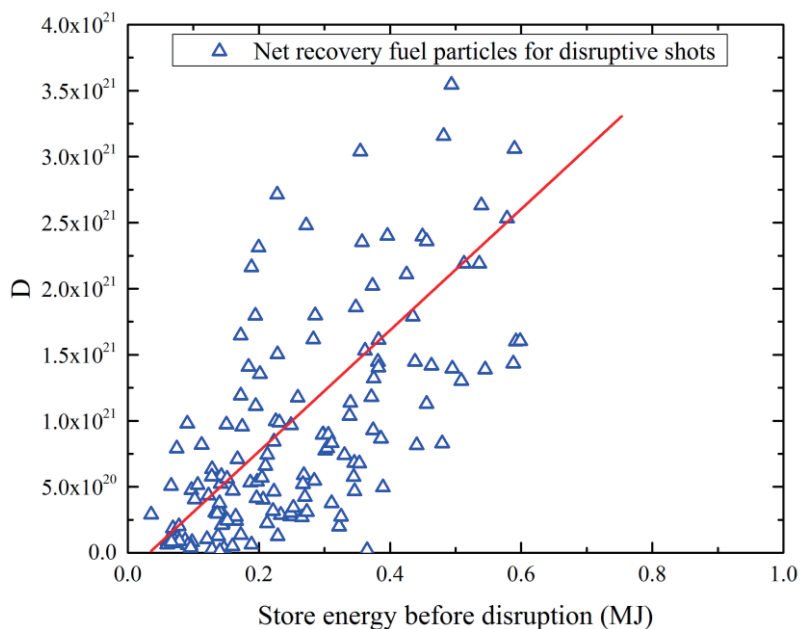
Fig. 10 Net fuel recovery for disruptive shots versus stored energy before distuption

In figure 10, we compared the net fuel recovery of these shots with different store energy just before disruption. The trend is more clearly than figure 9. With more stored energy, the disruption could lead more net fuel recovery.

5. Summary and conclusion

In KSTAR 2016 experiment campaign, particle balance is employed to be investigated fuel retention with different plasma parameters. During the whole campaign, the total retained Deuterium particles (not including the removed particles by GDC cleaning at night and early morning) are 1.99×10^{24} D with a averaged retention rate of 1.45×10^{20} Ds^{-1} (long-term retention). It is observed that the number of retained particles increased with number of injected particles in both non-disruptive and disruptive shots. During 58 days discharges in 2016 KSTAR experiment campaign, the average daily injected particles are 7.94×10^{22} D and average retained particles are 4.68×10^{22} D. The averaged retention rate during discharge is about 2.2×10^{22} D/s (long-term and dynamic retention).

Comparing fuel retention in different discharges, the retention is independent from plasma current, electron density, toroidal magnetic field, electron temperature and NBI injected power. For lower injected particles (less 6×10^{21} D), the retention fractions of H-mode discharges are lower than the retention fractions of Ohmic and L-mode discharges because of the higher fueling efficiency. In most cases, the retention rate increased as function of the number of injected particles. For different pulse length, the gradient of retention rate decreased with pulse length increased. For pulse length longer than 25s, the retention rate is around 1.9×10^{20} Ds^{-1}, which is quite similar with Tore Supra (2×10^{20} Ds^{-1}) [16]. The disruptive shots had lower retention than non-disruptive shots. Sometimes disruption could lead a negative retention (net fuel recovery) especially the disruptions with large store energy and high current quench rate.

References:

[1] G. Federici et al., Nucl. Fusion, 2001, 41, 1967-2137

[2] T. Loarer et al., Nucl. Fusion, 2007, 47, 1112-1120

[3] T. Loarer et al., J. Nucl. Mater., 2009, 390-391, 20-28

[4] J. Roth et al., Plasma Phys. Control. Fusion 2008, 50, 103001

[5] E. A. Unterberg et al., J. Nucl. Mater. 2011, 415, S740-7

[6] T. Loarer et al., 31st EPS Conf. on Plasma Phys. 2004, 28G, P-1.139

[7] Y. Y. Yu et al., Plasma Phys. Control. Fusion 2012, 54, 105006

[8] K. Kwon et al., Nucl. Fusion 2011, 51, 094006

[9] J. W. Juhn et al., J. Korean Phys. Society, 2014, 65

[10] C. Chen et al., J. Plasma Fusion Res. SERIES, 2010, 9

[11] L. Yao et al., Nucl. Fusion 2007, 47, 1399-1410

[12] X.W. Zhen et al., Plasma Phys. Control. Fusion 2013, 55, 115010

[13] ITER Physics Basis Chapter, Nucl. Fusion, 1999, 3

[14] ITER Joint Central Team, Nucl. Fusion, 39 (1999) 1295

[15] J. W. Juhn et al., J. Korean Phys. Soci., 65, 2014

[16] E. Tsitrone et al, Nucl. Fusion, 49, 2009, 075011

[17] C. Gormezano et al., 2007 Progress in the ITER Physics Basis Chapter 6: Steady State Operation, *Nucl. Fusio*n, 47, S285

[18] B. Cao et al., Nucl. Mater. Energy, in press

[19] V. Philipps et al., J. Nucl. Mater., 390-391, 2009, 478-481

[20] B. Pegourie et al., J. Nucl. Mater., 415, 2011, S809-812

[21] D. G. Whyte et al., 2006 Proc. 21st Int. Conf. on Fusion Energy (Chendu, China)

[22] E. M. Hollmann et al., Pegourie, J. Nucl. Mater., 390-391, 2009, 597-601

Acknowledgements

Characterization of hydrogen-like pellet ablation clouds in the LHD

G. Seguineaud[1], G. Motojima[1,2], Y. Narushima[1,2], M. Goto[1,2]

[1]Graduate University for Advanced Studies, Toki 509-5292, Gifu, Japan

[2]National Institute for Fusion Science, Toki 509-5292, Gifu, Japan

Abstract

Spatial resolution spectroscopy of hydrogen-like pellet ablation clouds is conducted in the LHD. With a focus on the Balmer lines, some ablation clouds are observed with enough clarity to attempt to characterize them. The spectrometer designed and built for the purpose of providing these results is thoroughly presented. Qualitative observations as well as preliminary fitting results are also mentioned.

1. Introduction

Spatial resolution analysis of pellet ablation clouds is carried out using a proof-of-concept approach. A spectrometer with a field-of-view narrow enough to observe slices of ablation clouds has been designed, built and installed on the LHD. To create a narrow field-of-view, a plano-convex cylindrical lens can be used. The field-of-view can be estimated using a laser beam. A Light beam passing through the plane side of such a lens would come out as a linearly redistributed image at the other side. Such a phenomenon could be reversed to collect the light emitted from an object into an optical fiber.

By combining a cylindrical plano-convex lens, an optical fiber and a spectrometer, it should be possible to record the light emitted by ablation clouds as they transit through a band-shaped field-of-view. Data thus obtained could give access to plasma parameters of slices of ablation clouds such as the electron density and temperatures. It means that by using this system, it should be possible to create the spatial profile of any ablation cloud at almost any time.

Should this new experimental device show that it can be used as designed, it could provide another way to study pellets injection and pellets ablation processes. Also, the validity of the Local Thermodynamic Equilibrium (LTE) condition which is usually assumed in this case could be tested.

The LTE assumption implies that the evolution of some (intensives) plasma parameters in a localized area is small enough to assume that the system can be considered as homogeneous. Here, the parameters would be the electron temperature and density, and the system would be the ablation cloud.

By using this assumption, a previous study [1] showed that the gradients of the electron density and temperature distributions of ablation clouds (from the core to the edges) were both decreasing. The latter observation needs to be considered in more depth as it is not an 'expected' result considering that the electron temperature of the background plasma surrounding the pellet is a lot higher (>>1.0keV). Indeed, it is more natural to think that the outer plasma shells of the ablation cloud are more 'thermalized' with the background plasma than the inner shells, meaning that the electron temperature gradient should be the opposite of what has been found.

2. Experimental setup

Plasma diagnostics of pellets ablation clouds are conducted in the Large Helical Device. The LHD is a heliotron-type experimental machine that study magnetically confined fusion plasmas. Hydrogen or deuterium fuel pellets are injected into the plasma of the LHD at an approximate velocity of 1000.00 m/s. Pellets interact with the background plasma of the LHD, leading to the formation of an ablation cloud around the pellets. Ablation clouds emit intense radiations, part of which are, first, collected by an observation system, then, sent to a spectrometer for analysis. A support flange fixed on the observation port points to a specific area on the trajectory of the pellet (cf. Fig.1).
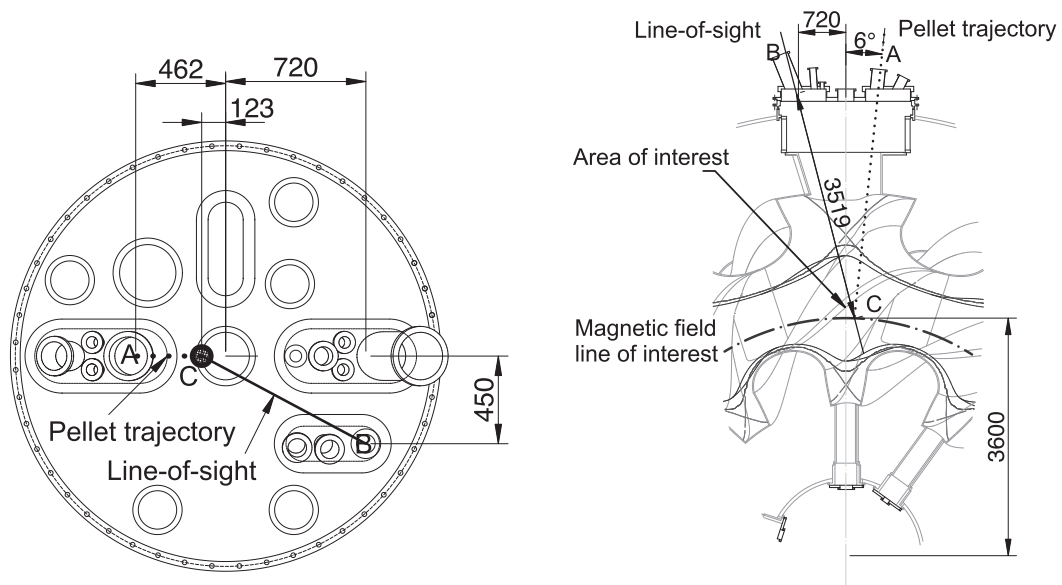
Fig.1 Experimental montage on the LHD of the observation port (left) and the mid-section at the observation port (right) where A is the pellet gun, B the observation port and C is the Area of interest.

The observation system is targeting an area where the magnetic field lines are as perpendicular as possible with the line-of-sight of the observation system (noted by the letter 'C' in Fig.1). Like so, the observation system is able to collect data of the 'best profile' of the ablation cloud possible, provided the pellet trajectory is not modified.

The observation system is comprised of a lens and an optical fiber which are both installed in a lens tube. The lens, from Thorlabs (ref: LJ1695RM), is an uncoated UV fused silica plano-convex cylindrical lens that has a focal length of 50.00 mm. The optical fiber is a 100.00 μm multimode optical fiber that has a numerical aperture of 0.2 (i.e. an acceptance angle of ~10.00º). These two components are combined so the field-of-view of the system has a vertical slit-like shape and a focal point where the pellet trajectory and line of sight decussate.

Let's consider an ablation cloud which is roughly elongated in the horizontal direction (i.e. along the magnetic field lines) in such a way that it crosses the line-of-sight from one side to another of the field-of-view of the observation system. If the time resolution of the measurement is fast enough, spatially resolved spectra of ablation cloud slices are obtained. Fig.2 illustrates the geometry between the pellet trajectory, the elongated ablation cloud, and the field-of-view of the experimental setup.
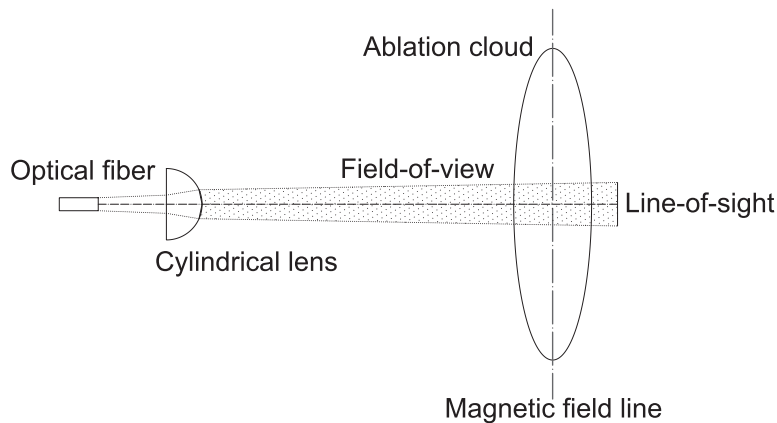
Fig.2 Ideal case illustration of the crossing between the trajectory of the pellet ablation cloud and the line-of-sight of the observation system. Dimensions are not to scale. Values given in [mm]

The optical fiber having a finite dimension, the lens having chromatic aberrations, the world is never how ones want it to be, the theoretical field-of-view of 7.00 mm estimated by the lens equation is actually not what has been measured. The width of the field-of-view at the focal point has been experimentally measured to be ~20.00 mm.

Also, it is important to note that the pellet trajectory, unless perturbed, does not coincide with the magnetic field line. It means that the light that observation system is collecting is never at the same distance. Although that may be of importance, the effect of this phenomenon has been neglected in the present study. To know where the spectrometer is looking at, a Phantom V7 fast camera is also used. It has a sampling rate set of 20.00 μs per frame with an effective exposure time of 1.00 μs. The light-source processed by the fast camera is obtained from Fujikura fiberscopes (ref: II-03D9057A) located on the same support flange as the lens tube.

The spectrometer (cf. Fig.3) comprised of a box containing a grating and a camera is located in a remote area to avoid signal-noise produced by neutral particles bombardment coming from the fusion device. The optical fiber which provides the light-source coming from the observation port is directly placed at the entrance of the box. No slit has been judged necessary as the observation system already fill a similar function. The light emitted from the optical fiber is both diffracted and focused on the detector thanks to the grating.
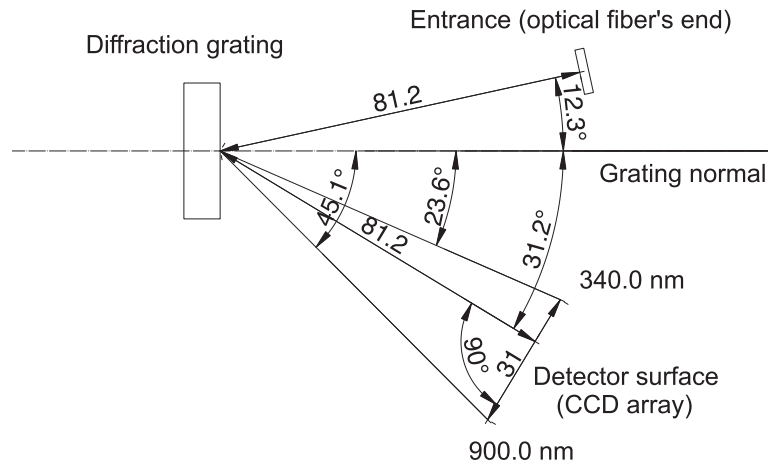
Fig.3 Simplified schematic of the spectrometer. Values given in [mm]

The grating used is a flat-field aberration-corrected holographic grating from Shimadzu (ref: P0550-01TR). It has an operating wavelength range comprised between 340.00 nm and 900.00 nm. Its nominal blaze wavelength is at 340.00 nm. Relative diffraction efficiency of the grating is given as being of 50.00% (minimum) at nominal blaze wavelength.

The camera used is a NEOPT (ref: NCAM2-BLD-04K070CL) which has an "announced" operating wavelength range comprised between 350.00 nm and 1050.00 nm. It is a 2 lines CCD camera, each line having 4096 pixels measuring 7x7μm each. In this experiment, the camera is set in a 2x2 binning mode where squares of 4 adjacent pixels are recombined into one bigger 'pixelsblock', emulating a one line CCD camera of 2048 pixels measuring 14x14μm each. The configuration of the camera is such that it outputs 12 bits frames at a sampling rate of approximately 71.4 kHz (i.e. 14.00 μs per frame with an effective exposure time of 11.00 μs).

The absolute sensitivity of the entire system has been calibrated with a uniform source sphere from labsphere (ref: AS-02576-100). The absolute wavelength range of observation of the spectrometer is estimated to be between 340.00 nm and ~830.00 nm.

It is also necessary to note that the Balmer-α line is often saturated due to the limited dynamic range of the detector. This is not problematic in this case because the Balmer-α line profile is influenced by the reabsorption effect which makes the analysis complicated anyway.

Instead, an emphasis is placed on measuring the continuum radiation as well as the Balmer-β and Balmer-γ lines which are more accessible to characterize ablation clouds. However, the weak quantum efficiency of the detector at wavelengths lower than 340.00 nm makes it difficult to obtain accurate spectra usually at and over the transition to the continuum point (i.e. where isolated lines are not observable anymore).

3. Results and discussion

Measurements were made for a plasma with a magnetic configuration of $R_{ax} = 3.6$ m and $B_{ax} = -1.5$ T, where R_{ax} is the major radius at the magnetic axis and B_{ax} is the magnetic field strength at the magnetic axis.

A discharge where a series of six deuterium pellets is injected between t ~ 3.7 s and 3.9 s is selected. Fig.4 shows the temporal evolution of some relevant parameters of the background plasma. The line-averaged electron density $<n_e>_{line}$ is increasing whereas the central electron temperature T_{e0} is decreasing. Data obtained from a spectrometer of the H-α line emitted by the ablation cloud show that there is a correlation between the ablation process and the quick evolution of the background plasma parameters. A focus is put on the last injected pellet as it has been deemed to be the most appropriate for analysis.
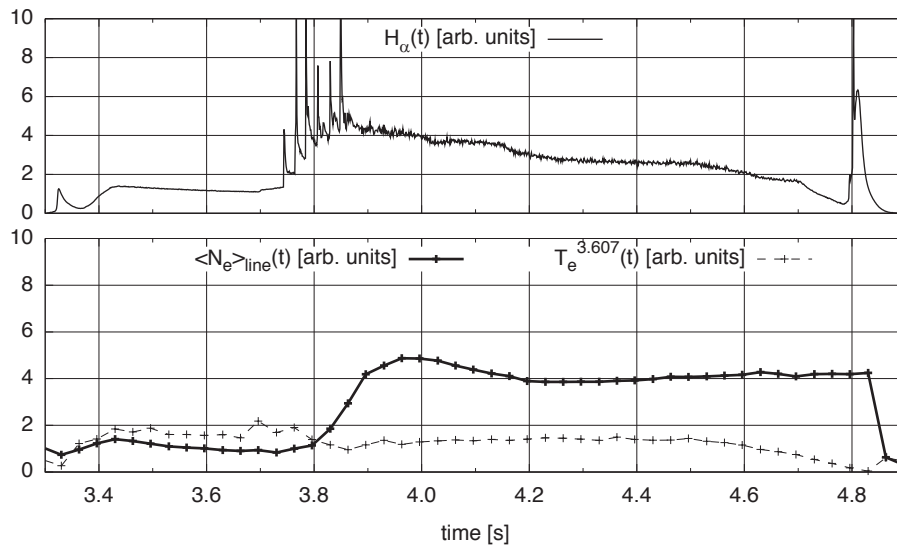
Fig.4 Background plasma parameters: H-α emission line (top), $<N\_\{e\}>_{line}$ and T_e^{core} (bottom). All are in function of time.

Fig.5 shows the comparison between the line-integrated data of the spectrometer with the simulated area of the line-of-sight on the fast camera data. Intensities have been re-adjusted for the sake of comparison. Time-stamps also require to be re-adjusted because there is a delay between the acquisition systems. It has been estimated to be of ~ 60.0 μs and is mainly due to the behavior of the trigger of the spectrometer which begin recording ~ 100.0 μs after that the initial trigger of the LHD has been sent. Discrepancies observed between 300.00 μs and 500.00 μs can be explained by two causes, although it is not clear yet which one is dominant. These causes are:

- a difference of effective exposure time between the fast camera (1.0 μs) and the spectrometer (11.0 μs).
- an imperfect lens-fiberscope alignment leading to the existence of an angle between the fields-of-view of the spectrometer and the fast camera.

A difference in effective exposure time means a difference in the quantity of light collected by the

apparels. Moreover, both devices have their own characteristics which makes them react slightly differently when exposed under the same light source.

A misalignment between both observation systems means that the angle with which they observe the pellet trajectory with is also different. Consequently, the 'way' light is sent to their respective detector has a different intensity profile.

A solution to the first problem would be to synchronize the effective exposure time of both apparels, whereas a solution to the second problem would be to correct the angles between both observation systems. For the rest of this study, the field-of-view of both apparels are supposed identical (i.e. no misalignment).
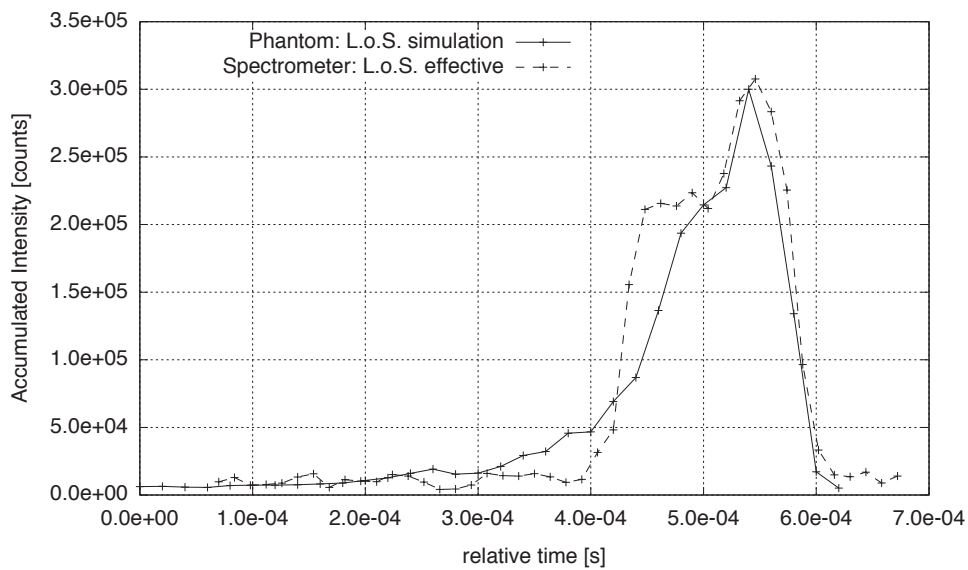
Fig.5 Accumulated intensity comparison between the effective line-of-sight of the spectrometer and the estimated one from the camera (represented by the white-delimited bands in the fast camera figures)

Fig.6 shows the temporal behavior of the H-β and H-γ lines intensity measured with the present observation system. It is clear from the Fig.6 that the pellet has indeed been recorded 'by slices'. The edges can be distinguished by the increasing and decreasing intensity signals between 300.0 μs and 400.0 μs for the front edge and between 500.0 μs and 600.0 μs for the back edge. As for the center region, it seems that a peak of intensity is located toward the back of the ablation cloud. The small intensity bump between 200.0 μs and 300.0 μs supposedly corresponds to a so called plasmoid drift. It is however not treated here.
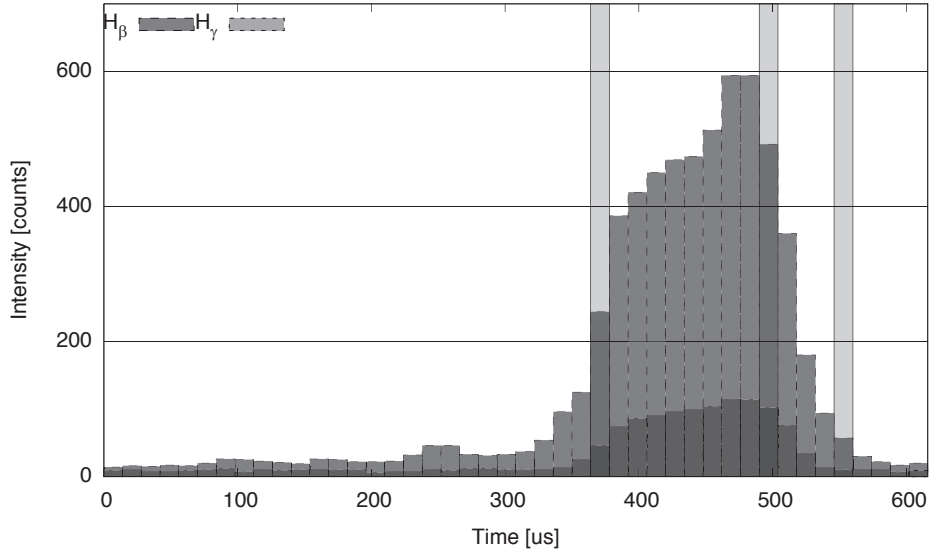
Fig.6 Timeline of the Intensity profile obtained by the spectrometer.

Fig.7(a) shows spectra observed with the spectrometer at three different timings which indicated by vertical bands in Fig.6. The same time positions obtain with the fast camera this time are given in Fig.7(b), 7(c) and 7(d).

The approximate field-of-view is indicated by the bands on the fast camera images. The first, second, and third measurements respectively corresponds to the front edge, center, and back edge regions of the ablation cloud crossing the field-of-view of the spectrometer. Discrepancies of shapes and intensities between each spectrum clearly indicate that the plasma conditions are different for each of these locations. The wider FWHM of the lines corresponding to the spectrum at the center region of the pellet hints toward a higher electron density. The continuum radiation between 525.00 nm and 625.00 nm usually hints toward the electron temperature behavior. However, in order to get clearer results, using a more quantitative method is necessary.

Fit using a least-squares minimization method of the measured spectra with a theoretical model that is to be introduced in an ulterior paper have been attempted.

Let the merit function of the fitting be f(Te, n_e, n(0),V), where V is a scale factor having a dimension of m^3, it is expressed as:

$$f(T_e, n_e, n(0), V) = \sum_{\lambda_n} \left(\frac{P_{\mathrm{obs}}(\lambda_n) - P_{\mathrm{th}}(\lambda_n)}{P_{\mathrm{obs}}(\lambda_n)} \right)^2$$

where λ_n takes the all wavelength values of the observed spectrum, $P_{\mathrm{obs}}(\lambda_n)$ and $P_{\mathrm{th}}(\lambda_n)$ are the observed and theoretical spectra, respectively. The wavelength range > 600.00 nm which includes the H-α line as well as the wavelength range < 400 nm are excluded from the fitting in order to avoid the complications noted at the end of the section 2.

241

Fitting results will not be shown here as they are still in their very preliminary stage. For now, it seems that what is given by the fittings corresponds to what has been previously found by the paper of reference [1]. That is to say, that the electron Temperature decreases as it gets toward the edges of the ablation cloud.

However, a lot of points that could completely change the results have to be addressed before a definitive answer is given.
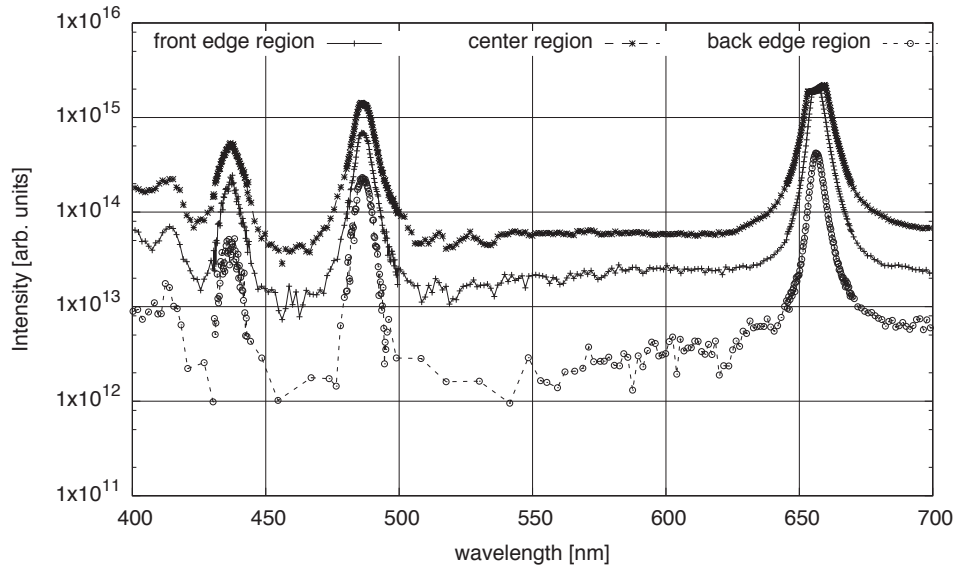
(a)   Spectra obtained at 3 locations (averaged to the 5 nearest neighbors)
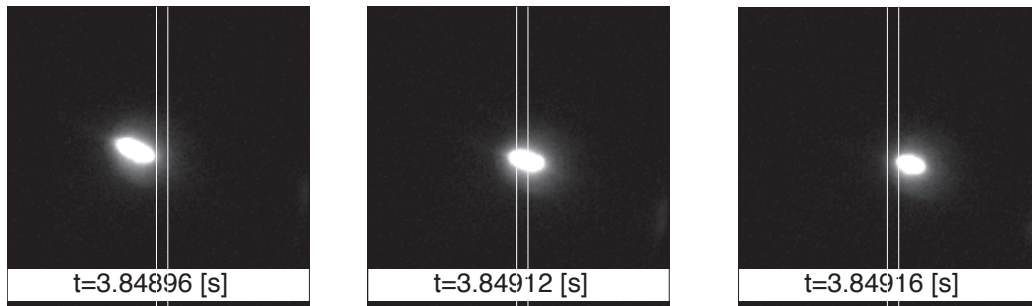
(b)   front edge   (c)   center region   (d)   back edge

Fig.7 Spectra (obtained by the spectrometer) and pictures (obtained
by the fast camera) of the ablation cloud at three different locations.

References

[1] G. Motojima et al., Review of Scientific Instruments **83**-9 (2012) 093506

Initial Results of Triton Burnup Study by Using Neutron Activation System in the Large Helical Device

Neng Pu[1], Takeo Nishitani[2], Kunihiro Ogawa[1,2], Hiroki Kawase[1],
Mitsutaka Isobe[1,2], Sadayoshi Murakami[3], and LHD Experiment Group[2]

[1]SOKENDAI (The Graduate University for Advanced Studies), Toki 509-5292, Gifu, Japan

[2]National Institute for Fusion Science, National Institutes of Natural Sciences, Toki 509-5292, Gifu,

Japan

[3]Kyoto University, Kyoto, 615-8540, Japan

Abstract

On the Large Helical Device, deuterium plasma experiments have been conducted from March 2017. Shot-integrated neutron yield reached up to 7×10^{14} and 3.5×10^{15} in first phase where NBI #1, 2, and 3 used hydrogen and NBI #4 and 5 used deuterium, and in full D-D phase, respectively. In this campaign, the neutron activation system (NAS) was utilized to perform cross checking with absolute total neutron yield measured by the neutron flux monitor (NFM) and to measure 14 MeV neutrons for the triton burnup study. Neutron yield evaluated by NAS was consistent with that measured with NFM. Most relative deviations between the NAS and NFM were less than 10%. The absolute value of the triton burnup ratio was defined as 14 MeV neutron yield divided by 2.45 MeV neutron yield. The values were evaluated to be 0.04% - 0.33% by the NAS measurement. We found that triton burnup ratio increased with electron density below about 3×10^{19} m^{-3}, and decreased above that density. Triton burnup ratio decreased as the magnetic axis position was shifted outward, which is supposed to be due to the orbit of helically trapped energetic tritons.

1. Introduction

The Large Helical Device (LHD) is a large superconducting heliotron device in Japan, having a major radius of 3.9 m and averaged plasma minor radius of ~0.6 m.[1] In LHD, deuterium plasma operation was started in March 2017 to explore further high-performance plasmas of LHD. Neutron yield measurement is essential for the LHD deuterium projects in terms of radiation safety, evaluation of fusion output, and study of energetic-particle confinement. To evaluate total neutron yield from LHD deuterium plasmas, wide dynamic range neutron flux monitor (NFM)[2] and neutron activation system (NAS) are employed in LHD.[3] The NFM on LHD consists of three [235]U fission chambers and three high-sensitivity thermal neutron detectors. The NFM plays a primary role in evaluating total

243

neutron yield. Although NAS does not provide time evolution of neutron emission rate, it is absolutely insensitive to gamma-ray and is of great value to perform cross check of neutron yield evaluated by NFM.[4,5] In the tokamaks such as TFTR[6], JET[7], ASDEX-U[8], and JT-60U[9], neutron activation techniques have been applied to measure neutron yield from deuterium plasmas. In deuterium plasmas, 2.45 MeV neutrons and 1 MeV tritons are produced with almost same production rate. Energetic tritons will undergo secondary D-T reaction with background deuteron while they slow down. Therefore, if secondary 14 MeV neutrons can be measured selectively, we can study the confinement of 1 MeV tritons. Kinematic properties such as Larmor radius and precessional drift frequency of 1 MeV tritons are almost the same as 3.5 MeV alphas. Therefore, the triton burnup study is useful to estimate the behavior of D-T born alphas. The triton burnup study is one of the important physics subjects in the LHD deuterium project to demonstrate alpha particle confinement in the LHD-type magnetic field configuration. NAS plays an important role in the triton burnup study through measurements of secondary 14 MeV neutron yield.

2. Neutron activation system on LHD

NAS on LHD consists of activation foil, capsule, pneumatic control system, two irradiation ends, pneumatic tubes, air compressor, launching/collecting station, and two high-purity germanium (HPGe) gamma-ray detectors as shown in Fig. 1(a). The system design of NAS is based on that used in JT-60U[9]. The activation foil is mounted into a capsule made of polyethylene. The capsule loaded with an activation foil is transferred through a pneumatic tube from the station to the irradiation end. There are two irradiation ends: one is at the 8-O horizontal port, which is located at the outboard side of the horizontally elongated poloidal cross section of the plasma, and the other is located at the 2.5-L lower port, which is under the vertically elongated cross section of the plasma as shown in Fig. 1(b). Each irradiation end is made of a stainless steel with coaxial structure. Outside of the port flange, the inner tube of the irradiation end is connected to a capsule transfer tube made of acrylonitrile-butadiene-styrene resin and the outer tube is connected to a vinyl chloride resin tube for compressed air supply and exhaust. The length of pneumatic tubes in the 8-O port line and the 2.5-L port line are 93 m and 80 m, respectively.

The size of activation foil is 10 mm in diameter and 1 mm in thickness as shown in Fig. 1 (c). The indium foil is employed for the 2.45 MeV measurements by utilizing ^{115}In(n, n')^{115m}In reaction, because the reaction has a threshold of 336 MeV, a half-life 4.486 h, and a rather large cross-section. For secondary 14 MeV neutron yield measurement, Silicon and aluminum are used with ^{28}Si(n, p)^{28}Al, ^{27}Al(n, p)^{27}Mg, and ^{27}Al(n, α)^{24}Na reactions.
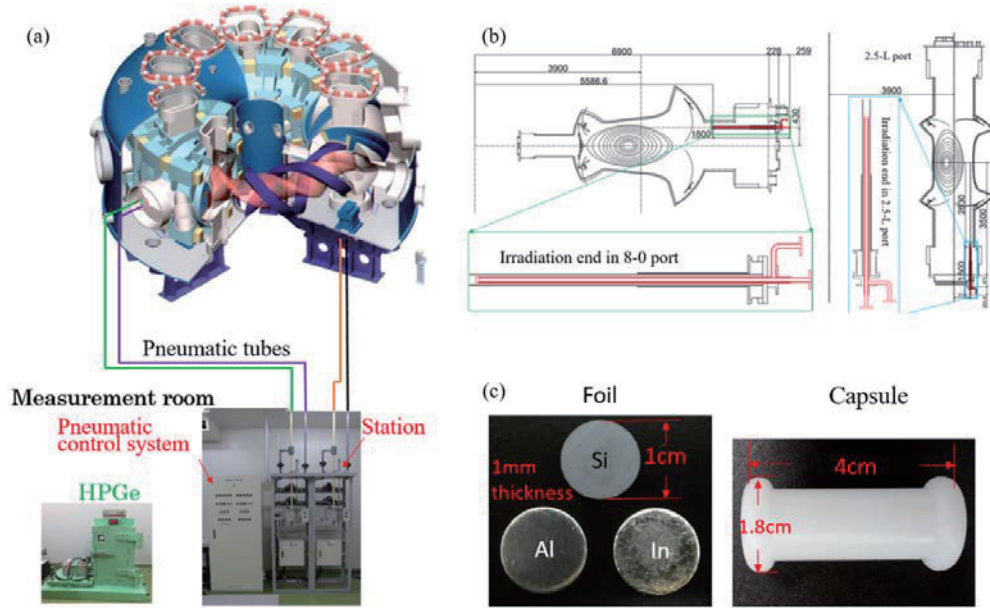
Figure 1. (a) Overview of neutron activation system on LHD, (b) two irradiation ends of neutron activation system at two poloidal cross-sections of 8-O and 2.5-L ports, (c) the right photograph is of capsule, and the left photograph shows indium, silicon and aluminum foil.

3. Principle of activation measurement

The neutron yield Y_n can be calculated by the expression:

$$Y_n = \frac{\lambda \cdot C}{N \cdot \alpha_\gamma \cdot \varepsilon \cdot (e^{-\lambda t_1} - e^{-\lambda t_2}) \cdot (1 - e^{-\lambda t_0}) \cdot \sum_E \sigma(E) \cdot \Phi(E)} \cdot t_0.$$

In the expressions, $\sigma(E)$ is cross section of sample, $\Phi(E)$ is neutron spectrum in the irradiation end for unit source neutron, E is neutron energy, $N = \alpha_{is} \cdot m \cdot N_A / M$ is the number of sample nuclei, α_{is} is the isotopic fraction of the sample nuclide, m is the mass of the sample, N_A is Avogadro's constant, M is the molar mass of the nuclide, α_γ is gamma ray abundance, t_0 is irradiation time, t_1 is start time of the gamma-ray measurement, t_2 is end time of the gamma-ray measurement, λ is the decay constant of activated nuclide in the sample, C is gamma-ray count under the specific gamma-ray peak measured during from t_1 to t_2, and ε is the efficiency of the HPGe detector in the specific gamma-ray peak.[10]

4. Comparison with neutron flux monitor

In situ calibration of NAS was performed by using ^{252}Cf source before the LHD first deuterium plasma campaign.[11] Shot-integrated neutron yields were evaluated by using ^{115}In(n,n')^{115m}In reaction with the results from in situ calibration experiment in deuterium plasmas heated by perpendicular deuterium NBIs. Those results were utilized to perform cross checking of absolute total neutron yield measured by NFM as shown in Fig. 2 (a). Relative deviations between the NAS and NFM are shown in Fig. 2 (b). Red line in Fig. 2 (a) is a relative deviation between the NAS and NFM equaled to 0. It

showed that neutron yield evaluated by NAS is consistent with that measured with NFM.
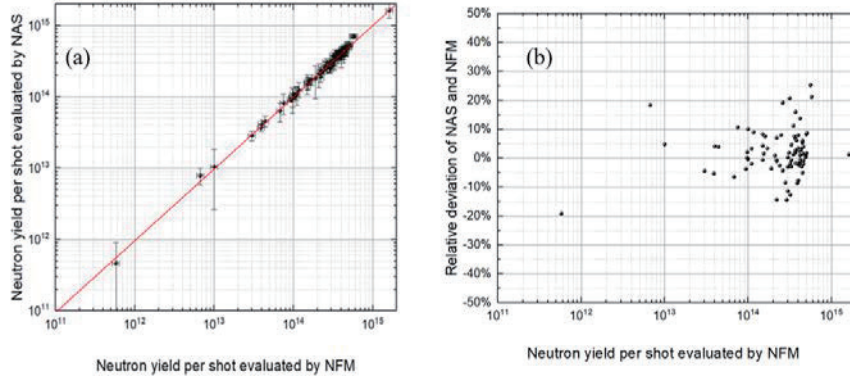
Figure 2. (a) Comparison of neutron yield measured with NAS and NFM in the LHD deuterium plasma experiment, (b) Relative deviations between the NAS and NFM.

5. Triton burnup study

Triton burnup ratio was defined as 14 MeV neutron yield divided by 2.45 MeV neutron yield.

$$\text{Triton burnup ratio} = \frac{14 \text{ MeV neutron yield}}{2.45 \text{ MeV neutron yield}}$$

In LHD first deuterium plasma campaign, triton burnup ratio was measured with NAS to be 0.04% ~0.33% in different magnetic axis and magnetic field as shown in Fig. 3. The NAS measurements indicated that triton burnup ratio increased with $\overline{n_e}$ below about 3×10^{19} m^{-3}, decreased from that density. In the low-density phase, confinement of energetic particles is very poor. Thus triton burnup ratio is low. The collision rate increases with increasing density. The slowing-down time decreases as the collision rate increases. When slowing-down time is reduced, a large amount of triton can be slowing-down in a short period of time to obtain a larger cross section of D-T reaction. Thus, triton burnup ratio increased with increasing density. When density was up to around 3×10^{19} m^{-3}, diffusion loss increases. At the same time, the slowing-down time is too short to lead a large number of energetic triton loss before slowing-down. Therefore, triton burnup ratio quickly decreased.
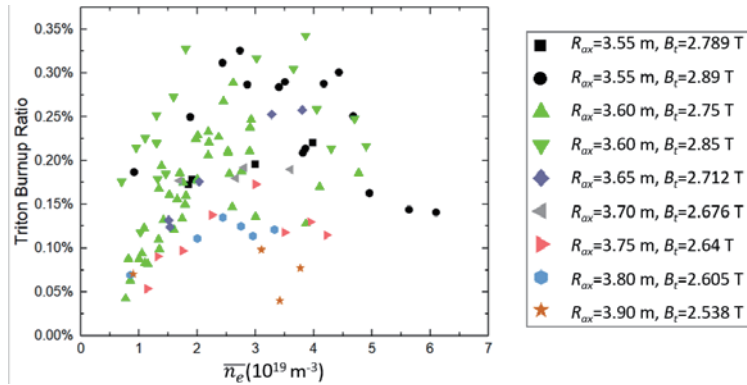
Figure 3. Line-averaged density dependence of triton burnup ratio in different magnetic field strengths and magnetic axis positions.

Confinement property of helically trapped energetic ions largely depends on magnetic field configurations. Collisionless orbits of helically trapped energetic ions in R_{ax} of 3.6 m, 3.75 m, and 3.9 m are shown in Fig. 4. Drift surface of trapped energetic ion in R_{ax} of 3.6 m matches with magnetic flux surfaces relatively. It tends to deviate largely from magnetic flux surfaces as magnetic axis position is shifted outward.[12] The triton burnup ratios in R_{ax} from 3.55 m to 3.9 m are plotted in Fig. 5. The triton burnup ratio tends to decrease as the plasma column is shifted outwardly as expected from orbit calculations. As can be seen in Fig.5 the high triton burnup ratio is obtained in inwardly shifted configuration (R_{ax}/B_t=3.55 m/2.89 T).
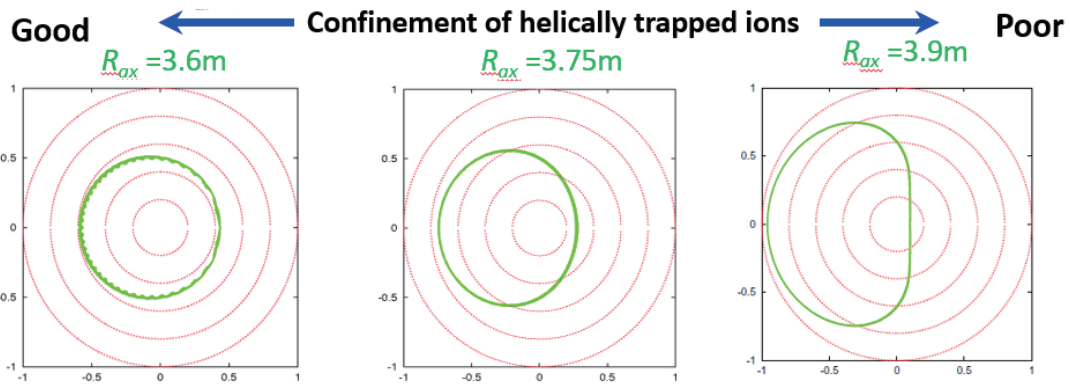
Figure 4. Collisionless orbits of helically trapped energetic ions in R_{ax} of 3.6 m, 3.75 m, and 3.9 m.
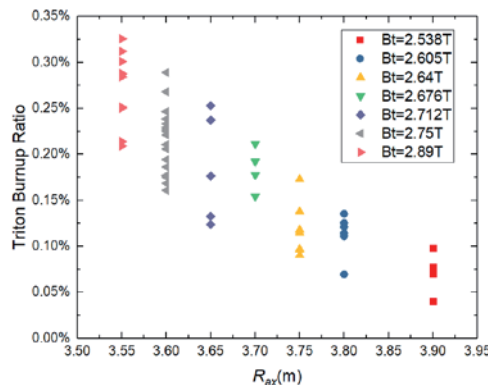
Figure 5. The triton burnup ratios in different magnetic axis R_{ax}

6.   Conclusion

In situ calibration of NAS was performed by using ^{252}Cf source before LHD first deuterium plasma campaign. NAS was utilized to perform cross checking of absolute total neutron yield measured by NFM. Neutron yield evaluated by NAS is consistent with that measured with NFM. Most

relative deviations between the NAS and NFM are less than 10%. It is the first time to measure 14 MeV neutron coming from stellarators in the word. Triton burnup ratio were obtained to be 0.04% ~ 0.34% by NAS in this campaign. Triton burnup ratio increased with $\overline{n_e}$ below about $3\times10^{19}\,\mathrm{m^{-3}}$, and decreased above that density. Triton burnup ratio decreased with the magnetic axis position shifted outward.

References

[1] A. Iiyoshi, et al, "Overview of the Large Helical Device project", *Nucl. Fusion* **39** (1999) 1245.

[2] M. Isobe, et al, "Wide dynamic range neutron flux monitor having fast time response for the Large Helical Device", Rev. Sci. Instrum, **85** (2014) 11E114.

[3] M. Isobe, et al, "Fusion product diagnostics planned for Large Helical Device deuterium experiment", Rev. Sci. Instrum. **81** (2010) 10D310.

[4] L. C. Johnson, et al, "Cross calibration of neutron detectors for deuterium-tritium operation in TFTR", Rev. Sci. Instrum, **66** 894 (1995).

[5] Cris W. Barnes, et al, "Operation and cross calibration of the activation foil system on TFTR", Rev. Sci. Instrum, **61** (1990) 3190.

[6] C. W. Barnes, et al, "Triton burnup measurements and calculations on TFTR", Nucl. Fusion **38** (1998) 597.

[7] S. Conroy, et al, "Time resolved measurements of triton burnup in JET plasmas", Nucl. Fusion **28** (1988) 2127.

[8] M. Hoek, et al, "Triton burnup measurements at ASDEX Upgrade by neutron foil activation", IPP-Report IPP-1/320 (1999).

[9] M. Hoek, et al, "Triton burnup measurements by neutron activation at JT-60U", Nucl. Instrum. Meth. Phys. Res., A **368** (1996) 804.

[10] M. Hoek, et al, "Initial Results from Neutron Yield Measurements by Activation Technique at JT-60U", Japan Atomic Energy Research Institute, JAERI-M 94-002 (1994).

[11]. N. Pu, et al, "In situ Calibration of Neutron Activation System on the Large Helical Device" Rev. Sci. Instrum, (processing).

[12] S. Murakami, et al, J. Plasma Fusion Res. SERIES, **5** (2002) 620-624.

Preliminary results of neutron emission profile measurements
in LHD deuterium plasmas

H. Kawase[1], K. Ogawa[1,2], T. Nishitani[2], N. Pu[1], M. Isobe[1,2],
and LHD Experiment Group[2]

[1]SOKENDAI (Graduate University for Advanced Studies), Toki 509-5292, Gifu, Japan

[2]National Institute for Fusion Science, National Institutes of Natural Sciences, Toki 509-5292, Gifu,

Japan

Abstract

The deuterium plasma experiments on the Large Helical Device (LHD) were carried out from March 7 to July 7 2017. Neutrons in the LHD deuterium plasma discharge were mainly generated by interaction between beam ions and bulk plasmas. Therefore, neutron emission profile measurement can potentially provide understanding of beam-ion profile and/or radial transport of beam ions. For this reason, the vertical neutron camera in the LHD was developed to investigate radial transport of beam ions. Time evolutions of neutron emission profile were measured in neutral beam-heated deuterium plasmas. Also, change of the neutron emission profile was clearly observed according to different magnetic axis positions of the LHD plasma.

1. Introduction

The Deuterium (D)-Tritium (T) fusion reactions will be used in a future nuclear fusion reactor. Because 3.5 MeV alpha particles born in a D-T plasma play a role as a main heating source in sustaining ignited condition, good confinement of energetic particles is required in magnetic confinement fusion. However, anomalous loss of energetic particle (EP) may occur due to unusual events such as energetic-particle-driven magnetohydrodynamics (MHD) and pressure-driven MHD modes in the future fusion reactor, leading to unwanted localized heat load and/or severe damage on the first wall. Therefore, deep understanding of the classical and non-classical behaviors of EPs is important. In currently performed fusion experiments, a plasma is heated by intensive neutral beam injection. In such a condition, neutrons are mainly generated by interaction between beam ions and

bulk plasma. Therefore, neutron emission profile measurement can potentially provide beam-ion profile and/or radial transport of beam-ion. Because of this, the neutron camera has been used on large tokamaks producing neutrons, such as the JET [1, 2], the TFTR [3, 4], and the JT-60U [5] in order to measure spatial profile of fusion neutron emission. In those devices, EPs transport caused by MHD instabilities such as sawtooth and energetic-particle-continuum mode were clearly observed by using the neutron camera [6, 7].

The Large Helical Device (LHD) deuterium plasma experiments were carried out from March 7 to July 7 2017. The deuterium experiments of the LHD provide a new opportunity to extend energetic particle physics study through neutron measurements. In order to investigate radial transport of energetic ions, the vertical neutron camera (VNC) has been developed in LHD [8]. The VNC on LHD is briefly described in Section 2. The experimentally measured time evolution of neutron emission profile is presented in Section 3. The results of measurement of neutron emission profile in various magnetic axis configurations are shown in Section 4. The summary of this work is given in Section 5.

2. The VNC for the LHD

The VNC scheme on the LHD is shown in Figure 1. The VNC consists of three sections: a multichannel collimator made of heavy concrete embedded in the 2.0 m thick concrete floor of the LHD torus hall, eleven channel radially aligned fast-neutron scintillation detectors, and a data acquisition system (DAQ) based on a leading edge fast-digitizer equipped with a field programmable logic circuit (FPGA). The size of the entire multichannel collimator is 0.8 m × 1.4 m and the thickness is 1.5 m. The multichannel collimator was made of heavy concrete and stainless steel pipes with an inner diameter of 30 mm arranged in the radial direction. Furthermore, the distance between each neighboring pipe center axis is 90 mm. The heavy concrete of which density is about 3.5 g/cm^3 is made from hematite (Fe_2O_3)-doped concrete. The fast-neutron detectors for the VNC consists of a stilbene scintillator with ϕ 20 mm and a thickness of 10 mm, and a photomultiplier tube (H 11934-100-10 MOD: HAMAMATSU Photonics K.K.) with booster power supplies to suppress the gain shift in the high-current operation regime. A stilbene scintillation detector was adopted as a fast-neutron detector in terms of high luminosity, fast-response, and good neutron-gamma (n-γ) discrimination capabilities. Discrimination between neutron and gamma pulses can be performed from the different decay time in the pulse shape. As shown in Figure 2(a), an arbitrary falling time t_l is set appropriately in the pulse waveform. Subsequently, two peaks appear in the histogram of Q_{long}/Q_{total} from Figure 2(b) when Q_{long} and $Q_{total}(=Q_{short}+Q_{long})$ are calculated. A peak with a large value of Q_{long}/Q_{total} results from neutrons,
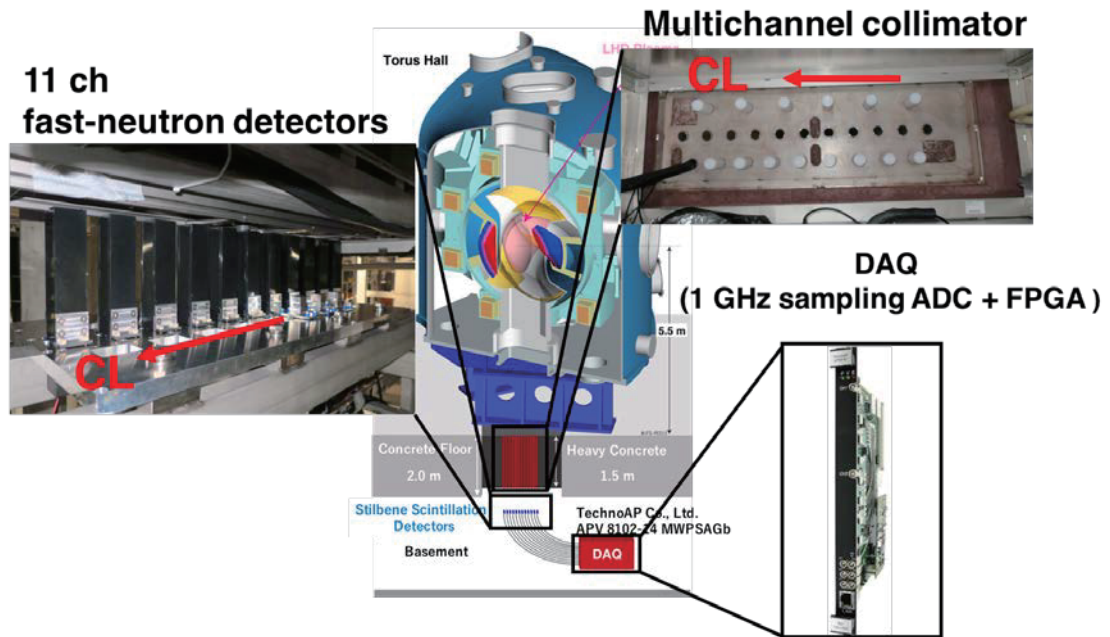
Fig. 1 Schematically drawn overview of vertical neutron camera on the LHD. The neutron collimator made of heavy concrete is embedded into the 2.0 m-thick concrete floor of the LHD torus hall. Stilbene detector array is installed at the collimator end in the basement.
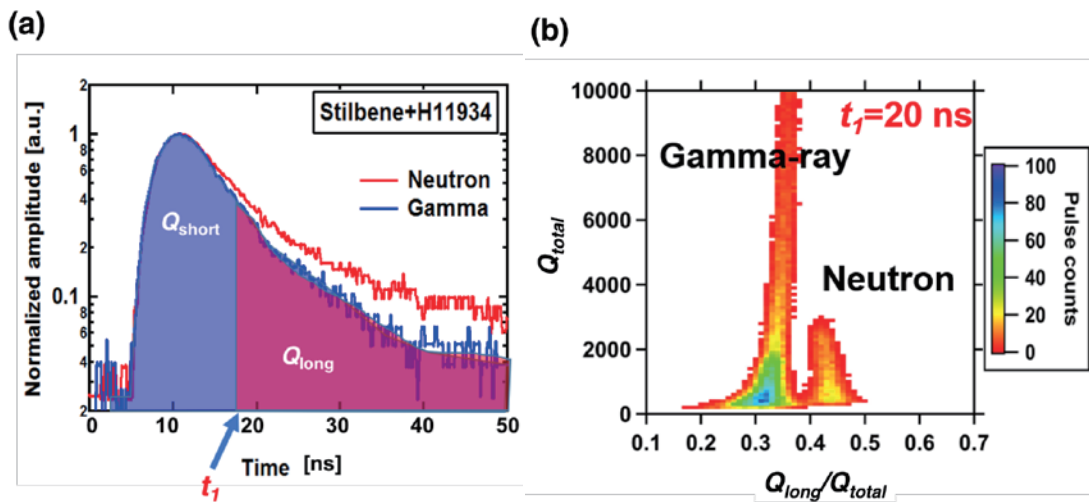
Fig. 2(a) Pulse shape discrimination method between neutron and gamma-ray pulses. There are two primary decay components. Appropriate t_1 is necessary to obtain good n-γ discrimination. (b) Result of n-γ discrimination. Two peaks are clearly discriminated when Q_{long}/Q_{total} histogram is plotted. A peak having large Q_{long}/Q_{total} corresponds to neutron, the other peak is gamma-ray. Here, t_1 was set to be 20 ns.

251

and the other peak corresponds to gamma-rays. The DAQ (Techno-AP Co., Ltd. APV 8102-14 MWPSAGb, V_{pp}: 6 V, 14 bits, DRAM: 2 GB) is characterized by high-speed sampling (1 GHz) ADC and FPGA, which enable both online and offline n-γ discrimination. The neutron measurement section of VNC on the LHD can be stably operated over $1×10^6$ cps to follow rapid events with good statistics on the number of pulse counts.

3. Experimental results

3-1. Time evolution of neutron emission profile

A typical time evolution of line-integrated neutron emission profiles was measured with VNC in deuterium plasmas with the following parameters: magnetic axis position R_{ax}=3.6 m and toroidal magnetic field strength B_t=2.75 T. Figure 3(a) shows waveform of plasma parameters at t from 3.0 to 5.0 s: ECH injection power P_{ECH}, the deposition power of neutral beam P_{NB}, line-averaged electron density n_{e_avg}, central electron temperature T_{e0}, and total neutron emission rate S_n measured with a calibrated fission chamber. Here, NB1 and NB2 inject hydrogen beams whereas NB3 and NB5 inject deuterium beams. Figure 3 (b) shows the time evolution of line-integrated neutron emission profiles at t from 3.0 to 5.0 s. Here, the size of time bin was 0.1 s. The line-integrated neutron counting rate had maximum at major radius R of 3.72 m. The peak position of line-integrated neutron counting rate
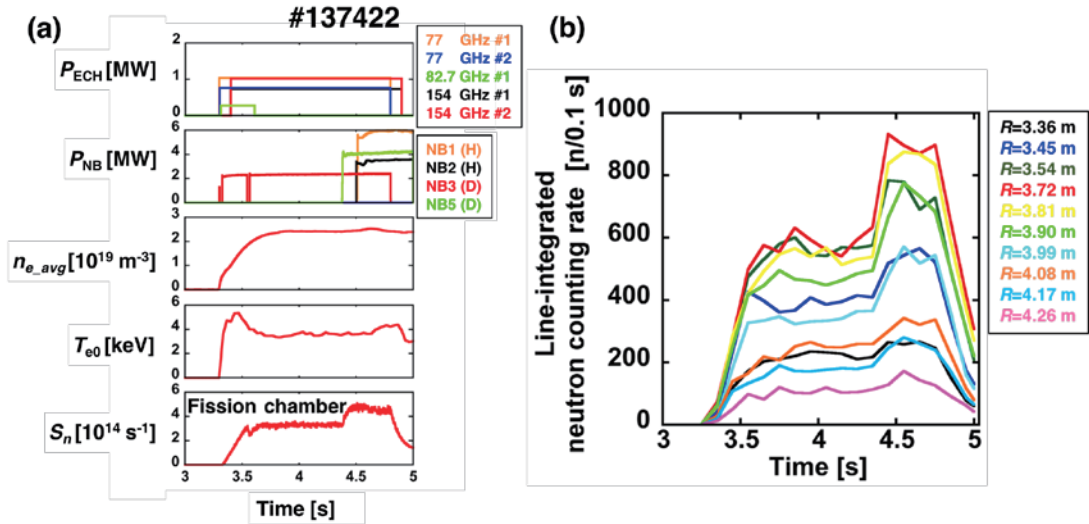
Fig. 3(a) Waveforms of the deuterium plasma discharge (#137422) in R_{ax}/B_t of 3.6 m/2.75 T. (b) Time evolution of line-integrated neutron emission profiles at t from 3.0 to 5.0 s for ten viewlines.

was similar to the plasma center R of 3.67 m measured by the Thomson scattering diagnostics. The line-integrated neutron counting rate rapidly increased when deuterium beams were injected into deuterium plasmas from at $t\sim$4.4 s.

3-2. Measurement of neutron emission profile in various magnetic axis configurations

The line-integrated neutron emission profiles were measured in plasmas with R_{ax} of 3.60 m, 3.75 m, and 3.90 m. Figure 4(a) shows poloidal cross sections at R_{ax} of 3.60 m, 3.75 m, and 3.90 m where measurements were performed. Experimental results of line-integrated neutron emission profile measurements at R_{ax} of 3.60 m, 3.75 m, and 3.90 m are shown in Figure 4(b). The red curve, the green curve, and the blue curve show the line-integrated neutron emission profiles at R_{ax} of 3.60 m, 3.75 m, and 3.90 m, respectively. As can be seen, the peak of line-integrated neutron emission profiles shifted outward with an increase of R_{ax} as expected.
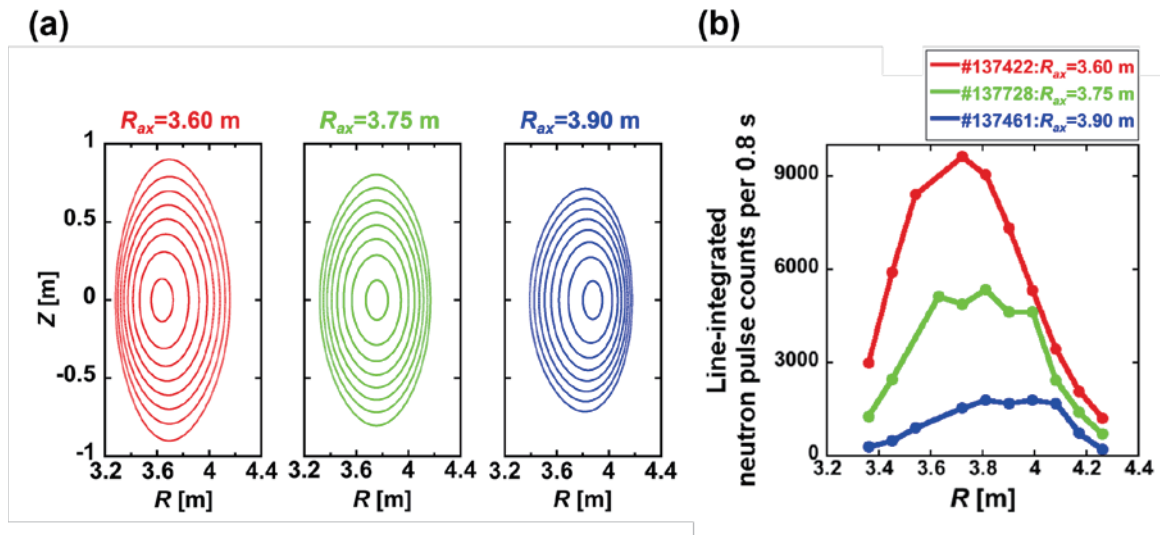
Fig. 4 (a) Poloidal cross sections at R_{ax} of 3.60 m, 3.75 m, and 3.90 m where measurements were performed. (b) Line-integrated neutron emission profiles at R_{ax} of 3.60 m (#137422), 3.75 m (#137728), and 3.90 m (#137461). Here, neutron pulses were integrated for 0.8 s. The peak of line-integrated neutron emission profiles shifted outward with an increase of R_{ax} as expected.

4. Summary

Measurements of neutron emission profiles were performed by using VNC in LHD deuterium plasma discharges. The line-integrated neutron counting rate obtained by VNC showed a similar time trend as the total neutron emission rate measured by the fission chamber. The peak of line-integrated neutron counting rate was R of 3.72 m which was close to the plasma center R of 3.67 m measured by

the Thomson scattering diagnostics. Neutron emission profiles were measured in three different magnetic axis configurations: R_{ax} of 3.60 m, 3.75 m, and 3.90 m. The peak of line-integrated neutron emission profile shifted outward as R_{ax} increased.

References

[1] J. M. Adams et al., Nucl. Instrum. Meth. **A329**, 277 (1993).

[2] O. N. Jarvis et al., Fus Eng. Des. **34-35**, 59 (1997).

[3] A. L. Roquemore et al., Rev. Sci. Instrum. **61**, 3163 (1990).

[4] A. L. Roquemore et al., Rev. Sci. Instrum. **68**, 544 (1997).

[5] M. Ishikawa et al., Rev. Sci. Instrum. **73**, 4237 (2002).

[6] F. B. Marcus et al., Plasma Phys. Control. Fusion **33**, 227 (1991).

[7] M. Ishikawa et al., Nucl. Fusion **45**, 1474 (2005).

[8] K. Ogawa et al., Rev. Sci. Instrum. **85**, 11E110 (2014).

Explicit High-order Noncanonical Symplectic Algorithms for Ideal Two-fluid Systems

Jianyuan Xiao[1], Hong Qin[1], Philip J. Morrison[2], Jian Liu[1], Yang He[1] and Ruili Zhang[1]

[1]University of Science and Technology of China, No. 96 Jinzhai Road, Hefei, China

[2]The University of Texas at Austin, Austin, Texas 78712-0262, U.S.

Abstract

In this work, an explicit high-order noncanonical symplectic algorithm for ideal two-fluid systems is developed. Fluids are discretized as particles, while the electromagnetic fields and internal energy are treated as discrete differential form fields on a fixed mesh. With the usage of Whitney interpolating forms and the Hamiltonian splitting method, this scheme preserves the gauge symmetry and charge conservation law of the ideal two-fluid systems and is high-order explicit, and the pressure is naturally derived from the discrete internal energy. This algorithm is especially suitable for large-scale simulations for physics problems that are multi-scale and require long-term fidelity and accuracy. Two examples are tested for the verification.

1. Introduction

The ideal two-fluid model, a basic non-dissipative model of plasma physics, has been widely used to study fusion and astrophysical plasmas. In this model, the electrons and ions are treated as ideal fluids separately, and they are coupling to the electromagnetic fields through the charge and current carried by them. The ideal two-fluid system has a Hamiltonian form, which was investigated in Refs. [1,2], its dynamics preserves the geometric structure and there is no dissipation of invariants such as the total energy and momentum in the system. Conventional algorithms for solving ideal two-fluid systems generally do not preserve the geometric structure and thus the truncation error can accumulate over all simulation time-steps. This will be a serious problem when simulating multiple time-scale physics that needs a lot of time steps. To solve this problem, people have developed the geometric structure preserving algorithms [3-6] which are able to preserve the discrete geometric structure very accurately for all time steps, and the numerical error of all invariants can be globally bounded by small values throughout simulations. Recently, in plasma simulations, geometric methods for charged particle dynamics and Particle-in-Cell (PIC) [7-12] are developed, and they have shown unparallelable long-term performance compared with conventional methods. There are some geometric methods for hydrodynamics [13-15], but they both have some shortage. For example methods in Refs. [13,14] are for incompressible fluids, and the method in Ref. [15] will fail when the deformation of fluids are large. In this work, an explicit, high-order, noncanonical symplectic algorithm for integrating the compressible ideal two-fluid system is developed. Fluids are discretized to particles in the Lagrangian description, which naturally guarantees conservation of the density. The electromagnetic fields and internal energy are discretized over a cubic mesh by using the theory of discrete exterior calculus (DEC) [16]. High-order Whitney interpolating forms [12] are used to ensure the gauge symmetry of Maxwell's equations. The discrete Poisson bracket for the ideal two-fluid system is obtained

by a similar technique that is used in obtaining the discrete Vlasov-Maxwell bracket, [12] and the final numerical scheme is constructed by the Hamiltonian split method [12,17]. Because we use a fix mesh to discretize the fields rather than a moving one, the final scheme will not suffer from the large deformation of fluids. The conservation of symplectic structure guarantees that the numerical errors of all invariants such as the total energy and momentum are bounded within a small value during the simulations, which means this method is most suitable for solving long-term multi-scale problems.

2. Structure Preserving Discretization for Ideal Two-fluid Systems

The starting point of the development is the Lagrangian of the ideal two-fluid system, which is quite similar to the Lagrangian of the Vlasov-Maxwell system except for the distribution functions are only in spatial and the additional internal energy terms. The Lagrangian is as follows.

$$
\mathcal{L} = \sum_s \int d\mathbf{x}_0 \left(\frac{1}{2} n_{s0}(\mathbf{x}_0) m_s |\dot{\mathbf{x}}_s|^2 + q_s n_{s0}(\mathbf{x}_0) \dot{\mathbf{x}}_s \cdot \mathbf{A}(\mathbf{x}_s) \right.
$$
$$
\left. - U_{ms}\left(\frac{n_{s0}(\mathbf{x}_0) m_s}{\mathcal{J}(\mathbf{x}_s)} \right) \right) + \frac{1}{2} \int d^3\mathbf{x} \left(|\dot{\mathbf{A}}(\mathbf{x})|^2 - |\nabla \times \mathbf{A}(\mathbf{x})|^2 \right), \tag{1}
$$

Where m_s, q_s and n_{s0} are charge, and initial number density distribution of species s, respectively, $\mathbf{x}_s$ and $\dot{\mathbf{x}}_s$ are current position and velocity of fluid elements for species s labeled by $\mathbf{x}_0$, which we take to be the initial value of $\mathbf{x}_s$ in the configuration space, $\mathcal{J}(\mathbf{x}_s)$ is the Jacobian of the coordinate transformation from the initial value $\mathbf{x}_0$ to $\mathbf{x}_s$. U_{ms} is the internal energy per unit mass for species s, and $\mathbf{A}$ is the electromagnetic vector potential. In the arguments of the fields $\mathbf{x}_s$ and $\mathbf{A}$ we suppress the time variable. In this Lagrangian, we have ignored the entropy term in the internal energy, assuming barotropic fluids, and adopted the temporal gauge (i.e. $\phi = 0$). The permittivity and permeability are set to 1 for simplicity. Evolution equations of this system are obtained by the variation.

$$
\frac{\delta S}{\delta \mathbf{x}_s} = 0, \tag{2}
$$

$$
\frac{\delta S}{\delta \mathbf{A}} = 0, \tag{3}
$$

where S is the action integral

$$
S = \int \mathcal{L} \, dt, \tag{4}
$$

which yields

$$
m_s \ddot{\mathbf{x}}_s = q_s (\dot{\mathbf{x}}_s \times \mathbf{B}(\mathbf{x}_s) + \mathbf{E}(\mathbf{x}_s)) - \frac{1}{n_{s0}(\mathbf{x}_s)} \frac{\partial U_{ms}\left(\frac{m_s n_{s0}(\mathbf{x}_0)}{\mathcal{J}(\mathbf{x}_s)} \right)}{\partial \mathbf{x}_s}, \tag{5}
$$

$$
\dot{\mathbf{E}}(\mathbf{x}) = \nabla \times \mathbf{B}(\mathbf{x}) - \sum_s \int d\mathbf{x}_0 (q_s n_{s0}(\mathbf{x}_0) \dot{\mathbf{x}}_s \delta(\mathbf{x}_s - \mathbf{x})), \tag{6}
$$

where $\mathbf{E} = -\dot{\mathbf{A}}$ and $\mathbf{B} = \nabla \times \mathbf{A}$ are the electromagnetic fields. These equations are exactly the ideal

two-fluid equations in the Lagrangian variable description.

Next is the discretization. The electromagnetic fields are discretized over a cubic mesh, while the fluid is discretized into finite-sized smooth particles [10,12,18] moving between mesh grids. The idea of fluid particles is also the key idea of smoothed-particle-hydrodynamics (SPH) method [18-20]. However, the difference is that our internal energy fields are calculated on fixed mesh grids. The resulting spatial-discretized Lagrangian is

$$
\mathcal{L}_d = \sum_{s,p} \left(\frac{1}{2} m_s n_{0,sp} |\dot{\mathbf{x}}_{sp}|^2 + q_s n_{0,sp} \dot{\mathbf{x}}_{sp} \cdot \sum_J \mathbf{A}_J W_{\sigma_{1J}}(\mathbf{x}_{sp}) \right) \\
- \sum_{s,I} U_s(\rho_{sI}) + \frac{1}{2} \sum_J \left(|\dot{\mathbf{A}}_J|^2 - |\mathrm{curl}_d \mathbf{A}_J|^2 \right),
$$

(7)

where

$$
\rho_{sI} = \sum_p m_s n_{0,sp} W_{\sigma_{0I}}(\mathbf{x}_{sp}).
$$

(8)

Here the subscript sp denotes the p-th particle of species s, $W_{\sigma_{0I}}$ and $W_{\sigma_{1J}}$ are Whitney interpolating maps for discrete 0-forms and 1-forms [12,16], U_s is the discrete internal energy per unit volume for species s, curl_d is the discrete curl operator which is defined in Eq. (24), I, J, K are indices for discrete 0-form, 1-form, 2-form, respectively. To simplify the notation, the grid size Δx has been set to unity. The Whitney maps are defined as follows:

$$
\sum_{i,j,k} W_{\sigma_{0,i,j,k}}(\mathbf{x}) \phi_{i,j,k} \equiv \sum_{i,j,k} \phi_{i,j,k} W_1(x) W_1(y) W_1(z),
$$

(9)

$$
\sum_{i,j,k} W_{\sigma_{1,i,j,k}}(\mathbf{x}) \mathbf{A}_{i,j,k} \equiv \sum_{i,j,k} \begin{bmatrix} A_{xi,j,k} W_1^{(2)}(x-i) W_1(y-j) W_1(z-k) \\ A_{yi,j,k} W_1(x-i) W_1^{(2)}(y-j) W_1(z-k) \\ A_{zi,j,k} W_1(x-i) W_1(y-j) W_1^{(2)}(z-k) \end{bmatrix}^T,
$$

(10)

$$
\sum_{i,j,k} W_{\sigma_{2,i,j,k}}(\mathbf{x}) \mathbf{B}_{i,j,k} \equiv \sum_{i,j,k} \begin{bmatrix} B_{xi,j,k} W_1(x-i) W_1^{(2)}(y-j) W_1^{(2)}(z-k) \\ B_{yi,j,k} W_1^{(2)}(x-i) W_1(y-j) W_1^{(2)}(z-k) \\ B_{zi,j,k} W_1^{(2)}(x-i) W_1^{(2)}(y-j) W_1(z-k) \end{bmatrix}^T,
$$

(11)

$$
\sum_{i,j,k} W_{\sigma_{3,i,j,k}}(\mathbf{x}) \rho_{i,j,k} \equiv \sum_{i,j,k} \rho_{i,j,k} W_1^{(2)}(x-i) W_1^{(2)}(y-j) W_1^{(2)}(z-k),
$$

(12)

$$
W_1^{(2)}(x) = -\begin{cases} W_1'(x) + W_1'(x+1) + W_1'(x+2), & -1 \le x < 2, \\ 0, & \text{otherwise}. \end{cases}
$$

(13)

$$
(\nabla_d \phi)_{i,j,k} = [\phi_{i+1,j,k} - \phi_{i,j,k}, \phi_{i,j+1,k} - \phi_{i,j,k}, \phi_{i,j,k+1} - \phi_{i,j,k}].
$$

(14)

$$(\text{curl}_d \mathbf{A})_{i,j,k} = \begin{bmatrix} \left(A_{zi,j+1,k} - A_{zi,j,k}\right) - \left(A_{yi,j,k+1} - A_{yi,j,k}\right) \\ \left(A_{xi,j,k+1} - A_{xi,j,k}\right) - \left(A_{zi+1,j,k} - A_{zi,j,k}\right) \\ \left(A_{yi+1,j,k} - A_{yi,j,k}\right) - \left(A_{xi,j+1,k} - A_{xi,j,k}\right) \end{bmatrix}^T , \tag{15}$$

$$(\text{div}_d \mathbf{B})_{i,j,k} = \left(B_{xi+1,j,k} - B_{xi,j,k}\right) + \left(B_{yi,j+1,k} - B_{yi,j,k}\right) \\ + \left(B_{zi,j,k+1} - B_{zi,j,k}\right) , \tag{16}$$

where the one-dimensional interpolation function W_1 is chosen in this paper to be

$$W_1(x) = \begin{cases} 0, & x \le -2, \\ -\frac{x^6}{48} - \frac{x^5}{8} - \frac{5x^4}{16} - \frac{5x^3}{12} + x + 1, & -2 < x \le -1, \\ \frac{x^6}{48} - \frac{x^5}{8} - \frac{5x^4}{16} - \frac{5x^3}{12} - \frac{5x^2}{8} + \frac{7}{12}, & -1 < x \le 0, \\ \frac{x^6}{48} + \frac{x^5}{8} - \frac{5x^4}{16} + \frac{5x^3}{12} - \frac{5x^2}{8} + \frac{7}{12}, & 0 < x \le 1, \\ -\frac{x^6}{48} + \frac{x^5}{8} - \frac{5x^4}{16} + \frac{5x^3}{12} - x + 1, & 1 < x \le 2, \\ 0, & 2 < x. \end{cases} \tag{17}$$

The equations of motion arising from the action with Lagrangian L_d of (7) are the following:

$$m_s n_{0,sp} \ddot{\mathbf{x}}_{sp} = q_s n_{0,sp} \left(\dot{\mathbf{x}}_{sp} \times \left(\nabla \times \sum_J \mathbf{A}_J W_{\sigma_{1J}}(\mathbf{x}_{sp}) \right) - \dot{\mathbf{A}}_J W_{\sigma_{1J}}(\mathbf{x}_{sp}) \right) \\ - \sum_I U'_s(\rho_{sI}) m_s n_{0,sp} \nabla W_{\sigma_{0I}}(\mathbf{x}_{sp}), \tag{18}$$

$$\ddot{\mathbf{A}}_J = -\text{curl}_d^T \text{curl}_d \mathbf{A}_J + \sum_{s,p} q_s n_{0,sp} \mathbf{x}_{sp} W_{\sigma_{1J}}(\mathbf{x}_{sp}). \tag{19}$$

Next, we introduce two discrete fields $\mathbf{E}_J = -\dot{\mathbf{A}}_J$ and $\mathbf{B}_K = \sum_J \text{curl}_{dKJ}\mathbf{A}_J$, which are discrete electromagnetic fields. We will make use of the following properties of the interpolating forms:

$$\nabla \sum_I W_{\sigma_{0I}}(\mathbf{x}) \phi_I = \sum_{I,J} W_{\sigma_{1J}}(\mathbf{x}) \nabla_{dJI} \phi_I, \tag{20}$$

$$\nabla \times \sum_J W_{\sigma_{1J}}(\mathbf{x}) \mathbf{A}_J = \sum_{J,K} W_{\sigma_{2K}}(\mathbf{x}) \text{curl}_{dKJ} \mathbf{A}_J, \tag{21}$$

$$\nabla \cdot \sum_K W_{\sigma_{2K}}(\mathbf{x}) \mathbf{B}_K = \sum_{K,L} W_{\sigma_{3L}}(\mathbf{x}) \text{div}_{dLK} \mathbf{B}_K, \tag{22}$$

$$(\nabla_d \phi)_{i,j,k} = \left[\phi_{i+1,j,k} - \phi_{i,j,k}, \phi_{i,j+1,k} - \phi_{i,j,k}, \phi_{i,j,k+1} - \phi_{i,j,k} \right]. \tag{23}$$

$$
(\mathrm{curl_d A})_{i,j,k} = \begin{bmatrix} \left(A_{zi,j+1,k} - A_{zi,j,k}\right) - \left(A_{yi,j,k+1} - A_{yi,j,k}\right) \\ \left(A_{xi,j,k+1} - A_{xi,j,k}\right) - \left(A_{zi+1,j,k} - A_{zi,j,k}\right) \\ \left(A_{yi+1,j,k} - A_{yi,j,k}\right) - \left(A_{xi,j+1,k} - A_{xi,j,k}\right) \end{bmatrix}^T , \tag{24}
$$

$$
\begin{aligned}
(\mathrm{div_d B})_{i,j,k} &= \left(B_{xi+1,j,k} - B_{xi,j,k}\right) + \left(B_{yi,j+1,k} - B_{yi,j,k}\right) \\
&\quad + \left(B_{zi,j,k+1} - B_{zi,j,k}\right) ,
\end{aligned} \tag{25}
$$

which hold for any ϕ_I, $\mathbf{A}_J$ and $\mathbf{B}_k$.

To construct the geometric structure preserving algorithm, the Hamiltonian theory for the discretized system is considered. Note that the only difference between the two-fluid Lagrangian and the Vlasov-Maxwell Lagrangian is the internal energy term, which can be written as a function of $\mathbf{x}_{sp}$. Thus, the discrete Poisson structure of the ideal two-fluid system can be chosen to be the same as that for the Vlasov-Maxwell system [12], which is

$$
\begin{aligned}
\{F,G\} = & \sum_J \left(\frac{\partial F}{\partial \mathbf{E}_J} \cdot \sum_K \frac{\partial G}{\partial \mathbf{B}_K} \mathrm{curl_{dKJ}} - \sum_K \frac{\partial F}{\partial \mathbf{B}_K} \mathrm{curl_{dKJ}} \cdot \frac{\partial G}{\partial \mathbf{E}_J} \right) \\
& + \sum_{s,p} \frac{1}{m_s n_{0,sp}} \left(\frac{\partial F}{\partial \mathbf{x}_{sp}} \cdot \frac{\partial G}{\partial \dot{\mathbf{x}}_{sp}} - \frac{\partial F}{\partial \dot{\mathbf{x}}_{sp}} \cdot \frac{\partial G}{\partial \mathbf{x}_{sp}} \right) + \sum_{s,p} \frac{q_s}{m_s} \\
& \times \left(\frac{\partial F}{\partial \dot{\mathbf{x}}_{sp}} \cdot \sum_J W_{\sigma_{1J}}(\mathbf{x}_{sp}) \frac{\partial G}{\partial \mathbf{E}_J} - \frac{\partial G}{\partial \dot{\mathbf{x}}_{sp}} \cdot \sum_J W_{\sigma_{1J}}(\mathbf{x}_{sp}) \frac{\partial F}{\partial \mathbf{E}_J} \right) \\
& - \sum_{s,p} \frac{q_s}{m_s^2 n_{0,sp}} \frac{\partial F}{\partial \dot{\mathbf{x}}_{sp}} \cdot \left[\sum_K W_{\sigma_{2K}}(\mathbf{x}_{sp}) \mathbf{B}_K \right] \times \frac{\partial G}{\partial \dot{\mathbf{x}}_{sp}}.
\end{aligned} \tag{26}
$$

And the discretized two-fluid Hamiltonian is

$$
\begin{aligned}
H = & \frac{1}{2} \left(\sum_J \mathbf{E}_J^2 + \sum_K \mathbf{B}_K^2 + \sum_{s,p} m_s n_{0,sp} |\dot{\mathbf{x}}_{sp}|^2 \right) \\
& + \sum_{sI} U_s(\rho_{sI}).
\end{aligned} \tag{27}
$$

Now the discrete algorithm can be developed. Using a Hamiltonian splitting technique similar to that in Refs. [12] and [17], H can be split into 6 parts

$$
H = H_E + H_B + H_x + H_y + H_z + H_U, \tag{28}
$$

where

$$
H_E = \frac{1}{2} \sum_J \mathbf{E}_J^2, \tag{29}
$$

$$
H_B = \frac{1}{2} \sum_K \mathbf{B}_K^2, \tag{30}
$$

$$
H_r = \frac{1}{2} \sum_{s,p} m_s n_{0,sp} \dot{r}_{sp}^2, \quad \text{for } r \in \{x, y, z\}, \tag{31}
$$

$$H_U = \sum_{s,I} U_s(\rho_{sI}).$$

(32)

It turns out that the exact solutions for all sub-systems can be found and computed explicitly. The exact

solutions for H_E, H_B, H_x, H_y, and H_z have been derived in Ref. [12]. They are

$$\Theta_E : \begin{cases} \mathbf{E}_J(t + \Delta t) = \mathbf{E}_J(t), \\ \mathbf{B}_K(t + \Delta t) = \mathbf{B}_K(t) - \Delta t \sum_J \mathrm{curl}_{\mathrm{d}\,KJ} \mathbf{E}_J(t), \\ \mathbf{x}_{sp}(t + \Delta t) = \mathbf{x}_{sp}(t), \\ \dot{\mathbf{x}}_{sp}(t + \Delta t) = \dot{\mathbf{x}}_{sp}(t) + \dfrac{q_s}{m_s} \Delta t \sum_J W_{\sigma_{1J}}(\mathbf{x}_{sp}(t)) \mathbf{E}_J(t), \end{cases}$$

(33)

$$\Theta_B : \begin{cases} \mathbf{E}_J(t + \Delta t) = \mathbf{E}_J(t) + \Delta t \sum_K \mathrm{curl}_{\mathrm{d}\,KJ} \mathbf{B}_K(t), \\ \mathbf{B}_K(t + \Delta t) = \mathbf{B}_K(t), \\ \mathbf{x}_{sp}(t + \Delta t) = \mathbf{x}_{sp}(t), \\ \dot{\mathbf{x}}_{sp}(t + \Delta t) = \dot{\mathbf{x}}_{sp}(t), \end{cases}$$

(34)

$$\Theta_x : \begin{cases} \mathbf{E}_J(t + \Delta t) = \mathbf{E}_J(t) - \displaystyle\int_0^{\Delta t} dt' \sum_{s,p} q_s n_{0,sp} \dot{x}_{sp}(t) \mathbf{e}_x W_{\sigma_{1J}}\left(\mathbf{x}_{sp}(t) + \dot{x}_{sp}(t) t' \mathbf{e}_x\right) \\ \mathbf{B}_K(t + \Delta t) = \mathbf{B}_K(t), \\ \mathbf{x}_{sp}(t + \Delta t) = \mathbf{x}_{sp}(t) + \Delta t \dot{x}_{sp}(t) \mathbf{e}_x, \\ \dot{\mathbf{x}}_{sp}(t + \Delta t) = \dot{\mathbf{x}}_{sp}(t) + \dfrac{q_s}{m_s} \dot{x}_{sp}(t) \mathbf{e}_x \times \displaystyle\int_0^{\Delta t} dt' \sum_K W_{\sigma_{2K}}\left(\mathbf{x}_{sp}(t) + \dot{x}_{sp}(t) t' \mathbf{e}_x\right) \mathbf{B}_K(t). \end{cases}$$

(35)

The solutions Θ_y and Θ_z are similar to Θ_x. For H_U, the exact evolution equations are

$$\begin{aligned} \dot{\mathbf{E}}_J &= \{\mathbf{E}_J, H_U\} = 0, \\ \dot{\mathbf{B}}_K &= \{\mathbf{B}_K, H_U\} = 0, \\ \dot{\mathbf{x}}_{sp} &= \{\mathbf{x}_{sp}, H_U\} = 0, \\ \ddot{\mathbf{x}}_{sp} &= \{\dot{\mathbf{x}}_{sp}, H_U\} = -\sum_I U_s'(\rho_{sI}) \nabla W_{\sigma_{0I}}(\mathbf{x}_{sI}). \end{aligned}$$

(36)

Using the property Eq. (20) of the Whitney interpolating forms, this exact solution can be written as

$$\Theta_U : \begin{cases} \mathbf{E}_J(t + \Delta t) = \mathbf{E}_J(t), \\ \mathbf{B}_K(t + \Delta t) = \mathbf{B}_K(t), \\ \mathbf{x}_{sp}(t + \Delta t) = \mathbf{x}_{sp}(t), \\ \dot{\mathbf{x}}_{sp}(t + \Delta t) = \dot{\mathbf{x}}_{sp}(t) - \Delta t \sum_{I,J} \nabla_{\mathrm{d}\,JI} U_s'(\rho_{sI}) W_{\sigma_{1J}}(\mathbf{x}_{sp}). \end{cases}$$

(37)

The final geometric structure-preserving scheme can be constructed from these exact solutions. For

example, a first-order scheme can be chosen as

$$\Theta_1(\Delta t) = \Theta_E(\Delta t)\Theta_B(\Delta t)\Theta_x(\Delta t)\Theta_y(\Delta t)\Theta_z(\Delta t)\Theta_U(\Delta t), \tag{38}$$

and a second-order symmetry scheme can be constructed as

$$\begin{aligned}
\Theta_2(\Delta t) = {}& \Theta_x(\Delta t/2)\Theta_y(\Delta t/2)\Theta_z(\Delta t/2)\Theta_B(\Delta t/2) \\
& \times \Theta_U(\Delta/2)\Theta_E(\Delta t)\Theta_U(\Delta t/2)\Theta_B(\Delta t/2) \\
& \times \Theta_z(\Delta t/2)\Theta_y(\Delta t/2)\Theta_x(\Delta t/2).
\end{aligned} \tag{39}$$

The $2(l+1)$ th-order scheme can be derived from the $2l$th-order scheme by using

$$\begin{aligned}
\Theta_{2(l+1)}(\Delta t) &= \Theta_{2l}(\alpha_l\Delta t)\Theta_{2l}(\beta_l\Delta t)\Theta_{2l}(\alpha_l\Delta t), \\
\alpha_l &= 1/(2 - 2^{1/(2l+1)}), \\
\beta_l &= 1 - 2\alpha_l.
\end{aligned} \tag{40}$$

3. Numerical Examples

We have implemented the second-order symplectic two-fluid method discussed above. To testify the practicability, we examine the dispersion relation of an electron-deuterium plasma, and its energy evolution. The simulation parameters are choosen as follows.

$$n_{i0} = n_{e0} = 4.0 \times 10^{19}\,\mathrm{m}^{-3},$$

$$\rho_{e0} = n_{e0}m_e,$$

$$\rho_{i0} = n_{i0}m_i,$$

$$m_i = 3671m_e = 3.344 \times 10^{-27}\,\mathrm{kg},$$

$$q_i = -q_e = 1.602 \times 10^{-19}\mathrm{C},$$

$$U_e(\rho_e) = U_{e0}\frac{3}{2}\left(\frac{\rho_e}{\rho_{e0}}\right)^{5/3},$$

$$U_i(\rho_i) = U_{i0}\frac{3}{2}\left(\frac{\rho_i}{\rho_{i0}}\right)^{5/3},$$

$$\mathbf{B}_0 = (3.17\mathbf{e}_z + 1.13\mathbf{e}_y)\mathrm{T},$$

where $U_{i0} = U_{e0} = m_e n_e v_{Te}^2/2, v_{Te} = 0.0450c$, c is the speed of light in the vacuum, $\mathbf{B}_0$ is the constant external magnetic field. The simulation domain is a $1 \times 1 \times 1500$ mesh, gird size is $\Delta x = 2 \times 10^{-4}$m, time step is $\Delta x/2c$, and the periodical boundary is chosen in all x, y and z directions. In the beginning of the time, 4 fluid particles are equally spaced in each cell. To numerically obtain the dispersion relation, the simulation is carried out with a small random perturbation. We have recorded the field evolution and the kinetic energy evolution. The dispersion relation is plotted in Fig. 1, and the total energy evolution is plotted in Fig. 2. We can easily see that the dispersion relation obtained by this scheme is complying with the theoretical results, and the total energy is bounded in 2×10^6 time steps.
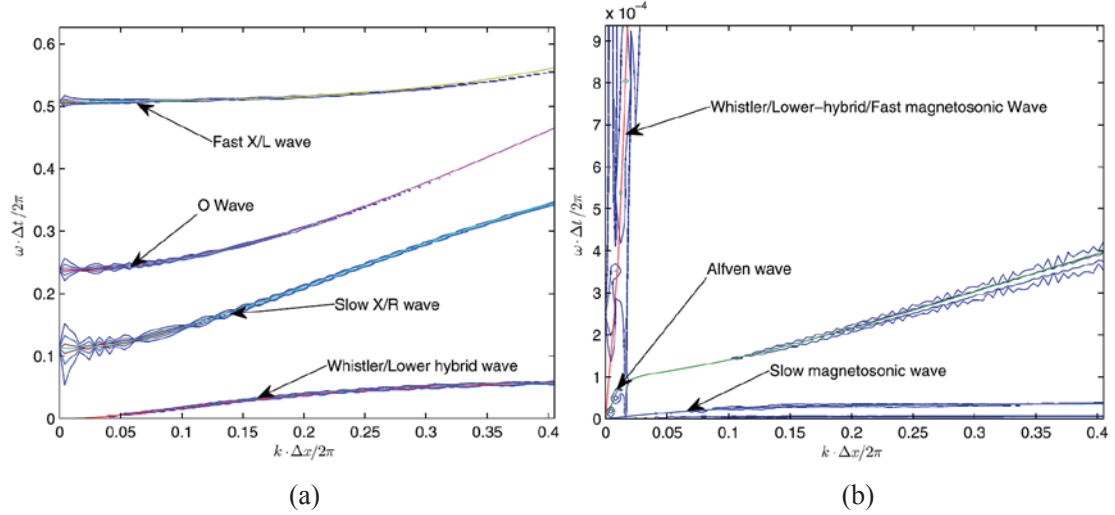
Figure 1. The dispersion relation of an electron-deuterium two-fluid plasma plotted against simulation results. The high frequency region is shown in (a) and the low frequency region in (b), with solid lines being theoretical dispersion relation.
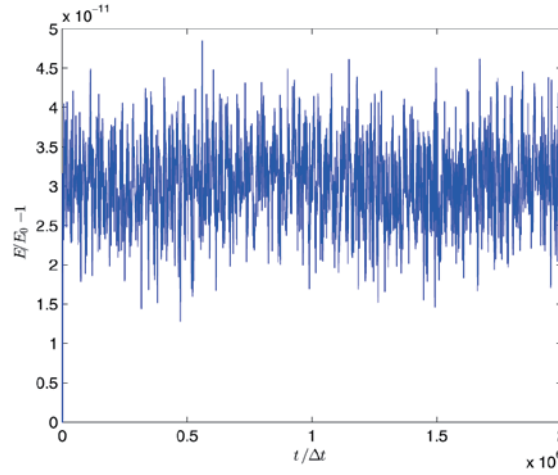
Figure 2. Evolution of the total energy obtained from the structure preserving two-fluid algorithm. In all 2×10^6 time steps, the energy deviates from its initial value by only a very small amount.

4. Conclusion

In summary, a geometric algorithm for ideal two-fluid systems has been developed. In this method, fluids are discretized as particles, and the conservation of mass is seen to be naturally satisfied. The electromagnetic and internal energy fields are discretized over a fixed cubic mesh using discrete differential forms. With the assistance of high-order Whitney interpolation forms, this scheme preserves the electromagnetic gauge symmetry. In the algorithm, the discrete pressure was obtained from the discrete internal energy field. The time integration was accomplished by adopting the high-order explicit Hamiltonian splitting technique, which preserves the whole symplectic structure of the two-fluid system. Numerical examples were given to verify the accuracy and conservative nature of the geometric algorithm. We expect that this algorithm will find a wide range of applications, especially in physical problems that are multi-scale and demand long-term accuracy and fidelity.

References

[1] R. G. Spencer and A. N. Kaufman, Phys. Rev. A 25, 2437 (1982).

[2] P. J. Morrison, Rev. Mod. Phys. 70, 467 (1998).

[3] T. Lee, Phys. Lett. B 122, 217 (1983).

[4] K. Feng, J. Comput. Math. 4, 279 (1986).

[5] T. Lee, J. Stat. Phys. 46, 843 (1987).

[6] R. D. Ruth, IEEE Trans. Nucl. Sci. 30, 2669 (1983).

[7] H. Qin and X. Guan, Phys. Rev. Lett. 100, 035006 (2008).

[8] R. Zhang, J. Liu, Y. Tang, H. Qin, J. Xiao, and B. Zhu, Phys. Plasmas 21, 032504 (2014).

[9] J. Squire, H. Qin, and W. M. Tang, Phys. Plasmas (1994-present) 19, 084501 (2012).

[10] J. Xiao, J. Liu, H. Qin, and Z. Yu, Phys. Plasmas 20, 102517 (2013).

[11] J. Xiao, J. Liu, H. Qin, Z. Yu, and N. Xiang, Phys. Plasmas (1994-present) 22, 092305 (2015).

[12] J. Xiao, H. Qin, J. Liu, Y. He, R. Zhang, and Y. Sun, Phys. Plasmas (1994-present) 22, 112504 (2015).

[13] D. Pavlov, P. Mullen, Y. Tong, E. Kanso, J. E. Marsden, and M. Desbrun, Phys. D: Nonlinear Phenom. 240, 443 (2011).

[14] E. S. Gawlik, P. Mullen, D. Pavlov, J. E. Marsden, and M. Desbrun, Phys. D: Nonlinear Phenom. 240, 1724 (2011).

[15] Y. Zhou, H. Qin, J. Burby, and A. Bhattacharjee, Phys. Plasmas (1994-present) 21, 102109 (2014).

[16] A. N. Hirani, "Discrete exterior calculus," Ph.D. thesis (California Institute of Technology, 2003).

[17] Y. He, H. Qin, Y. Sun, J. Xiao, R. Zhang, and J. Liu, Phys. Plasmas (1994-present) 22, 124503 (2015).

[18] J. J. Monaghan, Annu. Rev. Astron. Astrophys. 30, 543 (1992).

[19] J. Bonet and T.-S. Lok, Comput. Meth. Appl. Mech. Eng. 180, 97 (1999).

[20] D. J. Price and J. Monaghan, Mon. Not. R. Astron. Soc. 348, 139 (2004).

Automatic data cleaning using artificial intelligence for magnetic confinement fusion devices

Lan Ting[1], Liu Jian[1], Qin Hong[1, 2]

[1]School of Nuclear Science and Technology and Department of Modern Physics, University of Science and Technology of China, Hefei, Anhui 230026, China

[2]Plasma Physics Laboratory, Princeton University, Princeton, NJ 08543, USA

Abstract

To guarantee the availability and reliability of data source in Magnetic Confinement Fusion (MCF) devices, incorrect diagnostic data, which cannot reflect real physical properties of measured objects, should be sorted out before further analysis and study. Traditional data sorting cannot meet the growing demand of MCF research because of the low-efficiency, time-delay, and lack of objective criteria. In this paper, a Time-Domain Global Similarity (TDGS) method based on machine learning technologies is proposed for the automatic data cleaning of MCF devices. Traditional data sorting aims to the classification of original diagnostic data sequences, which are different in both length and evolution properties under various discharge parameters. Hence the classification criteria are affected by many discharge parameters and vary shot by shot. The focus of TDGS method is turned to the physical similarity between data sequences from different channels, which are more essential and independent of discharge parameters. The complexity arisen from real discharge parameters during data cleaning is avoided in the TDGS method by transforming the general data sorting problem into a binary classification problem about the physical similarity between data sequences. As a demonstration of its application to multi-channel measurement systems, the TDGS method is applied to the EAST POlarimeter-INterferomeTer (POINT) system. The optimized performance of the method has reached 0.9871 ± 0.0385.

1. Introduction

With the development of Magnetic Confinement Fusion (MCF) science and diagnostic techniques, massive diagnostic data are increasingly generated. Original diagnostic data could be unreliable due to various interference sources and complex measuring conditions in MCF devices, such as mechanical vibration, electromagnetic interference, signal saturation, and hardware failures. To guarantee the availability and reliability of data source, incorrect diagnostic data, dubbed dirty data, which cannot reflect real physical properties of measured objects, should be sorted out before further analysis and study. The identification of incorrect data can be regarded as a typical classification problem, i.e., how to properly divide the original data set into two groups, correct and incorrect one. Since experimental setups and discharge processes are diverse, measured quantities from different shots, diagnostic systems, and devices evolve in totally different ways. Incorrect diagnostic results also vary due to their uncertain causes. Therefore, it is difficult to define general and clear criteria for data cleaning. Traditionally, dirty data are searched and removed manually with the assistant of computer programs, mainly according to some simple rules, common experiences, and sometimes personal intuitions. These data cleaning programs and rules

only apply to certain specific data and usually performs poorly. Explosively increasing fusion data cannot be satisfactorily cleaned in time. Real-time processing and feed-back control require much faster data cleaning methods, which can remove dirty data in a short time, say millisecond. On the other hand, subjective factors in manual data cleaning processes lead to inconsistent results. To meet the demand of fusion energy research, the speed, efficiency, and accuracy of fusion data cleaning should be improved imperatively. Automatic data cleaning methods based on machine learning is a strong candidate for breaking through the bottleneck of massive data application in fusion research.

A new data cleaning method based on the Time-Domain Global Similarity (TDGS) among data sequences defined by typical machine learning technologies has been proposed [1]. The general-purposed TDGS method can be used to automatically sort dirty diagnostic data from MUlti-channel Measurement (MUM) systems in MCF experiments. Most diagnostic systems of MCF devices are MUM systems, which measure the time evolution of plasma parameters from different locations or directions with multiple independent measuring channels, such as common interferometer systems [2], polarimeter systems [3–5], electron cyclotron emission imaging systems [6], etc. Time sequences of diagnostic data from different channels of the MUM system reflect related yet distinct aspects of the same observed object. Therefore these diagnostic data are physically associated. We define this relation as physical similarity. The physical similarity just exists between correct data sequences from different channels of the MUM system. The dirty data, which are caused by a variety of interference sources, are physically dissimilar from correct data sequences or each other. To overcome the difficulty of direct classification, the TDGS method sorts the dirty data by classifying the physical similarity between diagnostic data sequences from different channels under the same discharge. Traditional data sorting aims to the classification of original diagnostic data sequences, which are different in both length and evolution properties under various discharge parameters. Hence the classification criteria are affected by many discharge parameters and vary shot by shot. The focus of TDGS method turns to the physical similarity between data sequences from different channels, which are more essential and independent of discharge parameters. Then the complexity arisen from real discharge parameters during data cleaning is avoided in TDGS method by transforming the general data sorting problem into a binary classification problem about the physical similarity between data sequences.

The rest parts of this paper are organized as follows. In Sec. II, the procedures of TDGS method for automatic diagnostic data cleaning of MUM systems are introduced. In Sec. III, the prospects of applying TDGS method to data cleaning in more MUM systems of MCF devices are discussed. Moreover, the further optimization of TDGS method is also proposed.

2. TIME-DOMAIN GLOBAL SIMILARITY METHOD

TDGS method aims to automatically sort out the incorrect diagnostic data of the MUM system. By transforming the direct data sequence classification problem into a binary classification problem about the physical similarity between diagnostic data sequences, TDGS method eliminates the complexity arisen from discharge parameters during data cleaning. In this section, the procedures of training TDGS model for data cleaning of MUM systems are explained.

In TDGS method, the sample set is generated by the direct sum of two original diagnostic data

sequences from two different channels of a MUM system in the same discharge. By combining two data sequences from different channels of an N-channel MUM system as one sample, C_N^2 samples can be generated for one discharge, and $P*C_N^2$ samples can be generated for P discharges. Each sample is tagged by several indices which indicates the corresponding physical similarity between two sequences. These indices span a high dimensional index-space, in which these samples can be classified into two groups, physical similar samples and physical dissimilar ones. A physical similar sample is constituted by two correct data sequences. If a sample is classified to be physical dissimilar, its constituents contain at least one dirty data sequence. According to this rule, the dirty diagnostic data can be properly identified by physical similarity. The transformation of TDGS method is exhibited with the database from a 4-channel MUM system for one discharge, see Fig. 1. In this example, the ratio of incorrect data to correct ones is $\frac{1}{3}$, which is the class structure in directly classifying the original data sequences. By combining any two data sequences from different channels as one sample, 6 samples are generated by TDGS method. 3 samples constituted by two correct data sequences are tagged with similarity. And the other 3 samples containing at least one incorrect data sequence are tagged with dissimilarity. The class structure of TDGS method is $\frac{1}{1}$. After the transformation of TDGS method, the class structure is more balanced in this case.
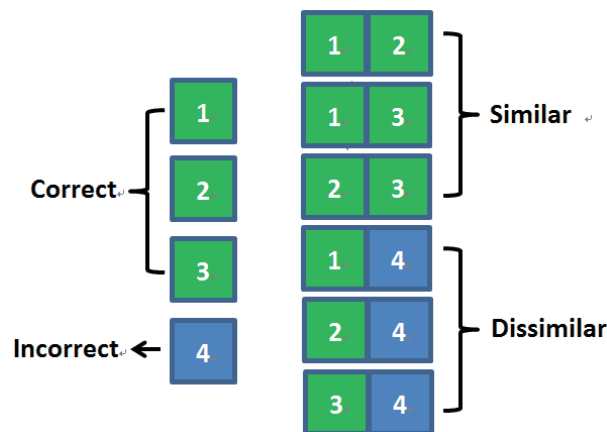
Fig.1 The class structure transformation by TDGS method is shown with an example in the database from a 4-channel MUM system for one discharge.

In many MUM systems of MCF devices, the physical similarity between diagnostic data exists in time domain rather than frequency domain. And the dissimilarity between dirty data, or dirty and clean data, is in global scale for most of the time, instead of local and small scale. TDGS method employs different definitions of distance between two time-series signals as tag indices of a sample, measuring this global time-domain similarity. To guarantee precise classification, different kinds of distance functions are adopted to map signals from a high-dimensional space of original data sequences into a lower-dimensional feature space. Because in different discharges the length of diagnostic data sequences changes, original data sequences should be normalized in distance functions to guarantee length independence. Then samples generated from different discharges can be joined together as a unified sample set, used as the training set or the test set. To demonstrate the performance of TDGS method, it is tested by the data cleaning of

POlarimetry-INTerferometry (POINT) system on EAST Tokamak. The performance in this paper refers to the accuracy rate of classification results about physical similarity. In this example, Support Vector Machine (SVM) is adopted as the classification algorithm, which has advantage in solving nonlinear, high-dimensional problems [7–8]. The k-fold cross-validation is used as model assessment method because it can provide an effectively unbiased error estimate. In k-fold cross-validation method, all samples contribute to both training and validation, and each sample is used for validation only once [9]. For practical purpose of data cleaning for MCF devices, the samples of a validation set are selected to be generated by the data from one discharge, rather than randomly from the whole set. Evaluated by 24-fold cross-validation, the accuracy rate of TDGS method in cleaning the dirty density data of POINT system can reach 0.9871 ± 0.0385, which meets the application requirements of POINT system. By applying TDGS method to the data cleaning of POINT system, the reliability and availability of data source from POINT system are evidently enhanced quickly and conveniently.

3. SUMMARY

In this paper, machine learning is applied to the automatic data cleaning of MCF devices for the first time. Correct diagnostic data sequences from different channels of MUM systems, which reflect related yet distinct aspects of the same observed object, are physical similar with each other. Based on this physical similarity, we propose a general-purposed TDGS method to sort out the dirty diagnostic data of MUM systems in MCF devices. The optimized performance of TDGS method in sorting the density data of POINT system has reached 0.9871 ± 0.0385.

In the future, we will apply TDGS method to clean the POINT data and other MUM systems in MCF devices. In large-scale applications of TDGS method, predication speed and robustness should be further considered as assessment indicators for model selection. Meanwhile, the algorithm for data cleaning based on physical similarity between data sequences should be further optimized to achieve less calculation amount and error accumulation. Moreover, the physical similarity in frequency-domain can also be utilized in some data cleaning problem of MUM systems.

References

[1] T. Lan, J. Liu, H. Qin, and L. Li Xu, ArXiv e-prints (2017), 1705.04947.

[2] K. Kawahata, K. Tanaka, Y. Ito, A. Ejiri, and S. Okajima, Review of scientific instruments 70, 707 (1999).

[3] A. Donné, M. Graswinckel, M. Cavinato, L. Giudicotti, E. Zilli, C. Gil, H. Koslowski, P. Mc Carthy, C.

Nyhan, S. Prunty, et al., Review of scientific instruments 75, 4694 (2004).

[4] D. Brower, Y. Jiang, W. Ding, S. Terry, N. Lanier, J. Anderson, C. Forest, and D. Holly, Review of Scientific Instruments 72, 1077 (2001).

[5] H. Liu, Y. Jie, W. Ding, D. Brower, Z. Zou, J. Qian, W. Li, Y. Yang, L. Zeng, S. Zhang, et al., Journal of Instrumentation 11, C01049 (2016).

[6] C. Luo, B. Tobias, B. Gao, Y. Zhu, J. Xie, C. Domier, N. Luhmann, T. Lan, A. Liu, H. Li, et al., Journal of Instrumentation 9, P12014 (2014).

[7] C. Cortes and V. Vapnik, Machine learning 20, 273 (1995).

[8] J. Platt, Tech. Rep. (1998).

[9] R. Kohavi et al., in Ijcai (Stanford, CA, 1995), vol. 14, pp. 1137–1145.

Program of A3 Seminar
(11-14 July 2017, Sapporo, Japan)

10 July 2017 (Monday) Registration: evening			

11 July (Tuesday)			
Session 1 (Opening & Category: I) Chair: L.Q.Hu	08:30	MORITA Shigeru (NIFS)	Opening
	08:40	DING Bojiang (ASIPP)	LHCD studies towards long-pulse plasma with high performance in EAST
	09:00	KIM Jayhyun (NFRI)	Counter current drive and counter torque discharges in KSTAR
	09:20	BAK Jun-Gyo (NFRI)	Characterization of the plasma current quench during disruptions in the KSTAR
	09:40	LYU Bo (ASIPP)	Experimental studies of LHCD's effect on plasma rotation on EAST
	10:00	CAI Huishan (USTC)	Influence of toroidal rotation on tearing modes
Coffee Break 10:20-10:40			
Session 2 (Category: I) **Chair:** Yeong-Kook OH	10:40	JEON YoungMu (NFRI)	Characteristics of KSTAR high poloidal beta operation scenario
	11:00	BAE Cheonho (NFRI)	Comparison of toroidal torque contributions in axisymmetric tokamak plasmas
	11:20	LIU Haiqingu (ASIPP)	Improve H-mode plasma with flat central magnetic shear on EAST
	11:40	YUN Gunsu (POSTECH)	Stability of the KSTAR H-mode plasma boundary with perpendicular shear flow
	12:00	TOI Kazuo (NIFS)	Precursors and Control of ELMs in Stellarator/Helical Plasmas
Lunch Break12:20-13:30			
Session 3 (Category: IIa) Chair: OHDACHI Satoshi	13:30	XIAO Bingjia (ASIPP)	Recent experiment on EAST in the quasi-snowflake diverted shape
	13:50	MAO Shifeng (USTC)	Simulation Study of Quasi-snowflake divertor with Ne seeding
	14:10	BANG Eun-nam (NFRI)	Carbon atom density in gap of tungsten block in 2016 KSTAR campaign
	14:30	HONG Suk-Ho (NFRI)	ELM heat load on castellated tungsten blocks
	14:50	ASHIKAWA Naoko (NIFS)	Retention on coated W with microcrystalline structures after plasma exposures in KSTAR and EAST
	15:10	CHEN Junling (ASIPP)	Recent progress of first mirror in-situ cleaning using radio frequency plasma in EAST
Coffee Break 15:30-15:50			

	15:50	KATO Daiji (NIFS)	Tungsten atomic data research using CoBIT and LHD
Session 4 (Category: IIa) Chair: HONG Suk-Ho	16:10	CUI Zhengying (SWIP)	Study of impurity transport in the HL-2A ECRH L-mode plasmas with radically different ECRH power depositions
	16:30	OISHI Tetsutaro (NIFS)	Dependence of carbon impurity flow in the edge stochastic magnetic field layer of LHD on the magnetic field configuration
	16:50	WANG Fuqiong (Donghua Univ.)	SOLPS-ITER modeling of EAST edge plasmas
	17:10	DAI Shuyu (DUT)	Studies of edge impurity transport in the scrape-off layer of EAST with EMC3-EIRENE modelling
	17:30	MORITA Shigeru (NIFS)	Island formation in stochastic magnetic field layer during RMP-triggered detached plasmas of LHD

12 July (Wednesday)			
Session 5 (Category: I & III) Chair: JEON YoungMu	08:30	ISOBE Mitsutaka (NIFS)	Summary of energetic-particle diagnostics and physics collaborations in Japan, Korea, and China for the last five years
	08:50	FAN Tieshuan (Peking Univ.)	Development of the TOFED and Bonner Sphere Spectrometers at EAST
	09:10	KIM Junghee (NFRI)	Research status of energetic particle physics and diagnostics in KSTAR
	09:30	OHDACHI Satoshi (NIFS)	The effects of the RMP application on the energetic particle driven resistive interchange (EIC) mode
	09:50	NAM Yoonbum (UNIST)	Double tearing modes driven by ECH/CD in sawtoothing discharges (tentative)
Coffee Break 10:10– 10:30			
Session 6 (Category: I & IV) Chair: LYU Bo	10:30	HU Liqun (ASIPP)	Recent progress of ITER Radial X-ray Camera
	10:50	OH Seung Tae (NFRI)	Progress of IR imaging video bolometer of KSTAR
	11:10	YE Minyou (USTC)	Development of Ultrafast Charge eXchange Recombination Spectroscopy diagnostic on EAST
	11:30	YU Yi (USTC)	Development of Beam Emission Spectroscopy diagnostics on EAST
	11:50	GAO Jinming (SWIP)	Dynamics of runaway electrons in HL-2A with infrared camera system
	12:10	WANG Hao (NIFS)	Simulation studies of chirping geodesic acoustic modes and nonlinearly-coupled modes in 3-dimensional LHD equilibrium
Lunch 12:30-13:30			
Session 7 (Category: I) Chair: S.Morita	13:30	TAKEIRI Yasuhiko (NIFS) WAN Baonian (ASIPP) LI Jiangang (ASIPP)	Welcome speech
	13:40	TAKEIRI Yasuhiko (NIFS)	Prospect towards steady-state helical fusion reactor based on progress of LHD project entering the deuterium experiment phase
	14:10	WAN Baonian (ASIPP)	Research of key issues for steady-state tokamak operation on EAST
	14:40	OH Yeong-Kook (NFRI)	Plasma discharge characteristics according to hot PFC temperature operation
Coffee Break & Seminar Photo 15:10– 15:40			

Session 8 (Category: I, IIa & IV) Chair: M.Isobe	15:40	LI Jiangang (ASIPP)	ECRH on CFETR- physics and technology needed
	16:10	GUO Houyang (ASIPP)	An innovative small angle slot divertor concept for long pulse advanced tokamaks
	16:30	LIU Yi (SWIP)	Recent Results from HL-2A on MHD control
	16:50	KISHIMOTO Yasuaki (Kyoto Univ.)	Numerical laboratory based on global gyro-kinetic modeling for studying turbulence and MHD events in tokamak
	17:10	XIANG Nong (ASIPP)	Development of full kinetic code to simulate lower hybrid wave and plasma interactions on EAST

13 July (Thursday)			
Session 9 (Category: Fostering of young scientists) PhD students & post-doctoral students Chair: XIAO Bingjia	08:00	ZHOU Chu (USTC)	Recent results of microwave reflectometer systems on EAST
	08:15	LEE Youngho (SNU)	Recent Progress on Hybrid Scenario in KSTAR
	08:30	HUANG Xianli (NIFS)	Analysis of impurity transport at different magnetic configurations in LHD based on impurity pellet injection and space-resolved EUV spectroscopy
	08:45	LIU Yang (Sokendai)	Determination of tungsten ion density in LHD using unresolved transition array at 27-34 Å
	09:00	ZHAO Zhenling (USTC)	Observation of MHD modes by ECEI at core and edge plasma in EAST
	09:15	BANDO Takahiro (SOKENDAI)	Characteristics of helically trapped energetic-ion-driven resistive interchange modes in deuterium plasma experiments of LHD
	09:30	KIM Minho (POSTECH)	Fast RF diagnostics in KSTAR ELMy H-mode plasma
	09:45	THATIPAMULA Shekar Goud (NFRI)	Edge Langmuir probes in KSTAR (tentative)
Coffee Break 10:00 - 10:20			
Session 10 (Category: Fostering of young scientists) PhD students & post-doctoral students Chair: TOI Kazuo	10:20	CAO Bin (NFRI)	The wall retention research by particle balance in KSTAR 2016 experiment
	10:35	SEGUINEAUD Guillaume (SOKENDAI)	Characterization of hydrogen-like pellet ablation clouds in the LHD
	10:50	PU Neng (SOKENDAI)	Initial results of triton burnup study by using neutron activation system in LHD
	11:05	KAWASE Hiroki (SOKENDAI)	Preliminary results of neutron emission profile measurements in LHD deuterium plasmas
	11:20	XIAO Jianyuan (USTC)	Explicit high-order noncanonical symplectic algorithms for ideal two-fluid systems
	11:35	LAN Ting (USTC)	Automatic data cleaning using machine learning technologies for magnetic confinement fusion
	11:50	S.Morita ((NIFS) Y.K.Oh (NFRI) L.Q.Hu (ASIPP)	Summary reports, closing and others (Proceedings with format, schedule after session etc.)
Lunch Break 12:20 - 14:00			

Session 11
Discussions on A3 program
Chair:
S.Morita
L.Q.Hu
Y.K.Oh
	14:00-17:00
	Discussions on future planning for collaborations including
	  - Education of young scientists
	  - Summary report of A3 collaboration
	  - New toroidal devices
	
	Budgetary and administrative works are informed by Prof. Shaohua DONG, Prof. Xiaodong ZHANG, Mr. Yoshio KAMIYA and Chihiro SAKO et al.

14 July
(Friday)

Session 12
Discussions on A3 collaboration
Chair:
S.Morita
L.Q.Hu
Y.K.Oh
	09:00-12:00
	
	Summaries of scientific activities of A3 Foresight Program on Critical Physics Issues Specific to Steady State Sustainment of High-Performance Plasmas are discussed at each category.
	
	Category I: Steady state sustainment of magnetic configurations
	        (Current drive and profile control)
	
	Category II: Edge and divertor plasma control
	   Category IIa: Transport of edge and divertor plasmas
	   Category IIb: Stability of edge plasma
	
	Category III: Confinement of alpha particles
	        (Interaction of energetic particle and bulk plasma)
	
	Category IV: Theory and simulation
	
	13:30-17:00
	
	- Individual discussion on personnel exchange
	- Individual discussion on hardware construction and operation of diagnostics and heating devices
	- Individual discussion on device operation and machine time
	
	- Scientific discussions on future collaborative studies
	- Discussions with PHD students, post-doctoral researchers and young scientists
	- Discussions on post-A3 program

(END)

Participants of the 11th A3 Workshop at Sapporo
July. 11-14, 2017, Sapporo ,Japan

No	Affiliation	& Name		M/F	e-mail
1	NFRI	오영국	OH Yeong-Kook	M	ykoh@nfri.re.kr
2	NFRI	전영무	JEON YoungMu	M	ymjeon@nfri.re.kr
3	NFRI	김재현	KIM Jayhyun	M	jayhyunkin@nfri.re.kr
4	NFRI	홍석호	HONG Suk-Ho	M	sukhhong@nfri.re.kr
5	NFRI	박준교	BAK Jun-Gyo	M	jgbak@nfri.re.kr
6	NFRI	방은남	BANG Eun-nam	F	bang14@nfri.re.kr
7	NFRI	셰카르고우드	THATIPAMULA Shekar Goud	M	shekaruh@nfri.re.kr
8	NFRI	배천호	BAE Cheonho	M	cbae@nfri.re.kr
9	NFRI	오승태	OH Seung Tae	M	stoh@nfri.re.kr
10	NFRI	샤오빈	CAO Bin	M	caobin@nfri.re.kr
11	NFRI	김정희	KIM Junghee	M	kimju@nfri.re.kr
12	POSTECH	윤건수	YUN Gunsu	M	gunsu@postech.ac.kr
13	UNIST	남윤범	NAM Yoonbum	M	yoonbumnam@unist.ac.kr
14	SNU	이영호	LEE Youngho	M	orzl56491@snu.ac.kr
15	POSTECH	김민호	KIM Minho	M	kmh415@postech.ac.kr
16	NIFS	森田 繁	MORITA Shigeru	M	morita@nifs.ac.jp
17	NIFS	大石 鉄太郎	OISHI Tetsutaro	M	oishi@nifs.ac.jp
18	NIFS	劉 洋	LIU Yang	M	liu.yang@nifs.ac.jp
19	NIFS	黄 賢礼	HUANG Xianli	M	huang.xianli@nifs.ac.jp
20	NIFS	芦川 直子	ASHIKAWA Naoko	F	ashikawa@nifs.ac.jp
21	NIFS	加藤 太治	KATO Daiji	M	dkato@nifs.ac.jp
22	NIFS	大舘 暁	OHDACHI Satoshi	M	ohdachi@nifs.ac.jp
23	NIFS	坂東 隆宏	BANDO Takahiro	M	bando.takahiro@nifs.ac.jp
24	NIFS	東井 和夫	TOI Kazuo	M	toi@toki-fs.jp
25	NIFS	磯部 光孝	ISOBE Mitsutaka	M	isobe@nifs.ac.jp
26	NIFS	普 能	PU Neng	M	pu.neng@nifs.ac.jp
27	NIFS	河瀬 広樹	KAWASE Hiroki	M	kawase.hiroki@nifs.ac.jp
28	NIFS	セギノ ギョーム	SEGUINEAUD Guillaume	M	guillaume.seguineaud@nifs.ac.jp
29	NIFS	王 灝	WANG Hao	M	wang.hao@nifs.ac.jp
30	NIFS	岸本 泰明	KISHIMOTO Yasuaki	M	kishimoto@energy.kyoto-u.ac.jp
31	NIFS	竹入 康彦	TAKEIRI Yasuhiko	M	takeiri@nifs.ac.jp
32	NIFS	迫 千尋	SAKO Chihiro	M	sako.chihiro@nifs.ac.jp
33	NIFS	伊藤 美貴子	ITO Mikiko	F	ito.mikiko@nifs.ac.jp
34	ASIPP	万宝年	WAN Baonian	M	bnwan@ipp.ac.cn

35	ASIPP	胡立群	HU Liqun	M	lqhu@ipp.ac.cn
36	ASIPP	项农	XIANG Nong	M	xiangn@ipp.ac.cn
37	ASIPP	肖炳甲	XIAO Bingjia	M	bjxiao@ipp.ac.cn
38	ASIPP	吕波	LYU Bo	M	blu@ipp.ac.cn
39	ASIPP	刘海庆	LIU Haiqingu	M	hqliu@ipp.ac.cn
40	ASIPP	董少华	DONG Shaohua	F	shdong@ipp.ac.cn
41	ASIPP	李建刚	LI Jiangang	M	j_li@ipp.ac.cn
42	ASIPP	张晓东	ZHANG Xiaodong	M	xdzhang@ipp.ac.cn
43	ASIPP	丁伯江	DING Bojiang	M	bjding@ipp.ac.cn
44	ASIPP	陈俊凌	CHEN Junling	M	jlch@ipp.ac.cn
45	ASIPP	郭后扬	GUO Houyang	M	hyguo@ipp.ac.cn
46	Peking Univ.	樊铁栓	FAN Tieshuan	M	tsfan@pku.edu.cn
47	USTC	肖建元	XIAO Jianyuan	M	xiaojy@mail.ustc.edu.cn
48	USTC	兰婷	LAN Ting	F	lanting@ustc.edu.cn
49	USTC	余羿	YU Yi	M	yuyi@ustc.edu.cn
50	USTC	毛世峰	MAO Shifeng	M	sfmao@ustc.edu.cn
51	USTC	周楚	ZHOU Chu	M	zhouchu@ustc.edu.cn
52	USTC	赵朕领	ZHAO Zhenling	M	zzl1212@mail.ustc.edu.cn
53	USTC	蔡辉山	CAI Huishan	M	hscai@mail.ustc.edu.cn
54	DUST	王福琼	WANG Fuqiong	F	wangfq@dhu.edu.cn
55	SWIP	刘仪	LIU Yi	M	yiliu@swip.ac.cn
56	SWIP	高金明	GAO Jinming	M	gaojm@swip.ac.cn
57	SWIP	崔正英	CUI Zhengying	F	cuizy@swip.ac.cn
58	DUT	戴舒宇	DAI Shuyu	M	daishuyu@dlut.edu.cn